Habilitationsschrift

Quantum Information Processing and Nuclear Spins in Nanostructures

Géza Giedke

2013

Physik-Department, Technische Universtität München und
Max-Planck–Institut für Quantenoptik, Garching

Contents

1 Introduction

Quantum Information

Quantum information proves strikingly that information science is fundamentally a *physical* science: what information processing tasks can be achieved and how efficiently this can be done, can depend strongly on whether the systems used to encode and process information follow the laws of classical or quantum physics. [1]

The information theoretical perspective on quantum physics [182] has had profound impact: On the one hand, it has given fresh impetus and clarity to foundational questions [e.g., attempts to base quantum mechanics (QM) on information theoretic axioms [107, 170, 42]], led to a deeper understanding of the potential and limitations of QM (e.g., quantum error correction [229, 135], the intimate relation of quantum states and quantum operations [43, 124], the identification of small families of quantum states comprising (or approximating) most of the physically relevant states and giving rise to novel approaches to simulate quantum systems [255], the identification of generically hard problems in quantum physics using idea from computational complexity [164, 224, 225, 53]). It has also provided a unifying language that simplifies and encourages the exchange and interaction between a broad range of disciplines from mathematical physics and quantum foundations to quantum optics, condensed matter physics and computer science.

On the other hand, it has yielded results of short- and long-term practical interest, most prominently the potential computational speed-up in concrete problems such as factorization [230] (and a large number of others as listed in [127]) and especially in the efficient simulation of many-body quantum dynamics [165, 48], but it has also added practical interest to many of the quirks and apparent paradoxes of QM, turning them into tools and the basis of information processing protocols. In this way, e.g., the no cloning theorem [271, 68] and Bell inequalities [77, 3] led to quantum key distribution [98], entanglement [115] gave rise to quantum teleportation [14], "Schrödinger-cat-like" states spurred advances in quantum-enhanced metrology [95, 97] [2].

This has inspired a worldwide sustained endeavor to realize quantum mechanical information processing, i.e., to identify and build physical systems that allow for both the control and the isolation from all unwanted couplings that are needed for a quantum computer (QC) [287, 249]. Recent major advances regarding the threshold for quantum error correction [139, 203, 259] and the possibility of QC in dissipative systems [256] provide further encouragement that this goal can be achieved.

[1] While it is still an open question, whether quantum computers are more efficient than classical ones ($P \stackrel{?}{=} BQP$ in terms of the two complexity classes – a serious challenge to the extended Church-Turing Thesis [1]) there are tasks in cryptography and communication where a strict gap between classical and quantum systems has been proved [204, 98, e.g.].

[2] See however [117, 82] for their limitation in the presence of noise.

Semiconductor quantum dots (QDs), which are considered in the main part of the Thesis, are one of the major approaches [166] to this goal. We only mention in passing the many other implementations that are currently being pursued. QIP based on trapped ions [47], neutral atoms in lattices [123], or superconducting circuits [228] are particularly successful. Each approach has its merits and each has yielded not only to impressive control of individual quantum systems but also led to new insight into the physics of the respective platform.

QIP in Quantum Dots

This technology platform has several attractive features: It is a solid system which makes trapping or the use of vacuum chambers unnecessary. It is an artificial, hence *designable* system for which many parameters can be tuned at fabrication. And it can tap into the highly developed toolbox of semiconductor electronics and nano-fabrication technologies for integration with (classical) computing technology, photonics, and for eventual scaling up the quantum devices. Moreover, QDs can be accessed both optically and electronically, thus combining the most advanced techniques of quantum and classical information processing.

These advantages do not come without cost: artificial atoms embedded in bulk solid-state material are exposed to many hard-to-control degrees of freedom which can cause decoherence of the quantum registers used for QIP (phonons, fluctuating charges, impurity spins) and usually require cryogenic temperatures to be operational. Moreover, they can never be fabricated fully identically leading to errors due to fabrication imperfections and inhomogeneities.

Charge, polarization, and spin degrees of freedom were investigated as qubit candidates. The most promising and fruitful idea in the QD setting was Loss and DiVincenzo's proposal to use the spin of single electrons trapped in QDs [166]. It exploits the spins' good isolation from phonons, which was estimated to allow coherence times T_2 many orders of magnitude longer than those that can be achieved for the charge-based qubits and sufficient to perform a large number of gate operations.

The Loss-DiVincenzo proposal was quickly followed by several others for using the spins associated with localized "defects" in solids, in particular the spins of phosphorus donors in silicon [128], electron spins in (optically active) self-assembled semiconductor QDs [119], and the spin associated with the Nitrogen-Vacancy (NV) center in diamond [273].

While the spin was specifically selected to reduce decoherence due to charge noise and phonons, it was soon noticed that this choice makes the qubit susceptible to another important "environment", namely the nuclear spins of the atoms of the semiconductor lattice. In the technologically best controlled materials (GaAs, InGaAs) all nuclei carry a nuclear spin and possess a strong hyperfine interaction (HFI), leading to fast dephasing of electron-spin qubits (within a few nanoseconds in the first experiments).

This led to a intense and detailed theoretical and experimental investigation of the HFI in nanostructures with the aim of reducing or controlling the interaction of the spin qubit with its nuclear-spin environment, e.g., by preparing the nuclear spins in states that are (partially) decoupled from the qubit ("reservoir engineering") or by dynamical decoupling [284]. In fact, there are many ways in which the nuclear spin system can even be made *useful* for QIP, either as a means to perform gate operations or as a quantum memory. In addition to the QIP interest, the HFI in QDs realizes a *central*

spin system [90], one of the important standard models of quantum many-body physics. Experimental and theoretical evidence shows that the HF-coupled QD spin supports many intriguing dynamical effects, from bistability to superradiance and phase transitions and merits investigation regardless of QIP applications. The present Thesis contributes to the theoretical investigation of spin physics in QDs both from the QIP and from the quantum many-body point of view.

This Thesis

This Thesis reports on three related topics addressed by the author from 2005 to today: In Ch. 2 treats the interaction of solid-state spin qubits with a surrounding spin bath and the question how to facilitate quantum information processing (QIP) in this setting. This motivates, in particular, the analysis of dissipative dynamics which prepare an advantageous (polarized or narrowed) state of the nuclear-spin bath. These dynamics give rise to interesting physical phenomena and lead us in Ch. 3 to the more general topic of the steady-state properties of open quantum many-body systems, in particular phase transition-like behavior. Finally, in Ch. 4, some more formal questions on quantum information processing using Gaussian states and operations, i.e., with the toolbox of linear quantum optics, are addressed.

The three parts of the Thesis are related by the focus on quantum information processing (QIP) in concrete, experimentally accessible physical systems and by the use of methods and intuitions from quantum optics (linear optics, atomic ensembles, cavity-QED, quantum optical master equation) which turn out to be very useful in the solid-state system with which most of this Thesis is concerned, namely single localized electron spins in semiconductor quantum dots coupled to their naturally occurring nuclear spin environment. This system is the main motivation to study the the central spin system and its steady-state phase diagram in the second part. The methods of Gaussian QIP turn out to be useful in this context since in certain situations the nuclear spins are well described by collective excitations ("spin waves") that are in an (approximately) Gaussian state and undergo an effectively linear evolution.

In the next chapter, we provide some common background and perspective to the publications that form the core of this work and which are collected and reprinted in Chapter 7. Comprehensive and current reviews of the different subjects are included among the references, in particular [49, 253, 40] for Chapter 2, [178] for Chapter 3, and [261] for Chapter 4.

A note on the references. The articles which are part of this Thesis are cited as G:*nn* and listed in Section 5. All other references are in the bibliography at the end of this Thesis.

2 State Engineering and QIP with Nuclear Spins in Quantum Dots and other Nanostructures

2.1 Introduction

This is the first of the three main chapters in which the background and context of the work comprising this Thesis is briefly summarized. The actual work is contained in the publications reprinted in Chapter 7.

We first give a very short introduction to quantum dots (QDs) and then briefly describe the history and status of QIP with QD spins before focusing on the role of QD nuclear spins in this context. All these topics have been the subject of excellent reviews to which we refer the interested reader in the respective sections.

2.1.1 Quantum Dots

Quantum dots (QDs) are nanostructures which confine charge carriers (conduction-band electrons or valence-band holes) in all three dimensions to lengths small compared to the particle's wavelength so that its motion becomes fully quantized.

This confinement can be achieved in several ways, e.g., by device geometry (e.g. etching/growth of 0d or 1d structures), by externally applied electrostatic potentials, or by the composition of different materials, see, e.g., [102] for a detailed and current presentation of different QDs.

Prime example for the latter type of confinement are *self-assembled quantum dots* (SAQDs) which can be formed in the process of epitaxial growth due to the strain between two lattice-mismatched materials (e.g., InAs deposited on a GaAs substrate). Due to the mismatched lattice constants the above a certain thickness the layer-by-layer deposition of InAs becomes unstable against the formation of InGaAs droplets. Depositing further GaAs on top yields a layer of InGaAs droplets enclosed in GaAs, cf. Fig. 2.1.1(B). Due to the differences in band gap between the two materials, both conduction-band electrons and valence-band holes can be trapped within the InGaAs droplets. Size, location and composition of the droplets can be partially controlled by growth conditions and pre-patterning of the surface on which the InGaAs is grown, but are still to some extent random. Typical dimensions of such SAQDs are $5 - 10$ nm in height and $10 - 30$ nm in diameter, comprising $10^4 - 10^5$ atoms and providing for a rather strong confinement of a few 10 meV [236], which allows to work at 4 K temperatures. [1]

A major advantage of SAQDs is that they are optically active since both electrons and holes and therefore also optical excitations (excitons) which are formed by promoting a valence band electron

[1] Closely related are so-called *interface-fluctuation quantum dots* (IFQDs) which are formed by monolayer fluctuations of the thickness of, e.g., a few atomic layers of GaAs embedded between AlGaAs substrates. If these fluctuations have suitable extent in plane, they can provide trapping potentials for electrons and holes, studied, e.g. in [23, 167].

to the conduction band are trapped by the QD. As a consequence, both neutral and charged SAQDs feature strong dipole transitions to the corresponding excitonic states. In recent years, clean QDs with lifetime-limited linewidths (and lifetimes on the order of 1 ns) are studied in many labs and provide fast and versatile access and control to the QD states and properties. It should be noted that SAQDs can additionally be contacted by gate electrodes, thus enabling both electronic and optical access and control. Among the disadvantages of SAQDs is the essentially random growth process which makes it difficult to control location, size, and composition of the QD although there is progress in all these respects. The very strong confinement has also made it more difficult to let electrons in different QDs interact with each other.

In *electrostatically defined quantum dots* (EDQDs; sometimes also called *lateral* QDs), carriers are confined to the interface between two semiconductor materials (e.g., GaAs on AlGaAs) with very nearly matched lattice constants (hence little strain) but different bad gap, cf. Fig. 2.1.1(A). Incorporating a doped layer close to the interface in the high-bandgap material (AlGaAs) ("modulation doping") leads to the accumulation of carriers at the interface in the low-bandgap material and the formation of a two-dimensional electron gas (2DEG) in the trapping potential provided by the positive donors in AlGaAs and the electrons in GaAs, see, e.g., [106, 102] and references therein.
Now metal electrodes ("gates") can be lithographically fabricated above the 2DEG. By applying voltages to the gates, the 2DEG can be depleted below the electrodes and with a suitable arrangement of electrodes (cf. Fig. 2.1.1A) a trapping potential for carriers can be realized. In contrast to SAQDs, only one type of carrier is trapped in EDQDs and therefore, excitons are not bound and EDQDs are not optically active. Also, the confinement is typically weaker than for SAQDs (a few meV) and experiments have to be done at very low temperatures (100 mK). The advantages of this system include the cleaner structure (due to the absence of strain), the deterministic fabrication which allows the construction of elaborate multi-dot geometries ("quantum dot molecules", cf., e.g., [232] for a four-QD chain allowing the realization of two logical qubits) and the built-in electronic access to the QDs.

Charge state – The number of electrons in a QDs can nowadays be very well controlled by doping and applied gate voltages, so that QDs are routinely operated at well-defined constant occupation number [106]. To study transport through the QD one tunes the gate voltages to the boundary between two charge configurations so that electrons can be exchanged with the surrounding 2DEG by tunneling [147, 206].

Carrier wave function and other properties – The details of the QD potential and the properties of the carrier wave function in the QD – and especially their prediction from phenomenological or microscopic dot and growth parameters – are in general difficult and still a subject of active research. However, it is usually possible to determine most quantities of interest (binding energies, wave functions, coupling matrix elements, g factors, effective masses) from experiment. And for our purposes, a very simple toy-model of QD confinement (e.g., by a harmonic confinement potential or a box) usually suffices. We consider temperatures sufficiently low so that only the lowest orbital in the QD confinement potential are occupied.

Optical Properties – The optical properties of QDs are largely determined by the dipole transitions between conduction and valence band supported by the host semiconductor. For the III-V materials we consider, the conduction band (CB) is formed mostly from s-type orbitals thus close to the atomic nuclei the electron wave function has s character (spherical symmetry, no angular momentum, finite overlap with the nucleus). In contrast, the valence band (VB) is constructed from p-type orbitals. Its

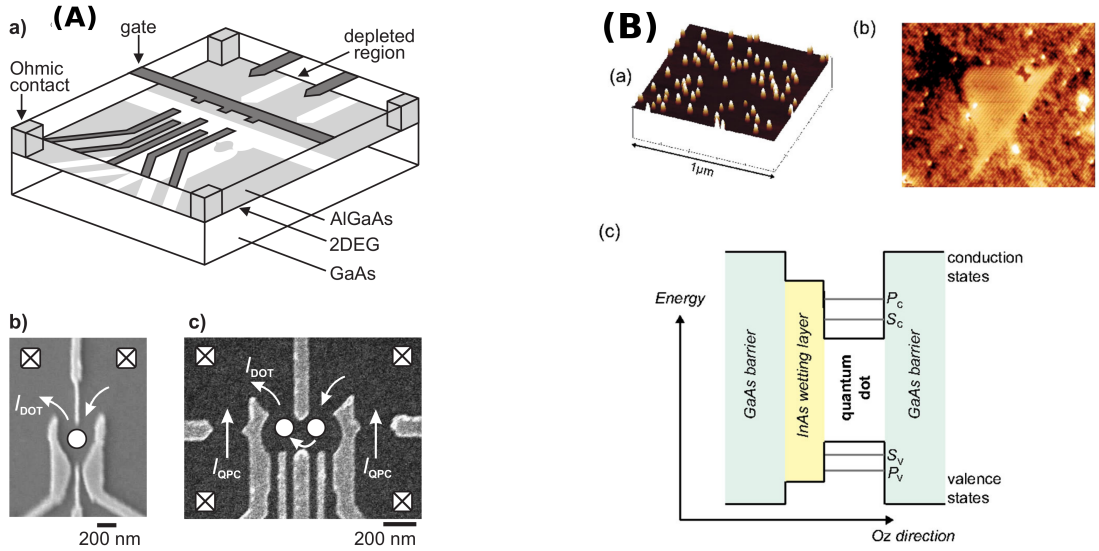

Fig. 2.1: Electrically defined (A) and self-assembled (B) quantum dots. The pictures are taken from the review articles by Hanson *et al.* [106] and Urbaszek *et al.* [253], respectively. (A) shows schematically the 2D heterostructure and the interface at which the 2DEG forms within which the QDs are defined by the metallic gates. The electron microscope picture of two EDQD structures (B) Shows a picture taken of a layer of InAs SAQDs and sketches the band structure of the QD and surrounding heterostructure (cut in growth direction through a QD). Bound QD states in both the conduction and valence band are indicated.

six-fold degeneracy is lifted by spin-orbit coupling and further by growth-induced strain (cf. [102]) and the highest-lying valence sub-band is formed by the ($J = 3/2, J_z = \pm 3/2$) heavy hole states (J_z defined along the growth direction).
From these consideration the properties of the QD spin qubits become clear: a CB electron trapped in the ground state of a QD is a spin-1/2 particle, and hence a clean qubit. The optical properties of a neutral or charged SAQD are determined by the dipole matrix elements which couple its ground state to the optically excited state containing one exciton, i.e., a bound state of a CB electron and a VB hole. The lowest-energy, most stable exciton consists of a VB heavy hole and a CB electron, each in the lowest QD orbital state. In the neutral QD, the "exciton ground state subspace" is four-dimensional; due to spin selection rules, there are two optically active and two inactive states ("bright" and "dark" excitons). The former characterized are by electron and heavy hole with antiparallel oriented spins, the latter by parallel spins of electron and hole. For the singly (negatively) charged QD, the charged exciton ("trion") is formed by a CB singlet and a VB hole, hence there are only two such states, both dipole-coupled to the singly-charged QD ground state.

These considerations lead to a simple level scheme for the QD [cf. Figs. 2.2 and 2.3 for SAQDs]; these sketches illustrate the dipole-allowed transitions from the ground state(s). The obvious ways to optically manipulate the electron spin in a SAQD are evident: the level scheme allows for spin-pumping to any of the two ground states, for spin-flip Raman transitions between the two and for spin-dependent AC Stark shifts, which can be used for phase gates or for QND spin measurement. For comprehensive review, see [102].

Quantum Dot Molecules – QDs are frequently called "artificial atoms" due to the atom-like properties

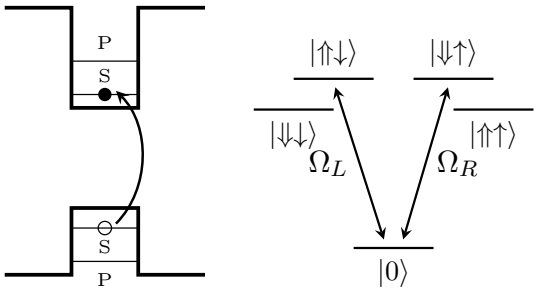

Fig. 2.2: Neutral exciton in self-assembled QD: a valence band electron is promoted to the conduction band (filled circle), leaving a valence band hole.

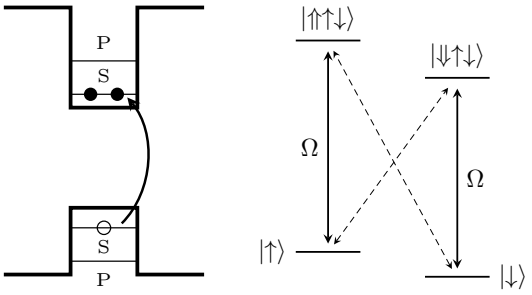

Fig. 2.3: Level structure of the singly charged QD (single-electron ground states and excited (trion) states); configuration for optical pumping is depicted. Dipole-allowed and (weakly) forbidden transitions are indicated by solid (dashed) arrows.

described above. Also like atoms, multiple QDs can also form "molecules", if they are close enough to interact. The best studied QD molecule is the double quantum dot (DQD), depicted in Fig. 2.1.1A, which has been the work horse for many of the pioneering QIP experiments with QDs [106]. It is formed by two EDQDs, which are coupled to each other by coherent tunneling and operated in the (1,1) charging region (i.e., with a single electron on each dot). The tunnel coupling gives rise to an exchange interaction which lifts the degeneracy in the four-dimensional (1,1) subspace by splitting the singlet from the three triplet states, cf. Fig. 2.4B. The exchange coupling can be used to implement quantum gates in this system [36]. Of particular interest for QIP work (and parts of this Thesis) is the *Pauli blockade regime* in which the DQD is tuned to the (1,1) charging region and the two QDs are biased such that transport occurs via the cycle $(1,1) \rightarrow (0,2) \rightarrow (0,1) \rightarrow (1,1)$, while states $(2,0)$ and $(1,0)$ are not accessible. Since the transition from $(1,1)$ to $(0,2)$ proceeds via the tunneling Hamiltonian which leaves the electrons' spin unchanged, only the $(1,1)$-singlet state S(1,1) can contribute to transport. Coupling to the $(0,2)$-triplet states is suppressed since they involve (due to the Pauli principle) the first orbital excited state of the right dot, with much higher energy.

Other Nanostructures – There are a number of nanostructures not mentioned in the brief sketch above that are of similar interest for QIP. One of the most promising such systems are nitrogen

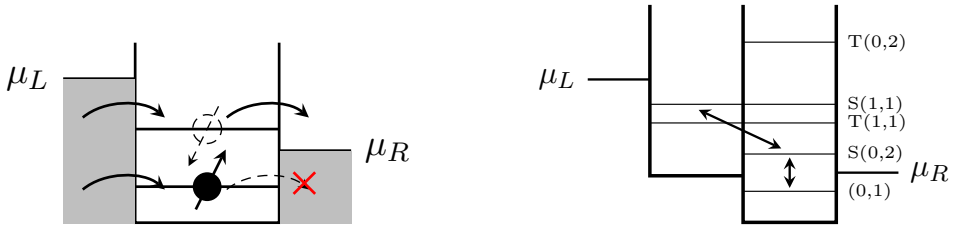

Fig. 2.4: (Left) Single-electron quantum dot in a magnetic field in the spin-blockade setting: both Zeeman levels can be filled from the right, electrons in the lower Zeeman state cannot escape to the right. (B) Ground state level scheme of a biased two-electron double quantum dot (DQD) in the Pauli blockade regime (cf. text). The eigenstates $X(n,m)$ are labeled by the number of electrons in the two dots and their singlet/triplet character.

vacancy centers in diamond [71]. These are point defects consisting of substitutional nitrogen atom next to a vacancy (missing carbon atom). These defects occur naturally or can be produced by ion implantation and annealing (allowing vacancies to wander until they find a N to for an NV center with). NV centers are very stable, have strong optical zero-phonon line and a spin triplet ground state with a characteristic zero-field splitting (2.88 GHz). The electrons are very tightly bound to the center (it's deep in diamond's huge band gap) and the spin ground states have a long coherence time of up to 1 ms [11] and can be manipulated with microwave fields. They can, moreover, be distinguished optically by their different fluorescence properties and optical pumping allows to initialize the NV center one of the spin states.

Other solid-state systems that are closely related to the QDs we mostly are concerned with and are currently investigated for QIP are phosphorus donors in silicon (Si:P), first proposed in [128], and quantum dots in carbon based systems such as graphene [205] and carbon nanotubes [35, 45, 88].

2.1.2 QIP with Electron Spins in QDs

Electron spins in quantum dots were among the first systems proposed to implement qubits in a potentially scalable way to eventually build a quantum computer [166]. The original proposal was to use the two spin states of a single QD electron as a qubit and to use the tunnel coupling between neighboring QDs to implement two-qubit gates It was made even before single electrons in QDs had been prepared much less single spin detection or manipulation had been demonstrated.

Within a few years these milestones were achieved in a series of ground-breaking experiments demonstrating single-shot readout of a single spin [78, 215] and single- and two-qubit gates [193, 141] in EDQDs and a little later also in SAQDs (high-fidelity state preparation [8, 274]; single-spin detection [176, 9], and single-qubit gates [199, 15, 262], two-qubit gates [132]).

There has been considerable progress towards building a light-matter quantum interface, essential for quantum communication between two quantum registers and a attractive route to long-range coupling of qubits within one processor. Milestone results were the demonstration of strong coupling of QDs to high-Q cavities [207, 280, 109, 158] and entanglement between QD spins and photons [89, 59, 219].

The interaction with the nuclear spin environment severely limited the observed coherence time and gate fidelities in the early experiments, see [142, 126]. Since then, advances in qubit design, nuclear spin preparation, and the use of dynamical decoupling techniques have lead to significantly improved (faster, cleaner) QD spin qubits with the coherence time of a DQD electron spin qubit now approaching 200 µs [18, 19], four orders of magnitude longer than typical gate operations times (∼10 ns). Thus the "problem" of nuclear spins is considered as "practically solved" [10] as other sources of decoherence (in particular gate noise) become the limiting factor while the useful aspects of the nuclear spins come into focus.

Greatly improved two-qubit gates in EDQDs were demonstrated recently [184, 34] and for the first time, all standard building blocks for a QC (single- and two-qubit gates, state preparation and measurement) have been achieved in a single system [232]. The fidelities achieved to date are still moderate ($F = 0.72$ for Bell state generation in [232] or readout fidelity of ~ 0.86 in [184]) and

significant technological improvements are needed to approach the regime required for fault-tolerant operation.

Other Nanostructures While the above summary has focused on spin qubits in (In)GaAs QDs, progress in some of the closely related solid-state systems already mentioned has also been great. Since many of the ideas and concepts presented here can be equally well (or better) applied to other atom-like nanostructures in solids such as NV centers [273, 71] or P donors in silicon (Si:P) [128, 197], and since some of the works to be presented later explicitly refer to them, a few words about NV center qubits and Si:P qubits may be in order.

These systems combine some of the advantages of QDs (the solid state material, potential for tight integration with electronics and photonics, and availability of nanofabrication technology) with those of atomic qubits (essentially identical, atomic-sized systems) and QIP in these systems has made great strides in recent years. The diamond-based approach is most notable for the possibility of operating a quantum device even at room temperature. In the NV center spin-triplet ground state (cf. p. 8) two levels can be designated as qubit and fast and accurate preparation and readout have been demonstrated. The electronic spin couples to proximal nuclear spins (^{13}C or ^{15}N). These spins can be accessed by NMR techniques and together with the hyperfine coupling this has allowed high-fidelity preparation of the nuclear spins and the creation of multi-particle entangled states [180]. The entanglement of two NV centers has been demonstrated very recently [72]. For a comprehensive review, see [71].

Si, on the other hand, is the favorite material of semiconductor technology, sporting very mature and advanced fabrication methods and the availability of very clean, isotopically pure samples (e.g., as used in recent projects to redefine the mass standard [5]). In [242] coherence times of 3 min were shown for the a nuclear spin qubit of a P donor. Coupling between different P qubits has not been achieved until now.
The technological advantages of Si have also motivated the work on QIP using lateral Si/SiGe quantum dots [233, 264, 172]. Detailed calculations of spin decoherence [61, 268, 267, 266] and already the first experiments have confirmed the expectation of good coherence properties and demonstrated T_2^* ∼360 ns [172] (more than a factor of 10 better than in the comparable first GaAs-QD experiments).

As described in the previous sections, nuclear spins are almost ubiquitous in solid-state structures considered for QIP. We have a closer look at their interaction with QD spin-qubits in the next section.

2.1.3 Nuclear Spins in QDs

Nuclear spins are among the most common and advanced qubits both in atomic and solid-state systems. In solids, two different situations can occur: in some systems, single nuclear spins located close to defects such as donor-bound electrons [128] or NV centers [273] are promising qubits – combining the strong experimental control (via the electron of the nearby defect) with a nuclear spin's good coherence properties. A coherence time of 180 s has been demonstrated at cryogenic temperatures (∼2 K) in ultrapure ^{28}Si [242] and in excess of 1 s at room temperature in diamond [173].
In contrast, in many cases the electron spins does not couple to just a few but to a large number of

nuclear spins. Then their most notable effect is that of a spin-bath that dephases and decoheres the electron spin. This effect is particularly strong in GaAs QDs [142, 126] with their 100% concentration of nuclei with spin and large magnetic moments, but in weaker form also present in Si:P and diamond systems [105, 252].

In QDs, the investigation of nuclear spin effects has focused the second role. Here, the electron is delocalized over thousands to millions of nuclei which are typically in an almost maximally mixed state even at the low temperatures and large magnetic fields available in experiments. The interaction with this environment dominates dephasing and decoherence of the electron spin qubit. The accurate theoretical description of decoherence due to interaction with this non-Markovian many-spin environment is a challenging task and many approaches have been suggested (see, e.g., [49] and also Section 2.1.3) differing in the regimes considered and in the extent to which correlations and interactions among the nuclear spins are taken into account.

Since the hyperfine interaction is central to this Thesis we sketch here its microscopic derivation as given, e.g. in [2, 237] or recently with a focus on quantum dots and QIP in [84].

Hyperfine interaction

Starting with the Dirac equation for an electron in the potential of the nucleus and taking into account only the lowest-order relativistic corrections, yields, in addition to the Zeeman term four terms containing the electron spin. In addition to the spin-orbit interaction of the electron these comprise three terms describing interactions between electron and nuclear spin, namely

$$H_{\mathrm{fc}} = \frac{\mu_0}{4\pi}\frac{8\pi}{3}\delta(\mathbf{r})2g_n\mu_n\mu_B\mathbf{S}\cdot\mathbf{I}, \tag{2.1}$$

$$H_{\mathrm{dip}} = \frac{\mu_0}{4\pi}2g_n\mu_n\mu_B\frac{3(\mathbf{n}\cdot\mathbf{S})(\mathbf{n}\cdot\mathbf{I})-\mathbf{S}\cdot\mathbf{I}}{r^3}, \tag{2.2}$$

$$H_{\mathrm{ang}} = \frac{\mu_0}{4\pi}2g_n\mu_n\mu_B\frac{\mathbf{L}\cdot\mathbf{I}}{r^3}, \tag{2.3}$$

where μ_0 is the vacuum permeability, μ_B the Bohr magneton, and $g_n\mu_n$ the nuclear gyromagnetic ratio with nuclear g-factor g_n and nuclear magneton μ_n; $\mathbf{r}$ is the vector pointing from the nucleus to the electron, $r = |\mathbf{r}|, \mathbf{n} = \mathbf{r}/r$, and $\mathbf{S}, \mathbf{L}$, and $\mathbf{I}$ denote the electron spin, electron angular momentum and nuclear spin operators, respectively.

In a QD, the electron's wave function is delocalized over $10^4 - 10^7$ lattice nuclei and it interacts with all their spins

$$H_{\mathrm{hfi}} = \sum_j H_{\mathrm{fc}}(\mathbf{r}_j, \mathbf{I}_j) + H_{\mathrm{dip}}(\mathbf{r}_j, \mathbf{I}_j) + H_{\mathrm{ang}}(\mathbf{r}_j, \mathbf{I}_j). \tag{2.4}$$

In the cases of interest in this Thesis, the hyperfine interaction (HFI) is weak compared to the level splitting between the electron's motional eigenstates of the confinement Hamiltonian provided by quantum dot potential (the "orbital part" of the Hamiltonian). Hence H_{hfi} can be treated as a perturbation of the electron's Hamiltonian and the leading term is given by the projection of H_{hfi} to the subspace of the ground-state electron, which is a pure spin Hamiltonian into which the electron's

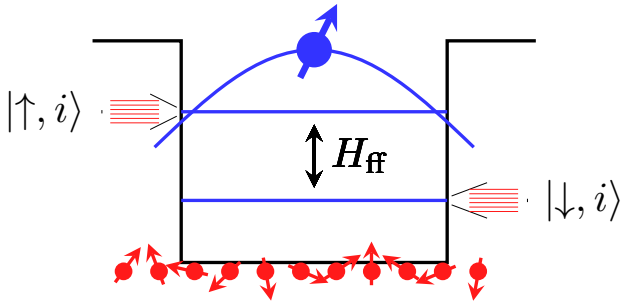

Fig. 2.5: A single-electron in the orbital ground state of a QD, delocalized over many lattice atoms carrying nuclear spins (unpolarized). The Zeeman split electron states split in many hyperfine levels due to the Overhauser term AS^zA^Z; $H_{\rm ff}$ couples the two manifolds.

wavefunction enters only parametrically by determining (a) the relative size of the three terms in Eq. (2.4) and (b) the effective interaction strength with the jth nucleus.

For conduction band electrons in III-V materials such as (In)GaAs, which have mainly s character (the conduction band is largely formed by s electrons) their hyperfine interaction is mainly given by the contact term (since s wave functions have a finite overlap with the atomic nucleus) while the dipolar and angular momentum terms are much smaller (due to symmetry and zero angular momentum) and are neglected in the following. This yields the dominant (Fermi contact) hyperfine Hamiltonian which is central to most of the investigations in the first two parts of this Thesis:

$$H_{\rm hf} = \mathbf{S} \cdot \sum_{j=1}^{N} \alpha_j \mathbf{I}_j \equiv A\mathbf{S} \cdot \mathbf{A}. \tag{2.5}$$

Here we have introduced the hyperfine coupling constant A and the collective nuclear spin operator $\mathbf{A} = \sum_j \alpha_j \mathbf{I}_j$ with normalization such that $\sum_{j=1}^{N} \alpha_j = 1$. [2]

Typically, we are interested in a situation with additionally applied external magnetic field $\mathbf{B}_{\rm ext} = B_{\rm ext}\mathbf{z}$ in z direction and associated electronic and nuclear Zeeman terms. Then, there are two distinct parts to $H_{\rm hf}$: the *Overhauser term* $\propto S^zA^z$, an additional, effective magnetic field in z direction provided by the nuclei ("Overhauser field") and the flip-flop term $\propto (S^+A^- + S^-A^+)$ describing the exchange of spin quanta between the electron and the nuclei.
We often distinguish the *detuned regime* in which $H_{\rm ff}$ is detuned $g^*\mu_B B_{\rm ext} \gg A/\sqrt{N}$ and the *resonant regime* in which the two energies are comparable (and the exchange of spin excitations between electron and nuclei is efficient).

Let us add here a remark on the applicable energy scales in discussing the hyperfine dynamics in QDs.

[2] With this normalization, A corresponds to the interaction energy of the electron spin with a fully polarized nuclear spin system. For a typical state, the value is a factor $\sim 1/\sqrt{N}$ smaller (reflecting the typical size of the matrix elements of the operators A^r). The number N of coupled nuclei is defined using some cutoff, neglecting very weakly coupled nuclei. Typical values for N vary from 10^4 in small SAQDs to several 10^6 in large EDQDs.

confinement energy	$10 - 100$ meV	
orbital energy differences	$1 - 10$ meV	
Zeeman energies	25 μeV/T	
hyperfine interaction	$A \sim$90 μeV	GaAs, fully polarized
	$A \sim$150 μeV	InAs, fully polarized
	$A/\sqrt{N} \sim 0.1 - 1$ μeV	random state, dot size $N = 10^4 - 10^6$
	$\sim A/N \sim 0.01 - 10$ neV	single nucleus i/a with electron ("Knight field")
nuclear Zeeman energy	4 neV/T	
quadrupole interaction	$\lesssim$10 neV	strain induced shifts, cf., e.g., [168]
nuclear dipole interaction	8 peV	for GaAs, [220]

Table 2.1: interaction energy scales in a quantum dot

Note that $A \sim$100 μeV gives the maximum interaction strength for fully polarized nuclei. It is often expressed in terms of the equivalent effective magnetic field strength $A/(g^*\mu_B)$, which can amount to several Tesla in fully polarized GaAs QDs. But the fraction of states showing such a strong interaction is small, and for a randomly chosen nuclear state (or, in case of a highly polarized system, when considering H_{ff} only), the effective strength of the hyperfine interaction is reduced by a factor $\sim \sqrt{N}$ to typical values of $0.1 - 1$ μeV depending on the size of the QD.

This yields a hierarchy of time scales which is useful in the analysis of the system: The electronic dynamics (both orbital and Zeeman) is much faster than the HFI which is again much faster than the nuclear Zeeman and dipolar dynamics. Moreover, HFI affects the electron much faster than it changes a single nuclear spin (ratio between $1/N$ and $1/\sqrt{N}$). These relations will

Note however, that for large nuclear polarization the HFI energy (Overhauser shift) is comparable to typical Zeeman energies and can have decisive influence on the electronic dynamics which becomes important, e.g., in the context of dynamical polarization of the nuclear spins (cf. Section 2.2.1, p. 17).

Electron Spin Decoherence Due to Nuclei

The most notable effect of the hyperfine interaction is a fast dephasing of the electron spin qubit (on a time scale of nanoseconds) in the random field of the (unpolarized) nuclear spin ensemble and a slower decoherence of the electron spin due to fluctuation of the nuclear field on a time scale set by the direct and mediated nuclear-nuclear interaction.

This interaction and its decohering effect on the electron spin has been studied in great detail and with increasing sophistication of the analytical and numerical methods.

The main effects can already be seen in a semiclassical treatment in which the electron precesses in a magnetic field including the quasistatic contribution of the Overhauser field which, in turn, precesses (much more slowly) in the average field of the electron spin (Knight field) [36, 81, 175]. This approach is supported by [41], which argues that as long as only (ensemble averaged) electronic properties are of interest a semiclassical treatment (classical approximation for the nuclear spins) is adequate.

In a finite magnetic field (the case of detuned flip-flops), two central time scales were identified [130, 131, 220]: the (hyperfine-induced) electron decoherence time $T_{2,hf} \sim \hbar N/A$ which arises from fluctuations of the nuclear spins (and thus the Overhauser field) due to the inhomogeneity of the coupling constants α_j. This can be in the range of $1 - 10$ µs for GaAs QDs. Much faster is the *ensemble dephasing time* $T^*_{2,hf} \sim \hbar A/\sqrt{N}$: it is given by the typical standard deviation of the Overhauser field and leads to a dephasing of the electron spin within 10 ns (which can be avoided with spin-echo techniques).

More involved quantum mechanical (perturbative) treatments analyze the highly non-Markovian character of the interaction [51], predicting power-law decay of coherences and collapses and revivals. The relaxation and dephasing of a DQD singlet-triplet qubit by the nuclear spin bath was analyzed in [52, 248]. For a "narrowed" nuclear spin bath (prepared in an A^z eigenstate) in a strong magnetic field, the coherence time of the electron spin qubit is prolonged and the decay becomes Markovian (exponential) [50].

Systematic expansions allowing to include intrinsic and mediated interaction between the nuclei and taking into account n orders of the interaction were developed [269, 278, 282, 12]. These approaches were used to evaluate the decoherence after dephasing was removed using spin-echo pulses and predict decoherence times no longer than 10 µs in GaAs unless more sophisticated dynamical decoupling techniques [227, 163, 284] are employed or by sufficiently strong polarization [283] achieved.

Analytical methods have been successfully employed to study the dynamics of the central spin system for specific initial conditions of the system such as the fully polarized spin-bath with flipped central spin [220]. The central spin system is *integrable* (even in the inhomogeneous case) and can be solved by a Bethe ansatz [90]. For small N, this solution has been used to analyze the dynamics of the system [22, 21], providing estimates for decoherence time as well as characteristic times of non-Markovian features such as the amplitude and dominant frequency components of the damped oscillations of the central spin.

We conclude this section by mentioning two very simple but useful approximations to the electron-nuclear dynamics, that give a simple intuitive picture and allow rough estimates for the electron-nuclear dynamics that often already contain the main qualitative features.

Homogeneous Coupling – It is often a good first approximation (especially for large QDs) to take the coupling constants $\alpha_j = 1/N$. In that case, the collective nuclear operators $A^{\pm,z}$ (multiplied by N) satisfy standard angular momentum commutation relations and the Hilbert space of the nuclear spins ($\mathcal{H} = \mathbb{C}^{2^n}$ for the case of spin-1/2 nuclei) decomposes into invariant subspaces $\mathcal{H} = \oplus_{J,\beta}\mathcal{H}_{J,\beta}$ labeled by the total angular momentum J and a set of permutation quantum numbers β [7]. Then $\dim\mathcal{H}_{J,\beta} = 2J + 1$ and it is spanned by the J^z-eigenvectors $|J, m, \beta\rangle, m = -J, \ldots, J$ (often referred to as *Dicke states*). Since HFI preserves these subspaces the dynamics can be discussed on each one separately.
Regarding decoherence of the electron spin, this can be readily obtained by letting the electron interact with a $|J, m, \beta\rangle$ and averaging over J, m, weighing each subspace with its (J-dependent) degeneracy [7].

Holstein-Primakoff approximation – A simple and useful theoretical method to analyze the dynamics of is *bosonization* of the spins by the Holstein-Primakoff (HP) transformation [114]. By this one refers to the following *exact* transformation expressing the spin operators $J^{\pm}, J^z$ of a spin-J system

in terms of bosonic creation and annihilation operators $b, b^\dagger$. Let us introduce it here although we will mainly use if It is straight forward to check that

$$J^- = \sqrt{2J - b^\dagger b}\, b \tag{2.6a}$$

$$J^+ = b^\dagger \sqrt{2J - b^\dagger b} \tag{2.6b}$$

$$J^z = -J + b^\dagger b \tag{2.6c}$$

hold on the subspace spanned by the first $2J + 1$ eigenstates of $b^\dagger b$ (and that this subspace is left invariant by the operators on the right hand side of Eqs. (2.6a)). The transformation becomes useful for highly polarized systems, i.e., if the square root can be expanded, leading to the HP approximation $J^- \approx \sqrt{2J} b + o(b^\dagger b/(2J))$. This description and variations thereof have been used in several of the results presented in this Thesis.

This picture [241] and its systematic extension to the inhomogeneous case [44], can be used to analyze the dephasing and decoherence of the electron spin for a (sufficiently) polarized spin bath and in an external magnetic field: the HP approximation then leads to a Jaynes-Cummings Hamiltonian for the hyperfine interaction. Depending on the applied field, it describes detuned or resonant Rabi oscillations of the electron spin. In the former case, the variance of the Overhauser term $b^\dagger b S^z$ leads to dephasing on a time scale $1/(A\sqrt{\mathrm{Var} t b^\dagger b})$. In the resonant case, there are Rabi oscillations induced by H_{ff} (with frequency $\sim A\sqrt{2J}$) which lead to decay and revivals of the electron spin. Unless the state is very narrow, they dephase under the influence of the Overhauser term [44]. Moreover, due the inhomogeneity there are correction terms to H_{JC} describing the coupling to other, independent bosonic modes, which eventually leads to decoherence and decay of the JC dynamics.

Three main remedies to decoherence by the nuclear spin bath have been pursued:

- *Dynamical Decoupling* – Spin-echo schemes [60] can remove the dephasing due to the (quasistatic) random mixture of effective Overhauser fields. But decoherence due to nuclear dynamics remains unless further efforts are taken, e.g., to dynamically decouple (some of the) nuclear spins from each other [284] or by suitable state preparation [283]. However, even without these more sophisticated techniques, nuclear spin dynamics is sufficiently slow [183, 138, 157] to allow for electron coherence times of 200 µs [19] (in principle) well above the 1% error-per gate rate required for fault tolerance [259].

- *State preparation through polarization or measurement* – Preparing the nuclear spins in an eigenstate of the Overhauser field operator A^z removes the main cause of dephasing (and also restores to some extent Markovian decay of the electron spin [50]). This has motivated numerous proposals for measuring A^z [33, 136, 243, 93].
  A second approach employs dissipative dynamics (typically, a suitable fast polarizing process applied to the electron) to drive the nuclear spins deterministically to a highly polarized state (with a large, sharp value of A^z), a process known as dynamical nuclear polarization (DNP). While for a purely thermal polarization procedure a noticeable reduction of ΔA^z requires very high polarizations (99% for a reduction by a factor 10) many DNP processes have a built-in resonance structure which leads to a narrow steady-state Overhauser field even at low polarizations, see Section 2.2.1.

- *New Materials* – As already mentioned, materials with low nuclear spin concentration have been proposed for QIP applications to avoid the decoherence by hyperfine interaction. Most notable and advanced among these are silicon-based systems such as P donors in Si [128] and SiGe quantum dots [233, 264] and those based on carbon such as NV centers in diamond [272] [3]. Very long coherence times have been demonstrated in these systems [242, 173]. Still, also these qubits are exposed to a spin-bath due to the non-zero fraction of spinful nuclei and spin-carrying defects, so that the methods to describe and cope with this environment are still applicable [60, 267].

This sets the stage for the work presented in this Thesis:

Preparing the State of the Nuclear Spins

Due to the weak interaction of the nuclear spins with external fields, direct thermal polarization is not practical to prepare them in a pure state. Even at B =10 T and T =100 mK the thermal polarization of GaAs nuclei would only be $P = p_+ - p_- = (e^{-\beta E_+} - e^{-\beta E_-})/(e^{-\beta E_+} + e^{-\beta E_-}) = 0.004$ with $E_\pm = \pm 40$ neV and β =0.1 /μeV. Instead, one uses the interaction with the electron (which itself can be controlled very well as demonstrated in the QIP experiments reviewed above) to change the nuclear state.

The standard approach is dynamical nuclear polarization (DNP), in which the electron spin is strongly polarized and HFI used to transfer this polarization (partially) to the nuclei, DNP has a long and successful history in bulk systems [188, 155, 174, 218] and afforded many insights in the spin dynamics in solids [189, 174]. The novel aspect in DNP in QDs [146] is that a single microscopic quantum system (two-level electron with fixed wave function) is used to polarize a mesoscopically small, well-isolated nuclear spin system. The small size enhances the coupling per nucleus, has allowed experimentalists to reach much higher polarization than in bulk, and the fixed wave function (and therefore fixed interaction strength which each nucleus) may make the quantum coherences between the nuclear spins relevant for the polarization process.

There are two main approaches to nuclear state preparation, either using *dissipation* (induced via HFI with the electron) to drive them to a well-defined stationary state (dynamical nuclear polarization (DNP)) or *measurement*, in which electronic and nuclear degrees of freedom are correlated by HFI and measurements of the electron, e.g., detection of an Overhauser shift of the Zeeman splitting, is used to extract information about the nuclear system. In Section 2.2 we present theoretical investigations into both approaches as well as one that combines both of them to reach the limit in which A^z is defined to a precision on the order of a single spin-flip. Let us mention results on nuclear spin preparation via transient unitary dynamics to prepare spin-squeezed states [214].

Using the QD Nuclear Spins for QIP

Nuclear spins can become useful for spin-qubit QIP in solid-state systems mainly as a high-quality quantum memory. Atomic qubits mostly use hyperfine levels to store quantum information, and with atom-like solid-state spin qubits (Si:P,NV centers) this direction has also been successfully pursued [173, 242]. The case of QDs is different, due to the large number of weakly coupled nuclear spins

[3] Other approaches such as QDs in carbon nanotubes (CNTs) [171, 88] or in graphene [205] are still in a very early stage of investigation and not further discussed here.

which makes initialization of the memory difficult and almost precludes individual addressing of the nuclei.

But similar to quantum memories (for light) proposed using spin-polarized atomic ensembles [148, 85], *collective* excitations of a highly polarized nuclear spin system might be used to store quantum information [247, 70, 153]. In Section 2.3 we present further applications in this vein.

2.2 Nuclear Spin State Engineering: Dynamical Polarization and Measurement

In this Section we present different approaches to the preparation of the nuclear spin ensemble in a desired state. We are interested in reaching states characterized by reduced standard deviation ΔA^z of the Overhauser field A^z compared to the maximally mixed state ($\Delta A^z|_{\mathbb{1}} \sim 1/\sqrt{N}$) and high polarization. The motivation is mainly, that reduced A^z-variance means longer electron T_2^* time and thus a better electron-spin qubit. In addition, the "internal" dynamics of the nuclear spin system (e.g., due to dipole-dipole interaction) is slowed down for highly polarized states, thereby increasing also the proper coherence time T_2 [266]. Moreover, preparation of a well-defined nuclear spin state is the starting point for using the nuclear spin system itself for QIP purposes, e.g., as a quantum memory [247] and may also open the door to interesting studies of the dipolar nuclear spin system to the detailed study of the nuclear spin system under the combined influence of the dipole-dipole and the electron-mediated interactions [210, 234]. Finally, as we shall see, the dynamics of the state-preparation process itself can be highly interesting, featuring bistability, cooperative effects, spin squeezing, and steady-state phase transitions. This will be further explored in the first part of the next Chapter (Section 3).

We consider first dynamical nuclear polarization (DNP) schemes, then measurement-based schemes and finally a combination of the two.

2.2.1 Dynamical Nuclear Polarization

In our theoretical treatment of the nuclear polarization process we consider strong optical or electronic driving of the electron and make use of the different timescales of electronic and hyperfine/nuclear dynamics (cf. Tab. 2.1, p. 13) to adiabatically eliminate the electronic degree of freedom and derive an effective quantum master equation for the nuclear spin system. This equation describes a situation in which the electronic subsystem quickly settles into a (quasi-)stationary state which then effectively drives a dissipative time evolution of the nuclear system.

Since the Overhauser field in GaAs QDs can be very strong, the separation of time scales is not complete and the change of dynamics of the nuclear system (in particular, the build-up of an Overhauser field) can significantly affect the electronic dynamics and thus its stationary state which then acts back on the nuclear dynamics. This feedback between electronic and nuclear system is responsible for the hysteretic and bistable dynamics observed in DNP.

Theoretically, cooling dynamics has mostly been considered using a semiclassical approximation in which the nuclear spin operators were replaced by mean values in the spin-temperature approximation [2, 174, 146, 63, 144, 212, 211, 58, 116, 213], in which coherences among the nuclear spins are neglected,

see however, [201, 100, 101] for a quantum treatment of DNP in a DQD and [25, 26] for the interplay of HFI and spin-orbit interaction.

This is appropriate if, as in bulk or quantum well systems, there is no fixed electron wave function and many motional states are involved, or if the nuclear dephasing rate is large. In quantum dots, however, the nuclei interact collectively with an electron in the motional ground state of the QD and the higher motional levels are far detuned. Therefore the coupling strength of each nucleus is fixed, and well-defined phase relationships between the nuclear spins can build up, necessitating a quantum treatment of the process. This was pointed out by Imamoğlu *et al.* [120], who showed that the cooling process can be inhibited by so-called dark states, which trap excitations and potentially result in serious constraints on the achievable polarizations. Inhomogeneities (either inherent in the system or introduced actively, e.g., by modulating the wave function of the electron) can mitigate this problem [120], but the ideas were tested numerically only in very small systems (10 nuclear spins).

Since the effect of inhomogeneities is expected to be reduced for larger systems [247], and thus limitations due to dark states may be more severe (in fully homogeneous systems, the achievable polarization would be negligible due to dark states) we developed in [G:5], reprinted on p. 49ff a full quantum model of DNP which was refined in later work [G:18, G:20] and is summarized in the following.

To exhibit most clearly the effects of collective coupling on the DNP dynamics, we consider the case of a singly-charged QD in which the electron is fully polarized, e.g., by ideal optical pumping or coupling to a fully polarized reservoir. The ensuing master equation for the reduced density matrix μ of the nuclear spins then describes an almost ideal polarization process

$$\dot{\mu} = c_r \left(A^- \mu A^+ - \{A^+ A^-, \mu\}_+ /2 \right) - i[\frac{g}{2} A^z + c_i A^+ A^- + g_n \mu_n B_{\text{ext}} I^z, \mu], \tag{2.7}$$

which besides the (first) spin pumping term only contains I^z-preserving Hamiltonian terms describing the nuclear Zeeman energy, the inhomogeneous Knight field of the electron ($\propto A^z$) and an electron-mediated interaction between the nuclear spins. The coefficients c_r, c_i are given by

$$c_r = \frac{g^2 \alpha}{4\Delta^2}, \tag{2.8}$$

$$c_i = \frac{g^2 \omega_0}{4\Delta^2}, \tag{2.9}$$

where Δ is the effective Zeeman splitting (including the instantaneous Overhauser field) between the two electronic spin states, $g = g_{\text{hf}} \sum_j \alpha_j^2$ the hyperfine coupling strength, ω_0 the bare Zeeman splitting, and α electron tunnel coupling to the leads. For details, see Fig. 2.6 and [G:20].

From this form of the master equation several conclusions can be drawn that were derived and explored more fully in [G:5, G:9, G:13, G:20]:

- Due to the collective nature of the spin pumping Lindblad operator A^-, there are many not fully polarized states $|D\rangle$ in the kernel of A^-. For these, DNP is significantly slowed down (or fully inhibited, if $|D\rangle$ is also eigenstate of the total Hamiltonian).
- This "blockade" is partially lifted by the inhomogeneous Knight field A^z in the Hamiltonian.

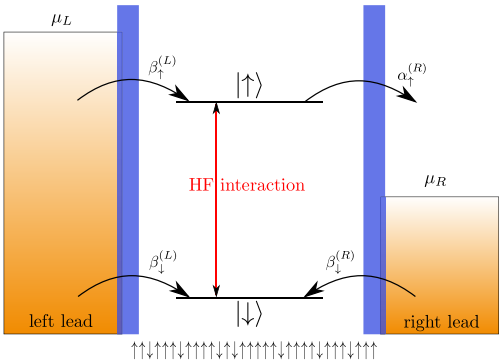

Fig. 2.6: Spin-blockade setting for DNP [G:20]. If electron tunneling described by the parameters α, β is fast, the electron reaches an $\downarrow$-polarized quasi-steady state and then polarizes the nuclei since spin-blockade can only be lifted by a hyperfine flip-flop.

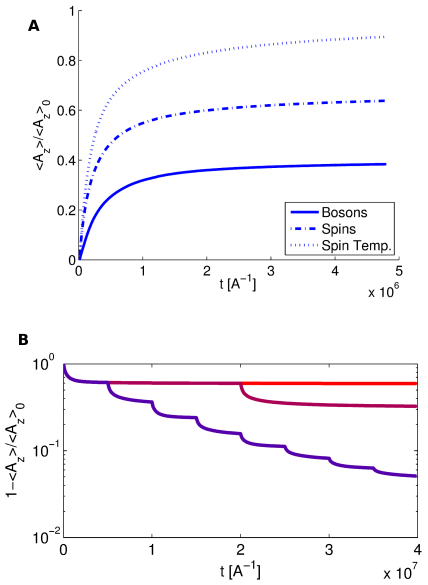

Fig. 2.7: Polarization dynamics: Time-evolution of Overhauser field in a generic DNP protocol [G:5]. (A) Note the reduced asymptotic polarization if nuclear coherences are taken into account (compared to the semiclassical model of a product nuclear state. (B) Changing the electron wave function can enhance the ultimate polarization by lifting dark-state coherences.

- For completely homogeneous coupling only a fraction $\leq 1/\sqrt{N}$ can be polarized.
- To reach very high polarization, it may be useful to change the quantum dot potential so that different electron wavefunctions (and hence different coupling constants α_j) are operative at different times, see Fig. 2.7.
- When solving the master equation Eq. (2.7) for $\langle I_j^z(t) \rangle$ we find that it depends only on the spin-spin correlations $\langle I_j^+ I_k^- \rangle$, which, in turn, depend on higher-order correlations, leading to a hierarchy of equations. It can be solved numerically only for rather small systems, but it suggests an approach to find approximate solutions by invoking factorization assumptions [6], e.g., neglecting correlations between different spins or approximating fourth-order correlations by Wick-like expressions of second order. Several of the standard The "semiclassical" approximation which assumes the nuclei to be in a product state at all times neglects all correlations between different spins $\langle I_j^+ I_k^- \rangle \propto \delta_{jk}$. We will make frequent use of factorization schemes that reduce fourth-order terms to products of second order terms to close the equation. This allows to keep coherences between nuclear spins and effects like dark states (and superradiant states) while still keeping the equations manageable and providing numerically accurate results for small systems for which comparison with exact numerics is possible [G:8, G:13].
- The master equation Eq. (2.7) is closely related to the one studied in the context of the quantum optical effect of *superradiance* [99]. This motivates the first studies reported in Section 3.

- Note that the separation of time scales used in the derivation of Eq. (2.7) requires that we work in the detuned regime. As seen in Eq. (2.8) this detuning slows DNP down.

- The coefficient of the master equation depends on the nuclear spin state via the Overhauser shift that contributes to Δ. This introduces and effective nonlinearity into the dynamics which can be understood as underlying, e.g., the bistable behavior predicted [57, 58, 145, 137] and [G:18] and observed [142, 27, 216, 151] in DNP in QDs.

In the general case, the nuclear spin master equation contains more terms. One the one hand, we have neglected any internal nuclear dynamics as, e.g., the slow depolarizing process that restores the $\langle A^z \rangle = 0$ stationary value in the absence of pumping. Other terms arise, since the electronic steady state is usually not pure and more electronic levels and hyperfine induced transitions may be involved (e.g., in a two-electron DQD, one usually has to consider five electronic states spanning the ground-state subspace). Together with the effect that the nuclear spin state can have on the electronic level scheme this can give rise to a very varied and rich dynamics, including "self-polarization" [73, 146, 212], nuclear-spin "narrowing" and "dragging" [156], bi- and multi-stability [186, 118, 142, 4, 27, 169, 246, 58]. A recent and thorough review of DNP in optically active QDs is provided [253].

In [G:14] and [G:23] we consider two such more complicated and realistic situations encountered in two specific DNP experiments. We adapt the derivation of the master equation to the cases of an optically driven neutral SAQDs (with five relevant levels – the empty QD and four excitonic states) and a two-electron DQD in the inhomogeneous field of an on-sample nanomagnet. In both cases we provide a simple model and show that the approximation by a rate equation for the nuclear spins that captures the main features of the observed steady-state behavior. It allows to identify the operative DNP mechanism and suggests how to improve the DNP process. The first is notable for the fact that no polarization of the electronic steady state is needed to impart a large polarization to the nuclear system. The polarizing dynamics occurs since one of the two possible flip-flop processes is far more detuned that the other, leading to a net polarization rate. The experiment [G:23] achieves the largest polarization reported in lateral QDs to date in an more usual way: the inhomogeneous field of the nanomagnet changes the electronic steady state population (compared with the case without a magnet) and selectively drains population two of the three main steady-state components by coupling them much more efficiently than the third, leading to a polarized electronic steady state which drive DNP.

Further theoretical development of the model in [G:13, G:20], where we explore, in particular, the cooperative aspect of the collective dynamics which becomes most evident when we use Eq. (2.7) to *depolarize* a nuclear spin system (that had previously been polarized by interaction with spin-$\uparrow$ electrons) (cf. Section 3.2, p. 32).

If the objective is only to reduce the Overhauser field variance, then DNP is not the best procedure to chose: DNP tries to increase $|A^z|$ by driving all nuclear spins into a polarized state and significant narrowing is only achieved for very high polarization, which requires to push all states into a very small subspace of the total Hilbert space. Other A^z eigenvalues (not close to maximal) are highly degenerate and it may be preferable to *measure* the Overhauser field in order to reduce its variance.

2.2.2 Measurement of the Ensemble Nuclear Spin

To measure the "Overhauser field operator" A^z the natural choice is to exploit the QND-type coupling $S^z A^z$ and measure it via the electron. To suppress $H_{\rm ff}$ which disturbs the QND coupling one works at sufficiently strong magnetic field. Measuring the resonance frequency of electronic states as shifted by the Overhauser term is one way to determine A^z which has been pursued [33], however, the natural linewidth of the QD exciton (1 μeV) corresponds to a width of several 100 nuclear spin flips, hardly reducing ΔA^z below its value in the fully mixed state. Instead, ESR, two-photon resonance techniques or quantum phase estimation may allow a significant narrowing [136, 243, 93, 38].

In [G:2], reprinted on p. 84ff we propose a method for estimating an unknown quantum field associated with a mesoscopic spin ensemble. By using an incoherent version of the *quantum phase estimation algorithm*, [133, 182] we show that the number of qubit measurements scales linearly with the number of significant digits of the estimation. We only assume the availability of single qubit operations such as preparation of a known qubit state, rotations in the xy-plane, and measurement, of which only rotations need to be fast. The estimation procedure that we describe would suppress the dephasing of the qubit induced by the reservoir. If the measurement of the reservoir observable is sufficiently fast and strong, it may in turn suppress the free evolution of the reservoir in a way that is reminiscent of a quantum Zeno effect.

While our scheme is relatively fast and uses a minimum number of interactions to extract information about A^z the experimental demands (especially electron shuttling and precise timing and high-fidelity single-electron spin measurements) are still quite demanding.

Our second approach [G:3], cf. p. 92 uses an optical method which only requires photon counting and relies on the effect of electromagnetically induced transparency (EIT). EIT is two-photon resonance effect in which a three-level atom with a Λ-configuration interacts with two lasers and is driven into a coherent superposition of the two ground states which is decoupled from the lasers: If two lasers are in two-photon resonance [4] so that in a suitable rotating frame the Hamiltonian of the atom reads

$$H = \omega_e |e\rangle\langle e| + (\Omega_1 |e\rangle\langle 1| + \Omega_2 |e\rangle\langle 2| + \text{h.c.}) \tag{2.10}$$

then $|D\rangle \propto \Omega_2 |1\rangle - \Omega_1 |2\rangle$ is an eigenstate of H and not coupled to the excited state, i.e., it does not scatter any laser light (it is "transparent" to the laser light; the atom remains "dark"). Spontaneous emission from $|e\rangle$ brings the atom to state $|D\rangle$ with a finite rate and after that no photons are scattered. This has also been referred to as "coherent population trapping" (CPT), cf., e.g., [226]. This effect depends very sensitively on the two-photon detuning between the levels/lasers: if one ground-state level shifts relative to the other, the dark state becomes bright and the atom scatters light. We propose to use this effect in a one-electron QD [5] to determine A^z: in the detuned regime, the number of scattered photons tells us, how far we are from resonance. By adjusting the laser detunings (which can be done fast on the timescale of nuclear dynamics so that we can treat the nuclei quasi-statically) until no more light is scattered we can determine AA^z to within the width of the two-photon resonance (which corresponds to a few nuclear spin flips).

[4] The detuning of the first laser from the transition $1 \leftrightarrow e$ should be the same as that of the second laser from $2 \leftrightarrow e$.

[5] A Λ-scheme connecting the states $|\uparrow_z\rangle$ and $|\downarrow_z\rangle$ is possible, since the "diagonal" transitions (cf. Fig. 2.3) is weakly allowed due to heavy-hole–light-hole mixing.

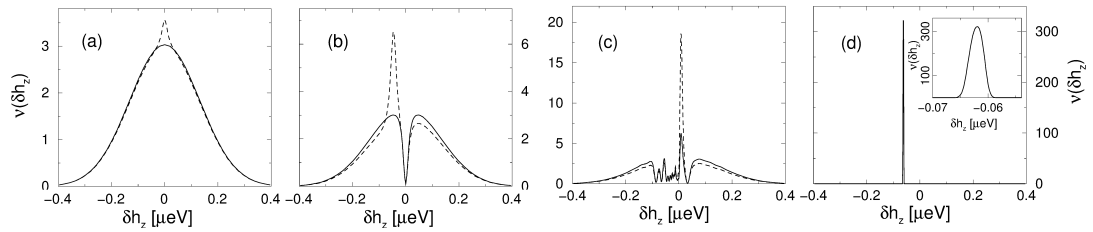

Fig. 2.8: EIT-based measurement scheme: conditional evolution of the Overhauser field distribution [G:3]. Given some prior Overhauser field distribution, we tune the lasers such that its maximum corresponds to two-photon resonance. Conditioned on *non*-detection for a time t the peak is enhanced (dashed lines). A scattered photon then modifies the OH distribution. Updatingteh distribution and tuning to the new peak leads to further narrowing conditioned on non-detection. The third plot depicts a typical conditional distribution after 11 photo detections, the last one after $\sim$100 μs.

In fact, the "narrowing" techniques that were most successful in practice so far did not fall in either of these classes. They are DNP schemes in which the DNP rate depends sensitively on the Overhauser field (cf., e.g. Eq. (2.7)); this can lead to sharp resonances in DNP as a function of $\langle A^z \rangle$. Combined with the slow decay of the nuclear spin polarization to the unpolarized states this result in very narrow "stationary state polarizations" [58] even if the total polarization is rather small [156, 275, 244, 18]

In the following section we present a method that builds on the EIT-measurement scheme to engineer such a narrow stationary-state condition. If combined with measurement and feedback, it may allow to prepare states of the nuclear system in which A^z is determined to a precision corresponding to a single nuclear spin flip. The scheme has already found application for state preparation in NV centers [250].

2.2.3 Nuclear Spin Cooling Using Overhauser-Field-Selective CPT

In [G:11, G:12], reprinted on p. 96ff, we show that EIT/CPT in the spin states of a solid-state emitter could be used to deterministically prepare a nuclear spin environment with ultra-narrow Overhauser field distribution. This scheme is an extension of the EIT-based measurement scheme just discussed. It considers again a single electron in an optically active QD under illumination by two lasers and takes into account the laser-induced nuclear spin diffusion that is mediated by H_{ff}. We show that the diffusion rate is proportional to the population in the optically excited state (trion) of the QD. Consequently, if for the given laser frequencies the current OH value does not satisfy the EIT condition (two-photon detuning = Overhauser shift), the excited state will be populated, the nuclear spins will diffuse and A^z will change. The diffusion comes to rest at the dark state resonance when the population in the excited state (ideally) drops to zero. We show that when the coupled system is in the dark state, the Overhauser field has a standard deviation on the order A/N (corresponding to a single spin flip).

It should be noted that the diffusion induced here is *undirected* (inducing a random walk) and there is a large range of A^z-eigenvalues to explore. However, the spectral density of A^z is concentrated in an interval $[-1/\sqrt{N}, +1/\sqrt{N}]$, while there are only exponentially few states with eigenvalues of

order 1 [G:12], see also [251]. This effectively restricts the interval to be explored by the random walk and ensures that if the system leaves the trapping region it returns sufficiently quickly to keep the steady-state A^z-variance small.

An additional feature of the scheme is the possibility of using resonant fluorescence to verify the preparation of a narrow nuclear spin distribution [G:3]; turning the laser fields off after a dark state has been reached ensures that the Overhauser field distribution remains in the single-spin regime within timescales determined by the (intrinsic) nuclear spin lifetime; the corresponding electron spin T_2^* time will then be prolonged by a factor $\sim \sqrt{N}$. Note that – by construction – this scheme narrows a "generalized Overhauser field" $\tilde{A}^z$ which is renormalized by a contribution $\propto \{A^+, A^-\}_+$ (representing the leading-order contribution of $H_{\rm ff}$). This implies that the nuclear spins in the prepared state do not evolve due to electron-mediated indirect interactions, eliminating a principal contribution to electron spin T_2 time [130, 248].

2.3 Using the Nuclear Spins for QIP protocols

In this section we propose and analyze different ways in which the nuclear spin ensemble may be made useful for quantum information processing purposes. The main motivation are their strong coupling to the electron and otherwise very good isolation and long life- and coherence time.

Broadly speaking, two ways to actively use nuclear spins in QDs for QIP have been explored. On the one hand, the nuclear spins can be of help to perform quantum gates on the electron spin qubit, since they can provide a stable, localized, effective magnetic field. Many single-qubit gates require the controlled, time-dependent application of strong magnetic fields acting on individual spin qubits in QDs, which is challenging to achieve. One solution is the inclusion of micro- or nanomagnets in the setup [196, 185, 192] and to move the electrons (by electrical control) in their inhomogeneous field to induce the desired gate [166, 104, 86]. Polarized nuclear spins could play a similar and potentially more versatile role: even a 10% polarization difference between the two QDs in a GaAs DQD amounts to a few 100 mT in effective field difference (much larger than nuclear field fluctuations) and thanks to the long nuclear spin lifetimes this can be considered static on the timescale of the electron dynamics. Combined with time-dependent voltages applied to the QD electrodes such a static field gradient can be utilized for (single-qubit) gate operations [209] in lieu of time-dependent magnetic fields which are difficult to produce quickly or in such a localized way. To implement a phase gate, a spin qubit can be moved into a partially polarized QD for a suitable time; for singlet-triplet qubits Overhauser-field gradients enable rotations between the computational states [86] or they can be exploited to allow individual addressing of single electrons in a DQD by resonant microwave radiation [154]; finally, NMR techniques allow the rapid rotation of the Overhauser field, thereby providing localized oscillatory magnetic fields [167]. More complicated transitions between multi-qubit states can be implemented via Landau-Zener type transitions in an inhomogeneous magnetic field [194, 209, 91].

For the "static" Overhauser field applications, the only requirements are sufficiently narrow Overhauser field and sufficiently long relaxation time (T_1) of the nuclear spins. Depending on the system, lifetimes from seconds to hours have been observed [G:14, G:23], all much longer than the time needed for Overhauser-field-based quantum gates (micro- to nanoseconds).

The second kind of QIP application involves quantum mechanical degrees of freedom of the nuclear system and exploits the long coherence time of nuclear spin to store and process quantum information in the nuclear spin system. These proposals of nuclear spin quantum memory [247, 153], quantum interface [G:17], or quantum register [G:1] require relatively high nuclear polarization and have not yet been implemented experimentally. For these applications, the coherence time (T_2) of the nuclear spin is crucial. In [62, 241, 282], T_2 times for the nuclear spin qubit on the order of 1 ms are predicted. There have been only a few studies of the nuclear spin T_2 time in quantum wells [187] and quantum dots [167], which confirm these values. Further improvements could be achieved with NMR dynamical decoupling techniques and improved state preparation (high polarization).

As mentioned above, for NV centers and for Si:P, this expectation has been confirmed, and coherence times above 180 s at few K temperatures [242] and still more than 1 s at room temperature [173] have been demonstrated. In these cases, *single* nuclear spins are used for storage [6]. They can be individually addressed spectroscopically due to the specific strength of their coupling to the central spin. In contrast, in QDs the hyperfine splitting is quasi-continuous due to the large number of inhomogeneously coupled spins [251] and only collective excitations can be accessed.

In this Thesis we present a number of QIP applications of nuclear spins as quantum memory.

Nuclear Spin Quantum Register

We build on the quantum memory proposal [247] and the quantum optical analogy of the polarized nuclear spin system and the electron spin as a (approximate) realization of the Jaynes-Cummings model [231]. The Jaynes-Cummings Hamiltonian

$$H_{\mathrm{JC}} = g\left(S^{+}a + S^{-}a^{\dagger}\right) \tag{2.11}$$

has been extensively analyzed in quantum optics and for quantum information processing. It allows (together with control over the two-level system) to prepare any state of the bosonic mode [159]. The realization of H_{JC} for cold trapped ions [7] was the basis for the seminal proposal of the trapped-ion quantum computer [47].

In [G:1], cf. Section 7, p. 113 we exploit this analogy to show how to couple, manipulate, and measure qubits realized as collective excitations of the nuclear spin ensemble. Ideally, the logical $|0\rangle$ is given by the fully polarized state and logical $|1\rangle \propto A^{+}|0\rangle$. For large N we can use the Holstein-Primakoff approximation $A^{+} \approx \sqrt{N}$ (cf. Eqs. (2.6a)) to turn H_{hf} into a JC-Hamiltonian. Consequently, quantum gates developed in the trapped-ion context can be used for the nuclear-spin-ensemble qubit as well. This allows, in particular, the implementation of a C-NOT gate between electron-spin and nuclear-ensemble qubits. Coupling between different nuclear-spin ensembles requires either to coherently shuttle electrons between quantum dots or the off-line generation of entanglement which can then be used to implement non-local gates by local operations and classical communication [46]. We estimate the error contributions due to different imperfections and find that the fidelity is limited by the width of the Overhauser field and that with polarizations above 90% and a factor

[6] Or a small number of individually addressable spins as demonstrated in [245].

[7] Two internal states of the ion were coupled via suitable lasers to the mode defined by ions' quantized collective in the harmonic trap.

10 reduction of the width of the Overhauser field, two-qubit gate fidelities above 0.99 should be achievable.

Nuclear Spin Quantum Interface

The quantum optical analogy used above is extended in [G:17, G:16] (cf. Section 7, p. 117) to show how to map states of the electromagnetic field coherently to (and from) the nuclear spin system. Specifically, we then show that the nuclear spin quantum memory can also be used as part of a light-matter *quantum interface*: a QD strongly coupled to a high-Q cavity can be used to engineer an effective coupling

$$\propto A^{\pm} b + A^{\mp} b^{\dagger} \tag{2.12}$$

between an optical field mode b of the cavity and the nuclear spin system (plus some additional terms as discussed in the paper). This is achieved as follows (cf. Fig. 2.9): cavity and control laser drive a (detuned) Raman spin-flip transition between the two electron spin states. However, we chose the laser frequency such that the two-photon detuning is large for the transition between the two ground states, but resonant with a transition between two adjacent hyperfine levels. This transition is made possible by H_{ff}. As we discuss in [G:16], both terms $\pm$ are present in general (due

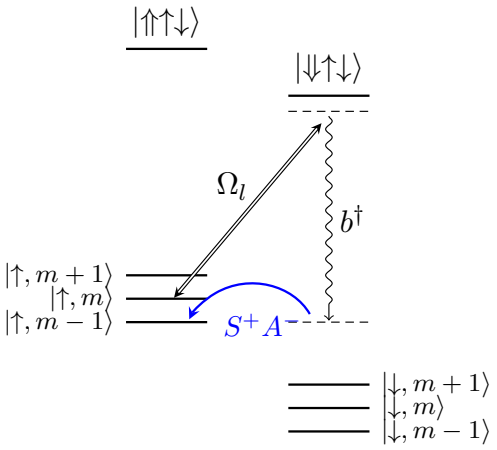

Fig. 2.9: Coupling the nuclear spins to a cavity mode. Laser (Ω_l and cavity photon ($a^\dagger$)) are two-photon detuned from the $|\uparrow\rangle \leftrightarrow |\downarrow\rangle$ transition, but resonant with flipping a single nuclear spin. The hyperfine flip-flop term enables the otherwise spin-forbidden transition $|\uparrow, m\rangle \leftrightarrow |\uparrow, m-1\rangle$ while emitting one cavity photon. Here m labels the number of nuclear spin excitations above the fully polarized state $m = 0$ ($|m+1\rangle = A^+ |m\rangle$). Solid lines indicate energy levels, dashed lines show the detuning of the operative transitions. The HF splitting is not drawn to scale. A second Λ scheme coupling to the other trion state is not drawn (see [G:16]).

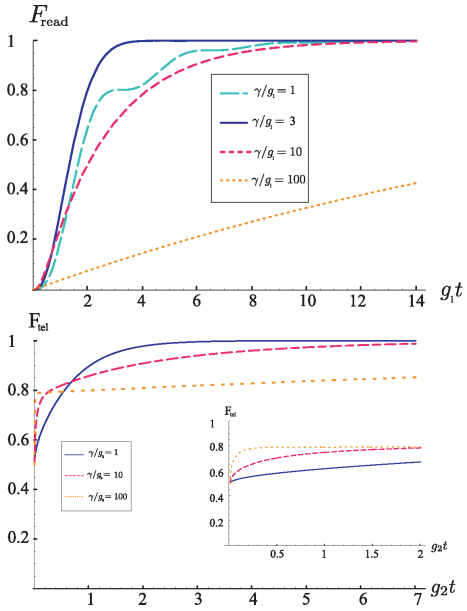

Fig. 2.10: Quantum interface performance: Optimal fidelities for readout (top) and write-in (bottom) of coherent states out of/into the quantum memory plotted as a function of the interaction time. The fidelities are computed based on the quadratic bosonic interaction (Holstein-Primakoff approximation) that approximates the actual coupling, see [G:16].

to a second Λ scheme via the other trion state), but by tuning the control laser one of them can

be made resonant while the other can then be neglected (rotating wave approximation). Thus one can obtain either a beamsplitter-type coupling between the two systems or a two-mode squeezing interaction, which then allows to choose between (i) mapping the nuclear spin-state to the mode (beamsplitter) or (ii) creating a two-mode squeezed state of nuclei and light. As we show in the paper, by properly including the losses of the cavity (linear coupling to its output field), mapping and squeezing can be achieved between nuclear spins and output mode, even for rather short-lived cavities. The achievable fidelities for readout and teleportation-based write-in are plotted in Fig. 2.10 as a function of interaction time, i.e., how long the beamsplitter (squeezing) Hamiltonian is applied. The classical limit ($F = 0.5$) is clearly overcome for a large range. The proposed set-up is clearly quite challenging (strong coupling to a good cavity with well-defined output mode, highly polarized nuclear spins), but if realized it would open several possibilities: the two-mode entangled state can be used for teleporting quantum information into the nuclear spin system (quantum interface, write-in) or, via entanglement swapping, to entangle two distant nuclear spin systems, which could, in turn, be used to implement long-range two-qubit gates on electron-spin qubits.

Entangling Electrons via a maximally mixed Spin Bath

The previous proposals require very high nuclear spin polarization. The opposite regime of a *completely mixed nuclear spin system* (with density matrix $\propto \mathbb{1}$) might be expected to be of no use whatsoever. But as we show in [G:8], p. 170 the very slow nuclear dynamics makes it possible to use this fully mixed systems to mediate a coherent interaction and create multiparticle entanglement between a sequence of electrons that sequentially interact with the same spin bath.

The idea is to couple a single electron spin (the "control electron") coherently and resonantly to the bath (via H_{ff}). This creates a correlation between an increased Overhauser field and the control electron spin. A sequence of N $\uparrow_x$-polarized electrons ("target electrons") then interacts off-resonantly with the Overhauser field, rotating $\uparrow_x$ to $\downarrow_x$ and back with a frequency depending on the value of A^z, i.e it differs depending on whether the control electron flipped or not. For a static bath, this shift is the same for a whole sequence of such electrons. Chosing the interaction time suitably we show that the target electrons can now be projected into a GHZ-state by an measurement of the control electron that *erases* the information whether the control electron had flipped or not. Surprisingly, the resulting state is uncorrelated with the state of the highly mixed spin bath.

In [G:8] we analyze the effects of inhomogeneity in the hyperfine coupling and nuclear Zeeman energies and conclude that our scheme could work even for realistic parameters, provided that the electrons can be stored with high fidelity. We also show that the scheme can be modified to prepare a larger class of multipartite entangled states (matrix product states of bond dimension 2). However, the main point we want to make is that even a maximally mixed system can be used to mediate coherent interaction and create entanglement.

After several QIP-applications of nuclear spin ensembles in QDs, we conclude this section with a proposal involving a different solid-state system, NV centers in diamond, where single nuclear spins close to the center can serve as a high-quality quantum memory.

Nuclear Spins Qubits in NV Centers

In [G:21], p. 162 we employ a nuclear spin quantum memory next to an NV center qubit (cf. p. 8 and 10).

Here, the NV center electron spin couples strongly to only a few proximal nuclear spins which can be individually addressed spectroscopically. In these cases, several nuclear-spin qubits associated to the defect have been addressed and entangled with the electron spin [180]. The nuclear spins have been exploited as quantum memory to extend the qubit lifetime by several orders of magnitude [173] and to improve the qubit measurement fidelity by repeated readout [125]. There have been very rapid and impressive advances towards production, characterization, and manipulation of high-quality qubits in diamond, with the especially attractive prospect that they might work almost at room temperature [71]. Coherent interaction between two dipole-coupled NV centers [179, 72] and even between NV centers in two different samples [16] (separated by a 3 m) was demonstrated.

Motivated by the rapid technological and theoretical progress of the diamond QIP platform, we combine recent advances into a proposal to integrate NV center qubits into a scalable architecture for a quantum computer.

The main (theoretical) challenge is to design the system such that qubits are close enough (to each other) for strong interaction and fast quantum gates, but also far enough that individual readout and parallel operation on different qubits is possible. The latter is important, since favorable error correction thresholds depend on applying many gates in parallel.

We describe and analyze a feasible diamond-based architecture, which uses of a 2D array of single NV centers, created, e.g., through implantation of ions and subsequent annealing [11]. Each NV center constitutes an individual quantum register containing a nuclear spin and a localized electronic spin [273]. The nuclear spin serves as the memory qubit, while the electronic spin will be used to initialize, read out, and mediate coupling between nuclear spins of adjacent registers.

To allow for a separation of several 100 nm between NV center qubits (this is needed both for the proposed methods of addressing and readout and to allow for finite implantation probability) we invoke and extend the proposal [277] to mediate an interaction between NV centers by an optically inactive "dark" spin chain data bus (DSCB), realized, e.g., by implanted Nitrogen impurities with spin 1/2.

With these ingredients, we propose the following hierarchy of control to achieve a scalable architecture: on the lowest level are *plaquettes* of $100 - 500$ nm in each direction. A single computational NV center (with associated nuclear spin) is implanted per plaquette. The plaquettes are combined into a *super-plaquettes* of $10{\times}10$ μm^2 each of which can be controlled by confined microwave (MW) fields. The full quantum register is then a square array of super-plaquettes.

The benefit of this structure is the following: having only one computational NV per plaquette allows individual optical addressing (initialization, readout) by standard far-field sub-wavelengths techniques such as STED [265] and, as we explain presently, is also sufficient for individual MW access. While the NV centers are then too far for direct dipole-dipole interaction, they can be coupled using a DSCB. The coupling via the DCSB (and single-qubit operations on the nuclear spins) are done by MW fields. In order to allow for individual addressing, different NVs (within one super-plaquette) must be distinguished spectroscopically. This can be achieved with a magnetic field gradient (in y direction across the super-plaquette) if the NV centers are implanted such that each one has a unique y coordinate (e.g., for an $M \times M$ super-plaquette one defines M rows within each plaquette and then in the (i, j)th plaquette the NV center is implanted in the ith row, thus column and row within the super-plaquette uniquely determine the y position and therefor a unique MW resonance frequency, enabling individual access. Different super-plaquettes can be accessed by their individual confined

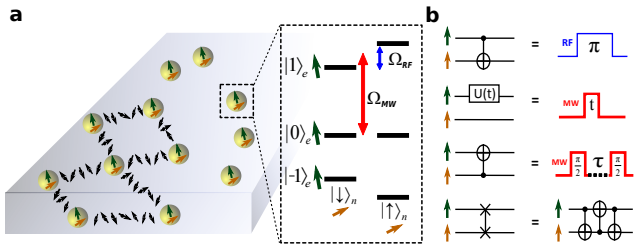

Fig. 2.11: Arrangement of NV centers on plaquettes; level scheme for the NV center quantum register and pulse sequences for quantum gates between electron and nuclear spin qubits, see [G:21].

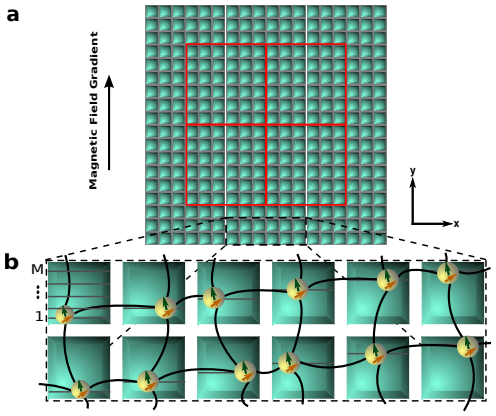

Fig. 2.12: Arrangement of plaquettes in super-plaquettes and staggered positioning of the NV centers within neighboring plaquettes to allow individual addressing (cf text and [G:21]).

MW field. By defining a dual lattice of super-plaquettes and switching between operating on either one, qubits in different super-plaquettes can be coupled.

In [G:21] we analyze in detail the technical requirements of the design, and, in particular, different methods to implement high-fidelity two-qubit gates via the DSCB [277] (the main idea is to use resonant MW driving and the natural (off-resonant) dipolar interaction of the spins to engineer a flip-flop (XX) interaction between neighbouring dark spins; this allows to swap qubits either sequentially or using an effective direct coupling between the NVs, mediated by the chain; note that this works even if the bus spins are completely mixed and no individual control of the dark spins is assumed), and estimate the errors contributed by various imperfections (mainly arising from off-resonant couplings in the spin-chain transfer and regarding the individual addressing of NV qubits and the effect of finite temperature, which affects the transfer via the T-dependent lifetime of the NV center electron spin). Gate fidelities of 0.99 could be achievable (at $\sim$250 K), which would be above the quantum error correction threshold derived in [259].

A majority of the elements required for the realization of individual qubits in our architecture have already been demonstrated, but the implementation and integration of the various proposed elements still requires substantial advances in areas ranging from quantum control to materials science. Nevertheless, the above considerations indicate the feasibility of experimentally realizing a solid-state quantum computer capable of operating under ambient conditions at or near room temperature.

3 Open Quantum Systems and Phase Transitions

3.1 Introduction

The most general time-evolution of a quantum system includes interaction with uncontrolled degrees of freedom (the "environment") and is therefore not unitary. Such coupling can cause decoherence [288] and typically destroys quantum effects. Therefore, avoidance of dissipative couplings has been a prime objective in most QIP experiments and central aspects of QIT such as quantum error correction and quantum Shannon theory deal with how to avoid and fight the decohering effect of open-system dynamics.
Recently, it was realized that, if properly designed, even purely dissipative coupling to uncontrolled degrees of freedom could lead to a variety of genuine quantum effects, including many-body and long-range entanglement and universal quantum computing [149, 257, 256]. This provides (yet another [83, 202]) alternative to the standard gate-array version of quantum computation for which the famous Di Vincenzo Criteria [69] (which listed pure, almost perfectly isolated qubits among the requirements for quantum computing), were formulated. This may even be particularly robust way to perform these tasks, since quantum properties are attained in the steady state of the open system dynamics. Hence they are unaffected by timing and preparation errors and are reached *while the system interacts with its environment*, which potentially facilitates observation of the effect.

Thus there is a twofold motivation for the study of open system dynamics in we can either design our system (codes, subspaces) to protect it against decoherence or we can tweak to environment and the coupling to it to make dissipation useful to perform QIP tasks or to observe quantum effects. The latter is the motivation of the contributions summarized in this Chapter.

Before summarizing the results on the occurrence and properties of phase transitions in open quantum systems, we touch upon a few concepts and models (Lindblad dynamics, phase transitions, central spin model) that are the common background to the research reported here.

3.1.1 Lindblad Dynamics

The simplest class of open-system time evolutions is the one described by a Lindblad-type master equation [32]. It encompasses the important class of systems that are weakly coupled to a memoryless (Markovian) environment. The corresponding time evolution $\mathcal{T}_t = e^{t\mathcal{L}}$ forms a semigroup of completely positive (CP) maps with constant generator $\mathcal{L}$. The generator is sometimes referred to as the *Liouville operator* or *Liouvillian* of the open system and can always be brought to the

form

$$\mathcal{L}(\rho) = -i[H, \rho] + \sum_k D(L_k)(\rho), \tag{3.1}$$

$$\text{with } D_k(\rho) = L_k \rho L_k^\dagger - \frac{1}{2}\left\{\rho, L_k^\dagger L_k\right\}. \tag{3.2}$$

for hermitian H. This class of evolutions generalizes the unitary (Hamiltonian) evolution ($L_k = 0$) to the case of non-hermitian generators. This analogy will by quite useful for some of our considerations below.

CP semigroups are *contractive* $\|\mathcal{T}_t\| \leq 1$ and consequently the real part of the spectrum of the generator $\mathcal{L}$ is ≤ 0. Generically, $\mathcal{T}_t$ describes the evolution of the quantum system towards a *steady state* ρ_s characterized by

$$\mathcal{L}(\rho_s) = 0. \tag{3.3}$$

It has been shown that every Liouvillian $\mathcal{L}$ (of Lindblad form) has at least one such steady state. For a more general analysis of the properties of Lindblad operators, cf. [13].

Our interest in the following focuses on the stationary state of a given $\mathcal{L}$ and how it depends on the system parameters, in particular, on points of abrupt/non-analytical change, which may be linked to phase transitions.

3.1.2 Phase Transitions

One of the central topics of statistical mechanics are the different phases a given physical system can be in, their classification and the means to change one phase into another. Sometimes, this change happens abruptly, a phenomenon called phase transition (PT). PTs are interesting since they often display anomalous or singular behavior and since the behavior is *universal*, i.e., independent of microscopic details of the system [279].

At zero temperature, a special kind of phase transition occurs, which is driven by quantum (instead of thermal) fluctuations. These quantum phase transitions (QPTs) are related to some of the most fascinating effects in quantum physics (BEC, quantum Hall effect, superconductivity) and have been a subject of intense research in the last decades [217]. QPT are related to exotic phases of matter, often intimately linked to many-body entanglement and pose a particular challenge for the classical simulation of quantum dynamics.

PTs can also occur away from thermal equilibrium [111, 161], e.g., when a system is in contact with reservoirs of different temperatures or if it is also driven by a coherent source. Dissipation drives the system into a steady state, which generally depends of the parameters of system, drive, and environment. As these parameters are changed, so is the steady state. At certain points in parameter space an abrupt (non-analytic) change of steady-state properties may occur, giving rise to a dissipative phase transition (DPT) [258, 263, 56, 177, 67, 161, 285, 75]. DPTs have been much less studied than QPTs. The aim of the contributions summarized in this Chapter is to shed some light on the physical and mathematical properties of DPTs. To this end we propose and analyze two toy models of open quantum systems that allow far reaching analytical results while still supporting a rich variety of physical effects.

Before turning to these results, let us briefly introduce to simple models that have been extensively studied as paradigmatic many-body quantum systems and that give rise to QPTs and DPTs and motivate and inform the work of this Thesis.

3.1.3 The Central Spin Model and the Dicke Model

The central spin model is one of the canonical models in which a small quantum system can be coupled to a large bath. Before coming in the focus of QIP as the model for hyperfine dynamics of electron spin qubits in QDs it had been studied in other contexts, from from electron dynamics in ferromagnetic grains to superconductors (see [281] for a brief overview) and as a model system for decoherence [31, 54, 79].

In its simplest form, it consists of a set of N spin-1/2 particles coupled to a single central spin-1/2 by an isotropic Heisenberg interaction and exposed to an external field:

$$H_{\mathrm{CSM}} = \omega S^z + \vec{S} \cdot \sum_{j=1}^{N} \alpha_j \vec{I}_j + \omega_n \sum_j I_j^z. \tag{3.4}$$

The Hamiltonian dynamics of this system and generalizations thereof (e.g., to larger spins, anisotropic coupling) has been thoroughly studied. Eq. (3.4) belongs to the integrable family of Gaudin magnets [90] and can be solved exactly by a Bethe ansatz [90, 235]. It is closely related to the BCS model of superconductivity [281]. Due to the infinite range of the interaction, the mean field approximation is exact in the thermodynamic limit (see discussion and references in [281]). The energy eigenvalues of Eq. (3.4) are given via a set of algebraic equations [90, 22], but extracting the eigenvalues is practical only for small systems and the physics of the CSM is still actively investigated [21, 80, 12].

In the next sections we study the dynamics under a central spin Hamiltonian augmented by dissipative and driving terms. First, we analyze cooperative effects akin to superradiance. Then we add driving and consider the steady state phase diagram of the driven and damped *homogeneous* central spin model.

The CSM is an interesting candidate to study QPTs since it is related to another well-studied system, the Dicke model [65] of a bosonic mode coupled to N two-level systems with Hamiltonian

$$H_{\mathrm{Dicke}} = \omega a^\dagger a + \nu \sum_j I_j^z + g \sum_{j=1}^{N} \left(I_j^+ a + I_j^- a^\dagger \right). \tag{3.5}$$

which is known to exhibit a transitions between a normal and a superradiant phase [110]. In the former, the bosonic occupation number per atom vanishes in the thermodynamic limit, in the latter there is a macroscopic occupancy. The (existence and character of the) transition is robust under many modifications of Eq. (3.5) such as counter-rotating terms, multiple bosonic modes, position-dependent coupling constants [112] (and [24] for a comprehensive review with special emphasis on mesoscopic systems and the solid-state setting).

Most prominently, superradiance is seen in the *transient* evolution the Dicke model: as N (initially fully excited and independent) two-level atoms couple jointly to a single mode, a spontaneous

build-up and reinforcement of correlations between the initially independent dipoles leads to strong enhancement of emission. This is reflected in an intensity burst that can be many orders of magnitude stronger than what one would be produced by the same number of independent emitters [99, 24].

SR can also be observed in the *stationary* state of a dissipative Dicke model, provided that a driving term ($\propto S^x$) is added that prevents that all excitations are lost from the system. It then describes the process of (cooperative) resonance fluorescence, which is the textbook example of a dissipative phase transition [39]. The model applies to two-level atoms in a cavity interacting with an external laser field. The cavity mode is coupled to the atoms and to the other modes of the electromagnetic field, which act as a reservoir and drive the atoms to a steady state. Without driving, in the steady state all atoms are de-excited. As driving strength is increased, the atoms' state is rotated on the Bloch sphere towards the equator. At that point, the steady state abruptly changes and the polarization and population inversion display a sudden change, indicating the appearance of a DPT. Experimental [92] and theoretical studies [160, 200, 20, 222] revealed interesting features such as optical multistability, first and second order phase transitions, and bipartite entanglement.

The close connection between H_{CSM} and H_{Dicke} is obvious. While there cannot be a "macroscopic" occupation of the central spin, in the case of a lossy "central" system a superradiantly enhanced de-excitation of the N two-level systems is possible. In the following section we investigate superradiant behavior in the dissipative central spin system realized by the electron and nuclear spins in a quantum dot.

3.2 Superradiance with Nuclear Spins in QDs

Nuclear spins in a QD are an attractive system to investigate the central spin dynamics since they combine the very well-isolated mesoscopic nuclear system with the clean and well-controlled central electron spin. The Hamiltonian H_{CSM} is the standard model used to describe the HFI in QDs. The tools available to control the electron spin allows to introduce efficient damping, driving and monitoring of the dynamics. The CSM in the QD is far from the homogeneous limit, but the robustness of the superradiant phase transition under position-dependent coupling constants in the Dicke model [112] suggests that of SR behavior might still be observed for the inhomogeneous CSM.

3.2.1 SR with Nuclear Spins in in SAQDs

In [G:13], reprinted on p. 175ff we explore the close similarity of the DNP master equation Eq. (2.7) with the master equation of quantum optical superradiance (SR). We consider a singly-charged self-assembled QD optically pumped to the spin-$\downarrow$ state, for a sketch of the system see Fig. 3.1. The fast decaying excited state is negligibly populated throughout and we can adiabatically eliminate it to obtain the master equation for a dissipative central spin model

$$\dot{\rho} = \Gamma_r(S^-\rho S^+ - \frac{1}{2}S^+S^-\rho - \frac{1}{2}\rho S^+S^-) - i[H_{\mathrm{CSM}}, \rho], \tag{3.6}$$

where Γ_r is the effective optical pumping rate from the $S^z = +1/2$ to the $S^z = -1/2$ state and $H_{\rm CSM} = \frac{g}{2}(A^+S^- + A^-S^+) + gA^zS^z + \omega_S S^z$. A QD electron in state $|+\rangle$ scatters laser photons until it decays into $|-\rangle$ when the QD becomes dark. The flip-flop term in $H_{\rm CSM}$ can return it to the bright state $|+\rangle$. Thus every photon scattered by the QD is preceded by a HF spin flip. The superradiant effect occurs in the rate with which the bright state is repopulated: for a fully polarized nuclear system, the operative matrix element of $\langle A^+A^-\rangle$ is of order $O(1/N)$ and increases up to $O(1)$ as nuclear spin polarization decays and coherence between the nuclear spin builds up.

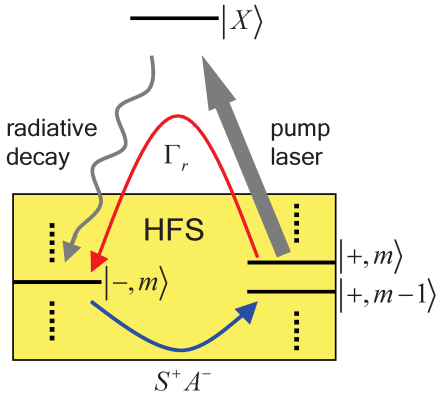

Fig. 3.1: Superradiant dynamics of nuclear spins in an optically driven QD: A shows the system: the electron spin is optically pumped to the $S^z = -1/2$-state $|-\rangle$ where it no longer interacts with the driving field. HFI can return the electron to $|+\rangle$ so that it can again scatter light.

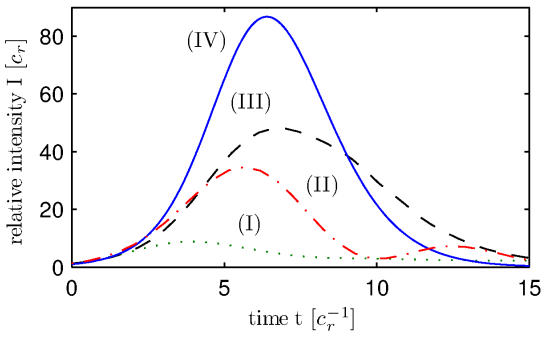

Fig. 3.2: Superradiant signature of the scattered light: scattered intensity as a function of time for $N = 21^2$ spins in (IV) the ideal Dicke system, and (III-I) the CSM for different values of $\epsilon = A/(2|\gamma_r/2 + i\omega_S|) = 0.99, 0.7, 0.3$. We take $\omega_S = A/2$ and dynamically compensate the instantaneous Overhauser field.

In [G:13] we show that this behavior occurs in QD and NV systems with realistic parameters despite the imperfections of the nuclear spin system compared to the Dicke model, i.e., the inhomogeneity of the coupling constants α_j, the Overhauser term S^zA^z (not present in $H_{\rm Dicke}$), and finite initial polarization.

As the signature of SR we consider the strong intensity peak and its (linear) scaling with system size (cf. Fig. 3.2). For product states of the nuclear spins, the intensity is maximized for the initial (fully polarized) state. Hence any increase in intensity beyond the initial value could be taken as sign of nuclear spin coherence and SR. By numerically integrating Eq. (3.6) (exactly for small systems and using a factorization method for larger ones) we find intensity profiles as in Fig. 3.2, displaying a large increase in intensity even for the small ($N < 400$) systems we can handle, and see that the peak height increases linearly with N , which extrapolates to an increase by a factor > 1000 for QDs with $N \sim 10^4$. We show that in rather small systems ($N \sim 10$ as expected for NV centers in ^{13}C-enriched diamond) still an enhancement of 100% is predicted and the for QDs the SR effect persists even for finite initial polarization.

3.2.2 SR with Nuclear Spins in in EDQDs

Since the SR effect scales with particle number, it is tempting to turn to larger QDs such as lateral EDQDs to observe it. However, in that case optical pumping is not available to drive the electron spin. In [G:20], reprinted on p. 179ff we show that spin-dependent tunneling of the electron can lead to a SR master equation predicting an $\propto N$ enhancement of the leakage current through an initially polarized spin-blocked QD.

We consider a single QD in a magnetic field and tunnel coupled to two leads. The QD is tuned to the spin-blockade regime, cf. Fig. 2.4A in which the spin ground state can be filled from the left but not leave to the right and transport is only possible with assistance of spin-flip processes such as HFI. We identify the conditions for which the leads can be eliminated and use the projection operator technique to derive a Markovian master equation (similar to Eq. (2.7)) which describes the lifting of the spin blockade by HFI. We show that this process is superradiantly enhanced for initially polarized nuclear spins leading to a strong increase in current through the QD scaling linear with N. Although the initial current is very weak (inversely proportional to N) it is of the order of currents already measured in Pauli-blocked QDs and the rate of HF flips is fast compared to nuclear interactions as long as $N \lesssim 10^5$. Therefore the N-fold increase over this initial value should be observable with current setups for sufficient nuclear polarization in lateral QDs.

Let us now turn from transient to *steady state* signatures of superradiance. Following the analogy of CSM and Dicke model and the existence of a dissipative superradiant PT in the driven and damped Dicke model, we study a driven and damped central spin system in detail in the next section. This provides a simple model to study general properties of phase transitions (e.g., their relation to spectral properties of the Liouvillian) and it might help to understand the behavior observed in QD experiments such as [152] with features reminiscent of a phase transition and possibly relate them to dissipative many-body dynamics.

3.3 Dissipative Phase Transitions in the Central Spin System

In [G:18], reprinted on p. 196ff we analyze the steady-state phase diagram of a driven and damped central spin system (CSS). In the model we consider, the central spin is externally driven and decays through interaction with a Markovian environment, leading (in a rotating frame and under the rotating wave approximation) to the master equation

$$\dot{\rho} = \mathcal{L}\rho \equiv J\gamma \left(S^- \rho S^+ - \frac{1}{2}\{S^+ S^-, \rho\}_+ \right) - i[H'_{\mathrm{CSM}}, \rho], \tag{3.7}$$

where

$$H'_{\mathrm{CSM}} = J\Omega S^x) + \delta\omega I_z + \frac{a}{2}(S^+ I^- + S^- I^+) + a S^+ S^- I_z \tag{3.8}$$

and S^α and $I^\alpha = \sum \sigma_i^\alpha$ ($\alpha = +, -, z$) denote electron and (homogeneous) collective nuclear spin operators, respectively. $J\Omega$ is the Rabi frequency of the resonant external driving of the electron while $\delta\omega = \omega - a/2$ is the difference of hyperfine detuning ω and half the individual hyperfine coupling strength a.

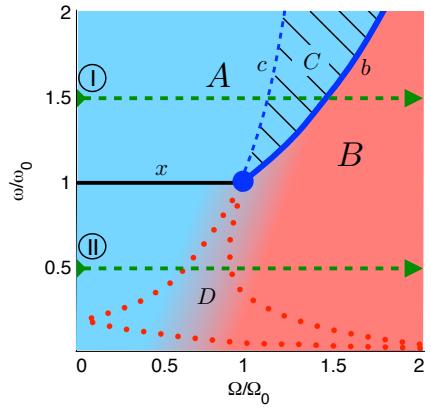

Fig. 3.3: Schematic of the different phases and transitions of master equation (3.7) studied in [G:18] as driving Ω and detuning ω are varied. In the two main phases of the system A (blue) and B (red) – which together cover the whole phase diagram – the system is found in a thermal squeezed spin state. The different phase boundaries, region of bistability (C) and the critical point (ω_0, Ω_0) are fully described in [G:18], reprinted on p. 196ff.

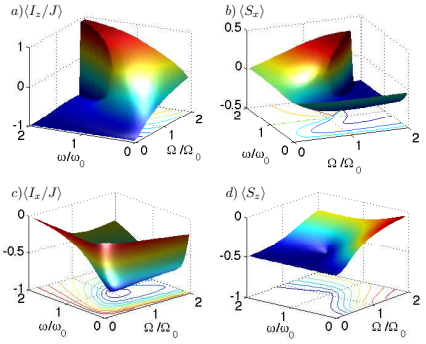

Fig. 3.4: Displays steady-state expectation values of electron and nuclear spin observables. Note the abrupt transition from almost fully positive to negative polarization at the boundary b.

Our main tool for the analysis of the dynamics and phase diagram is the Holstein-Primakoff transformation (cf. p. 15). We generalize it to allow for arbitrary direction of the polarization of the spin bath by including a semiclassical displacement $b \to b + \sqrt{J}\beta, |\beta|^2 < 2$. Expanding the square root terms $(\sqrt{2J - b^\dagger b})$ in orders $\epsilon = 1/\sqrt{J}$ introduces a hierarchy in the terms of the Liouvillian which then allows for a perturbative treatment of Eq. (3.7).

The leading order term acts only on the central spin but depends on the semiclassical displacement β. Thus the timescales of central spin and bath spin evolutions are separated by ϵ. The central spin quickly reaches its (quasi)steady state $\rho_{s,e}(\beta)$ and can be adiabatically eliminated (for given β), yielding a effective master equation for the nuclear spin operators b that depends on $\rho_{s,e}(\beta)$. Keeping only terms up to second order in ϵ we can then self-consistently determine the steady-state displacements (the "semiclassical solution") and their stability by analyzing the dynamics of the quantum fluctuations b. Since the effective master equation is quadratic in the bosonic operators, exact analytical treatment is possible. In the thermodynamic limit $J \to \infty$ the description becomes exact (as long as the stationary $|\beta| < \sqrt{2}$).

This allows to reach a detailed understanding of the system's phase diagram, sketched in Fig. 3.3. We can distinguish two phases of normal and anomalous polarization (A,B) which are separated by transition regions of bistability (C) and overdamping (D). The C and B are separated by a first-order phase boundary at which the steady state polarization changes non-analytically. The line culminates in a critical point at which the system undergoes a second order phase transition

These characterizations are supported by spectral analysis of the system's Liouvillian. When crossing b, the "dissipative gap" (or asymptotic decay rate (ADR): the largest non-zero real part of the Liouvillian's eigenvalues) closes indicating a PT. Away from the critical point, the corresponding

imaginary parts remain different (cf. Fig. 3.5a) and we have a "direct crossing" of eigenstates, reminiscent of first-order PTs. In contrast, at the critical point, the complex eigenvalues become degenerate (cf. Fig. 3.5b). This behavior is related to an avoided crossing (for finite systems) which vanishes in the thermodynamic limit (second-order PT). We show that at the critical point the system becomes macroscopically spin-squeezed (Fig. 3.6), i.e. is driven to an N-particle entangled state.

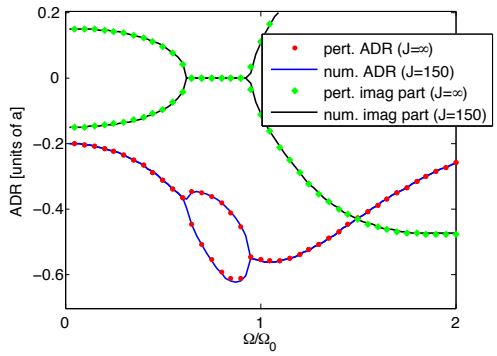

Fig. 3.5: Complex energy of the two modes corresponding to the semiclassical solutions $\beta_\pm$ (for $\gamma = a$). The solid line in the non-shaded area represents the ADR. (a) Along the line I ($\omega = 1.5\omega_0$): The eigenvalues miss each other in the complex plane, only the real parts cross. (b) Along x ($\omega = \omega_0$): The complex eigenvalues degenerate asymptotically at the critical point.

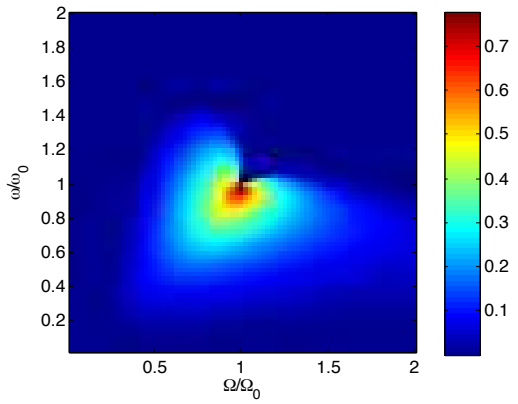

Fig. 3.6: The squeezing measure $C = \max_{\vec{n}} \left\{1 - \frac{2}{J}\langle \Delta J^2_{\vec{n}}\rangle - \frac{1}{J^2}\langle I_{\vec{n}}\rangle^2\right\}$ [143] in the thermodynamic limit. C approaches 1 at $(\omega_0, 0)$, indicating diverging entanglement in the system.

Whether these features survive in the actual, inhomogeneous CSM realized in a QD remains to be seen. The experience from the Dicke model suggests this to be the case. We provide some confirming evidence.

To further explore the relation between characteristics of the steady-state phase diagram and the spectrum of the system's Liouvillian, we looked at several other simple open quantum systems, namely 1d spin chains [G:24] and 1d quasifree fermionic systems [G:22].

3.4 Dissipative 1D Spin Chains

3.4.1 Quasifree Fermions

Dissipative fermionic systems and their critical behavior have received much attention recently. Quasifree fermionic systems, described by quadratic Hamiltonians in the anticommuting creation and annihilation operators combine several advantages. They are relatively simple both in mathematical terms (fully described by their covariance matrix, scaling only quadratically in the number of systems involved) and experimental demands (only linear couplings between the modes are required). Nevertheless, they encompass many intriguing effects including phase transitions [75, 286],

Majorana fermions [134], topological ground states [66]. An important subset of 1D fermionic systems is related to spin chains (studied, e.g., as model of spin transport and used in Section 2.3, p. 26 a means to couple spin-qubits in solids [277]) by the Jordan-Wigner transformation, see e.g., [181].

In [G:22], reprinted on p. 217ff we consider fermionic systems with quadratic Liouvillian, that is with a Hamiltonian quadratic in the Fermi operators and a dissipator of Lindblad form with Lindblad operators that are linear combinations of Fermi operators. For these systems we develop a general formalism to study the time-evolution and steady-state behavior of the covariance matrix (see also the independent (and more general) results in [75]). We focus on 1d translationally invariant systems in which the thermodynamic limit can readily be obtained and derive, in particular, expressions for the steady-state covariance matrix in the limit of weak dissipation.

Our methods can be extended to also include *quadratic* Lindblad operators as long as they are hermitian, since in that case (of a dephasing interacting with an environment) the dynamical equation for the covariance matrix is still closed.

We relate spectral properties of the Liouvillian $\mathcal{L}$ to steady-state properties of the fermionic system. We see that phase transitions in the Hamiltonian part can be reflected in non-analytic behavior of low-lying eigenvalues of $\mathcal{L}$ even in cases where the steady-state itself no longer bears any sign of critical behavior.

3.4.2 Dissipative Spin Chains

One very clean and versatile realization of 1d (and 2d) spin systems are ultra-cold atoms in an optical lattice [17, 162], which offer through laser cooling and manipulation powerful methods the engineer effective Hamiltonians and cool many-body quantum systems close to their ground state. In view of the interest in the dissipative dynamics of quantum systems it would therefore be interesting to add *controlled* dissipation to the toolbox available in this setting.

In [G:24], reprinted on p. 230ff pursue a twofold aim: First, we propose a scheme to realize a quantum spin system using ultra-cold atoms in an optical lattice in which both coherent interaction and dissipation can be engineered and controlled, enabling the study the non-equilibrium and steady-state physics of open and driven spin systems. To this end, we consider bosonic atoms in a 1d optical lattice in the Mott regime with filling factor 1. In the Lamb-Dicke regime, so that we can access the atoms' motional degree of freedom optically. The anharmonicity of the trapping potential and the decay we engineer restricts the dynamics to the two lowest motional bands, realizing an effective spin-$\frac{1}{2}$ system. We show engineer the Hamiltonian for a XXZ chain in a tunable transverse magnetic field and how to use far-detuned couplings to two internal atomic levels to obtain effective decay of the spin-$\frac{1}{2}$ in the internal ground state (see Fig. 3.7).

In the second part, we highlight a peculiar feature of the steady-state diagram for small spin chains: in the limit of weak dissipation, abrupt changes of steady-state expectation values for certain critical values of the system parameters are observed. We explain this feature by relating it to degeneracy of the system Hamiltonian and derive a sufficient condition for the occurrence of sharp peaks at critical system parameters, see Fig. 3.8. This shows that in dissipative systems spectral properties of the operative Hamiltonian can be accessible even far from the ground state.

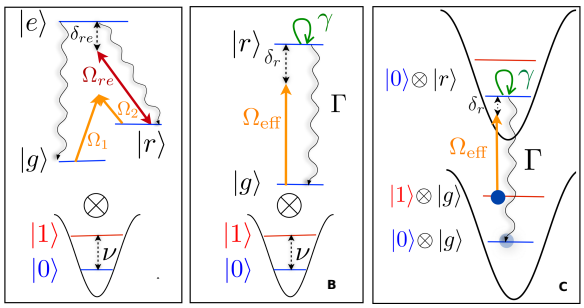

Fig. 3.7: Engineering effective decay in the ground-state subspace. (A) detuned two-photon transition between two ground states g, r combined with detuned coupling of r to spontaneously decaying level e. Eliminating the fast, detuned e yields an effective decay of r with tunable rates γ, Γ, depicted in (B). Tuning the effective driving on resonance with the red phonon sideband leads to the effective cooling dynamics in the ground state (C).

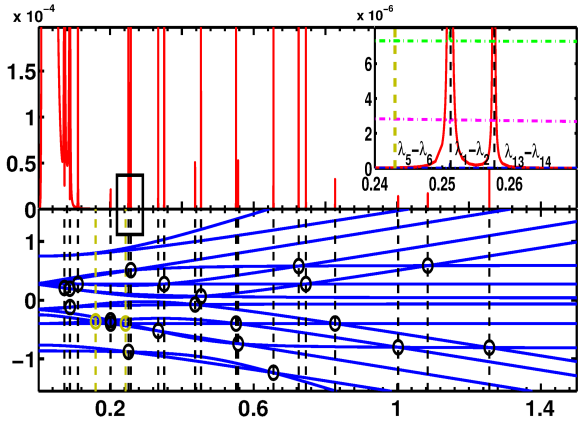

Fig. 3.8: Degeneracies in the Hamiltonian are accompanied by rapid changes in the steady state. Depicted is the infidelity $1-F(\rho_s(B), \rho_s(B+\delta B))$ of the steady state at magnetic field B with the that at $B+\delta B$, cf. [G:24]. The inset resolves the the peak around 0.25 (black box).

4 QIP with Gaussian States and Channels

4.1 Introduction

Quantum systems with infinite-dimensional Hilbert space supporting observables with continuous spectrum ("continuous variables"(CV)) were a something of a late-comer in QIP. They were first discussed in the context of quantum teleportation [254, 28], where they gave rise to the first demonstration of *deterministic* or *unconditional* teleportation [87]. All previous demonstration using two-qubit entangled states realized with single photons worked only probabilistically, since no full Bell-state analyzer can be built from purely linear-optics elements [37]. There are excellent and extensive recent reviews on Gaussian states and QIP [29, 260, 261], hence this introduction will be very brief.

The states of modes of the electromagnetic field are best described using the symmetric Fock space. Among the states in this space, the family of *Gaussian* (or *quasifree* [195]) states plays a special role.

Mathematically, these states are fully characterized by the first and second moments (the *displacement vector* and the *covariance matrix* (CM)) of the field quadrature operators (with position-momentum-like commutation relations). Each pair of canonically conjugate operators X_j, P_j defines a *mode* and we consider only systems consisting of finitely many modes in the following. Thus a simple finite description exists although the states are defined on an infinite-dimensional Hilbert space. This simple description is related to the states' description on "phase space", a $2N$ dimensional symplectic space to which almost all questions regarding Gaussian states and their transformations can be translated [270] and which is the starting point for the "canonical quantization" of linear classical systems.

From the practical point of view, most of the readily prepared states in quantum optical experiments (vacuum, coherent, thermal states) are in this class. Crucially, also the (two-mode) squeezed states that are central to the teleportation protocol belong to the Gaussian family. This reflects the fact that all these states can be prepared starting with a simple initial state (such as the vacuum) by applying only standard optical elements (beam splitters, interferometers, phase plates, squeezers) and discarding modes. In fact, the set of Gaussian states is *invariant* under these operations and under an important class of measurements (homodyne or heterodyne measurements).

Moreover, Gaussian states also naturally arise in material systems both from mechanical degrees of freedom [121, 221, 198] and from central limit arguments [55, 195]: large ensembles of independent, identically prepared quantum systems can be readily described by Gaussian quantum states. This has been most extensively used in the QIP context for atomic vapors [103] where continuous-variable quantum information has been readily exchanged between optical and atomic degrees of freedom. This Thesis provides yet another example, namely the nuclear spin ensembles in the Holstein-Primakoff approximation [114], cf., e.g. [G:17, G:18].

The Gaussian setting is of especial interest from the perspective of quantum communication, since the Gaussian channels are arguably the practically most important class of channels: quantum information is almost invariably sent using photons (using optical fibers, free space, or, in the microwave range, via superconducting transmission lines (part of the quantum computing architecture discussed in, e.g., [223]). To a excellent approximations the corresponding channels, including the perfect, the lossy, and the amplification channel fall in the class of Gaussian-preserving quantum operations ("Gaussian operations") [76, 261]. Therefore, large parts of quantum communication protocols can be entirely formulated in Gaussian terms.

In addition to the transmission in space, bosonic channels also play a major role for "transmission in time", i.e., in *quantum memories*. Several of the most advanced light-matter interfaces [103] make use of atomic ensembles to store photonic quantum information in collective atomic degrees of freedom which are in turn well described by bosonic modes. The quantum capacity of the corresponding channel is the adequate figure of merit for such devices.

The entanglement properties of multipartite Gaussian states and the capabilities and limitations of Gaussian operations for QIP tasks have been widely explored (see [261] for a very recent review). Most notable is maybe the fact that the Gaussian setting alone does not allow for entanglement distillation and hence neither for quantum error correction. On the other hand, it was shown that for cryptography, the Gaussian setting is enough, i.e., when using Gaussian states for quantum key distribution, the most general quantum operations do not provide a better attack than Gaussian operations only [208].

Despite steady progress, many quantitative and qualitative questions in QIP remain open even in the Gaussian setting. Most prominent here are questions concerning the capacity of Gaussian quantum channels – both for the transmission of classical or of quantum information. In particular, it is a long-standing and still open conjecture that the classical capacity of Gaussian channels can be attained by Gaussian input states. Until now, it has been proved only for the (important) case of the lossy channel [96].

The contribution of this Thesis to the field of Gaussian QIP is twofold, addressing the entanglement properties of Gaussian states and the capacities of Gaussian channels.

4.2 Extremality of Gaussian States

In [G:4], reprinted on p. 242ff, we provide a novel characterization of multipartite Gaussian states by an extremality property with respect to a class of functionals that contains, in particular, certain entanglement measures. This result implies not only that Gaussian states are the least entangled (e.g., in terms of "distillable entanglement") among all states with the same second moments, but can also help to show that Gaussian states are optimal for certain communication tasks. Our result based on a general method, which exploits the central limit theorem as a active and local *Gaussification* operation. Besides adding to previously known extremal characterizations of Gaussian states (e.g., those with the highest entropy for given second moments) it may also used as a justification of the frequently made Gaussian approximation to general quantum states (as it excludes an overestimation of entanglement [1], even in cases where the actual state is highly non-Gaussian.

[1] At least for certain standard measures of this quantity.

Another important application has been obtained in quantum cryptography, proving the optimality of the Gaussian attack, as was already mentioned [208]. Further applications can be found regarding channel capacities.

4.3 Quantum Capacities of Gaussian Channels

This leads to the second result presented here, namely the determination of the quantum capacity of certain Gaussian quantum channels. In [G:7], reprinted on p. 246ff, the task is to use Gaussian channels (completely positive maps preserving the Gaussian character of all input states) to transmit quantum information. The quantum capacity $Q(T)$ of a channel T is the asymptotic rate at which quantum information can be transmitted for many parallel uses of the channel. In general, Q is given by the regularization of the highly non-additive coherent information $J(\rho, T)$ and no simple way to compute the quantum capacity of (even finite-dimensional) channels is known.

We prove two results: First, given an arbitrary quantum channel T we construct a Gaussian channel that lower-bounds its quantum capacity. To this end consider the state ρ_T obtained by letting T act on an entangled state. There is a unique Gaussian state $\mathcal{G}(\rho_T)$ with the same first and second moments. The lower bound is given by the teleportation channel, using a $\mathcal{G}(\rho_T)$ as the entangled resource. That it is a lower bound follows since the quantum capacity of T is not smaller than the one-way distillable entanglement in ρ_T (Q is not increased by a classical side-channel) which, by the result of the previous section is lower-bounded by the same quantity computed for $\mathcal{G}(\rho_T)$. Using the teleportation channel T_G provided by $\mathcal{G}(\rho_T)$ is one (but not necessarily the best) way to distill the state, hence

$$Q(T) \geq D_{\leftarrow}(\rho_T) \geq D_{\leftarrow}(\mathcal{G}(\rho_T)) \geq Q(T_G). \tag{4.1}$$

Second, building on previous results [64] that show that for *degradable* channels (i.e. channels, from whose output the output of the complementary channel can be obtained) the coherent information $J(\rho, T)$ can be expressed in terms of a conditional entropy. The latter is known to be strongly subadditive and can therefore be shown to be maximized for Gaussian states by the argument of [G:4]. This implies that the quantum capacity is additive for Gaussian channels

$$Q\big(\otimes_i T_i\big) = \sum_i \sup_{\rho_G} J\big(\rho_G, T_i\big) \tag{4.2}$$

and can be computed by maximizing the righthand side over Gaussian states; as an example we provide a simple formula of the quantum capacity of the attenuation and amplification channels. We conclude by providing a necessary and sufficient criterion for degradability Gaussian channels and show that generically, Gaussian channels are neither degradable nor antidegradable.

An especially striking example of the non-additivity of quantum capacity is *super-activation* [240]: here, two quantum channels that have each *zero* quantum capacity (i.e., no quantum information whatsoever can be transmitted no matter how many times the channel is used in parallel) are combined into a channel with finite quantum capacity. This effect, first derived for finite-dimensional systems, has also been shown to occur for Gaussian channels [239]. The known examples for Gaussian superactivation require a large amount of squeezing. We address the question whether that is necessary and provide a partial result towards a "yes" answer to this question. All presently know examples of superactivation combine two channels that fail to have quantum capacity for two

very different reasons, namely channels that are entanglement-breaking (or, equivalently [113], which have a symmetric extension, i.e. which provide two identical outputs and thus would violate the no-cloning theorem if they had finite quantum capacity) and "ppt-channels" that can produce only output states that have positive partial transpose. In [G:19], reprinted on p. 250ff, we show that for this type of superactivation, squeezing is indeed needed in the Gaussian context, since without squeezing the ppt channel would also have a symmetric extension and therefore be unable to activate another symmetric-extension channel. Whether there are other way to achieve superactivation (or even other Gaussian channels with zero quantum capacity [238]) remains an interesting open problem.

4.4 Pairing of Fermionic States

Finally, we include in this Part a result that is not concerned with bosonic Gaussian states but rather uses concepts and methods developed in this context and applies them to states describing *fermionic* states (quasifree or general) instead. A central notion for fermions is *pairing* which is prototypically realized in the BCS states of superconductivity. Motivated by a controversy on how to certify the presence of pairing in experimentally prepared states [190, 289, 191] we attempt to clarify the matter in [G:10], reprinted on p. 255ff, by proposing a clear mathematical definition of pairing intended to capture its two-particle nature and to allow a systematic study of the set of paired states and its properties.

Since pairing is a correlation between fermions, totally uncorrelated states (Slater rank 1 [74]) are certainly not paired. Moreover, the property should be independent of our choice of (single-particle) basis. The two-particle nature of pairing then leads us to define a state as *paired* if its expectation values for two-particle observables (represented by hermitian elements in the linear hull of operators containing no more than two creation and two annihilation operators) cannot be reproduced by a separable state. We show that BCS state are indeed paired according to this definition.

We then exploit that definition to obtain pairing criteria and to quantify pairing. For Gaussian (quasifree) states a simple necessary and sufficient condition is obtained. For these states, pairing can (loosely) be seen as the analog of (bosonic) squeezing in the fermionic setting.

For the general case, we derive a family of *pairing witnesses* (observables that have positive expectation value for all unpaired states, but that attain a negative expectation value for some states which are thus certified as paired), which, in particular, can be used to prove all BCS states as paired.

We conclude by showing that pairing can be exploited for enhanced interferometry / phase estimation and introduce a pairing measure that allows to quantify this resource-character of paired states.

5 Conclusions and Outlook

In the preceding Chapters we have provided background and context to and an extended summary of the publications comprising this Thesis, which are reprinted in the subsequent Chapter.

We have seen that QIP using spins in quantum dots and other nanostructures has made great progress as a quantum computing in recent years and that the nuclear spin environment which is almost inevitably present in these systems can now be controlled to such an extent that its inclusion as a useful agent for QIP purposes becomes feasible. We presented state preparation procedures (by dissipation or measurement) and proposed QIP protocols that exploit the long nuclear coherence time for quantum register or a light-matter interface.
At the same time, these investigations revealed an interesting dissipative quantum many-body dynamics that lead us to the study of the dissipative central spin model as a paradigmatic open quantum system for the study of dissipative phase transitions. We showed that hyperfine interaction in a QD could allow the observation of superradiant dynamics and first and second order phase transitions. This suggested a relation of DPTs to spectral (degeneracy) properties of the operative Liouvillian which we studied for the central spin model and 1d spin chains.
Turning to quantum information theory, we focused on Gaussian states and operations which are central for (optical) communication. We proved an entanglement-related extremality property of Gaussian states which is useful for security and optimality proofs in communication protocols and we used it to obtain the quantum capacity of certain Gaussian channels (and general lower bounds).

Let us conclude with some forward looking remarks.

Thanks to state engineering and dynamical decoupling, the interaction with nuclear spins is no longer the main source of decoherence in QD but is beginning to be put to good use for gate implementations. In order to go further and involve the nuclei coherently in QIP, nuclear state preparation needs to be enhanced beyond the current 60%-80% polarization.

It would be highly interesting to explore the limits of DNP via the QD electron spin and see whether it is possible to approach the fully polarized state. At some point the nuclear interactions may no longer be neglected, and dynamical decoupling techniques may be needed to suppress them. Besides the QIP application, interesting physics may become accessible when studying the dynamics of the mesoscopic nuclear spin system under the influence of direct and mediated dipolar coupling [234].

Dissipative state preparation has been a fruitful approach in quantum optics and can be applicable in the solid-state setting as well. Going beyond spin-squeezing [214, 129] it would be interesting to exploit ideas from quantum optics [150, 257] to entangle distant quantum dots possible exploiting the recently demonstrated coherent (electron) transport [276].

Also apart from QIP, the dissipative dynamics of the QD central spin system holds plenty of interest. Can the DPT obtained in the simple homogeneous model system be observed in realistic inhomogeneous systems? Can the model be used to explain the observation of anomalous Hanle effect (including build-up and abrupt collapse of a transversal Overhauser field) observed in [152]? More generally, can a theory of DPTs be developed, that gives a spectral condition for their occurrence and classification? Is the concept of universality applicable to the dissipative case and what are the corresponding classes and their relation to those occurring in QPTs?

In the field of Gaussian QIP, several hard, quantitative questions concerning channel capacities and entanglement measures remain open, most prominently the calculation of the classical capacity of Gaussian channels.
The characterization of the zero-quantum-capacity Gaussian channels would be interesting, in particular with regard to the possibility to discover new examples of superactivation.
Computation of the entanglement of formation for states beyond the symmetric two-mode states would be interesting in itself, especially the question if it is additive. While the existence for which $E_F[\rho\otimes\rho] < 2E_F(\rho)$ is known due to Hastings' result [108], no examples have been constructed. While there is no particular reason to expect a Gaussian example, the fact E_F can be computed for some of these states [94] (and generalizations seem possible [122]) may give some hope to make progress.
Since the Gaussian toolbox is not enough for the most general QIP tasks, it is interesting to ask what is the best way to upgrade it by a non-Gaussian ingredient? Are there "magic states" as the ones that can complement Clifford circuit to fault-tolerant universal quantum computation circuits [30]? We know that single-photon states can do that [140] – but are they the best and can they be distilled by Gaussian means?

6 List of Publications

[G:1] J. M. Taylor, G. Giedke, H. Christ, B. Paredes, J. I. Cirac, P. Zoller, M. D. Lukin, and A. Imamoğlu, *Quantum information processing using localized ensembles of nuclear spins*. unpublished (2004), `cond-mat/0407640`.

[G:2] G. Giedke, J. M. Taylor, D. D'Alessandro, M. D. Lukin, and A. Imamoğlu, *Quantum measurement of a mesoscopic spin ensemble*. Phys. Rev. A **74**, 032316 (2006), `quant-ph/0508144`.

[G:3] D. Stepanenko, G. Burkard, G. Giedke, and A. Imamoğlu, *Enhancement of electron spin coherence by optical preparation of nuclear spins*. Phys. Rev. Lett. **96**, 136401 (2006), `cond-mat/0512362`.

[G:4] M. M. Wolf, G. Giedke, and J. I. Cirac, *Extremality of Gaussian quantum states*. Phys. Rev. Lett. **96**, 080502 (2006), `quant-ph/0509154`.

[G:5] H. Christ, J. I. Cirac, and G. Giedke, *Quantum description of nuclear spin cooling in a quantum dot*. Phys. Rev. B **75**, 155324 (2007), `cond-mat/0611438`.

[G:6] M. França Santos, G. Giedke, and E. Solano, *Noise-free measurement of harmonic oscillators with instantaneous interactions*. Phys. Rev. Lett. **98**, 020401 (2007), `quant-ph/0606004`.

[G:7] M. M. Wolf, D. Pérez-García, and G. Giedke, *Quantum capacities of bosonic channels*. Phys. Rev. Lett. **98**, 130501 (2007), `quant-ph/0606132`.

[G:8] H. Christ, J. I. Cirac, and G. Giedke, *Entanglement generation via a completely mixed nuclear spin bath*. Phys. Rev. B **78**, 125314 (2008), `arXiv:0710.4120`.

[G:9] H. Christ, J. I. Cirac, and G. Giedke, *Nuclear spin polarization in quantum dots-the homogeneous limit*. Solid State Sciences **11(5)**, 965 (2009).

[G:10] C. V. Kraus, M. M. Wolf, J. I. Cirac, and G. Giedke, *Pairing in fermionic systems: A quantum information perspective*. Phys. Rev. A **79**, 012306 (2009), `arXiv:0810.4772`.

[G:11] M. Issler, E. Kessler, G. Giedke, S. Yelin, I. Cirac, M. Lukin, and A. Imamoğlu, *Nuclear spin cooling using Overhauser field selective coherent population trapping*. Phys. Rev. Lett. **105**, 267202 (2010), `arXiv:1008.3507`.

[G:12] M. Issler, E. Kessler, G. Giedke, S. Yelin, I. Cirac, M. Lukin, and A. Imamoğlu, *Supplement: Nuclear spin cooling using Overhauser field selective coherent population trapping*. Phys. Rev. Lett. **105**, 267202 (supp) (2010), `arXiv:1008.3507`.

[G:13] E. M. Kessler, S. Yelin, M. D. Lukin, J. I. Cirac, and G. Giedke, *Optical superradiance from nuclear spin environment of single photon emitters*. Phys. Rev. Lett. **104**, 143601 (2010), `arXiv:1002.1244`.

[G:14] F. Klotz, V. Jovanov, J. Kierig, E. C. Clark, M. Bichler, G. Abstreiter, M. S. Brandt, J. J. Finley, H. Schwager, and G. Giedke, *Asymmetric optical nuclear spin pumping in a single uncharged quantum dot*. Phys. Rev. B **82**, 121307(R) (2010), arXiv:1007.2145.

[G:15] A. E. B. Nielsen, C. A. Muschik, G. Giedke, and K. G. H. Vollbrecht, *Quantum state engineering, purification, and number resolved photon detection with high finesse optical cavities*. Phys. Rev. A **81**, 043832 (2010), arXiv:1002.0127.

[G:16] H. Schwager, J. I. Cirac, and G. Giedke, *Interfacing nuclear spins in quantum dots to cavity or traveling-wave fields*. New J. Phys. **12**, 043026 (2010), arXiv:0903.1727.

[G:17] H. Schwager, J. I. Cirac, and G. Giedke, *A quantum interface between light and nuclear spins in quantum dots*. Phys. Rev. B **81**, 045309 (2010), arXiv:0810.4488.

[G:18] E. M. Kessler, G. Giedke, A. Imamoğlu, S. F. Yelin, M. D. Lukin, and J. I. Cirac, *Dissipative phase transition in central spin systems*. Phys. Rev. A **86**, 012116 (2012), arXiv:1205.3341.

[G:19] D. Lercher, G. Giedke, and M. M. Wolf, *Super-activation for Gaussian channels requires squeezing*. (accepted as contribution to TQC'13) (2012), arXiv:1209.5574.

[G:20] M. J. A. Schuetz, E. M. Kessler, J. I. Cirac, and G. Giedke, *Superradiance-like electron transport through a quantum dot*. Phys. Rev. B **86**, 085322 (2012), arXiv:1206.2573.

[G:21] N. Y. Yao, L. Jiang, A. V. Gorshkov, P. C. Maurer, G. Giedke, J. I. Cirac, and M. D. Lukin, *Scalable architecture for a room temperature solid-state quantum information processor*. Nature Comm. **3**, 800 (2012), arXiv:1012.2864.

[G:22] B. Horstmann, J. I. Cirac, and G. Giedke, *Dissipative dynamics and phase transitions in fermionic systems*. Phys. Rev. A **87**, 012108 (2013), arXiv:1207.1653.

[G:23] G. Petersen, E. A. Hoffmann, D. Schuh, W. Wegscheider, G. Giedke, and S. Ludwig, *Large nuclear spin polarization in gate-defined quantum dots using a single-domain nanomagnet*. Phys. Rev. Lett. p. (accepted) (2013), arxiv:1212.3140.

[G:24] H. Schwager, J. I. Cirac, and G. Giedke, *Dissipative spin chains: Implementation with cold atoms and steady-state properties*. Phys. Rev. A **87**, 022110 (2013), arXiv:1207.5768.

Acknowledgments

The work summarized in this Thesis has been the fruit of many long and valuable collaborations with friends and colleagues in many different places. It is a very welcome opportunity and great pleasure to thank them here for their insight, inspiration, patience, and comradeship, which were instrumental for the success (such as it is) of this work.

First of all, I thank Ignacio Cirac, Director of the MPI of Quantum Optics and head of the MPQ Theory Division where most of this work has been done. It has been a huge privilege and very rewarding scientific experience to work with him over many years. It is hard to overstate how much I have profited from his deep and broad knowledge of physics, from the many insightful and focused discussions with him, from the freedom he provides to pursue one's own idea, and from his encouragement, good advice, and support, and, last but not least, from and the excellent group of people (both scientifically and personally) that he has assembled and maintained at MPQ. I am deeply grateful for the opportunity to be part of this team; this work would not have been possible elsewhere.

Much of the work in this Thesis has been done in collaboration with a number of great Diploma and PhD students that I had the good fortune to work with. Henning Christ, Heike Schwager, Eric Kessler, and Martin Schütz worked on different aspects of the physics of nuclear spins in quantum dots, Heike, Eric, and Martin as well as Birger Horstmann studied different aspects of phase transitions in open quantum systems, while Christina Kraus and Eliška Greplová investigated quantum informational aspects of fermionic systems. While their scientific contribution is evident from the authorship of the papers included in this Thesis, I would like to thank them here especially for the skill, curiosity, enthusiasm, and endurance that they brought to their work. With such students, it is easy and fun to be a Thesis (co-)advisor. It was (and is) great to work with you!

Many thanks to the senior collaborators on the different projects, especially to Michael Wolf, from whose mathematical insight and precision I learned a lot (not only on Gaussian quantum information), to Ataç Imamoğlu, who taught me much about quantum dots and who first made me aware of the fascinating physics of nuclear spins in quantum dots, and to Misha Lukin for many visits (in both directions) and especially his insight on NV centers.

The Munich area is great for doing quantum physics, and I am glad and thankful that I had the opportunity to collaborate with colleagues from experimental physics at TUM and LMU within the Sonderforschungsbereich 631: in particular, many thanks to John Finley and Stefan Ludwig and their co-workers Florian Klotz, Gunnar Petersen and Eric Hoffmann from all of whom I learned much about DNP experiments.

The MPQ Theory group has been an highly inspiring and stimulating place to work: I am grateful to Miguel, Mari Carmen, Gemma, Oriol, Matteo, Raúl, Maarten, Kike, Kalle, Christine, Johannes, Tao, Yue, Juanjo, Diego, and many others (including the group members already mentioned before) for uncounted talks, scientific and not-so-scientific discussions, fun group outings, and generally making this an enjoyable and rewarding place to work at.

That it was always easy to focus on the science was due in large part to the great dedication and helpfulness of the secretaries of the Theory Division – Renate, Verena, Veronika, and Andrea you all did a terrific job, thank you very much.

For proper balance, I am always glad to mix some sports with the science, and also like to give thanks to the many colleagues with which kept me running on the track or football field, especially the SV MPQ Quantenkick, the MPQ Running Team, the Lauftreff Garching and the Benasque Quantum Information Football Team (still looking for that first victory against the locals ;-).

Finally, I would like to thank my parents, sister, and brothers for their steady and continuing support. It is great to be embedded in such a family! In particular, I acknowledge their gentle, but persistent reminders about this Thesis when I preferred to do other things rather than writing it up.

7 Selected Reprints

PHYSICAL REVIEW B **75**, 155324 (2007)

Quantum description of nuclear spin cooling in a quantum dot

H. Christ, J. I. Cirac, and G. Giedke
Max-Planck-Institut für Quantenoptik, Hans-Kopfermann-Strasse 1, D-85748 Garching, Germany
(Received 1 December 2006; revised manuscript received 1 February 2007; published 18 April 2007)

We study theoretically the cooling of an ensemble of nuclear spins coupled to the spin of a localized electron in a quantum dot. We obtain a master equation for the state of the nuclear spins interacting with a sequence of polarized electrons that allows us to study quantitatively the cooling process including the effect of nuclear spin coherences, which can lead to "dark states" of the nuclear system in which further cooling is inhibited. We show that the inhomogeneous Knight field mitigates this effect strongly and that the remaining dark-state limitations can be overcome by very few shifts of the electron wave function, allowing for cooling far beyond the dark-state limit. Numerical integration of the master equation indicates that polarizations larger than 90% can be achieved within a millisecond time scale.

DOI: 10.1103/PhysRevB.75.155324 PACS number(s): 71.70.Jp, 73.21.La

I. INTRODUCTION

Nuclear spins are one of the best studied quantum systems, and highly developed techniques such as NMR have allowed detailed studies of the properties and dynamics of molecular and solid-state systems.[1] Due to their very long decoherence time, nuclear spins (and hyperfine levels) have also played a central role in many approaches to the implementation of quantum information processing (QIP).[2–6]

Recently, the localized ensemble of nuclear spins in a quantum dot (QD) has received special attention in the context of QIP with electron spins in QDs: the nuclei couple via a Fermi contact interaction to the electron spin[7] and, as predicted by theory,[8–12] have been shown in recent experiments to constitute the major source of decoherence of electron spin qubits in some of the most promising QD-based implementations.[13,14] The vice of this strong coupling is turned into a virtue when the electron is used to manipulate the state of the nuclear ensemble. This has long been exploited in dynamical nuclear polarization[15–18] (DNP) in bulk systems and has afforded many insights into the spin dynamics in solids.[17,19]

DNP *in quantum dots* has come into focus more recently in the context of QIP, since strongly polarized nuclei could lead to much longer electron spin dephasing times,[12] provide strong local magnetic field gradients required in quantum information proposals,[20,21] and even allow one to utilize the nuclear spins themselves as long-lived quantum memory.[22,23] More generally, a highly polarized nuclear spin ensemble in a QD provides, together with the electron spin, a strongly coupled, well-isolated mesoscopic quantum system with close similarities to the Jaynes-Cummings model in quantum optics,[23–25] with the fully polarized state corresponding to the vacuum in all cavity modes. Thus ultrahigh DNP in QDs may open the door to realize cavity-QED in quantum dots and implement tasks such as state engineering.

Experimentally, significant nuclear polarization in self-assembled QDs has been achieved.[26–30] However, the degree of polarization in these experiments was still too low to improve electron spin coherence times considerably and still far from the ground state.

Theoretically, cooling dynamics has mostly been considered in the spin temperature approximation,[1,17,31,32] in which coherences among the nuclear spins are neglected. This is appropriate if, as in bulk or quantum well systems, there is no fixed electron wave function and many motional states are involved, or if the nuclear dephasing rate is large. In quantum dots, however, the nuclei interact collectively with an electron in the motional ground state of the QD and the higher motional levels are far detuned. Therefore the coupling strength of each nucleus is fixed, and well-defined phase relationships between the nuclear spins can build up, necessitating a quantum treatment of the process, which was first pointed out by Imamoğlu *et al.*[33] who showed that the cooling process can be inhibited by so-called dark states, which trap excitations and potentially result in serious constraints on the achievable polarizations. While it was pointed out in Ref. 33 that inhomogeneities (either inherent in the system or introduced actively by modulating the wave function of the electron) can mitigate this problem, these ideas were put to numerical test only in very small one-dimensional (1D) systems of ten nuclear spins. However, the effect of inhomogeneities is expected to be reduced for realistic larger systems,[22] and thus limitations due to dark states are more severe.[60]

We consider the cooling of N nuclear spins in a QD through interaction with polarized electrons. One cooling cycle consists of (a) initialization of the electron spin in a well-defined direction and (b) evolution of the combined system for a "short" time. In this way the electron spin acts effectively as a $T=0$ reservoir for the nuclear spin bath and pumps excitation out of it.

We derive in a consistent manner a full quantum model of this process, which allows us to numerically study particle numbers of up to $N\sim 10^3$. We show that a sufficient inhomogeneity of the couplings leads to a dephasing of nuclear spin states and thus limitations due to dark states are partially lifted. We demonstrate that enhanced cooling protocols involving only a few ($\leqslant 10$) modulations of the electron wave function allow one to fully overcome these limitations, indicating that Overhauser fields above 90% of the maximal value can be created within the nuclear spin diffusion time.

The paper is organized as follows: In Sec. II we present the generic cooling protocol and analyze its performance in Sec. III; the applicability of the scheme to some specific physical systems is studied in Sec. IV.

 ©2007 The American Physical Society

II. COOLING SCHEME

Interaction. The Fermi contact interaction between an (s-type conduction band) electron spin $\mathbf{S}$ and the spins $\mathbf{I}_i$ of the lattice nuclei leads to a Heisenberg-like coupling $A\alpha_i\mathbf{I}_i\cdot\mathbf{S}$ to the nuclear spin at lattice site i, where A sets the overall strength of the hyperfine interaction and the factor $0<\alpha_i<1$ is determined by the probability to find the electron at site i and the gyromagnetic ratio of the ith nucleus.[7] In the presence of an external magnetic field B_{ext} we write the Hamiltonian of the spin system with the collective nuclear spin operators $A^\mu=\Sigma_i g_i I_i^\mu$ ($\mu=\pm,z$) as ($\hbar=1$)

$$H=\frac{g}{2}(A^+S^-+S^+A^-)+gA^zS^z+g^*\mu_B B_{\text{ext}}S^z, \tag{1}$$

where we have defined $g=A\sqrt{\Sigma_i\alpha_i^2}$ and $g_i=\alpha_i/\sqrt{\Sigma_i\alpha_i^2}$, such that $\Sigma_i g_i^2=1$, and denoted the electron g factor by g^* and the Bohr magneton by μ_B.

We do not consider the Zeeman energy of the nuclear spins, because for typical QDs it is much (10^3 times) smaller than the electron's Zeeman energy,[7] and similarly we neglect the even smaller dipolar interaction between the nuclei. The effects of these are briefly discussed at the end of Sec. III. Finally, we restrict the analysis to nuclear spins $I=1/2$ and one nuclear species only in this article.

The first part of the above Hamiltonian exchanges spin excitation between the electron and the nuclei, and it is this mechanism that is used to create polarization. The second part of the Hamiltonian constitutes a "quantum" magnetic field, the Overhauser field, for the electron spin generated by the nuclei.

The cooling scheme. We assume initially the electron spin to be pointing in the $-z$ direction $|\psi_e\rangle=|\downarrow\rangle$. In the absence of a magnetic field this initial state defines the axis of quantization. The cooling cycle we consider is an iteration between evolution with Hamiltonian, Eq. (1), and reinitialization of the electron to $|\downarrow\rangle$. The nuclei effectively "see" a large cold reservoir of electron spins, and the concatenated evolution of the nuclear spin density matrix becomes

$$\rho\to\cdots U_t\text{tr}_e[U_t(\rho\otimes|\downarrow\rangle\langle\downarrow|)U_t^\dagger]\otimes|\downarrow\rangle\langle\downarrow|U_t^\dagger\cdots. \tag{2}$$

Here $U_t=\exp(-iHt)$ is the time evolution operator, tr_e denotes the trace over the electron, and here and in the following ρ will denote the state of the nuclear spin system only. Spin-polarized currents or optical pumping with polarized light give rise to a polarized electron bath, but also the fast electrical control available in double QDs[13] allows for the creation of nuclear spin polarization without the need for preprepared electrons, as we will detail in the last section of this article.

Considering small times for the evolution in each individual step of the cooling protocol, we expand the time evolution operators in Eq. (2) to second order. The standard deviation of the $A^{\pm,z}$ terms scales as $A\sqrt{\Sigma_i\alpha_i^2}=g\sim\mathcal{O}(A/\sqrt{N})$ for the initially totally mixed nuclear spin state, and thus for $\Delta t\ll g^{-1}\sim\sqrt{N}/A$ we neglect higher orders. The readily obtained master equation

$$\rho_{t+\Delta t}-\rho_t=i\frac{g\Delta t}{2}[A^z,\rho_t]-\frac{g^2(\Delta t)^2}{8}[A^z,[A^z,\rho_t]]-\frac{g^2(\Delta t)^2}{8}(A^+A^-\rho_t+\rho_tA^+A^--2A^-\rho_tA^+) \tag{3}$$

contains a Hamiltonian part arising from the Overhauser field and a contribution in Lindblad form. The latter generates the nuclear spin polarization and has been studied in the limit of homogeneous coupling constants in the context of superradiance.[34–36]

As polarization builds up and $g\langle A^z\rangle\gg A/\sqrt{N}$ the Hamiltonian terms on the right-hand side of Eq. (3) may become large (for fixed time step Δt). To preserve the validity of the master equation one can either reduce the interaction time $\Delta t<A^{-1}$ or assume that the Overhauser field $\langle A^z\rangle$ is approximately compensated by an applied magnetic field, so that $\langle gA^z-g^*\mu_B B_{\text{ext}}\rangle\Delta t\ll 1$ for all times. In the latter case Δt is short enough to ensure quasiresonant hyperfine flips despite the random detunings stemming from the fluctuating Overhauser field and at the same time large enough to guarantee a fast cooling rate.[61] This is the situation we investigate in the following. Without retuning the system in this manner the polarization rate becomes dependent on the polarization itself and the emerging nonlinearities give rise to the bistability effects observed in Refs. 14, 30, and 37–41 and limit the final polarization.

Homogeneous coupling. Before we discuss general inhomogeneous couplings, consider for a moment the homogeneous case $\alpha_i\propto 1/N$ as a demonstration of some interesting features of the above master equation. In this case, the operators $A_{\pm,z}$ appearing in Eq. (3) form a spin algebra $I_{\pm,z}$ and the collective angular momentum states (Dicke states) $|I,m_I,\beta\rangle$ provide an efficient description of the system dynamics:[42,22] the total spin quantum number I is not changed by $A_{\pm,z}$ and the effect of Eq. (3) is simply to lower [at an (I,m_I)-dependent rate] the I_z quantum number. If $m_I=-I$ is reached, the system cannot be cooled any further, even if (for $I\ll N/2$) it is far from being fully polarized. These dark states[22,33] are a consequence of the collective interaction, Eq. (1). Thus spin excitations are trapped and cooling to the ground state prevented. We evaluate the steady-state polarization $\langle I^z\rangle_{\text{ss}}=\langle\Sigma_i I_i^z/\sqrt{N}\rangle_{\text{ss}}$ as

$$\frac{\langle I^z\rangle_{\text{ss}}}{\langle I^z\rangle_0}=\frac{2}{2^N N}\sum_{I=0}^{N/2}I(2I+1)D_I=\sqrt{\frac{8}{\pi N}}+\mathcal{O}(1/N); \tag{4}$$

i.e., for a mesoscopic number of particles the obtained polarization is negligible. In the above equation $\langle I^z\rangle_0$ is the expectation value in the completely polarized state, $D_I=\binom{N}{N/2-I}-\binom{N}{N/2-I-1}$ is the degeneracy of the subspaces of different total angular momentum, and the last equality has been obtained by employing the Stirling formula.

Evolving the nuclei according to Eq. (3), we find the exact time evolution of the polarization as shown in Fig. 1. In these and the following simulations $g\Delta t=0.1$—i.e., $\Delta t=0.1g^{-1}\sim 0.1\sqrt{N}/A$. As expected the polarization decreases as $1/\sqrt{N}$ as N increases, which underlines the importance of the nuclear spin coherences. In particular this shows that an in-

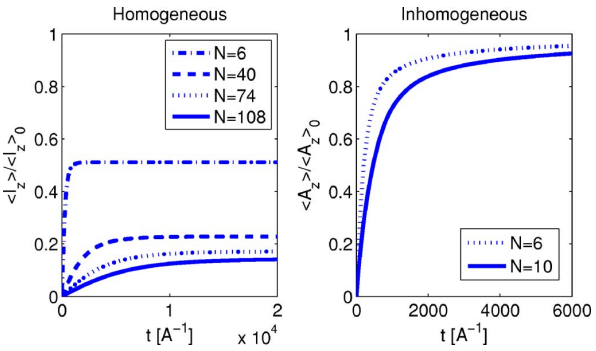

FIG. 1. (Color online) Exact polarization dynamics. Left: Homogeneous case, $g_j=1/\sqrt{N}$. Right: In the inhomogeneous case, $g_j \propto \exp(-(j-N/2-1/4)^2/w^2)$. The term 1/4 is added to account for asymmetry between electron wave function and the lattice and avoid symmetry effects for this small scale system.

coherent spin temperature description of the process would give even qualitatively wrong results. The time scale over which the steady state is reached is $\sim N/(g\Delta t A)$.

Inhomogeneous coupling. Consider now an inhomogeneous wave function. The results for the exact evolution of the quantity of interest, $\langle A^z\rangle$, are shown in Fig. 1. The coupling constants g_j in this example are taken from a 1D Gaussian distribution with width $N/4$.[62] The most important and striking feature is that in this situation almost complete polarization is obtained.

The reason that this is possible here is *not* that there are no dark states in the case of inhomogeneous coupling constants. On the contrary it has been shown that there exists a one-to-one mapping[22] from the familiar homogeneous dark states $(|I,-I,\beta\rangle$ in the Dicke basis) to their inhomogeneous counterparts, defined by $A^-|D\rangle=0$. The reason for obtaining high polarization beyond the homogeneous limit is the Hamiltonian part of the master equation (3). To illustrate this point, consider two spins with coupling constants $g_1 \neq g_2$. Then the dark state $|\Psi_D\rangle \propto g_2|\uparrow\downarrow\rangle - g_1|\downarrow\uparrow\rangle$ evolves due to the A^z term in Eq. (3) to $e^{i\delta_g t}g_2|\uparrow\downarrow\rangle - e^{-i\delta_g t}g_1|\downarrow\uparrow\rangle$, where δ_g is proportional to g_1-g_2. Obviously this state will become "bright" again after a time $\propto 1/|g_i-g_j|$ and $A^-|D\rangle \neq 0$. This process is first order and, as we will detail later, "delivers" coolable excitations sufficiently fast to maintain a high cooling rate.

III. POLARIZATION DYNAMICS

The polarization dynamics of the nuclear ensemble is governed by Eq. (3). While for homogeneous systems the collective angular momentum Dicke basis enables an efficient description of the problem, for realistic large and inhomogeneous systems more effort is required.

To study the evolution of the nuclear polarization, we are interested in the individual spin expectation values $\langle\sigma_i^+\sigma_i^-\rangle$. These depend, via Eq. (3), on all the elements of the covariance matrix

$$\gamma_{ij} = \langle\sigma_i^+\sigma_j^-\rangle,$$

which, in turn, depend on higher-order correlations as seen from the equations of motion

$$\frac{\Delta\gamma_{ij}}{\Delta t} = \xi_{ij}\gamma_{ij} - \kappa\sum_k g_k(-g_i\langle\sigma_k^+[\sigma_i^+,\sigma_i^-]\sigma_j^-\rangle + g_j\langle\sigma_i^+[\sigma_j^-,\sigma_j^+]\sigma_k^-\rangle), \quad (5)$$

where $\xi_{ij}=ig(g_j-g_i)/2-g^2\Delta t(g_j-g_i)^2/8$ and $\kappa=g^2\Delta t/8$ and the σ_i^μ refer to the Pauli matrices at site i.

The simultaneous solution of the ensuing hierarchy of equations is only feasible for very small particle numbers N, and further approximations are needed to treat the large systems of interest. We introduce several ways, labeled (i)–(v), of closing this set of equations and discuss their validity and implications in detail below.

In the strongest approximation (i) all coherences between different spins are neglected, yielding independent rate equations for each individual nuclear spin. This reproduces essentially the spin-temperature description commonly employed in the discussion of bulk DNP[1,17] (each subset of spins with identical coupling strengths g_i is assigned its own effective temperature). This approach cannot reproduce the quantum effects we want to study, but it can serve as a benchmark for how strongly these are influencing the cooling process.

The simplest approximations that take quantum coherences between nuclear spins into account close the hierarchy of equations at the level of second-order correlations. Our approximation (ii) is motivated by the generalized Holstein-Primakoff description,[43] which in lowest order treats the nuclei as bosonic modes $\sigma_i^- \to a_i$. The bosonic commutation relations $[a_i,a_j^\dagger]=\delta_{ij}$ yield a closed set of equations for the elements of the covariance matrix γ. The bosonic description is known to be accurate for highly polarized and moderately inhomogeneous systems[25] and allows one to bring results and intuition from quantum optics to bear in the spin system discussed here. Dark states are included in the form of the vacuum of the collective mode $b=\Sigma_i g_i a_i$ coupled to the electron in Eq. (1). For unpolarized systems (with on average 1/2 excitations per bosonic mode a_i), this description provides a lower bound on the performance of the cooling protocol, since in the absence of an inhomogeneous Knight field cooling is limited to $\mathcal{O}(1)$ excitations per mode rather than the $\mathcal{O}(\sqrt{N})$ coolable excitations expected at the beginning of the cooling process for spins; cf. Eq. (4). In the two limiting cases discussed so far, Eq. (5) simplifies to

$$\frac{\Delta\gamma_{ij}}{\Delta t} = \begin{cases} -2\kappa\delta_{ij}g_i^2\gamma_{ii} & \text{(i) spin temp.,} \\ \xi_{ij}\gamma_{ij} - \kappa\sum_k g_k(g_i\gamma_{kj}+g_j\gamma_{ik}) & \text{(ii) bosonic.} \end{cases}$$

One can take into account more aspects of the spin algebra by replacing some higher-order expectation values by lower orders using the properties of Pauli matrices $[\sigma_i^+,\sigma_i^-]=\sigma_i^z$ and $\sigma_i^z\sigma_i^\pm=\pm\sigma_i^\pm$, obtaining

$$\frac{\Delta\gamma_{ij}}{\Delta t} = \xi_{ij}\gamma_{ij} - \kappa\delta_{ij}\sum_k g_k(g_i\gamma_{kj}+g_j\gamma_{ik}) - \kappa(1-\delta_{ij})\Big(-\sum_{k\neq i} g_k g_i\langle\sigma_k^+\sigma_i^z\sigma_j^-\rangle + g_i^2\gamma_{ij} - \sum_{k\neq j} g_k g_j\langle\sigma_i^+\sigma_j^z\sigma_k^-\rangle + g_j^2\gamma_{ij}\Big). \quad (6)$$

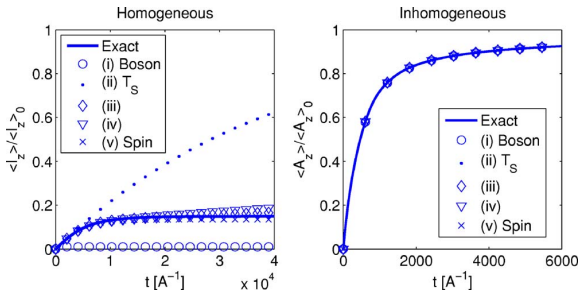

FIG. 2. (Color online) Comparison of different approximation schemes for the homogeneous situation with $N=100$ (left) and the case of Gaussian couplings (as in Fig. 1) and $N=10$ nuclear spins (right).

The remaining higher-order expectation values (now having distinct indices $i\neq j, j\neq k$) can be approximated in a Hartree-like way[44] (iii) or, having the bosonic limit in mind, by the Wick theorem (iv),

$$\frac{1}{2}\langle\sigma_k^+\sigma_i^z\sigma_j^-\rangle=\begin{cases}\left(\gamma_{ii}-\frac{1}{2}\right)\gamma_{kj} & \text{(iii)},\\ -\frac{1}{2}\gamma_{kj}+\gamma_{ki}\gamma_{ij}+\gamma_{kj}\gamma_{ii} & \text{(iv)}.\end{cases}$$

The fifth and final approximation scheme we invoke has been introduced in the context of superradiance as a Wick-type factorization, which takes into account the partly bosonic, partly fermionic properties of spin-1/2 operators.[36] In contrast to the last two factorization schemes, it does not rely on a distinction of cases. It is directly based on the exact equation (5) and approximates the three-operator-expectation values in the following way:

$$\frac{1}{2}\langle\sigma_k^+\sigma_i^z\sigma_j^-\rangle=-\frac{1}{2}\gamma_{kj}-\gamma_{ki}\gamma_{ij}+\gamma_{kj}\gamma_{ii}\quad\text{(v) "spin."}$$

Direct comparison of the approximation schemes (i)–(v) with the exact solution for both homogeneous and inhomogeneous couplings is shown in Fig. 2. In the homogeneous case the spin temperature description (i) is clearly qualitatively wrong, because it neglects correlations in the bath. The bosonic description (ii) captures the feature of dark states, but it overestimates their influence: Instead of $\sim\sqrt{N}$, only one excitation can be removed. The two schemes based on a distinction of cases, (iii) and (iv), give very good results initially, until roughly $\sqrt{N}$ spins have been flipped. Then, however, the polarization keeps increasing on a slow time scale and does not reach a steady state in the correct time. The (v) "spin" approximation gives very good results and gets both the polarization time scale and the finally obtained value of the polarization right within a few percent.

The comparison of the different approaches to the exact solution for inhomogeneous couplings is restricted to small particle numbers (see Fig. 2). In this regime all introduced approximation schemes reproduce the exact dynamics correctly. The reason for the good correspondence is the strong dephasing of dark states and generally coherences between nuclear spins for small inhomogeneous systems.

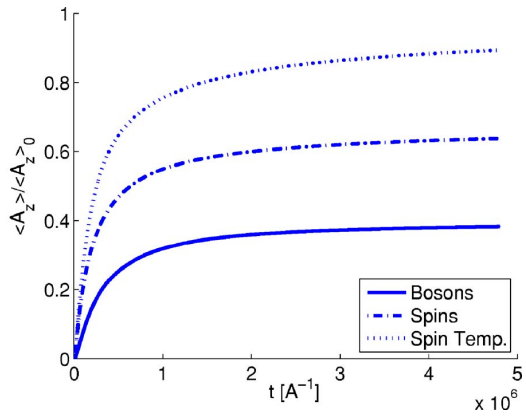

FIG. 3. (Color online) The polarization dynamics for $N=1000$ spins coupled with a 2D Gaussian wave function, which is shifted from the origin by $1/3$ in the x and y directions.

Using these approximations we present the polarization dynamics for $N=10^3$ spins coupled through a 2D Gaussian wave function in Fig. 3. For the data presented in this and the following figure, we considered the spins in a 2D square lattice geometry, with the lattice constant set to unity. The bosonic description displays the lowest final polarization and polarization rate (for the same reasons as in the homogeneous case) and is expected to give lower bounds on the performance on the polarization procedure. Of particular interest are the predictions of the (v)-"spin"-approximation scheme, because its good performance in the completely homogeneous situation gives us confidence that also partial homogeneities are correctly accounted for. The achieved polarizations of $\sim$60% in this setting show the importance of the intrinsic dephasing due to the inhomogeneity (homogeneous coupling would allow for $<5\%$ polarization). However, the intrinsic inhomogeneity alone does not allow for ultrahigh polarizations and we are thus led to investigate more sophisticated cooling schemes. As shown later, in these enhanced protocols all approximation schemes lead to the same conclusions.

To gain a better understanding of the presented phenomena in the inhomogeneous situation, we go to an interaction picture $\rho_I=U_0\rho U_0^\dagger$, with $U_0=\exp(-iA^z t/2)$, which shows very clearly the oscillating coherences between spins with $g_i\neq g_j$:

$$\frac{\Delta\rho_I}{\Delta t}=-\kappa\left[\sum_{ij}g_ig_je^{-ig(g_i-g_j)t/2}\sigma_i^+\sigma_j^-,\rho_I\right]_+ +2\kappa\sum_{ij}g_ig_je^{-ig(g_i-g_j)t/2}\sigma_j^-\rho_I\sigma_i^+. \quad (7)$$

In the rotating-wave approximation (RWA), the rotating terms ($g_i\neq g_j$) are neglected and in the absence of exact symmetries the above equation reduces to the spin temperature description. A partial rotating-wave approximation neglects only the coherences between spins with considerably differ-

ent coupling constants; i.e., the ratio between dephasing and polarization rate is required to be large $[4|g_i-g_j|/(g\Delta t g_i g_j) > 1]$. This procedure gives a block-diagonal Liouvillian which allows for the extension of the numerical studies to particle numbers up to $N=10^4$.

In the RWA we evaluate the buildup time τ_p for the polarization as the inverse of the weighted average of the individual spin decay times,

$$\tau_p = \left(\frac{\sum_i g_i \kappa_i}{\sum_i g_i}\right)^{-1} = \frac{4\sum_i g_i}{g(g\Delta t)\sum_i g_i^3} = \mathcal{O}\left(\frac{4N^{3/2}}{A(g\Delta t)}\right), \quad (8)$$

and find good agreement with the numerically obtained time scale to reach the steady state in all discussed schemes. For example, for the data presented in Fig. 3 we find times of 3.4×10^5 (spin temp.), 4.6×10^5 (bosonic), and 3.3×10^5 ("spin") in units of A^{-1} to reach $(1-e^{-1})\approx0.63$ of the quasi-steady-state Overhauser field. This agrees well with the analytical estimate $\tau_p\approx2.4\times10^5/A$, despite the differences in the final polarizations obtained in the different approximation schemes. This correspondence between the RWA-based estimate and the numerically obtained polarization times for the coherent evolution indicates that the inhomogeneous Knight field provides coolable excitations at a rate larger than the polarization rate, thus not slowing down the process.

When the inhomogeneity of the coupling is large enough to justify the rotating-wave approximation, each spin evolves with its own Liouvillian and the nuclei remain in a product state during the whole evolution. To keep the errors in the derivation of the master equation [due to higher-order terms of the expansion of the time evolution operators in Eq. (2)] small, it is sufficient to do so for each spin individually in this case. This allows a larger time step $\Delta t \ll (A\alpha_{\max})^{-1} = \mathcal{O}(N/A)$ in each cycle, and therefore the cooling rate can be significantly enhanced. The cooling time effectively scales only linearly in the particle number

$$\tilde{\tau}_p = \mathcal{O}\left(\frac{4N}{A(\Delta t A/N)}\right). \quad (9)$$

Taking $A=100\ \mu$eV~40 ps, a value typical for GaAs QDs, and 0.1 as the value for the terms $g\Delta t$ and $A/N\Delta t$ in the denominators of Eqs. (8) and (9), respectively, we find that approximately 4×10^3 and 3×10^5 spins can be cooled to more than 90% of the steady-state value $\langle A^z\rangle_{ss}$ within a millisecond.

We now study enhanced cooling protocols that lift the dark-state limitations and which rely solely on the ability to shift the center of the electron wave function. These shifts can be effected by applying dc gate voltages to the QD. After such a shift only very few spins will have the same coupling constants for *both* wave functions and therefore singletlike coherences are broken up. We confirm this expectation numerically as shown in Fig. 4 for some exemplarily chosen shifts of the electron wave function. The shifts range from a few lattice sites to roughly the width of the electron wave function. The timing of the shifts we have performed for obtaining the data presented in Fig. 4 can be inferred from the plots, as it is accompanied by a rapid increase in the cooling rate.

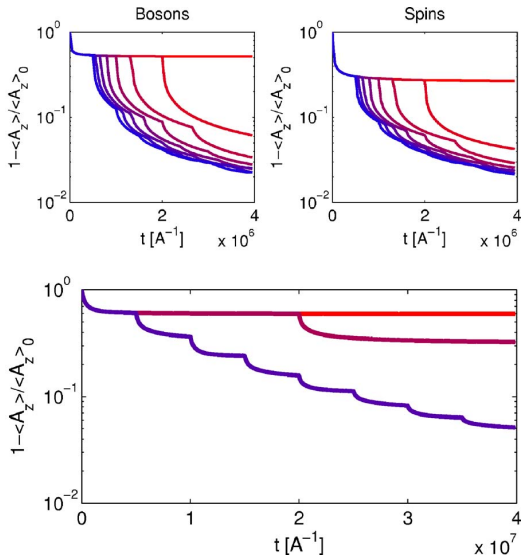

FIG. 4. (Color online) Polarization dynamics in the enhanced cooling protocol for $N=196$ (upper plots) and $N=1000$ (lower plot). In the upper plots approximation schemes (ii) (left) and (v) (right) have been invoked; the lower plot is based on the bosonic model and the partial rotating-wave approximation (see text). In all plots the different lines are representing cooling procedures with different numbers of mode changes. In the upper plots the randomly chosen Gaussian modes with width $w=N/4$ are defined by the centers $\{(1/3,1/3),(1.35,-0.81),(0.32,-0.04),(1.17,0.79),(-0.13,-1.44),(0.96,-0.17),(0.35,0.88),(1.27,0.71)\}$. In the lower plot only two modes with centers $\{(1/3,1/3),(-3.15,-1.5)\}$ have been iterated.

Regarding the approximation schemes, we have found that all schemes taking into account coherences, (ii)–(v), predict the same behavior and the spin-based factorization (v) offers the quantitatively best description. It is important to note that all these descriptions coincide at the end of the cooling protocol [shown in Fig. 4 only for (ii) and (v)]. In particular the limiting bosonic model predicts the same high ($\geqslant$95%) polarizations and cooling rates as the other schemes, which leads us to conclude that the $\mathcal{O}(10)$-mode changes are sufficient to achieve near-ground-state cooling for realistically large numbers of nuclei in QDs.

Despite being a radical approximation at low polarization, the bosonic scheme (ii) captures the cooling dynamics qualitatively and we remark that it can be generalized to provide an accurate and conceptually simple description of the electron-nuclear spin dynamics at high polarizations.[25]

The cooling schemes we have presented are governed by the optimal time scale set by the hyperfine interaction constant A, but the schemes themselves leave room for optimization: The cooling rate can be tuned by choosing Δt adaptively during the cooling process. The mode changes can be optimized by a careful choice of the size and the timing of the shifts, and through more sophisticated deformations of the electron wave function. These and further modifications

are implementation dependent and will be the topic of future work.

In using the Hamiltonian, Eq. (1), we have neglected a number of weak interactions that are present in actual systems and, while being much smaller than the dominant hyperfine term, may become important on the long time scales required to reach high polarization. We argue in the following that these terms do not affect the quantitative conclusions obtained. While nuclear Zeeman energies are large enough to cause additional dephasing between the nuclear spins, similar to the inhomogeneous Knight fields, this will only be effective between nuclei of *different* Zeeman energy—i.e., belonging to different nuclear species. This leads to two to three mutually decohered subsystems (in a partial rotating-wave approximation), each of which is described by our model.

The nuclear dipole-dipole interaction[45] can lead to both diffusion and dephasing processes, both of which are of minor importance as shown below. Dipolar processes that change A^z are off-resonant and hence expected to be slow, as indicated by the nuclear spin diffusion rates measured, e.g., in Ref. 46, and should not significantly affect the polarizations reached. Resonant processes such as terms $\propto I_i^z I_j^z$ affect the cooling process only insofar as they can cause dephasing of dark states similar to the inhomogeneous Knight shift. The rate at which coolable excitations are provided is set by the energy difference for two nuclear spins in a dark pair. The interaction energy for two neighboring spins is about $\sim 10^{-5}$ μeV (Ref. 7); hence, a singlet of neighboring spins can dephase in ~ 100 μs (or slower if all surrounding spins are polarized). Even widely separated spins interacting with differently polarized environments dephase only up to a few 10 times faster than this (depending on the geometry). Thus we see that the dipolar dephasing is considerably slower than that caused by the inhomogeneous Knight field, and only if the latter becomes inefficient due to homogeneities (towards the end of cooling a given mode) can the dipolar dephasing contribute coolable excitations, but at a much slower rate than what can be achieved by changing the electron wave function and the ensuing return to a situation of strong Knight inhomogeneity. Thus, one does not expect the cooling process to be affected except for a slight additional dephasing. However, on much longer time scales of tens of milliseconds the dipole-dipole interaction provides the depolarizing mechanism (mainly affecting nuclei with a weak hyperfine interaction) that needs to be considered, e.g., when cooling much beyond 90% polarization is studied.

Clearly a polarization $<100\%$ of the electron "reservoir" directly translates into limitations on the final polarization of the nuclei. A quantification of this necessarily needs to refer to the details of a concrete physical realization of our model, which is not the topic of this article. The limitations can be minute—e.g., in the case of the double-dot setup presented in the next section.

IV. ADAPTING THE MODEL TO CONCRETE PHYSICAL SETTINGS

The generic model of a single spin-1/2 particle coupled inhomogeneously to an ensemble of N nuclear spins can readily be adapted to various experimental settings.

If a source of spin-polarized electrons is available, single electron tunneling into the QD provides the initialization. Controlled tunneling into and out of the QD with rates >10 ns^{-1} appears feasible,[47,48] justifying the description of the dynamics by a suddenly switched on and off interaction.

For self-assembled QDs, optical pumping with polarized light has been shown to provide a spin-polarized bath of electrons that cools the nuclei.[26–30] However, in this setup the average dwell time of a single polarized electron in the dot is large and the detuning due to the z component of the Overhauser field leads to instabilities[39–41] in the nuclear polarization which are avoided in our scheme.

In double QDs in the two-electron regime[49,50] the role of the states $|\downarrow\rangle,|\uparrow\rangle$ is played by the two-electron singlet $|\tilde{S}\rangle$ and one of the triplet states; in the following, we consider $|T_+\rangle = |\uparrow\rangle|\uparrow\rangle$. Tunnel coupling between the two dots and the external magnetic field is chosen such that the other triplet states are off-resonant and cause only small corrections to the dynamics sketched here.

As discussed in more detail in Refs. 49–51, the hyperfine interaction in this system is described by the Hamiltonian $\Sigma_l \mathbf{S}_l \cdot \mathbf{A}_l$, where $l=L,R$ refers to the orbital state of the electron. Coupling between $|\tilde{S}\rangle$ and $|T_+\rangle$ is mediated by the *difference* $\delta A^\pm = (A_L^\pm - A_R^\pm)/2$ of the collective nuclear spin operators of the two dots L,R, while the effective Overhauser field is given by the sum $(A_L^z + A_R^z)/2$. Thus we have that the analysis of the previous sections applies to the double-dot case in this regime (to zeroth order; cf. Ref. 52) with the replacements

$$|\downarrow\rangle \to |\tilde{S}\rangle, \quad |\uparrow\rangle \to |T_+\rangle,$$

$$A^\pm \to -\sqrt{2}(\cos\theta)\delta A^\pm, \quad A^z \to \frac{1}{2}(A_L^z + A_R^z).$$

The adiabatic singlet has contributions from both the delocalized (1,1) and localized (0,2) charge states, and with $\cos\theta$ we denote the amplitude of the (1,1) contribution[50] [with (m,n) we denote a state with m electrons on the left and n electrons on the right dot]. The effect of higher-order terms (e.g., of the nuclear spin components $\delta A^z, A_L^\pm + A_R^\pm$) merits more detailed analysis.

This system is of particular interest since fast electrical control of gate voltages can provide a highly spin-polarized electron system through near-unity fidelity initialization of a singlet in the right-hand dot $|S(0,2)\rangle$.[13,53] Starting from this singlet, rapid adiabatic passage [1 ns (Ref. 13)] by means of tuning the asymmetry parameter ϵ between the dots, initializes the electrons to the adiabatic singlet $|\tilde{S}\rangle$ and brings the system to the S-T_+ resonance.

The transitions from the singlet to the other two triplets $T_{0,-}$ are detuned by an external magnetic field (of order 100 mT in the experiments of Ref. 13). After a time Δt the system is ramped back to the (0,2) charge region and the electrons relax to the singlet ground state, completing one cooling cycle. If relaxation to the state $S(0,2)$ is fast, the limiting time scale for this cycle is given by the hyperfine

coupling constant A, showing that here the polarization rate is governed by the natural and optimal time scale (and not other, slower time scales, like, e.g., cotunneling in Refs. 32 and 37).

In the GaAs double-dot setup the sudden approximation is justified for typical tunnel couplings ~ 10 μeV, which have to be compared to the typical time scale for a hyperfine flip $\leqslant 0.1$ μeV and the fact that additionally all spin flip transitions are off-resonant during the adiabatic ramp. At the S-T_+ resonance selecting a suitable combination of external magnetic field and time step Δt detunes the unwanted transitions and at the same time ensures resonance for the polarizing transition. Note also that the Overhauser field increases the external magnetic field in materials with negative electron g factor, like GaAs ($g^* \approx -0.44$), thus further suppressing unwanted transitions and requiring retuning of the end point of the adiabatic ramp. Given the availability of fast (100 ps) voltage pulses, the reinitialization of $|S(0,2)\rangle$ via a (0,1) charge state is likely to be limited by the tunneling rate from the reservoir to the QD. For optimal cooling efficiency this rate should and could be made large $\gtrsim 10A/\sqrt{N}$.[47,48]

Since in the double-dot setup the "polarized" state is a spin singlet, there is no inhomogeneous Knight field to dephase the dark states and DNP will be severely limited. However, there are many ways of providing it—for example, by extending the cooling cycle to include a third step in which a single-electron state of the double dot is realized or by increasing the time spent at the S-T_+ resonance in each cooling cycle [the latter would require a reformulation of the master equation (3) not presented here]. At the same time it would be interesting to find evidence for quantum coherence between nuclear spins in QDs by comparison of the obtained Overhauser field in the case of strong and weak inhomogeneous Knight fields.[54]

V. CONCLUSIONS AND OUTLOOK

In summary we have presented a quantum treatment of a dynamical nuclear spin polarization scheme in single-electron quantum dots that takes into account quantum coherences between nuclei and allows numerical study of the cooling dynamics for thousands of spins. We have quantified limitations due to dark states and shown that these limits are overcome by the inhomogeneous Knight shift and active mode changes. From this we conclude that cooling to more than 90% (of the maximal Overhauser field) is feasibly faster than typical nuclear spin diffusion processes. Setups for the experimental realization of our scheme have been proposed.

In order to go beyond the presented results to polarizations larger than 99%, which would bring the system of coupled nuclei close to a pure state and significantly reduce electron spin decoherence, the presented scheme can be optimized, both in terms of timing (length of the individual cooling step and wave function changes) and in terms of the electron wave functions chosen. A further enhancement may be achieved by combining the polarization scheme with A^z measurements[56–58] to reduce the A^z variance and to tailor the interaction times and the external field to the measured A^z value. Dipolar interactions and other depolarizing processes will become more important in later stages of the cooling and need to be considered carefully in the development of ground-state cooling techniques. More detailed studies of these processes may, in addition, lead to schemes to monitor the intrinsic (dipolar) nuclear dynamics via the hyperfine interaction.

The combination of high polarization and long coherence times makes the nuclear spin ensemble itself a candidate for an active role in quantum computation. Like the actively explored single-nucleus-spin qubits,[5] collective excitations of a polarized ensemble of spins could also be used for quantum information purposes.[23] Similar to their atomic counterparts,[59,63] the ensembles might become more suited than their isolated constituents for certain quantum information tasks.

ACKNOWLEDGMENTS

We thank Belén Paredes for very valuable discussions and Ataç Imamoğlu for fruitful comments. This work was supported by the DFG within SFB 631.

[1] A. Abragam, *Principles of Nuclear Magnetism* (Clarendon Press, Oxford, 1961).
[2] J. I. Cirac and P. Zoller, Phys. Rev. Lett. **74**, 4091 (1995).
[3] N. Gershenfeld and I. Chuang, Science **275**, 350 (1997).
[4] D. G. Cory, A. F. Fahmy, and T. F. Havel, Proc. Natl. Acad. Sci. U.S.A. **94**, 1634 (1997).
[5] B. E. Kane, Nature (London) **393**, 133 (1998).
[6] J. Wrachtrup, S. Y. Kilin, and A. P. Nizovtsev, Opt. Spectrosc. **91**, 459 (2000).
[7] J. Schliemann, A. Khaetskii, and D. Loss, J. Phys.: Condens. Matter **15**, R1809 (2003).
[8] G. Burkard, D. Loss, and D. P. DiVincenzo, Phys. Rev. B **59**, 2070 (1999).
[9] S. I. Erlingsson, Y. V. Nazarov, and V. I. Fal'ko, Phys. Rev. B **64**, 195306 (2001).
[10] A. V. Khaetskii, D. Loss, and L. Glazman, Phys. Rev. Lett. **88**, 186802 (2002).
[11] I. A. Merkulov, A. L. Efros, and M. Rosen, Phys. Rev. B **65**, 205309 (2002).
[12] W. A. Coish and D. Loss, Phys. Rev. B **70**, 195340 (2004).
[13] J. R. Petta, A. C. Johnson, J. M. Taylor, E. A. Laird, A. Yacoby, M. D. Lukin, C. M. Marcus, M. P. Hanson, and A. C. Gossard, Science **309**, 2180 (2005).
[14] F. H. L. Koppens, J. A. Folk, J. M. Elzerman, R. Hanson, L. H. Willems van Beveren, I. T. Vink, H.-P. Tranitz, W. Wegscheider, L. P. Kouwenhoven, and L. M. K. Vandersypen, Science **309**, 1346 (2005).
[15] A. W. Overhauser, Phys. Rev. **92**, 411 (1953).
[16] G. Lampel, Phys. Rev. Lett. **20**, 491 (1968).
[17] *Optical Orientation*, edited by F. Meier and B. Zhakharchenya, Modern Problems in Condensed Matter Sciences Vol. 8 (North-Holland, Amsterdam, 1984).
[18] G. Salis, D. D. Awschalom, Y. Ohno, and H. Ohno, Phys. Rev. B **64**, 195304 (2001).

[19] D. Paget, G. Lampel, B. Sapoval, and V. I. Safarov, Phys. Rev. B **15**, 5780 (1977).
[20] J. M. Taylor, H.-A. Engel, W. Dür, A. Yacoby, C. M. Marcus, P. Zoller, and M. D. Lukin, Nat. Phys. **1**, 177 (2005).
[21] W. A. Coish and D. Loss, cond-mat/0610443 (unpublished).
[22] J. M. Taylor, A. Imamoğlu, and M. D. Lukin, Phys. Rev. Lett. **91**, 246802 (2003).
[23] J. M. Taylor, G. Giedke, H. Christ, B. Paredes, J. I. Cirac, P. Zoller, M. D. Lukin, and A. Imamoğlu, cond-mat/0407640 (unpublished).
[24] Z. Song, P. Zhang, T. Shi, and C.-P. Sun, Phys. Rev. B **71**, 205314 (2005).
[25] H. Christ *et al.* (unpublished).
[26] A. S. Bracker, E. A. Stinaff, D. Gammon, M. E. Ware, J. G. Tischler, A. Shabaev, A. L. Efros, D. Park, D. Gershoni, V. L. Korenev, and I. A. Merkulov, Phys. Rev. Lett. **94**, 047402 (2005).
[27] B. Eble, O. Krebs, A. Lemaitre, K. Kowalik, A. Kudelski, P. Voisin, B. Urbaszek, X. Marie, and T. Amand, Phys. Rev. B **74**, 081306(R) (2006).
[28] A. Greilich, R. Oulton, S. Y. Verbin, D. Yakovlev, M. Bayer, V. Stavarache, D. Reuter, and A. Wieck, cond-mat/0505446 (unpublished).
[29] C.-W. Lai, P. Maletinsky, A. Badolato, and A. Imamoğlu, Phys. Rev. Lett. **96**, 167403 (2006).
[30] I. A. Akimov, D. H. Feng, and F. Henneberger, Phys. Rev. Lett. **97**, 056602 (2006).
[31] C. Deng and X. Hu, Phys. Rev. B **71**, 033307 (2005).
[32] M. S. Rudner and L. S. Levitov, cond-mat/0609409 (unpublished).
[33] A. Imamoğlu, E. Knill, L. Tian, and P. Zoller, Phys. Rev. Lett. **91**, 017402 (2003).
[34] R. Bonifacio, P. Schwendimann, and F. Haake, Phys. Rev. A **4**, 302 (1971).
[35] M. Gross and S. Haroche, Phys. Rep. **93**, 301 (1982).
[36] A. V. Andreev, V. I. Emelyanov, and Y. A. Ilinski, *Cooperative Effects in Optics: Superradiance and Phase Transitions* (IOP, Bristol, 1993).
[37] K. Ono and S. Tarucha, Phys. Rev. Lett. **92**, 256803 (2004).
[38] A. K. Hüttel, J. Weber, A. W. Holleitner, D. Weinmann, K. Eberl, and R. H. Blick, Phys. Rev. B **69**, 073302 (2004).
[39] P.-F. Braun, B. Urbaszek, T. Amand, X. Marie, O. Krebs, B. Eble, A. Lemaitre, and P. Voisin, Phys. Rev. B **74**, 245306 (2006).
[40] P. Maletinsky, C.-W. Lai, A. Badolato, and A. Imamoğlu, Phys. Rev. B **75**, 035409 (2007).
[41] A. I. Tartakovskii, T. Wright, A. Russell, V. I. Fal'ko, A. B. Van'kov, J. Skiba-Szymanska, I. Drouzas, R. S. Kolodka, M. S. Skolnick, P. W. Fry, A. Tahraoui, H.-Y. Liu, and M. Hopkinson, Phys. Rev. Lett. **98**, 026806 (2007).
[42] F. T. Arecchi, E. Courtens, R. Gilmore, and H. Thomas, Phys. Rev. A **6**, 2211 (1972).
[43] T. Holstein and H. Primakoff, Phys. Rev. **58**, 1098 (1940).
[44] G. S. Agarwal, Phys. Rev. A **4**, 1791 (1971).
[45] C. P. Slichter, *Principles of Magnetic Resonance* (Springer-Verlag, Berlin, 1980).
[46] D. Paget, Phys. Rev. B **25**, 4444 (1982).
[47] M. Førre, J. P. Hansen, V. Popsueva, and A. Dubois, Phys. Rev. B **74**, 165304 (2006).
[48] S. Ludwig and M. Atatüre (private communication).
[49] W. A. Coish and D. Loss, Phys. Rev. B **72**, 125337 (2005).
[50] J. M. Taylor, J. R. Petta, A. C. Johnson, A. Yacoby, C. M. Marcus, and M. D. Lukin, cond-mat/0602470 (unpublished).
[51] S. I. Erlingsson and Y. V. Nazarov, Phys. Rev. B **66**, 155327 (2002).
[52] W. A. Coish and D. Loss, *Quantum Computing with Spins in Solids*, Handbook of Magnetism and Advanced Magnetic Materials Vol. 5 (Wiley, Hoboken, NJ, 2006).
[53] F. H. L. Koppens, C. Buizert, K. J. Tielrooij, I. T. Vink, K. C. Nowack, T. Meunier, L. P. Kouwenhoven, and L. M. K. Vandersypen, Nature (London) **442**, 766 (2006).
[54] Subradiance is not easily demonstrated in quantum optical systems; it was experimentally observed many years after superradiance; see Ref. 55.
[55] D. Pavolini, A. Crubellier, P. Pillet, L. Cabaret, and S. Liberman, Phys. Rev. Lett. **54**, 1917 (1985).
[56] D. Stepanenko, G. Burkard, G. Giedke, and A. Imamoğlu, Phys. Rev. Lett. **96**, 136401 (2006).
[57] D. Klauser, W. A. Coish, and D. Loss, Phys. Rev. B **73**, 205302 (2006).
[58] G. Giedke, J. M. Taylor, D. D'Alessandro, M. D. Lukin, and A. Imamoğlu, Phys. Rev. A **74**, 032316 (2006).
[59] A. Kuzmich and E. S. Polzik, in *Quantum Information with Continuous Variables*, edited by S. L. Braunstein and A. K. Pati (Kluwer Academic, Dordrecht, 2003).
[60] In a fully homogeneous system only a fraction of $\mathcal{O}(1/\sqrt{N})$ spins can be cooled before the system is trapped in dark states.
[61] Ensuring the validity of Eq. (3) for all times by retuning B_{ext} assumes that the standard deviation of gA^z remains bounded by $\mathcal{O}(A/\sqrt{N})$ thus keeping the error in each cooling step small. Computing $\text{Var}A^z$ in each step and choosing Δt accordingly guarantees correctness. In general, the polarizing process is expected to *decrease* $\text{Var}A^z$ from the initial value in the maximally mixed state. This is confirmed by exact numerical calculations for small particle numbers. We are confident that this holds for large N, too, since the generic states exhibit standard deviation $\leqslant\mathcal{O}(A/\sqrt{N})$ (as evidenced by the variance of the maximally mixed state). Moreover, the standard deviation in the maximal entropy state of total polarization P is $\mathcal{O}((1-P^2)A/\sqrt{N})$ for all P. Similar reasoning holds for the x and y directions.
[62] In this article we focus on Gaussian electron wave functions, which approximate experimental conditions well. For the coherent phenomena we discuss, the distribution of the groups of similarly coupled spins is of major importance. This property is generally mainly determined by the width and dimensionality of the wave function, and only to a smaller extent by its exact functional form.
[63] L.-M. Duan, J. I. Cirac, P. Zoller, and E. S. Polzik, Phys. Rev. Lett. **85**, 5643 (2000).

Available online at www.sciencedirect.com
ScienceDirect
Solid State Sciences 11 (2009) 965–969
Solid State Sciences
www.elsevier.com/locate/ssscie

Nuclear spin polarization in quantum dots – The homogeneous limit

H. Christ*, J.I. Cirac, G. Giedke

Max–Planck–Institut für Quantenoptik, Hans–Kopfermann–Strasse, 1, D-85748 Garching, Germany

Received 6 June 2007; received in revised form 12 September 2007; accepted 28 September 2007
Available online 9 October 2007

Abstract

We theoretically discuss the dynamical quantum process of polarizing the nuclear spins in a quantum dot via the hyperfine interaction with the electron spin. The limit of homogeneous couplings, i.e. a flat electronic wave function, is analyzed in detail and approximate analytical solutions are shown to provide accurate results, allowing for the determination of cooling potential and rates, both of which reflect the effect of polarization-limiting dark states. We further provide a detailed microscopic description of these states that proves useful for the analysis of the effect of electron wave function changes during the cooling procedure.
© 2007 Elsevier Masson SAS. All rights reserved.

PACS numbers: 71.70.Jp; 73.21.La

Keywords: Nuclear spins; Quantum dots; Quantum information

1. Introduction

Nuclear spin polarization in quantum dots (QD) has received tremendous attention in recent years (see Ref. [1] and references therein), because of its strong influence on the electron spin coherence, which is crucial for quantum computation [2], and because the nuclear spins themselves are an interesting physical system with possibly long coherence times [3] and interesting many body (dipolar) effects [4,5]. While most previous studies neglected quantum effects in the cooling process it has been shown [1,6] that coherences between nuclei can indeed strongly influence and limit the polarization process. We present here further evidence for these observations by considering the limit of a spatially homogeneous electron wave function, which is commonly assumed in studies of electron spin decoherence. Indeed we show in the present work that for the cooling process the level of homogeneity plays an important role. Naturally our theory is directly applicable to QD potentials and shapes producing a quasi-homogeneous electron distribution. Furthermore, as an inhomogeneous wave function can be approximated by a step function and our results bear relevance for the dynamics in each of the steps, the results presented here can be transferred to more general situations (cf. e.g. Ref. [7]).

We consider the cooling of N nuclear spins in a QD through interaction with polarized electrons, as in Ref. [1]. One cooling cycle consists of (i) initialization of the electron spin in a well-defined direction $|\uparrow\rangle$, and (ii) evolution of the combined system for a "short" time Δt.

The hyperfine (HF) interaction for homogeneous coupling constants reads

$$H = \frac{A}{2N}\left(I^+S^- + S^+I^-\right) + \frac{A}{N}I^zS^z + B_{\text{ext}}S^z. \tag{1}$$

S is the spin operator for the electron, A the HF coupling constant, $\hbar = 1$, and $I^\mu = \sum_i I_i^\mu$ are the three components of the homogeneous collective nuclear spin operators ($\mu = \pm,\ z$). The collective operators fulfill the angular momentum commutation relations $[I^+,\ I^z] = -I^+$, $[I^+,\ I^-] = 2I^z$. We take $I = 1/2$ and neglect nuclear dipolar interactions, nuclear Zeeman energies and species inhomogeneities (see Ref. [1] for

* Corresponding author. Tel.: +49 089 32905368.
E-mail address: hcc@mpq.mpg.de (H. Christ).

1293-2558/$ - see front matter © 2007 Elsevier Masson SAS. All rights reserved.
doi:10.1016/j.solidstatesciences.2007.09.027

a discussion of these effects). If the relevant system dynamics happens on a timescale larger than Δt, as is the case in the present study, we arrive at the continuous version of the master equation of Ref. [1] for the density matrix ρ of the nuclei

$$\frac{\mathrm{d}}{\mathrm{d}t}\rho = i\frac{A}{2N}[I^z,\rho] - \frac{A^2\Delta t}{8N^2}[I^z,[I^z,\rho]] - \frac{A^2\Delta t}{8N^2}\left(I^+I^-\rho + \rho I^+I^- - 2I^-\rho I^+\right). \quad (2)$$

Although we consider in our model the polarization process in a single dot, the results bear relevance for spin cooling in the recently investigated double QDs [8,9]. There, the polarizing dynamics happens in the subspace of a two-electron singlet and a polarized triplet; coupling between the two is mediated by the *difference* $\delta I^\pm = (I_L^\pm - I_R^\pm)/2$ of the collective nuclear spin operators of the two dots L and R, while the effective Overhauser field is given by the sum $(I_L^z + I_R^z)/2$. In the homogeneous limit these operators obey the same algebra as the "bare" ones of our model, thus making our results directly applicable.

2. Achievable polarization

Due to the collective coupling, singlet-like "dark states" can trap spin excitation and prevent cooling to the ground state. This effect is for homogeneous couplings most conveniently described in the Dicke basis [10], which is well-known for example from the literature on superradiance. The basis states are $|I,m,\beta\rangle$ where $I(I+1)$ is the eigenvalue of the collective angular momentum operator $\mathbf{I}^2$, and the eigenvalue of I^z is given by m. The possible values of I are $N/2$, $N/2-1$, …, the smallest value being 0 if N is even and 1/2 if N is odd; $|m| \le I$. The β is the permutation quantum number, which labels the different degenerate states with the same quantum numbers I and m. The degeneracy D of the states depends only on I and not on m, $D(I) = \binom{N}{N/2-1} - \binom{N}{N/2-I-1}$.

When acting on a state $|I,m,\beta\rangle$, the operator I^- decreases the quantum number m by one $I^-|I,m,\beta\rangle = \sqrt{I(I+1)-m(m-1)}|I,m-1,\beta\rangle$. For $m=-I$ the action of I^- yields zero, and thus the states $|I,-I,\beta\rangle$ can not be polarized further in a system evolving according to Eq. (2). The steady state of the cooling process described by the master Eq. (2) starting from a completely mixed state is thus

$$\rho_{\mathrm{ss}} = 1/2^N \sum_I D(I)(2I+1)|I,-I\rangle\langle I,-I|, \quad (3)$$

where the trace over the permutation quantum number β has been performed.

We now evaluate the polarization of the steady state Eq. (3) normalized to the polarization of the ground state

$$\frac{\langle I^z\rangle_{\mathrm{ss}}}{\langle I^z\rangle_0} = \frac{2}{2^N N}\left[\frac{4(N-1)!}{([(N-1)/2]!)^2} - \frac{1}{2}\left(2^N - \binom{N}{(N/2)}\right)\right],$$

where for the fully polarized state one has a polarization $\langle I^z\rangle = -N/2$. As an example this expression can applied to the case $N=2$, where one finds a final polarization of 3/4. This is the expected result because one out of the four two-spin states cannot be cooled (the singlet). In Fig. 1 it is shown that for increasing particle number the possible polarization quickly decreases from 75% of the two-particle case. The negative indications for cooling purposes are obvious.

Application of the Stirling formula $N! \approx \sqrt{2\pi}N^{N+1/2}\mathrm{e}^{-N}$ gives the approximate result for $N \gg 1$

$$\frac{\langle I^z\rangle_{\mathrm{ss}}}{\langle I^z\rangle_0} = \sqrt{\frac{8}{\pi N}} + \mathcal{O}(1/N). \quad (4)$$

For the mesoscopic particle numbers of interest in the study of quantum dots, the obtainable polarization is thus negligible. In Fig. 1 it is shown that the approximate first order formula matches the exact value very well, as expected.

3. Time evolution

The study of the time evolution of the nuclear spin system under the master Eq. (2) is similar to the study of the evolution of the atomic population in superradiant light emission from an ensemble of atoms. The latter problem has received considerable attention in the quantum optics literature, see e.g. the textbook [11] and review [12]. The focus of these studies was slightly different than it is in the cooling protocol we are considering. In quantum optics an ensemble with all atoms excited is the most studied situation, because for this initial condition one has pronounced signatures in the emitted light pulses *and* it is experimentally accessible. Here on the other hand, we are dealing with a completely mixed initial state. This complicates the situation because in this mixture superradiant as well as subradiant states occur. Nevertheless we

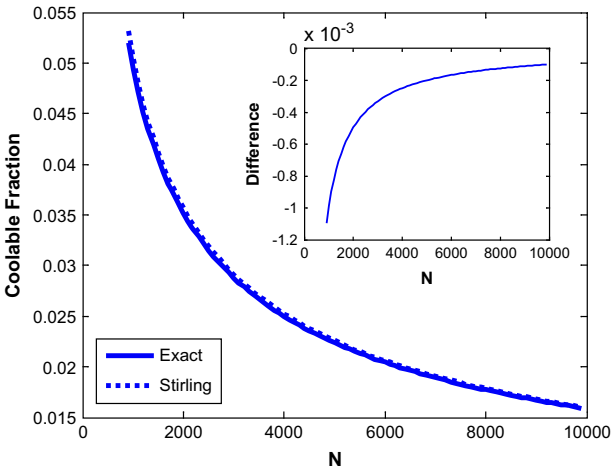

Fig. 1. The fraction of the nuclei that can be polarized in the case of homogeneous coupling constants. Shown are both the exact and the approximate numbers; the inset shows the difference between the two.

extract and present here approximate explicit analytic expressions for the evolution of the nuclear spin polarization.

Instead of solving the dynamics of the density matrix of the nuclei, we concentrate on the evolution of the variable of our interest, $\langle I^z\rangle$. It obeys the equation of motion

$$\frac{\mathrm{d}}{\mathrm{d}t}\langle I^z\rangle = \mathrm{tr}\left(I^z\frac{\mathrm{d}}{\mathrm{d}t}\rho\right) = -2\kappa\langle I^+I^-\rangle,$$

where we have introduced $\kappa = A^2\Delta t/8N^2$. The equation for the polarization $\langle I^z\rangle$ does not close, but couples to the variable $\langle I^+I^-\rangle$. The time evolution of this quantity depends on $\langle I^+I^zI^-\rangle$. Continuing this procedure leads to a hierarchy of coupled equations. Following the quantum optics literature on superradiance we make a factorization assumption

$$\langle (I^z)^2\rangle = \langle I_z\rangle^2, \tag{5}$$

which is equivalent to the assumption that $\langle I_i^zI_j^z\rangle = \langle I_i^z\rangle\langle I_j^z\rangle$. In the following we apply this factorization to obtain analytical results for the time evolution of the polarization and check its validity by comparison with the exact numerical solution.

Using this assumption the equation of motion for the polarization becomes

$$\frac{\mathrm{d}}{\mathrm{d}t}\langle I^z\rangle = -2\kappa\big(\langle \mathbf{I}^2\rangle - \langle I^z\rangle^2 + \langle I^z\rangle\big), \tag{6}$$

where $\mathbf{I}^2 = (I^z)^2 + (1/2)(I^+I^- + I^-I^+)$ was used. For each given initial state $|I,m,\beta\rangle$ this equation is solved by

$$\langle I^z(t)\rangle_{I,m} = 1/2 - \nu_I\tanh(\nu_I(2\kappa t - c_0)), \tag{7}$$

where $\nu_I = \sqrt{4I(I+1)+1}/2$ and the initial condition depends on the value of m and enters through the constant $c_0 = \mathrm{arctanh}[-2(m-1/2)/\nu_I]/(2\nu_I)$. In Fig. 2 we compare the evolution of the polarization averaged over all initial states

$$\langle I^z(t)\rangle_{\mathrm{averaged}} = \sum_{I,m} D(I)\langle I^z(t)\rangle_{I,m} \tag{8}$$

with the exact numerical calculation. The curves show good agreement, which serves as an indication that the factorization assumption captures the correct physics of the polarization process.

To gain further insight into the evolution of the population, we consider the evolution of a pure initial state with total angular momentum and z-projection equal to the mean value of the totally mixed state, i.e. $m=0$ and $I_{\mathrm{mean}} = (1/2^N)\sum_{I=0}^{N/2} I(2I+1)D(I)$. Using the same approximations as for the evaluation of the total obtainable polarizations (Eq. (4)) one gets $I_{\mathrm{mean}} = \sqrt{2N/\pi} + \mathcal{O}(1)$. In this limit the polarization develops according to

$$\langle I^z(t)\rangle_{\mathrm{mean}} = -\frac{1}{2}\sqrt{\frac{8N}{\pi}}\tanh\left(\sqrt{\frac{8N}{\pi}}\frac{A^2\Delta t}{8N^2}t\right), \tag{9}$$

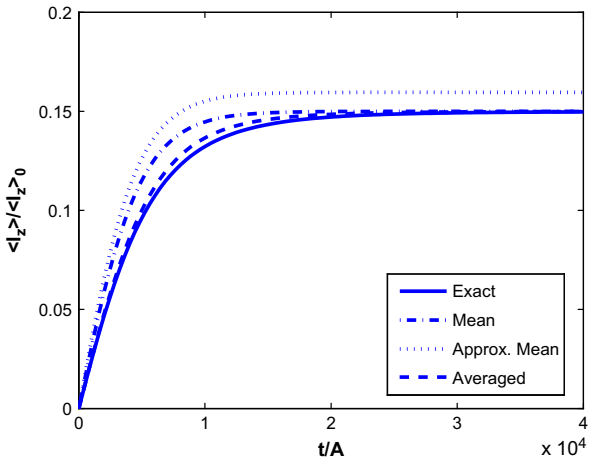

Fig. 2. Comparison between the various (semi-)analytical solutions based on Eq. (5) and the exact numerical result for $N=100$ particles. The "average" (dashed) line is averaged over all states in the initially totally mixed nuclear state, see Eq. (8). The two other curves are directly obtained from Eq. (7) by substituting one specific value for the angular momentum I that enters the solution as a parameter; for the dashed–dotted line the average value of the total angular momentum I has been calculated exactly and for the dotted curve the approximate expression $I = \sqrt{2N/\pi}$ was used.

where we used $\sqrt{N}\gg 1$. Fig. 2 shows the evolution in the "mean state" for both the exact and the approximate expressions for the mean value of the average spin I_{mean}. Using the exact mean the results are very close to the actual evolution: Both the timescale and the final polarization are correctly predicted. When the approximate expression for the mean is employed, the timescale of the process is still correct. However, the predicted final polarization differs from the real polarization. This is to be expected, since the approximated mean value of I is only correct to order 1, which translates into a $\mathcal{O}(1/N)$ error for the polarization.

From Eq. (9) we can thus extract the timescale for reaching the steady state of the polarization

$$\tau_{\mathrm{hom}} = \frac{N}{A}\frac{\sqrt{8\pi}}{0.1}, \tag{10}$$

where we used $\Delta t = 0.1\sqrt{N}/A$, i.e. Δt is chosen such that the condition necessary for the expansion of the time evolution operator is fulfilled.

4. Microscopic description of dark states

In this section a new microscopic description of dark states is introduced, which, besides providing handy intuition, will serve in Section 5 as the basis for our estimations regarding ground state cooling in homogeneous situations. We prove that one can understand all dark states $I^-|I,-I,\beta\rangle = 0$ as a superposition of states describing $n = N/2 - I$ singlets and $2I = N - 2n$ polarized spins $|\downarrow\rangle$. Let us denote a singlet of spins i and j as $|S_{ij}\rangle$ and by $|S\{s_i\}_{i=1}^{2S},\downarrow\rangle$ the state with S singlets $|S_{s_is_{i+1}}\rangle$ and the remaining states spins in state $|\downarrow\rangle$. The

idea is to show that the statistical mixture of all permutations of $|S\{i\}_{i=1}^{2S}, \downarrow\rangle$

$$P_I = \frac{1}{N!}\sum_{\pi\in S_N} X(\pi)P_{|S\{1,\ldots,2S\},\downarrow\rangle}X(\pi)^\dagger$$

(where for a permutation $\pi \in S_N$ let $X(\pi)|S\{s_i\},\downarrow\rangle = |S\{\pi(s_i)\},\downarrow\rangle$) is equal to the projector on the the $(I, -I)$-subspace:

$$P_I = \frac{1}{D(I)}\sum_\beta |I,-I,\beta\rangle\langle I,-I,\beta|.$$

To see this, we first observe that $S_N \ni \pi \mapsto X_{(I,M)}(\pi) \in M_{2^N}$ with $X_{(I,\ M)}(\pi)$ acting (as above) on the space spanned by the vectors $|I,M;\beta\rangle$ with $\beta = 1,\ldots,D(I)$ a label for the eigen values of a set of permutation operators extending $\vec{I}^2$, and I^z to a complete commuting set (e.g. $P_{2i-1,2i}, i = 1,\ldots,N/2$ cf. [10]) is a *representation* of the permutation group S_N. The representation must be *irreducible*, since if it were not, there would exist at least two sets of vectors in $\mathcal{H}_{(I,M)}$ that are *not* connected by S_N, hence the projector on one of those would be an operator commuting with $\{\vec{I}^2, I^z, P_{2i-1,2i}\}$, contradicting that this is a *complete* set of commuting observables on $(\mathbb{C}^2)^{\otimes N}$. Finally, we clearly have $X_{I,-I}(\pi)P_I X_{(I,-I)}(\pi)^\dagger = P_I$ and by Schur's Lemma (which states that any operator commuting with all elements of a irrep is proportional to the identity see, e.g. Ref. [13]) it follows that $P_I \propto \mathbb{1}_{I,-I}$. Counting the number of permutations respectively the degeneracy of the $(I, -I)$-subspace gives the normalization factor.

This shows that the projector on the (I, m)-subspace is given by the equal-weight mixture of all permutations of $N/2 - I$ singlets and the remaining $2I$ spins in the state $|I, m\rangle$.

5. Mode changes

To cool beyond the dark state, the coupling operator I^- needs to be changed. In view of the analogy between a (collectively addressed) system of spins and a bosonic mode, such a transformation of I^- can be viewed as addressing a different "mode" of the system [1]. Any $\tilde{I}^- = \sum_i g_i I_i^-$ with $\vec{g}$ not parallel to $(1,\ldots,1)$ represents a different mode in this terminology. The number of modes that are needed to cool the nuclear spins to the ground state is in general not easily estimated due to the fact that orthogonal spin modes do not commute [14].

In order to get an estimate for the number of modes needed for cooling the spins, we use the simple Hadamard basis for the modes. The Hadamard matrices are recursively defined by $H_0 = 1$, and

$$H_{m+1} = \frac{1}{\sqrt{2}}\begin{pmatrix} H_m & H_m \\ H_m & -H_m \end{pmatrix}.$$

The size of the matrix is 2^m. Its columns are mutually orthogonal and represent the different modes we aim to address. Changing from the standard homogeneous coupling to the ith Hadamard mode could be achieved, e.g. by performing phase flips $|\downarrow\rangle_j \to -|\downarrow\rangle_j$ for all j with $(H_m)_{ji} = -1$.

When applied after cooling with the first mode, such a mode change has no effect on nuclei already in state $|\downarrow\rangle$ but singlets are transformed to triplets (with zero z-projection) if the phase of only one of the two spins is flipped, so that the state in the new mode is

$$\sum_n p(n)\sum_{\pi\in S_N}\sum_{u=0}^{n} q(n,u)\times X(\pi)P_{|S1,\ldots,2(n-u),\downarrow\rangle}X(\pi)^\dagger \otimes |T_0\rangle\langle T_0|^{\otimes u}$$

where $q(n, u)$ denotes the probability that u of the n singlets become a triplet after the mode change. We assume that changing from one Hadamard mode to the next typically breaks up half the singlets in each of the terms in the mixture, i.e. $\overline{u} = n/2$.

We now calculate the total angular momentum $\mathbf{I}^2$ of this state, by first noting that in each of the above terms in the mixture one can split the collective operators up into terms that act on spins which remained untransformed by the mode change, and the rest $\Sigma_{\text{all spins}} = (\Sigma_{\text{in some } T_0} + \Sigma_{\text{rest}})$. The mixed terms between the two sums can be seen to be 0 readily. The terms involving the unchanged (rest) spins have the same total spin as before the mode change: Only singlets have been taken away. For the spins that have turned from singlets to triplets one can easily verify that their contribution to the new total angular momentum is $(N/2 - I_{\text{old}})/4$.

In a semiclassical treatment we now calculate in the way outlined above the average angular momentum after k mode changes and arrive at the recursive formula

$$I_{k+1}(I_{k+1}+1) = I_k(I_k+1) + (N/2 - I_k)/4, \tag{11}$$

where k is the index for the number of modes changes, and from which we extract the minimal compatible polarization, $I_k^z = -I_k$. The numerical solution of the above recursive formula presented in Fig. 3 indicates that order of $\mathcal{O}(N)$ modes

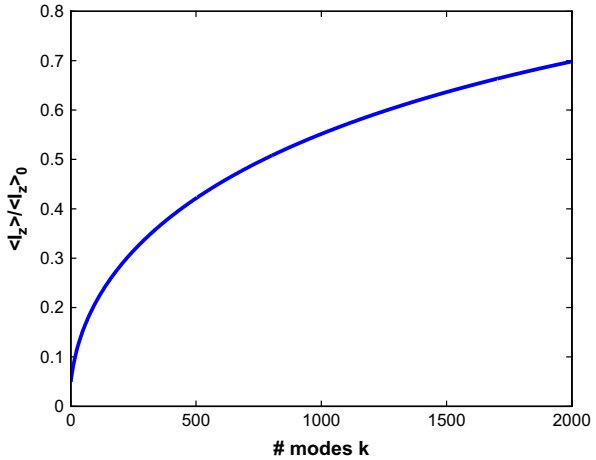

Fig. 3. Estimate of the achieved cooling after a given number of (Hadamard-) mode changes for $N = 10^3$ nuclear spins.

are necessary to completely cool the nuclear spins. We have verified this scaling behavior for a wide range of particle numbers.

Note that a scheme employing Hadamard modes is not optimal: if one had complete freedom in the choice of modes, one could cool each spin individually and therefore cool everything to the perfect ground state in N steps; which is already better than the cooling procedure shown in Fig. 3.

We are thus lead to the conclusion that achieving high polarization for strictly homogeneous couplings is hard: Sophisticated and undesirable control mechanisms for the electron wave function might be needed. As seen in Ref. [1], an *inhomogeneous* coupling will significantly simplify the cooling process.

6. Conclusions

We have presented a study of nuclear spin cooling in quantum dots in the limit of a homogeneous electron wave function. We calculated exactly the cooling potential, presented analytical formulas for the time evolution of the polarization and, after introducing a handy intuition for the microscopic description of the dark states in the nuclear ensemble, showed that many different (Hadamard-) electron wave function profiles are needed to completely polarize the nuclei. The results underline the importance of the inhomogeneous Knight shift in nuclear spin cooling, which mitigates these limitations so strongly, that polarizations above 90% are achievable in realistic setups [1].

References

[1] H. Christ, J.I. Cirac, G. Giedke, Phys. Rev. B 75 (2007) 155324.
[2] D. Loss, D.P. DiVincenzo, Phys. Rev. A 57 (1998) 120 cond-mat/9701055.
[3] J.M. Taylor, G. Giedke, H. Christ, B. Paredes, J.I. Cirac, P. Zoller, M.D. Lukin, A. Imamoğlu, 2004, cond-mat/0407640.
[4] D.H. Feng, I.A. Akimov, F. Henneberger, Phys. Rev. Lett. 99 (2007) 036604 cond-mat/0703386.
[5] P. Maletinsky, A. Badolato, A. Imamoglu, Phys. Rev. Lett. 99 (2007) 056804.
[6] A. Imamoğlu, E. Knill, L. Tian, P. Zoller, Phys. Rev. Lett. 91 (2003) 017402 cond-mat/0303575.
[7] S.I. Erlingsson, Y.V. Nazarov, Phys. Rev. B 70 (2004) 205327.
[8] J. Baugh, Y. Kitamura, K. Ono, S. Tarucha, Phys. Rev. Lett. 99 (2007) 096804.
[9] J.R. Petta, J.M. Taylor, A.C. Johnson, A. Yacoby, M.D. Lukin, C.M. Marcus, M.P. Hanson, A.C. Gossard, 2007, arXiv:0709.0920.
[10] F.T. Arecchi, E. Courtens, R. Gilmore, H. Thomas, Phys. Rev. A 6 (1972) 2211.
[11] A.V. Andreev, V.I. Emelyanov, Y.A. Ilinski, Cooperative Effects in Optics: Superradiance and Phase Transitions, IOP Publishing, London, 1993.
[12] M. Gross, S. Haroche, Phys. Rep. 93 (1982) 301.
[13] T. Inui, Y. Tanabe, Y. Onodera, Group Theory and its Applications in Physics, second ed, Springer, Berlin, 1996.
[14] In the bosonic approximation [1] the number of required modes is easily seen to be N, because the modes are mutually independent and initially all N modes are occupied and consequently have to be cooled one by one (neglecting the effects of inhomogeneous Knight fields). The bosonic model is only exact for high polarization, and in general is expected to be a lower bound on the performance of the cooling protocol for the spins. It is unclear, if the scaling behavior of the number of required modes is the same for spins. One might think, for example, that one needs only $\mathcal{O}(\sqrt{N})$ modes in the spin case, because in the first mode $\sim\sqrt{N}$ excitations can be removed from the spin system.

RAPID COMMUNICATIONS

PHYSICAL REVIEW B **82**, 121307(R) (2010)

Asymmetric optical nuclear spin pumping in a single uncharged quantum dot

F. Klotz, V. Jovanov, J. Kierig, E. C. Clark, M. Bichler, G. Abstreiter, M. S. Brandt, and J. J. Finley
Walter Schottky Institut, Technische Universität München, Am Coulombwall 3, 85748 Garching, Germany

H. Schwager and G. Giedke
Max-Planck-Institut für Quantenoptik, Hans-Kopfermann-Straße 1, 85748 Garching, Germany
(Received 12 July 2010; revised manuscript received 25 August 2010; published 21 September 2010)

Highly asymmetric dynamic nuclear spin pumping is observed in a single self-assembled InGaAs quantum dot subject to resonant optical excitation of the neutral exciton transition. A large maximum polarization of 54% is observed and the effect is found to be much stronger upon pumping of the higher energy Zeeman level. Time-resolved measurements allow us to directly monitor the buildup of the nuclear spin polarization in real time and to quantitatively study the dynamics of the process. A strong dependence of the observed dynamic nuclear polarization on the applied magnetic field is found, with resonances in the pumping efficiency observed for particular magnetic fields. We develop a model that accounts for the observed behavior, where the pumping of the nuclear spin system is due to hyperfine-mediated spin-flip transitions between the states of the neutral exciton manifold.

DOI: 10.1103/PhysRevB.82.121307 PACS number(s): 73.21.La, 78.67.Hc

Nuclear spin effects in semiconductor quantum dot (QD) nanostructures have attracted much attention over recent years.[1–14] The hyperfine (hf) interaction of the 10^4–10^5 nuclear spins within the dot and the spin of an individual electron that is electrically or optically generated is key to address and control the nuclear spin system. This may provide optoelectronic access to the mesoscopic nuclear spin system with strong potential for future applications in quantum information technologies.[2] The hf interaction limits the electron-spin coherence in QDs (Refs. 3 and 15) making reliable strategies to control the nuclear field highly desirable.[4,5] From both perspectives, a highly polarized ensemble of nuclear spins would be advantageous. To date, the vast majority of experiments on dynamical nuclear polarization (DNP) have been carried out on charged QDs containing a resident electron.[6–8] However, this system is subject to fast depolarization effects that are typically mediated by the residual electron in the dot.[6] Comparatively few studies of DNP in neutral QDs have been reported,[9–14,16] for which a stable polarization of the nuclear spin system over time scales exceeding 1 h has been demonstrated.[13]

In this Rapid Communication we demonstrate pumping of the nuclear spin system in an InGaAs QD via resonant optical excitation of the neutral exciton X^0. Most surprisingly, a strong asymmetry is found in the DNP efficiency for excitation of the two transitions of the orbital ground state of the dot. DNP predominantly occurs for pumping of the higher energy Zeeman level. A theoretical model is presented that accounts for the experimental results. Our results show that the asymmetric and efficient resonant DNP arises from hf-mediated spin-flip transitions between neutral exciton states.

As depicted schematically in the inset of Fig. 1(a), the samples investigated were GaAs *n-i*-Schottky photodiode structures grown by molecular-beam epitaxy. A single layer of nominally $In_{0.5}Ga_{0.5}As$ self-assembled QDs was grown in the i region using a partially covered island growth mechanism. The diode is formed by a heavily n^+-doped back contact and a 3-nm-thick semitransparent Ti top contact which allows the application of dc electric fields along the growth direction of the QDs. The Ti top contact is covered with an opaque Au layer in which 1-μm-wide circular apertures are opened to facilitate optical access to single QDs. Photocurrent (PC) measurements were carried out on this structure at 10 K for different magnetic fields B_{ext} using linearly polarized light from a tunable external cavity Littman-Metcalf diode laser. We employ the quantum-confined Stark effect (QCSE) to tune the transitions of the QD into resonance with the laser by sweeping the applied electric field while keeping the laser energy fixed. Figure 1(a) shows the dc Stark shift of the examined X^0 state measured at $B_{ext}=0$ T in both PC at high (>30 kV/cm) and photoluminescence (PL) at lower electric fields (<30 kV/cm), which can be well described

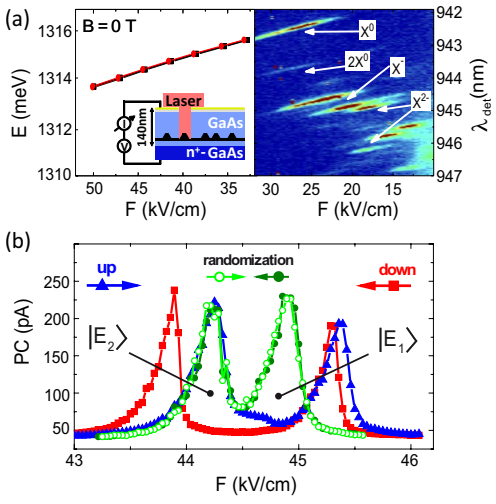

FIG. 1. (Color online) (a) Combined PL and PC measurements at $B_{ext}=0$ T. Inset: schematic of the structure investigated consisting of a single layer of self-assembled QDs is embedded in the intrinsic region of a Schottky photodiode. (b) Both X^0 *s*-shell states measured in PC electric field sweeps at $B_{ext}=5$ T. The individual curves were measured as described in the text.

 ©2010 The American Physical Society

using a second-order polynomial fit allowing a direct conversion of applied electric field into transition energy.[17] Figure 1(b) shows an example of an electric field sweep PC measurement performed at $B_{ext}=5$ T. The measurement clearly reveals the two optically active (bright) s-shell states of X^0, denoted $|E_1\rangle$ and $|E_2\rangle$, as they are tuned into and out of resonance with the laser by the QCSE. The levels $|E_1\rangle$ and $|E_2\rangle$ are separated by an energy gap $\Delta E=\sqrt{E_Z^2+\delta_1^2}$ in an externally applied magnetic field, where E_Z is the Zeeman energy and δ_1 the fine-structure splitting due to anisotropic exchange coupling.[18] For $E_Z \gg \delta_1$, the states $|E_{1,2}\rangle$ correspond to the bright excitons with angular momentum projection $J_z=+1(|\downarrow\Uparrow\rangle)$ and $J_z=-1(|\uparrow\Downarrow\rangle)$, respectively, where $\uparrow, \downarrow(\Uparrow, \Downarrow)$ denote the electron- (hole-) spin orientation. A clear difference is observed between the two measurements performed with opposite sweep directions of the electric field; from low to high values ["sweep up"—blue trace, closed triangles in Fig. 1(b)] and high to low values ["sweep down"—red trace, closed squares in Fig. 1(b)]. These observations are shown to arise from DNP and the resulting effective Overhauser magnetic field B_N. Partial polarization of the nuclear spin bath in the QD arises from hf coupling to the spins of the electrons pumped through the dot during the measurement and introduces an Overhauser energy shift $\delta_N=g_e\mu_B B_N$, where μ_B is the Bohr magneton and g_e the electron g factor. To study DNP it is important to obtain a reference measurement for an unpolarized state of the QD nuclear spin system. We obtain such data by first randomizing the nuclear spins prior to every measurement point recorded during an electric field sweep and also ensuring that our measurement does not induce significant DNP. To achieve this, the sample was tuned close to flatband and excited nonresonantly in the wetting layer for 10 s with linearly polarized light. This procedure pumps randomly oriented electron spins through the QD, whereupon hf interactions efficiently depolarize the nuclear spin system. This expectation is confirmed by the observations presented in Fig. 1(b); when applying this randomization procedure the sweep direction is found to have no influence on the measured resonance curves, the light green (open circles) and dark green (closed circles) traces in Fig. 1(b) corresponding to sweep-up and sweep-down directions, respectively. We note that the observed insensitivity to sweep direction when employing the randomization procedure is in strong contrast to the results obtained without randomization during the sweep [red trace, closed squares and blue trace, closed triangles in Fig. 1(b)]. For all measurements without randomization, the electric field sweep was performed at a speed that was slow compared to the time required to reach the steady-state polarization of the nuclear spin system. Therefore, each of the measurement points presented in Fig. 1(b) represents the steady-state situation of the nuclear spin system. However, before every sweep we applied the randomization process once to ensure a well-defined initial state without residual DNP.

Figure 1(b) reveals an asymmetric behavior of DNP upon pumping of the two bright exciton states of X^0. For the up sweep [blue trace, closed triangles in Fig. 1(b)], first $|E_2\rangle$ comes into resonance with the laser as the energies of the states are shifted via the QCSE. No significant DNP effects are observed upon exciting $|E_2\rangle$ since the measured PC signal coincides exactly with the reference curve recorded without DNP effects. However, as $|E_1\rangle$ is tuned into resonance with the excitation laser, the nuclear spin bath is clearly subject to DNP since a shift of the $|E_1\rangle$ resonance to higher energies is observed. When the electric field is swept in the opposite direction [red trace, closed squares in Fig. 1(b)], first the $|E_1\rangle$ state is tuned into resonance with the laser leading to a buildup of B_N. After the $|E_1\rangle$ state has been tuned through the laser, the energetically lower $|E_2\rangle$ state approaches the laser energy. The measurements presented in Fig. 1(b) clearly show that the $|E_2\rangle$ peak in the PC signal is now redshifted as compared to the reference measurement. This observation unequivocally shows that the nuclear field created by optical pumping of $|E_1\rangle$ is still present.

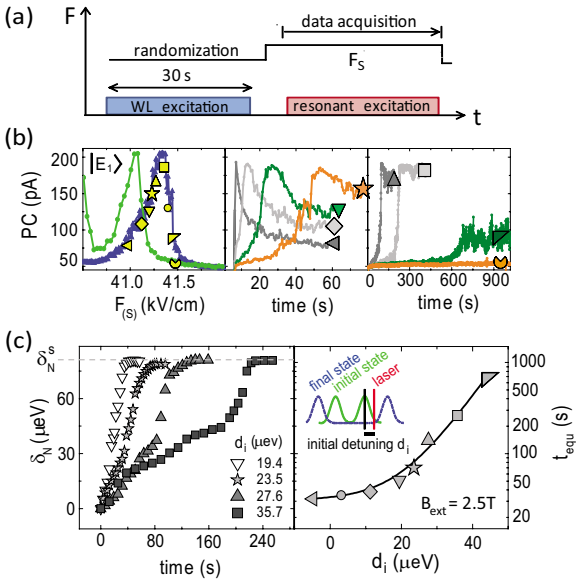

FIG. 2. (Color online) (a) Timing of electric field sequence and laser excitation of the sample used for time resolved measurements of δ_N. (b) Center and right panel: time-dependent PC signal of $|E_1\rangle$ for different initial detunings of the spin state from the laser d_i (defined by F_S). Left panel: steady-state PC values of the time-dependent measurements as a function of F_S [yellow/light gray symbols] in comparison with corresponding electric field sweep measurements [green trace, closed circles and blue trace, closed triangles; color and symbol coding identical to Fig. 1(b)]. (c) Left panel: δ_N^S as a function of time for different d_i. Right panel: time t_{equ} until δ_N^S is reached as a function of d_i. The black solid line is a exponential fit, where an offset of 30 s is included. Identical symbols ($\Delta, \nabla, \ldots$) in different panels refer to the same d_i.

Figure 2 presents time-resolved PC measurements performed at $B_{ext}=2.5$ T. These measurements allow us to investigate the buildup dynamics of δ_N. The timing and electric field sequence used for the measurements is depicted schematically in Fig. 2(a). First, we employed the randomization procedure to delete any residual DNP. Following this, the electric field is set to a value F_S that defines a specific initial (red) detuning (d_i) of $|E_1\rangle$ from the laser. Finally, the laser is switched on and we record the PC signal as a function of time. The middle and right panel of Fig. 2(b) shows the

temporal dependence of the PC for different d_i. For all detunings $d_i < 36$ μeV, the PC signal first increases to a common maximum value and then decreases to a steady-state value I_{PC}^{equ} characteristic of each d_i. For $d_i > 36$ μeV a monotonic increase in the PC signal toward the individual I_{PC}^{equ} value is observed. Plotting I_{PC}^{equ} versus d_i and comparing the result with the electric field sweep measurements presented in the left panel of Fig. 2(b) clearly shows that they directly map out the sweep-up curve [yellow/light gray symbols and blue trace, closed triangles in Fig. 2(b)]. This observation directly confirms that the electric field sweeps presented in Fig. 2(b) are indeed performed adiabatically, such that the system remains in a steady state during measurement. Time-resolved control experiments performed at different B_{ext} confirm that this is also the case for all electric field sweeps. The initial increase in the PC signal arises from the buildup of an Overhauser shift that serves to reduce the red detuning of $|E_1\rangle$ from the laser. The maximum PC signal is reached when the $|E_1\rangle$ state is exactly in resonance with the laser. As δ_N increases further, $|E_1\rangle$ becomes blue detuned from the laser until the system reaches the steady-state value δ_N^s. These measurements allow us to directly monitor the time evolution of the Overhauser shift of $|E_1\rangle$. To do this, we mapped the steady-state PC spectrum recorded with randomization [green trace, closed circles in Fig. 2(b)] onto the time-resolved data by shifting it such as to reproduce the instantaneous PC signal measured at a time t. The instantaneous Overhauser shift $\delta_N(t)$ can then be extracted from this shift and the results of this procedure are plotted in the left panel of Fig. 2(c) for different values of d_i. A characteristic behavior is observed for all curves that becomes more pronounced for larger d_i. A first slow linear increase in δ_N is followed by a faster buildup as the steep slope on the high-energy flank of the resonance approaches the laser energy. This direct resonance is accompanied by a strong increase in excitation rate of the QD and thus, a much higher nuclear spin pumping rate. Finally, the increase in δ_N slows down as the system approaches the steady state. In the right panel of Fig. 2(c), we plot the time required to reach saturation t_{equ} (Ref. 19) as a function of d_i. The dependence of t_{equ} on d_i can be well described using a monoexponential fit with an offset (solid black line) that reflects the asymptotic approach of the system toward the steady state. Even for initial detunings far below one linewidth (≈ 15 μeV), where the QD excitation rate is highest, we always find $t_{equ} > 30$ s. For $d_i > 15$ μeV, the initial overlap of $|E_1\rangle$ with the laser is much smaller. The lower excitation rate results in a slower δ_N buildup. We measured the buildup dynamics of δ_N for d_i up to 40 μeV, leading to t_{equ} in excess of 700 s. For $d_i > 40$ μeV, no DNP is observed over a time scale of 1000 s. These measurements allow us to directly estimate the net electron-nuclear spin-flip-flop rate Γ_{ff} and the efficiency of the process. At $B_{ext} = 2.5$ T, we obtain $\delta_N^s = 80$ μeV, corresponding to a nuclear spin bath polarization of $P = 32\%$,[7] i.e., $\sim 10^4$ polarized nuclei. For small detunings ($d_i < 15$ μeV), t_{equ} is typically on the order of 10 s or longer indicating an average $\Gamma_{ff} \sim 10^3$ s^{-1}. We note that this is an average value since the detuning and, therefore, the dynamics change continuously throughout the measurement. In our experiment the amplitude of typical PC signals are 100–200 pA, corresponding to the generation of $\sim 10^{10}$ excitons per second. These observations show that only one electron in 10^7 actually undergoes a net spin-flip-flop event with a nucleus before tunneling out of the dot.

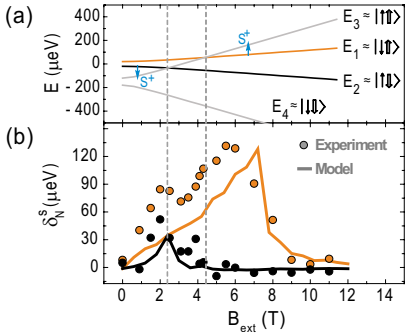

FIG. 3. (Color online) (a) Calculated Breit-Rabi diagram for the bright ($|E_{1,2}\rangle$) and dark ($|E_{3,4}\rangle$) exciton states. (b) Steady-state Overhauser shift δ_N^s created by resonant excitation of either of the two X^0 states $|E_1\rangle$ and $|E_2\rangle$ as a function of B_{ext} obtained from experiment (circles) and calculated using the model described in the text (solid line). The dashed vertical lines indicate the crossing of $|E_3\rangle$ and $|E_{1,2}\rangle$ in the absence of DNP, respectively.

A systematic investigation of δ_N^s as a function of the applied magnetic field is presented in Fig. 3(b). For $B_{ext} = 0-6$ T, δ_N^s created via resonant excitation of $|E_1\rangle$ increases with increasing B_{ext} and then decreases monotonically for $B_{ext} \geq 6$ T. The maximum observed Overhauser shift of $\delta_N^s \approx 135$ μeV obtained for $B_{ext} \approx 6$ T corresponds to a nuclear polarization of $P = 54\%$ (Ref. 7) and an Overhauser field of $B_N = 3.8$ T [using $g_e = -0.6$ calculated for our InGaAs QDs (Ref. 20) and similar to values found in the literature[21,22]]. In strong contrast, resonant excitation of $|E_2\rangle$ does not result in any pumping of the nuclear spin bath for $B_{ext} \geq 4$ T. For $B_{ext} \leq 4$ T a small Overhauser shift is observed. However, the magnitude of δ_N^s is always significantly smaller than that induced by pumping of $|E_1\rangle$ at the same B_{ext}. Most remarkably, the direction of B_N with respect to B_{ext} is found to be identical for excitation of both $|E_1\rangle$ and $|E_2\rangle$ since in both cases δ_N is found to result in an increase in ΔE over the value measured without DNP effects.

The pumping of the nuclear spin bath can be explained via hf-mediated electron-nuclear spin-flip-flop processes that exchange the orientation of the electron and a nuclear spin. This process is described by the flip-flop part of the hf Hamiltonian $H_{ff} \sim S^+ \Sigma_j I_j^- + S^- \Sigma_j I_j^+$,[23] where $S^\pm$ and $I_j^\pm$ are the raising and lowering operators for the electron and jth nuclear spin, respectively. To understand the principle characteristics of the DNP curve in Fig. 3(b) we consider the exciton level structure shown in Fig. 3(a). The two bright exciton states $|E_{1,2}\rangle$ are split from the two optically inactive (dark) excitons $|E_{3,4}\rangle$ by the large isotropic exchange splitting (~ 150 μeV).[18] Bright and dark doublets are also split by anisotropic exchange δ_1 (with $\delta_1^{bright} = 40$ μeV measured at $B_{ext} = 0$ T) and are, therefore, a superposition of the pure spin states with a mixing ratio that decreases with increasing B_{ext}. The hf flip-flops couple bright and dark excitons, $|\uparrow\Downarrow\rangle \xrightarrow{S^-} |\downarrow\Downarrow\rangle$ and $|\downarrow\Uparrow\rangle \xrightarrow{S^+} |\uparrow\Uparrow\rangle$. Since only bright excitons are

excited by the laser and tunneling quickly removes all excitons from the QD, the hf flip flops occur only from bright to dark states. As we see from Fig. 3(a) the dark exciton state $|E_3\rangle \approx |\uparrow\Uparrow\rangle$ is energetically closer to both bright states than $|E_4\rangle \approx |\downarrow\Downarrow\rangle$. This makes hf-induced transitions to $|E_3\rangle$ in which the electron spin flips up (S^+) more likely than those to $|E_4\rangle$ in which it flips down [see Fig. 3(a)] since the flip rate scales with the inverse of the energy difference squared (and the matrix elements between the two states).[24] Consequently, the resonant optical pumping has the result that nuclear spins are predominantly flipped to align antiparallel with B_{ext}. This qualitatively explains why we observe *unidirectional* nuclear polarization independent of the net polarization of the electrons pumped through the dot. The peaks observed in Fig. 3(b) are related to the crossing of different exciton levels: as $|E_3\rangle$ crosses either $|E_2\rangle$ or $|E_1\rangle$, hf flips become very likely and nuclear polarization builds up. This process is particularly efficient for the higher energy exciton $|E_1\rangle$ [orange/dark gray curve in Fig. 3(b)] since the coupling matrix element $\langle E_3|H_{\text{ff}}|E_1\rangle$ is close to a maximum as $|E_1\rangle$ is of predominant $|\downarrow\Uparrow\rangle$ character. Efficient coupling between $|E_1\rangle$ and $|E_3\rangle$ is preserved over a wide range of electric fields since DNP causes both an energy shift of $|E_1\rangle$ and shifts the magnetic field for which $|E_1\rangle$ and $|E_3\rangle$ cross to larger values. This leads to a stronger and higher peak in the achieved nuclear polarization that is also shifted to higher B_{ext} values than expected from the crossing of the states without B_{N}. In contrast, for the lower energy exciton $|E_2\rangle$ DNP is much less effective since this state has predominant $|\uparrow\Downarrow\rangle$ character and $\langle E_3|H_{\text{ff}}|E_2\rangle$ is small but nonzero due to the (weak) admixture of $|\downarrow\Uparrow\rangle$ in $|E_2\rangle$ arising from the anisotropic exchange. This leads to the small DNP peak at low magnetic field around the crossing of $|E_2\rangle$ and $|E_3\rangle$ [black curve in Fig. 3(b)]. No DNP is observed at $B_{\text{ext}} \approx 0$ T since now both doublets are of strongly mixed spin character[18] and the energy difference to both dark states is almost identical for each bright state. For large B_{ext}, hf flip-flops are ineffective since the bright and dark exciton states are strongly detuned with the result that DNP is suppressed.

All these features are reproduced by our simulations shown in Fig. 3(b). Our theoretical approach makes use of the separation of time scales between the fast excitonic and slow nuclear dynamics. The exciton experiences the Overhauser field of quasistatic nuclei and quickly reaches a steady state determined by optical driving, tunneling, and the hf coupling. Dark exciton populations in this steady state arise from the transverse components of B_{N} (hf flip flops) and determine (on the slow nuclear time scale) the "instantaneous" nuclear polarization rate. This rate is used in the simulation of the PC measurements: for given magnetic field B_{ext}, laser frequency ω_{L}, and nuclear polarization P we determine the rate, change P accordingly and repeat until the steady-state polarization is reached. Keeping P fixed, the detuning is then shifted and the process is repeated. From the average exciton population (at given B_{ext}, ω_{L}, and d_{i}) the photocurrent is deduced and from the peaks in the PC curve δ_{N} is obtained as described before. In the simulations we assumed a finite laser-induced nuclear depolarization rate, as without it the nuclear steady state would be almost fully polarized throughout. A more detailed analysis of the nuclear dynamics subject to optical pumping in the presence of tunneling will be presented elsewhere. At this point we would like to mention that we were recently made aware of a paper that describes optically mediated DNSP in a single InP/GaInP QD interrogated via photoluminescence.[25] The model utilized to explain the results of that paper is fully consistent with the one proposed here.

This work was financially supported by the DFG via SFB 631 and NIM as well as by the EU via SOLID.

[1] W. A. Coish and J. Baugh, Phys. Status Solidi B **246**, 2203 (2009).
[2] J. M. Taylor, C. M. Marcus, and M. D. Lukin, Phys. Rev. Lett. **90**, 206803 (2003).
[3] A. V. Khaetskii, D. Loss, and L. Glazman, Phys. Rev. Lett. **88**, 186802 (2002).
[4] R. Oulton *et al.*, Phys. Rev. Lett. **98**, 107401 (2007).
[5] X. Xu *et al.*, Nature (London) **459**, 1105 (2009).
[6] P. Maletinsky, A. Badolato, and A. Imamoglu, Phys. Rev. Lett. **99**, 056804 (2007).
[7] B. Eble, O. Krebs, A. Lemaitre, K. Kowalik, A. Kudelski, P. Voisin, B. Urbaszek, X. Marie, and T. Amand, Phys. Rev. B **74**, 081306 (2006).
[8] A. S. Bracker *et al.*, Phys. Rev. Lett. **94**, 047402 (2005).
[9] D. Gammon, A. L. Efros, T. A. Kennedy, M. Rosen, D. S. Katzer, D. Park, S. W. Brown, V. L. Korenev, and I. A. Merkulov, Phys. Rev. Lett. **86**, 5176 (2001).
[10] A. I. Tartakovskii *et al.*, Phys. Rev. Lett. **98**, 026806 (2007).
[11] T. Yokoi, S. Adachi, H. Sasakura, S. Muto, H. Z. Song, T. Usuki, and S. Hirose, Phys. Rev. B **71**, 041307 (2005).
[12] E. S. Moskalenko, L. A. Larsson, and P. O. Holtz, Phys. Rev. B **80**, 193413 (2009).
[13] P. Maletinsky *et al.*, Nat. Phys. **5**, 407 (2009).
[14] M. N. Makhonin *et al.*, Appl. Phys. Lett. **93**, 073113 (2008).
[15] D. Loss and D. P. DiVincenzo, Phys. Rev. A **57**, 120 (1998).
[16] V. L. Korenev, JETP Lett. **70**, 129 (1999).
[17] P. W. Fry *et al.*, Phys. Rev. Lett. **84**, 733 (2000).
[18] M. Bayer *et al.*, Phys. Rev. B **65**, 195315 (2002).
[19] Defined as the time for the PC signal to reach 98% of $I_{\text{PC}}^{\text{equ}}$, the asymptotic PC value for long times.
[20] T. Andlauer, Ph.D. thesis, TU München, 2009.
[21] M. Kroner *et al.*, Phys. Rev. Lett. **100**, 156803 (2008).
[22] M. Bayer, A. Kuther, A. Forchel, A. Gorbunov, V. B. Timofeev, F. Schafer, J. P. Reithmaier, T. L. Reinecke, and S. N. Walck, Phys. Rev. Lett. **82**, 1748 (1999).
[23] J. Schliemann, A. Khaetskii, D. Loss, and J. Phys, J. Phys.: Condens. Matter **15**, R1809 (2003).
[24] For example, J. J. Sakurai, *Modern Quantum Mechanics*, 2nd ed. (Addison-Wesley, Reading, Massachusetts, 1994).
[25] E. A. Chekhovich, A. B. Krysa, M. S. Skolnick, and A. I. Tartakovskii, arXiv:1007.1241v2 (unpublished).

arXiv:1212.3140v1 [cond-mat.mes-hall] 13 Dec 2012

Large nuclear spin polarization in gate-defined quantum dots using a single-domain nanomagnet

Gunnar Petersen,[1,*] Eric A. Hoffmann,[1,*] Dieter Schuh,[2] Werner Wegscheider,[3,2] Geza Giedke,[4] and Stefan Ludwig[1]

[1] *Center for Nanoscience and Fakultät für Physik, Ludwig-Maximilians-Universität München, Geschwister-Scholl-Platz 1, 80539 München, Germany*
[2] *Institut für Experimentelle Physik, Universität Regensburg, D-93040 Regensburg, Germany*
[3] *Solid State Physics Laboratory, ETH Zurich, 8093 Zurich, Switzerland*
[4] *Max-Planck-Institut für Quantenoptik, 85748 Garching, Germany*

(Dated: December 14, 2012)

The electron-nuclei (hyperfine) interaction is central to spin qubits in solid state systems. It can be a severe decoherence source but also allows dynamic access to the nuclear spin states. We study a double quantum dot exposed to an on-chip single-domain nanomagnet and show that its inhomogeneous magnetic field crucially modifies the complex nuclear spin dynamics such that the Overhauser field tends to compensate external magnetic fields. This turns out to be beneficial for polarizing the nuclear spin ensemble. We reach a nuclear spin polarization of $\simeq 50\,\%$, unrivaled in lateral dots, and explain our manipulation technique using a comprehensive rate equation model.

PACS numbers: 76.70.Fz, 81.07.Ta, 31.30.Gs, 07.55.Db

The hyperfine interaction (HFI) between few electrons and a bath of nuclear spins induces a complex quantum many-body dynamics which has been studied in a variety of systems including phosphorus donors in silicon [1], nitrogen vacancy centers in diamond [2], quantum Hall systems [3], and semiconductor-based quantum dots, both optically [4] and in transport [5, 6]. In GaAs double quantum dots (DQDs), each electron interacts with $\sim 10^6$ nuclear spins, which fluctuate thermally even at cryogenic temperatures. Their HFI causes electron spin decoherence [6–9], but it also offers a means to control the nuclear spins dynamically [10–13]. As has been proposed [14–17] and demonstrated [18–20], nuclear spin manipulation facilitates nuclear state preparation, which can enhance spin coherence times [21, 22]. Nuclear spin manipulation has also motivated theoretical proposals [23, 24] and experimental realizations [25, 26] of nuclear spins as quantum memory.

Here, we present a novel nuclear spin manipulation technique. We couple a DQD with a single-domain nanomagnet whose inhomogeneous magnetic field does not depend on external fields. This allows measurements in a new regime, which will increase our fundamental understanding and control of the coupled electron-nuclei system common to a variety of platforms. As an example, we demonstrate unusually strong dynamic nuclear spin polarization (DNSP). In laterally defined DQDs, adiabatic pumping experiments have produced polarizations of 1–5 % [11–13], and using electron dipole spin resonance, 16 % has been realized [10]. Using a simpler experimental technique, we report $\simeq 50\,\%$ polarization, achieved by exploiting the benefits of our nanomagnet.

We measure the current, I, which results from a dc voltage, here $V = 1\,\mathrm{mV}$, applied across the DQD exposed to the inhomogeneous magnetic field of a nanomagnet (see Figures 1a,c). As detailed in Figure 1b, electrons tunnel sequentially through the DQD via the occupation

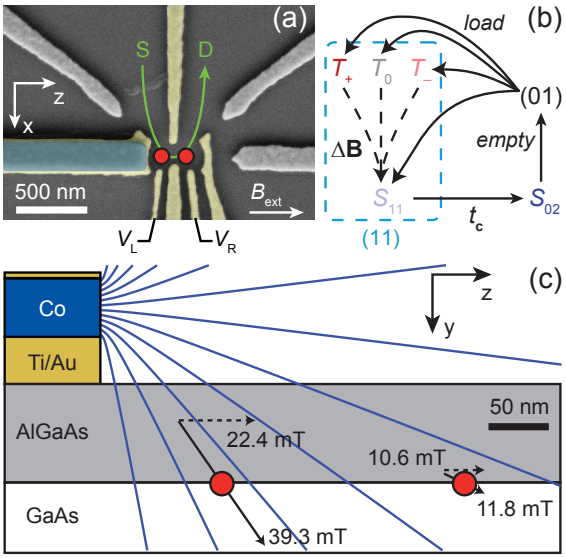

FIG. 1. (a) Scanning electron micrograph showing the Ti/Au gates (yellow) used to define the DQD. Electrons tunnel sequentially from source (S) to drain (D) through the two QDs located near ●. The (blue) single-domain Co nanomagnet (200 (width) × 50 (height) × 2000 nm^3, 2/5 visible) generates an inhomogeneous magnetic field, $\mathbf{B}_{\mathrm{nm}}$. (b) The tunneling sequence $(0\,1) \rightarrow (1\,1) \rightarrow (0\,2) \rightarrow (0\,1)$. Triplet-singlet transitions $\{T_-, T_0, T_+\} \rightarrow S_{11}$ require lifting of the PSB. (c) The relevant layers of the heterostructure, gates, and nanomagnet. The magnetic field lines (blue) are calculated according to ref. 27. The black arrows indicate the local magnetic fields $\mathbf{B}^{\mathrm{L}}_{\mathrm{nm}} = (0, 32.3, 22.4)\,\mathrm{mT}$ and $\mathbf{B}^{\mathrm{R}}_{\mathrm{nm}} = (0, 5.2, 10.6)\,\mathrm{mT}$. The 3 mT radius of ● represents the typical Overhauser field fluctuations.

cycle $(0\,1) \rightarrow (1\,1) \rightarrow (0\,2) \rightarrow (0\,1)$, where $(m\,n)$ indicates the number, m (n), of electrons in the left (right) dot. The transition $(0\,1) \rightarrow (1\,1)$ loads one of four $(1\,1)$ states, which consist of the singlet state, S_{11}, and the three triplet states, $T_{11} = \{T_-,\ T_0,\ T_+\}$. Only $T_\pm$ have a nonzero spin projection along the quantization axis, which we choose parallel to the external magnetic field, $B_{\rm ext}$ (along the z-axis in Figure 1a). The only energetically accessible $(0\,2)$ state is the singlet state, S_{02}. The corresponding eigenenergies are plotted in Figure 2a as a function of the energy detuning, Δ, between the diabatic singlet states S_{11} and S_{02}. The singlet eigenstates, $S_{\rm s}$ and $S_{\rm a}$, are the symmetric and antisymmetric combinations of S_{11} and S_{02} mixed by the interdot tunnel coupling, $t_{\rm c}$. T_0 is at zero energy (neglecting exchange coupling), while $T_\pm$ are split by their Zeeman energies, $E_{\rm z}^{\pm} = \pm g\mu_{\rm B}\left(\left|\mathbf{B}^{\rm L} + \mathbf{B}^{\rm R}\right|\right)/2$, where $\mathbf{B}^{\rm L}$ ($\mathbf{B}^{\rm R}$) is the local magnetic field in the left (right) dot, g the Landé g-factor, and $\mu_{\rm B}$ the Bohr magneton. For $\Delta > 0$, the triplets are well separated from $S_{\rm s}$, but not from $S_{\rm a}$.

In a homogeneous magnetic field $\left(\mathbf{B}^{\rm L} = \mathbf{B}^{\rm R}\right)$, transitions between triplets and singlets are forbidden by Pauli spin blockade [28] (PSB) (dashed arrows in Figure 1b). Eventually the occupation cycle stalls in one of the triplets resulting in $I = 0$ (neglecting cotunneling). DNSP requires $I \neq 0$, which can be induced by a local field difference, $\mathbf{B}^{\rm L} - \mathbf{B}^{\rm R}$, that lifts the PSB by coupling triplets to singlets. One way to produce inhomogeneous fields is to include on-chip micromagnets, which have been used for all-electric control of a single electron spin [29–31]. However, at external fields below a few hundred mT, micromagnets form magnetic domains, which greatly reduce their fields. Here, we use a nanomagnet (see Figure 1a), which forms a single magnetic domain (due to its shape anisotropy) and a sizable $\Delta\mathbf{B} = \left(\mathbf{B}^{\rm L} - \mathbf{B}^{\rm R}\right)/2$ even if $B_{\rm ext} = 0$ [32]. This previously unexplored regime proves to be highly beneficial for controlling DNSP.

Even in the absence of on-chip magnets, the HFI between thermally fluctuating nuclear spins and electrons creates an *effective* (Overhauser) field, $\mathbf{B}_{\rm nuc}$, which statistically varies between the two dots resulting in a small leakage current near $B_{\rm ext} \simeq 0$ and $\Delta \simeq 0$ [33, 34]. Compared to $\mathbf{B}_{\rm nuc}$, the nanomagnet's inhomogeneous field, $\mathbf{B}_{\rm nm}$, is more stable in time, and $|\Delta\mathbf{B}_{\rm nm}| \gg |\Delta\mathbf{B}_{\rm nuc}|$ (see Figure 1c). $B_{\rm ext}$ is aligned along the easy axis (z-axis) of the nanomagnet, which has a coercive field of 52 mT. Because the nanomagnet forms a single domain, $B_{\rm ext}$ does not affect the magnitude of $\mathbf{B}_{\rm nm}$. The associated $\Delta\mathbf{B}_{\rm nm}$ results in a leakage current over a broad range of Δ and $B_{\rm ext}$ including distinct current maxima along the $S_{\rm a}$–$T_\pm$ resonances (Figure 2b). These current features are seen at small $B_{\rm ext}$ and, hence, are not accessible with multidomain magnets (see above). Our observed current features are very different from measurements performed without an on-chip magnet [33].

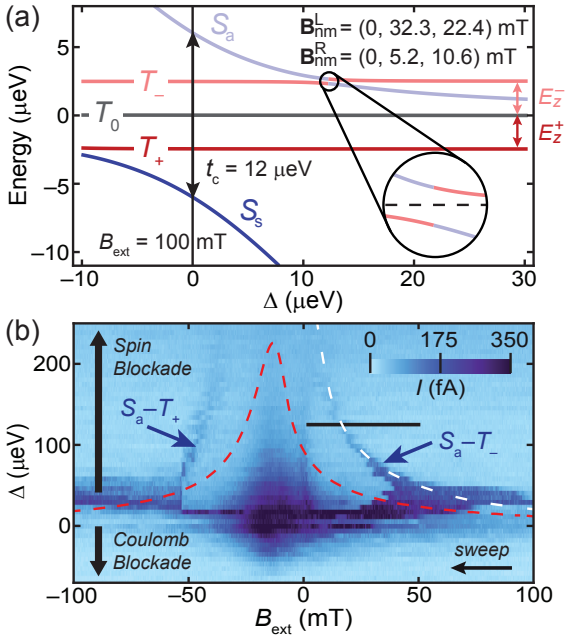

FIG. 2. (a) The relevant eigenenergies as a function of Δ, for $\mathbf{B}_{\rm nuc} = 0$. The inhomogeneous $\mathbf{B}_{\rm nm}$ causes singlet-triplet mixing (see enlarged $S_{\rm a}$–T_- avoided crossing) and lifts the PSB. (b) Leakage current, I, through the DQD versus Δ (stepped from top to bottom) and $B_{\rm ext}$ (swept at -50 mT/min). The red dashed line is a numerical prediction of the $S_{\rm a}$–$T_\pm$ resonances without DNSP using $t_{\rm c} = 12\,\mu$eV. The white dashed line includes DNSP (via the $S_{\rm a}$–T_- resonance) using eq 1 with $\Gamma_{\rm rel} = 0.043\,{\rm s}^{-1}$, $\gamma = 10$ mT, and $\alpha = 35\,{\rm nA}^{-1}\,{\rm s}^{-1}$.

However, consideration of $\mathbf{B}_{\rm nm}$ alone does not explain all features in Figure 2b. We must include the HFI and its effect on DNSP, as has proven necessary in other experiments [19, 35–37]. The dashed red line in Figure 2b is a prediction of the position of the $S_{\rm a}$–$T_\pm$ resonances as a function of $B_{\rm ext}$ and Δ. It takes into account $\mathbf{B}_{\rm nm}$, but neglects $\mathbf{B}_{\rm nuc}$ [33]. Compared to this prediction, however, the measured resonances (blue arrows in Figure 2b) occur at larger $|B_{\rm ext}|$. As we will show, this shift can be explained by including DNSP, which produces a $B^z_{\rm nuc}$ that compensates $B_{\rm ext}$, e. g., $B^z_{\rm nuc} < 0$ when $B_{\rm ext} > 0$.

The connection to DNSP becomes evident with the data shown in Figure 3a, which probes the $S_{\rm a}$–T_- resonance as a function of time for a fixed Δ. We prepared the nuclear spin polarization, P, to $P \simeq 0$ by waiting three minutes at $I = 0$ before turning on the voltage across the DQD. The current maximum, $I_{\rm max}$, at the $S_{\rm a}$–T_- resonance occurs later in time at larger $B_{\rm ext}$. Again, this can be explained if $B^z_{\rm nuc} < 0$ and compensates $B_{\rm ext}$. Because the GaAs g-factor is negative, $P = -B^z_{\rm nuc}/B^{\rm max}_{\rm nuc}$, where

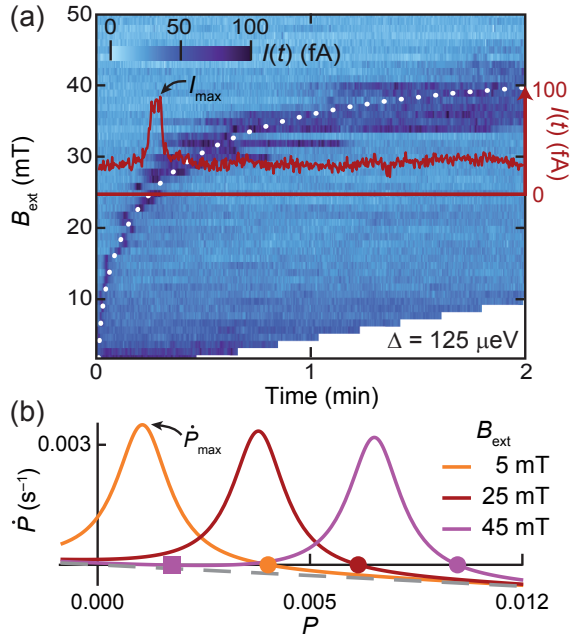

FIG. 3. (a) Current versus time, $I(t)$, as a function of $B_{\rm ext}$ along the horizontal line in Figure 2b (we prepared $P(0) = 0$). *Density Plot:* $I(t, B_{ext})$. The white dotted line predicts the moment of maximal current, $t\,(I_{\rm max})$, using eq 1 and the same parameters as in Figure 2b. *Red Trace:* $I(t)$ measured at $B_{\rm ext} = 25\,{\rm mT}$. (b) $\dot{P}(P)$ for three different $B_{\rm ext}$ using eq 1 and the same parameters as in Figure 2b. Far from resonance an exponential decay $\dot{P} = -\Gamma_{\rm rel}P$ remains (gray dashed line). ●,●,● mark the $B_{\rm ext}$–dependent "adjustable" fixed point and ■ a "trivial" fixed point, which appears near $P = 0$ when $B_{\rm ext} \gtrsim 45\,{\rm mT}$.

$B^{\rm max}_{\rm nuc} \simeq 6.1\,{\rm T}$ is the Overhauser field magnitude produced when all nuclear spins are aligned [33]. $B^z_{\rm nuc} < 0$ implies that $P > 0$, which can only be explained if DNSP from T_+ outweighs that from T_-, despite the system being near the $S_{\rm a}$–T_- resonance. This peculiar situation results from spin-selective lifting of the PSB (of T_-) and bolsters DNSP, as discussed below.

Our explanation starts with a rate equation model [19, 20, 38] including only polarization generated by T_+ near the $S_{\rm a}$–T_- resonance (A comprehensive calculation in [33] Sec. III includes all (1 1) states). As a simplification, we use the average polarization $P = \left(P^{\rm L} + P^{\rm R}\right)/2$. ($P^{\rm L} \neq P^{\rm R}$ would mainly affect the decay of T_0, not $T_\pm$.) The overall rate equation is

$$\dot{P}(t) = \Gamma_{\rm pol}(t)\,[1 - P(t)] - \Gamma_{\rm rel}P(t), \qquad (1)$$

where the polarization decay rate, $\Gamma_{\rm rel}$, is constant, while the build-up rate, $\Gamma_{\rm pol}(t)$, is proportional to current, $\Gamma_{\rm pol}(t) = \alpha I(t) > 0$, as observed experimentally. For convenience, we describe the current maximum at the $S_{\rm a}$–T_- resonance as a Lorentzian

$$I(t) = I_{\rm max}\frac{(\gamma/2)^2}{\left(E_z^- - E_{\rm a}\right)^2 + (\gamma/2)^2}, \qquad (2)$$

where $I_{\rm max}$ is the (measured) resonant current and γ is the effective width of the resonance. (Nonresonant states contribute weakly to $I(t)$.) Here

$$E_{\rm a} = \left(-\Delta + \sqrt{t_{\rm c}^2 + \Delta^2}\right)/2 \qquad (3)$$

is the energy of $S_{\rm a}$. We approximate $E_{\rm z}$ by only including the average z-component of $\mathbf{B}_{\rm nm}$, $\overline{B}^z_{\rm nm}$, so that

$$E_{\rm z}^- \approx |g|\,\mu_{\rm B}\left(B_{\rm ext}(t) - B^{\rm max}_{\rm nuc}P(t) + \overline{B}^z_{\rm nm}\right). \qquad (4)$$

Example $\dot{P}(P)$ curves are plotted in Figure 3b and are used to model the data in Figure 3a. $P\,(t = 0) = 0$ in this measurement, and the model predicts $\dot{P}(P = 0) > 0$ (evident in Figure 3b). Therefore, P increases in time until it reaches a stable fixed point at $\dot{P} = 0$ (and ${\rm d}\dot{P}/{\rm d}P < 0$). For $B_{\rm ext} < 43\,{\rm mT}$, P passes through the $S_{\rm a}$–T_- resonance, which coincides with $\dot{P}_{\rm max}$ in Figure 3b. As $B_{\rm ext}$ is increased, the $S_{\rm a}$–T_- resonance moves to larger P, and with it move $\dot{P}_{\rm max}$ and the stable "adjustable" fixed point (A-FP, circles in Figure 3b). Accordingly, the measured (resonant) $I_{\rm max}$ in Figures 3a appears later in time with increasing $B_{\rm ext}$. When $B_{\rm ext} \approx 45\,{\rm mT}$, a second stable "trivial" fixed point (T-FP, square in Figure 3b) appears near $P = 0$ and remains there for $B_{\rm ext} > 45\,{\rm mT}$. Hence, we expect P to remain near zero (far from resonance) at the T-FP. Indeed, no resonant current maximum is observed for $B_{\rm ext} \gtrsim 43\,{\rm mT}$ in Figure 3a.

Eq 1 provides quantitative predictions of the time evolution of the $S_{\rm a}$–T_- resonance associated with the measured $I_{\rm max}$. Namely, it yields the white fits in Figures 2b and 3a. These two separate fits share altogether four fit parameters. The agreement between our model and data indicates that the model captures the DNSP in both experiments. In addition, $\Gamma_{\rm rel}$ agrees with reported values [13].

Our model reveals a straightforward procedure to maximize P. We start at small $B_{\rm ext}$ where the T-FP is absent and P is initialized at the A-FP (see top panel of Figure 4a). This initialization requires small $B_{\rm ext}$ and sufficient singlet–triplet mixing and is only possible with a single-domain nanomagnet. To reach a large P, we increase $B_{\rm ext}$ (with a sufficiently slow sweep rate) dragging the A-FP, and P along with it (see middle panel of Figure 4a). This dragging procedure works up to a maximum polarization, $P_{\rm max}$, occurring when the decay of P overwhelms its build-up and $\dot{P}_{\rm max} = 0$ (see bottom panel of Figure 4a). $P_{\rm max}$ is defined by solving eq 1 for $\dot{P}(P_{\rm max}) = 0$:

$$P_{\rm max}/\left(1 - P_{\rm max}\right) = \alpha I_{\rm max}/\Gamma_{\rm rel} \equiv \Gamma^{\rm max}_{\rm pol}/\Gamma_{\rm rel}, \qquad (5)$$

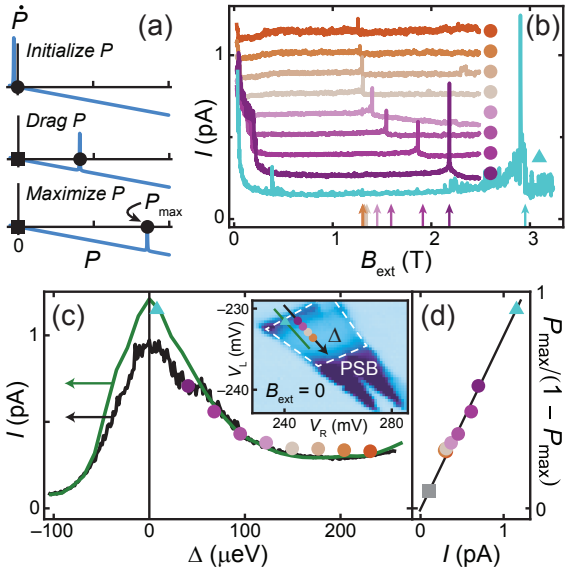

FIG. 4. (a) $\dot{P}(P)$ for three $B_{\rm ext}$ using eq 1 with $I_{\rm max} = 1.2\,$pA and the fit parameters from Figure 2b. ■ marks the T-FP and ● the A-FP. (b) Leakage current, I, for various Δ in the PSB regime [see (c)] measured while continuously increasing $B_{\rm ext}$ (at 30 mT/min) after initialization at the A-FP at $B_{\rm ext} = 50\,$mT. (All but the lowest trace are vertically offset in increments of 125 fA.) Sharp current peaks (marked by arrows) correspond to the maximum polarization, $P_{\rm max}(\Delta)$, in (a). (c) $P_{\rm max}/(1-P_{\rm max})$ from (b) (filled circles) and I (black/green traces), measured along the (black/green) lines in the inset, versus Δ. *Inset*: I measured as a function of gate voltages $V_{\rm L,R}$ (see Figure 1a). The region of suppressed I within the double triangle of finite current marks PSB. (d) $P_{\rm max}/(1-P_{\rm max})$ versus I, extracted from the traces in (c). The gray square is predicted from the data in Figure 2b. The black line expresses eq 5 with $\alpha/\Gamma_{\rm rel} = 0.81\,{\rm pA}^{-1}$ using the fit parameters from Figure 2b.

where $\Gamma_{\rm pol}^{\rm max}, P_{\rm max} > 0$ and both depend on Δ via $I_{\rm max}$. At $B_{\rm ext}^{\rm max}$ (the field corresponding to $P_{\rm max}$), the A-FP coincides with the $S_{\rm a}$–T_- resonance, and we expect a current maximum.

Indeed, the leakage current measured during such DNSP sweeps, displayed for various Δ in Figure 4b, features a sharp current maximum at a particular $B_{\rm ext}$ (see arrows), which we identify as $B_{\rm ext}^{\rm max}(\Delta)$. For $B_{\rm ext} > B_{\rm ext}^{\rm max}$, the A-FP is lost, and the nuclear spin polarization decays ($\dot{P} < 0$) with rate $\Gamma_{\rm rel}$.

$P_{\rm max}(\Delta)$ compensates $B_{\rm ext}^{\rm max}(\Delta)$ so that we can equate $P_{\rm max}(\Delta) = B_{\rm ext}^{\rm max}(\Delta)/B_{\rm nuc}^{\rm max}$. $P_{\rm max}/(1-P_{\rm max})$ and I measured versus Δ are shown side-by-side in Figure 4c demonstrating a striking correlation between $P_{\rm max}/(1-P_{\rm max})$ and I. In fact, in accordance with eq 5, Figure 4d shows that $P_{\rm max}/(1-P_{\rm max}) \propto I$ confirming our assumption that $\Gamma_{\rm pol} \propto I$. The straight black line in Figure 4d expresses eq 5 using the fit parameters from Figure 2b.

The ability to explain three very different data sets (Figures 2b, 3a, 4d) with one set of fit parameters corroborates the interpretation of the current peaks in Figure 4b and the validity of our rate equation model [33].

Our highest $B_{\rm ext}^{\rm max} \simeq 2.9\,$T (green data in Figure 4b) corresponds to $P \simeq 50\,\%$ (and generates an Overhauser field gradient of $\sim 1\,$T/100nm across the DQD boundary). This exceeds by far previously reported polarizations in laterally defined DQDs [10–13](a complementary measurement of P in [33] Sec. VI).

To detail how $\mathbf{B}_{\rm nm}$ and the HFI combine to lift the PSB and induce DNSP, we compare our system with two simpler scenarios. If the HFI were the only mechanism to lift PSB, no DNSP would be expected since all triplets are loaded equally often resulting in as many up as down nuclear spin flips. In experiments without a nanomagnet [36, 39], cotunneling weakly lifts the PSB (in competition with the HFI) and does so equally for each triplet, nearly irrespective of its energy. In contrast, the hyperfine-induced decay rate is strongly energy dependent. Therefore, near the $S_{\rm a}$–T_- resonance, T_- generates more nuclear spin flips than T_+, and $P < 0$ is observed without nanomagnet.

In our case, $\mathbf{B}_{\rm nm}$ mixes T_- and $S_{\rm a}$ strongly near their resonance, resulting in two (1 1) states that are no longer in PSB. Hyperfine-induced decay is heavily suppressed in these mixed states. In this situation, the HFI still contributes to the decay of T_+ (and T_0) thereby producing DNSP and $P > 0$. In an alternative approach, DNSP has been studied for large $t_{\rm c}$ ($\sim 100\,\mu$eV) by sweeping Δ[36, 37, 39]. However, when $t_{\rm c} \sim$ 1–10 μeV, which is favorable for spin qubits, P is limited by the energy of $S_{\rm a}$ in the PSB regime, so that $|P| \lesssim t_{\rm c}/(2\,|g|\,\mu_{\rm B} B_{\rm nuc}^{\rm max}) \sim 10\,\%$. Moreover, $B_{\rm nuc}^{z} < 0$ in our system provides a distinct advantage because $B_{\rm nuc}^{z}$ compensates $B_{\rm ext}$ such that the total effective magnetic field is constant during the polarization build-up; therefore, P is only limited by $\alpha I_{\rm max}/\Gamma_{\rm rel}$ when dragging P with $B_{\rm ext}$.

We have demonstrated a nuclear spin polarization of $\simeq 50\,\%$ in a DQD based on the enhanced ability to manipulate the nuclear spin ensemble using an on-chip nanomagnet. Larger polarizations can be expected upon further optimization of the electronic spectrum, sample geometry and materials. Our results demonstrate the flexibility offered by an on-chip nanomagnet, which could be used for all-electric ESR [29] while simultaneously polarizing the nuclear spin ensemble at small $t_{\rm c}$ values ideal for spin qubit operation. Such a system could be used to improve nuclear state preparation techniques [12, 40–42] or for measuring complex nuclear phenomena such as spin squeezing [43], quantum memory [23, 24], dark states [44], quantum phase transitions [45], and superradiance [46].

We thank S. Cammerer as well as J. P. Kotthaus for helpful discussions regarding the nanomagnet design and S. Manus for technical support. Financial support from

the German Science Foundation DFG via SFB 631 and the German Excellence Initiative via the "Nanosystems Initiative Munich (NIM)" is gratefully acknowledged. E. A. H. thanks the Alexander von Humboldt Foundation and S. L. the Heisenberg program of the DFG.

* These authors contributed equally to this work.

[1] B. E. Kane, Nature **393**, 133 (1998).
[2] F. Jelezko and J. Wrachtrup, Physica Status Solidi A **203**, 3207 (2006).
[3] A. Kou, D. T. McClure, C. M. Marcus, L. N. Pfeiffer, and K. W. West, Phys. Rev. Lett. **105**, 056804 (2010).
[4] B. Urbaszek, X. Marie, T. Amand, O. Krebs, P. Voisin, P. Maletinsky, A. Hogele, and A. Imamoglu, ArXiv e-prints ***arXiv:1202.4637v2 [cond-mat.mes-hall]*** (2012).
[5] J. Schliemann, A. Khaetskii, and D. Loss, J. Phys.-Condes. Matter **15**, R1809 (2003).
[6] J. Fischer, M. Trif, W. A. Coish, and D. Loss, Solid State Commun **149**, 1443 (2009).
[7] W. Yao, R. B. Liu, and L. J. Sham, Phys. Rev. B **74**, 195301 (2006).
[8] L. Cywinski, W. M. Witzel, and S. Das Sarma, Phys. Rev. Lett. **102**, 057601 (2009).
[9] H. Bluhm, S. Foletti, I. Neder, M. Rudner, D. Mahalu, V. Umansky, and A. Yacoby, Nature Phys. **7**, 109 (2011).
[10] E. A. Laird, C. Barthel, E. I. Rashba, C. M. Marcus, M. P. Hanson, and A. C. Gossard, Phys. Rev. Lett. **99**, 246601 (2007).
[11] J. R. Petta, J. M. Taylor, A. C. Johnson, A. Yacoby, M. D. Lukin, C. M. Marcus, M. P. Hanson, and A. C. Gossard, Phys. Rev. Lett. **100**, 067601 (2008).
[12] S. Foletti, H. Bluhm, D. Mahalu, V. Umansky, and A. Yacoby, Nature Phys. **5**, 903 (2009).
[13] D. J. Reilly, J. M. Taylor, J. R. Petta, C. M. Marcus, M. P. Hanson, and A. C. Gossard, Phys. Rev. Lett. **104**, 236802 (2010).
[14] G. Burkard, D. Loss, and D. P. DiVincenzo, Phys. Rev. B **59**, 2070 (1999).
[15] D. Klauser, W. A. Coish, and D. Loss, Phys. Rev. B **73**, 205302 (2006).
[16] M. S. Rudner and L. S. Levitov, Phys. Rev. Lett. **99**, 036602 (2007).
[17] J. Danon and Y. V. Nazarov, Phys. Rev. Lett. **100**, 056603 (2008).
[18] C. Latta, A. Högele, Y. Zhao, A. N. Vamivakas, P. Maletinsky, M. Kroner, J. Dreiser, I. Carusotto, A. Badolato, D. Schuh, W. Wegscheider, M. Atature, and A. Imamoglu, Nature Phys. **5**, 758 (2009).
[19] I. T. Vink, K. C. Nowack, F. H. L. Koppens, J. Danon, Y. V. Nazarov, and L. M. K. Vandersypen, Nature Phys. **5**, 764 (2009).
[20] J. Danon, I. T. Vink, F. H. L. Koppens, K. C. Nowack, L. M. K. Vandersypen, and Y. V. Nazarov, Phys. Rev. Lett. **103**, 046601 (2009).
[21] H. Bluhm, S. Foletti, D. Mahalu, V. Umansky, and A. Yacoby, Phys. Rev. Lett. **105**, 216803 (2010).
[22] B. Sun, W. Yao, X. D. Xu, A. S. Bracker, D. Gammon, L. J. Sham, and D. Steel, J Opt Soc Am B **29**, A119 (2012).
[23] J. M. Taylor, A. Imamoglu, and M. D. Lukin, Phys. Rev. Lett. **91**, 246802 (2003).
[24] Z. Kurucz, M. W. Sorensen, J. M. Taylor, M. D. Lukin, and M. Fleischhauer, Phys. Rev. Lett. **103**, 010502 (2009).
[25] P. C. Maurer, G. Kucsko, C. Latta, L. Jiang, N. Y. Yao, S. D. Bennett, F. Pastawski, D. Hunger, N. Chisholm, M. Markham, D. J. Twitchen, J. I. Cirac, and M. D. Lukin, Science **336**, 1283 (2012).
[26] M. Steger, K. Saeedi, M. L. W. Thewalt, J. J. L. Morton, H. Riemann, N. V. Abrosimov, P. Becker, and H. J. Pohl, Science **336**, 1280 (2012).
[27] R. Engel-Herbert and T. Hesjedal, J. Appl. Phys. **97**, 074504 (2005).
[28] K. Ono, D. G. Austing, Y. Tokura, and S. Tarucha, Science **297**, 1313 (2002).
[29] M. Pioro-Ladriere, T. Obata, Y. Tokura, Y. S. Shin, T. Kubo, K. Yoshida, T. Taniyama, and S. Tarucha, Nature Phys. **4**, 776 (2008).
[30] T. Obata, M. Pioro-Ladriere, Y. Tokura, Y. S. Shin, T. Kubo, K. Yoshida, T. Taniyama, and S. Tarucha, Phys. Rev. B **81**, 085317 (2010).
[31] R. Brunner, Y. S. Shin, T. Obata, M. Pioro-Ladriere, T. Kubo, K. Yoshida, T. Taniyama, Y. Tokura, and S. Tarucha, Phys. Rev. Lett. **107**, 146801 (2011).
[32] S. Heedt, C. Morgan, K. Weis, D. E. Bürgler, R. Calarco, H. Hardtdegen, D. Grützmacher, and T. Schäpers, Nano. Lett. **12**, 4437 (2012).
[33] See attached Supplementary Material for additional information.
[34] F. H. L. Koppens, J. A. Folk, J. M. Elzerman, R. Hanson, L. H. W. van Beveren, I. T. Vink, H. P. Tranitz, W. Wegscheider, L. P. Kouwenhoven, and L. M. K. Vandersypen, Science **309**, 1346 (2005).
[35] K. Ono and S. Tarucha, Phys. Rev. Lett. **92**, 256803 (2004).
[36] T. Kobayashi, K. Hitachi, S. Sasaki, and K. Muraki, Phys. Rev. Lett. **107**, 216802 (2011).
[37] S. M. Frolov, J. Danon, S. Nadj-Perge, K. Zuo, J. W. W. van Tilburg, V. S. Pribiag, J. W. G. van den Berg, E. P. A. M. Bakkers, and L. P. Kouwenhoven, Phys. Rev. Lett. **109**, 236805 (2012).
[38] M. S. Rudner, F. H. L. Koppens, J. A. Folk, L. M. K. Vandersypen, and L. S. Levitov, Phys. Rev. B **84**, 075339 (2011).
[39] J. Baugh, Y. Kitamura, K. Ono, and S. Tarucha, Phys. Rev. Lett. **99**, 096804 (2007).
[40] G. Giedke, J. M. Taylor, D. D'Alessandro, M. D. Lukin, and A. Imamoglu, Phys Rev A **74**, 032316 (2006).
[41] D. J. Reilly, J. M. Taylor, J. R. Petta, C. M. Marcus, M. P. Hanson, and A. C. Gossard, Science **321**, 817 (2008).
[42] M. Issler, E. M. Kessler, G. Giedke, S. Yelin, I. Cirac, M. D. Lukin, and A. Imamoglu, Phys. Rev. Lett. **105**, 267202 (2010).
[43] M. S. Rudner, L. M. K. Vandersypen, V. Vuletic, and L. S. Levitov, Phys. Rev. Lett. **107**, 206806 (2011).
[44] M. Gullans, J. J. Krich, J. M. Taylor, H. Bluhm, B. I. Halperin, C. M. Marcus, M. Stopa, A. Yacoby, and M. D. Lukin, Phys. Rev. Lett. **104**, 226807 (2010).
[45] M. S. Rudner and L. S. Levitov, Phys. Rev. B **82**, 155418 (2010).
[46] M. J. A. Schuetz, E. M. Kessler, J. I. Cirac, and G. Giedke, Phys. Rev. B **86**, 085322 (2012).

SUPPLEMENTARY INFORMATION FOR "LARGE NUCLEAR SPIN POLARIZATION IN GATE-DEFINED QUANTUM DOTS USING A SINGLE-DOMAIN NANOMAGNET"

CONTENTS

I. OVERVIEW

The following supplementary material provides additional information related to various aspects of the main article. We start in Section II with details about the sample design and the experimental setup of the measurements. In Section III we introduce a model Hamilton operator which describes the hyperfine interaction (HFI) in our double quantum dot (DQD) setup including the inhomogeneous magnetic field of the nanomagnet. Based on a rate equation model, in Section IV, we perturbatively solve the dynamic nuclear spin polarization (DNSP) problem by explicitly taking into account the contributions of all four (1 1) states. We show that the perturbative solution justifies the simplified model used in the main article. Section V provides detailed explanations of the current features in Fig. 2b of the main article. In Section VI we present results of a complementary experiment that gives additional evidence of the validity of our model and of our interpretation of the data in Fig. 4 of the main article in terms of a large nuclear spin polarization. Section VII describes the fitting procedure for the data in Figs. 2b, 3a of the main article.

II. SAMPLE DESIGN AND EXPERIMENTAL SETUP

The samples have been fabricated from a GaAs / AlGaAs heterostructure containing a two-dimensional electron system (2DES) 85 nm below the surface. At cryogenic temperatures, the 2DES has a carrier density of $1.19 \times 10^{11}\,\mathrm{cm}^{-2}$ and a mobility of $0.36 \times 10^{6}\,\mathrm{cm}^{2}\,\mathrm{V}^{-1}\,\mathrm{s}^{-1}$. Metallic gate electrodes (30 nm gold on top of 5 nm titanium) have been fabricated on the sample surface by electron-beam lithography and standard evaporation/lift-off techniques (Fig. S1a). The Co nanomagnet with a thickness of 50 nm was evaporated directly on top of the leftmost gate and capped with 5 nm of Au to prevent oxidization. Negative voltages applied to these electrodes are used to deplete locally the 2DES and thereby define the DQD. The absolute electron occupation, $(m\ n)$, was determined by quantum-point-contact charge detection[R1]. All measurements have been performed in a dilution refrigerator at an electron temperature of $\sim 100\,\mathrm{mK}$. Fig. S1b sketches the experimental situation in this Letter. A source-drain voltage of $V = (\mu_\mathrm{S} - \mu_\mathrm{D})/e$ is applied across the DQD between degenerate leads. The DQD is in the Pauli-spin blockade, where a triplet state can only contribute to current if it is coupled to a singlet state, e.g., by field inhomogeneity or interaction with the ensemble of $N_{\mathrm{L(R)}} \sim 10^6$ nuclei.

III. THE HAMILTONIAN

The total Hamiltonian of the system includes electrostatic, magnetic, and hyperfine contributions and is given (in the relevant subspace depicted in Fig. S1b) by

$$H = H_\mathrm{el} + H_\mathrm{B} + H_\mathrm{hf}. \tag{S1}$$

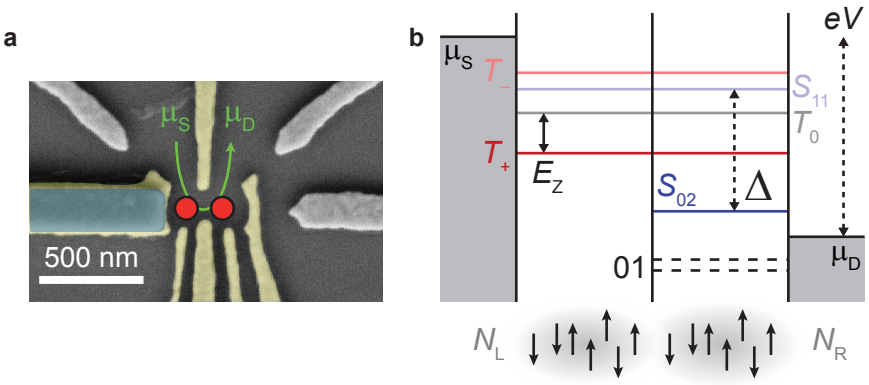

FIG. S1. **Experimental setup a)** SEM image of the DQD device used in the experiments. **b)** A DQD in Pauli-spin blockade (typical experimental situation), while a voltage V is applied between the degenerate 2D leads with chemical potentials $\mu_{\rm S}$ and $\mu_{\rm D}$. Vertical lines are tunnel barriers. The right dot always contains at least one electron. The dashed horizontal lines are the spin-split chemical potentials of the spin up/down (0 1) states, where the chemical potential of a quantum dot is defined as the energy needed to add one more electron. The solid horizontal lines are the chemical potentials of the five relevant two-electron basis states, where $E_{\rm Z}$ is the Zeeman energy and Δ is the energy detuning between the singlet states, S_{11} and S_{02}.

Using the diabatic singlet-triplet basis $\{T_+, T_0, T_-, S_{11}, S_{02}\}$, the electrostatic contribution is

$$H_{\rm el} = t_{\rm c}/2\left(|S_{11}\rangle\langle S_{02}| + |S_{02}\rangle\langle S_{11}|\right) - \Delta\,|S_{02}\rangle\langle S_{02}|\,, \tag{S2}$$

where Δ is the interdot energy detuning (see Fig. S1) and $t_{\rm c}$ is the interdot tunnel splitting (see Fig. 2a of the main article). The interaction between the local magnetic fields and the electron spins in the two dots is described by

$$H_{\rm B} = g\mu_{\rm B}\left[\left(\mathbf{B}_{\rm ext} + \mathbf{B}^{\rm L}_{\rm nm}\right)\cdot\mathbf{S}^{\rm L} + \left(\mathbf{B}_{\rm ext} + \mathbf{B}^{\rm R}_{\rm nm}\right)\cdot\mathbf{S}^{\rm R}\right], \tag{S3}$$

where $\mathbf{B}_{\rm ext}$ is the external magnetic field, $\mathbf{B}^{\rm L,R}_{\rm nm}$ the local magnetic field of the nanomagnet, $\mathbf{S}^{\rm L,R}$ the local electron spin operator, g the electron g-factor, and $\mu_{\rm B}$ the Bohr magneton.

The wave function of an electron confined in a lateral GaAs-dot overlaps with $\sim 10^6$ nuclei. The hyperfine interaction between the electron spin and the nuclear spins is dominated by the contact term $H^{\rm L,R}_{\rm con} = \sum_k A^{\rm L,R}_k \mathbf{I}^{\rm L,R}_k \cdot \mathbf{S}^{\rm L,R}$, where $\mathbf{I}^{\rm L,R}_k$ is the kth nuclear spin operator and $A^{\rm L,R}_k$ the hyperfine coupling constants. $A^{\rm L,R}_k$ is proportional to the overlap between the wavefunctions of the kth nucleus in left/right dot and the electron and varies by isotope type. It is common to define an average A reflecting the natural abundance of isotope type and the average overlap with the electron wavefunction. In this approximation, the contact Hamiltonian is $H^{\rm L,R}_{\rm con} = A\mathbf{I}^{\rm L,R}\cdot\mathbf{S}^{\rm L,R}$, where $\mathbf{I}^{\rm L,R}$ is the average nuclear spin (ensemble) operator and $A = 85\,\mu$eV in GaAs[R2]. Electrons in the left/right dot couple to different sets of nuclei, and we can write

$$H_{\rm hf} = H^{\rm L}_{\rm con} + H^{\rm R}_{\rm con} = A\left(\mathbf{I}^{\rm L}\cdot\mathbf{S}^{\rm L} + \mathbf{I}^{\rm R}\cdot\mathbf{S}^{\rm R}\right) = A\sum_{i={\rm L,R}}\left(I^i_z S^i_z + \frac{I^i_+ S^i_- + I^i_- S^i_+}{2}\right), \tag{S4}$$

where $S^{\rm L,R}_z$ and $I^{\rm L,R}_z$ are the corresponding z-projection operators; and $S^{\rm L,R}_\pm = S^{\rm L,R}_x \pm iS^{\rm L,R}_y$ and $I^{\rm L,R}_\pm = I^{\rm L,R}_x \pm iI^{\rm L,R}_y$ are the spin raising and lowering operators. In a semiclassical approximation $\mathbf{I}^{\rm L,R}$ can be replaced by the effective nuclear magnetic (Overhauser) field[R3] $\mathbf{B}^{\rm L,R}_{\rm nuc} = A\langle\mathbf{I}^{\rm L,R}\rangle/(g\mu_{\rm B})$, where $\langle\ldots\rangle$ denotes the expectation value, and $\langle I\rangle_{\rm max} = 3/2$ in GaAs. In ESR experiments (not shown), we measured $g \simeq -0.36$ in our system. This predicts, for fully polarized nuclear spins ($P = 1$), an Overhauser field magnitude of $B^{\rm max}_{\rm nuc} = A\langle I\rangle_{\rm max}/(|g|\,\mu_{\rm B}) \simeq 6.1\,$T. The semiclassical version of $H_{\rm hf}$ has the same form as $H_{\rm B}$ (see Eq. (S3)), and we can summarize

$$H_{\rm B} + H_{\rm hf} = g\mu_{\rm B}\left(\mathbf{B}^{\rm L}\cdot\mathbf{S}^{\rm L} + \mathbf{B}^{\rm R}\cdot\mathbf{S}^{\rm R}\right), \tag{S5}$$

where $\mathbf{B}^{\rm L,R} = \mathbf{B}_{\rm ext} + \mathbf{B}^{\rm L,R}_{\rm nm} + \mathbf{B}^{\rm L,R}_{\rm nuc}$ is the total effective magnetic field acting on an electron in the left and right dot, respectively.

In analogy to $\overline{\mathbf{B}} = \left(\mathbf{B}^{\rm L} + \mathbf{B}^{\rm R}\right)/2$ and $\Delta\mathbf{B} = \left(\mathbf{B}^{\rm L} - \mathbf{B}^{\rm R}\right)/2$, we define the symmetric and antisymmetric spin operators $\overline{\rm S} = \left(\mathbf{S}^{\rm L} + \mathbf{S}^{\rm R}\right)/2$ and $\Delta{\rm S} = \left(\mathbf{S}^{\rm L} - \mathbf{S}^{\rm R}\right)/2$. We then use $\overline{B}_\pm = \overline{B}_x \pm i\overline{B}_y$, $\Delta B_\pm = \Delta B_x \pm i\Delta B_y$, $\overline{\rm S}_\pm = \overline{\rm S}_x \pm i\overline{\rm S}_y$

and $\Delta \mathrm{S}_{\pm} = \Delta \mathrm{S}_x \pm i \Delta \mathrm{S}_y$, defined akin to the spin raising and lowering operators in equation (S4), to write equation (S5) analogous to the right hand side of equation (S4):

$$H_{\mathrm{B}} + H_{\mathrm{hf}} = g\mu_{\mathrm{B}} \left(2\overline{B}_z \overline{\mathrm{S}}_z + 2\Delta B_z \Delta \mathrm{S}_z + \Delta B_+ \Delta \mathrm{S}_- + \Delta B_- \Delta \mathrm{S}_+ + \overline{B}_+ \overline{S}_- + \overline{B}_- \overline{S}_+ \right). \tag{S6}$$

With the quantization axis, $\hat{z}$, defined parallel to $\mathbf{B}_{\mathrm{ext}}$, the matrix representation of the (semiclassical) total Hamiltonian in the basis spanned by the diabatic singlet and triplet states $\{T_+,\, T_0,\, T_-,\, S_{11},\, S_{02}\}$ is

$$H = \mu^\star \begin{array}{c} \begin{array}{ccccc} T_+ & T_0 & T_- & S_{11} & S_{02} \end{array} \\ \left(\begin{array}{ccccc} \sqrt{2}\,\overline{B}_z & \overline{B}_- & 0 & -\Delta B_- & 0 \\ \overline{B}_+ & 0 & \overline{B}_- & \sqrt{2}\Delta B_z & 0 \\ 0 & \overline{B}_+ & -\sqrt{2}\,\overline{B}_z & \Delta B_+ & 0 \\ -\Delta B_+ & \sqrt{2}\Delta B_z & \Delta B_- & 0 & t_{\mathrm{c}}^\star/2 \\ 0 & 0 & 0 & t_{\mathrm{c}}^\star/2 & -\Delta^\star \end{array} \right) \end{array} \quad \begin{array}{l} T_+ = |\uparrow\uparrow\rangle \\ T_0 = \left(|\uparrow\downarrow\rangle + |\downarrow\uparrow\rangle\right)/\sqrt{2} \\ T_- = |\downarrow\downarrow\rangle \\ S_{11} = \left(|\uparrow\downarrow\rangle - |\downarrow\uparrow\rangle\right)/\sqrt{2} \\ S_{02} = |0,\uparrow\downarrow\rangle \end{array} \tag{S7}$$

where $\mu^\star = g\mu_{\mathrm{B}}/\sqrt{2}$, $t_{\mathrm{c}}^\star = t_{\mathrm{c}}/\mu^\star$ and $\Delta^\star = \Delta/\mu^\star$. The matrix representation (S7) illustrates that the x- and y-components of $\mathbf{\Delta B}$ mix $T_\pm$ with S_{11}, while the z-component of $\mathbf{\Delta B}$ mixes T_0 (which has no spin component along the z-axis) with S_{11}. Instead, $\overline{B}_z$ leads to the Zeeman splitting of the $T_\pm$ states. Note that the off-diagonal terms $\overline{B}_\pm$, which mix $T_\pm$ with T_0, vanish if the quantization axis is chosen parallel to $\overline{\mathbf{B}}$.

IV. PERTURBATION CALCULATION OF DNSP

In the main article, we use a simplified approximation that only considers the hyperfine contribution from T_+. In this section, we calculate the hyperfine-induced decay of all (1 1) states using perturbation theory (Fermi's golden rule) similar to reference [R4] in which, however, the effects of a nanomagnet were not included. Here we show that the simplified model produces the pertinent features of the perturbation theory, justifying the approximation used in the main article.

We start by writing equation (S1) as $H = H_0 + H_{\mathrm{ff}}^+ + H_{\mathrm{ff}}^-$, where

$$H_0 = H_{\mathrm{el}} + H_{\mathrm{B}} + 2g\mu_{\mathrm{B}} \left(\overline{B}_{\mathrm{nuc}}^z \overline{S}_z + \Delta B_{\mathrm{nuc}}^z \Delta S_z \right), \tag{S8}$$

$$H_{\mathrm{ff}}^\pm = g\mu_{\mathrm{B}} \left(\overline{B}_{\mathrm{nuc}}^\pm \overline{\mathrm{S}}_\mp + \Delta B_{\mathrm{nuc}}^\pm \Delta \mathrm{S}_\mp \right), \tag{S9}$$

are the bare Hamiltonian and hyperfine flip-flop Hamiltonians, respectively. We treat $H_{\mathrm{ff}}^+ + H_{\mathrm{ff}}^-$ as a perturbation of H_0. Diagonalization of H_0 provides the unperturbed eigenvalues, E_n, of the nth eigenstate, $|n\rangle$. We account for coupling to the leads by a simple master equation with four Lindblad operators (eliminating the intermediate stage in the sequential tunneling process $(0\,2) \to (0\,1) \to (1\,1)$) and assuming that the four (1 1) states $\{T_+, T_0, T_-, S_{11}\}$ are populated with equal rate:

$$\frac{d}{dt}\rho = \frac{1}{i\hbar}[H_0, \rho] + \frac{\Gamma_R}{4} \sum_{x \in \{T_+, T_0, T_-, S_{11}\}} \left(|x\rangle \langle S_{02}|\, \rho\, |S_{02}\rangle \langle x| - \frac{1}{2} \left(|S_{02}\rangle \langle S_{02}|\, \rho + \rho\, |S_{02}\rangle \langle S_{02}| \right) \right). \tag{S10}$$

We approximate the dynamics by a rate equation for the populations $\boldsymbol{\rho} = (\rho_{11}, \rho_{22}, \rho_{33}, \rho_{44}, \rho_{55})$ in the five energy eigenstates.

$$\frac{d\boldsymbol{\rho}}{dt} = G^{(0)} \boldsymbol{\rho}. \tag{S11}$$

The transition matrix $G^{(0)} = (G_{ij}^{(0)})_{ij}$, describes decay of the level n with a rate $\Gamma_n^0 = \Gamma_R s_n$, determined by $s_n = |\langle S_{02}|\, n\rangle|^2$, the overlap of $|n\rangle$ with the localized singlet state. Since only (1 1) states are refilled, the rate with which

$|m\rangle$ is populated is proportional to $(1 - s_m)$: Hence the matrix elements of $G^{(0)}$ are

$$G^{(0)}_{nm} = \frac{\Gamma_R}{4}(1 - s_n)s_m \ \ (n \neq m), \tag{S12}$$

$$G^{(0)}_{nn} = -\frac{\Gamma_R}{4}s_n\,(3 + s_n)\,. \tag{S13}$$

The width of the level $|n\rangle$ is given by $\hbar\Gamma^0_n = \hbar\Gamma_R s_n$.

We include the hyperfine flip-flop processes using Fermi's golden rule (assuming a constant density of states over the range of energies of the (1 1) states) to determine the flip-flop rate from an initial state, $|n\rangle$, to the final state, $|f\rangle$ as

$$\begin{aligned}\Gamma^{\pm}_{n\to f} &= \frac{2\pi}{\hbar}\left|\langle f|\, H^{\pm}_{\rm ff}\,|n\rangle\right|^2 \frac{1}{2\pi}\frac{\hbar\left(\Gamma^0_f + \Gamma^0_n\right)}{(E_n - E_f)^2 + \left(\hbar\frac{\Gamma^0_f+\Gamma^0_n}{2}\right)^2}\frac{1 \mp P}{2} \\ &= \frac{\left|\langle f|\, H^{\pm}_{\rm ff}\,|n\rangle\right|^2\left(\Gamma^0_f + \Gamma^0_n\right)}{(E_n - E_f)^2 + \left(\hbar\frac{\Gamma^0_f+\Gamma^0_n}{2}\right)^2}\frac{1 \mp P}{2},\end{aligned}$$

where the factor $(1 \mp P)/2$ expresses the influence of polarization on the nuclear-spin flip rates. The total escape rate from $|n\rangle$ is then

$$\Gamma_n = \Gamma^0_n + \sum_{f\neq n}(\Gamma^+_{n\to f} + \Gamma^-_{n\to f}). \tag{S14}$$

We can neglect cotunneling in our sample, since its contribution to the leakage current is negligible compared to that of the nanomagnet. The full rate equation is now given by

$$\frac{d\boldsymbol{\rho}}{dt} = G\boldsymbol{\rho}, \tag{S15}$$

with $G_{nm} = G^{(0)}_{nm} + \Gamma^+_{n\to m} + \Gamma^-_{n\to m} (n \neq m)$ and $G_{nn} = G^{(0)}_{nn} - \sum_{m\neq n}(\Gamma^+_{n\to m} + \Gamma^-_{n\to m})$.

We determine the leakage current and the DNSP rates by numerically solving for $\dot{\boldsymbol{\rho}} = 0$, obtaining the steady state populations $\rho^{\rm ss}_n$. The magnitude of the total current is given by

$$I = I^0 + I^+ + I^- = e\sum_n \rho^{\rm ss}_n \Gamma_n,$$

where e is the magnitude of the electron charge. I^0 is the non-polarizing current induced by the nanomagnet, while $I^{\pm}$ are the hyperfine-generated currents that polarize in opposite directions. $I^{\pm}$ are expressed as

$$I^{\pm} = e\sum_n \rho_n \Gamma^{\pm}_n.$$

To convert these currents into nuclear polarization rates, we write

$$\Gamma^{\pm}_{\rm pol} = \frac{2I^{\pm}}{eN},$$

where we have normalized by e and included that the polarization, $P = \left(N^{\uparrow} - N^{\downarrow}\right)/N$, changes by $2/N$ per nuclear spin flip for N nuclei in total. The overall polarization rate equation is

$$\dot{P} = \Gamma^+_{\rm pol} - \Gamma^-_{\rm pol} - P\Gamma_{\rm rel}. \tag{S16}$$

In the main article, we neglect $\Gamma^-_{\rm pol}$ and approximate

$$\dot{P} \simeq \Gamma^+_{\rm pol} - P\Gamma_{\rm rel} \simeq \alpha I\,(1 - P) - P\Gamma_{\rm rel}, \tag{S17}$$

where α is taken as a constant ($\sim 35\,{\rm nA}^{-1}\,{\rm s}^{-1}$).

To compare the above theoretical model with the simplified version used in the main text, Fig. S2 shows $\dot{P}$ versus P and $B_{\rm ext}$ predicted using the two models represented by equations (S16) and (S17). The simple model, shown in Fig. S2a, predicts a narrow region of positive $\dot{P}$ running diagonally through the P–$B_{\rm ext}$ plane. The perturbation theory calculation, shown in Fig. S2b, predicts this same feature, which is associated with the $S_{\rm a}$–T_- resonance, as well as more complicated behavior associated with other singlet–triplet resonances (see Fig. S2c). Both models predict that the $S_{\rm a}$–T_- resonance is the only resonance which creates a stable fixed point at large P and $B_{\rm ext}$. Figs. S2c-e demonstrate the good agreement between the simplified model (orange lines) and the perturbation calculation (black lines) at the $S_{\rm a}$–T_- resonance. (The orange lines here are the same as the lines in Fig. 4a of the main article.) Compared to the other two resonances, $\dot{P}$ at the $S_{\rm a}$–$T_\pm$ resonances is very steep and provides strong feedback of the nuclear spins toward the A-FP, a distinct advantage for DNSP. From Fig. S2, it is evident that equations (1–4) of the main article are sufficient to model the nuclear polarization associated with the $S_{\rm a}$–T_- resonance.

The leftmost and rightmost $\dot{P}$ extrema in Figs. S2c-d are generated by the $S_{\rm s}$–$T_\pm$ resonances, while the small feature between the $S_{\rm a}$–$T_\pm$ resonances corresponds to the crossing of the triplet levels at $B^z = B_{\rm ext} + \overline{B}^z_{\rm nm} - PB^{\rm max}_{\rm nuc} \approx 0$. Note that the nuclear field components $\bar{B}^{x,y}_{\rm nuc}, \Delta B^{x,y,z}_{\rm nuc}$ play an important role for our treatment, determining directly the strength of the hyperfine flip-flop rates. For the DNSP rates depicted in Fig. S2 we have averaged calculations for different values of the nuclear field fluctuations chosen according to a Gaussian distribution with zero mean and standard deviation of $\sim 3\,$mT.

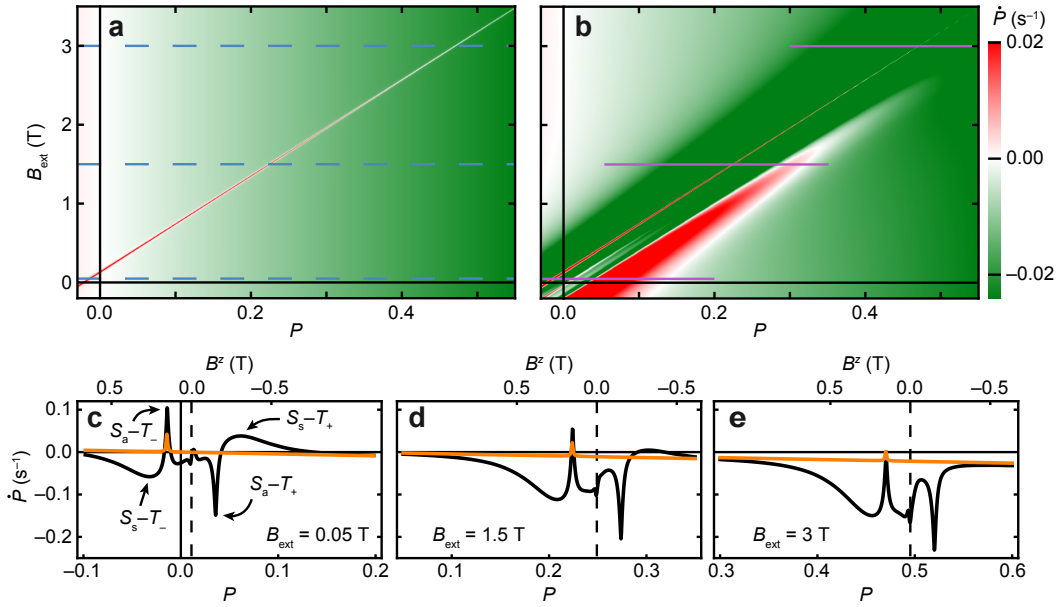

FIG. S2. **Nuclear polarization rate a)** The nuclear polarization rate, $\dot{P}$, calculated analytically using equation (1) of the main article. The dashed horizontal lines correspond to the constant $B_{\rm ext}$ slices shown in Fig. 3b of the main article. **b)** $\dot{P}$ calculated numerically using equation (S16) with $\Gamma_{\rm R} = 4.5\,$GHz and $N = 10^6$ nuclei. A random Gaussian distribution was used for $B^x_{\rm nuc}$ and $B^y_{\rm nuc}$ as in reference [R5]. The scale bar applies to both **a** and **b**. Both calculations were performed using $t_c = 12\,\mu$eV, $\Delta = 8\,\mu$eV, $\Gamma_{\rm rel} = 0.04\,{\rm s}^{-1}$, and the magnetic field distribution of the nanomagnet (Fig. 1c, main article). **c-d)** $\dot{P}$ as a function of P at constant $\mathbf{B}_{\rm ext}$ (lines in **a**,**b**) comparing the rate equation model [orange, equation (1) of the main article] with the perturbation calculation [black, equation (S16)]. The ranges in P of these slices are indicated by the magenta lines in **b**. The polarization rate extrema associated with the four singlet-triplet resonances are labeled in **c**. The top axis indicates the z-component of the total effective magnetic field, $B^z = B_{\rm ext} + \overline{B}^z_{\rm nm} - PB^{\rm max}_{\rm nuc}$. In addition to the extrema associated with the singlet-triplet resonances small polarization features appear near $B^z = 0$ (dashed vertical lines) where triplets become degenerate.

V. HYPERFINE- AND NON-HYPERFINE–INDUCED LEAKAGE CURRENT

The leakage current through the DQD shown in Fig. 2b of the main article contains a number of features which can be traced back to the inhomogeneous field produced by the single domain nanomagnet. To illustrate this, in Fig. S3 we show the PSB leakage current through two different DQD devices with identical gate layout. The data in Figs. S3**a** and S3**b** show measurements for opposite sweep directions acquired on the sample also presented in the main article but for a larger interdot tunnel coupling $t_c \sim 15\,\mu eV$. These data are more richly featured compared to those in Fig. S3c in which no nanomagnet was present ($t_c \sim 1\,\mu eV$).

In Fig. S3c, the measured current is approximately symmetric with respect to the $B_{ext} = 0$ axis, and the main features are increased current along the $\Delta = 0$ and $B_{ext} = 0$ axes (for $\Delta \gtrsim 0$, that is, outside of Coulomb blockade) and a global maximum at $\Delta = B_{ext} \simeq 0$. Similar data have already been published and discussed in detail in reference [R6]. In short, current is created by t_c in combination with the hyperfine interaction, which mixes triplet and singlet states strongly when $\Delta \simeq 0$ or $B_{ext} \simeq 0$. The width of the current maximum along the $B_{ext} = 0$ axis is determined by the standard deviation of the fluctuating $\mathbf{B}_{nuc}$[R5, R6]. The data in Figs. S3a and S3b illustrate that the sizeable $\mathbf{B}_{nm}$ adds complexity. The following list provides a short explanation for each of the features specific for the sample with nanomagnet:

- The most obvious response to expect when sweeping B_{ext} is hysteresis of the magnetization of the single domain nanomagnet. Because of its single-domain character, we expect the nanomagnet to switch polarization abruptly when B_{ext} passes the coercive field. An abrupt switch in magnetic field, in turn, should cause an equally abrupt change in the leakage current signal. Such features are indeed observed in Figs. S3a,b at $B_{ext} \simeq \mp 52\,mT$, respectively (see white arrows), and are also seen in Fig. 2b of the main article.

- In the presence of $\mathbf{B}_{nm}$, the eigenenergies of the $T_\pm$–like states are never zero. However, the relevant magnetic field, $\left|\mathbf{B}^L + \mathbf{B}^R\right|$ can be minimized by B_{ext}, and at this minimum, the $T_\pm$ are most degenerate and a local maximum of the leakage current is expected. For our $\mathbf{B}_{nm}$ values, $\left|\mathbf{B}^L + \mathbf{B}^R\right|$ is minimized at $B_{ext} \simeq \pm 12\,mT$, depending on the polarization of the nanomagnet. These fields are indicated in Figs. S3a,b with red arrows and faithfully identify the current maxima.

- The observation of distinct local current maxima at the S_a–$T_\pm$ resonance (black arrows in Figs. S3a and S3b) and in Fig. 2b of the main article) is unique to samples containing a single domain nanomagnet. The sharpness of these peaks can only be explained by taking into account the hyperfine induced dynamics of the nuclear spins. The actual position of the S_a–$T_\pm$ resonance is shifted towards larger $|B_{ext}|$ compared to its prediction (see Fig. 2b of the main article). In the main article we explain this shift by taking into account the hyperfine induced DNSP.

- $\mathbf{B}_{nm}$ mixes triplet and singlet states weakening the spin blockade and allowing leakage current to flow. However, B_{ext} tunes this mixing. In fact, the condition $\Delta\mathbf{B} \parallel \overline{\mathbf{B}}$ defines a local minimum of the singlet mixture with the $T_\pm$ states [R5]. This can be readily seen from the Hamiltonian in equation (S7) if the quantization axis is chosen parallel to $\overline{\mathbf{B}}$. For our system, this condition is satisfied when $B_{ext} \simeq \pm 8\,mT$. We actually observe current minima at slightly shifted values (see yellow arrows in Fig. S3a,b) owing to the complex DNSP that occurs while sweeping B_{ext} (see Fig. S2).

The current at finite B_{ext} and small Δ in Figs. S3a and S3b is characterized by strong switching noise and dragging effects which has also been observed in samples without on-chip magnet[R6, R7]. We forgo a detailed discussion of these effects, which can be explained in terms of the hyperfine dynamics in the presence of more than one stable fixed point at $\Delta \sim 0$[R4].

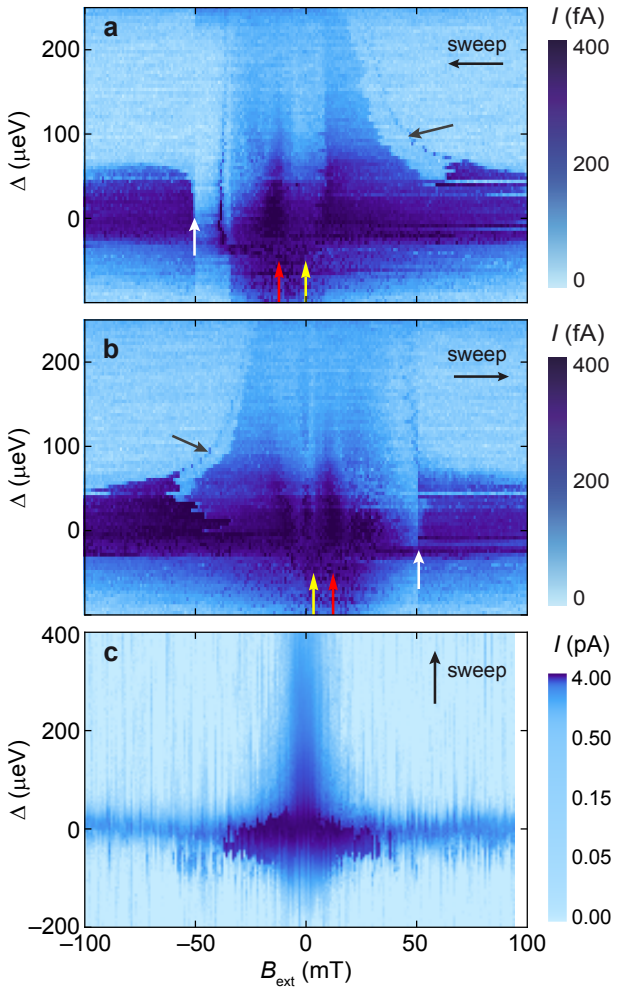

FIG. S3. **Spin-blockaded leakage current. a)** The dc leakage current, I, as a function of B_{ext} (swept from positive to negative) and Δ (stepped from positive to negative) ($t_c \sim 15\,\mu$eV. **b)** Same as in **a** but for the opposite sweep direction of $\mathbf{B}_{\mathrm{ext}}$ (from negative to positive). Arrows in **a** and **b** mark specific features explained in the main text. **c)** I as a function of B_{ext} and Δ measured using a sample with an identical gate layout as the sample used in the main article, but without the on-chip nanomagnet. Overall, maximum I values are one order of magnitude larger than in **a** and **b** owing to stronger source/drain coupling with this particular gate tunning, but the region of enhanced I is much smaller. The magnetic field was stepped from right to left and the energy detuning was swept from bottom to top. The perpendicular sweep direction compared to **a** and **b** does not affect the main features of this measurement. It does however cause a noisy background which is typical for this sweep direction and is caused by charge noise triggered by sweeping gate voltages.

VI. NUCLEAR POLARIZATION BUILD-UP

Here we present additional data to support our interpretation of the DNSP data. Fig. S4 demonstrates that the polarization dragging in Fig. 4b of the main article is reproducible. All the main features in Fig. S4a are reproducible, especially the position of $B_{\rm ext}^{\rm max}$ where polarization is lost. The current measured at the beginning of each field sweep near $B_{\rm ext} = 0$ is the typical leakage current that appears near $B_{\rm ext} = 0$ (see, for example, Fig. S5) and is extended somewhat because of DNSP. We interpret the sharp current maximum (labeled $B_{\rm ext}^{\rm max}$) as the point of maximum polarization (see main article). The δI in Fig. S4b results from losing the stable polarization condition and related resonant current as the polarization decays and the system drifts away from resonance.

Fig. S5 shows a second technique for demonstrating the polarization created during fixed-point dragging measurements. In Fig. S5a, we show I measured as a function of $B_{\rm ext}$ and Δ over a much larger range of $B_{\rm ext}$ than Fig. 2b of the main article. The current features at low $B_{\rm ext}$ in S5**a** differ from those in Fig. 2b of the main article mostly because Δ was swept rather than $B_{\rm ext}$.

The current traces in Fig. S5b, measured at $B_{\rm ext} = 250\,{\rm mT}$ after the nuclei have been polarized to $P \approx 4\,\%$, are very similar to the trace in Fig. S5c, which shows current measured at $B_{\rm ext} = 17.5\,{\rm mT}$ and $P = 0\,\%$. The quantitative similarity between the $P \approx 4\,\%$ current traces in Fig. S5b and the trace in Fig. S5c allows us to conclude that $B_{\rm nuc}^{z}$ compensates $B_{\rm ext}$ ($B_{\rm nuc}^{z} \simeq -B_{\rm ext}$ for $B_{\rm ext} \gg |\mathbf{B}_{\rm nm}|$) thereby reducing the total effective field. In contrast to the polarized traces in Fig. S5b, which are almost symmetric with respect to $\Delta = 0$, the $P = 0\,\%$ curve in Fig. S5c is asymmetric and exhibits switching noise for $\Delta > 0$. We attribute this behavior to small changes in nuclear spin polarization, while in Fig. S5b, the polarization is stabilized at the adjustable fixed point (A-FP). The current traces in Fig. S5b measured at $P \approx 4\,\%$ are repeatable and much larger than the trace measured at $P = 0\,\%$. This demonstrates that the polarization is finite and stable.

Current features, such as the local maxima in Fig. 2a of the main article and Fig. S4 at $B_{\rm ext} > 1\,{\rm T}$, are not seen in Fig. S5a. These features are missing because Δ is swept, and significant polarizations are not obtained. Taken together with Figs. 2,3 of the main article, Figs. S4 and S5 demonstrate the ability of our system to generate large nuclear spin polarization—and detect it.

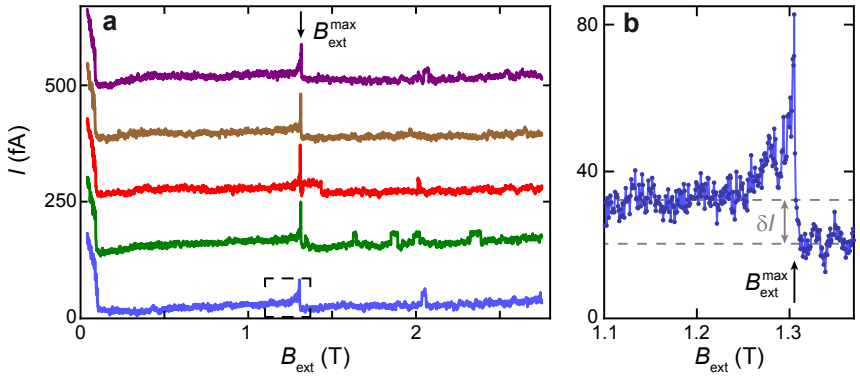

FIG. S4. **Polarization sweep repeatability a)** Five polarization sweeps measured at a rate $\dot{B}_{\rm ext} = 35\,{\rm mT/min}$ and $\Delta = 150\,\mu{\rm eV}$. The traces are offset by $N \times 120\,{\rm fA}$; $N = 0, 1, 2, 3, 4$ for clarity. The current bistabilities observed beyond $B_{\rm ext}^{\rm max}$ are consistent with DNSP[R4, R6]. **b)** The details of a current trace near $B_{\rm ext}^{\rm max}$ taken from within the boxed region of **a** demonstrate a sharp resonance and clear change in current, $\delta I \simeq 11\,{\rm fA}$, before and after sweeping through $B_{\rm ext}^{\rm max}$.

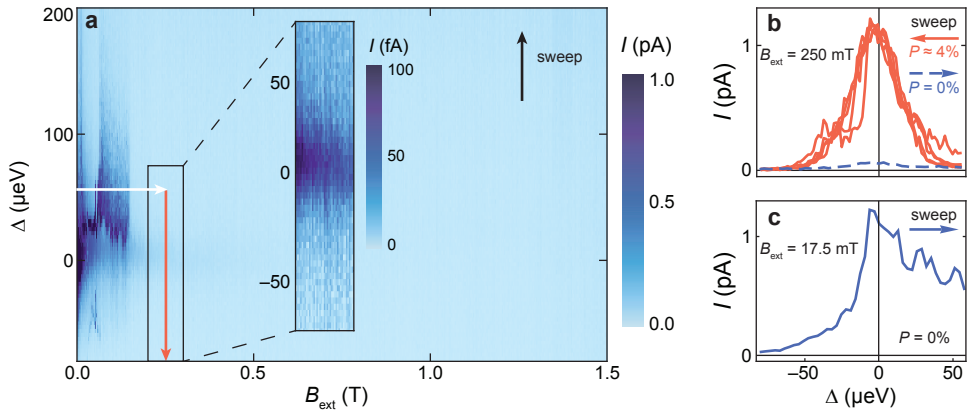

FIG. S5. **PSB leakage current at large $B_{\mathbf{ext}}$ a)** Leakage current, I, as a function of Δ and a large range of B_{ext}. The magnetic field has been stepped and Δ has been swept from negative to positive to minimize DNSP effects. *Inset*: Enlarged region centered at $B_{\mathrm{ext}} = 250\,\mathrm{mT}$ showing the small ($\sim 100\,\mathrm{fA}$) leakage current when $P = 0\,\%$. **b)** The solid orange lines are I measured while sweeping Δ multiple times through $\Delta = 0$ into Coulomb blockade along the orange arrow in **a**. These data were measured after ramping B_{ext} from $B_{\mathrm{ext}} \simeq 0$ to $B_{\mathrm{ext}} \simeq 250\,\mathrm{mT}$ (along the white arrow in **a**) creating a polarization of $P \simeq 4\,\%$. The dashed blue line is I at $P = 0\,\%$ extracted from **a** at $B_{\mathrm{ext}} = 250\,\mathrm{mT}$ and is negligible compared to I with polarization. **c)** I measured versus Δ starting with unpolarized nuclei extracted from **a** at $B_{\mathrm{ext}} = 17.5\,\mathrm{mT}$.

VII. DATA FITTING

The fitting procedure of the data in article Figs. 2b and 3a involves solving numerically the nonlinear differential equation given by equation (1) of the main article for a given set of parameters. This produces $P(t)$, which is then fed into equation (2) to find $I(t)$. Our goal is not to reproduce the details of the measured $I(t)$ traces, but only the position of its maximum at the S_{a}–T_- resonance, that is, the position of the resonant current I_{max}. Therefore, the final step is to calculate the position of I_{max} using the numerical $I(t)$. This procedure was repeated with different parameter sets until an agreement between theory and data was found.

The numerical fit needs the following parameters: t_{c}, γ, α, I_{max}, and Γ_{rel} (see equations (1–3) of the main article). I_{max} and the ratio $\alpha/\Gamma_{\mathrm{rel}} = 0.8\,\mathrm{pA}^{-1}$ (see main article Fig. 4d) were measured, thus reducing the overall number of fit parameters to three.

For the time-dependent data (see main article Figs. 3), $I_{\mathrm{max}} = 100\,\mathrm{fA}$ is the measured peak height. I_{max} values for the Δ-dependent data (see main article Fig. 2b) are unique for each value of Δ because I is Δ dependent. Fig. S6 details how $I_{\mathrm{max}}(\Delta)$ is extracted from the I measured as a function of B_{ext} and Δ. The main result is that $I_{\mathrm{max}}(\Delta)$ is identical to $I(\Delta)$ measured near $B_{\mathrm{ext}} = 0$, where spin blockade is lifted.

When $\mathbf{B}_{\mathrm{nm}}$ and $\mathbf{B}_{\mathrm{nuc}}$ are known, the Δ–B_{ext} position of the S_{a}–T_- resonance can be approximated analytically. This approximation is used in equation (4) of the main article and includes only B^z_{nm} providing $E_z^{\pm} \simeq \pm g\mu_{\mathrm{B}} \left(B_{\mathrm{ext}} - B^{\mathrm{max}}_{\mathrm{nuc}} P + \overline{B}^z_{\mathrm{nm}} \right)$. In Fig. S7, we compare exact numerical results with the analytical approximations for all four singlet–triplet resonances. The analytical approximation for the S_{a}–T_- resonance is in excellent agreement with the numerical calculation for $B_{\mathrm{ext}} \geq 0$.

One set of fit parameters ($t_{\mathrm{c}} = 12\,\mu\mathrm{eV}$, $\Gamma_{\mathrm{rel}} = 0.043\,\mathrm{s}^{-1}$, $\gamma = 10 \pm 1\,\mathrm{mT}$, and $\alpha = 35\,\mathrm{nA}^{-1}\,\mathrm{s}^{-1}$) reproduces the data of two very different experiments in Figs. 2b,3a of the main text. The data sets were measured using identical gate voltages. For a slightly different system tuning, only two parameters are expected to change, namely t_{c} and α, because they reflect the various hyperfine and non-hyperfine system rates, which are strongly gate dependent. γ depends mostly on $\mathbf{B}_{\mathrm{nm}}$, which is constant, while Γ_{rel} should be independent of gate tuning because it is a property of the nuclei. These expectations are supported in Fig. S8 where I versus B_{ext} and time has been measured after making the voltage of the top center gate more positive (see the gate design in Fig. 1a of the main article). The ability to describe disparate sets of data in different tuning regimes with either no change or only justifiable adjustments to fit parameters demonstrates the validity of our model.

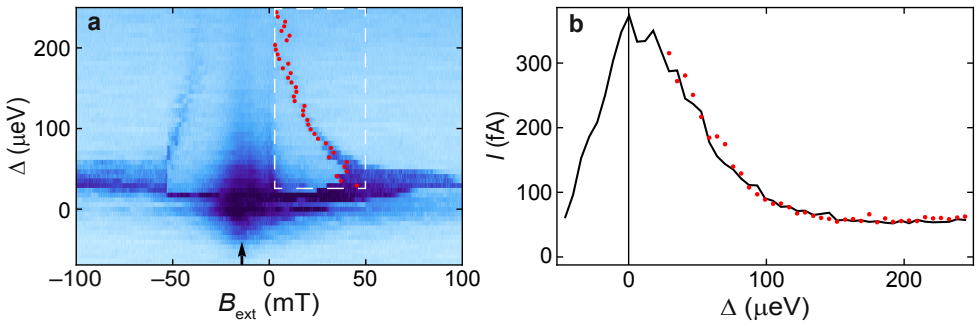

FIG. S6. **Determination of I_{max}. a)** Leakage current, I, measured versus B_{ext} and Δ repeated from Fig. 2b of the main article. After searching within the boxed region, the ● indicate the B_{ext}-Δ position of I_{max} along the S_a–T_- resonance. **b)** Here ● are the I_{max} values from **a** plotted as a function of Δ. In comparison, the black line is I measured versus Δ along the symmetry axis (black arrow in **a**). As expected, $I_{max}(\Delta)$ along the S_a–T_- resonance follows the general $I(\Delta)$ trend. A smoothed version of $I(\Delta)$ is used to create the smooth numerical fit in Fig. 2b of the main article.

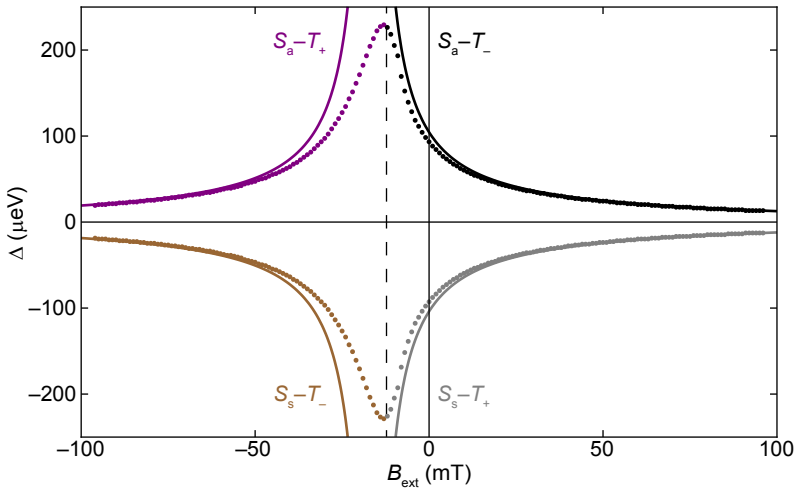

FIG. S7. **Location of singlet–triplet resonances.** The numerically calculated data points indicate the position in the B_{ext}–Δ plane where singlet and triplet states are resonant. The solid lines are approximated values calculated analytically. Each line is labeled to identify which states are resonant. In particular, the black line is the analytic approximation for the S_a–T_- resonance and was used to fit the DNSP data (see Fig. 2 of the main article). The exact and approximate values are in excellent agreement for $B_{ext} \geq 0$, where all DNSP measurements were performed. The upper branch of the numerical calculation is included in Fig. 2b of the main article. The vertical dashed line at $B_{ext} = -12\,\mathrm{mT}$, which is the minimizing value of $|\mathbf{B}^L + \mathbf{B}^R|$, defines the symmetry axis where the triplets are most degenerate. Here $t_c = 12\,\mu\mathrm{eV}$.

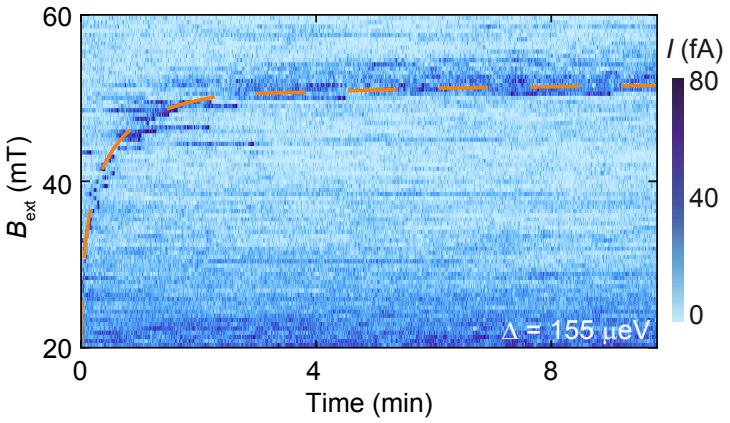

FIG. S8. **Nuclear Spin Dynamics.** Current measured as a function of time demonstrating DNSP at the S_a–T_- resonance. The dashed orange line is a numerical fit of the data. Here the system is tuned to a larger tunnel coupling compared to the tuning used in Fig. 3 of the main article. As a result, $t_c = 22\,\mu\text{eV}$ is larger, which makes E_a larger, and the current peak is not observed until $B_{ext} \approx 20\,\text{mT}$. Meanwhile, $\alpha = 14\,\text{nA}^{-1}\,\text{s}^{-1}$ suffers from the increased t_c. The other fit parameters are unchanged, that is, $\gamma = 10\,\text{mT}$ and $\Gamma_{rel} = 0.04\,\text{s}^{-1}$.

* These authors contributed equally to this work.

[R1] A. C. Johnson, J. R. Petta, C. M. Marcus, M. P. Hanson, and A. C. Gossard, Phys. Rev. B **72**, 165308 (2005).
[R2] W. A. Coish and J. Baugh, Phys Status Solidi B **246**, 2203 (2009).
[R3] A. W. Overhauser, Phys. Rev. **92**, 411 (1953).
[R4] M. S. Rudner, F. H. L. Koppens, J. A. Folk, L. M. K. Vandersypen, and L. S. Levitov, Phys. Rev. B **84**, 075339 (2011).
[R5] O. N. Jouravlev and Y. V. Nazarov, Phys. Rev. Lett. **96**, 176804 (2006).
[R6] F. H. L. Koppens, J. A. Folk, J. M. Elzerman, R. Hanson, L. H. W. van Beveren, I. T. Vink, H. P. Tranitz, W. Wegscheider, L. P. Kouwenhoven, and L. M. K. Vandersypen, Science **309**, 1346 (2005).
[R7] T. Kobayashi, K. Hitachi, S. Sasaki, and K. Muraki, Phys. Rev. Lett. **107**, 216802 (2011).

PHYSICAL REVIEW A **74**, 032316 (2006)

Quantum measurement of a mesoscopic spin ensemble

G. Giedke,[1,2] J. M. Taylor,[3] D. D'Alessandro,[4] M. D. Lukin,[3] and A. Imamoğlu[1]
[1]*Institut für Quantenelektronik, ETH Zürich, Wolfgang-Pauli-Straße 16, 8093 Zürich, Switzerland*
[2]*Max-Planck-Institut für Quantenoptik, H.-Kopfermann-Str., 85748 Garching, Germany*
[3]*Department of Physics, Harvard University, Cambridge, Massachusetts 02138, USA*
[4]*Department of Mathematics, Iowa State University, Ames, Iowa 50011, USA*
(Received 19 August 2005; revised manuscript received 19 June 2006; published 15 September 2006)

We describe a method for precise estimation of the polarization of a mesoscopic spin ensemble by using its coupling to a single two-level system. Our approach requires a minimal number of measurements on the two-level system for a given measurement precision. We consider the application of this method to the case of nuclear-spin ensemble defined by a single electron-charged quantum dot: we show that decreasing the electron spin dephasing due to nuclei and increasing the fidelity of nuclear-spin-based quantum memory could be within the reach of present day experiments.

DOI: 10.1103/PhysRevA.74.032316 PACS number(s): 03.67.Lx, 71.70.Jp, 73.21.La, 76.70.−r

I. INTRODUCTION

Decoherence of quantum systems induced by interactions with low-frequency reservoirs is endemic in solid-state quantum information processing (QIP) [1,2]. A frequently encountered scenario is the coupling of a two-level system (qubit) to a mesoscopic bath of two-level systems such as defects or background spins. The manifestly non-Markovian nature of system-reservoir coupling in this scenario presents challenges for the description of the long term dynamics as well as for fault tolerant quantum error correction [3,4]. The primary experimental signature of a low-frequency reservoir is an unknown but slowly changing effective field that can substantially reduce the ability to predict the system dynamics. A possible strategy to mitigate this effect is to carry out a quantum measurement which allows for an estimation of the unknown reservoir field by controlled manipulation and measurement of the qubit. A precise estimation of the field acting on the large Hilbert space of the reservoir requires, however, many repetitions of the procedure: this constitutes a major limitation since in almost all cases of interest projective measurements on the qubit are slow [5] and in turn will limit the accuracy of the estimation that can be achieved before the reservoir field changes.

In this work, we propose a method for estimating an unknown quantum field associated with a mesoscopic spin ensemble. By using an incoherent version of the *quantum phase estimation algorithm* [6,7], we show that the number of qubit measurements scale linearly with the number of significant digits of the estimation. We only assume the availability of single-qubit operations such as preparation of a known qubit state, rotations in the x-y plane, and measurement, of which only rotations need to be fast. The estimation procedure that we describe would suppress the dephasing of the qubit induced by the reservoir; indeed, an interaction with the estimated field leads to coherent unitary evolution that could be used for quantum control of the qubit. If the measurement of the reservoir observable is sufficiently fast and strong, it may in turn suppress the free evolution of the reservoir in a way that is reminiscent of a quantum Zeno effect.

After presenting a detailed description of the measurement procedure and discussing its performance and limitations, we focus on a specific application of the procedure for the case of a single quantum dot (QD) electron spin interacting with the mesoscopic nuclear spin ensemble defined by the QD. It is by now well known that the major source of decoherence for the electron-spin qubits in QDs [8] is the hyperfine interaction between the spins of the lattice nuclei and the electron [9–15]. A particular feature of the hyperfine-related dephasing is the long correlation time (t_c) associated with nuclear spins. This enables techniques such as spin echo to greatly suppress the dephasing [16]. In [12] it was suggested to measure the nuclear field to reduce electron-spin decoherence times; precise knowledge of the instantaneous value of the field would even allow for controlled unitary operations. For example, knowledge of the field in adjacent QDs yields an effective field gradient that could be used in recently proposed quantum computing approaches with pairs of electron spins [17]. Moreover, with sufficient control, the collective spin of the nuclei in a QD may be used as a highly coherent qubit-implementation in its own right [18–20].

II. PHASE ESTIMATION

In the following we consider an indirect measurement scheme in which the system under investigation is brought into interaction with a probe spin (a two-level system in our case) in a suitably prepared state. Measuring the probe spin after a given interaction time t yields information about the state of the system. We assume the mesoscopic system evolves only slowly compared to the procedure, and further that the measurement does not directly perturb the system. In essence, we are performing a series of quantum nondemolition (QND) measurements on the system with the probe spin.

We consider an interaction Hamiltonian of the form

$$H_{\mathrm{int}} = \hbar A_z \otimes S_z \tag{1}$$

which lends itself easily to a measurement of the observable A_z. The QND requirement is satisfied for $[H_{\mathrm{int}}, H_{\mathrm{bath}}] \to 0$. The applicability of H_{int} in situations of physical interest is discussed in Sec. VI. Given this interaction, the strategy to

 ©2006 The American Physical Society

measure A_z is in close analogy to the so-called Ramsey interferometry approach, which we now briefly review.

For example, an atomic transition has a fixed, scalar value for A_z which corresponds to the transition frequency. By measuring A_z as well as possible in a given time period, the measurement apparatus can be locked to the fixed value, as happens in atomic clocks. The probe spin S is prepared in a state $|+\rangle=(|\uparrow\rangle+|\downarrow\rangle)/\sqrt{2}$. It will undergo evolution under H according to $U_t=\exp(-itA_zS_z)$. After an interaction time t, the probe spin's state will be

$$\cos(\Omega t)|+\rangle + i\sin(\Omega t)|-\rangle, \tag{2}$$

where $\Omega=A_z/2$ is the precession frequency for the probe spin. A measurement of the spin in the $|\pm\rangle$ basis yields a probability $\cos^2(\Omega t)$ of being in the $|+\rangle$ state. Accumulating the results of many such measurements allows one to estimate the value for Ω (and therefore A_z). In general, the best estimate is limited by interaction time: for an expected uncertainty in A_z of Δ_0 and an appropriate choice of t, M measurements with fixed interaction times $1/\Delta_0$ can estimate A_z to no better than $\sim\Delta_0/\sqrt{M}$ (see [21], and references therein).

In our scenario, the situation is slightly different in that A_z is now a quantum variable. For a state $|s\rangle$ in the Hilbert space of the system $\mathcal{H}$ which is an eigenstate of A_z with eigenvalue $2\Omega_s$, the coupling induces oscillations:

$$U_t|s\rangle|+\rangle = |s\rangle[\cos(\Omega_s t)|+\rangle + i\sin(\Omega_s t)|-\rangle]. \tag{3}$$

Thus, the probability to measure the probe spin in state $|+\rangle$ given that the system is in a state $|s\rangle$ is $p(+|s)=\cos^2(\Omega_s t)$ at time t, providing information about which eigenvalue of A_z is realized. Comparing Eq. (2) to Eq. (3) indicates that the same techniques used in atomic clocks (Ramsey interferometry) could be used in this scenario to measure Ω_s and thus project the bath in some eigenstate of A_z with an eigenvalue of Ω_s to within the uncertainty of the measurement.

Beyond the Ramsey approach, there are several ways to extract this information, which differ in the choice of interaction times t_j and the subsequent measurements. The general results on quantum metrology of [22] show, however, that the standard Ramsey scheme with fixed interaction time t is already optimal in that the scaling of the final variance with the inverse of the total interaction time cannot be improved without using entangled probe states. Nevertheless, the Ramsey scheme will not be the most suitable in all circumstances. For example, we have assumed so far that preparation and measurement of the probe spin is fast when compared to $1/\Delta_0$. However, in many situations with single quantum systems, this assumption is no longer true, and it then becomes desirable to minimize the number of preparation and/or measurement steps in the scheme.

III. THE MEASUREMENT SCHEME

We now show that by varying the interaction time and the final measurements such that each step yields the maximum information about Ω_s, we can obtain the same accuracy as standard Ramsey techniques with a similar interaction time, but only a *logarithmic* number of probe spin preparations and measurements. As a trivial case, if A_z had eigenvalues 0 and 1 only, then measuring the probe in the $\pm$ basis after an interaction time $t_1=\pi$, we find $+$ $(-)$ with certainty, if the systems are in an $A_z=0$ (1) eigenstate; if they were initially in a superposition, measuring the probe projects the system to the corresponding eigenspaces. We can extend this simple example (in the spirit of the quantum phase estimation algorithm [6,7] and its application to the measurement of a classical field [23]) to implement an A_z measurement by successively determining the binary digits of the eigenvalue. We start with the ideal case, then generalize to a more realistic scenario.

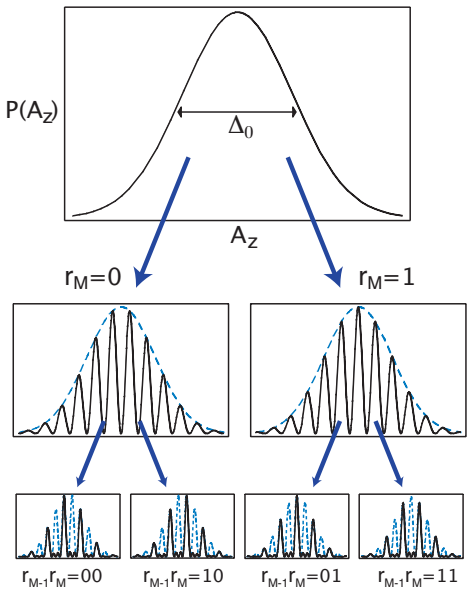

FIG. 1. (Color online) Illustration of the first two steps of the measurement procedure. The original distribution $P(A_z)$, with rms width Δ_0 is shown at the top. After the first measurement, with result $r_M=0,1$, the conditional distribution (middle plots) reflects the knowledge of the least significant bit. The next measurement result r_{M-1} further reduces the distribution (bottom plots).

A. Ideal case

If all the eigenvalues of A_z are an integer multiple of some known number α and bounded by $2^M\alpha$, then this procedure yields a perfect A_z measurement in M steps: let us write all eigenvalues as $2\Omega_s=\alpha 2^M\Sigma_{l=1}^M s_l 2^{-l}$. The sum we denote by s and also use the notation $s=0.s_1s_2\ldots s_M$. Starting now with an interaction time $t_1=\pi/\alpha$, we have $\Omega_s t_1=s_M\pi/2 \bmod \pi$. Hence the state of the probe electron is flipped if and only if $s_M=1$. Therefore measuring the probe electron in state $+$ $(-)$ projects the nuclei to the subspace of even (odd) multiples of α (see Fig. 1). We denote the result of the first measurement by $r_M=0(1)$ if the outcome was "$+$ $(-)$." All the higher digits have no effect on the measurement result since they

induce rotations by an integer multiple of π which have no effect on the probabilities $p(\pm|s)$.

To measure the higher digits, we reduce the interaction time by half in each subsequent step: $t_{j+1}=2^{-j}t_1$ until we reach $t_M=\pi/\alpha$ in the final and shortest step. For $j>1$ the rotation angle $\Omega_s t_j \pmod{\pi}$ in the jth step does not only depend on the jth binary digit of s but also on the previous digits (which have already been measured, giving results $r_{M+1-l}=s_{M+1-l}$, $l=1,\ldots,j-1$). The angle $\Omega_s t_j \pmod{\pi}$ is given by $s_{M+1-j}\pi/2+\varphi_j$ with $\varphi_j=\pi/2\Sigma_{l=1}^{j-1} r_{M+1-l}2^{l-j}$, where we have used the results r_l already obtained. This overrotation by the angle φ_j can be taken into account in the choice of the measurement basis for the jth step: if the jth measurement is performed in a *rotated basis* $|\pm_j\rangle$ that is determined by the previous results r_l, namely,

$$|+_j\rangle := \cos\varphi_j|+\rangle - i\sin\varphi_j|-\rangle, \tag{4a}$$

$$|-_j\rangle := \sin\varphi_j|+\rangle + i\cos\varphi_j|-\rangle, \tag{4b}$$

then the jth measurement yields "+" ($r_{M+1-j}=0$) if $s_{M+1-j}=0$ and "−" ($r_{M+1-j}=1$) otherwise. Thus, after M measurements we obtain $r_l=s_l$, $\forall l=1,\ldots,M$ and have performed a complete measurement of A_z (where the number M of probe particles used is the smallest integer such that $2^M \geqslant A_z/\alpha$).

Before proceeding, we note that the proposed scheme is nothing but an "incoherent" implementation of the quantum phase estimation algorithm: As originally proposed, this algorithm allows measurement of the eigenvalue of a unitary U by preparing M qubits (the control register) in the state $|+\rangle^{\otimes M}$ (i.e., the equal superposition of all computational basis states $|j\rangle, j=0,\ldots,2^M-1$) and performing controlled-$U^{2^{j-1}}$ gates between the jth qubit and an additional register prepared in an eigenstate $|s\rangle$ of U with $U|s\rangle=e^{i2\pi s}|s\rangle$. The controlled-$U$ gates let each computational basis state acquire a s-dependent phase: $|l\rangle \mapsto e^{i2\pi l s}|l\rangle$. Then the inverse quantum Fourier transformation (QFT) is performed on the control register, which is then measured in the computational basis, yielding the binary digits of s. Performing the QFT is still a forbidding task, but not necessary here: the sequence of measurements in the rotated basis $|\pm_j\rangle$ described above is in fact an implementation of the combination of QFT and measurement into one step. This was previously suggested in different contexts [24–26].

B. Realistic case

In general, there is no known α such that all eigenvalues s of A_z are integer multiples of α. Nevertheless, as discussed below, the above procedure can still produce a very accurate measurement of A_z if sufficiently many digits are measured. Now we evaluate the performance of the proposed measurement scheme in the realistic case of noninteger eigenvalues. Since here we are interested in the fundamental limits of the scheme, we will for now assume all operations on the probe qubit (state preparation, measurement, and timing) to be exact; the effect of these imperfections is considered in Sec. V. Without loss of generality, let A and 0 denote the largest and smallest eigenvalues of A_z, respectively [46], and choose $\alpha=2A$ such that the eigenvalues of A_z/α are all $\in[0,\frac{1}{2}]$. These are the eigenvalues s we measure in the following.

The function from which all relevant properties of our strategy can be calculated is the conditional probability $p_M(R|s)$ to obtain (after measuring M electrons) a result $R=0.r_1r_2\ldots r_M$ given that the system was prepared in an eigenstate with eigenvalue s. The probability to measure R is given by the product of the probabilities to measure r_{M+1-j} in the jth step, which is $\cos^2(\Omega_s t_j-\varphi_j+r_{M+1-j}\pi/2)=\cos^2(\pi[s-R]2^{M-j})$. Hence

$$p_M(R|s)=\prod_{k=0}^{M-1}\cos^2(\pi[s-R]2^k), \tag{5}$$

see also [23]. This formula can be simplified by repeatedly using $2\sin x=\sin(x/2)\cos(x/2)$ to give

$$p_M(R|s)=\left(\frac{\sin(2^M\pi[s-R])}{2^M\sin(\pi[s-R])}\right)^2. \tag{6}$$

Assume the nuclei are initially prepared in a state ρ with prior probability $p(s)$ to find them in the eigenspace belonging to the eigenvalue s. After the measurement, we can update this distribution given our measurement result. We obtain, according to Bayes' formula

$$p_M(s|R)=\frac{p_M(R|s)p(s)}{\sum_s p_M(R|s)p(s)}, \tag{7}$$

with the expectation value denoted by $\bar{s}_R$.

IV. PERFORMANCE OF THE SCHEME

As the figure of merit for the performance of the measurement scheme we take the improvement of the average uncertainty in A_z of the updated distribution

$$\overline{\Delta A_{z,\mathrm{est}}}^{(M)} := \sum_R p_M(R)\sqrt{\sum_s (s-\bar{s}_R)^2 p_M(s|R)} \tag{8}$$

over the initial uncertainty $\Delta_0=\Delta A_z^{(0)}$. An upper bound to $\overline{\Delta A_{z,\mathrm{est}}}^{(M)}$ is given by the square root of the average variance $\bar{V}$

$$\bar{V}_M := \sum_R p_M(R)\sum_s (s-\bar{s}_R)^2 p_M(s|R), \tag{9}$$

as easily checked by the Cauchy-Schwarz inequality. We now show that $\bar{V}_M \leqslant 2^{-M}$. We replace $\bar{s}_R \to \tilde{R}=\min\{R,1-R\}$; we can use any such replacement to obtain an upper bound, as the expectation value $\bar{x}=\Sigma_x p(x)x$ minimizes $v(y)=\Sigma_x p(x)(x-y)^2$. This choice means that measurement results $R>\frac{1}{2}$ are interpreted as $1-R$, which is appropriate since the scheme does not distinguish the numbers $s=\delta$ and $s'=1-\delta$ and due to the choice of α only $s\in[0,\frac{1}{2}]$ occur. Thus

$$\bar{V}_M \leqslant \sum_s p(s)\sum_R (s-\tilde{R})^2 p_M(R|s) =: \sum_s p(s)\bar{V}_M(s).$$

The terms $\bar{V}_M(s)$ can be shown [47] to be $\leqslant b_V 2^{-M}$ with $b_V=(1+2^{-M})/2$. This means that performing M measure-

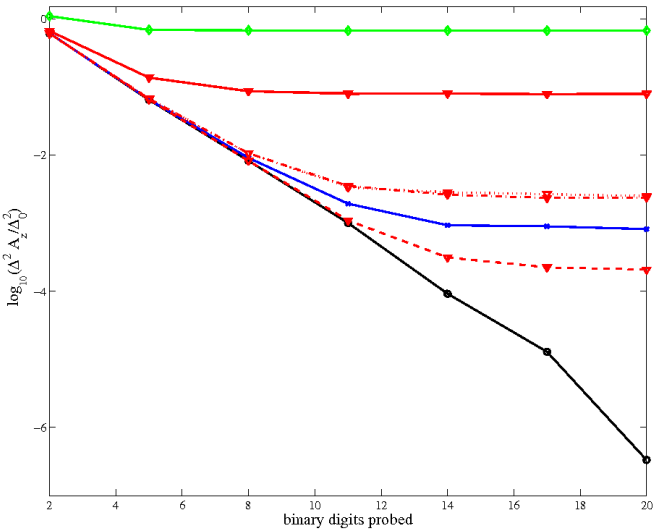

FIG. 2. (Color online) Estimation in the presence of preparation and measurement error p: the logarithm of the improvement $\Delta A_{z,\mathrm{est}}/\Delta_0$ is plotted versus the number M of binary digits measured. The solid lines represent different error rates ($p=0$: black circles; $p=10^{-4}$ blue crosses; $p=10^{-2}$: red triangles; and $p=10^{-1}$: green diamonds). The broken red curves (triangles) demonstrate the benefit of simple error correction (for $p=10^{-2}$): strategy I (3 repetitions per digit: use the majority result, either for all digits or only for leading $M/2$ digits); (dash-dotted, dotted—almost undistinguishable); strategy II (increase number of repetitions for more significant digits to 7 repetitions for leading $M/8$ digits, 5 for next $M/8$, and 3 for next $M/4$); dashed. We see that the latter provides a better accuracy than the uncorrected $p=10^{-4}$ curve.

ments yields a state with A_z uncertainty $\Delta A_{z,\mathrm{est}} \leqslant \alpha 2^{-M/2}$. For example, we need about 13 interactions with the probe spin to reach the 1% level in $\Delta A_{z,\mathrm{est}}/\alpha$ and about 7 more for every additional factor of 10.

The overall procedure requires a total time $T_M = \sum_{j=1}^{M}(t_j+\tau_m) = 2t_1(1-2^{-M}) + M\tau_m$, which is an interaction time (determined mainly by the time $t_1 = \pi/\alpha 2^M = \pi(2f\Delta_0)^{-1}2^M$ needed for the least significant digit probed) and the time to make M measurements (τ_m is the time to make a single measurement). We obtain for the average uncertainty an upper bound in terms of the interaction time $T_{\mathrm{int}} = T_M - M\tau_m$ needed:

$$\frac{\Delta A_{z,\mathrm{est}}}{\Delta_0} \leqslant \sqrt{\frac{\pi f}{\Delta_0 T_{\mathrm{int}}}}. \tag{10}$$

Immediately the similarity with standard atomic clock approaches is apparent, as the uncertainty decreases with the square root of the interaction time. However, while for an atomic clock scheme, in which the interaction time per measurement is kept fixed to $\sim\pi/(f\Delta_0)$, the total time to reach the precision of Eq. (10) is $T_M^{\star} = 2t_1 + \tau_m 2^M$. For our method the measurement time is reduced dramatically by a time $T_M^{\star} - T_M = \tau_m(2^M - M)$. In this manner our approach requires a polynomial, rather than exponential, number of measurements for a given accuracy, though the overall interaction time is the same for both techniques.

It may be remarked that even the scaling in interaction time differs significantly if other figures of merit are considered. For example, our scheme provides a *square-root speed-up* in T_{int} over the standard Ramsey scheme if the aim is to maximize the information gain or to minimize the confidence interval [27].

V. ERRORS AND FLUCTUATIONS IN A_z

Up until now we have considered an idealized situation in which the value of A_z does not change over the course of the measurement and in which preparation and measurement of the probe system work with unit fidelity. Let us now investigate the robustness of our scheme in the presence of these errors.

A. Preparation and measurement errors

By relying upon a small number of measurements, the scheme we described becomes more susceptible to preparation and measurement errors. An error in the determination of the kth digit leads to an increase of the error probability in the subsequent digits. This error amplification leads to a scaling of the final error of $\sqrt{p}$, where p is the probability of incurring a preparation or measurement error in a single step. We confirm this with Monte Carlo simulations of the measurement procedure [Fig. 2(a)], leading to an asymptotic bound:

$$\Delta A_{z,\mathrm{est}} \leqslant (2f\Delta_0)\sqrt{p}. \tag{11}$$

Standard error correction (EC) techniques can be used to overcome this problem. For example, by performing three measurements for each digit and using majority vote, the effective probability of error can be reduced to $\sim 3p^2$—at the expense of tripling the interaction time and number of measurements. While this may look like a big overhead, it should be noted that the scheme can be significantly improved: the least significant digits do not require any EC. For them, the scheme gives noisy results even for error rate $p=0$ due to the undetermined digits of A_z, this does not affect the most significant $M/2$ digits. This indicates that it may be enough to apply EC for the leading digits.

As can be seen from Fig. 2(b), this simple EC strategy provides a significant improvement in the asymptotic ΔA_z. This is hardly changed, when EC is applied only to the leading half of the digits. Thus only twice as many measurements (and an additional interaction time $\sim 2^{M/2+2}$ which is $\ll T_M$) is needed for an order-of-magnitude improvement in ΔA_z. By

repeating the measurement of more important digits even more often, the effect of technical errors can be reduced even further, as confirmed by Monte Carlo simulations [Fig. 2(b)]. We also note that further improvements (beyond M digits) can be achieved by this technique. In essence, choosing a digital approach to error correction for our digital technique yields substantially better performance than adapting the digital technique to an analog approach.

B. Estimation of bath decorrelation errors

In practice, internal bath dynamics will lead to fluctuations in A_z, such that $A_z(t) \neq A_z(t')$ for times t and t' that are sufficiently different. Furthermore, apparatus errors, as outlined above, lead to errors in our measurement procedure. We will assume that the variations of A_z are slow over short time intervals, allowing us to approximate the M bit measurement process as a continuous measurement over the time T_M with some additional noise with variance $\approx \Delta A_{z,\mathrm{est}}(M)^2 \ll \Delta_0^2$. Then we will find the expected difference in our measurement result and the value of A_z at a later time.

Under the above approximations the value of the kth such measurement (where a complete set of M bits takes a time T_M and the kth such measurement ends at time t_k) is

$$m_k = \frac{1}{T_M}\int_{t_k - T_M}^{t_k} A_z(t)dt + G_k, \tag{12}$$

where the noise from measurement is incorporated in the stochastic noise variable G_k with $\langle G_k G_{k'}\rangle \approx \delta_{kk'}\Delta A_{z,\mathrm{est}}(M)^2$. We can estimate A_z at a later time, and find the variance of this estimate from the actual value:

$$\begin{aligned}\bar{V}_M(t > t_k) &= \langle [m_k - A_z(t)]^2\rangle \\ &= \langle G_k^2\rangle + \Delta_0^2 + \frac{1}{2T_M^2}\int_{t_k - T_M}^{t_k}\int_{t_k - T_M}^{t_k}\langle\{A_z(t'), A_z(t'')\}_+\rangle dt''dt' \\ &\quad - \frac{1}{T_M}\int_{t_k - T_M}^{t_k}\langle\{A_z(t'), A_z(t)\}_+\rangle dt'\end{aligned}$$

If we assume A_z is a Gaussian variable with zero mean, described by a spectral function $S(\omega)$ [i.e., $\langle A_z(t)A_z(t+\tau)\rangle = \int_{-\infty}^{\infty} S(\omega)e^{i\omega\tau}d\omega$], then

$$\begin{aligned}\bar{V}_M(t) &= \Delta A_{z,\mathrm{est}}(M)^2 + \Delta_0^2 + \frac{1}{T_M^2}\int_{-\infty}^{\infty} S(\omega)\frac{\sin^2(T_M\omega/2)}{(\omega/2)^2}d\omega \\ &\quad - \int_{-\infty}^{\infty} S(\omega)\frac{\sin[(t - t_k + T_M)\omega] - \sin[(t - t_k)\omega]}{T_M\omega/2}d\omega.\end{aligned}$$

For A_z that fluctuates slowly in time and corresponds to a non-Markovian, low-frequency noise, the second moment of $S(\omega)$ converges. We define

$$\frac{1}{t_c^2} = \frac{1}{\langle A_z^2\rangle}\int_{-\infty}^{\infty} S(\omega)\omega^2 d\omega. \tag{13}$$

When $T_M, t - t_k + T_M \ll t_c$, we may expand the sine terms in the integrals. Taking $t = t_k + T_M$, the expected variance to order $(T_M/t_c)^2$ is

$$\bar{V}_M(t) \approx \Delta A_{z,\mathrm{est}}(M)^2 + \Delta_0^2\left[\frac{T_M}{t_c}\right]^2\left(\tfrac{7}{3} - \tfrac{1}{12}\right). \tag{14}$$

As an example case, we consider as realistic parameters $t_c \approx 1$ ms and $T_M = 16$ μs with $\Delta A_{z,\mathrm{est}}^2/\Delta_0^2 = 0.025^2$. These parameter choices are described in detail in Sec. VI. We find that our variance 16 μs *after* the measurement is approximately $0.035^2\Delta_0^2$ with equal contributions from the measurement noise and from the bath decorrelation. Substantially faster decorrelation would dominate the noise in the estimate, and render our technique unusable.

In the limit of slow decorrelation, this approach would allow one to use the (random) field A_z to perform a controlled unitary of the form $\exp(-im_k S_z\tau)$ at a time t, with a fidelity

$$F = \exp\left\{-\left\langle\left[\int_{t-\tau}^{t} A_z(t')dt' - m_k\right]^2\right\rangle/4\right\}. \tag{15}$$

For example, a π rotation around the probe spins' z axis would have a fidelity $\approx 1 - \bar{V}_M(t)\pi^2/\Delta_0^2$, or 0.998 for the above parameters.

We remark that this approach for estimation in the presence of bath fluctuations is not optimal (Kalman filtering [28] would be more appropriate for making an estimation of A_z using the measurement results). Furthermore, it does not account for the nonlinear aspects of our measurement procedure, nor does it incorporate any effect of the measurement on the *evolution* of the bath (e.g., quantum Zeno effect). More detailed investigations of these aspects of the process should be considered in an optimal control setting. Nonetheless, our simple analysis above indicates that slow decorrelation of the bath will lead to modest additional error in the estimate of A_z.

VI. EXAMPLE: ESTIMATING COLLECTIVE NUCLEAR SPIN IN A QUANTUM DOT

Now we apply these general results to the problem of estimating the collective spin of the lattice nuclei in a QD.

The interaction of a single electron spin in a QD with the spins of the lattice nuclei $\vec{I}_j$ is described by the Fermi contact term [11]

$$\vec{S}\cdot\sum_j \alpha_j\vec{I}_j, \tag{16}$$

where the sum in Eq. (16) runs over all the N lattice nuclei. The α_j are constants describing the coupling of the jth nuclear spin with the electron. They are proportional to the modulus squared of the electron wave function at the location of the jth nucleus and are normalized such that $\Sigma_j\alpha_j I^{(j)} = A$, which denotes the hyperfine coupling strength.

Due to the small size of the nuclear Zeeman energies, the nuclei are typically in a highly mixed state even at dilution refrigerator temperatures. This implies that the electron experiences an effective magnetic field (Overhauser field, $\vec{B}_{\mathrm{nuc}}$) with large variance, reducing the fidelity of quantum memory and quantum gates. This reduction arises both from

the inhomogeneous nature of the field ($\vec{B}_{\mathrm{nuc}}$ varies from dot to dot) [29] and the variation of $\vec{B}_{\mathrm{nuc}}$ over time due to nuclear-spin dynamics (even a single electron experiences different field strengths over time, implying loss of fidelity due to time-ensemble averaging).

In a large external magnetic field in the z direction the spin flips described by the x and y terms are suppressed and—in the interaction picture and the rotating wave approximation—the relevant Hamiltonian is of the type given in Eq. (1), where A_z is now the collective nuclear-spin operator

$$A_z = \sum_{j=1}^{N} \alpha_j I_z^{(j)}, \tag{17}$$

which gives the projection of the Overhauser field along the external field axis by $B_{\mathrm{nuc},z}=\hbar A_z/g^*$. Before continuing, let us remark here that one can expect to obtain an effective coupling of the type Eq. (1) in a similar fashion as a good approximation to a general spin-environment coupling $\vec{S}\cdot\vec{A}$, whenever the computational basis states of the qubit are nondegenerate (as guaranteed in the system studied here by the external field) and the coupling to the environment is sufficiently weak such that bit-flip errors are detuned.

To realize the single-spin operations needed for our protocol—preparation, rotation, and read-out—many approaches have been suggested as part of a quantum computing implementation with electron spin qubits in QDs using either electrical or optical control (see, e.g., [30] for a recent review).

The experimental progress towards coherent single-spin manipulation has been remarkable in recent years. In particular, the kind of operations needed for our protocol have already been implemented in different settings: For self-assembled dots, state preparation with $F\geqslant 0.99$ has been realized [31], while for electrically defined dots, a single-spin measurement with a fidelity of $F\geqslant 0.72$ was reported [32]. In the double-dot setting [16], all three operations have recently been demonstrated, and we estimate the combined fidelity to be $F\geqslant 0.7$.

As can be seen from Fig. 2, at the level of 1% accuracy of state preparation, rotation, and read-out, the proposed nuclear-spin measurement should be realizable. As discussed in many specific proposals [30] these error rates appear attainable in both the transport and the optical setting. Apart from single qubit operations, our proposal also requires precise control of the interaction time. Fast arbitrary wave form generators used in the double-dot experiments, have time resolutions better than 30 ps [48] and minimum step sizes of 200 ps, which translates into errors of a few percent in estimating A_z with initial uncertainties of order 1 ns^{-1}. Uncertainties of this order are expected for large QDs ($N\sim 10^6$) even if they are unpolarized and for smaller ones at correspondingly higher polarization (see below).

For GaAs and InAs QDs in the single electron regime, $A\sim 50-200\ \mathrm{ns}^{-1}$ and $N\sim 10^4-10^6$. The uncertainty $\Delta_0^2=\langle A_z^2\rangle-\langle A_z\rangle^2=(T_2^*)^{-2}$ determines the inhomogeneous dephasing time T_2^* [12]. Especially at low polarization P, this uncertainty is large $\Delta_0^2\approx A^2(1-P^2)/N$, and without correction H_{zz} leads to fast inhomogeneous dephasing of electron-spin qubits: $T_2^*\gtrsim 10$ ns has been observed [1,33,34]. However, as A_z is slowly varying [9,10,16], it may be estimated, thereby reducing the uncertainty in its value and the corresponding dephasing. This is expected to be particularly effective, when combining the estimation with recent progress in polarizing the nuclear-spin ensemble [33,35,36].

In a QD system such as [5], with $\tau_m\simeq 1\ \mu$s and for $1/\Delta_0\simeq 10$ ns we can estimate 8 digits ($M=8$) (improving $\Delta A_{z,\mathrm{est}}$ by a factor of at least 16) in a total time $T_M=16\ \mu$s. In contrast, a standard atomic clock measurement scheme would require a time $\simeq 280\ \mu$s.

We now consider limits to the estimation process, focusing on expected variations of A_z due to nuclear-spin exchange and preparation and measurement errors. Nuclear-spin exchange, in which two nuclei switch spin states, may occur directly by dipole-dipole interactions or indirectly via virtual electron spin flips. Such flips lead to variations of A_z as spins i and j may have $\alpha_i\neq\alpha_j$.

The dipole-dipole process, with a $1/r^3$ scaling, may be approximated by a diffusive process at length scales substantially longer than the lattice spacing [15,37]. The length scale for a spin at site i to a site j such that $\alpha_j\approx\alpha_i$ is not satisfied is on the order of the QD radius (5–50 nm); for diffusion constants appropriate for GaAs [38], the time scale for a change of A_z comparable to ΔA_z by this process is $\sim 0.01-10$ s.

However, nuclear-spin exchange mediated by virtual electron-spin flips may be faster. This process is the first correction to the rotating wave approximation, and is due to the (heretofore neglected) terms in the contact interaction, $H_{\mathrm{ff}}=\hbar/2(A_+S_-+A_-S_+)$, which are suppressed to first order by the electron Larmor precession frequency ϵ_z. These have been considered in detail elsewhere [10,12,39–42]. Using perturbation theory to fourth order, the estimated decorrelation time for A_z is $t_c^{-1}=A^2/(\epsilon_z N^{3/2})$, giving values $0.1-100\ \mathrm{ms}^{-1}$ for our parameter range [42]. Taking $t_c=1$ ms, we may estimate the optimal number of digits to measure. Using Eq. (14), the best measurement time is given by $T_M\sim t_c/2^{M/2}$ and for the values used above, $M\approx 10-11$ is optimal. We note as a direct corollary that our measurement scheme provides a sensitive probe of the nuclear-spin dynamics on nanometer length scales.

We now consider implications of these results for improving the performance of nuclear-spin ensembles, both as quantum memory [19] and as a qubit [20]. The dominant error mechanism is the same as for other spin-qubit schemes in QDs: uncertainty in A_z. The proposed measurement scheme alleviates this problem. However, the nuclear-spin ensembles operate in a subspace of collective states $|0\rangle$ and $|1\rangle$, where the first is a "dark state," characterized by $A_-|0\rangle=0$ (and the second is $\propto A_+|0\rangle$, where $A_\pm=\Sigma_j\alpha_j I_\pm^{(j)}$). Thus $|0\rangle$ is an A_- eigenstate and cannot be an A_z eigenstate when $\alpha_k\neq$ const (except for full polarization). Therefore, the measurement (which essentially projects to certain A_z eigenspaces ($A_z\in[a-\Delta a,a+\Delta a]$)) moves the system out of the computational space, leading to leakage errors. The incommensurate requirements of measuring A_z and using an A_-

eigenstate place an additional restriction on the precision of the measurement. The optimal number of digits can be estimated in perturbation theory, using an interaction time $T_{\mathrm{int}} \approx 2t_1$ and numerical results [19] on the polarization dependence of Δ_0. We find that for high polarization $P > 90\%$ a relative error of $\Delta a/a \lesssim 1\%$ is achievable.

VII. CONCLUSIONS

We have shown that a measurement approach based on quantum phase estimation can accurately measure a slowly varying mesoscopic environment coupled to a qubit via a pure dephasing Hamiltonian. By letting a qubit interact for a sequence of well-controlled times and measuring its state after the interaction, the value of the dephasing variable can be determined, thus reducing significantly the dephasing rate.

The procedure requires fast single qubit rotations, but can tolerate realistically slow qubit measurements, since the phase estimation approach minimizes the number of measurements. Limitations due to measurement and preparation errors may be overcome by combining our approach with standard error correction techniques. Fluctuations in the environment can also be tolerated, and our measurement still provides the basis for a good estimate, if the decorrelation time of the environment is not too short.

In view of the implementation of our scheme, we have considered the hyperfine coupling of an electron spin in a quantum dot to the nuclear-spin ensemble. Our calculations show that the Overhauser field in a quantum dot can be accurately measured in times shorter than the nuclear decorrelation time by shuttling suitably prepared electrons through the dot. Given recent advances in electron measurement and control [5,16] this protocol could be used to alleviate the effect of hyperfine decoherence of electron-spin qubits and allow for a detailed study of the nuclear-spin dynamics in quantum dots. Our approach complements other approaches to measuring the Overhauser field in a quantum dot that have recently been explored [43,44].

While we discussed a single electron in a single quantum dot, the method can also be applied, with modification to preparation and measurement procedures [49], to the case of two electrons in a double dot [1,34,45].

As we have seen, the Hamiltonian Eq. (1) can serve as a good approximation to more general qubit-environment coupling in the case of weak coupling and a nondegenerate qubit. Therefore, we expect that this technique may find an application in other systems with long measurement times and slowly varying mesoscopic environments.

ACKNOWLEDGMENTS

J.M.T. would like thank the quantum photonics group at ETH for their hospitality. The authors thank Ignacio Cirac and Guifré Vidal for sharing their notes on the performance of the QFT scheme for different figures of merit. The work at ETH was supported by NCCR Nanoscience, at Harvard by ARO, NSF, Alfred P. Sloan Foundation, and David and Lucile Packard Foundation, and at Ames by the NSF Career Grant No. ECS-0237925, and at MPQ by SFB 631.

[1] A. C. Johnson, J. R. Petta, J. M. Taylor, A. Yacoby, M. D. Lukin, C. M. Marcus, M. P. Hanson, and A. C. Gossard, Nature (London) **435**, 925 (2005); e-print cond-mat/0503687.
[2] G. Ithier, E. Collin, P. Joyez, P. J. Meeson, D. Vion, D. Esteve, F. Chiarello, A. Shnirman, Y. Makhlin, and J. Schriefl, Phys. Rev. B **72**, 134519 (2005).
[3] R. Alicki, M. Horodecki, P. Horodecki, and R. Horodecki, Phys. Rev. A **65**, 062101 (2002).
[4] B. M. Terhal and G. Burkard, Phys. Rev. A **71**, 012336 (2005).
[5] J. M. Elzerman, R. Hanson, L. H. Willems van Beveren, B. Witkamp, L. M. K. Vandersypen, and L. P. Kouwenhoven, Nature (London) **430**, 431 (2004).
[6] A. Kitaev, e-print quant-ph/9511026.
[7] M. A. Nielsen and I. L. Chuang, *Quantum Computation and Quantum Information* (Cambridge University Press, Cambridge, 2000).
[8] D. Loss and D. P. DiVincenzo, Phys. Rev. A **57**, 120 (1998).
[9] A. V. Khaetskii, D. Loss, and L. Glazman, Phys. Rev. Lett. **88**, 186802 (2002).
[10] I. A. Merkulov, A. L. Efros, and M. Rosen, Phys. Rev. B **65**, 205309 (2002).
[11] J. Schliemann, A. Khaetskii, and D. Loss, J. Phys.: Condens. Matter **15**, R1809 (2003).
[12] W. A. Coish and D. Loss, Phys. Rev. B **70**, 195340 (2004).
[13] S. I. Erlingsson and Y. V. Nazarov, Phys. Rev. B **70**, 205327 (2004).
[14] R. de Sousa, N. Shenvi, and K. B. Whaley, Phys. Rev. B **72**, 045330 (2005).
[15] C. Deng and X. Hu, Phys. Rev. B **72**, 165333 (2005).
[16] J. R. Petta, A. C. Johnson, J. M. Taylor, E. A. Laird, A. Yacoby, M. D. Lukin, C. M. Marcus, M. P. Hanson, and A. C. Gossard, Science **309**, 2180 (2005).
[17] J. M. Taylor, H.-A. Engel, W. Dür, A. Yacoby, C. M. Marcus, P. Zoller, and M. D. Lukin, Nat. Phys. **1**, 177 (2005).
[18] J. M. Taylor, C. M. Marcus, and M. D. Lukin, Phys. Rev. Lett. **90**, 206803 (2003).
[19] J. M. Taylor, A. Imamoğlu, and M. D. Lukin, Phys. Rev. Lett. **91**, 246802 (2003).
[20] J. M. Taylor, G. Giedke, H. Christ, B. Paredes, J. I. Cirac, P. Zoller, M. D. Lukin, and A. Imamoğlu, e-print cond-mat/0407640.
[21] D. J. Wineland, J. C. Bergquist, J. J. Bollinger, W. M. Itano, F. L. Moore, J. M. Gilligan, M. G. Raizen, D. J. Heinzen, C. S. Weimer, and C. H. Manney, in *Laser Manipulation of Atoms and Ions*, Proceedings of the Enrico Fermi Summer School, Course CXVIII, Varenna, 1991, edited by E. Arimondo, W. D. Phillips, and F. Strumia (North-Holland, Amsterdam, 1992), p. 539.
[22] V. Giovannetti, S. Lloyd, and L. Maccone, Phys. Rev. Lett. **96**, 010401 (2006).

[23] L. Vaidman and Z. Mitrani, Phys. Rev. Lett. **92**, 217902 (2004).
[24] R. B. Griffiths and C.-S. Niu, Phys. Rev. Lett. **76**, 3228 (1996).
[25] S. Parker and M. B. Plenio, Phys. Rev. Lett. **85**, 3049 (2000).
[26] A. Tomita and K. Nakamura, Int. J. Quantum Inf. **2**, 119 (2004).
[27] L. Masanes, G. Vidal, and J. I. Cirac (unpublished).
[28] R. E. Kalman, ASME J. Basic Eng. **82**, 35 (1960).
[29] S. Lee, P. von Allmen, F. Oyafuso, G. Klimeck, and K. B. Whaley, J. Appl. Phys. **97**, 043706 (2005); e-print quant-ph/0403122.
[30] V. Cerletti, W. A. Coish, O. Gywat, and D. Loss, Nanotechnology **16**, R27 (2005); e-print cond-mat/0412028.
[31] M. Atature, J. Dreiser, A. Badolato, A. Hogele, K. Karrai, and A. Imamoglu, Science **312**, 551 (2006).
[32] R. Hanson, L. H. Willems van Beveren, I. T. Vink, J. M. Elzerman, W. J. M. Naber, F. H. L. Koppens, L. P. Kouwenhoven, and L. M. K. Vandersypen, Phys. Rev. Lett. **94**, 196802 (2005).
[33] A. S. Bracker, E. A. Stinaff, D. Gammon, M. E. Ware, J. G. Tischler, A. Shabaev, A. L. Efros, D. Park, D. Gershoni, and V. L. Korenev, Phys. Rev. Lett. **94**, 047402 (2005).
[34] F. H. L. Koppens, J. A. Folk, J. M. Elzerman, R. Hanson, L. H. Willems van Beveren, I. T. Vink, H.-P. Tranitz, W. Wegscheider, L. P. Kouwenhoven, and L. M. K. Vandersypen, Science **309**, 1346 (2005).
[35] B. Eble, O. Krebs, A. Lemaitre, K. Kowalik, A. Kudelski, P. Voisin, B. Urbaszek, X. Marie, and T. Amand, e-print cond-mat/0508281.
[36] C. W. Lai, P. Maletinsky, A. Badolato, and A. Imamoglu, Phys. Rev. Lett. **96**, 167403 (2006).
[37] C. P. Slichter, *Principles of Magnetic Resonance* (Springer-Verlag, Berlin, 1980).
[38] D. Paget, Phys. Rev. B **25**, 4444 (1982).
[39] N. Shenvi, R. de Sousa, and K. B. Whaley, Phys. Rev. B **71**, 224411 (2005).
[40] W. Yao, R.-B. Liu, and L. J. Sham, Phys. Rev. Lett. **95**, 030504 (2005).
[41] C. Deng and X. Hu, Phys. Rev. B **73**, 241303(R) (2006).
[42] J. M. Taylor, J. R. Petta, A. C. Johnson, A. Yacoby, C. M. Marcus, and M. D. Lukin, e-print cond-mat/0602470.
[43] D. Klauser, W. A. Coish, and D. Loss, Phys. Rev. B **73**, 205302 (2006).
[44] D. Stepanenko, G. Burkard, G. Giedke, and A. Imamoglu, Phys. Rev. Lett. **96**, 136401 (2006).
[45] W. A. Coish and D. Loss, Phys. Rev. B **72**, 125337 (2005).
[46] In practice one may want to make use of prior knowledge about the state of the system to reduce the interval of possible eigenvalues that need to be sampled. Hence A may be understood as an effective maximal eigenvalue given, e.g., by the expectation value of A_z plus f standard deviations. The values outside this range will not be measured correctly by the schemes discussed, but we assume f to be chosen sufficiently large for this effect to be smaller than other uncertainties.
[47] For this we make use of Eq. (6) and $(\sin x)/x \geq 1-\pi^{-1}|x|$ (for $|x| \leq \pi$) to bound all terms of the sum over R.
[48] J. R. Petta (private communication).
[49] In the strong field case a two-level approximation for the spin system is appropriate [45]. Preparing superpositions in the $S_z=0$ subspace such as the singlet, and measuring in this basis as well [16], the scheme would measure the z component of the nuclear-spin difference between the dots. To measure the total Overhauser field, superpositions of the $S_z \neq 0$ triplet states have to be used.

PRL **96,** 136401 (2006) PHYSICAL REVIEW LETTERS week ending 7 APRIL 2006

Enhancement of Electron Spin Coherence by Optical Preparation of Nuclear Spins

Dimitrije Stepanenko and Guido Burkard
Department of Physics and Astronomy, University of Basel, Klingelbergstrasse 82, CH-4056 Basel, Switzerland

Geza Giedke and Atac Imamoglu
Institute of Quantum Electronics, ETH Zürich, CH-8093 Zürich, Switzerland
(Received 15 December 2005; published 3 April 2006)

We study a large ensemble of nuclear spins interacting with a single electron spin in a quantum dot under optical excitation and photon detection. At the two-photon resonance between the two electron-spin states, the detection of light scattering from the intermediate exciton state acts as a weak quantum measurement of the effective magnetic (Overhauser) field due to the nuclear spins. In a coherent population trapping state without light scattering, the nuclear state is projected into an eigenstate of the Overhauser field operator, and electron decoherence due to nuclear spins is suppressed: We show that this limit can be approached by adapting the driving frequencies when a photon is detected. We use a Lindblad equation to describe the driven system under photon emission and detection. Numerically, we find an increase of the electron coherence time from 5 to 500 ns after a preparation time of 10 μs.

DOI: 10.1103/PhysRevLett.96.136401 PACS numbers: 71.70.Jp, 03.67.Pp, 78.67.Hc

Introduction.—Single electron spins localized in small artificial structures, such as semiconductor quantum dots (QDs), have become available and to a large extent controllable [1–4]. Of particular interest is the phase coherence of electron spins as single quantum objects, both from a fundamental physics point of view and because of their potential use as quantum bits (qubits) for quantum information processing [5,6].

A number of physical mechanisms that lead to the gradual reduction of the quantum phase coherence (decoherence) of the electron spin have been analyzed [7]. It has been established experimentally [2–4] and theoretically [8–13] that, in a GaAs QD, the predominant decoherence mechanism is the hyperfine coupling to the nuclear spins in the host material. For an unpolarized ensemble of N nuclei and an effective hyperfine interaction energy A, the dephasing time in a weak magnetic field is $T_2^* \sim 1/\sigma \sim \sqrt{N}/A$, where σ is the width of the distribution of nuclear field values h_z parallel to the field. In a typical GaAs QD with $A \sim 90$ μeV or $A/g\mu_B = 3.5$ T [14], the number of Ga and As nuclei (spin $I = 3/2$) is $N \sim 5 \times 10^5$ and $T_2^* \sim 5$ ns; this value is supported by the experimental evidence [4,15]. The T_2^* decay originates from nuclear ensemble averaging and can be prolonged by narrowing the nuclear spin distribution [12]. Another strategy is to polarize the nuclear spins [8], but this requires a polarization close to 100% which is currently not available [12]. Two schemes have been proposed to achieve a narrowing of the nuclear spin distribution, based on electron transport [16] and gate-controlled electronic Rabi oscillations [17].

Here we analyze an optical scheme for nuclear spin preparation that makes use of spin-flip two-photon (Raman) resonance in a driven three-level system (TLS), in analogy to electromagnetically induced transparency (EIT) in atoms [18,19]. The lowest electronic states in a QD formed in a III-V semiconductor (e.g., GaAs) that are optically active under σ_+ circularly polarized excitation are the Zeeman-split ground state of a single localized conduction-band (E_C) electron and the negatively charged exciton (trion) $|X\rangle$, i.e., two electrons (spin up and down) plus one valence band heavy hole (hh) with angular momentum $J_{z'} = +3/2$ (Fig. 1). The $J = 3/2$ sector in the valence band is split into light hole and hh states along the axis z' of strong QD confinement. Here we assume excitation from the hh ($J_{z'} = \pm 3/2$) subband only. The axis z in

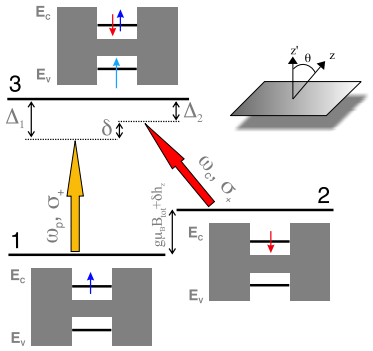

FIG. 1 (color online). Three-level system. State 1 (2) is a spin-up (-down) conduction-band (E_C) electron, with splitting $g\mu_B B_{\text{tot}} + \delta h_z$, where δh_z is the z component of the nuclear (Overhauser) field fluctuations. State 3 is a trion with $J_{z'} = 3/2$. Two laser fields with frequencies ω_p and ω_c are applied near the 13 and 23 resonances with detunings $\Delta_{1,2}$. For a σ_+ circularly polarized excitation (along z'), both transitions are allowed for $\theta \neq 0$ and transitions to the $J_{z'} = -3/2$ states are forbidden. Inset: Structural axis z', leading to a splitting in E_V and spin quantization axis $z \parallel \mathbf{B}_{\text{tot}}$ in E_C where $\cos\theta = z \cdot z' < 1$.

 © 2006 The American Physical Society

PRL 96, 136401 (2006) PHYSICAL REVIEW LETTERS week ending 7 APRIL 2006

E_C is parallel to the total magnetic field $\mathbf{B}_{\rm tot}$, and we assume that the axes z and z' enclose an angle $\theta > 0$. The spin-up and -down states in E_C are then $|\uparrow\rangle \equiv |\uparrow\rangle_z = \cos(\theta)|\uparrow\rangle_{z'} + \sin(\theta)|\downarrow\rangle_{z'}$ and $|\downarrow\rangle \equiv |\downarrow\rangle_z = \cos(\theta)|\downarrow\rangle_{z'} - \sin(\theta)|\uparrow\rangle_{z'}$. Two circularly polarized (σ_+) continuous-wave lasers at the frequencies $\omega_p = \omega_X - \omega_\uparrow - \Delta_1$ and $\omega_c = \omega_X - \omega_\downarrow - \Delta_2$ stimulate the transitions between $|\uparrow\rangle$ and $|X\rangle$ and between $|\downarrow\rangle$ and $|X\rangle$, while the trion with $J_{z'} = -3/2$ is not excited.

The narrowing of the nuclear field distribution ν is based on light scattering in a TLS, where two long-lived (spin) states are coupled resonantly to an excited state that decays by spontaneous emission. When the two lasers satisfy exact two-photon resonance $\delta = \Delta_1 - \Delta_2 = 0$, one of the eigenstates of the system is a superposition of the two spin states with a vanishing excited state $|X\rangle$ component. The TLS at $\delta = 0$ is driven to this dark state with a vanishing light scattering rate [19]. The population of $|X\rangle$ and, thus, the photon scattering rate is nonzero for $\delta \neq 0$. In the presence of the nuclear spins, this resonance moves to $\delta = \delta h_z$, where δh_z is the deviation of the nuclear field (along z) from its mean $\langle h_z\rangle$. The absence of photon emission during a waiting time t constitutes a weak measurement of the quantum operator δh_z. In the limit $t \to \infty$, it becomes a strong measurement, projecting the nuclear state onto $|\delta h_z = 0\rangle$ (width $\sigma = 0$), thus eliminating electron decoherence due to the fluctuating field δh_z.

Model.—The Hamiltonian for the TLS coupled to nuclei is $H = H_0 + H_{\rm int} + H_{\rm hf}$, where $H_0 = -(\hbar\omega_z/2)\Sigma_z + \hbar\omega_X P_X$, with $\Sigma_i = \sigma_i \oplus 0$, the block-diagonal 3×3 matrix with the Pauli matrix σ_i in the upper left corner and 0 elsewhere, and $P_X = |X\rangle\langle X| = (001)^T(001)$. The spin splitting is given as $\hbar\omega_z = g\mu_B B_{\rm tot} = |g\mu_B\mathbf{B} + \langle\mathbf{h}\rangle|$, the sum of the external magnetic and the mean nuclear fields. The nuclear (Overhauser) field operator is $\mathbf{h} = \sum_{i=1}^N A_i \mathbf{I}_i$, where $A_i = a_i v_0 |\Psi(\mathbf{r}_i)|^2$, and $\Psi(\mathbf{r}_i)$ denotes the electron wave function at the position $\mathbf{r}_i$ of the ith atomic nucleus, v_0 is the volume of the unit cell, and a_i is the hyperfine coupling strength for the nuclear species at site i. The classical laser fields in the rotating wave approximation (RWA) are described by [19] $H_{\rm int} = \Omega_p e^{i\omega_p t}|X\rangle\times\langle\uparrow| + \Omega_c e^{i\omega_c t}|X\rangle\langle\downarrow| + \text{H.c.}$ The coupling of the electron spin to the quantum fluctuations of $\mathbf{h}$ is described by $H_{\rm hf} = -\frac{1}{2}\delta\mathbf{h}\cdot\mathbf{\Sigma}$, where $\delta\mathbf{h} = \mathbf{h} - \langle\mathbf{h}\rangle$. In the rotating frame $\tilde\Psi(t) = U(t)\Psi(t)$, with $U(t) = e^{-i\omega_p t}P_\uparrow + e^{-i\omega_c t}P_\downarrow + P_X$, where $P_\uparrow = |\uparrow\rangle\langle\uparrow|$ and $P_\downarrow = |\downarrow\rangle\langle\downarrow|$, we find $\tilde H(t) = U(t)\times[H(t) + \hbar\omega_p P_\uparrow + \hbar\omega_c P_\downarrow]U(t)^\dagger$ and, up to a constant (we drop the tilde and use H for the Hamiltonian henceforth),

$$H(t) = -\frac{\hbar}{2}\begin{pmatrix}\delta & 0 & \Omega_p\\ 0 & -\delta & \Omega_c\\ \Omega_p & \Omega_c & -\Delta\end{pmatrix} - \frac{\hbar}{2}\delta h_z\Sigma_z + H_\perp, \quad (1)$$

where $\Delta = \Delta_1 + \Delta_2$. The hyperfine flip-flop terms $H_\perp = \hbar(\delta h_+\Sigma_- e^{it(\omega_p-\omega_c)} + \delta h_-\Sigma_+ e^{-it(\omega_p-\omega_c)})/4$ are oscillating rapidly at the frequency $\omega_p - \omega_c = g\mu_B B_{\rm tot}/\hbar - \delta$ and can be neglected in the RWA [20], leading to a block-diagonal Hamiltonian $H = \text{diag}(H_1, H_2, \ldots, H_K)$, with

$$H_k = -\frac{\hbar}{2}\begin{pmatrix}\delta h_z^k + \delta & 0 & \Omega_p\\ 0 & -\delta h_z^k - \delta & \Omega_c\\ \Omega_p & \Omega_c & -\Delta\end{pmatrix}, \quad (2)$$

where δh_z^k for $k = 1, 2, \ldots, K$ are the eigenvalues of the operator δh_z and $K = (2I+1)^N$ is the dimension of the nuclear spin Hilbert space. The state of the TLS combined with the nuclear spins is described by the density matrix ρ, which we divide up into 3-by-3 blocks $\rho_{kk'}$ and which evolves according to the generalized master equation [19]

$$\dot\rho = \mathcal{L}\rho \equiv \frac{1}{i\hbar}[H,\rho] + \mathcal{W}\rho, \quad (3)$$

with the Hamiltonian equation (1) and the dissipative term $\mathcal{W}\rho = \sum_{\alpha=\uparrow,\downarrow}\Gamma_{X\alpha}(2\sigma_{\alpha X}\rho\sigma_{X\alpha} - \sigma_{XX}\rho - \rho\sigma_{XX})/2 + \sum_{\beta=\downarrow,X}\gamma_\beta(2\sigma_{\beta\beta}\rho\sigma_{\beta\beta} - \sigma_{\beta\beta}\rho - \rho\sigma_{\beta\beta})/2$, where $\sigma_{ij} = \sigma_{ij}\otimes\mathbb{1} = |i\rangle\langle j|$. The rate $\Gamma_{X\alpha}$ describes the radiative decay of $|X\rangle$ into $\alpha = |\uparrow\rangle, |\downarrow\rangle$, while γ_β is the pure dephasing rate of state $\beta = |\downarrow\rangle, |X\rangle$ with respect to $|\uparrow\rangle$. Since H is block-diagonal, Eq. (3) leads to the closed form

$$\dot\rho_{kk'} = \frac{1}{i\hbar}(H_k\rho_{kk'} - \rho_{kk'}H_{k'}) + \mathcal{W}\rho_{kk'}. \quad (4)$$

The diagonal blocks obey the familiar Lindblad equation,

$$\dot\rho_{kk} = \mathcal{L}_k\rho_{kk}, \qquad \mathcal{L}_k = -i[H_k,\rho] + \mathcal{W}\rho. \quad (5)$$

Stationary state.—We start with the factorized state $\rho_0 = \chi_0\otimes\nu_0$, with arbitrary initial density matrices χ_0 and $\nu_0 = \sum_{kk'}\nu_{kk'}|\delta h_z^k\rangle\langle\delta h_z^{k'}|$ of the TLS and the nuclear ensemble, where $|\delta h_z^k\rangle$ are eigenstates of δh_z. We assume a Gaussian $\nu_{kk} = (2\pi)^{-1/2}\sigma^{-1}\exp[-(\delta h_z^k)^2/2\sigma^2]$, with the width $\sigma = \sigma_0 = A/\sqrt{N}$, plotted as a solid line in Fig. 2(a). For our numerics, we choose $A = 90$ μeV, $N \approx 5\times 10^5$, corresponding to $\sigma_0 \simeq 0.13$ μeV $\simeq 0.2\hbar\Gamma$, with $\Gamma = 1$ ns, and a sample of $n \ll K$ states ($n \sim 4000$) [21]. Because of the hyperfine coupling, the TLS and the nuclei are entangled in the stationary state $\bar\rho = \sum_{kk'}\bar\rho_{kk'}\otimes|\delta h_z^k\rangle\langle\delta h_z^{k'}|$ with $\dot{\bar\rho} = \mathcal{L}\bar\rho = 0$. We derived an analytical expression for the 3-by-3 diagonal blocks $\bar\rho_{kk}$ of $\bar\rho$ as a function of all parameters, including δh_k.

Evolution of the observed system.—In order to enhance the electron-spin coherence, we aim at *narrowing* the nuclear spin distribution ν_{kk}. For a Gaussian distribution, this amounts to decreasing the width σ, thus increasing the electron coherence time $t_0 \simeq 1/2\sigma$. Ideally, we would perform a projective measurement P on the nuclear spins, $P\bar\rho_{kk}P \propto \delta(\delta h_z^k - \delta)$. A successive approximation of P is achieved by monitoring the photon emission from the QD. The longer the period t during which no photon is emitted, the higher is the probability for δh_z to be at the two-photon resonance, $\delta h_z = \delta$.

To describe the state of the system conditional on a measurement record, we use the *conditional density matrix*

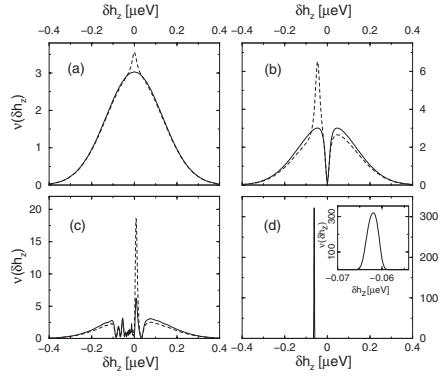

FIG. 2. Conditional evolution of the nuclear spin distribution $\nu(\delta h_z^k) = \nu_{kk}$. (a) During the first period t_1 without photon emission, the initial Gaussian distribution (solid line) develops a peak at the two-photon resonance (dashed line). (b) Change of $\nu(\delta h_z)$ after emission at t_1 (solid line), until before emission time t_2 of the second photon (dashed line). The two-photon resonance δ is shifted to the position of the left maximum (adaptive technique). The depleted region around $\delta h_z^k = 0$ develops at t_1. (c) Analogous situation between t_{11} and t_{12}. (d) $\nu(\delta h_z)$ is obtained after a total time of 10 μs. Inset: Magnification of peak in (d). The width of $\nu(\delta h_z)$ is reduced by a factor of ≈ 100 compared to the initial width in (a). The parameters are $\Omega_c = \Omega_p = 0.2$ ns^{-1}, $\Delta = 0$, $\Gamma_{X\uparrow} = \Gamma_{X\downarrow} = 1$ ns^{-1}, and $\gamma_\downarrow = \gamma_X = 0.001$ ns^{-1}.

ρ^c. In the absence of photon emission, ρ^c obeys Eq. (5) with $\mathcal{L}_k$ replaced by $\mathcal{L}_k - \mathcal{S}$, where the collapse operator $\mathcal{S}$ describes spontaneous emission of the state $|X\rangle$ into $|\uparrow\rangle$ and $|\downarrow\rangle$ with rates $\Gamma_{X\uparrow}$ and $\Gamma_{X\downarrow}$ [22],

$$\dot{\rho}^{\,c}_{kk} = (\mathcal{L}_k - \mathcal{S})\rho^c_{kk}, \qquad \mathcal{S}\rho = \sum_{\alpha=\uparrow,\downarrow} \Gamma_{X\alpha}\sigma_{\alpha X}\rho\sigma_{X\alpha}. \quad (6)$$

We have numerically calculated ρ^c in the absence of emitted photons for a duration t. We plot the updated distribution ν_{kk} from $\nu = \mathrm{Tr}_\Lambda \rho^c$ as a dashed line in Fig. 2(a). We find that the *a posteriori* ν_{kk} is concentrated around the two-photon resonance. As the off-diagonal elements (coherences) of ν are constrained by positivity, $|\nu_{kk'}| \le \sqrt{\nu_{kk}\nu_{k'k'}}$, they are also reduced by the narrowing of ν_{kk}. This process is eventually stopped by a photon emission.

Photon emission.—The stationary emission rate is [22]

$$\Gamma_{\mathrm{em}} = \mathrm{Tr}\mathcal{S}\bar{\rho}(t) = \Gamma\sum_k (\rho_{kk})_{XX}\nu_{kk}, \quad (7)$$

where $\Gamma = \Gamma_{X\uparrow} + \Gamma_{X\downarrow}$. The average photon number during time t is $\langle N_{\mathrm{ph}}\rangle = t\Gamma_{\mathrm{em}}$, and the *a priori* probability for $N_{\mathrm{ph}} = 0$ is, according to Poissonian statistics, $P_{\mathrm{dark}}(t) = \exp(-\Gamma_{\mathrm{em}}t)$. The waiting time distribution for photon emissions is $p_{\mathrm{wait}}(t) = \Gamma_{\mathrm{em}}^{-1}\exp(-\Gamma_{\mathrm{em}}t)$ with mean $\langle t\rangle = \Gamma_{\mathrm{em}}^{-1}$. The narrowing of ν_{kk}, Eqs. (6) and (7), leads to a decreasing Γ_{em} and an increasing $\langle t\rangle$.

With Eq. (7), we find the update rule for ν upon photon emission, $\nu' = \mathrm{Tr}_\Lambda\mathcal{S}\rho^c/\mathrm{Tr}\mathcal{S}\rho^c$, or

$$\nu'_{kk} = \frac{\nu_{kk}(\rho_{kk})_{XX}}{\sum_j \nu_{jj}(\rho_{jj})_{XX}}, \quad (8)$$

where ν_{kk} and $(\rho_{kk})_{XX} = \langle X|\rho_{kk}|X\rangle$ are taken before the emission. The population in the Overhauser field δh_z corresponding to the two-photon resonance $\delta h_z = \delta$ is depleted by the photon emission [Fig. 2(b), solid line].

Adaptive technique.—The stationary, isolated TLS at the two-photon resonance is in a dark state. However, the coupling to the nuclei introduces a nonzero probability for occupation of $|X\rangle$ and for photon emission. Since the detection of a photon provides information about δh_z, the photon emission does not necessarily signify a failed attempt to narrow the nuclear field distribution but can be used as an input for the next weak measurement with adjusted frequencies of the driving lasers, $\omega'_p = \omega_p + \epsilon/2$ and $\omega'_c = \omega_c - \epsilon/2$, so that the new two-photon resonance condition is $\delta h_z = \delta'$, where $\delta' = \delta + \epsilon$ while $\Delta' = \Delta$. We choose ϵ such that the new resonance with the Overhauser field lies in one of the two maxima $\delta h_z^{\max}$ formed after the photon emission; see Fig. 2(b). This situation is described by Eq. (2) with the substitution $\delta \to \delta + \delta h_z^{\max}$. The adaptive technique also works by changing only one of the laser frequencies. Right after the photon emission, the TLS is in one of the single electron states $|\uparrow\rangle$ or $|\downarrow\rangle$. Within a time $1/\Gamma$, much faster than any nuclear time scale, the system will reach the new stationary state. The photon emission from the QD can again be monitored, leading to an enhanced nuclear population at the new resonance [Fig. 2(b), dashed line], thus further narrowing the nuclear distribution. Repeating this procedure leads to a nuclear width that is limited only by the width of the EIT resonance [Figs. 2(c) and 2(d)].

Electron-spin decoherence.—The electron-spin coherence is quantified using the expectation value of the raising operator $S_+(t)$ in a state $|x_+\rangle$ that is prepared perpendicular to the total field $\mathbf{B}_{\mathrm{tot}}$ and is freely precessing about the fluctuating nuclear field δh_z, $\langle S_+(t)\rangle \equiv \langle x_+|S_+(t)|x_+\rangle$. We obtain $\langle S_+(t)\rangle = (\hbar/2)\sum_k \nu_{kk}\exp(it\delta h_z^k)$, which we plot in Fig. 3 at various stages in an adaptive optical measurement scheme. As the off-diagonal elements $\nu_{kk'}$ for $k \neq k'$ do not enter $\langle S_+(t)\rangle$ and Eq. (4) decouples, these results are valid for any ν_0 consistent with the chosen Overhauser field probability distribution. We make a Gaussian fit $\langle S_+(t)\rangle \propto \exp(-t^2/t_0^2)$ for short times t and plot the coherence time t_0 as a function of the total waiting time in Fig. 4. This is the main result of our theoretical analysis: The repeated observation of the QD photon emission and adaptation of the laser frequencies ω_c and ω_p after each photon emission leads to a pronounced enhancement of the electron coherence time, for the realistic parameters chosen, from $t_0 =$ 5 ns to $\approx$500 ns within a total observation time of 10 μs.

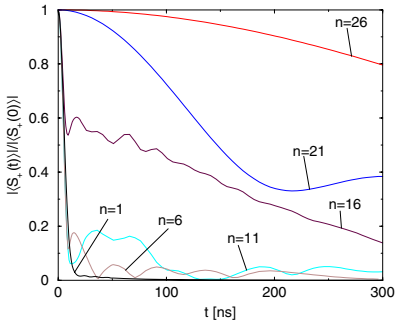

FIG. 3 (color online). Electron coherence function $|\langle S_+(t)\rangle|/|\langle S_+(0)\rangle|$ vs electronic precession time t calculated from $\nu(\delta h_z)$ in Fig. 2 after emission of the nth photon ($n = 1, 6, \ldots, 26$). The initial decay is approximately Gaussian.

Imperfect detectors.—We cannot expect to have perfect photon detectors at our disposal; therefore, we discuss here the case of a detector with efficiency $e < 1$. For an imperfect detector, Eq. (6) becomes $\dot{\rho}^c_{kk} = (\mathcal{L}_k - e\mathcal{S})\rho^c_{kk}$, reflecting that photons are detected with probability e. We have numerically analyzed the case of $e = 10\%$ (other parameters as above) and find $t_0 \approx 460$ ns after a somewhat longer preparation time $t = 50$ μs. This is still much shorter than the time after which the nuclear spin decays, around 0.01 s due to higher-order hyperfine flip-flop terms [17], but possibly longer due to Knight-shift gradient effects. Nuclear flip-flop processes occur on a time scale of ≈ 100 μs [14] but are ineffective in changing h_z in a magnetic field that enforces nuclear spin conservation and, thus, preserve h_z for short-range flip-flops while long-range flip-flops are suppressed by the Knight-shift gradient. This picture is supported by the observed slow ($\gtrsim 1$ s) decay of polarized nuclear spins in contact with donors in GaAs [23]. While a quantitative theory for the relevant time scale of nuclear spin decay due to nuclear-dipole interactions is missing, the arguments given above suggest that our picture of a slow decay is reasonable.

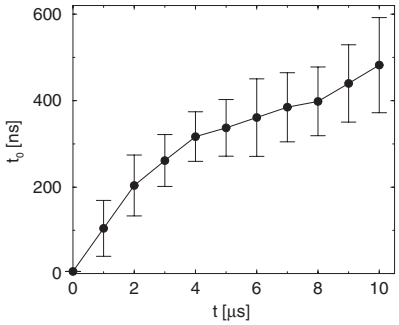

FIG. 4. Characteristic time t_0 of the initial Gaussian decay of $|\langle S_+(t)\rangle|/|\langle S_+(0)\rangle|$ in Fig. 3 as a function of the optical preparation time t, averaged over 50 numerical runs (error bars indicate the standard deviation).

Conclusions.—We find that it is possible to efficiently enhance the quantum phase coherence of an electron spin in a QD surrounded by a large ensemble of nuclear spins by a continuous weak measurement of the Overhauser field using optical excitation at a two-photon resonance of the TLS formed by $|\uparrow\rangle$, $|\downarrow\rangle$, and $|X\rangle$. An intriguing question is whether the electron-spin coherence can be enhanced by a quantum Zeno type effect to the point where it is ultimately determined by spin-orbit interaction: Since the reservoir correlation time of dominant electron-spin decoherence due to flip-flop terms of the hyperfine interaction is ~ 1 μs, this would most likely require high efficiency detection of the scattered photons.

We thank W. A. Coish, D. Klauser, D. Loss, M. D. Lukin, and J. M. Taylor for discussions. We acknowledge funding from the Swiss National Science Foundation (SNF) and through NCCR Nanoscience.

[1] J. M. Elzerman *et al.*, Phys. Rev. B **67**, 161308 (2003).
[2] A. C. Johnson *et al.*, Nature (London) **435**, 925 (2005).
[3] F. H. L. Koppens *et al.*, Science **309**, 1346 (2005).
[4] J. R. Petta *et al.*, Science **309**, 2180 (2005).
[5] D. Loss and D. P. DiVincenzo, Phys. Rev. A **57**, 120 (1998).
[6] A. Imamoglu *et al.*, Phys. Rev. Lett. **83**, 4204 (1999).
[7] V. Cerletti *et al.*, Nanotechnology **16**, R27 (2005).
[8] G. Burkard, D. Loss, and D. P. DiVincenzo, Phys. Rev. B **59**, 2070 (1999).
[9] A. Khaetskii, D. Loss, and L. Glazman, Phys. Rev. Lett. **88**, 186802 (2002).
[10] I. A. Merkulov, A. L. Efros, and M. Rosen, Phys. Rev. B **65**, 205309 (2002).
[11] A. Khaetskii, D. Loss, and L. Glazman, Phys. Rev. B **67**, 195329 (2003).
[12] W. A. Coish and D. Loss, Phys. Rev. B **70**, 195340 (2004).
[13] W. A. Coish and D. Loss, Phys. Rev. B **72**, 125337 (2005).
[14] D. Paget *et al.*, Phys. Rev. B **15**, 5780 (1977).
[15] The decay of a spin echo envelope, being a measure for $T_2 \geq T_2^*$, can be much slower [4].
[16] G. Giedke *et al.*, quant-ph/0508144.
[17] D. Klauser, W. A. Coish, and D. Loss, cond-mat/0510177 [Phys. Rev. B (to be published)].
[18] S. E. Harris, Phys. Today **50**, No. 7, 36 (1997).
[19] M. Fleischhauer, A. Imamoglu, and J. P. Marangos, Rev. Mod. Phys. **77**, 633 (2005).
[20] The neglected flip-flop terms contribute to electron-spin decoherence due to higher-order terms.
[21] Smaller sample sizes ($n \sim 100$) also give reliable results due to the block-diagonal H. Denser sampling is used to resolve the sharp final distribution.
[22] H. J. Carmichael, *An Open Systems Approach to Quantum Optics* (Springer, Berlin, 1993).
[23] D. Paget, Phys. Rev. B **25**, 4444 (1982).

PRL **105,** 267202 (2010) PHYSICAL REVIEW LETTERS week ending 31 DECEMBER 2010

Nuclear Spin Cooling Using Overhauser-Field Selective Coherent Population Trapping

M. Issler,[1] E. M. Kessler,[2,*] G. Giedke,[2] S. Yelin,[3] I. Cirac,[2] M. D. Lukin,[4] and A. Imamoglu[1,†]

[1]*Institute of Quantum Electronics, ETH-Zürich, CH-8093 Zürich, Switzerland*

[2]*Max-Planck-Institut für Quantenoptik, Hans-Kopfermann-Straße 1 85748 Garching, Germany*

[3]*Department of Physics, University of Connecticut, 2152 Hillside Road, U-3046 Storrs, Connecticut 06269-3046, USA*

[4]*Department of Physics, Harvard University, Cambridge, Massachusetts 02138, USA*

(Received 19 September 2010; revised manuscript received 17 November 2010; published 21 December 2010)

We show that a quantum interference effect in optical absorption from two electronic spin states of a solid-state emitter can be used to prepare the surrounding environment of nuclear spins in well-defined states, thereby suppressing electronic spin dephasing. The coupled electron-nuclei system evolves into a coherent population trapping state by optical-excitation-induced nuclear-spin diffusion for a broad range of initial optical detunings. The spectroscopic signature of this evolution where the single-electron strongly modifies its environment is a drastic broadening of the dark resonance in optical absorption experiments. The large difference in electronic and nuclear time scales allows us to verify the preparation of nuclear spins in the desired state.

DOI: 10.1103/PhysRevLett.105.267202 PACS numbers: 75.40.Gb, 03.65.Yz, 78.67.Hc

The phenomenon of coherent population trapping (CPT) in three-level emitters [1] is at the heart of a number of key advances in quantum optics, such as subrecoil cooling of atoms [2] and slow-light propagation [3,4]. In these experiments, optical excitation from two low-energy (spin) states to a common optically excited state vanishes due to a quantum interference effect, leading to the formation of a dark resonance whenever the two driving laser fields satisfy the two-photon resonance condition. The fundamental limit on how well quantum interference eliminates optical absorption is provided by the decoherence rate (T_2^{-1}) of the two low-energy spin states. Typically, this decoherence rate is assumed to be induced by a Markovian reservoir which is not influenced by its coupling to the emitter.

Unlike their atomic counterparts, solid-state spins are subject to non-Markovian dephasing [5,6] due to their coupling to reservoirs with long correlation times. In particular, hyperfine coupling to nuclear spins constitutes the most important source of decoherence for spin qubits. It was proposed that polarizing or measuring nuclear spins could alleviate the (T_2^*) decoherence process [5], which prompted theoretical [7,8] and experimental efforts aimed at narrowing down the Overhauser-field (OF) distribution [9–11]. Remarkably, recent experiments achieved a substantial manipulation of the nuclear spins (reservoir) by using the electron spin (system) itself [10–15].

In this Letter, we show that CPT in the spin states of a solid-state emitter could be used to deterministically prepare a nuclear-spin environment with ultranarrow OF distribution. This is achieved via anomalous diffusion processes associated with optical excitation [2]. As a consequence of the anomalous diffusion, the coupled electron-nuclei system dynamically switches back and forth between a trapped regime where nuclear-spin diffusion slows down drastically due to the formation of an electronic dark state and a nontrapped regime where optical excitation leads to fast diffusion [16]. When the coupled system is in the dark state, the nuclear-spin distribution has a standard deviation that is close to the single-spin limit. An additional feature of the scheme is the possibility of using resonant fluorescence to verify the preparation of a narrow nuclear-spin distribution [17]; turning the laser fields off after determining the coupled system to be in the dark state ensures that the OF distribution remains in the single-spin regime within time scales determined by the (intrinsic) nuclear-spin lifetime. The electron spin T_2^* time is then prolonged by a factor $\sim\sqrt{N}$, where N is the number of nuclear spins. Remarkably, nuclear spins in the prepared state do not evolve due to electron-mediated indirect interactions, eliminating a principal contribution to electron spin T_2 time [5,6].

We consider a solid-state emitter where two ground electronic spin states ($|\uparrow\rangle, |\downarrow\rangle$) are coupled by two laser fields to a common optically excited state $|t\rangle$ [Fig. 1(a)]. The laser with frequency ω_p (ω_c) coupling the $|\uparrow\rangle \leftrightarrow |t\rangle$ ($|\downarrow\rangle \leftrightarrow |t\rangle$) transition with Rabi frequency Ω_p (Ω_c) is referred to as the probe (coupling) field. The state $|t\rangle$ decays via spontaneous emission back to the two ground spin states (for simplicity we assume the rates $\Gamma_{t\uparrow} = \Gamma_{t\downarrow} = \Gamma/2$). Denoting the Zeeman energy of the electron spin due to the external field B_z with ω_z and the energy of $|t\rangle$ with ω_t, we express the bare optical detunings relevant for the CPT system as $\Delta\omega_p = \omega_t + \omega_z/2 - \omega_p$ and $\Delta\omega_c = \omega_t - \omega_z/2 - \omega_c$. In the absence of any spin interactions or decoherence, laser fields satisfying the two-photon resonance condition ($\delta = \Delta\omega_p - \Delta\omega_c = 0$) pump the electron spin into the dark state $|D\rangle \propto \Omega_c|\uparrow\rangle - \Omega_p|\downarrow\rangle$, which is decoupled from optical excitation. When $\Delta\omega_c = 0$ and $\Omega_p, \Omega_c \ll \Gamma$, the absorption line shape of the emitter is a Lorentzian with a quantum interference induced transparency in the center, that has a width $\delta\nu_{\text{trans}} \sim (\Omega_p^2 + \Omega_c^2)/\Gamma$.

 © 2010 The American Physical Society

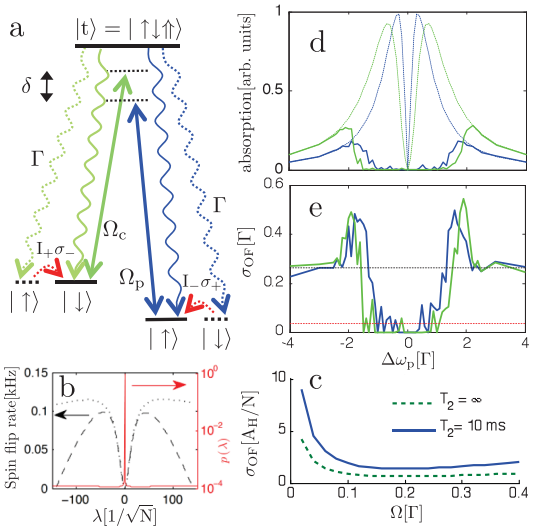

FIG. 1 (color). (a) The energy level diagram of a solid-state emitter exhibiting coherent population trapping (CPT). (b) Nuclear-spin diffusion rates depending on the nuclear-spin projection λ assuming homogeneous coupling. Parameters are $N = 4 \times 10^4$, $\Gamma = 1$ GHz, $A_H = \omega_z = 100$ μeV, and $\Omega = \Omega_p = \Omega_c = 0.1$ GHz. The rates calculated using the quantum mechanical (for the subspace $J = \sqrt{N/2}$, dashed line) and the semiclassical (dotted line) descriptions show both qualitative and quantitative agreement. The solid (red) curve shows the nuclear-spin distribution for $\Omega = 0.02\Gamma$ and $T_2^{-1} = 100\ \mathrm{s}^{-1}$. (c) The dependence of the steady-state OF standard deviation σ_{OF} as a function of Ω in the limit of homogeneous coupling; the solid (dashed) line is obtained by taking $T_2^{-1} = 100\ \mathrm{s}^{-1}$ ($T_2^{-1} = 0\ \mathrm{s}^{-1}$). (d) The absorption line shape (arb. units) for $\Omega = 0.2\Gamma$ (blue lines) and $\Omega = 0.4\Gamma$ (green lines): in stark contrast to the standard CPT profile (dotted lines), the dark resonance is drastically broadened (solid lines). (e) σ_{OF} for $\Omega_p = \Omega_c = 0.2\Gamma$ (blue line) and $\Omega_p = \Omega_c = 0.4\Gamma$ (green line) is reduced to the level below that of a single nuclear-spin flip (red line). The black line shows σ_{OF} in the absence of lasers.

In practice, the electronic spin states of most solid-state emitters are mutually coupled via hyperfine interactions with a nuclear-spin ensemble consisting of N nuclei $H_{\mathrm{hyp}} = g\sum_i^N a_i[I_z^i\sigma_z + \frac{1}{2}(I_+^i\sigma_- + I_-^i\sigma_+)]$. Here, a_i defines the normalized (unitless) hyperfine coupling constant between the emitter electron and the ith nucleus ($\sum a_i^2 = 1$). In this convention $g \equiv A_H/\sum a_i$ quantifies the collective hyperfine coupling strength, with A_H denoting the hyperfine interaction constant of the material [18]. σ_α and I_α^i ($\alpha = +, -, z$) are the electronic and nuclear-spin operators, respectively; $\sigma_+ = |\uparrow\rangle\langle\downarrow|$. Collective nuclear-spin operators can be defined as $I_\alpha \equiv \sum_i a_i I_\alpha^i$; in general, these operators do not satisfy angular momentum commutation relations. In the limit of a large external field ($\omega_z \gg g$), the direct electron-nuclei flip-flop processes $I_+\sigma_- + I_-\sigma_+$ are strongly suppressed due to the large mismatch in the electronic and nuclear Zeeman splitting. In contrast, optical excitation does allow for energy conservation in an optically assisted electron-nuclear spin-flip process.

Our analysis of CPT in the presence of hyperfine interactions with a (single-isotope) nuclear-spin reservoir starts with the master equation, obtained by eliminating the radiation field reservoir using a Born-Markov approximation. We then apply a Schrieffer-Wolff transformation and use $\epsilon = g/(2\omega_z)$ as a small expansion parameter to eliminate the direct hyperfine flip-flop interaction. The resulting master equation then reads

$$\dot{\rho} = \underbrace{\frac{\Gamma}{2}(\mathbb{1}_S \otimes \rho_{tt} - \{|t\rangle\langle t|, \rho\}_+) - i[H, \rho]}_{\mathcal{L}_0(\rho)} + \underbrace{\epsilon^2\frac{\Gamma}{4}\mathbb{1}_S \otimes D(\rho_{tt})}_{\epsilon^2\mathcal{L}_1(\rho_{tt})}, \tag{1}$$

where $\rho_{tt} = \langle t|\rho|t\rangle$ acts on the Hilbert space of nuclear spins, $\mathbb{1}_S = |\uparrow\rangle\langle\uparrow| + |\downarrow\rangle\langle\downarrow|$, $\{\}_+$ denotes the anticommutator, and $H = H_{\mathrm{laser}} + \tilde{H}_{\mathrm{spin}}$. Here, $\tilde{H}_{\mathrm{spin}} = g\sigma_z(I_z - \frac{\epsilon}{2} \times \{I_+, I_-\}_+ - \delta/g)$ describes the effective magnetic field experienced by the electron, with contributions from the two-photon detuning and the hyperfine interactions; we refer to the latter as the generalized OF $g\tilde{I}_z = g(I_z - \frac{\epsilon}{2} \times \{I_+, I_-\}_+)$; the second term in the generalized OF stems from electronic energy renormalization due to virtual hyperfine flip-flop processes. $H_{\mathrm{laser}} = \Omega_c|\downarrow\rangle\langle t| + \Omega_p|\uparrow\rangle \times \langle t| + \mathrm{H.c.}$ denotes the laser coupling, and the term

$$D(\rho) = I_+\rho I_- + I_-\rho I_+ - \tfrac{1}{2}\{I_+I_- + I_-I_+, \rho\}_+ \tag{2}$$

describes an optically assisted nuclear diffusion process that is lowest order in ϵ [19]. At this point we neglect intrinsic nuclear-spin evolution in the absence of hyperfine interaction, which we address when we analyze the cooling time scales. If $M > 1$ nuclear species (isotopes) are present, a simple extension of Eq. (1), where each isotope couples to the electron independently, will be valid provided that $\epsilon g/|\omega_z^s - \omega_z^r| \ll 1\ \forall\ s \neq r$; here ω_z^s is the Larmor frequency of the sth nuclear species [20].

The term $\mathcal{L}_0(\rho)$ describes the evolution of the coupled system that leaves $\tilde{I}_z$ a constant of motion; for a two-photon detuning δ each eigenvector $|\lambda\rangle$ of $\tilde{I}_z$ (with eigenvalue λ) corresponds to a steady-state solution $\mathcal{L}_0(\rho_\lambda) = 0$ with $\rho_\lambda = \rho^e(\lambda) \otimes |\lambda\rangle\langle\lambda|$. Here, $\rho^e(\lambda) = \langle\lambda|\rho_\lambda|\lambda\rangle$ is the steady-state solution of the optical Bloch equations (OBE). In the OBE $\delta_{\mathrm{eff}} = g\lambda - \delta$ gives the effective two-photon detuning that determines the CPT condition. The term $\mathcal{L}_1$ describes the evolution of $\tilde{I}_z$ due to hyperfine-assisted light scattering, taking place on time scales longer than that of the electron by a factor ϵ^{-2}. The corresponding nuclear spin-flip rates in positive (D^+) and negative direction (D^-) are $D^\pm = \epsilon^2\frac{\Gamma}{2}\rho_{tt}^e(\lambda)\langle I_\mp I_\pm\rangle$, where $\rho_{tt}^e(\lambda) = \langle t|\rho^e(\lambda)|t\rangle$ is the population in state $|t\rangle$. $D^\pm$ are directly obtained from Eq. (1) [Fig. 1(b), dashed black lines]. Each nuclear spin-flip event changes $\langle\tilde{I}_z\rangle$ by a value of order a_i.

The interplay of dynamics due to $\tilde{H}_{\mathrm{spin}}$ and $\mathcal{L}_1$ is at the heart of the nuclear-spin cooling scheme we analyze in this

work. For nuclear states with $\delta_{\rm eff} = 0$ the system is in two-photon resonance and the electronic system is transparent such that $\mathrm{Tr}\{\rho_{tt}\} = 0$: as a consequence, the nuclear-spin diffusion vanishes and the system is trapped in a dark state. Since the generalized OF in an electronic-nuclear dark state is locked to a fixed value, its variance will be strongly reduced (nuclear state narrowing) suppressing hyperfine-induced electron spin decoherence. Strikingly, by narrowing the $\tilde{I}_z$, the second order contribution to hyperfine-induced electron spin decoherence is eliminated as well. For all nuclear states satisfying $\delta_{\rm eff} \approx 0$, the excited electronic state population is small ($\mathrm{Tr}\{\rho_{tt}\} \propto \delta_{\rm eff}^2$), ensuring that the spin diffusion rate remains vanishingly small: we refer to this subspace as the "trapping region." In contrast, nuclear states with $\delta_{\rm eff} \not\approx 0$ render the electron optically active and the generalized OF experiences diffusion ("recycling region"). Through successive spin-flip events, the nuclear reservoir probes different spin configurations with distinct $\langle \tilde{I}_z \rangle$. Eventually, the diffusion allows the nuclei to reach a configuration with $\delta_{\rm eff} \approx 0$, the system becomes locked in the trapping region. Because of the quasicontinuous nature of the $\tilde{I}_z$ spectrum in the limit $N \gg 1$ (see Sec. D of [21]), the dark-state condition $\delta_{\rm eff} = 0$ can be satisfied for a wide range of initial detunings $\Delta\omega_p$.

To confirm these predictions derived from Eq. (1), we consider, for simplicity, nuclear spin-1/2 systems. While our analysis applies to a broad class of solid-state emitters from various types of quantum dots (QD) to nitrogen-vacancy (N-V) centers, we now focus on a single-electron-charged QD in Voigt geometry where the optically excited state has an electron-singlet and a hole [17,22,23]. A numerical analysis is feasible in two limits.

For homogeneous coupling ($a_i = 1/\sqrt{N}$) we calculate the dependence of the steady-state OF standard deviation $\sigma_{\rm OF}$ directly from the full master equation (see Sec. A of [21]), which contains all orders of the hyperfine interaction including processes that result in a (small) finite decay rate out of the dark state [24] as well as a finite electron spin decoherence rate T_2^{-1}. Figure 1(c) shows $\sigma_{\rm OF}$ for the case $\delta = 0$ and $T_2^{-1} = 100\ \mathrm{s}^{-1}$ ($T_2^{-1} = 0\ \mathrm{s}^{-1}$) as a function of Ω, where we find that $\sigma_{\rm OF}$ decreases with decreasing Ω until it reaches a minimum of $\sigma_{\rm OF} \simeq 2A_H/N$ ($\sigma_{\rm OF} \simeq 0.7A_H/N$) for $\Omega \simeq 0.2\Gamma$. This result can be understood by recalling that the width of the transparency dip in CPT scales as Ω^2/Γ, implying that the range of OF values yielding transparency can be narrowed simply by reducing Ω. However, for $\Omega < 0.2\Gamma$, we find that $\sigma_{\rm OF}$ increases rapidly; for such small values of Ω, the coupled electron-nuclei system spends a substantial amount of time outside the transparency region due to finite decay out of the dark state, leading to the observed increase in steady-state value of $\sigma_{\rm OF}$. Nevertheless, we find that even for $\Omega_p = \Omega_c = 0.02\Gamma$, where $\sigma_{\rm OF} \approx 9A_H/N$, the nuclear-spin distribution is strongly peaked around states $|\lambda_0\rangle$ such that $\tilde{I}_z|\lambda_0\rangle = 0$ [Fig. 1(b), solid red line].

In the weak excitation limit $\Omega_p = \Omega_c \ll \Gamma$, the electron degrees of freedom can be eliminated adiabatically from Eq. (1), yielding a reduced master equation for the nuclear-spin evolution. For $\delta = 0$ we obtain

$$\dot{\rho}^n = \mathrm{Tr}_S(\dot{\rho}) = D(\Gamma_{\rm nuc}\rho^n), \tag{3}$$

where $\Gamma_{\rm nuc} = \epsilon^2[1 - (\frac{\Gamma_{\rm eff}}{|\Delta_{\rm eff}|})^2]\Gamma_{\rm eff}$ is the nuclear spin-flip rate and $|\Delta_{\rm eff}|^2 = \Gamma_{\rm eff}^2 + (g\tilde{I}_z)^2$. $\Gamma_{\rm eff} = 2\Gamma\Omega^2[\Gamma^2 + (g\tilde{I}_z)^2]$ is an operator valued electron spin decay rate. Since $\Gamma_{\rm nuc}$ vanishes for all zero eigenstates of $\tilde{I}_z$, Eq. (3) implies, in accordance with the considerations above, that every state in the kernel of $\tilde{I}_z$—i.e., a state of vanishing generalized OF—is a steady state of the dynamics.

To analyze the inhomogeneous coupling limit with a quasicontinuous OF, we adopt a semiclassical approach where nuclear spins are described at all times by a product of I_z^i eigenstates [25]. In this case, the master equation Eq. (1) reduces to rate equations which can be simulated using Monte Carlo techniques, and allows us to uncover the spectroscopic signatures of the CPT OF cooling scheme. Figure 1(d) shows the result of such simulations as the probe field is scanned across the (bare) resonance while keeping $\Delta\omega_c = 0$, in the limit of a vanishing decay rate out of the dark state. We use a toy model where the QD has a total of 100 nuclei divided into 5 classes with different a_i (see Sec. B of [21]). To obtain the probe absorption line shape as well as the OF variance, we assume that for each probe field detuning we start out from a completely mixed nuclear state ρ^n and evolve the coupled system until $t_{\rm fin} = 10^{12}\Gamma^{-1}$. We find that instead of exhibiting a narrow transparency dip at (bare) two-photon resonance [as in the absence of hyperfine coupling, Fig. 1(d), dashed curve), the coupled electron-nuclei system displays a drastically broadened transparency window with width significantly larger than Γ [Fig. 1(d), green ($\Omega = 0.4\Gamma$) and blue ($\Omega = 0.2\Gamma$) lines]. Concurrently, the OF distribution is narrowed dramatically from its value in the absence of optical excitation [Fig. 1(e), black line] such that $\sigma_{\rm OF}$ is smaller than the change induced by flipping one nuclear spin of the most weakly coupled class [Fig. 1(e), green and blue lines]. These simulations show the striking features that are consequences of the optically induced nuclear-spin diffusion which allows the coupled system to evolve into the electronic-nuclear dark state $\rho_D = |D\rangle\langle D| \otimes \rho_D^n$, where ρ_D^n is a nuclear-spin density operator that yields $\delta_{\rm eff} = 0$.

To estimate the time scale for reaching the dark state [26], we consider the limit $\Omega^2/\Gamma \lesssim A_H/N$; i.e., a typical single nuclear spin flip takes the system out of the transparency window. If we take the nuclear spin-flip rate in the recycling region to be constant with rate $\tau_0^{-1} \approx \epsilon^2\Omega^2/\Gamma$, then the random walk of the OF is unbiased, has a step size $\sim A_H/N$, and is restricted in its range to $A_H/\sqrt{N}$. Thus the number of flips required to reach the trapping region is $\langle M \rangle \approx (\frac{A_H/\sqrt{N}}{A_H/N})^2 \approx N$ (see Sec. C of [21]). The corresponding time to reach the dark state is $\langle \hat{t} \rangle = \langle M \rangle \tau_0 \approx \frac{N^2}{A_H\epsilon^2}$. For $\omega_z \simeq A_H$ this simplifies to $\langle \hat{t} \rangle \approx N^3/A_H$.

Given the strong N dependence of $\langle \hat{t} \rangle$ corresponding to the time scale needed to establish $\sigma_{\mathrm{OF}} \sim A_H/N$, it is important to consider nuclear-spin dynamics arising from optical-excitation-independent nuclear-spin diffusion or decay processes, as well as the electron T_2. The ultimate limit for the latter is due to spin-flip phonon emission with a rate $\sim 10^{-7}\Gamma$ for $\omega_z \simeq A_H$ [27]. Physical processes leading to nuclear-spin diffusion in the dark state include (a) nuclear-spin diffusion mediated by dipole-dipole interactions, (b) electric field fluctuations leading to spatial shifts in the QD electron wave function, (c) quadrupolar interaction with axis $\nparallel B_z$. If we denote the intrinsic nuclear-spin diffusion rate that arises from any of these mechanisms with γ_n, the effective width of the trapping region will be given by $\tilde{\delta} = \epsilon^{-1}\Omega\sqrt{N\gamma_n/\Gamma}$ (see Sec. C of [21]). We emphasize that earlier QD experiments have demonstrated $\gamma_n^{-1} > 100$ s [12,28], suggesting that intrinsic nuclear-spin time scales could be longer than $\langle \hat{t} \rangle$ [29].

The steady-state σ_{OF} for a small trapping region is dominated by the optical-excitation-induced fluctuations in the OF in the recycling region. A strategy to reduce the σ_{OF} below its steady-state value is to monitor the light scattering rate W_{scat} of the coupled system. Since $W_{\mathrm{scat}} \propto \delta_{\mathrm{eff}}^2$ in the neighborhood of the trapping region, a drastic reduction in W_{scat} verifies that the nuclear spins are in the desired state; turning the laser fields then off will ensure that σ_{OF} will be given by the width $\tilde{\delta} \sim A_H/N$ of the trapping region. This feedback is possible due to the fact that the time scale for flipping a nuclear spin is longer by a factor ϵ^{-2} than that for a photon scattering event.

Even though we have analyzed nuclear-spin diffusion associated with the ground-state hyperfine coupling, the conclusions remain unchanged if the solid-state emitter has hyperfine coupling leading to nuclear-spin diffusion in the optically excited state [22]; in fact, such processes shorten $\langle \hat{t} \rangle$. This would be the case, for example, in QDs with vanishing heavy-light hole mixing leading to near-resonant hole-mediated nuclear-spin flips in the excited state.

While prior experimental results on pulsed excitation of an ensemble of QDs strongly suggest the feasibility of our proposal in self-assembled QDs [28], we expect our findings to be relevant for a range of solid-state emitters. Of particular interest are N-V centers in diamond where CPT has also been previously observed [30].

We acknowledge support by an ERC Advanced Investigator Grant (M. I. and A. I.), the DFG within SFB 631 and the Nano Initiative Munich (E. M. K., G. G., and I. C.), and NSF under Grant No. 0653417 (S. Y.).

*Corresponding author.
Eric.Kessler@mpq.mpg.de
†Corresponding author.
imamoglu@phys.ethz.ch

[1] G. Alzetta *et al.*, Nuovo Cimento Soc. Ital. Fis. B **36**, 5 (1976).
[2] A. Aspect *et al.*, Phys. Rev. Lett. **61**, 826 (1988).
[3] L. V. Hau *et al.*, Nature (London) **397**, 594 (1999).
[4] M. Fleischhauer and M. D. Lukin, Phys. Rev. Lett. **84**, 5094 (2000).
[5] A. V. Khaetskii, D. Loss, and L. Glazman, Phys. Rev. Lett. **88**, 186802 (2002).
[6] J. M. Taylor *et al.*, Phys. Rev. B **76**, 035315 (2007).
[7] G. Giedke *et al.*, Phys. Rev. A **74**, 032316 (2006).
[8] D. Klauser, W. A. Coish, and D. Loss, Phys. Rev. B**73**, 205302 (2006).
[9] D. Reilly *et al.*, Science **321**, 817 (2008).
[10] I. T. Vink *et al.*, Nature Phys. **5**, 764 (2009).
[11] C. Latta *et al.*, Nature Phys. **5**, 758 (2009).
[12] P. Maletinsky, A. Badolato, and A. Imamoglu, Phys. Rev. Lett. **99**, 056804 (2007).
[13] E. Chekhovich *et al.*, Phys. Rev. Lett. **104**, 066804 (2010).
[14] B. T. Eble *et al.*, Phys. Rev. B **74**, 081306(R) (2006).
[15] S. W. Brown *et al.*, Phys. Rev. B **54**, R17 339 (1996).
[16] F. Bardou *et al.*, Phys. Rev. Lett. **72**, 203 (1994).
[17] D. Stepanenko *et al.*, Phys. Rev. Lett. **96**, 136401 (2006).
[18] If the ensemble consists of different atomic species, one can define an effective A_H that corresponds to the electron spin splitting when all nuclei are polarized; a_i then reflects the probability of finding the electron on site i as well as the hyperfine constant of the ith nucleus.
[19] In Eq. (1) we have neglected terms $\propto \epsilon^2$ that only affect the electron evolution.
[20] Generalized OH terms describing flip-flops between different species will then also be off resonant and can be neglected provided $|\omega_z^s - \omega_z^r| \gg \Omega^2/\Gamma$, ϵg. In this limit, we obtain an intraspecies generalized OH field: $\tilde{I}_z = I_z - \frac{\epsilon}{2}\sum_s \{I_+^s, I_-^s\}_+$; see Sec. A6 of [21].
[21] See supplementary material at http://link.aps.org/supplemental/10.1103/PhysRevLett.105.267202 for a derivation of Eqs. (1)–(3) (Sec. A), a description of the semiclassical simulations (Sec. B), a description of the system dynamics using Lévy flights (Sec. C), and a detailed analysis of $\tilde{I}_z$ (Sec. D).
[22] X. Xu *et al.*, Nature (London) **459**, 1105 (2009).
[23] D. Brunner *et al.*, Science **325**, 70 (2009).
[24] An example of such a process is off-resonant hyperfine-assisted laser scattering $\propto \epsilon^2(\Gamma/\omega_z)^2$.
[25] For simplicity, we simulate the dynamics with I_z. This is justified since the relevant characteristics of I_z and $\tilde{I}_z$, namely, the spectrum, the density of states, and the dynamics induced by $I_\pm$, coincide; see Sec. D of [21].
[26] There exists a close analogy between the problem of CPT in the presence of inhomogeneous hyperfine interactions with a nuclear-spin ensemble and that of a one-dimensional velocity selective CPT [2,16]; the role of atomic momentum in the latter case is assumed by $\tilde{I}_z$ in the present problem.
[27] M. Kroutvar *et al.*, Nature (London) **432**, 81 (2004).
[28] A. Greilich *et al.*, Science **317**, 1896 (2007).
[29] If the nuclear spin T_2 (T_2^*) $\neq 0$, e.g., due to dipolar fields or inhomogeneous quadrupolar interactions, the light scattering in the dark state can be neglected in the limit $1/T_2 < A_H/N^2$ (see Sec. A6 of [21]).
[30] C. Santori *et al.*, Opt. Express **14**, 7986 (2006).

EPAPS
Nuclear spin cooling using Overhauser field selective coherent population trapping

E.M. Kessler[1,*] , M. Issler[2,*], G. Giedke[1], S. Yelin[3], J.I. Cirac[1], M.D. Lukin[4], A. Imamoglu[2]
[1] *Max-Planck-Institut für Quantenoptik, Hans-Kopfermann-Str. 1 85748 Garching, Germany*
[2] *Institute of Quantum Electronics, ETH-Zürich, CH-8093 Zürich, Switzerland*
[3] *Department of Physics, University of Connecticut 2152 Hillside Road, U-3046 Storrs, CT 06269-3046, USA and*
[4] *Department of Physics, Harvard University, Cambridge, MA 02138, USA*

The following supplementary material is divided into four sections. Each section provides background information related to specific topics of the main text. The sections are not built upon each other and can be read independently. Section A provides a detailed derivation of the master Eqs. (1) and (3) of the main text as well as a discussion of potential limitations of the scheme due to state independent diffusion processes. The details of the semiclassical Monte Carlo simulations of the coherent population trapping based Overhauser field cooling scheme can be found in Section B. In Section C the description of the system dynamics in the context of Lévy flights is presented and relevant system timescales are discussed. Finally, Section D contains a detailed analysis of the properties of the generalized Overhauser field.

A. Derivation of the master equation

In the subsections 1-4 of this Section, we present the intermediate steps for the derivation of Eqs. (1), (2) and (3) of the main text. A detailed justification for neglecting higher-order terms appearing after the Schrieffer-Wolff transformation is given in subsection 5. The modification of the model considered in the main text in the presence of multiple nuclear species/isotopes and nuclear T_2 processes is analyzed in subsection 6.

1. Preliminaries

In order to derive nuclear diffusion rates in the CPT setting, we consider the master equation describing the coupled electron and nuclear system, obtained after eliminating the radiation field reservoir using a Born-Markov approximation:

$$\begin{aligned}\dot{\rho} =&\frac{\Gamma}{2}(|\uparrow\rangle\langle t|\rho|t\rangle\langle\uparrow| - \frac{1}{2}\{|t\rangle\langle t|,\rho\}_+)\\ &+\frac{\Gamma}{2}(|\downarrow\rangle\langle t|\rho|t\rangle\langle\downarrow| - \frac{1}{2}\{|t\rangle\langle t|,\rho\}_+) - i[\mathcal{H},\rho]\\ =&\frac{\Gamma}{2}(\mathbb{1}_S\otimes\rho_{tt} - \{|t\rangle\langle t|,\rho\}_+) - i[\mathcal{H},\rho],\end{aligned} \tag{A.1}$$

where $\rho_{tt} = \langle t|\rho|t\rangle$ acts on the Hilbert space of nuclear spins, $\mathbb{1}_S = |\uparrow\rangle\langle\uparrow| + |\downarrow\rangle\langle\downarrow|$ and we defined $\{A,B\}_+ = AB+BA$. The Hamiltonian of the system consists of a diagonal part $\mathcal{H}_0$ and the laser and hyperfine Hamiltonians,

$$\mathcal{H} = \mathcal{H}_0 + \mathcal{H}_{\rm laser} + \mathcal{H}_{\rm hyp}, \tag{A.2}$$

$$\mathcal{H}_0 = \omega_t |t\rangle\langle t| - \omega_z\sigma_z, \tag{A.3}$$

$$\mathcal{H}_{\rm laser} = \Omega_c e^{i\omega_c t}|\downarrow\rangle\langle t| + \Omega_p e^{i\omega_p t}|\uparrow\rangle\langle t| + h.c., \tag{A.4}$$

$$\mathcal{H}_{\rm hyp} = g\left(I_z^{(1)}\sigma_z + \frac{1}{2}(I_+^{(1)}\sigma_- + I_-^{(1)}\sigma_+)\right). \tag{A.5}$$

Here, ω_t and ω_z denote the trion state and electron Zeeman energies, whereas $\omega_{c/p}$ and $\Omega_{c/p}$ are the coupling and probe laser's frequencies and Rabi energies, respectively. The nuclear quasi-spin operators are defined as $I_\alpha^{(n)} = \sum_{i=1}^N a_i^n I_\alpha^i$ ($\alpha = +,-,z$); we note that in the main text, we used the simplified notation $I_\alpha^{(1)} = I_\alpha$ since there we did not

---

* These authors have contributed equally to this work.

introduce collective operators with $n \neq 1$. For the analysis below, we (initially) neglect the nuclear Zeeman energy. The hyperfine coupling coefficients a_i are normalized such that $\sum a_i^2 = 1$ (in this convention the hyperfine interaction constant of the material is given by $A_H = g \sum a_i$) and the electron operators σ_α are the usual spin 1/2 operators. We assume that in the absence of optical excitation, the electron spin is well isolated from all reservoirs other than the nuclear spins [1], and spin-flip co-tunneling or phonon emission rates are negligible within the timescales of interest.

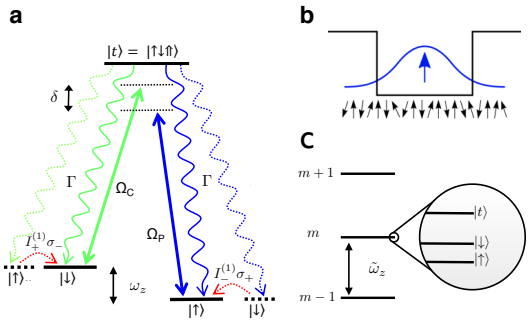

Figure 1: (a) Scheme of the electronic levels in the CPT setting. The dashed lines illustrate the hyperfine assisted decay processes, which are responsible for the nuclear spin diffusion in an optically active system. (b) The confined electron spin of the charged quantum dot interacts with a large nuclear spin bath ($N \sim 10^4 - 10^5$) via hyperfine contact interaction. (c) In a rotating frame that renders the Hamiltonian time-independent the spectrum of the diagonal part of H' splits into submanifolds, labelled by the nuclear quantum number m (spin projection in z-direction), which consist of the three different electronic states (and further degenerate states due to nuclear total spin and permutation quantum numbers). The weak coupling between the different manifolds motivates a perturbative treatment.

The basis transformation

$$H' = e^{i\xi t}(\mathcal{H} - \xi)e^{-i\xi t}, \tag{A.6}$$

with

$$\xi = \left[\omega_t - \frac{1}{2}(\Delta\omega_c + \Delta\omega_p)\right] |t\rangle\langle t| - [\omega_z + (\Delta\omega_c - \Delta\omega_p)]\,(I_z^{(0)} + \sigma_z), \tag{A.7}$$

renders the Hamiltonian time independent,

$$\begin{aligned} H' = {} & \tilde{\omega}_z I_z^{(0)} + \frac{1}{2}(\Delta\omega_c + \Delta\omega_p)\,|t\rangle\langle t| - \delta\sigma_z \\ & + H_{\text{laser}} + H_{\text{hyp}}, \end{aligned} \tag{A.8}$$

where $H_{\text{laser}} = \Omega_c\,|\downarrow\rangle\langle t| + \Omega_p\,|\uparrow\rangle\langle t| + h.c.$ and $H_{\text{hyp}} \equiv \mathcal{H}_{\text{hyp}}$. The laser detunings are given as $\Delta\omega_p = -\omega_p + (\omega_t + \omega_z/2)$ and $\Delta\omega_c = -\omega_c + (\omega_t - \omega_z/2)$. The effective nuclear energy in the rotating frame is $\tilde{\omega}_z = \omega_z + \Delta\omega_c - \Delta\omega_p \approx \omega_z$ and the two-photon detuning is denoted by $\delta = \Delta\omega_p - \Delta\omega_c$. The dissipative part of Eq. (A.1) - containing secular terms exclusively - remains unchanged under the transformation.

In the limit of a large external field ($\tilde{\omega}_z \gg g$), the direct electron-nuclei flip-flop processes $I_+^{(1)}\sigma_- + I_-^{(1)}\sigma_+$ are strongly suppressed due to the large mismatch in the electronic and nuclear Zeeman splitting. In the following we derive the second order effects of the energetically suppressed hyperfine flip-flop interaction in a systematic approach using quasidegenerate perturbation theory [2, 3] (sometimes referred to as Schrieffer-Wolff transformation). We will find that the higher order corrections to the flip-flop interaction account for an optically assisted nuclear diffusion process [Fig. 1 (a)] and motivate the introduction of the novel concept of a generalized Overhauser field.

2. Quasidegenerate perturbation theory

The clear separation of energy scales in the Hamiltonian of Eq. (A.8) [$\tilde{\omega}_z \gg g,\ \delta,\ \Omega_{c/p},\ \Delta\omega_{c/p}$; see Fig. 1 (c)] allows us to partition the full Hamiltonian into a zero-order part $H_0' = \tilde{\omega}_z I_z^{(0)}$ and a small perturbation $V = H' - H_0'$. The eigenvectors of H_0' are grouped into well separated manifolds, labeled by the nuclear spin projection quantum number

m [see Fig. 1 (c)]. According to this spectrum any operator O can be partitioned into a block diagonal O_D operator - containing terms that conserve m - and a block off-diagonal O_N operator - containing terms that drive transitions between different manifolds (m non-conserving terms). For the Hamiltonian this separation yields

$$H'_D = H'_0 + V_D, \tag{A.9}$$
$$H'_N = V_N, \tag{A.10}$$

where

$$V_D = +\frac{1}{2}(\Delta\omega_c + \Delta\omega_p)\,|t\rangle\langle t| - \delta\sigma_z + (\Omega_c\,|\downarrow\rangle\langle t| + \Omega_p\,|\uparrow\rangle\langle t| + h.c.) + gI_z^{(1)}\sigma_z \tag{A.11}$$
$$V_N = \frac{g}{2}\left(I_+^{(1)}\sigma_- + I_-^{(1)}\sigma_+\right). \tag{A.12}$$

Note that the above choice of H'_0 is not unique. Other choices that for instance render V_N purely block-off-diagonal are equivalent, but complicate the fine-structure within the manifolds.

In the following we are going to construct a similarity transformation, generated by an anti-hermitian operator $S = -S^\dagger$

$$H = e^{-S}H'e^{S} \tag{A.13}$$

that renders the transformed Hamiltonian block diagonal and thus decoupling the different manifolds from each other. Since the above condition does not define S uniquely [4], we further demand $S_D = 0$ (canonical choice). Expanding the operators in orders of the perturbation

$$H = \sum_{n=0}^{\infty} H^{[n]}, \qquad S = \sum_{n=0}^{\infty} S^{[n]}, \tag{A.14}$$

one can derive conditional equations for S order by order. Exploiting the fact that V_N^2 is block diagonal ($\sigma_-^2 = \sigma_+^2 = 0$) one finds the simple recursive equations:

$$\begin{aligned}
S^{[0]} &= 0,\\
[H'_0, S^{[1]}] &= -V_N,\\
[H'_0, S^{[2]}] &= -[V_D, S^{[1]}],\\
[H'_0, S^{[3]}] &= -[V_D, S^{[2]}] - \frac{1}{3}[[V_N, S^{[1]}], S^{[1]}],\\
&\vdots
\end{aligned} \tag{A.15}$$

The expansion of the transformed Hamiltonian yields

$$\begin{aligned}
H^{[0]} &= H'_0,\\
H^{[1]} &= V_D,\\
H^{[2]} &= \frac{1}{2}[V_N, S^{[1]}],\\
H^{[3]} &= \frac{1}{2}[V_N, S^{[2]}],\\
&\vdots
\end{aligned} \tag{A.16}$$

Note that $H^{[n]}$ only depends on lower orders of the transformation matrix. Higher order expressions and a detailed derivation are given in [3].

3. Second order corrections

We are going to expand our system's master equation Eq. (A.1) to second order in the perturbation in order to identify the dominant hyperfine processes in the electron-nuclear CPT setting. From Eqs. (A.15) we readily derive the form of $S^{[1]}$,

$$S^{[1]} = \epsilon(\sigma_+ I_-^{(1)} - \sigma_- I_+^{(1)}), \tag{A.17}$$

where we defined the expansion parameter $\epsilon = \frac{g}{2\tilde{\omega}_z}$. $S^{[1]}$ generates the second order corrections to the Hamiltonian [Eqs. (A.16)]:

$$H^{[2]} = -\frac{1}{2}\epsilon g(\sigma_z\{I_+^{(1)}, I_-^{(1)}\}_+ - I_z^{(2)}). \tag{A.18}$$

The full transformed Hamiltonian then reads,

$$\begin{aligned} H &= H_0' + V_D + H^{[2]}, \\ &= \tilde{\omega}_z I_z^{(0)} + \frac{1}{2}(\Delta\omega_c + \Delta\omega_p)\,|t\rangle\langle t| + (\Omega_c\,|\downarrow\rangle\langle t| + \Omega_p\,|\uparrow\rangle\langle t| + h.c.) \\ &+ g\sigma_z(I_z^{(1)} - \frac{1}{2}\epsilon\{I_+^{(1)}, I_-^{(1)}\}_+ - \delta/g) + \epsilon g\frac{1}{2}I_z^{(2)}. \\ &= \tilde{\omega}_z I_z^{(0)} + \frac{1}{2}(\Delta\omega_c + \Delta\omega_p)\,|t\rangle\langle t| + H_{\text{laser}} + g\sigma_z(\tilde{I}_z^{(1)} - \delta/g) + \epsilon g\frac{1}{2}I_z^{(2)}, \end{aligned} \tag{A.19}$$

where we have introduced the notion of the *generalized Overhauser field (GOF)* $g\tilde{I}_z^{(1)} = g(I_z^{(1)} - \frac{1}{2}\epsilon\{I_+^{(1)}, I_-^{(1)}\}_+)$, which contains all electron-nuclear interactions up to second order and can be interpreted in our context as an effective two-photon detuning, which adds to the external laser detuning δ.

In a similar procedure the system Liouvillian $\mathcal{K}'(\rho) = \frac{\Gamma}{2}(\mathbb{1}_S \otimes \rho_{tt} - \{|t\rangle\langle t|, \rho\}_+)$ is transformed under S and expanded in orders of the perturbation

$$\mathcal{K}(\rho) = \sum_{n=0}^{\infty} \mathcal{K}^{[n]}(\rho). \tag{A.20}$$

Realizing that the transformation leaves the excited electron state invariant $e^{-S^{[1]}}\,|t\rangle = |t\rangle$ (and thus the second term of the Liouvillian $\propto \{|t\rangle\langle t|, \rho\}_+$) we only have to transform the jump term $\mathbb{1}_S \otimes \rho_{tt}$. The *Baker-Hausdorff formula* yields,

$$e^{-S^{[1]}}(\mathbb{1}_S \otimes \rho_{tt})e^{S^{[1]}} \approx \mathbb{1}_S \otimes \rho_{tt} + [\mathbb{1}_S \otimes \rho_{tt}, S^{[1]}] + \frac{1}{2}[[\mathbb{1}_S \otimes \rho_{tt}, S^{[1]}], S^{[1]}], \tag{A.21}$$

which is particularly simple to calculate since $\mathbb{1}_S\sigma_\alpha = \sigma_\alpha$. Grouped into orders of ϵ one finds

$$\begin{aligned} \mathcal{K}^{[0]}(\rho) =& \frac{\Gamma}{2}(\mathbb{1}_S \otimes \rho_{tt} - \{|t\rangle\langle t|, \rho\}_+), \\ \mathcal{K}^{[1]}(\rho) =& -\epsilon\frac{\Gamma}{2}\left(\sigma_-[\rho_{tt}, I_+^{(1)}] + \sigma_+[I_-^{(1)}, \rho_{tt}]\right), \\ \mathcal{K}^{[2]}(\rho) =& \epsilon^2\frac{\Gamma}{4}\mathbb{1}_S \otimes D_1(\rho_{tt}) + \epsilon^2\frac{\Gamma}{2}\sigma_z \otimes D_2(\rho_{tt}). \end{aligned} \tag{A.22}$$

Note that the above procedure is equivalent to a straightforward transformation of the electronic jump operators $|\downarrow\rangle\langle t|$ and $|\uparrow\rangle\langle t|$ of the Liouvillian. The superoperators

$$\begin{aligned} D_1(\rho) =& I_+^{(1)}\rho I_-^{(1)} + I_-^{(1)}\rho I_+^{(1)} - \frac{1}{2}\{I_+^{(1)}I_-^{(1)} + I_-^{(1)}I_+^{(1)}, \rho\}_+, \\ D_2(\rho) =& I_-^{(1)}\rho I_+^{(1)} - I_+^{(1)}\rho I_-^{(1)} + \{I_z^{(2)}, \rho\}_+, \end{aligned} \tag{A.23}$$

describe optically induced random nuclear spin diffusion processes caused by optically assisted electron-nuclear spin flip events. Since this nuclear diffusion depends on the electron population in the excited state $\propto \rho_{tt}$ it will vanish for electronic dark states, which are defined via the condition $\rho_{tt} = 0$. Note that second order terms in the transformed Liouvillian arising from $S^{[2]}$ are non-secular and consistently neglected. $\mathcal{K}^{[1]}$ and the second summand in $\mathcal{K}^{[2]}$ do not affect the nuclear evolution governed by $\dot{\rho}_I = \text{Tr}_S(\dot{\rho})$, since $\text{Tr}_S(\sigma_z) = \text{Tr}_S(\sigma_\pm) = 0$ (Tr_S denotes the trace over all electronic degrees of freedom). For the electron evolution, which occurs on timescales $\propto \Gamma$ these terms merely represent a small ϵ^2-correction ($\mathcal{K}^{[1]}$ acquires an additional factor $\propto \epsilon$ since it is non-secular) and are consequently neglected in the following. If we further assume resonance ($\Delta\omega_c = \Delta\omega_p = 0$) and neglect the last term of Eq. (A.19) - which accounts for a small state independent nuclear diffusion and will be discussed in Section A 5 - we arrive at the master equation Eq. (1) of the main text (note that in the notation of the main text $I_\alpha \equiv I_\alpha^{(1)}$),

$$\begin{aligned} \dot{\rho} =& \frac{\Gamma}{2}(\mathbb{1}_S \otimes \rho_{tt} - \{|t\rangle\langle t|, \rho\}_+) + \epsilon^2\frac{\Gamma}{4}\mathbb{1}_S \otimes D_1(\rho_{tt}) \\ &- i[H_{\text{laser}} + \tilde{H}_{\text{spin}}, \rho], \end{aligned} \tag{A.24}$$

where we further applied the trivial transformation into a frame rotating with $\tilde{\omega}_z I_z^{(0)}$. $\tilde{H}_{\rm spin} = g\sigma_z(\tilde{I}_z^{(1)} - \delta/g)$ contains all electron nuclear interactions to leading order and can be interpreted as an effective two-photon detuning. If the nuclear system is in an eigenstate $|\lambda\rangle$ of the GOF operator $\tilde{I}_z^{(1)}$ with eigenvalue $\lambda = \delta/g$ the two photon detuning vanishes and the product state $|\lambda\rangle \otimes |D\rangle$ (with $|D\rangle = \frac{1}{\sqrt{\Omega_c^2+\Omega_p^2}}(\Omega_c |\uparrow\rangle - \Omega_p |\downarrow\rangle)$ being the electronic dark state) is a steady state of the dynamics. If, in contrast, the nuclear system is in a state where $\lambda \neq \delta/g$ (i.e. the two-photon resonance condition is violated) the electronic system is bright ($\rho_{tt} \neq 0$) inducing nuclear diffusion given by the term $\propto D_1(\rho_{tt})$.

4. Nuclear rate equation

In the weak excitation limit $\Omega_p, \Omega_c \ll \Gamma$, we can eliminate the state $|t\rangle$, yielding a master equation involving the nuclear and electronic spins only. For simplicity we assume the external two-photon detuning $\delta = 0$ as well as $\Omega_c = \Omega_p = \Omega$, which ensures that the relevant dark and bright electron spin states in the rotating frame are states polarized in $\hat{x}$-direction $|D(B)\rangle = (|\uparrow\rangle - (+)\,|\downarrow\rangle)/\sqrt{2}$. A generalization to a finite detuning δ and arbitrary Rabi frequencies is straightforward, but offers no further insight. In the case of homogeneous nuclear coupling we then obtain from Eq. (A.24) the reduced master equation

$$\begin{aligned}\dot{\rho} =& \Gamma_{\rm eff}(\sigma_-^x \rho \sigma_+^x - \frac{1}{2}\{\sigma_+^x\sigma_-^x, \rho\}_+) \\ &+ \frac{\Gamma_{\rm eff}}{2}[\sigma_x, [\sigma_x, \rho]] - ig\tilde{I}_z^{(1)}[\sigma_z, \rho] \\ &+ \epsilon^2 \mathbb{1}_S \otimes D_1(\Gamma_{\rm eff}\rho_{BB}),\end{aligned} \tag{A.25}$$

where $\sigma_\pm^x$ are the electron spin flip operators in $\hat{x}$-basis ($\sigma_-^x |B\rangle = |D\rangle$, $\sigma_+^x |D\rangle = |B\rangle$) and $\Gamma_{\rm eff} = \frac{\Omega^2}{(\Gamma/2)^2 + (g\tilde{I}_z^{(1)}/2)^2}\frac{\Gamma}{2}$ is an operator valued effective (electron) spin decay rate. The last line of Eq. (A.25) describes the nuclear spin diffusion determined by the nuclear operator proportional to the bright state population $\rho_{BB} = \langle B|\rho|B\rangle$ [5].

In order to eliminate the electronic degrees of freedom from Eq. (A.25) we use the fact that on the timescales of the electron evolution, the nuclear field can be considered as quasi-static and hence the electron settles quickly (on nuclear timescales) to its interim steady state. We find that on this coarse grained timescale $\rho_{BB} = \frac{1}{2}[1 - (\frac{\Gamma_{\rm eff}}{|\Delta_{\rm eff}|})^2]{\rm Tr}_S(\rho)$, with ${\rm Tr}_S$ denoting the trace over electron spin and $|\Delta_{\rm eff}|^2 = \Gamma_{\rm eff}^2 + (g\tilde{I}_z^{(1)})^2$. Using this relation, the electron spin can be eliminated from Eq. (A.25), yielding a nuclear rate equation

$$\dot{\rho^n} = {\rm Tr}_S(\dot{\rho}) = D(\Gamma_{\rm nuc}\rho^n), \tag{A.26}$$

where we defined the state dependent nuclear diffusion rate $\Gamma_{\rm nuc} = \epsilon^2[1 - (\frac{\Gamma_{\rm eff}}{|\Delta_{\rm eff}|})^2]\Gamma_{\rm eff}$. In concordance with the above considerations $\Gamma_{\rm nuc}$ vanishes for all states in the kernel of $\tilde{I}_z^{(1)}$, i.e. states of zero GOF that fulfill the two-photon resonance condition are steady states of the dynamics. For large detunings ($\tilde{I}_z^{(1)} \sim 1$) the optically induced change of $\tilde{I}_z^{(1)}$ is of order $\frac{d}{dt}{\rm Tr}(\rho\tilde{I}_z^{(1)}) \sim \Gamma_{\rm nuc}N^{-1/2} \sim \epsilon^2\frac{\Omega^2}{\Gamma}$ which provides the fast diffusion driving the system into the dark state.

5. Higher order corrections

We have seen in the foregoing section that nuclear states in the kernel of $\tilde{I}_z^{(1)} - \delta/g$ decouple completely from the electron degrees of freedom and the evolution of these states comes to rest and the system is trapped. However, higher order corrections - which we have neglected so far - can contribute to a finite, state-independent nuclear diffusion rate out of the trapping region. In the following we identify and discuss these corrections.

First we consider the effect of the second order term $\epsilon g\frac{1}{2}I_z^{(2)}$, which we neglected in Eq. (A.19) and which does not commute with the GOF $g\tilde{I}_z^{(1)}$. Consequently GOF eigenstates evolve under its action. To estimate the corresponding

nuclear diffusion rate we consider the equation of motion of the corresponding Heisenberg operator

$$\begin{aligned}\frac{d}{dt}\tilde{I}_z^{(1)} =& -i[\tilde{I}_z^{(1)}, \epsilon g\frac{1}{2}I_z^{(2)}], \\ =& -i\frac{1}{4}\epsilon^2 g(I_+^{(3)}I_-^{(1)} - I_+^{(1)}I_-^{(3)} + I_-^{(1)}I_+^{(3)} - I_-^{(3)}I_+^{(1)}) \\ =& -i\frac{1}{2}\epsilon^2 g(I_+^{(3)}I_-^{(1)} - I_+^{(1)}I_-^{(3)}).\end{aligned} \tag{A.27}$$

Note that, since the perturbation commutes with the zero order (i.e. standard OF) part of the GOF ($[I_z^{(1)}, I_z^{(2)}] = 0$) the effect is of higher order $\propto \epsilon^2$. Furthermore the spin operators are normalized such that typical matrix elements of $I_+^{(n)}I_-^{(m)}$ are of order $\sim N^{1-(n+m)/2}$. In fact, the number of larger matrix elements (at most by a factor N) is exponentially small. Thus it can only reduce the trapping region (which is defined as the set of eigenvectors with sufficiently small eigenvalues of $\tilde{I}_z^{(1)} - \delta/g$, and which is shown to be sizeable in Section D) insignificantly. Therefore we can roughly estimate the rate of change in the subspace of relevant states ψ

$$\left|\frac{d}{dt}\langle\tilde{I}_z^{(1)}\rangle_\psi\right| \sim \frac{\epsilon^2}{N}g. \tag{A.28}$$

which is smaller than the optically induced nuclear diffusion rate by a factor $\frac{A_H/N}{\Omega^2/\Gamma}$. Note however, that Eq. (A.28) is a pessimistic estimate, since it does not take into account the Hamiltonian character of the perturbation $\epsilon I_z^{(2)}$: every nuclear dark state (small-eigenvalue eigenstate of$\tilde{I}_z^{(1)}$) that is also an eigenstate of $I_z^{(2)}$ maintains its dark state character. Since $I_z^{(2)}$ and $I_z^{(1)}$ (of which $\tilde{I}_z^{(1)}$ is a perturbation) commute, this subspace may be substantial. In particular, in the limiting case of homogeneous coupling, Eq. (A.27) vanishes exactly. While Eq. (A.28) is slow enough not to interfere with the measurement-based scheme, its influence on the steady-state scheme is subject of ongoing work.

Next we consider higher order corrections in the perturbation theory by expanding the Hamiltonian to third order. The generator of the third order correction $S^{[2]}$ can be calculated using Eqs. (A.15):

$$\begin{aligned}S^{[2]} =& \epsilon\epsilon_\delta(\sigma_+ I_-^{(1)} - \sigma_- I_+^{(1)}) \\ &+ \epsilon\epsilon_c(I_-^{(1)}\left|\uparrow\right\rangle\left\langle t\right| - h.c.) + \epsilon\epsilon_p(I_+^{(1)}\left|\downarrow\right\rangle\left\langle t\right| - h.c.) \\ &+ \epsilon^2\left[\sigma_- I_+^{(2)} - \sigma_+ I_-^{(2)} - 2(\sigma_+ I_z^{(1)} I_-^{(1)} - \sigma_- I_+^{(1)} I_z^{(1)})\right],\end{aligned} \tag{A.29}$$

with the expansion parameters $\epsilon_\delta = \frac{\delta}{\tilde{\omega}_z}$, $\epsilon_{p/c} = \frac{\Omega_{p/c}}{\tilde{\omega}_z} \ll 1$. The third order Hamiltonian [Eqs. (A.16)] is then given by

$$\begin{aligned}H^{[3]} =& -\epsilon^2\delta(\sigma_z\{I_+^{(1)}, I_-^{(1)}\}_+ - I_z^{(2)}) \\ &+ \frac{1}{4}\epsilon^2\{I_+^{(1)}, I_-^{(1)}\}_+ H_{\text{laser}} \\ &+ \frac{1}{2}\epsilon^2 I_z^{(2)}(\Omega_c\left|\downarrow\right\rangle\left\langle t\right| - \Omega_p\left|\uparrow\right\rangle\left\langle t\right| + h.c.) \\ &+ \epsilon^2 g\sigma_z(I_+^{(1)} I_z^{(1)} I_-^{(1)} + h.c.) \\ &+ \frac{1}{8}\epsilon^2 g(\{I_+^{(2)}, I_-^{(1)}\}_+ + \{I_+^{(1)}, I_-^{(2)}\}_+ - I_z^{(1)} I_z^{(2)}),\end{aligned} \tag{A.30}$$

The first term is of the exact form as $H^{[2]}$ and can easily be incorporated in the above considerations of Section A 3 as a small (ϵ) correction. The second and third term describe two different types of laser assisted nuclear diffusion. The first type supports the scheme, since H_{laser} only couples to the electronic bright state $\left|B\right\rangle$. Thus this diffusion comes to rest whenever the electron is in the dark state $\left|D\right\rangle$. The second type of laser assisted nuclear diffusion couples to the dark state and thus, in principle, represents a possible escape mechanism from trapping states. However, since - as discussed above - the diffusion operator $I_z^{(2)}$ commutes with the zero order part of the GOF the contribution of the third term is yet of one order ϵ smaller than the process of Eq. (A.28) and thus safely negligible. The fourth and fifth term of Eq. (A.30) originate in third order contributions of the hyperfine interaction. While the fourth term can be incorporated in the definition of the GOF, the fifth term represents a state independent nuclear diffusion, effectively of the same order as the one of Eq. (A.28).

All these processes are taken into account exactly in the homogeneous simulations [based on Eq. (A.1)] and account for the small but finite standard deviation in the steady state.

6. Inhomogeneous nuclear Zeeman terms

We have so far neglected the Zeeman energy of the nuclei, which is typically three orders of magnitude smaller than ω_z. A *homogeneous* nuclear Zeeman term $\propto I_z^{(0)}$ has no effect on the analysis carried out in the subsections 1-5 since it commutes with the GOF $g\tilde{I}_z^{(1)}$. However, if different nuclear species with different gyromagnetic ratios are involved, this is no longer the case since the correction $\propto I_+^{(1)}I_-^{(1)}$ in $\tilde{I}_z^{(1)}$ includes the exchange of nuclear spin excitations between different nuclear species. Different Larmor frequencies associated with different species/isotopes will in general lead to a modulation of the GOF. Here, we will show that in the limit of large differences in Larmor frequencies, the dominant contribution to GOF stems from intra-species flip-flop terms; the fast time dependence of the inter-species flip-flop terms in this limit ensures that their contribution averages out.

For the relevant nuclei the energy differences (between different species) are often so large (up to 10 MHz per Tesla) that they cannot be neglected on the timescales of nuclear spin diffusion (see Table I).

Isotope	^{69}Ga	^{71}Ga	^{75}As	^{113}In	^{115}In
Natural Abundance (%)	60.1	39.9	100	4.3	95.7
gyromagnetic ratio ($10^7 \mathrm{rad} s^{-1} T^{-1}$)	6.44	8.18	4.60	5.90	5.88

Table I: Natural abundances and gyromagnetic ratios of typical isotopes. Source: WebElements [http://www.webelements.com/]

We consider here the case that $\mathcal{H}$ also contains an inhomogeneous nuclear Zeeman term

$$H_{nz} = \sum_j \omega_{nz,j} I_z^j. \tag{A.31}$$

We assume a number of different nuclear species labeled by s and define nuclear operators referring to species s by $I_\alpha^{(n,s)} \equiv \sum_{j\in s} a_j^n I_\alpha^j$ (where the sum runs only over the indices j of nuclei belonging to species s). Then the correction term in the generalized Overhauser field splits into an intra-species part which commutes with H_{nz} and a second (inter-species) part describing the exchange of spin excitations between different species:

$$\{I_+^{(1)}, I_-^{(1)}\}_+ = \sum_s \{I_+^{(1,s)}, I_-^{(1,s)}\}_+ + 2\sum_{s>s'} \left(I_+^{(1,s)} I_-^{(1,s')} + I_-^{(1,s)} I_+^{(1,s')} \right). \tag{A.32}$$

We show in the following that for sufficiently large magnetic fields the latter terms are off-resonant and thus suppressed to leading order. Only the intra-species terms $\sum_s \{I_+^{(1,s)}, I_-^{(1,s)}\}_+$ survives in the GOF. To higher orders, the inter-species terms provide small additional state-independent GOF-diffusion terms similar to the one generated by $I_z^{(2)}$ [see Eq. (A.27)].

Generalizing the considerations of Section A 3 we consider H_{nz} to be part of V_D and modify the generator of the Schrieffer-Wolff transformation such that the terms connecting different species in Eq. (A.32) are canceled. This is achieved by adding

$$T = \sigma_z \sum_{s>s'} \frac{\epsilon g}{2(\omega_{nz,s} - \omega_{nz,s'})} \left(I_+^{(1,s)} I_-^{(1,s')} - I_-^{(1,s)} I_+^{(1,s')} \right) \equiv \sigma_z X \tag{A.33}$$

to S. This modification has the following effects: $H = e^{-S-T}(H' + H_{nz})e^{S+T} = H' + H_{nz} - [S, H'] - [T, H'] - [S, H_{nz}] - [T, H_{nz}] + \frac{1}{2}[S+T, [S+T, H' + H_{nz}]] + \ldots$, which leads to several new first and second order terms like $[S^{[1]}, H_{nz}], [T, H_0 + V_N + V_D], [T + S^{[1]}, [T + S^{[1]}, H_{nz}]]$ etc. Most of these terms are off-resonant either by ω_z or $\omega_{nz,s} - \omega_{nz,s'}$ and the secular terms lead to $I_z^{(0,s)}$-conserving second order corrections, which either modify the GOF or induce a small state-independent GOF-diffusion (similar to $I_z^{(2)}$ in Eq. (A.27)). Since they are similar to and smaller (by $\epsilon\omega_{nz,s}/g$ or $\epsilon g/(\omega_{nz,s} - \omega_{nz,s'})$, respectively) than terms already considered, we do not discuss them in detail.

To determine the conditions under which it is allowed to neglect all non-secular terms, denote by $\Delta_{nz} = \min\{|\omega_{nz,s} - \omega_{nz,s'}| : s \neq s'\}$ the nuclear Zeeman inhomogeneity [6] and introduce $\epsilon_{nz} = g\epsilon/\Delta_{nz}$. Exemplarily we consider the laser term arising from $[T, V_D]$, which represents one of the major perturbations. It reads

$$\frac{\Omega_p}{2} |\uparrow\rangle\langle t| X - \frac{\Omega_c}{2} |\downarrow\rangle\langle t| X + \text{h.c.} \propto |D\rangle\langle t| + \text{h.c.} \tag{A.34}$$

It describes laser-assisted nuclear spin dynamics that changes the GOF and is only detuned by Δ_{nz}. Thus we need

$$\frac{\Omega\epsilon g}{\Delta_{nz}} \ll \Delta_{nz} \Leftrightarrow \Delta_{nz}^2 \gg \frac{\Omega g^2}{2\tilde{\omega}_z}. \tag{A.35}$$

With typically $\Delta_{nz} \sim 10^{-3}\tilde{\omega}_z$ we need $10^{-6} \gg \frac{\Omega}{\tilde{\omega}_z}\frac{g^2}{\tilde{\omega}_z^2}$. In terms of ϵ_{nz} we need $\Omega\epsilon_{nz} \ll \Delta_{nz}$. For typical values (all energies in μeV) of $g \sim 1$ and $\Delta_{nz} \sim 10^{-3}\tilde{\omega}_z$ we could take $\tilde{\omega}_z \sim 100$, which yields $\epsilon_{nz} \sim 10^{-1}$ and thus would require $\Omega \sim 0.1$. Thus if Δ_{nz} is sufficiently large ($g\epsilon, \Omega\epsilon_{nz} \ll \Delta_{nz}$) these contributions are small and the non-secular terms can be neglected. This can always be ensured by sufficiently strong magnetic field. Using the same arguments one can show that under condition Eq. A.35 also the other terms arising from T can safely be neglected.

Similarly, we have to transform the jump operators in the Liouvillian. Here we consider only the first-order correction to $\mathcal{I}^{[1]}$ arising from $|\downarrow\rangle\langle t| \to |\downarrow\rangle\langle t| - [S^{[1]} + T, |\downarrow\rangle\langle t|] \pm \ldots$. The new terms such as $[T, |\downarrow\rangle\langle t|] = -\frac{1}{2}X|\downarrow\rangle\langle t|$ describe an additional slow nuclear spin dynamics that occurs only in the optically excited state, thus enhancing nuclear diffusion outside the trapping region and improving the scheme.

In realistic systems, there may be other processes affecting the nuclear spins which have to be taken into account for a full description – in particular the dipolar interaction between nuclear spins and on-site quadrupolar terms; these terms would lead to a non-zero T_2^* time of the nuclear spin ensemble. In addition, there may be T_2 processes affecting the nuclei, arising from fluctuating local magnetic fields. While these processes will be discussed in detail in future work, we provide here some simple estimates of how these processes relate quantitatively to other corrections considered in previous sections.

We consider pure dephasing of nuclear spins with rate T_2^{-1}

$$\dot{\rho} = \frac{1}{T_2}\sum_j (I_z^j \rho I_z^j - \rho)$$

affecting all nuclei. Computing the contribution to $\frac{d}{dt}\tilde{I}_z^{(1)}$ arising from this process we find in the subspace of relevant states ψ

$$|\frac{d}{dt}\langle \tilde{I}_z^{(1)}\rangle_\psi| \sim \epsilon\frac{1}{T_2}, \tag{A.36}$$

as the effective T_2-induced diffusion rate of $\tilde{I}_z^{(1)}$. This contribution is of the same order as the leading higher-order correction discussed in the preceding section if $1/T_2 \sim \epsilon N^{-3/2}A_H \sim 10^3\mathrm{s}^{-1}$. For the measurement based nuclear spin cooling to yield $\sigma_{OF} \leq A_H/N$, the condition $1/T_2 < A_H/N^2 \sim 10^3\mathrm{s}^{-1}$ needs to be satisfied (see the discussion in Sec. C).

B. Rate equation description of nuclear spin dynamics

In this Section, we present the details of the model used to obtain the semi-classical Monte Carlo simulation of the quantum dot absorption rate and the Overhauser field standard deviation presented in Fig. 1d-e of the main text.

The semiclassical limit can be derived from the master Eq. (A.24) by replacing the collective spin decay by independent decay of individual spins. This is accomplished by making the following substitutions in the master equation:

$$\begin{aligned} I_+\rho^n I_- = \sum_{ij} a_i a_j I_+^i \rho^n I_-^j &\to \sum_i a_i^2 I_+^i \rho^n I_-^i, \\ I_-\rho^n I_+ = \sum_{ij} a_i a_j I_-^i \rho^n I_+^j &\to \sum_i a_i^2 I_-^i \rho^n I_+^i, \\ \{I_+I_- + I_-I_+, \rho\}_+ = \{\sum_{ij} a_i a_j (I_+^i I_-^j + I_-^i I_+^j), \rho\}_+ &\to \{\sum_i a_i^2 (I_+^i I_-^i + I_-^i I_+^i), \rho\}_+. \end{aligned}$$

The replacement of the collective spin operators by single spin operators is justified in the limit where coherences between nuclear spin product states vanish on timescales short compared to their lifetime; this condition would be satisfied in systems with large inhomogeneities - either in the nuclear spin splitting or in hyperfine coupling. Since the spectrum, the density of states, and the nuclear spin dynamics $I_\pm$ resulting from $\tilde{I}_z$ and I_z are equivalent, we replace the generalized OF $\tilde{I}_z$ by the OF I_z in the simulations. The proofs that justify this latter replacement will

be given in the last section. We now coarse grain the nuclear motion with respect to the electron dynamics and from the resulting master equation we obtain rate equations that describe the nuclear spin evolution.

In order to mimic the inhomogeneous character of the hyperfine coupling we introduce a shell model of the QD with M different classes of nuclear spins; the nuclei in class (ν) have identical a_ν and their net spin polarization is $m_\nu = \frac{1}{2}(N_\nu^+ - N_\nu^-) = \langle \sum_{i\epsilon\nu} I_z^i \rangle$, where N_ν^+ (N_ν^-) denote the total number of up (down) spins in class (ν). The derived rate equation for the joint probabilities $\mathcal{P}(\{m_\mu\})$ associated with the nuclear spin configuration $\{m_\mu\}$ is given by

$$\begin{aligned}\frac{\partial \mathcal{P}(\{m_\mu\})}{\partial t} &= \sum_\nu^M \mathcal{P}(\{\bar{m}_\mu\}) N_\nu^-(\{\bar{m}_\mu\}) \Gamma_+^\nu(\{\bar{m}_\mu\}) \\ &+ \sum_\nu^M \mathcal{P}(\{\tilde{m}_\mu\}) N_\nu^+(\{\tilde{m}_\mu\}) \Gamma_-^\nu(\{\tilde{m}_\mu\}) \\ &- \sum_\nu^M \mathcal{P}(\{m_\mu\}) [N_\nu^- \Gamma_+^\nu(\{m_\mu\}) + N_\nu^+ \Gamma_-^\nu(\{m_\mu\})],\end{aligned} \tag{B.1}$$

where $\Gamma_\pm^\nu(\{m_\mu\}) = (\frac{g a_\nu}{4\omega_x})^2 \frac{\Gamma}{2} \rho_{tt}(\{m_\mu\})$ are the rates at which nuclear spins of the νth class are flipped if the nuclear spin polarizations in each class are given by $\{m_\mu\}$. $\{\bar{m}_\mu\}$ ($\{\tilde{m}_\mu\}$) denotes the nuclear spin configuration that differs from the configuration $\{m_\mu\}$ only in the νth class, with polarization $m_\nu - 1$ ($m_\nu + 1$). The factors N_ν^- (N_ν^+) account for the number of nuclear spins in the configuration $\{\bar{m}_\mu\}$ ($\{\tilde{m}_\mu\}$) that could be flipped to reach $\{m_\mu\}$.

We simulate the evolution of the nuclear spins with a Monte Carlo method. We assume in our numerical simulations that the QD contains 100 nuclear spins, grouped into five concentric shells ($M = 5$) with different hyperfine coupling constants that are determined by the 3D Gaussian electronic envelope function. The coupling constants a_i for these shells are chosen to be 0.0934Γ, 0.0828Γ, 0.0678Γ, 0.0513Γ, 0.0358Γ and the corresponding total numbers of nuclear spins in each shell are chosen to be 2, 8, 16, 28, 46. The coupling constants are chosen to ensure that the standard deviation of the Overhauser field seen by the QD electron for nuclei in a completely mixed state satisfies $\sigma_{OF}(\rho) = \frac{\Gamma}{4}$. We do not keep track of the exact configuration within each class (ν) of nuclear spins and assume that any configuration of spins leading to the same m_μ is equally likely and that the nuclear spin distribution in each shell is independent of the other shells.

As discussed in the main text, we keep $\Delta\omega_c = 0$ and then scan the probe laser across the resonance. For each probe laser detuning $\Delta\omega_p$ we assume that the initial nuclear state ρ^n is completely mixed and then we evolve the system until $t_{fin} = 10^{12}\Gamma^{-1}$. Figure 1d and 1e of the main text show the formation of an electronic-nuclear dark state and the concurrent reduction in Overhauser field standard deviation σ_{OF} for a range of probe laser detunings $\Delta\omega_p$. The two-photon resonance condition $\delta_{\text{eff}} = g\lambda - \delta = 0$ can be satisfied for a large range of initial detunings because the set of Overhauser fields resulting from all possible nuclear spin configurations of the toy model QD described above is quasi-continuous. However, the density of states in the toy model is not a smooth function of the Overhauser field, which explains the observed variations in the absorption strength and σ_{OF} within the *extended transparency region.*: the Overhauser field required to fulfill $\delta_{\text{eff}} = 0$ for some detunings $\Delta\omega_p$ is composed of a nuclear spin configuration that requires a large polarization in one of the nuclear spin classes. It will take many nuclear spin flips to reach such a state, since the initial state is taken to be Gaussian in all classes.

C. Lévy flight analysis

In this Section, we present details of the Lévy flight analysis used to obtain the time needed for the coupled electron-nuclei system to reach the dark state (Eq. (4) of the main text) and the effective minimum width of the trapping region $\tilde{\delta}$ in the presence of intrinsic nuclear spin diffusion.

For the nuclear spin cooling scheme we analyze, the time needed to reach the dark state is of key interest: since the optically-assisted nuclear spin flips take place at a rate that is smaller by a factor ϵ^2 than the rate of photon scattering events without nuclear spin flips, it is possible to monitor the sharp decrease in QD resonance fluorescence to verify that the coupled system is in the trapping region on timescales short compared to average nuclear spin flip time. Once the system is found to be in the trapping region, a feedback mechanism can be used to turn the laser excitation off, ensuring that the desired/attained σ_{OF} is preserved.

Continuous-time random walks are used in a wide range of fields to describe stochastic processes that are characterized by two probability distributions: one for the spatial jump length and another for the waiting time between

two consecutive jumps. If one allows the jump length distribution to assume a Lévy-type distribution that is marked by so-called "fat tails", extremely long spatial jumps will occur. This is due to the fact that, asymptotically, Lévy distributions decay as power laws rather than exponentially, which gives rise to larger probabilities for extreme events that dominate the evolution of the system. These "fat tails" are also responsible for diverging variance and possibly infinite mean. Compared to the Brownian motion, the described random walk will show superdiffusive behavior. On the other hand, if the waiting time distribution obeys Lévy distribution, the system can become trapped for long times between jumps, which leads to subdiffusion [10]. Lévy distributions have been used to describe a very wide variety of phenomena ranging from human travel [11] to anomalous transport of photons[12, 13], and in particular, to subrecoil laser cooling [8]. The problem of subrecoil laser cooling shares many features with the anomalous diffusion process that appears in the cooling of nuclear spins in Overhauser field (OF) selective coherent population trapping (CPT).

Here we analyze the anomalous diffusion of the nuclear OF due to optical excitation. The jump length distribution of the continuous-time random walk that describes this physical process is not of Lévy type, but is given by the distribution of the hyperfine coupling strength of the nuclei. The hyperfine interaction depends on the electronic envelope wave function, which is assumed to be Gaussian in the QD. A typical jump will thus induce a change in the OF by A_H/N. However, the waiting time distribution $P(t)$ between consecutive nuclear spin flips shows signatures of Lévy statistics.

For fixed laser detunings $\Delta\omega_p$ and $\Delta\omega_c$ the absorption depends on the value that the nuclear OF assumes. In particular, for $\delta_{\text{eff}} = g\lambda - \delta = 0$ with δ fixed, absorption vanishes due to the formation of a dark state. We define the region around this dark state in the CPT dip to be the trapping region, while the remaining part is called the recycling region. For all practical purposes, the waiting time distribution in the recycling region does not exhibit Lévy statistics (see below). On the other hand, in the trapping region one finds an infinite average trapping time if no optical-excitation-independent nuclear diffusion processes are present. The fact that $P(t)$ in the trapping region is a Lévy distribution is responsible for the overall subdiffusive behavior of the random walk of the nuclear spins.

The temporal evolution of the system shows switching between two regimes: diffusion in the recycling region and locking in the trapping region. To describe these dynamics, we introduce the recycling time $\hat{t}$ and the associated probability distribution function $\hat{P}(\hat{t})$. The recycling time is the time an initially trapped OF would diffuse in the recycling region before returning to the the trap. In other words, it is a measure for the timescales of switching between the diffusive and trapping regimes.

First, we will neglect optical-excitation independent nuclear spin diffusion and focus on the case where $\Delta\omega_p = \Delta\omega_c = 0$ and $\Omega_p = \Omega_c$. To simplify the estimation of the recycling and trapping (waiting) time, we consider a limiting case where the width for the CPT transparency dip fulfills $\Omega^2/\Gamma \ll A_H/N$; i.e., a typical single nuclear spin flip will take the system out of the transparency window. We remark that the condition $\Omega^2/\Gamma \ll A_H/N$ is not necessarily optimal for nuclear spin cooling since it requires very small Ω, which in turn leads to a small nuclear spin flip rate in the recycling region (see below) and longer than optimal return times. On the other hand, in this limit a single nuclear spin flip takes the system out of the trapping region, simplifying the analysis.

We assume that the width of the recycling region is determined by $A_H/\sqrt{N} \approx \Gamma/4$; since the density of states of the OF quickly drops for large polarizations, the OF cannot explore extreme polarizations. This observation is supported by numerical simulations, justifying the assumption of hard walls at $A_H/\sqrt{N} \approx \Gamma/4$. For the assumed parameter range, the light scattering rate is nearly constant outside the transparency dip and up to the hard walls that define the recycling region. We therefore take the light scattering rate to be constant in the recycling region and equal to Ω^2/Γ in this simplified model. As mentioned above, the nuclear spin flip rate is suppressed by a factor ϵ^2 compared to the light scattering rate, which leads to the nuclear spin flip rate $\tau_0^{-1} \approx \epsilon^2\Omega^2/\Gamma$ in the recycling region. In the limit of many nuclear spin flips, the number of steps in the recycling region required to return to the trapping region is thus given by the total range of OF values the system explores divided by the size of the trap: $\langle M\rangle = \frac{A_H/\sqrt{N}}{\Omega^2/\Gamma}$. This expression is valid provided $\langle M\rangle \gg N$, where $N = (\frac{A_H/\sqrt{N}}{A_H/N})^2$ is the number of spin flips that allows the system to diffuse to the hard walls, starting from an arbitrary polarization within the recycling region [14]. Since the time for a single spin flip is taken to be independent of the Overhauser field, the average (recycling) time to return to the trapping region is given by

$$\langle\hat{t}\rangle = \langle M\rangle\tau_0 = \frac{A_H/\sqrt{N}}{\Omega^2/\Gamma}\frac{\Gamma}{\Omega^2}\frac{1}{\epsilon^2}. \tag{C.1}$$

Since we assumed $\langle M\rangle \gg N$, this estimate is valid only in the limit $\Omega^2/\Gamma \ll A/N^{3/2}$.

Given the measurement-feedback strategy for minimizing σ_{OF} that we described earlier, we are strictly speaking interested in the time for an OF that is initially in the recycling region to reach the trapping region. In contrast, $\langle\hat{t}\rangle$ gives the average return time from the recycling to the trapping region, starting from an OF that is initially in the trap. Since the analysis for the recycling time we presented is valid in the limit of many nuclear spin flips in

the recycling region before the system reaches the trap, it follows that the OF explores the whole recycling region uniformly. In this case, the starting point of the OF becomes irrelevant in the sense that if the OF initially was in the trap, events where the OF returned to the trap after only a few spin flips in the recycling region are excluded from the analysis. As a consequence, the recycling (first return) time and the time for an OF that initially was in the recycling region to reach the trap, are comparable.

In the experimentally interesting limit $\Omega^2/\Gamma \geq A_H/N$, the number of steps needed to reach the trapping region is no longer given by Eq. (C.1). Since the step size is now comparable to the width of the trap, reaching the middle of the recycling region (where the trapping region is) starting from an arbitrary point within the hard walls is sufficient for trapping. The number of steps is then given by the whole interval divided by the step size squared: $\langle \tilde{M} \rangle = (\frac{A_H/\sqrt{N}}{A_N/N})^2 \simeq N$. Consequently, the time required to find the trap is given by $\langle \hat{t} \rangle = \langle \tilde{M} \rangle \tau_0 = N \frac{\Gamma}{\Omega^2} \frac{1}{\epsilon^2} = N \frac{N}{A_H} \frac{1}{\epsilon^2} = \frac{N^2}{A_H \epsilon^2} \approx \frac{N^3}{A_H}$, where the last expression follows for $\omega_z \approx A_H$.

The unfavorable scaling of $\langle \hat{t} \rangle$ with the number of nuclear spins, N, necessitates considering the effect of optical-excitation-independent nuclear spin diffusion or decay processes. Such processes would lead to a non-vanishing rate of nuclear spin flips that take the system out of the dark state. In the long term limit, this would establish a steady state between diffusion in the recycling region and finite-time trapping in the transparency region. Clearly, the presence of optical-excitation-independent nuclear spin diffusion processes limits the reduction in the standard deviation of the OF. We denote the single nuclear spin diffusion rate of any such mechanism by γ_n. If we assume that $N\gamma_n < \epsilon^2 \Omega^2/\Gamma$, we can write the steady-state standard deviation of the OF as

$$\sigma_{\rm OF} \simeq \tilde{\delta} \frac{\langle t \rangle}{\langle t \rangle + \langle \hat{t} \rangle} + \frac{A_H}{\sqrt{N}} \frac{\langle \hat{t} \rangle}{\langle t \rangle + \langle \hat{t} \rangle} \tag{C.2}$$

where the average time spent in the trapping region is $\langle t \rangle = (N\gamma_n)^{-1}$ (assuming that a single spin-flip takes the system out of the trap) and $\tilde{\delta}$ is the effective width of the trap; the latter is determined as the detuning for which the intrinsic scattering rate in the trap ($N\gamma_n$) equals the expected optically induced nuclear spin flip rate in the CPT dip given by $\epsilon^2 \frac{\Gamma}{\Omega^2} \langle \tilde{I}_z \rangle^2$; i.e. $\tilde{\delta}$ satisfies $\epsilon^2 \frac{\Gamma}{\Omega^2} \tilde{\delta}^2 = N\gamma_n$, yielding $\tilde{\delta} = \epsilon^{-1} \Omega \sqrt{N\gamma_n/\Gamma}$. The dependence $\propto \langle \tilde{I}_z \rangle^2$ comes from the coupling between the states $|B\rangle$ and $|D\rangle$ by $H_{\rm hyp}$ with the matrix element $\langle B|H_{\rm hyp}|D\rangle \propto \langle \tilde{I}_z \rangle$. The rate of this coupling is proportional to $|\langle B|H_{\rm hyp}|D\rangle|^2 \propto \langle \tilde{I}_z \rangle^2$, which leads to $P(t) \propto t^{-3/2}$. This asymptotic decay of $P(t)$ is responsible for the infinite average trapping times [8] in the absence of optical-excitation independent nuclear spin diffusion.

The smallest steady-state (measurement-free) $\sigma_{\rm OF}$ is obtained when the contribution from the trapping region (first term) and from the recycling region (second term) to $\sigma_{\rm OF}$ are comparable. However, substantial OF narrowing in this case is only possible provided $\langle \hat{t} \rangle \ll \langle t \rangle$. This condition is unlikely to be satisfied for self-assembled QDs if one aims at $\sigma_{OF} = A_H/N$, since $\langle \hat{t} \rangle \sim 10$s for $N = 10^4$ and $\gamma_n = 10^{-3}{\rm s}^{-1}$. On the other hand, a more modest narrowing yielding $\sigma_{OF} = 10A_H/N$ (achieved by choosing $\Omega^2/\Gamma = 10A_H/N$) would give $\langle \hat{t} \rangle \sim 1{\rm s} \ll \langle t \rangle \simeq 100(N\gamma_n)^{-1}$.

As we have discussed in the main text, the use of feedback from the scattered light intensity could be used to turn the laser that cause the optically induced nuclear spin diffusion off as soon as it is determined that the coupled system is in the trapping region. When this procedure is used, the (conditional) σ_{OF} is only limited by the effective width of the trapping region $\tilde{\delta}$. To achieve OF narrowing in the single spin limit $\sigma_{\rm OF} \sim \tilde{\delta} \sim A_H/N$, it is necessary to ensure $\gamma_n < A_H/N^3$ and $1/T_2 < A_H/N^2$.

D. Generalized Overhauser field

In this Section, we show that the spectrum and the density of states of the Generalized Overhauser Field (GOF) does not differ significantly from that of the standard Overhauser field. This property is important for justifying the assumptions leading to the semi-classical Monte Carlo simulations (see Fig. 1d-e of the main text), where we used the standard Overhauser field to reproduce the diffusive dynamics of the GOF.

For the main part of the nuclear Hilbert space – namely the domain where the operator $\tilde{I}_z^{(1)} - \delta/g$ is large (recycling region) – the ϵ-correction in the GOF represents a negligible perturbation to the hyperfine interaction. However, in the domain of small eigenvalues of $\tilde{I}_z^{(1)} - \delta/g$ (we define this trapping region within a small interval $L(\delta, \eta) = (\delta - \eta, \delta + \eta)/g$ centered around δ/g) this perturbative picture is not trivially justified.

Using Monte Carlo simulations we first show that the density of eigenstates of the homogeneous ($a_i = a_j = 1/\sqrt{N}$) and inhomogeneous operator $I_z^{(1)}$, respectively, is identical (up to small corrections) for our system parameters ($N = 10^4$, Gaussian distribution of coupling strengths), see Fig. 2 (a). Therefore, the number of eigenstates for the

inhomogeneous operator $I_z^{(1)}$ with small eigenvalues is exponentially large in the number of spins (in the homogeneous case every eigenvalue $m/\sqrt{N}$ has degeneracy $B_m = \binom{N}{N/2+m}$). This implies that neglecting the ϵ-correction, trapping regions close to the center of the spectrum $|\delta/g| \lesssim 1$ constitute a substantial part of the Hilbert space and can be reached in reasonable times by the nuclear random diffusion. For trapping regions $|\delta/g| \gtrsim 1$, i.e. very large laser detunings, the size of the trapping region drops exponentially [Fig. 2 (a)] and cannot be explored by the nuclear diffusion (see Fig. 1 (d) of the main text).

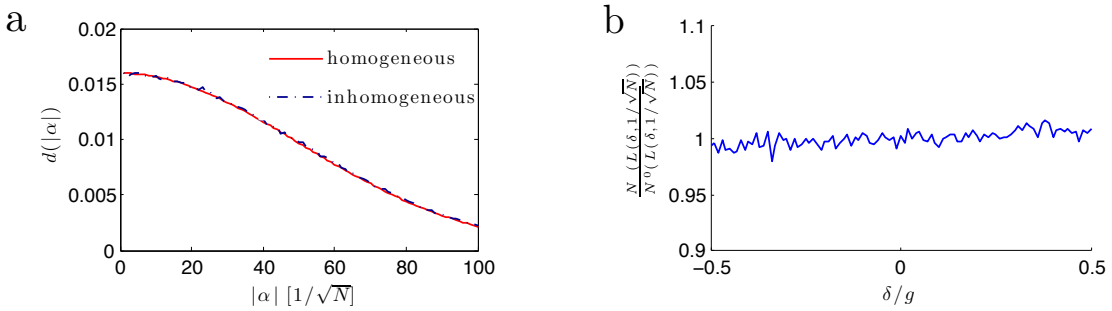

Figure 2: (a) Comparison of the density of eigenstates $d(|\alpha|)$ of the homogeneous and inhomogeneous nuclear operator $I_z^{(1)}$. The density of states is averaged over segments of size $1/\sqrt{N}$. While in the homogeneous case the density of states can be calculated exactly, in the inhomogeneous case it is evaluated using Monte Carlo simulations (b) The number of eigenvalues in small intervals of size $1/\sqrt{N}$ of the GOF approximately equals the number of states for the standard OF. In the simulations we assumed $N = 10^4$ and coupling coefficients a_i arising from a Gaussian electron wave function.

Next we are going to show that the GOF fulfills the same property by deriving a relation between the spectrum of the operators $\tilde{I}_z^{(1)}$ and $I_z^{(1)}$. In the homogeneous case the ϵ-correction commutes with the unperturbed part $[I_z^{(1)}, \{I_+^{(1)}, I_-^{(1)}\}_+] = 0$, and a common eigenbasis is given by the well known Dicke states $|J, m\rangle$, where J denotes the total spin and m the spin projection in $\hat{z}$-direction. The vast majority states within the kernel of $I_z^{(1)}$ lie in J subspaces around $J = \sqrt{N}/2$ (the degeneracy of each subspace J is given by $D_J = \binom{N}{N/2-I} - \binom{N}{N/2-I-1}$). Thus, up to a negligible fraction, most states will be shifted in energy by a small amount of order ϵ. The same can be shown for states with finite eigenvalue of $I_z^{(1)}$ in the range $\sim (-1, 1)$. The positive operator of the correction $\frac{1}{2}\epsilon\{I_+^{(1)}, I_-^{(1)}\}_+$ shifts the whole spectrum in the region of interest by a small amount $\propto \epsilon$ and thus preserves the required property of large density of states in any trapping region $L(\delta, \epsilon)$ close to the center of the spectrum.

In the inhomogeneous case this simple argument fails, since one cannot easily construct an eigenbasis of the GOF. We are going to estimate the density of states in the following. For the inhomogeneous GOF operator $\tilde{I}_z^{(1)}$ the number of states within the trapping region $L(\delta, \eta)$ is given by $N^\epsilon(L(\delta, \eta)) = \int_{L(\delta,\eta)} dE\ \mathrm{Tr}(\delta(E - I_z^{(1)} + \frac{1}{2}\epsilon\{I_+^{(1)}, I_-^{(1)}\}_+))$. Approximating the δ-functions by Lorentzians of width $\gamma \ll \eta$: $\delta(E - \tilde{I}_z^{(1)}) \approx \frac{\gamma}{(E-\tilde{I}_z^{(1)})^2+\gamma^2}$, and using the expansion $\frac{1}{A-\epsilon B} = \frac{1}{A}\sum_{n=0}^{\infty}(\epsilon B \frac{1}{A})^n$ with the definitions

$$A = \gamma^2 + (E - I_z^{(1)})^2, \tag{D.1}$$

$$B = -\frac{1}{2}\{(E - I_z^{(1)}), \{I_+^{(1)}, I_-^{(1)}\}_+\}_+ - \frac{1}{4}\epsilon(\{I_+^{(1)}, I_-^{(1)}\}_+)^2 =: Q + \epsilon P, \tag{D.2}$$

we find

$$N^\epsilon(L(\delta, \eta)) = \sum_{n=0}^{\infty} U^{(n)} = N^0(L(\delta, \eta)) + \sum_{n=1}^{\infty} U^{(n)}, \tag{D.3}$$

$$U^{(n)} = \gamma\epsilon^n \int_{L(\delta,\eta)} dE\ \mathrm{Tr}\left(\frac{1}{A}\left[B\frac{1}{A}\right]^n\right). \tag{D.4}$$

A pessimistic approximation shows that the sum $\sum_{n=1}^{\infty} U^{(n)}$ can be upper bounded by $\sim N^0(L(\delta, \eta))$ for large trapping regions $\eta \gg \epsilon$, i.e. the number of eigenstates changes at most by a factor of order 1.

Using the above definitions the quotient of the number of states in the perturbed and unperturbed case can be written to first order in ϵ as

$$\frac{N^{\epsilon}(L(\delta,\eta))}{N^{0}(L(\delta,\eta))} = \frac{\int_{L(\delta,\eta)} dE\ \mathrm{Tr}(\frac{1}{A}(1+\epsilon Q\frac{1}{A}))}{\int_{L(\delta,\eta)} dE\ \mathrm{Tr}(\frac{1}{A})} = \frac{\sum_{\vec{n}} \int_{L(\delta,\eta)} dE\ g(\vec{n},E) f(\vec{n},E)}{\sum_{\vec{n}} \int_{L(\delta,\eta)} dE\ g(\vec{n},E)}, \tag{D.5}$$

where we defined

$$g(\vec{n},E) = \langle\vec{n}|\,\frac{1}{A}\,|\vec{n}\rangle\,, \tag{D.6}$$

$$f(\vec{n},E) = 1 + \epsilon\,\langle\vec{n}|\,Q\frac{1}{A}\,|\vec{n}\rangle\,, \tag{D.7}$$

for a nuclear product state $|\vec{n}\rangle$. Expressions like the one of Eq.(D.5) can be efficiently evaluated using Monte Carlo simulation with *importance sampling* [9]. This method uses a more efficient sampling according to the probability distribution $g(\vec{n},E)$ (i.e. strongly weighted regions are favored in the sampling) instead of the sampling of random configurations $(\vec{n},E)$ within the entire state space. In particular it can be shown that

$$\frac{\sum_{\vec{n}} \int_{L(\delta,\eta)} dE\ g(\vec{n},E) f(\vec{n},E)}{\sum_{\vec{n}} \int_{L(\delta,\eta)} dE\ g(\vec{n},E)} = \lim_{t\to\infty} \frac{1}{t} \sum_{i=1}^{t} f(\vec{x}_i), \tag{D.8}$$

where the vectors $\vec{x}_i$ stand for particular configurations of the random variables $(\vec{n},E)$ which are distributed according to $g(\vec{x}_i)$.

The algorithm realizing the above scheme contains the following steps: (0.) We start from a random sample $\vec{x} := (\vec{n},E)$ $(E \in L(\delta,\eta))$ and then (1.) create a new sample $\vec{x}'$ by randomly changing one coordinate x_i (the ratio of spin flips and change of E is defined a priori). (2.) If $g(\vec{x}')/g(\vec{x}) > s$ - where s is an (in each step) randomly created number $\in (0,1)$ - we add $f(\vec{x}')$ to a variable F, if not we discard the new state, return to $\vec{x}$ and add $f(\vec{x})$ to F. Successive repetition of steps (1.) and (2.) lets the quantity F/t (t denotes the number of steps) converge to the desired quotient in Eq. (D.5). The method ensures that regions of higher importance are explored more frequently than others (according to $g(\vec{n},E)$), increasing the performance of the algorithm. The simulations for $N = 10^4$ inhomogeneously coupled spins suggest that even for $\eta \sim \epsilon$ the number of states in both the perturbed and unperturbed case differ by less than a few percent [see Fig. 2 (b)].

Furthermore, since $[\tilde{I}_z^{(1)}, I_-^{(1)}] = [I_z^{(1)}, I_-^{(1)}] + \mathcal{O}(\epsilon)$ the diffusion rate of the generalized Overhauser field equals the one in the unperturbed case up to an ϵ correction. This justifies the conclusion that the diffusive dynamics of the GOF is well reproduced by that of the standard OF.

---

[1] Atatüre, M. *et al.* Quantum-Dot Spin-State Preparation with Near-Unity Fidelity. *Science* **312**, 551 (2006).
[2] Cohen-Tannoudji, C. *et al.* Atom-Photon Interactions. New York: Wiley, 1998
[3] Shavitt, I. and Redmond, L. T. Quasidegenerate perturbation theories. A canonical van Vleck formalism and its relationship to other approaches. *J. Chem. Phys.* **73**(11), 5711 (1980).
[4] Klein, D. J. Degenerate perturbation theory. *J. Chem. Phys.* **61**(3), 786 (1973)
[5] For Eq. (A.25) to generate a physical (completely positive) dynamics, $\tilde{I}_z^{(1)}$ must commute with ρ at all times. This is ensured by Eq. (A.25) (in the homogeneous case) provided it holds initially, (e.g. for initially fully mixed nuclear spins).
[6] Only species with sizably different g factors are distinguished. The two In isotopes, e.g., are treated as one species for typical magnetic fields.
[7] This assumption is justified by the fact that the degeneracy of the the available Overhauser field configuration drops for larger $\langle\tilde{I}_z^{(1)}\rangle > A_H/\sqrt{N}$. In addition, the random walk of the Overhauser field is biased since the rates of flipping a spin up or down come with a factor proportional to the number of available final configurations. This bias becomes large for $\langle\tilde{I}_z^{(1)}\rangle > A_H/\sqrt{N}$ and prevents the Overhauser field from exploring extreme polarizations.
[8] Bardou, F., Bouchaud, J. P., Emile, O., Aspect, A., and Cohen-Tannoudji, C. Subrecoil Laser Cooling and Lévy Flights. *Phys. Rev. Lett.* **72**, 203 (1994).
[9] Hastings, W. K. Monte Carlo sampling methods using Markov chains and their applications. *Biometrika* **57**(1), 97 (1970).
[10] Chechkin, A. V. *et al.* Introduction to the Theory of Levy Flights in Anomalous Transport: Foundations and Applications. (eds Klages, R., Radons, G., and Sokolov, I. M.) 129-162 *WILEY VCH* (2008).
[11] Brockmann, D. *et al.* The scaling laws of human travel. *Nature* **439**, 462 (2006).
[12] Barthelemy, P. *et al.* A Lévy flight for light. *Nature* **453**, 495 (2008).
[13] Mercadier, N. *et al.* Lévy flights of photons in hot atomic vapours. *Nature Phys.* **5**, 602 (2009).
[14] F. Bardou, J.-P. Bouchaud, A. Aspect and C. Cohen-Tannoudji *Levy Statistics and Laser Cooling*, (Cambridge University Press, Cambridge, 2002).

Quantum information processing using localized ensembles of nuclear spins

J. M. Taylor[1], G. Giedke[2], H. Christ[3], B. Paredes[3], J. I. Cirac[3], P. Zoller[4], M. D. Lukin[1], and A. Imamoğlu[2]
[1] *Department of Physics, Harvard University, Cambridge, Massachusetts 02138, USA*
[2] *Institut für Quantenelektronik, ETH Zürich, Wolfgang-Pauli-Straße 16, CH-8093 Zürich, Switzerland*
[3] *Max-Planck-Institut für Quantenoptik, Hans-Kopfermann-Straße 1, Garching, D-85748, Germany*
[4] *Institut für Theoretische Physik, Universität Innsbruck, Technikerstraße 24, A-6020 Innsbruck, Austria*

We describe a technique for quantum information processing based on localized ensembles of nuclear spins. A qubit is identified as the presence or absence of a collective excitation of a mesoscopic ensemble of nuclear spins surrounding a single quantum dot. All single and two-qubit operations can be effected using hyperfine interactions and single-electron spin rotations, hence the proposed scheme avoids gate errors arising from entanglement between spin and orbital degrees of freedom. Ultra-long coherence times of nuclear spins suggest that this scheme could be particularly well suited for applications where long lived memory is essential.

PACS numbers: 03.67.Lx, 71.70Jp, 73.21.La, 76.70.-r

arXiv:cond-mat/0407640 v2 23 Jul 2004

Nuclear spin degrees of freedom have attracted considerable attention as potential carriers of quantum information due to their exceptionally long coherence times. Early bulk NMR work [1] has substantially enriched our understanding of the key features of quantum computation [2, 3]. The fundamental difficulties in scaling bulk NMR to a large number of qubits motivated efforts to use single, individually addressable nuclear spins in semiconductors as qubits [4], where computation is primarily mediated by the hyperfine interaction between electron and nuclear spin. While possibly scalable, such a scheme is limited by the fact that the electron wave-function is spread over many lattice sites, reducing the strength of the hyperfine interaction. In addition, two-qubit operations in Ref. [4] rely upon exchange coupling, making them susceptible to fast orbital decoherence mechanisms.

Recently, a method for robust storage of quantum information in localized ensembles of nuclear spins was suggested [5, 6], where it was shown that the collective hyperfine coupling between nuclear and electron spin degrees of freedom provides a controllable mechanism for coherent storage and manipulation of quantum states. These nuclear spin ensembles correspond, for example, to the lattice nuclei in a quantum dot. As a quantum memory, such nuclear ensembles are robust with respect to variations in dot characteristics, rely upon proven fabrication techniques, and provide high fidelity storage without requiring a high-degree of nuclear spin polarization.

In this Letter, we describe a technique to efficiently process quantum information stored in localized nuclear spin ensembles. Specifically, these ensembles enable a robust, scalable implementation of quantum computation protocols, unencumbered by the difficulties faced by single spin impurity or bulk NMR approaches. The fundamental interaction that allows for spin manipulation in our scheme is hyperfine coupling: as a result, the orbital and spin degrees of freedom remain unentangled throughout the two-qubit gate operations, mitigating the effects of orbital decoherence on gate fidelity. While collective enhancement of hyperfine interaction allows for fast quantum gates, the ultra-long nuclear spin coherence times render the scheme particularly attractive for memory intensive quantum information processing tasks.

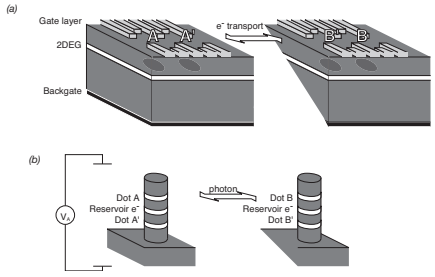

FIG. 1: Quantum dot based approaches for nuclear ensemble-based computation. (a) Electrically defined (lateral) quantum dots connected by ballistic transport *e.g.* through a series of quantum dots. Nearby rf-SETs (not shown) would provide measurement. (b) Nanowhiskers [7] with several optically active dots. Tasks between A and A' are achieved via shuttling of an electron from the reservoir dot via a potential difference, V_A. Long distances tasks are performed through photon-based entanglement generation between A' and B'. [19]

The scheme proposed here can be realized using either electrically [8] or optically [9] manipulated quantum dots that are defined as in Fig. 1. The nuclear ensemble in each dot is prepared using polarized electron spins [6, 10]. We illustrate our technique by considering the fully polarized case (when the nuclear state is $|0\rangle = |-I, \ldots, -I\rangle$ for N spin-I nuclei), demonstrate how to perform single qubit and two-qubit gates, and consider sources of error.

The Hamiltonian describing a single electron interacting with the nuclear spins in a quantum dot is [11]

$$H = \hbar B\gamma_S \hat{S}_z + \hbar B \sum_k \gamma_I^{(k)} I_z^{(k)} + \hbar a \hat{\vec{S}} \cdot \hat{\vec{A}}. \qquad (1)$$

The first and second terms describe the coupling of the

electron and the nuclear spins to an external magnetic field, with effective gyromagnetic ratios $\gamma_S, \gamma_I^{(k)}$. The last term is the electron coupling to collective nuclear degrees of freedom, defined by $\hat{A}_{\pm,z} = \sum_k \alpha_k \hat{I}^{(k)}_{\pm,z}$. The α_k's are proportional to the probability density of the electron at the location of the corresponding nuclei and are normalized such that $\sum_k \alpha_k = N$; $a = A/N$ is the average hyperfine interaction per nucleus. Both A and N depend upon the specific material and dot construction; typical numbers are $A \sim 10-100\ \mathrm{ns}^{-1}$ and $N = 10^4-10^6$ nuclei. Excitations out of the fully polarized state form an orthonormal set of collective nuclear spin states $|m\rangle \propto (\hat{A}_+)^m |0\rangle$, where m is the number of excitations.

When an electron is confined in the dot, evolution over times much shorter than a^{-1} is restricted to subspaces spanned by $\{|m-1\rangle|\uparrow\rangle, |m\rangle|\downarrow\rangle\}$. Using Pauli matrices, the Hamiltonian for each subspace with a fixed excitation number m is $H^{(m)} = \hbar\delta_m \sigma_z^{(m)} + \hbar\Omega_m \sigma_x^{(m)}$, with

$$\Omega_m = a/2\sqrt{\langle m-1|\hat{A}_-\hat{A}_+|m-1\rangle}; \quad (2a)$$

$$\delta_m = a/4(\langle m|\hat{A}_z|m\rangle + \langle m-1|\hat{A}_z|m-1\rangle) + [\gamma_S - (\langle m|K_z|m\rangle - \langle m-1|K_z|m-1\rangle)]B/2, \quad (2b)$$

where $K_z = \sum \gamma_I^{(k)} I_z^{(k)}$ is a sum over nuclear spin operators, weighted by individual nuclear spin gyromagnetic ratios. When Overhauser shift and Zeeman energy sum to zero ($|\delta_m| \ll \Omega_m$) and coherent flip-flop (Rabi) oscillations occur at rate Ω_m. The energy level structure of the coupled electron-nuclear system is shown in Fig. 2 along with the coupling strengths for $m \leq 2$: since $\Omega_{m+1} = \eta_m \Omega_m$ where $\eta_m = \sqrt{m+1}[1 - \mathcal{O}(m/N)]$, it is easy to note the analogy with the celebrated Jaynes-Cummings (JC) model of quantum optics [12]. We use the nonlinearity of such a JC-type two-level system coupled to a nearly-bosonic mode to effect elementary quantum gates.

Quantum information stored in the $m = 0, 1$ manifold can be mapped reliably from nuclear states to electron spin and back [6] via a generalized rotation :

$$R^{xy}_{en}(\pi/2, 0)(\alpha|0\rangle + \beta|1\rangle)|\downarrow\rangle = |0\rangle(\alpha|\downarrow\rangle + i\beta|\uparrow\rangle), \quad (3)$$

where

$$R^{xy}_{en}(\theta, \phi) = e^{i\phi\hat{S}_z} e^{-i\theta H/(\hbar\Omega_1)} e^{-i\phi\hat{S}_z}. \quad (4)$$

The transfer of quantum information from the nuclear ensemble to electron spin allows for fast single qubit operations to be performed: after a $|\downarrow\rangle$ electron is injected into the dot, the quantum information is transferred to the electron spin, and then the operation is performed on the electron. Finally, the quantum information is mapped back to the nuclear ensemble. A z-axis rotation can be accomplished by waiting in a static magnetic field or through a laser-induced spin-dependent AC Stark shift [16]. x-axis rotations can be done via

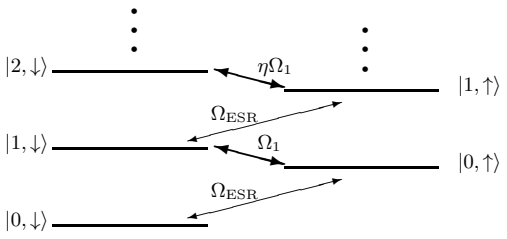

FIG. 2: Level structure of the combined electron spin and nuclear dark state plus excited states. For $N \to \infty$, the coupling between the two excitation manifold is stronger by $\eta \to \sqrt{2}$.

ESR [8, 13] (with $\Omega_{\mathrm{ESR}} \gtrsim 1\ \mathrm{ns}^{-1}$) or optical Raman spin flips through a virtual trion state (with $\Omega_{\mathrm{opt,ESR}} \gtrsim 10\ \mathrm{ns}^{-1}$) [9]. Measurement of the ensemble nuclear spin state can be implemented by mapping the quantum information to electron spin, and carrying out an electron spin measurement either by state selective ionization followed by charge measurement with a rf-SET [14] or by detecting fluorescence in a spin-dependent cycling transition [15, 16].

To perform a two-qubit gate between quantum dots A and A', a single electron can be used as to transfer quantum information between the dots: the state of nuclear spin qubit A is mapped onto the electron, which is then moved to A', where a controlled-phase (CP) gate between the nuclear and the electronic qubit is applied using the nonlinearity of the interaction. Following Ref. [17], a two-qubit CP-gate (up to single qubit gates) is given by

$$R^{xy}_{en}(\pi/4, 0) R^{xy}_{en}(\pi/\eta, -\pi/2) R^{xy}_{en}(-\pi/4, 0). \quad (5)$$

In the computational basis, this corresponds to

$$\begin{pmatrix} 1 & 0 & 0 & 0 \\ 0 & e^{i\pi/\eta} & 0 & 0 \\ 0 & 0 & e^{-i\pi/\eta} & 0 \\ 0 & 0 & 0 & -1 \end{pmatrix}. \quad (6)$$

After this operation, the quantum information carried by the electron spin is mapped back onto the nuclear spin ensemble A. Applying a z-rotation of $-\pi/\eta$ to qubit A and one of π/η to qubit A' yields a CP gate.

For distant dots, where electron spin transport between ensembles is difficult or impossible, it may be easier to generate entanglement off-line, apply local purification protocols and then use it to effect non-local gates, following [18]. Entanglement between distant electron spins can be generated optically, using spin-flip optical Raman transitions [19], or electronically, such as through adiabatic splitting of a spin singlet in a double dot [20]. The electron-nuclear state mapping procedure can then ensure that the distant nuclear spin ensembles are entangled. Starting with the entangled nuclear state $\frac{1}{\sqrt{2}}(|01\rangle + |10\rangle)$ (between dots A' and B', cf. Fig. 1), we can implement a CP gate on dots A and B (deterministically) by performing local unitaries and measurements

of AA' and BB' as follows: (i) perform a $\mathrm{CNOT}_{A\to A'}$ then measure A'. (ii) Perform a CP gate $|10\rangle \to -|10\rangle$ at BB' followed by a Hadamard gate and measurement at B'. (iii) Local phase flips $|0\rangle \to -|0\rangle$ at A (B) if the measurement outcomes at B'(A') were "1" complete the CP gate between A and B [21].

We next analyze various sources of errors due to finite polarization, inhomogeneity, nuclear spin dynamics, and electron spin decoherence. To understand the role of finite polarization, the specific cooling procedure must be examined. When the nuclear ensemble starts as a thermal mixture, cooling to dark states can be achieved by coupling polarized electron spins to the nuclear ensemble [10]. Regardless of the details of cooling, the final density matrix will be a statistical mixture of dark states $|\mathcal{D}(n,\beta)\rangle$, where $\hat{A}_-\,|\mathcal{D}(n,\beta)\rangle = 0$. n is the number of spin excitations ($n = 0$ is the fully polarized state) and β is the permutation group quantum number [22]. It was recently shown [6] that dark states have the same symmetry properties as the fully polarized state, and a manifold of excited states can be defined from a given dark state, $|m(n,\beta)\rangle \propto (\hat{A}_+)^m\,|\mathcal{D}(n,\beta)\rangle$. Hence the above considerations for perfectly polarized nuclei map directly to the case when the nuclear ensembles start in any given dark state, not just the fully polarized state.

In practice, the cooled nuclear ensemble density matrix is a mixture of different dark states, i.e. $\hat{\rho} = \sum_{n,\beta}\rho_{n,\beta}|\mathcal{D}(n,\beta)\rangle\langle\mathcal{D}(n,\beta)|$. As each dark state has a different $\delta_m(n,\beta), \Omega_m(n,\beta)$, interaction times and applied magnetic fields can only produce $R^{xy}_{en}(\theta,\phi)$ with the desired angle θ for some fraction of the given mixture. The inhomogeneous mixture effects can be characterized by examining the subgroups of dark states with different detunings, which lead to errors in Rabi oscillations $p \simeq (\sigma_\delta/\Omega_1)^2$, where σ_δ is the standard deviation of possible δ_1 values over the distribution $\rho_{n,\beta}$. In the homogeneous case with spin-1/2 nuclei,

$$\sigma_\delta \simeq a\sqrt{N(1-P^2)}\ . \tag{7}$$

Even at high ($P \sim 0.95$) polarizations, the effect of different detunings can be substantial ($p \sim 0.03$). This provides the strongest limit to realization of R^{xy}_{en} [23].

The inhomogeneous nature of the hyperfine coupling leads to further errors. In this case, the logical states of the system (the m-excitation manifolds) are no longer eigenstates of $\hat{J}_z = \hat{A}_z + \hat{S}_z$ and of $\hat{A}^2$. As a consequence, there is a nonzero probability that the system moves out of the computational subspace during the gate operation. We estimate these leakage errors using the techniques developed in Refs.[5, 6], and find that the resulting gate error p_{inhom} decreases with increasing number of nuclei: for $N \sim 10^5$ at high polarizations ($P > 0.95$) $p_{\mathrm{inhom}} \lesssim 10^{-3}$ [24]. We note that a similar error emerges due to the differences in Zeeman energy associated to different nuclear species. For materials like GaAs, with gyromagnetic ratios varying greatly from species to species, this limits the effectiveness of gate operations at high magnetic field, resulting in the errors in the range of 10^{-3} as indicated in Fig.3. Optical manipulation (e.g. tuning the system into resonance via spin-dependent AC optical Stark shifts) may mitigate this difficulty. Finally, in between gate operations the errors associated with inhomogeneous evolution may be eliminated by refocusing sequences of NMR pulses.

The nuclear spin diffusion due to dipole-dipole interactions with rate $\gamma_{DD} \sim 60\mathrm{ms}^{-1}$ leads to a decay of the coherences which form the dark states [25]. Active corrections can be performed with NMR pulse sequences that average the dipole-dipole Hamiltonian, such as WaHuHa, improving the error rate to $\tau^2_{whh}\gamma^3_{DD}$ [26, 27]. After correction dark state coherences could have lifetimes on the order of 0.1-1s for moderate cycle times τ_{whh}. Quadrupolar terms due to inhomogeneous strain can cause additional differential phase evolution of different nuclear spins. However, this type of phase inhomogeneity leads to an error second order in the interaction which is negligible ($\sim 10^{-7}$ per cycle of computation).

The errors of manipulation of single electron spins in quantum dots via microwave or optical fields have been considered in detail elsewhere [8, 9, 13, 15], and only the relevant results are quoted here. Electron spin decoherence will most likely be limited by different Overhauser shifts corresponding to different detunings, with error going as $p \simeq (\sigma_\delta/\Omega_{\mathrm{ESR}})^2$; fast ESR ($\sim 6\mathrm{ns}^{-1}$) will mitigate this effect; with optical fields, even faster effective Rabi-oscillations are predicted ($\Omega_{\mathrm{opt,ESR}} \sim 50\mathrm{ns}^{-1}$) with errors then limited by spontaneous emission to $\sim 10^{-3}$. As for measurement, the fundamental limit will be set by relaxation of the electron spin, which has a time scale $\Gamma^{-1} \sim$ 0.1-10ms, based on recent measurements of the spin relaxation time [14, 29].

Moving individual electron spins over short distances incurs phase errors due to uncertainty in the local nuclear field of the transport channel. The error induced by randomly oriented nuclei during transit can be estimated by the time-averaged hyperfine field the electron wavepacket encounters over the whole process, $A/\sqrt{nLhl}$, where n is the density of lattice nuclei, L is the length of the channel, and hl is the transverse area of the channel. For a 50nm wide, 10nm high channel, and a quantum dot separation of 1μm, the expected dephasing probability due to thermal nuclei is $\simeq 5\times 10^{-5}$ for a 3ns transfer time.

We consider three materials with demonstrated electronic and optical quantum dots (GaAs, $N = 10^5$; InAs, $N = 10^{4.6}$; CdSe, $N = 10^4$). The expected error of a two-qubit gate operation, defined as $\mathrm{Tr}[U_{\mathrm{perfect}}U^\dagger_{\mathrm{actual}}]/4$, where U_{perfect} is given by Eqn. 6, is plotted in Fig. 3. As the error is dominated by detuning error, it is material independent, and is a few percent at 95% polarizations.

To combat these errors, a series of measurements may be made to determine the effective detuning of the system better than the thermal mixture limit σ_δ. This can

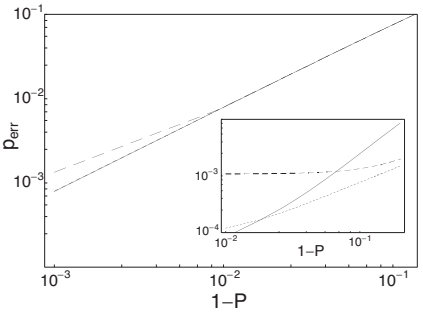

FIG. 3: For a cooled dark state density matrix (c.f. [6]), expected error for a controlled-phase operation between electron spin and nuclear spin as a function of polarization (CdSe: solid, InAs: dotted, GaAs: dashed; in the main figure, CdSe and InAs are indistinguishable). Inset shows effects of narrowing by a factor of 10 for different materials.

be done *e.g.* by a measurement made with the single electron in the quantum dot, in direct analogy to single ion Ramsey interferometry in atomic clocks [30]; the distribution is then narrowed, with $\tilde{\sigma}_\delta \simeq \sigma_\delta/\sqrt{n}$, where n is the number of measurements. An improvement in the uncertainty of the mixture's detuning of a factor of 10 yields high fidelity operation, as shown in the inset to Fig. 3 [31]. Smaller dots produce better results at higher polarizations due to their greater coupling strengths. The limits for GaAs are due to the large species inhomogeneity and the incommensurate requirement of sufficient magnetic field to perform effective coherent averaging of dipole-dipole interactions. Low species inhomogeneity allows for higher magnetic field, faster WaHuHa-type correction sequences, and fewer errors in the transfer operation. This would be the case for quantum dots defined in nanotubes with isotopically enhanced ^{13}C or in CdSe quantum dots. Materials with low spin-orbit interaction will also reduce electron spin dephasing.

In conclusion, we have detailed a scheme for quantum information processing using dynamically defined qubits composed of collective excitations of nuclear spins in a quantum dot. For small dots with near-homogeneous Zeeman splittings (e.g. CdSe, InAs) large but finite polarization (95%) is already sufficient to reach an error rate in two-qubit operations of order a few percent. Given the suppression of dipolar diffusion in lithographically isolated structures (e.g. vertical quantum dots, nanowhiskers, self-assembled quantum dots) these polarizations may be within reach. Moderate polarizations [32] have been already achieved, and techniques to improve upon this have been considered [10]. Our calculations indicate that the dominant source of error may be mitigated through narrowing the mixture of dark states.

We gratefully acknowledge helpful conversations with A. Sørensen. The work at Harvard was supported by ARO, NSF, Alfred P. Sloan Foundation, and David and Lucile Packard Foundation. I. Cirac acknowledges DFG (SFB 631). The work at ETH was supported by Nanoscience NCCR.

[1] D. G. Cory *et al.*, Proc. Nat. Acad. Sci. USA **94**, 1634 (1997).
[2] S. L. Braunstein *et al.*, Phys. Rev. Lett. **83**, 1054 (1999).
[3] R. Schack and C. M. Caves, Phys. Rev. A **60**, 4354 (1999).
[4] B. Kane, Nature **393**, 133 (1998).
[5] J. M. Taylor *et al.*, Phys. Rev. Lett. **90**, 206803 (2003).
[6] J. M. Taylor *et al.*, Phys. Rev. Lett. **91**, 246802 (2003).
[7] M. T. Björk *et al.*, Appl. Phys. Lett. **80**, 1058 (2002).
[8] D. Loss and D. DiVincenzo, Phys. Rev. A **57**, 120 (1998).
[9] A. Imamoğlu *et al.*, Phys. Rev. Lett. **83**, 4204 (1999).
[10] A. Imamoğlu *et al.*, Phys. Rev. Lett. **91**, 017402 (2003).
[11] J. Schliemann *et al.*, J. Phys: Cond. Matter **15**, R1809 (2003).
[12] Detailed study of this analogy will be reported elsewhere; H. Christ *et al.*, in preparation.
[13] L. M. K. Vandersypen *et al.*, in *Quantum Computing and Quantum Bits in Mesoscopic Systems* (Kluwer Academic Plenum Publishers, 2002).
[14] R. Hanson *et al.*, Phys. Rev. Lett. **91**, 196802 (2003).
[15] O. Gywat *et al.*, Phys. Rev. B **69**, 205303 (2004).
[16] A. Imamoğlu, Fortschr. Phys. **48**, 987 (2000).
[17] A. M. Childs and I. L. Chuang, Phys. Rev. A **63**, 012306 (2000).
[18] J. I. Cirac *et al.*, Phys. Rev. Lett. **86**, 544 (2001).
[19] C. Cabrillo *et al.*, Phys. Rev. A **59**, 1025 (1999).
[20] J. M. Taylor *et al.*, in preparation.
[21] Both imperfect entanglement and measurement errors lead only to phase-flip errors; thus, error correcting codes optimized for such errors may yield more favorable fault-tolerant thresholds.
[22] F. T. Arecchi *et al.*, Phys. Rev. A **6**, 2211 (1972).
[23] A similar analysis shows that $\sigma_\Omega \simeq (a/\Omega_1)\sigma_\delta$ and is negligible in comparison to detuning-based errors.
[24] For a manifold based on a dark state $|\mathcal{D}(n,\beta)\rangle$ the value of $p_{\rm inhom}$ can be estimated, using Fig. 2 of Ref. [6], as $(\chi_n^2+\omega_n^2)/\Omega^2$.
[25] C. Deng and X. Hu, e-print: cond-mat/0406478
[26] J. Waugh *et al.*, Phys. Rev. Lett. **20**, 180 (1968).
[27] M. Mehring, *High Resolution NMR Spectroscopy in Solids* (Berlin: Springer-Verlag, 1976).
[28] V. N. Golovach *et al.*, (2003), cond–mat/0310655.
[29] T. Fujisawa *et al.*, Phys. Rev. B. (Rapid Comm.) **63**, 081304 (2001).
[30] S. A. Diddams *et al.*, Science, **293**, 825 (2001).
[31] This technique will be detailed elsewhere, G. Giedke *et al.*, in preparation.
[32] D. Gammon *et al.*, Phys. Rev. Lett. **86**, 5176 (2001)

PHYSICAL REVIEW B **81**, 045309 (2010)

Quantum interface between light and nuclear spins in quantum dots

Heike Schwager, J. Ignacio Cirac, and Géza Giedke
Max-Planck-Institut für Quantenoptik, Hans-Kopfermann-Str. 1, D-85748 Garching, Germany
(Received 30 September 2009; revised manuscript received 9 December 2009; published 12 January 2010)

The coherent coupling of flying photonic qubits to stationary matter-based qubits is an essential building block for quantum-communication networks. We show how such a quantum interface can be realized between a traveling-wave optical field and the polarized nuclear spins in a singly charged quantum dot strongly coupled to a high-finesse optical cavity. By adiabatically eliminating the electron a direct effective coupling is achieved. Depending on the laser field applied, interactions that enable either write-in or read-out are obtained.

DOI: 10.1103/PhysRevB.81.045309 PACS number(s): 03.67.Lx, 42.50.Ex, 78.67.Hc

I. INTRODUCTION

The coherent conversion of quantum information between mobile photonic qubits for communication and stationary material qubits for storage and data processing is an important building block of quantum networks. In atomic systems several ideas to realize such a *quantum interface* have been suggested and experimentally demonstrated in recent years (see Ref. 1 for a review). For semiconductor quantum dots (QD) proposals for interfaces in analogy to the cavity-based atomic schemes have been put forward[2,3] and major prerequisites such as strong coupling to a nanocavity[4] have been realized (see Ref. 5 for a review). Here we will show how to realize a QD-based quantum interface between the *nuclear spins* in a QD and the optical field. The read-out we propose maps the nuclear state to the output mode of the cavity directly while the write-in proceeds by deterministic creation of entanglement between the nuclear spins and the cavity output mode and subsequent teleportation. Our scheme has several attractive features: the very long nuclear-spin lifetimes make the nuclei attractive for storing quantum information[6] and the use of collective states makes it possible to map not just qubits but also multiphoton states. In addition, typical electron-spin decoherence processes will be suppressed: the major process—hyperfine interaction with the lattice nuclear spins[7]—is harnessed to achieve the desired coupling and the influence of other processes is weakened since the electronic states can be adiabatically eliminated from the dynamics. The price for this is a reduction in the speed of the mapping process and the necessity to initialize the nuclear spin ensemble in a highly polarized state. In view of the high nuclear polarization of above 80% reported recently[8] the proposed protocol enables the high-fidelity mapping between a (traveling) optical field and the nuclear spin ensemble in a realistic setup.

The paper is organized as follows: first, we introduce the system in Sec. II. In Sec. III we sketch the adiabatic elimination that yields the Hamiltonians that describe the effective coupling between light and nuclear spins (for a detailed derivation see Appendix A). Next, we explain the interface protocol in Sec. IV and finally give an example for the implementation of the protocol in Sec. V.

II. SYSTEM

We consider a self-assembled QD charged with a single conduction-band electron, whose spin-states $|\uparrow\rangle, |\downarrow\rangle$ are split in a magnetic field. For clarity we first consider a simplified model, in which both electronic states are coupled by electric dipole transitions to the same charged exciton (trion) state $|X\rangle$ in a Λ configuration, cf. Fig. 1. Note that the selection rules in QDs often make it necessary to consider more complicated level schemes. After introducing our protocol using this simplified model, we will present a setting to realize the required coupling and discuss the effect of corrections to Eq. (1) in Sec. V.

The QD is strongly coupled to a high-Q nanocavity.[4] The two transitions are, respectively, off-resonantly driven by the cavity mode (frequency ω_c) and a laser of frequency ω_l, cf. Fig. 1, described by the Hamiltonian

$$H_{\text{opt}} = \frac{\Omega_c}{2} a^\dagger |\downarrow\rangle\langle X| + \frac{\Omega_l}{2} e^{+i\omega_l t} |\uparrow\rangle\langle X| + \text{H.c.} + \omega_c a^\dagger a + \omega_X |X\rangle\langle X| + \omega_z S^z, \tag{1}$$

where $\hbar = 1$ and Ω_l, Ω_c are the Rabi frequencies of laser and cavity fields, $a^\dagger$ and a are the cavity photons, ω_X denotes the trion energy, ω_z is the Zeeman splitting of the electronic states, and $S^z = 1/2(|\uparrow\rangle\langle\uparrow| - |\downarrow\rangle\langle\downarrow|)$. In Sec. V, we discuss how to effectively realize such a three-level system in a quantum dot. A detailed discussion of cavity decay ($\ll \Omega_l, \Omega_c$) will be considered later on.

As already mentioned, in most QDs the electron spin also has a strong hyperfine interaction with $N \sim 10^4 - 10^6$ lattice nuclear spins.[7] For s-type electrons it is dominated[9] by the Fermi contact term

$$H_{\text{hf}} = \frac{A}{2}(S^+ A^- + \text{H.c.}) + A S^z A^z, \tag{2}$$

where A is the hyperfine coupling constant, $S^\pm$ are the electron-spin operators, and $A^{\pm,z} = \Sigma_j \alpha_j I_j^{\pm,z}$ are the collective

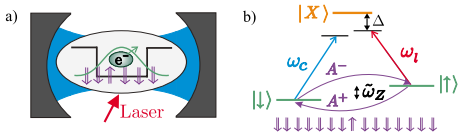

FIG. 1. (Color online) (a) Singly charged QD coupled to high-Q optical cavity. (b) Level scheme of the QD. Optical and hyperfine transitions.

 ©2010 The American Physical Society

nuclear-spin operators (we consider spin-1/2 nuclei for simplicity). The individual coupling constants α_j are proportional to the electron-wave function at site j and normalized to $\Sigma_j \alpha_j = 1$.

A prerequisite for using nuclear spins as a quantum memory is to initialize them in a highly polarized state which also satisfies $A^-|\psi_0\rangle = 0$, i.e., is decoupled from the electron in state $|\downarrow\rangle$ (dark state). Recently, nuclear polarization $P = \langle A^z\rangle/(-1/2)$ of $P > 80\%$ has been reported[8] (see also Refs. 10 and 11). The dark state condition is the natural consequence of using $H_{\rm hf}$ to polarize the nuclei[12] but has not yet been verified experimentally. It is useful to separate the large expectation value of A^z, which describes the effective magnetic field experienced by the electron spin due to the nuclei and write $A^z = \langle A^z\rangle_{\psi_0} + \delta A^z$. Henceforth we include the first term in $H_{\rm opt}$ by introducing $\tilde{\omega}_z = \omega_z + A\langle A^z\rangle_{\psi_0}$.

In the high-polarization regime $1 - P \ll 1$ a very convenient *bosonic description* for the nuclear spins becomes available: all excitations out of the fully polarized state and, in particular, the collective spin operator A^+ are approximated by bosonic creation operators applied to the N-mode vacuum state.[13,14] Replacing $A^- \to (\Sigma_j \alpha_j^2)^{1/2} b$ and $A^z \to (-\frac{1}{2} + \frac{1}{N} b^\dagger b)$, Eq. (2) reads (small corrections omitted in these replacements are discussed in Appendix B)

$$\tilde{H}_{\rm hf} = \frac{g_n}{2}(b^\dagger S^- + S^+ b) + \frac{A}{N} S^z \left(b^\dagger b - \frac{N}{2} \right), \tag{3}$$

where $g_n = A\sqrt{\Sigma_j \alpha_j^2}$. The expression $N_1 = (\Sigma_j \alpha_j^2)^{-1}$ can be seen as the effective number of nuclear spins to which the electron couples. In the homogeneous case $\alpha_j = \text{const}$ we have $N_1 = N$. Neglecting very weakly coupled nuclei we have $N_1 \approx N$ and we will just use N in the following.

The bosonic description emphasizes the relation to quantum optical schemes, gives access to the toolbox for Gaussian states and operations and allows a more transparent treatment of the corrections to the ideal Jaynes-Cummings-type coupling of Eq. (3); we will make use of this description later on.

III. COUPLING CAVITY AND NUCLEAR SPINS

Our aim is to obtain from $H = H_{\rm opt} + H_{\rm hf}$ a direct coupling between nuclear spins and light. The Hamiltonian H describes a complicated coupled dynamics of cavity, nuclei, and quantum dot. Instead of making use of the full Hamiltonian (and deriving the desired mapping, e.g., in the framework of optimal control theory) we aim for a simpler, more transparent approach. To this end, we adiabatically eliminate[15] the trion and the electronic degrees of freedom, which leads to a Hamiltonian H_{el} that describes a direct coupling between nuclear spins and light. As explained later, this can be achieved if the couplings (the Rabi frequency of the laser/cavity, the hyperfine coupling, respectively) are much weaker than the detunings to the corresponding transition:

$$\Delta' \gg \Omega_l, \Omega_c\sqrt{n}, \tag{4a}$$

$$\sqrt{\Delta' \tilde{\omega}_z} \gg \Omega_l, \Omega_c\sqrt{n}, \tag{4b}$$

$$\tilde{\omega}_z \gg g_n\sqrt{m}. \tag{4c}$$

Here, $\Delta' = \omega_X - \omega_l + \tilde{\omega}_z/2$ is the detuning, n is the number of cavity photons, and m is the number of nuclear excitations. Note that typically $\tilde{\omega}_z < \Delta'$ such that condition (4a) becomes redundant. In addition to Eqs. (4a)–(4c), we choose the adjustable parameters such that all first-order and second-order processes described by H are off-resonant but the (third-order) process in which a photon is scattered from the laser into the cavity while a nuclear spin is flipped down (and its converse) is resonant. This leads to the desired effective interaction.

The idea of adiabatic elimination is to perturbatively approximate a given Hamiltonian by removing a subspace from the description that is populated only with a very low probability due to chosen initial conditions and detunings or fast decay processes. If initially unpopulated states (in our case the trion state $|X\rangle$ and the electronic spin-up state $|\uparrow\rangle$) are only weakly coupled to the initially occupied states, they remain essentially unpopulated during the time evolution of the system and can be eliminated from the description. The higher-order transitions via the eliminated levels appear as additional energy shifts and couplings in the effective Hamiltonian on the lower-dimensional subspace.

The starting point is the Hamiltonian $H = H_{\rm opt} + H_{\rm hf}$ given by Eqs. (1) and (2). In order to get a time-independent Hamiltonian, we go to a frame rotating with $U^\dagger = \exp[-i\omega_l t(a^\dagger a + |X\rangle\langle X|)]$

$$H' = \frac{\Omega_c}{2}(a^\dagger|\downarrow\rangle\langle X| + \text{H.c.}) + \frac{\Omega_l}{2}(|\uparrow\rangle\langle X| + \text{H.c.}) + \delta a^\dagger a + \tilde{\omega}_z S^z + \frac{A}{2}(A^+S^- + S^+A^-) + AS^z\delta A^z + \Delta|X\rangle\langle X| \tag{5}$$

with detunings $\Delta = \omega_X - \omega_l$ and $\delta = \omega_c - \omega_l$.

Choosing the cavity and laser frequencies, ω_c and ω_l, far detuned from the exciton transition and the splitting of the electronic states $\tilde{\omega}_z$ much larger than the hyperfine coupling g_n, such that conditions (4a)–(4c) are fulfilled, we can adiabatically eliminate the states $|X\rangle$ and $|\uparrow\rangle$. A detailed derivation of the adiabatic elimination can be found in Appendix A. It yields a Hamiltonian that describes an effective coupling between light and nuclear spins

$$H_{el} = \frac{\Omega_c\Omega_l A}{8\Delta'\tilde{\omega}_z}(aA^+ + \text{H.c.}) + \omega_1 a^\dagger a - \frac{A}{2}\delta A^z - \frac{A^2}{4\tilde{\omega}_z}A^+A^- + T_{nl}, \tag{6}$$

where the energy of the photons $\omega_1 = \delta - \frac{\Omega_c^2}{4\Delta'}$ and the energy of the nuclear spin excitations $\sim -\frac{A}{2N} - \frac{A^2}{4N\tilde{\omega}_z}$. By T_{nl} we denote the nonlinear terms $T_{nl} = \frac{A^3}{8\tilde{\omega}_z^2}A^+\delta A^z A^- + \frac{A^2}{4\tilde{\omega}_z^2}\delta a^\dagger a A^+ A^- + \frac{\Omega_c^2\delta}{4\Delta'^2}a^\dagger a^\dagger a a$, which are small ($\|T_{nl}\| \ll \frac{\Omega_c\Omega_l A}{8\Delta'\tilde{\omega}_z}$) in the situation we consider ($\delta \ll \Omega_c, g_n/\tilde{\omega}_z \sim \Omega_l/\Delta' \ll 1$) and neglected in the following. In the bosonic description of the nuclear spins that we introduced in Eq. (3) the Hamiltonian given by Eq. (6) then reads

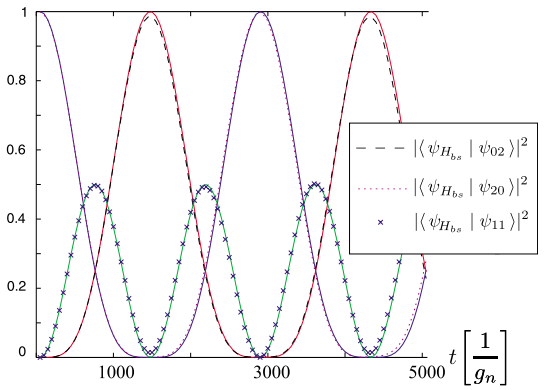

FIG. 2. (Color online) Evolution of the two-photon Fock state ψ_{20} under the full Hamiltonian H' (solid lines) and Hamiltonian H_{bs} ($\times$, dashed and dotted lines), where the trion and the electronic spin-up state have been eliminated.

$$H_{\mathrm{bs}} = g(ab^\dagger + \mathrm{H.c.}) + \omega_1 a^\dagger a + \omega_2 b^\dagger b \tag{7}$$

with coupling strength g given by

$$g = \frac{\Omega_c \Omega_l g_n}{8\Delta' \tilde{\omega}_z}. \tag{8}$$

The energy of the nuclear-spin excitations can now be written as $\omega_2 = -\frac{A}{2N} - \frac{g_n^2}{4\tilde{\omega}_z}$. For resonant exchange of excitations between the two systems, we choose $\omega_1 = \omega_2$. Then H_{bs} describes a beamsplitterlike coupling of the modes a and b. Processes in which absorption (or emission) of a cavity photon is accompanied by a nuclear spin flip are resonant and we have thus derived the desired effective interaction between light and nuclear spins. Since $\sqrt{\Omega_c \Omega_l/(\Delta' \tilde{\omega}_z)} \ll 1$ the effective coupling g is typically two to three orders of magnitude smaller than the hyperfine coupling g_n.

To illustrate the validity of the adiabatic elimination and the approximations leading to Eq. (7), we have simulated the evolution of the two-photon Fock state ψ_{20} (the first subscript denotes the number of photons and the second denotes the number of nuclear-spin excitations) under the full Hamiltonian H' given by Eq. (5) and compared it to the evolution under the Hamiltonian H_{bs} given by Eq. (7). We assume full nuclear spin-down polarization and the validity of the bosonic description. In the simulation, we choose $\Omega_l = \Omega_c$, $\Omega_l/\Delta = 1/10$, $\Omega_l^2/(\Delta \tilde{\omega}_z) = 1/100$, and $g_n/\tilde{\omega}_z = 1/50$, such that the conditions given by Eqs. (4a)–(4c) are fulfilled. Figure 2 shows, that H' is well approximated by H_{bs}, and that the nonlinear terms T_{nl} can be neglected. Almost perfect Rabi oscillations between the two-photon Fock state ψ_{20} and the state with two nuclear-spin excitations ψ_{02} can be seen in Fig. 2. For ψ_{01}, the adiabatic elimination is an even better approximation to the full Hamiltonian as the nonlinear terms T_{nl} and the conditions (4a)–(4c) depend on the excitation number.

In the process leading to the beamsplitter coupling, a photon is scattered from the cavity into the laser mode while a nuclear-spin excitation is created (and vice versa). If we interchange the role of laser and cavity field (i.e., the laser drives the $|\downarrow\rangle \leftrightarrow |X\rangle$ transition and the cavity couples to $|\uparrow\rangle$) then creation of a nuclear-spin excitation is accompanied by scattering of a laser photon *into* the cavity, i.e., the effective coupling becomes $a^\dagger b^\dagger + ab$. Tuning the energies such that $\omega_1 = -\omega_2$, the driving laser now facilitates the *joint* creation (or annihilation) of a spin excitation and a cavity photon, realizing a two-mode squeezing effective Hamiltonian

$$H_{\mathrm{sq}} = g(a^\dagger b^\dagger + ab) + \omega_1 a^\dagger a + \omega_2 b^\dagger b. \tag{9}$$

Here, the energy of the photons is $\omega_1 = \delta(1 + \frac{\Omega_c^2}{4\Delta'^2})$, the energy of the nuclear-spin excitations is $\omega_2 = -\frac{A}{2N} - \frac{g_n^2}{4\tilde{\omega}_z}$, and the nonlinear terms are now given by $T_{nl} = \frac{g_n^2}{4\tilde{\omega}_z^2}\frac{A}{2N} b^\dagger b^\dagger b b + \frac{g_n^2}{4\tilde{\omega}_z^2}\delta a^\dagger a b^\dagger b$. As before, they are much smaller than g and can be neglected for low excitation number. To be able to freely switch between H_{bs} and H_{sq} simply by turning on and off the appropriate lasers, both the "driven" and the empty mode should be supported by the cavity.

IV. QUANTUM INTERFACE

Now the obvious route to a quantum interface is via the Hamiltonian H_{bs}: acting for a time $t = \pi/g$ it maps $a \to ib$ and $b \to ia$ thus realizing (up to a phase) a swap gate between cavity and nuclear spins. This and related ideas are explored in Ref. 16. There are two problems with this approach: compared to the effective coupling, present-day cavities are "bad" with cavity lifetime $\tau_{\mathrm{cavity}} \ll 1/g$, i.e., the cavity field will decay before its state can be mapped to the nuclei. Moreover, it is notoriously difficult to couple quantum information into high-Q cavities, despite proposals[17] that address this issue. Both problems can be circumvented for our system by two key ideas: (i) to include the field modes into which the cavity decays in the description and (ii) to realize write-in via quantum teleportation. Moreover, read-out can be realized with similar techniques. In the following, we assume that all the light leaving the cavity can be collected and accessed optically. The combination of strong coupling and high collection efficiency has not yet been demonstrated for solid-state cavities, although there is remarkable progress toward that goal.[18]

Let us first consider the more complicated part, write-in. In the first step, the squeezing Hamiltonian H_{sq} (assisted by cavity decay) generates a strongly entangled two-mode squeezed state (TMSS) between the nuclear spins and the traveling-wave *output field* of the cavity. Then quantum teleportation[19] is used to deterministically write the state of another traveling-wave light field onto the nuclear mode. Similarly, H_{bs} can be used for read-out, by writing the state of the nuclei to the output field.

Let us now consider H_{sq} and quantitatively derive the entangled state and discuss the quality of the interface it provides. The Langevin equation of cavity and nuclear operators is (for $t \geq 0$)

$$\dot{a}(t) = -igb(t)^\dagger - \frac{\gamma}{2}a - \sqrt{\gamma}c_{\mathrm{in}}(t),$$

$$\dot{b}(t) = -igа(t)^\dagger, \tag{10}$$

where we have specialized to the case $\omega_1=-\omega_2$, transformed to an interaction picture with $H_0=\omega_1(a^\dagger a-b^\dagger b)$, and performed the rotating-wave and Markov approximations in the description of the cavity decay.[20] Here, $c_{\rm in}$ describes the vacuum noise coupled into the cavity and satisfies $[c_{\rm in}(t),c_{\rm in}^\dagger(t')]=\delta(t-t')$. Integrating Eqs. (10), we get

$$a(t) = \alpha_1^-(t)a + \alpha_2(t)b^\dagger + \sqrt{\gamma}\int_0^t \alpha_1^-(t-\tau)c_{\rm in}(\tau)d\tau,$$

$$b(t) = \alpha_2(t)a^\dagger + \alpha_1^+(t)b + \sqrt{\gamma}\int^t \alpha_2(t-\tau)c_{\rm in}^\dagger(\tau)d\tau, \tag{11}$$

where $\alpha_1^\pm(t)=e^{-\gamma t/4}[\cosh(\nu t)\pm\gamma/(4\nu)\sinh(\nu t)]$, $\alpha_2(t)=-ig/\nu e^{-\gamma t/4}\sinh(\nu t)$, and $\nu=\sqrt{(\gamma/4)^2+g^2}$; and $a,b\equiv a(0),b(0)$ in this equation. It may be remarked here that the analogous equations with $H_{\rm bs}$ instead of $H_{\rm sq}$ lead to almost identical solutions: now $a(t)$ is coupled to $b(t)$ instead of $b^\dagger(t)$ and the only other change to Eq. (11) is to replace ν by $\tilde{\nu}=\sqrt{(\gamma/4)^2-g^2}$.

While Eq. (11) describes a nonunitary time evolution of the open cavity-nuclei system, the overall dynamics of system plus surrounding free field is unitary. It is also Gaussian since all involved Hamiltonians are quadratic. Since all initial states are Gaussian as well the joint state of cavity, nuclei, and output field is a pure Gaussian state at any time. This simplifies the analysis of the dynamics and, in particular, the entanglement properties significantly: for pure states, the entanglement of one subsystem (e.g., the nuclei) with the rest is given by the entropy of the reduced state of the subsystem. Gaussian states are fully characterized by the first and second moments of the field operators $R_1=(a+a^\dagger)/\sqrt{2}$ and $R_2=-i(a-a^\dagger)/\sqrt{2}$ via the covariance matrix (CM) $\Gamma_{kl}=\langle\{R_k,R_l\}\rangle-2\langle R_k\rangle\langle R_l\rangle$ (where $\{,\}$ denotes the anticommutator). The CM of the reduced state of a subsystem [e.g., $\Gamma_{\rm nuc}(t)$ for the CM of the nuclei at time t] is given by the submatrix of Γ that refers to covariances of system operators only. For a single mode, the entropy of the reduced system can be obtained from the determinant of the reduced CM and with $x(t)\equiv\det\Gamma_{\rm nuc}(t)$ we get a simple expression for the entropy (i.e., entanglement)

$$E(t) = x(t)\log_2 x(t) - [x(t)-1]\log_2[x(t)-1]. \tag{12}$$

Since the state at hand (including the output field) is pure and Gaussian it is fully determined by $x(t)$ up to local Gaussian unitaries[21]: it is locally equivalent to a TMSS $|\psi(r)\rangle=(\cosh r)^{-1}\Sigma_n(\tanh r)^n|nn\rangle$ with CM (in 2×2 block matrix form)

$$\Gamma_{\rm TMSS} = \begin{pmatrix} \cosh(2r)\mathbb{1}_2 & \sinh(2r)\sigma_z \\ \sinh(2r)\sigma_z & \cosh(2r)\mathbb{1}_2 \end{pmatrix}.$$

The squeezing parameter r is determined by $x(t)=\cosh^2(2r)$. From Eq. (11) we find that $\Gamma_{\rm nuc}(t)=\cosh[2r(t)]\mathbb{1}_2$ for all $t\geq0$, where $\cosh[r(t)]$ is given by

$$\cosh r = e^{-\gamma t/4}\left[\frac{\gamma}{2\nu}\sinh(2\nu t) + \frac{g^2+\frac{\gamma^2}{8}}{2\nu^2}\cosh(2\nu t) + \frac{g^2}{2\nu^2}\right]^{1/2} \tag{13}$$

and quantifies how strongly the nuclei are entangled with cavity and output field. After turning off the coupling g at time $t_{\rm off}$ the nuclei are stationary while the cavity decays to the vacuum. Therefore, the final entanglement of nuclei and output field at time $t-t_{\rm off}\gg1/\gamma$ is given by Eq. (12) with $x(t)=\cosh[2r(t_{\rm off})]^2$. Note that for $\gamma\gg g$, $1/t$ and keeping only the leading terms in Eq. (13), $\cosh[2r(t)]$ simplifies to $3[1-8(g/\gamma)^2]e^{4g^2/\gamma t}$, i.e., two-mode squeezing $r(t)$ grows linearly with time at rate $\sim\frac{4g^2}{\gamma}$.

In order to perform the teleportation, a Bell measurement has to be performed on the output mode of the cavity and the signal state to be teleported. This is achieved by sending the two states through a 50:50 beam splitter and measuring the output quadratures.[19] Hence the output mode of the cavity, B_0, needs to be known to properly match it with the signal mode at the beam splitter. It can be expressed as a superposition of the bath operators $c(x,t)$ as $B_0(t)=\int_{\mathbb{R}}z^0(x,t)c(x,t)dx$. By definition, the mode B_0 contains all the photons emitted from the cavity, hence all other modes $B_{k\neq0}$ (from some complete orthonormal set of modes containing B_0) are in the vacuum state. This implies $\langle B_k(t)B_l(t)\rangle\propto\delta_{k0}\delta_{l0}$, from which the mode function z^0 can be determined as

$$z^0(x,t) = \alpha_2(t-x)/\sqrt{\int_{\mathbb{R}}|\alpha_2(t-x)|^2dx}. \tag{14}$$

The procedure for write-in then is: let $H_{\rm sq}$ act for a time t_1 to create the TMSS $\psi[r(t_1)]$ of the nuclei entangled with cavity and output field. To obtain a state in which the nuclei are only entangled to the output field, we switch the driving laser off ($g=0$) and let the cavity decay for a time $t_2\gg\tau_{\rm cav}$, obtaining an (almost) pure TMSS of the nuclei and the output mode, which is used for quantum teleportation. Teleportation maps the state faithfully up to a random displacement d, which depends on the measurement result. This can be undone with the help of $H_{\rm bs}$ (Ref. 16) to complete the write-in.

The read-out step follows identical lines, except that $H_{\rm sq}$ is replaced by $H_{\rm bs}$ and no teleportation is necessary since the state of the nuclei is directly mapped to the output mode of the cavity; for more details see Ref. 16.

As mentioned, we assume that all light that leaves the cavity can be collected and further processed. Losses could be modeled by mixing the outgoing light with yet another vacuum and tracing over the latter. Considering a fully decayed cavity, the reduced state of nuclei and output mode is now mixed but still entangled (unless the losses are $f=100\%$). Whether or not the state still allows for better-than classical teleportation depends on f and r. For example, for $r=1$ even at losses of 40%, $F_{\rm tel}>0.7$ (and >0.5 even at 75% loss). Note, however, that our read-out scheme is much less tolerant of losses.

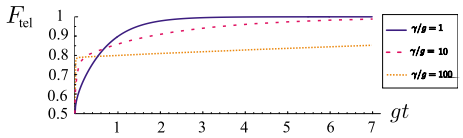

FIG. 3. (Color online) Average fidelity for the mapping of coherent states to the nuclei via teleportation (after complete decay of the cavity) plotted as a function of the interaction time $t_{\rm off}$ for different values of $g/\gamma=1$, 10, and 100 (solid, dash-dotted, and dashed). All fidelities converge to 1 as $gt\to\infty$.

The fidelity with which a quantum state can be teleported onto the nuclei using the protocol[19] is a monotonic function of the two-mode squeezing parameter $r(t_{\rm off})$. A typical benchmark[22] is the average fidelity F with which an arbitrary coherent state can be mapped. For $F\geq 2/3$ the quantum channel given by teleportation has a positive quantum capacity. If a TMSS is used for teleportation, F has a simple dependence on the squeezing parameter[23] and is given by $F(r)=1/(1+e^{-2r})$. Thus, if our system parameters g, γ, and the interaction time $t=t_{\rm off}$ lead to $\cosh[2r(t_{\rm off})]$ we have an interface that provides a write-in fidelity $F[r(t_{\rm off})]$, cf. Fig. 3. The fidelity for other subsets of states (including, e.g., finite dimensional subspaces) can be computed from the coherent state fidelity.[24] Already for $r(t_{\rm off})\sim 1$ fidelities above 0.8 are obtained. As seen from Fig. 3 this is achieved for $gt_{\rm off}\lesssim 5$ even for strong decay. After switching off the coupling we have to wait for the cavity to decay. Since typically $\gamma\gg g$ this does not noticeably prolong the protocol.

V. IMPLEMENTATION

Quantum dots generally have a richer level structure than the Λ scheme depicted in Fig. 1. This and the applicable selection rules imply that $H_{\rm opt}$ is not exactly realized. In this section we take this into account and discuss a setting that allows to realize the desired coupling.

We now consider the two spin states $|\Downarrow\rangle, |\Uparrow\rangle$ of the trion in addition to the two electronic-spin states. We focus on a setup where these states are Zeeman split by an external magnetic field in growth/z direction (Faraday geometry). The electronic state $|\uparrow\rangle$ is coupled to $|\Uparrow\rangle$ (with angular momentum $+3/2$) by σ^+ circularly polarized light (and $|\downarrow\rangle$ to $|\Downarrow\rangle$ with σ^--polarized light). We can stimulate these transitions by a σ^--polarized cavity field and a σ^+-polarized classical laser field, respectively, but this will not lead to a Λ scheme, cf. Fig. 4(a). The cleanest way to obtain the desired coupling is to mix the trion states with a resonant microwave field. The electronic eigenstates are unchanged (being far detuned from the microwave frequency) and are now both coupled to the new trion eigenstates $|-\rangle=1/\sqrt{2}(|\Uparrow\rangle-|\Downarrow\rangle)$ and $|+\rangle=1/\sqrt{2}(|\Uparrow\rangle+|\Downarrow\rangle)$, see Fig. 4(b) in a double Λ system.

There are other ways to couple both ground states to the same excited state, e.g., taking advantage of weakened selection rules (due to heavy-hole/light-hole mixing or an in-plane magnetic field) or using linearly polarized light (also in an in-plane magnetic field, i.e., Voigt geometry). They avoid the need of an additional microwave field at the expense of additional couplings (which have to be kept off-resonant) and are explored further in Ref. 16.

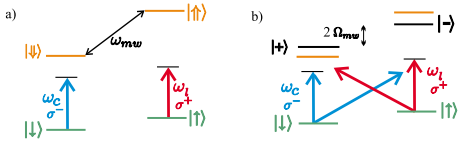

FIG. 4. (Color online) Level scheme of the QD (a) electronic and trion states split in an external magnetic field in growth direction. They are coupled by a σ^--polarized laser and a σ^+-polarized cavity field with frequencies ω_l and ω_c, respectively. (b) Additional to the setting in (a), a microwave field resonant with the splitting of the trion states in the magnetic field ($\omega_{\Uparrow}-\omega_{\Downarrow}=\omega_{mw}$) mixes the trion states. Laser and cavity couple both electronic states to the trion states $|+\rangle$ and $|-\rangle$.

The Hamiltonian of the system is now given by

$$H=\frac{\Omega_c}{2}a^\dagger|\downarrow\rangle\langle\Downarrow|+\frac{\Omega_l}{2}e^{i\omega_l t}|\uparrow\rangle\langle\Uparrow|+\Omega_{mw}e^{i\omega_{mw}t}|\Downarrow\rangle\langle\Uparrow|$$
$$+\text{H.c.}+\omega_c a^\dagger a+\omega_{\Uparrow}|\Uparrow\rangle\langle\Uparrow|+\omega_{\Downarrow}|\Downarrow\rangle\langle\Downarrow|+\tilde{\omega}_z S^z+H_{\rm hf}, \tag{15}$$

where $\omega_{\Uparrow},\omega_{\Downarrow}=\omega_X\pm\omega_{zh}/2$ include the hole Zeeman splitting $\omega_{zh}=\omega_{mw}$ and $H_{\rm hf}$ is given by Eq. (2). In a frame rotating with

$$U^\dagger=\exp[-i(\omega_{mw}+\omega_l)t(|\Uparrow\rangle\langle\Uparrow|+a^\dagger a)-i\omega_l t|\Downarrow\rangle\langle\Downarrow|)]$$

the Hamiltonian reads

$$H=\frac{\Omega_c}{2\sqrt{2}}(a^\dagger|\downarrow\rangle\langle+|-a^\dagger|\downarrow\rangle\langle-|)+\frac{\Omega_l}{2\sqrt{2}}(|\uparrow\rangle\langle+|+|\uparrow\rangle\langle-|)$$
$$+\delta' a^\dagger a+\Delta_+|+\rangle\langle+|+\Delta_-|-\rangle\langle-|+\tilde{\omega}_z S^z+H_{\rm hf}, \tag{16}$$

where $\delta'=\omega_c-\omega_l-\omega_{mw}$ and $\Delta_\pm=\omega_{\Downarrow}-\omega_l\pm\Omega_{mw}$. We adiabatically eliminate $|\pm\rangle$ and $|\uparrow\rangle$ as explained in Sec. III and Appendix A. This yields

$$H_{el}=g'(aA^+ +\text{H.c.})+\omega_1' a^\dagger a-\frac{A}{2}\delta A^z-\frac{A^2}{4\tilde{\omega}_z}A^+A^-+T_{nl}', \tag{17}$$

which is of exactly the same form as the Hamiltonian of our toy model given by Eq. (6), and differs only by the replacements $\Delta'^{-1}\to\frac{1}{2}(\Delta_+'^{-1}-\Delta_-'^{-1})$ in the coupling, $\Delta'^{-1}\to\frac{1}{2}(\Delta_+'^{-1}+\Delta_-'^{-1})$ in the nuclear energy and $\Delta'^{-2}\to\frac{1}{2}(\Delta_+'^{-2}+\Delta_-'^{-2})$ in the nonlinear terms. As before, the nonlinear terms T_{nl}' are small and are neglected in the following. Using the bosonic description, we then obtain again a beam splitter Hamiltonian Eq. (7), where the coupling is now given by

$$g'=\frac{\Omega_c\Omega_l g_n}{16\tilde{\omega}_z}\left(\frac{1}{\Delta_+'}-\frac{1}{\Delta_-'}\right) \tag{18}$$

with $\Delta_\pm'=\Delta_\pm+\frac{\tilde{\omega}_z}{2}$. Compared to Eq. (8) the effective coupling g is reduced by a factor $\Delta'(\Delta_+'^{-1}-\Delta_-'^{-1})$, i.e., $\approx 2\Omega_{mw}/\Delta'$ for $\Omega_{mw}\ll\Delta'$.

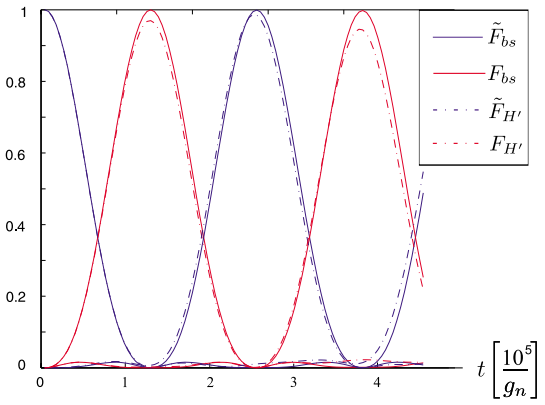

FIG. 5. (Color online) Performance of the quantum interface for the maximally entangled input state $\psi_{in} \propto \Sigma_{k=1}^{2} |k\rangle_R |k\rangle_c$ (subscript c indicates the cavity). The red solid curve shows the fidelity F_{bs} of ψ_{in} evolved under H_{bs} with the ideal target state $|\psi_{map}\rangle \propto \Sigma_{k=1}^{2} (-1)^{lk} (i)^k |k\rangle_R |k\rangle_n$ (subscript n indicates the nuclei) for $gt \in [l\pi, (l+1)\pi]$, where l takes into account the phases acquired during mapping, see text. The blue solid curve shows the fidelity $\tilde{F}_{\mathrm{bs}}$ with $|\tilde{\psi}_{map}\rangle \propto \Sigma_{k=1}^{2} (-1)^{lk} |k\rangle_R |k\rangle_c$ for $gt \in [\frac{2l+1}{2}\pi, \frac{2l+3}{2}\pi]$. Dashed curves depict the same fidelities for evolution under H' (denoted by $F_{H'}/\tilde{F}_{H'}$). (Parameters chosen as in the text.)

To illustrate that H_{el}, in the bosonic description, which we denote by H_{bs}, provides a good approximation to H and allows to implement a good quantum interface, we consider a maximally entangled state $\Sigma_k |k\rangle_R |k\rangle_c$ of cavity and some reference system R and then use the interface to map the state of the cavity to the nuclei. If a maximally entangled state of R and nuclei is obtained, it shows that the interface is perfect for the whole subspace considered. The fidelity of the state $\mathbb{1}_R \otimes U(t) \Sigma_{k=1}^{2} |k\rangle_R |k\rangle_c |0\rangle_n$ with the maximally entangled state $\Sigma_k |k\rangle_R |0\rangle_c |k\rangle_n$ fully quantifies the quality of the interface. In Fig. 5 we plot this fidelity for the evolutions $U(t)$ generated by the two Hamiltonians H and H_{el} of Eqs. (16) and (17) to show that a high-fidelity mapping is possible with the chosen parameters and that the simple Hamiltonian H_{el} well describes the relevant dynamics. Since $U(\pi/g) a U(\pi/g)^{\dagger} = ib$ some care must be taken concerning the phases of the number state basis vectors in the nuclear spin mode $[|k\rangle_c \mapsto (i)^k |k\rangle_n]$ and different phases at $t = 3\pi/g$. For the numerical simulation, we chose the parameters as follows: the number of nuclei $N = 10^4$, the hyperfine coupling constant $A = 100$ μeV, the laser and cavity Rabi frequency $\Omega_c = \Omega_l = 6$ μeV, the detuning of the trion $\omega_X - \omega_l = 700$ μeV, the microwave Rabi frequency $\Omega_{mw} = 50$ μeV and the effective Zeeman splitting $\tilde{\omega}_z = 50$ μeV. This corresponds to ~ 4 T using an electron g factor of 0.48 (external and Overhauser field are counter aligned) and the corresponding hole Zeeman splitting $\omega_{mw} \sim 700$ μeV. With these parameters, a value of $g \sim 5 \times 10^{-5}$ μeV is obtained, leading to times of ~ 10 microseconds for an interface operation.

Throughout the discussion we have neglected the internal nuclear dynamics and corrections to the bosonic description. Nuclear dynamics is caused by direct dipole-dipole interaction and electron-mediated interaction.[7,25,26] In Ref. 16 we consider these processes in detail and show that they are negligible: the coupling of the bosonic mode b to bath modes b_k is by a factor 10^{-2} smaller than the coupling g in H_{bs} given by Eq. (18).

The bosonic description of the nuclear spin system can be introduced in a formally exact way.[13] However, to obtain the simple Jaynes-Cummings-type Hamiltonian (7) instead of Eq. (6) we have made several approximations. As discussed in more detail in Appendix B, these can lead to two types of errors, (i) an inhomogeneous broadening of ω_2 and (ii) leakage from the mode b due to inhomogeneity. High polarization reduces both effects. The broadening of ω_2 can be further reduced by an accurate determination of the Overhauser shift A^z. Reduced Overhauser variance has already been seen experimentally.[27–29] Leakage is suppressed by the energy difference of excitations in the mode b and the other modes not directly coupled to the electron[14] (cf. also the Appendix B).

Finally, sufficiently small electron and cavity decoherence must be ensured. In particular, we assume the strong coupling limit of cavity QED and neglect spontaneous emission for the whole duration of our protocol, which requires that $(\Omega_l/\Delta_{\pm})^2 \gamma_{\mathrm{spont}} 1/g \ll 1$, where γ_{spont} comprises spontaneous emission of the quantum dot into noncavity modes. With the parameters chosen above this requires $\gamma_{\mathrm{spont}} \gg 1$ μs^{-1}. Electron-spin relaxation is sufficiently slow in QDs at large Zeeman splitting ($\gtrsim 1$ ms) compared to our interaction. The effect of electron-spin dephasing processes is suppressed by elimination of the electron: they lead to an inhomogeneous broadening of g and ω_i which is small as long as the energy scale of the dephasing is small compared to the detuning $\tilde{\omega}_z$.

VI. CONCLUSION

We have shown how to realize a quantum interface between the polarized nuclear-spin ensemble in a singly charged quantum dot and a traveling optical field by engineering beam splitter and two-mode squeezer Hamiltonians coupling the collective nuclear-spin excitation and the mode of the open cavity. This indicates how to optically measure and coherently manipulate the nuclear-spin state and opens a path to include nuclear-spin memories in quantum information and communication applications. Moreover, together with a photo detector for the output mode of the cavity, the quantum-dot-cavity system provides a means to monitor nuclear-spin dynamics on a microsecond time scale and would allow to precisely study the effect of internal nuclear-spin dynamics and the corrections to the bosonic description used here.

ACKNOWLEDGMENTS

We acknowledge support by the DFG within SFB 631 and the NIM Cluster of Excellence.

APPENDIX A: ADIABATIC ELIMINATION

In this section, we give a detailed derivation of the adiabatic elimination that yields the Hamiltonian that describes the effective interaction between light and nuclei, given by

Eq. (6). The starting point is the Hamiltonian given by Eq. (5).

Choosing the cavity and laser frequencies, ω_c and ω_l, far detuned from the exciton transition and the splitting of the electronic states $\tilde{\omega}_z$ much larger than the hyperfine coupling g_n, such that conditions (4a)–(4c) are fulfilled, we can adiabatically eliminate the states $|X\rangle$ and $|\uparrow\rangle$: denote by $\mathbb{Q}=|X\rangle\langle X|+|\uparrow\rangle\langle\uparrow|$ and $\mathbb{P}\equiv\mathbb{1}-\mathbb{Q}=|\downarrow\rangle\langle\downarrow|$ the projectors on the eliminated subspace and its complement, respectively. Then the Schrödinger equation in the two subspaces reads

$$E\mathbb{P}|\Psi\rangle = \mathbb{P}H'(\mathbb{P}+\mathbb{Q})|\Psi\rangle, \tag{A1a}$$

$$E\mathbb{Q}|\Psi\rangle = \mathbb{Q}H'(\mathbb{P}+\mathbb{Q})|\Psi\rangle. \tag{A1b}$$

Our goal is to derive an approximation of the Hamiltonian in the $\mathbb{P}$ subspace which we denote by H_{el}. From Eq. (A1b) we obtain

$$\mathbb{Q}|\Psi\rangle = \frac{1}{E-\mathbb{Q}H'\mathbb{Q}}\mathbb{Q}H'\mathbb{P}|\Psi\rangle. \tag{A2}$$

Inserting Eq. (A2) into Eq. (A1a), we arrive at the (still exact) equation

$$E\mathbb{P}|\Psi\rangle = \left(\mathbb{P}H'\mathbb{P}+\mathbb{P}H'\mathbb{Q}\frac{1}{E-\mathbb{Q}H'\mathbb{Q}}\mathbb{Q}H'\mathbb{P}\right)\mathbb{P}|\Psi\rangle \tag{A3}$$

for the wave function in the electron spin-down subspace with the unknown E appearing both on the right-hand side (rhs) and the left-hand side of Eq. (A3).

Now we use that (i) the range of (unperturbed) energies in the $\mathbb{P}$ subspace is small compared to the energy difference between the $\mathbb{P}$ and $\mathbb{Q}$ subspaces and (ii) the coupling term $\mathbb{P}H'\mathbb{Q}$ is small compared to this difference, i.e.,

$$\left\|\frac{1}{E-\mathbb{Q}H'\mathbb{Q}}\mathbb{Q}H'\mathbb{P}\right\| \ll 1. \tag{A4}$$

Then the second part on the rhs of Eq. (A3) is small and E can be approximated by E^0, an eigenvalue of $\mathbb{P}H'\mathbb{P}=-(\frac{\tilde{\omega}_z}{2}+\frac{A}{2}\delta A^z-\delta a^\dagger a)|\downarrow\rangle\langle\downarrow|$, which is here given by $E^0\approx-\tilde{\omega}_z/2$. Since for our purposes the energy of the nuclear excitations $[\sim g_n^2/(4\tilde{\omega}_z)]$ and cavity photons (δ) are chosen equal and are $\ll\tilde{\omega}_z$, and $\|\frac{A}{2}\delta A^z\|$ is of order $\frac{A}{2N}$ and $\ll\tilde{\omega}_z$, condition (i) is fulfilled. Condition (ii) given by Eq. (A4) is satisfied if the conditions of Eq. (4a) hold. This yields the effective Hamiltonian in the electron-spin down subspace

$$H_{el} = \left(\mathbb{P}H'\mathbb{P}-\mathbb{P}H'\mathbb{Q}\frac{1}{\tilde{\omega}_z+\mathbb{Q}H'\mathbb{Q}}\mathbb{Q}H'\mathbb{P}\right)\mathbb{P}. \tag{A5}$$

To simplify the second term in H_{el} (the denominator is an operator containing $a,a^\dagger,A^-,A^+$), we split it into two parts: $\tilde{\omega}_z+\mathbb{Q}H'\mathbb{Q}=B_1+B_2$, where

$$B_1 = \tilde{\omega}_z|\uparrow\rangle\langle\uparrow| + (\Delta+\tilde{\omega}_z/2)|X\rangle\langle X| \tag{A6}$$

contains the energetically large part and is easy to invert and

$$B_2 = \frac{\Omega_l}{2}(|\uparrow\rangle\langle X| + \text{H.c.}) + \delta a^\dagger a\mathbb{Q} + \frac{A}{2}A^+A^-|\uparrow\rangle\langle\uparrow|. \tag{A7}$$

contains the Rabi frequency of the laser field Ω_l that couples the spin-up state and the trion and the energies of photons and nuclear spins. From the conditions in Eq. (4a) follows that the cavity field is weak and the energies of photons and nuclear spins are small compared to the energy scale given by Δ' and $\tilde{\omega}_z$, therefore

$$\left\|\frac{1}{\sqrt{B_1}}B_2\frac{1}{\sqrt{B_1}}\right\| \ll 1 \tag{A8}$$

and we can approximate the denominator of Eq. (A3) by

$$\frac{1}{B_1+B_2} \approx \frac{1}{B_1}-\frac{1}{B_1}B_2\frac{1}{B_1}. \tag{A9}$$

Thus, inserting Eq. (A9) in Eq. (A3) and assuming the conditions given by Eqs. (4a)–(4c) to be fulfilled, we can write the Hamiltonian in the electron spin-down subspace as

$$H_{el} = \mathbb{P}H'\mathbb{P}-\mathbb{P}H'\mathbb{Q}\left(\frac{1}{B_1}-\frac{1}{B_1}B_2\frac{1}{B_1}\right)\mathbb{Q}H'\mathbb{P} \tag{A10}$$

with $\mathbb{P}H'\mathbb{Q}=\frac{\Omega_c}{2}a^\dagger|\downarrow\rangle\langle X|+AA^+|\downarrow\rangle\langle\uparrow|$, which yields

$$H_{el} = \frac{\Omega_c\Omega_l A}{8\Delta'\tilde{\omega}_z}(aA^+ + \text{H.c.}) + \omega_1 a^\dagger a - \frac{A}{2}\delta A^z - \frac{A^2}{4\tilde{\omega}_z}A^+A^- + T_{nl}, \tag{A11}$$

where the energy of the photons $\omega_1=\delta-\frac{\Omega_c^2}{4\Delta'}$ and the energy of the nuclear-spin excitations $\sim-\frac{A}{2N}-\frac{A^2}{4N\tilde{\omega}_z}$. By T_{nl} we denote the nonlinear terms $T_{nl}=\frac{A^3}{8\tilde{\omega}_z^2}A^+\delta A^zA^-+\frac{A^2}{4\tilde{\omega}_z^2}\delta a^\dagger aA^+A^-+\frac{\Omega_c^2\delta}{4\Delta'^2}a^\dagger a^\dagger aa$, which are small ($\|T_{nl}\|\ll\frac{\Omega_c\Omega_lA}{8\Delta'\tilde{\omega}_z}$) in the situation we consider ($\delta\ll\Omega_c, g_n/\tilde{\omega}_z\sim\Omega_l/\Delta'\ll1$).

APPENDIX B: BOSONIC DESCRIPTION OF NUCLEAR SPINS

The description of collective spin excitations in a large, highly polarized system of N spins[30] $\sigma_j^{\pm,z}$ as bosonic excitations out of the vacuum states goes back at least to the introduction of the Holstein-Primakoff transformation.[31] If the collective spin operators involved are $A^{\pm,z}\equiv J^{\pm,z}=\Sigma_j\sigma_j^{\pm,z}$ and the system is initialized in the symmetric fully polarized state $|\downarrow\downarrow\ldots\downarrow\rangle$ then the symmetric space spanned by the Dicke states[32] $|J=N/2,m\rangle$ is never left under the action of $A^{\pm,z}$ and up to a n-dependent correction the matrix elements of J^- in the basis $|N/2,n-N/2\rangle$ coincide with the matrix elements of the bosonic annihilation operator b in the Fock basis $|n\rangle$. In fact we have

$$\langle J,n-J|J^-|J,n'-J\rangle = \sqrt{2J}\sqrt{1-\frac{n-1}{2J}}\sqrt{n}\,\delta_{n,n'-1}. \tag{B1}$$

As long as $n\ll2J$ (in the whole subspace significantly populated throughout the evolution) the factor $\Sigma_n\sqrt{1-n/(2J)}P_{|J,n-J\rangle}\approx\mathbb{1}$ and the association

$$J^+ \to \sqrt{2J}b, \tag{B2a}$$

$$|J,n-J\rangle \to |n\rangle, \tag{B2b}$$

$$J^z \to -J\mathbb{1} + b^\dagger b \tag{B2c}$$

is accurate to $o[n_{\max}/(2J)]$. To obtain a more accurate description, we can even express the factor $\Sigma_n\sqrt{1-\frac{n-1}{2J}}$ in Eq. (B1) in bosonic terms, i.e., as $\sqrt{1-b^\dagger b/(2J)}$ leading to an *exact* mapping between the spin and bosonic operators.

The intuition we are following is that this association still is useful if we are dealing with (i) *not fully polarized* systems (i.e., $2J<N$) and (ii) the collective spin operators appearing in the dynamics are *inhomogeneous*, i.e., $A^{\pm,z}=\Sigma_j\alpha_j\sigma_j^{\pm,z}$.

Let us first discuss the two issues separately. If the system is homogeneous and $J<N/2$ but known, e.g., by measuring J_z and J^2, then by Eq. (B1) compared to the fully polarized case only the parameter $2J$ has to be adapted and the bosonic description is still good as long as $n_{\max}\ll 2J$.

If J is not precisely known, we get an inhomogeneous broadening of the coupling constants appearing in front of $A^\pm$ [due to the scaling factor $\sqrt{2J}$ in Eq. (B2a)] and of the constant in Eq. (B2c).

If $A^{\pm,z}$ are inhomogeneous, the three operators no longer form a closed algebra and the dynamics cannot be restricted to the symmetric subspace even if starting from the fully polarized state. However, it is still possible to associate A^- to an annihilation operator $A^-\to(\Sigma_j\alpha_j^2)^{1/2}(1+f)b$ where the correction factor $1+f$ is close to one for highly polarized systems ($\|f\|\sim 1-P$) and depends on the excitation number not only of the mode b but also of other bosonic modes, associated with collective spin operators different from $A^\pm$. These can be introduced, e.g., by choosing a complete orthonormal set of coupling vectors $\{\vec{\alpha}^{(k)}\}$ with $\alpha^{(0)}\propto\vec{\alpha}$ and defining a complete set $\{A_k^\pm=\Sigma_j\alpha_j^{(k)}\sigma_j^\pm, k=0,\ldots,N-1\}$ of collective spin operators. We refer to the modes $b_{k\neq 0}$ as "bath modes."

Generalizing the single-mode case discussed before, an exact mapping $A_k^-\to(1+f_k)b_k$ and $A^z\to-\frac{1}{2}+\frac{1}{N}\Sigma_k b_k^\dagger b_k+C_z$ with operators f_k, C_z describing corrections to the ideal case can be obtained. It was shown in Ref. 13 that the corrections f_k, C_z are of order $1-P$ for high polarization. Thus the mapping used in our analysis of the quantum interface is correct to zeroth order in $1-P$.

Corrections to that description can be obtained by including the corrections $1-f_k$ and C_z. The analysis is simplified by the fact that coupling between the mode b and the bath modes is weak (first order in the small parameter $1-P$) and we are interested only in the mode b. Thus by the replacements[13]

$$A^- \to (\sum \alpha_j^2)^{1/2}(1-f)b, \tag{B3a}$$

$$A_k^- \to b_k, \tag{B3b}$$

$$A^z \to -\frac{1}{2} - \frac{1}{N}\sum_{k=0}^{N-1} b_k^\dagger b_k + C_z \tag{B3c}$$

with quadratic Hermitian operators $f=\Sigma_{kk'}\tilde{F}_{kk'}b_k^\dagger b_{k'}$ and $C_z=\Sigma_{k,k'}C_{kk'}b_k^\dagger b_k$ we obtain a first-order description of the dynamics of the mode b (and the electron and photons coupled to it). Here $C=U\,\mathrm{diag}(\alpha_j-1/N)U^\dagger$ and $F=(\Sigma_j\alpha_j^2)U\,\mathrm{diag}(\alpha_j^2)U^\dagger$ and U transforms from the canonical basis to $\{\vec{\alpha}^{(k)}\}$. The matrix $\tilde{F}$ is obtained from F by multiplying F_{00} by 1/2 and F_{k0}, F_{0k} by 2/3. The operators f, D have been chosen such that the commutation relations of $A^\pm$ are preserved to first order. And while $A_k^\pm, k>0$ are not as accurately preserved, this affects the dynamics of $A^{\pm,z}$ only to second order.[13]

From Eq. (6) we see that there are three main effects of the corrections: (i) inhomogeneous broadening of $\tilde{\omega}_z$ and g_n (and consequently ω_2 and g) due to the finite variance in P; (ii) inhomogeneous broadening of g due to the variance in the correction factor $1-f$; and (iii) losses of excitations from the b mode to baths modes due to inhomogeneity.

Since $\tilde{\omega}_z\gg g_n$, the broadening due to the variance in the Overhauser field is $\ll\tilde{\omega}_z$ and thus has only a small effect. Similarly, the broadening of g affects the form of the output mode z^0 [cf. Eq. (14)] but since it appears there only via the parameter $\nu=\sqrt{(\gamma/4)^2\pm g^2}$ the effect is negligible since $g\ll\gamma$. However, the effective energy of the nuclear excitations, $\omega_2=g_n^2/(4\tilde{\omega}_z)$, can be more strongly affected: e.g., a standard deviation of 10% in P translates to a 10% variation in ω_2. It must be assured that this variation is small compared to g so that the resonance condition is maintained.

Concerning leakage, the strongest term is the one arising from A^z and it is not necessarily small compared to g. However, as was pointed out in Ref. 14 the mode b is detuned from the others due to the "ac Stark shift" arising from the off-resonant interaction with the electron [the term $\sim A^2/(4\tilde{\omega}_z)A^+A^-$]. As long as this energy shift is large compared to leakage, losses are suppressed and the mode b is only coupled dispersively to the bath (via the inhomogeneous broadening). To work in that regime, $\tilde{\omega}_z$ must not be too large, i.e., external and Overhauser field should partially compensate each other while still keeping $\Omega_l\ll\sqrt{\Delta'\tilde{\omega}_z}$.

[1] H. J. Kimble, Nature (London) **453**, 1023 (2008).
[2] A. Imamoğlu, D. D. Awschalom, G. Burkard, D. P. DiVincenzo, D. Loss, M. Sherwin, and A. Small, Phys. Rev. Lett. **83**, 4204 (1999).
[3] W. Yao, R.-B. Liu, and L. J. Sham, Phys. Rev. Lett. **95**, 030504 (2005).
[4] K. Hennessy, A. Badolato, M. Winger, D. Gerace, M. Atature, S. Gulde, S. Fält, E. L. Hu, and A. Imamoğlu, Nature (London) **445**, 896 (2007).
[5] R. Hanson and D. D. Awschalom, Nature (London) **453**, 1043

(2008).
[6] J. M. Taylor, A. Imamoğlu, and M. D. Lukin, Phys. Rev. Lett. **91**, 246802 (2003).
[7] J. Schliemann, A. Khaetskii, and D. Loss, J. Phys.: Condens. Matter **15**, R1809 (2003).
[8] P. Maletinsky, Ph.D. thesis, ETH Zürich, 2008.
[9] We neglect the noncontact parts of the hyperfine interaction (Ref. 33) and other small nuclear interactions such as the nuclear Zeeman term and the interaction between the nuclear spins.
[10] A. S. Bracker, E. A. Stinaff, D. Gammon, M. E. Ware, J. G. Tischler, A. Shabaev, A. L. Efros, D. Park, D. Gershoni, V. L. Korenev, and I. A. Merkulov, Phys. Rev. Lett. **94**, 047402 (2005).
[11] J. Skiba-Szymanska, E. A. Chekhovich, A. V. Nikolaenko, A. I. Tartakovskii, M. N. Makhonin, I. Drouzas, M. S. Skolnick, and A. B. Krysa, Phys. Rev. B **77**, 165338 (2008).
[12] A. Imamoğlu, E. Knill, L. Tian, and P. Zoller, Phys. Rev. Lett. **91**, 017402 (2003).
[13] H. Christ, Ph.D. thesis, TU München, 2008.
[14] Z. Kurucz, M. W. Sørensen, J. M. Taylor, M. D. Lukin, and M. Fleischhauer, Phys. Rev. Lett. **103**, 010502 (2009).
[15] E. Brion, L. Pedersen, and K. Mølmer, J. Phys. A: Math. Theor. **40**, 1033 (2007).
[16] H. Schwager, J. I. Cirac, and G. Giedke, arXiv:0903.1727 (unpublished).
[17] J. I. Cirac, P. Zoller, H. J. Kimble, and H. Mabuchi, Phys. Rev. Lett. **78**, 3221 (1997).
[18] M. Toishi, D. Englund, A. Faraon, and J. Vuckovic, Opt. Express **17**, 14618 (2009).
[19] S. L. Braunstein and H. J. Kimble, Phys. Rev. Lett. **80**, 869 (1998).
[20] C. W. Gardiner and P. Zoller, *Quantum Noise*, 2nd ed. (Springer-Verlag, Berlin, 2000).
[21] G. Giedke, J. Eisert, J. I. Cirac, and M. B. Plenio, Quantum Inf. Comput. **3** (3), 211 (2003).
[22] K. Hammerer, M. M. Wolf, E. S. Polzik, and J. I. Cirac, Phys. Rev. Lett. **94**, 150503 (2005).
[23] J. Fiurášek, Phys. Rev. A **66**, 012304 (2002).
[24] K. Hammerer, E. S. Polzik, and J. I. Cirac, Phys. Rev. A **74**, 064301 (2006).
[25] W. Yao, R.-B. Liu, and L. J. Sham, Phys. Rev. B **74**, 195301 (2006).
[26] W. M. Witzel and S. Das Sarma, Phys. Rev. B **74**, 035322 (2006).
[27] A. Greilich, A. Shabaev, D. R. Yakovlev, A. L. Efros, I. A. Yugova, D. Reuter, A. D. Wieck, and M. Bayer, Science **317**, 1896 (2007).
[28] X. Xu, W. Yao, B. Sun, D. G. Steel, A. S. Bracker, D. Gammon, and L. J. Sham, Nature (London) **459**, 1105 (2009).
[29] C. Latta, A. Högele, Y. Zhao, A. N. Vamivakas, P. Maletinsky, M. Kroner, J. Dreiser, I. Carusotto, A. Badolato, D. Schuh, W. Wegscheider, M. Atature, and A. Imamoğlu, Nat. Phys. **5**, 758 (2009).
[30] The *relevant* number N of nuclei coupled to the electron is obtained by neglecting all very weakly coupled nuclei. For typical choices of the electron-wave function it is on the order of $N_1 = (\Sigma_j \alpha_j^2)^{-1}$, which can be determined experimentally by measuring the variance of A^z in the fully depolarized state.
[31] T. Holstein and H. Primakoff, Phys. Rev. **58**, 1098 (1940).
[32] F. T. Arecchi, E. Courtens, R. Gilmore, and H. Thomas, Phys. Rev. A **6**, 2211 (1972).
[33] J. Fischer, M. Trif, W. A. Coish, and D. Loss, Solid State Commun. **149**, 1443 (2009).

New Journal of Physics
The open-access journal for physics

Interfacing nuclear spins in quantum dots to a cavity or traveling-wave fields

Heike Schwager[1], **J Ignacio Cirac and Géza Giedke**
Max-Planck-Institut für Quantenoptik, D-85748 Garching, Germany
E-mail: heike.schwager@mpq.mpg.de

New Journal of Physics **12** (2010) 043026 (36pp)
Received 19 November 2009
Published 13 April 2010
Online at http://www.njp.org/
doi:10.1088/1367-2630/12/4/043026

Abstract. In this paper, we show how to realize a quantum interface between optical fields and the polarized nuclear spins in a singly charged quantum dot, which is strongly coupled to a high-finesse optical cavity. Effective direct coupling between cavity and nuclear spins is obtained by adiabatically eliminating the (far detuned) excitonic and electronic states.

The requirements for mapping qubit and continuous variable states of cavity or traveling-wave fields to the collective nuclear spin are investigated: for cavity fields, we consider adiabatic passage processes to transfer the states. It is seen that a significant improvement in cavity lifetimes beyond present-day technology would be required for a quantum interface. We then turn to a scheme that couples the nuclei to the output field of the cavity and does not require a long-lived cavity. We show that the lifetimes reported in the literature and the recently achieved nuclear polarization of $\sim 90\%$ allow both high-fidelity read-out and write-in of quantum information between the nuclear spins and the output field.

We discuss the performance of the scheme and provide a convenient description of the dipolar dynamics of the nuclei for highly polarized spins, demonstrating that this process does not affect the performance of our protocol.

[1] Author to whom any correspondence should be addressed.

© IOP Publishing Ltd and Deutsche Physikalische Gesellschaft

Contents

1. Introduction

An important milestone on the path to quantum computation and quantum communication networks is the coupling of 'stationary' qubits for storage and data processing (usually assumed to be realized by material systems such as atoms or electrons) and mobile 'flying' qubits for communication (typically photons) [1, 2]. Detection and subsequent storage of information are inapplicable to quantum information as an unknown quantum state cannot be determined faithfully by a measurement. Hence, the development of 'light–matter interfaces' that allow the coherent write-in and read-out of quantum information has been the subject of intense theoretical research [3]–[5]. Two paths have been identified to make light efficiently couple to a single atomic quantum system: the use of a high-finesse cavity coupled to a single atom or the use of an optically thick ensemble of atoms, in whose collective state the quantum information is to be stored. Both have resulted in the experimental demonstration of such interfaces [6]–[10]. Even without strong coupling, a quantum interface can be realized by combining the probabilistic creation of entanglement between atoms and light with teleportation. This approach has been demonstrated with trapped ions [11].

For qubits realized by electron spins in quantum dots (QDs) [12, 13] such interfaces are yet to be realized, although in particular for self-assembled QDs [14], which have many atom-like properties, several proposals exist to map photonic states to an electron in a QD [13, 15] in analogy to the atomic schemes. Strong coherent coupling between a single quantum system and a single mode of high-Q micro- and nano-cavities has been demonstrated experimentally [16]–[19], raising the prospect of coupling light to the QD's electronic state by adapting protocols such as that in [3].

Despite their good isolation from many environmental degrees of freedom, the electron-spin coherence time in today's QDs is limited, mainly due to strong hyperfine coupling to lattice nuclear spins. Moreover, the capacity of such an interface is one qubit only, making the interfacing difficult for many-photon states of the light field as used in continuous variable quantum information processing. In contrast, the ensemble of lattice nuclear spins could provide a high-dimensional and long-lived quantum memory [20].

We show in the following how to couple an optical field directly to the nuclear spin ensemble, thus interfacing light to an exceptionally long-lived mesoscopic system that enables the storage and retrieval of higher-dimensional states and is amenable to coherent manipulation via the electron spin [21]. The system we consider is a charged QD strongly coupled to a high-finesse optical cavity by a detuned Raman process, introduced in section 2. In section 3, we show that by adiabatically eliminating the trion and the electron spin, different effective couplings (that can be tuned on- and off-resonant) between light and nuclear spins are achieved. In sections 4 and 5, we demonstrate that the state of the cavity field can be directly mapped to the nuclear spins using the methods of Landau–Zener transitions [22, 23] and stimulated Raman adiabatic passage (STIRAP) [24], respectively, where the latter yields a reduction in the time required for write-in. However, the drawback of this approach is that it requires very long cavity lifetimes. To address this problem, we discuss at length in section 6 a scheme that is robust against cavity decay: the read-out maps the nuclear state to the output mode of the cavity, while the write-in proceeds by deterministic creation of entanglement between the nuclear spins and the cavity output-mode and subsequent teleportation [25]. A similar scheme was first proposed by us in [35]. Here, we describe a modified setting, which is significantly simpler to realize[2] and discuss its dynamics in considerably more detail, including the full-time evolution of the system, the fidelity of both write-in and read-out processes, and the intermediate entanglement properties of the involved systems. Moreover, we show that apart from mapping light states to the nuclear spins, the interaction we describe can be used to generate an arbitrary Gaussian state. In section 7, we discuss different aspects concerning the experimental realization and the approximations used in our scheme such as the internal nuclear dynamics, dominated by dipolar interactions, which we model numerically, and corrections to the first-order bosonic description.

2. The system

We consider a self-assembled III–V QD with a single conduction-band electron strongly coupled to a high-Q nano-cavity (see figure 1(a)). At zero magnetic field, the two electronic ground states $|\pm 1/2\rangle$ (s-type conduction band states) are degenerate and the only dipole allowed transitions are to the trion states $|\pm 3/2\rangle$ with spin $+3/2$ and spin $-3/2$

[2] In contrast to [35], no microwave field is needed to split the trion states.

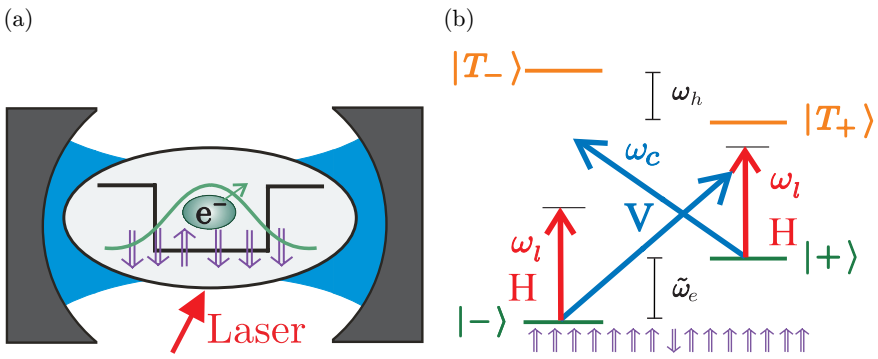

Figure 1. (a) A singly charged QD coupled to a high-Q optical cavity. (b) Level scheme of the QD. Optical and hyperfine driven transitions.

(heavy-hole valence band state) with $\sigma^{\pm}$ polarized light. An external magnetic field B_z in the z-direction, perpendicular to the growth (y-) direction, Zeeman splits the two electronic states and the trion states and leads to eigenstates $|\pm\rangle = (1/\sqrt{2})(|1/2\rangle \pm \mathrm{i}|-1/2\rangle)$ and $|T_{\pm}\rangle = (1/\sqrt{2})(|3/2\rangle \pm \mathrm{i}|-3/2\rangle)$. The states $|+\rangle \Leftrightarrow |T_+\rangle$ and $|-\rangle \Leftrightarrow |T_-\rangle$ can be coupled (see figure 1(b)) by horizontally polarized light, and $|+\rangle \Leftrightarrow |T_-\rangle$ and $|-\rangle \Leftrightarrow |T_+\rangle$ can be coupled by vertically polarized light:

$$H_{\mathrm{opt}} = \frac{\Omega_{\mathrm{c}}}{2}\left(a^{\dagger}|-\rangle\langle T_+| + a^{\dagger}|+\rangle\langle T_-| + \mathrm{h.c.}\right) + \frac{\Omega_{\mathrm{l}}}{2}\left(\mathrm{e}^{+\mathrm{i}\omega_{\mathrm{l}}t}(|+\rangle\langle T_+| + |-\rangle\langle T_-|) + \mathrm{h.c.}\right)$$
$$+\omega_{\mathrm{c}}\, a^{\dagger}a + \omega_{T_+}|T_+\rangle\langle T_+| + \omega_{T_-}|T_-\rangle\langle T_-| + \omega_{\mathrm{e}}S^z. \qquad (1)$$

Here, $\hbar = 1$, S^z is the electron spin operator, $a^{\dagger}$ and a are creation and annihilation operators of the single mode cavity field, ω_{c} and ω_{l} denote the cavity and the laser frequency (which are vertically/horizontally polarized, respectively) and Ω_{c} and Ω_{l} are the Rabi frequencies of the cavity and the laser field, respectively. The energies of the trion states $|T_+\rangle$, $|T_-\rangle$ are $\omega_{T_+} = \omega_{\mathrm{T}} + \omega_{\mathrm{h}}/2$ and $\omega_{T_-} = \omega_{\mathrm{T}} - \omega_{\mathrm{h}}/2$, where ω_{T} is the energy of the trion (without magnetic field), ω_{h} is the energy of the hole Zeeman splitting and $\omega_{\mathrm{e}} = g_{\mathrm{e}}\mu_b B_y$ denotes the Zeeman splitting of the electronic states. The first term of the Hamiltonian given by equation (1) describes the coupling to the cavity field and the second term the coupling to a classical laser field in the rotating wave approximation. We assume both cavity decay and spontaneous emission rate of the QD to be much smaller than Ω_{c} and omit both processes in equation (1). Besides the coupling to optical fields, the electron spin in a QD also has a strong hyperfine interaction with the lattice nuclear spins, which is for s-type electrons dominated by the Fermi contact term

$$H_{\mathrm{hf}} = \frac{A}{2}(A^{+}S^{-} + S^{+}A^{-}) + AS^zA^z, \qquad (2)$$

where $S^{\pm,z}$ are the electron spin operators and $A^{\pm,z} = \sum_j \alpha_j I_j^{\pm,z}$ are the collective nuclear spin operators (in a typical GaAs QD, the number of Ga and As nuclei lies between $N \sim 10^4$–10^6). The individual coupling constants α_j are proportional to the electron wavefunction at site j (and the magnetic dipole moment of the jth nucleus) [26] and are normalized to $\sum_j \alpha_j = 1$. The requirement for using nuclear spins as a quantum memory is to initialize them in a well-defined, highly polarized state. By this we mean that $\langle A^z\rangle$ is close to its minimum value $\langle A^z\rangle_{\mathrm{min}}$

($\approx -1/2$ for spin-1/2 nuclei) and define the polarization as $P = \langle A^z\rangle/\langle A^z\rangle_{\min}$. Due to their small magnetic moments, nuclear spins are almost fully mixed even at dilution-fridge temperatures and fields of several Teslas. Over the past years, significant progress in dynamical polarization experiments [27]–[30] has been reported with nuclear polarization up to 60%; recently, nuclear polarization >80% has been achieved [31].

A convenient and intuitive description of the highly polarized nuclei with homogeneous coupling to the electron is provided by the Holstein Primakoff transformation [32], by which collective nuclear spin operators $A^{\pm,z}$ can be mapped to the bosonic operators b, $b^\dagger$, associating $A^- \to (1/\sqrt{N})\sqrt{1-(b^\dagger b/N)}\,b$ and $A^z \to (1/N)(b^\dagger b - (N/2))$. Assuming high polarization, the electron spin couples to a bosonic 'spin wave' described by $A^- = (1/\sqrt{N})b$ and $A^z = (1/N)(b^\dagger b - N/2)$ by a Jaynes–Cummings (JC)-like interaction

$$H_{\rm hf} = \frac{g_n}{2}(b^\dagger S^- + S^+ b) + \frac{g_n}{\sqrt{N}} S^z \left(b^\dagger b - \frac{N}{2}\right), \tag{3}$$

with $g_n = A/\sqrt{N}$. The initial state of the nuclear spins is represented by a collection of bosonic modes, with b in the vacuum state. One can generalize this description to the case of inhomogeneous coupling to the electron ($g_n = A\sqrt{\sum_i \alpha_i^2}$) and obtain an identical description in the 0th order in $\langle b^\dagger b/N\rangle = (1-P)/2$ [33]. Corrections to this description arising from inhomogeneous coupling and not fully polarized nuclear spins will be discussed briefly in section 7.2 and a detailed discussion can be found in [34]. It should be noted that the scheme we present does not require the bosonic description and could also be discussed directly in terms of the collective spin operators. The Fock basis would be replaced by $(A^+)^n|\downarrow \ldots \downarrow\rangle$ and errors due to the inhomogeneity would have to be treated along the lines of [20, 35]. The bosonic picture, however, allows a much more transparent treatment of the corrections to the ideal case, emphasizes the relation to quantum optical schemes and gives access to the Gaussian toolbox of entanglement criteria and transformations.

3. Effective coupling between nuclei and cavity

Our aim is to obtain from $H = H_{\rm opt} + H_{\rm hf}$ a direct coupling between nuclear spins and light. The Hamiltonian H describes a complicated coupled dynamics of cavity, nuclei and QD. Instead of making use of the full Hamiltonian (and deriving the desired mapping, e.g. in the framework of optimal control theory), we aim for a simpler, more transparent approach. Closely following [35], we adiabatically eliminate [36] the trion and the electronic spin degree of freedom, which leads to a Hamiltonian $H_{\rm el}$ that describes a direct coupling between nuclear spins and light. As explained later, this can be achieved if the couplings (the Rabi frequency of the laser/cavity, the hyperfine coupling, respectively) are much weaker than the detunings to the corresponding transition:

$$\Delta'_{T_\pm} \gg \Omega_{\rm l}, \Omega_{\rm c}\sqrt{n}, \tag{4a}$$

$$\sqrt{\Delta'_{T_\pm}\,\tilde{\omega}_{\rm e}} \gg \Omega_{\rm l}, \Omega_{\rm c}\sqrt{n}, \tag{4b}$$

$$\tilde{\omega}_{\rm e} \gg g_n\sqrt{m}. \tag{4c}$$

Here, $\tilde{\omega}_{\rm e} = \omega_{\rm e} - (A/2)$, $\Delta'_{T_\pm} = \omega_{\rm T} - \omega_{\rm l} \pm \omega_{\rm h}/2 + \tilde{\omega}_{\rm e}/2 = \Delta' \pm \omega_{\rm h}/2 + \tilde{\omega}_{\rm e}/2$ with $\Delta' = \omega_{\rm T} - \omega_{\rm l}$, n is the number of cavity photons and m the number of nuclear excitations. Note that typically

$\tilde{\omega}_e < \Delta'_{T_\pm}$ such that condition (4*a*) becomes redundant. In addition to (4*a*)–(4*c*), we choose the adjustable parameters such that all first-order and second-order processes described by H are off-resonant, but the (third-order) process in which a photon is scattered from the laser into the cavity while a nuclear spin is flipped down (and its converse) is resonant. This leads to the desired effective interaction.

The idea of adiabatic elimination is to perturbatively approximate a given Hamiltonian by removing a subspace from the description that is populated only with a very low probability due to chosen initial conditions and detunings or fast decay processes. If initially unpopulated states (in our case the trion state $|X\rangle$ and the electronic spin-up state $|\uparrow\rangle$) are only weakly coupled to the initially occupied states, they remain essentially unpopulated during the time evolution of the system and can be eliminated from the description. The higher order transitions via the eliminated levels appear as additional energy shifts and couplings in the effective Hamiltonian on the lower-dimensional subspace.

The starting point is the Hamiltonian $H = H_{\rm opt} + H_{\rm hf}$ given by equations (1) and (2). In order to obtain a time-independent Hamiltonian, we proceed to a frame rotating with $U^\dagger = \exp[-i\omega_l t\,(a^\dagger a + |T_+\rangle\langle T_+| + |T_-\rangle\langle T_-|)]$ and obtain

$$H' = \frac{\Omega_c}{2}\,(a^\dagger|-\rangle\langle T_+| + a^\dagger|+\rangle\langle T_-| + \text{h.c.}) + \frac{\Omega_l}{2}\,(|+\rangle\langle T_+| + |-\rangle\langle T_-|) + \text{h.c.})$$
$$+\delta\, a^\dagger a + \Delta_{T_+}|T_+\rangle\langle T_+| + \Delta_{T_-}|T_-\rangle\langle T_-| + \omega_e S^z + H_{\rm hf}, \tag{5}$$

where $\Delta_{T_\pm} = \omega_{T_\pm} - \omega_l$ and $\delta = \omega_c - \omega_l$.

Choosing the cavity and laser frequencies, ω_c and ω_l, far detuned from the exciton transition and the splitting of the electronic states $\tilde{\omega}_e$ much larger than the hyperfine coupling g_n, such that conditions (4*a*)–(4*c*) are fulfilled, we can adiabatically eliminate the states $|T_\pm\rangle$ and $|+\rangle$. A detailed derivation of the adiabatic elimination can be found in [35]. It yields a Hamiltonian that describes an effective coupling between light and nuclear spins

$$H_{\rm el} = \frac{\Omega_c\Omega_l A}{8\Delta'_{T_+}\tilde{\omega}_e}(aA^+ + \text{h.c.}) + \frac{\Omega_c\Omega_l A}{8\Delta'_{T_-}\tilde{\omega}_e}(aA^- + \text{h.c.}) + \omega_l a^\dagger a - \frac{A}{2}\delta A^z - \frac{A^2}{4\tilde{\omega}_e}A^+A^- + T_{\rm nl}, \tag{6}$$

where the energy of the photons $\omega_l = \delta - (\Omega_c^2/4\Delta'_{T_+}) + (\Omega_l^2/4\Delta'^2_{T_-})\delta$ and the energy of the nuclear spin excitations $\sim -(A/2N) - (A^2/4N\tilde{\omega}_e)$. $T_{\rm nl}$ denotes the nonlinear terms

$$T_{\rm nl} = \frac{A^3}{8\tilde{\omega}_e^2}A^+\delta A^z A^- + \frac{A^2}{4\tilde{\omega}_e^2}\delta a^\dagger a A^+A^- + \frac{\Omega_c^2\delta}{4\Delta'^2_{T_+}}a^\dagger a^\dagger aa, \tag{7}$$

which are small ($\|T_{\rm nl}\| \ll \Omega_c\Omega_l A/8\Delta'\tilde{\omega}_e$) in the situation we consider ($\delta \ll \Omega_c$, $g_n/\tilde{\omega}_z \sim \Omega_l/\Delta'_{T_+,T_-} \ll 1$) and neglected in the following. We also neglect the nuclear Zeeman term, which is of the order of 10^{-3} smaller than the Zeeman energy of the electron. In the bosonic description of the nuclear spins that we introduced in equation (3), the Hamiltonian given by equation (6) reads

$$H_{\rm eff} = g_1(ab^\dagger + \text{h.c.}) + g_2(ab + \text{h.c.}) + \omega_1 a^\dagger a + \omega_2 b^\dagger b, \tag{8}$$

with coupling strengths g_1 and g_2 given by

$$g_1 = \frac{\Omega_c\Omega_l g_n}{8\Delta'_{T_+}\tilde{\omega}_e}, \qquad g_2 = \frac{\Omega_c\Omega_l g_n}{8\Delta'_{T_-}\tilde{\omega}_e}. \tag{9}$$

The energy of the nuclear spin excitations can now be written as $\omega_2 = -(A/2N) - (g_n^2/4\tilde{\omega}_e)$. The first term in the Hamiltonian is a beamsplitter-type interaction $\sim (ab^\dagger + \text{h.c.})$, whereas the

second term is a two-mode squeezing (TMS)-type interaction $\sim (ab + \text{h.c.})$. Both interactions can be made dominant by choosing the resonance condition to be either $\omega_1 = \omega_2$ or $\omega_1 = -\omega_2$. This will be discussed in detail in the following and illustrated numerically.

First, we validate the adiabatic elimination by a numerical simulation that compares the evolution of states Ψ_{20} (where the first subscript indicates the number of photons and the second the number of nuclear excitations) (under the condition $\omega_1 = \omega_2$, see figure 2) and Ψ_{00} (under the condition $\omega_1 = -\omega_2$, see figure 3) under the full Hamiltonian given by equation (5) to the evolution under the eliminated Hamiltonian given by equation (8). The solid lines show the evolution under the full Hamiltonian H' and the dashed lines the evolution under the eliminated Hamiltonian H_{eff}, and we find that H' is well approximated by H_{eff} and that the nonlinear terms T_{nl} can indeed be neglected.

For the simulation, we choose the parameters as follows: we assume a hole g-factor $g_{\text{h}} = -0.31$ and an electron g-factor $g_{\text{e}} = 0.48$ [37]; the number of nuclei $N = 10^4$, the hyperfine coupling constant $A = 100\,\mu\text{eV}$, the laser and cavity Rabi frequency $\Omega_{\text{c}} = \Omega_{\text{l}} = 15\,\mu\text{eV}$, the detuning of the trion $\Delta' = 1000\,\mu\text{eV}$, the effective Zeeman splitting of the electronic states $\tilde{\omega}_{\text{e}} = 13.9\,\mu\,\text{eV}$ (the magnetic field in the x-direction is 4 T) and the Zeeman splitting of the hole $\omega_{\text{h}} = -71.8\,\mu\text{eV}$. With these parameters, the conditions given by equations (4*a*)–(4*c*) are fulfilled and values $g_1 = 2.1 \times 10^{-3}\,\mu\text{eV}$ and $g_2 = 1.9 \times 10^{-3}\,\mu\text{eV}$ are obtained. We assume full nuclear (spin-down) polarization and use the bosonic description.

As already mentioned, two distinct resonance conditions are chosen in figures 2 and 3, leading to different dynamics of the system.

For resonant exchange of excitations between the two systems, we choose $\omega_1 = \omega_2$, where the tuning can be done by changing $\delta = \omega_{\text{c}} - \omega_{\text{l}}$. Then H_{eff} describes a beamsplitter-like coupling of the modes a and b and the effective interaction is described by

$$H_{\text{bs}} = g_1(ab^\dagger + \text{h.c.}) + \omega_1 a^\dagger a + \omega_2 b^\dagger b. \tag{10}$$

Processes in which absorption (or emission) of a cavity photon is accompanied by a nuclear spin excitation are resonant, whereas the squeezing interaction given by $g_2(a^\dagger b^\dagger + ab)$ is off-resonant. This can be seen going to a frame rotating with ω_1: g_2 is rotating with $2\omega_1$ and as $2\omega_1 \gg g_2$, the squeezing type interaction is off-resonant.

Tuning the energies such that $\omega_1 = -\omega_2$, the creation of a nuclear spin excitation is accompanied by scattering of a laser photon into the cavity, i.e. the effective coupling becomes $g_2(a^\dagger b^\dagger + ab)$ and the beamsplitter-type interaction $g_1(ab^\dagger + a^\dagger b)$ is off-resonant. The driving laser now facilitates the joint creation (or annihilation) of a spin excitation and a cavity photon, realizing a TMS Hamiltonian

$$H_{\text{sq}} = g_2(a^\dagger b^\dagger + ab) + \omega_1 a^\dagger a + \omega_2 b^\dagger b. \tag{11}$$

The plots in figures 2 and 3 illustrate that the dynamics of the system can indeed be approximated by equations (10) and (11). To simulate the beamsplitter-type coupling given by equation (10), we choose $\omega_1 = \omega_2$ and let the two-photon Fock state ψ_{20} evolve under the Hamiltonian given by equation (8) (see dashed lines in figure 3). Almost perfect Rabi oscillations can be seen between the two-photon Fock state ψ_{20} and the state with two nuclear spin excitations ψ_{02}, showing that $g_2(a^\dagger b^\dagger + \text{h.c.})$ in equation (8) can indeed be neglected. To simulate the squeezing-type interaction, we choose $\omega_1 = -\omega_2$ and study the evolution of the state ψ_{00} under the Hamiltonian given by equation (8) (see dashed blue lines in figure 3). It can be seen that the state ψ_{00} evolves into the states ψ_{11}, ψ_{22} and ψ_{33} with coupling strengths $g_2\sqrt{n}$, depending on the number of excitations n. We have thus shown that in this

IOP Institute of Physics DEUTSCHE PHYSIKALISCHE GESELLSCHAFT

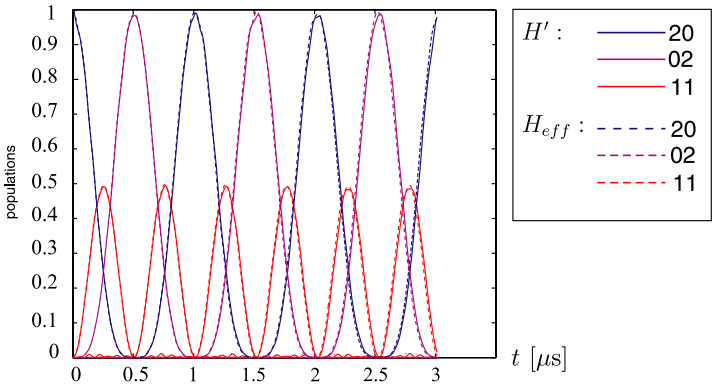

Figure 2. Evolution of the two-photon Fock state ψ_{20} under the full Hamiltonian H' (solid lines) and the eliminated Hamiltonian H_{eff} (dashed lines) tuning the energies such that $\omega_1 = \omega_2$ (beamsplitter-type interaction). Populations in the states ψ_{00}, ψ_{10}, ψ_{01}, ψ_{12}, ψ_{21} and ψ_{33} are plotted here but not mentioned in the legend as they are small.

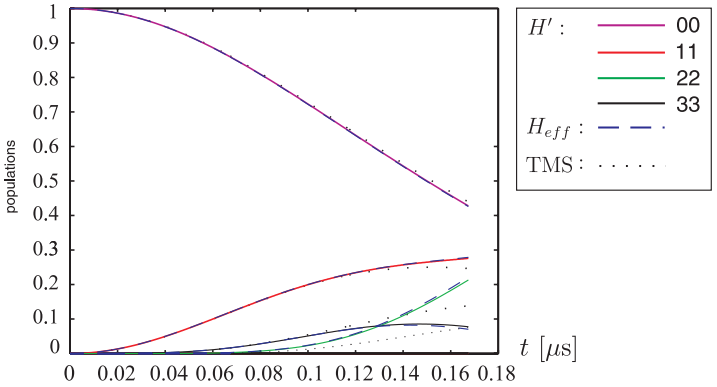

Figure 3. Evolution of the state ψ_{00} under the full Hamiltonian H' (solid lines) and the eliminated Hamiltonian H_{eff} (dashed blue lines) tuning the energies such that $\omega_1 = -\omega_2$ (squeezing interaction). The dotted black lines show the evolution under exact TMS (up to $n = 3$).

case, the beamsplitter-type interaction can indeed be neglected. For simplicity, we restricted the number of photons and nuclear excitations to three in our simulation, such that states ψ_{44} and higher excitation states do not occur and the evolution of the states ψ_{22} and ψ_{33} does only correspond to its evolution in a space with higher excitation numbers at very short times. This can be seen by comparing the evolution to the exact TMS that generates the state $\sqrt{1-\tanh^2(g_2 t)}\sum_{n=0}^{\infty}\tanh^n(g_2 t)|nn\rangle$ for which the populations up to $n = 3$ are plotted in figure 3 (dotted black lines).

4. Landau–Zener transitions

To map the state of the cavity to the nuclear spins, we take advantage of a formal analogy between the linear two-mode interaction given by equation (10) in the Heisenberg picture and the Landau–Zener problem [22, 23]. In the conventional Landau–Zener problem, initially uncoupled Hamiltonian eigenstates of a two-level system interact at an avoided crossing. This interaction is achieved by slowly changing an external parameter such that the level separation is a linear function of time. If the system starts in the ground state, the probability of finding it in the excited state is given by the Landau–Zener formula [22, 23].

Here, we invoke this idea in the Heisenberg picture to achieve a mapping of the photon annihilation operator a to the collective nuclear spin operator in the bosonic approximation b, i.e. $a \to b$ (the bosonic operators a and b are initially uncoupled). In the following, we show that our system can be transformed to a system that corresponds to the standard Landau–Zener problem.

In the Heisenberg picture, the linear two-mode interaction between the cavity mode and the nuclear spins in the QD, given by equation (10), is described by a set of coupled differential equations for the mode operators:

$$\frac{\mathrm{d}}{\mathrm{d}t}\begin{pmatrix} a(t) \\ b(t) \end{pmatrix} = -\mathrm{i}\begin{pmatrix} \omega_1 & g_1 \\ g_1 & \omega_2 \end{pmatrix}\begin{pmatrix} a(t) \\ b(t) \end{pmatrix}. \tag{12}$$

The available control parameters used to effect the change of $\omega_1 - \omega_2$ are the laser Rabi frequency Ω_l and the laser frequency ω_l. We consider a linear time dependence of

$$\omega_1 - \omega_2 = \beta t \tag{13}$$

for simplicity while the coupling g_1 is constant.

Let $a\left(\binom{u}{v}\right)$ denote the operator $ua_{-\infty} + vb_{-\infty}$ (a normalized linear combination of the purely photonic $a_{-\infty}$ and purely nuclear $b_{-\infty}$) and let $a_t\left(\binom{u}{v}\right) \equiv a\left(\binom{u_1}{v_1}\right)$ denote its image under time evolution; then the two operator equations of (12) can be combined into

$$\frac{\mathrm{d}}{\mathrm{d}t}a_t\left(\begin{pmatrix} u \\ v \end{pmatrix}\right) = -\mathrm{i}a_t\left[\begin{pmatrix} \omega_1 & g_1 \\ g_1 & \omega_2 \end{pmatrix}\begin{pmatrix} u \\ v \end{pmatrix}\right],$$

which can be written completely in terms of the mode function:

$$\frac{\mathrm{d}}{\mathrm{d}t}\begin{pmatrix} u_t \\ v_t \end{pmatrix} = -\mathrm{i}\begin{pmatrix} \omega_1 & g_1 \\ g_1 & \omega_2 \end{pmatrix}\begin{pmatrix} u_t \\ v_t \end{pmatrix}. \tag{14}$$

This is the same kind of coupled differential equation as that encountered in the Landau–Zener problem [22, 23]. Following the calculation done in [22, 23], we find that

$$|v(t=\infty)|^2 = K^2 U_1(\infty)U_1^*(\infty) = 1 - \epsilon^2, \tag{15}$$

where $\epsilon \equiv \mathrm{e}^{-\pi\gamma_z}$ and

$$\lim_{t\to\infty} U_1(t) = -K\frac{\sqrt{2\pi}}{\Gamma(\mathrm{i}\gamma_z + 1)}\mathrm{e}^{-(1/4)\pi\gamma_z}\mathrm{e}^{\mathrm{i}\beta t^2}(\sqrt{\beta}t)^{\mathrm{i}\gamma_z}, \tag{16}$$

with $\gamma_z = g_1^2/\beta$ and the constant $K = \sqrt{\gamma_z}\exp(-\gamma_z\pi/4)$ (for a detailed discussion, see appendix B). We thus find that the cavity mode operator a is mapped to

$$a_{+\infty} = \sqrt{1-\epsilon^2}\, b_{-\infty} + \epsilon\, a_{-\infty}, \tag{17}$$

a dominantly nuclear operator for small enough β so that ϵ is small, which effectively means that, for large enough times, $\omega_1 - \omega_2 \equiv \beta t$.

4.1. Quality of the mapping for Fock and coherent states

In the following sections, we will consider the quality of the mapping within the model given by equations (1) and (3); other imperfections will be discussed in section 7. To evaluate the quality of the mapping, we return to the Schrödinger picture. The mapping of an n-photon Fock state of the cavity to the nuclei leads to a mixture of Fock states with photon numbers $\leqslant n$. The fidelity with which an n-photon Fock state is mapped is given by

$$F_{\mathrm{F}}(n) = \langle n|\mathrm{tr}_{\mathrm{c}}\left(\left[\frac{a_\infty^\dagger}{\sqrt{n!}}\right]^n |0\rangle\langle 0| \left[\frac{a_\infty}{\sqrt{n!}}\right]^n\right)|n\rangle = (1-\epsilon^2)^n, \tag{18}$$

where the cavity mode is traced out. In a next step, we want to know which fidelities can be achieved for superpositions of number states, e.g. for coherent states.

Coherent states are representatives of the family of Gaussian states, which play an important role in quantum optics and quantum information processing. A Gaussian state is fully characterized by its first and second moments (γ, d), where γ is the state's covariance matrix and d its displacement (see appendix A). Since the dynamics generated by equation (18) is Gaussian, the mapping can be fully characterized in terms of covariance matrices. The mapping of a Gaussian state of light onto the nuclear spins corresponds to

$$(\gamma_{\mathrm{c}}, d_{\mathrm{c}})_{\mathrm{c}} \xrightarrow{\mathrm{map}} ((1-\epsilon^2)\gamma_{\mathrm{c}} + \epsilon^2\gamma_{\mathrm{ns}}, \quad \sqrt{1-\epsilon^2}d_{\mathrm{c}} + \epsilon d_{\mathrm{ns}})_{\mathrm{ns}'}, \tag{19}$$

where $(\gamma_{\mathrm{c}}, d_{\mathrm{c}})_{\mathrm{c}}$ and $(\gamma_{\mathrm{ns}}, d_{\mathrm{ns}})_{\mathrm{ns}}$ describe the states of cavity and nuclear spins, respectively, prior to the mapping, and $(\gamma_{\mathrm{ns}'}, d_{\mathrm{ns}'})_{\mathrm{ns}'}$ describes the state of the nuclei after the mapping. For a coherent state mapped to the nuclei, this corresponds to the map

$$(\mathbb{1}, \alpha)_{\mathrm{c}} \xrightarrow{\mathrm{map}} (\mathbb{1}, \sqrt{1-\epsilon^2}\alpha)_{\mathrm{ns}'}. \tag{20}$$

The fidelity of the mapping is given by [38]

$$F_{\mathrm{c}} = |\langle\, \alpha \mid \sqrt{1-\epsilon^2}\alpha\,\rangle|^2 = \exp\left[-|\left(1-\sqrt{1-\epsilon^2}\right)\alpha|^2\right]. \tag{21}$$

The minimal goal of a quantum interface is to achieve a better fidelity than can be achieved by classical means. As proved in [39, 40], the classical benchmark fidelity of coherent states distributed in phase space according to $p(\alpha) = \frac{\lambda}{\pi}\exp(-\lambda|\alpha|^2)$ is given by $F_{\max} = (1+\lambda)/(2+\lambda)$. Averaging F_{c} over all possible coherent input states with a Gaussian distribution, the fidelity reads

$$\bar{F}_{\mathrm{c}} = \int \mathrm{d}^2\alpha\; p(\alpha) F_{\mathrm{c}} = \frac{\lambda}{1-\epsilon^2/2-\sqrt{1-\epsilon^2}+\lambda}. \tag{22}$$

For a flat distribution with $\lambda \to 0$, large photon numbers that lead to high losses are dominant and therefore $\bar{F}_{\mathrm{c}} \to 0$.

A way to improve the average fidelity is to amplify the coherent state at either the write-in or the read-out stage, thus compensating for losses due to the imperfect mapping. Optimal phase-insensitive amplification would map $(\gamma, \mathrm{d}) \longrightarrow \left(\kappa^2\gamma + (\kappa^2-1)\mathbb{1}, \kappa\mathrm{d}\right)$ [41]. Choosing κ such that $\kappa \stackrel{!}{=} 1/\sqrt{1-\epsilon^2}$, amplification and subsequent mapping can be written as

$$(\mathbb{1}, \alpha)_{\mathrm{c}} \xrightarrow{\mathrm{amp.}} \left(\kappa\,\mathbb{1}, \frac{1}{\sqrt{1-\epsilon^2}}\alpha\right)_{\mathrm{c}} \xrightarrow{\mathrm{map}} \left(\kappa(1-\epsilon^2)+\epsilon^2)\,\mathbb{1}, \alpha\right)_{\mathrm{ns}'}. \tag{23}$$

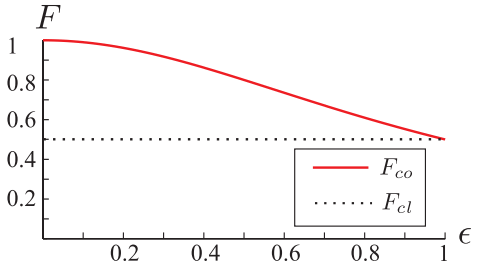

Figure 4. The (solid) red line indicates the fidelity of the mapping of an amplified coherent state of light to the nuclear spins versus the losses of the mapping ϵ. The fidelity is, even for large losses, higher than the fidelity $F_{\rm cl}$ that can be achieved by classical means, indicated by the (dotted) black line.

The fidelity of the mapping of the amplified state ρ_m, calculated using the relations for transition amplitudes of Gaussian states in [42], is given by

$$F_{\rm co} = \langle\alpha|\rho_{\rm m}(\alpha)|\alpha\rangle = \det\left(\frac{\gamma_c+\gamma_{\rm ns'}}{2}\right)^{-1/2} {\rm e}^{-(d_{\rm ns'}-d_{\rm c})^{\rm T}(\gamma_c+\gamma_{\rm ns'})(d_{\rm ns'}-d_{\rm c})}$$
$$= \det\left(\frac{\kappa(2-\epsilon^2)+\epsilon^2}{2}\mathbb{1}\right)^{-1/2} = \frac{1}{1+\epsilon^2}. \quad (24)$$

A plot of $F_{\rm co}$ is shown in figure 4. The fidelity of the mapping of the amplified coherent state is always higher than the classical benchmark fidelity $F_{\rm cl} = \frac{1}{2}$ for a flat distribution, i.e. the quantum interface shows high performance even for large losses ϵ.

4.2. Storage of an entangled state

So far, we have shown that it is possible to transfer Fock and coherent states of light to the nuclear spin memory. However, the ultimate test for a quantum memory is whether it is capable of faithfully storing part of an entangled quantum system. As an example of entangled light states, we consider a two-mode squeezed state where one of its light modes, M_1, is coupled to the cavity and mapped onto the nuclear spins of the QD (see figure 5(a)). To see how well the entanglement is preserved, we compute the entanglement between the nuclear spins and the light mode M_2 using Gaussian entanglement of formation (gEoF) [43]. We found it to be a monotonically decreasing function of the mapping error $\epsilon \in [0,1]$. As can be seen from figure 5(b), the nuclear spins of the QD are entangled with the light mode M_2. This allows remote access to the memory via teleportation, required for e.g. quantum repeaters.

4.3. Mapping time

A lower bound for the timescale of the mapping can be easily found considering the Hamiltonian $H_{\rm bs}$, where the parameters are chosen such that $\omega_1 = \omega_2$ and set to zero in a rotating frame: acting for a time $t = \pi/g_1$ (which is of the order of 6 μs) it maps $a \to b$ and $b \to a$, thus realizing a swap gate between cavity and nuclear spins[3]. The adiabatic procedure takes longer: to estimate a timescale, we consider the three conditions that need to be fulfilled: (i) $\epsilon < \epsilon_0$, i.e. the mapping

[3] This setting, however, would, in contrast to the adiabatic methods discussed in this and the following sections, be sensitive to exact time control because letting $H_{\rm bs}$ act for too long would reverse the mapping.

IOP Institute of Physics DEUTSCHE PHYSIKALISCHE GESELLSCHAFT

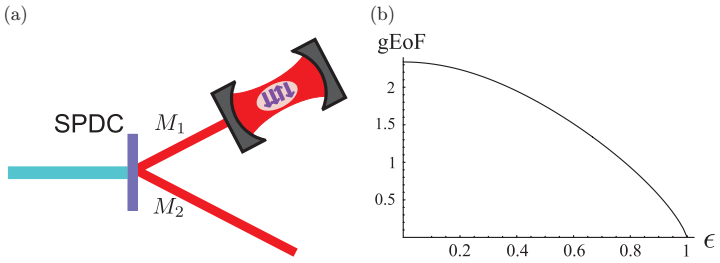

Figure 5. (a) One part (M_1) of a two-mode squeezed state, arising from a spontaneous parametric downconversion source, is coupled to the cavity and mapped to the nuclear spins of the QD. Thereby, the other part (M_2) gets entangled with the nuclear spins. (b) Plot of the Gaussian entanglement of formation (gEoF) for squeezing parameter $r = 1$ versus mapping error ϵ. The entanglement of the nuclear spins with part of a two-mode squeezed state (M_2) is a decreasing function of increasing mapping error ϵ.

error has to be smaller than some (small) value ϵ_0, which can be fixed depending on the fidelity that one wants to achieve (the fidelity depends only on ϵ). This condition can be written as $\beta > \pi/\ln(1/\epsilon_0)g_1^2$. (ii) In the beginning and at the end of the process, $|\omega_1 - \omega_2| \gg g_1$, i.e. the energy splitting between the levels has to be much larger than the coupling. As $|\omega_1 - \omega_2| = \beta t$, this condition leads to $\beta \gg g_1/t_0$. (iii) $\langle E_m(t)|(\mathrm{d}/\mathrm{d}t)H_{\mathrm{bs}}|E_n(t)\rangle \ll |E_m - E_n|^2$ for $t \in [-t_0, t_0]$ to make sure that the process is adiabatic. At $t = 0$, this condition reads $\beta \ll 4g_1^2$.

Depending on how ϵ is chosen, either condition (i) or (iii) is stronger. To map coherent states with average fidelity $F > 0.9$, we find $\epsilon < 1/3$ and with conditions (ii) and (iii) (here, condition (ii) is stronger than (i)) we estimate the time $t_0 \approx 20\pi/g_1 \approx 120\,\mu$s.

5. STIRAP

Mapping the state of the cavity to the nuclear spins is also possible considering a system where only the trion states are adiabatically eliminated and elimination of the electronic states is not required to achieve the desired interaction. We show that, with this system, the process of storing a state of light to the nuclear spins can be achieved by the well-known technique of STIRAP [24], which has been studied for multilevel systems [44] and has been demonstrated in several experiments [24]. This scheme allows us to coherently transfer population between two suitable quantum states via a so-called counterintuitive sequence of coherent light pulses that drive transitions of a lambda or a multilevel system. It has some advantages over the Landau–Zener method as the choice of control parameters is easier and less constraints have to be fulfilled as we do not eliminate the electronic states, which allows for faster mapping times compared to the Landau–Zener method.

Note that the main source of error, the decay of the cavity, is not considered here. Up to now, the experimentally achieved cavity decay rate γ of a photonic crystal microcavity that couples to a QD is of the order of $\gamma \approx 10^{10}\,\frac{1}{s}$ [45]. However, we do propose this scheme here, as cavity decay rates might improve and the scheme might also be used in a different setup.

For the system proposed in section 2, the STIRAP method is not as straightforward as for the setup we investigated in [35, section V]. The reason for this is that, after the elimination

of the trion states in the system used so far, there are two different couplings: $g_{a-}(S^+a^\dagger + \text{h.c.})$ and $g_{a+}(S^-a^\dagger + \text{h.c.})$, with $g_{a\pm} = \Omega_c\Omega_l/4\Delta_{T_\pm}$, where the first one has to be made off-resonant: $g_{a-} \gg g_{a+}$, which means that ω_h sets an upper limit to the coupling g_{a+} (as the condition for the adiabatic elimination is $\Delta_{T_\pm} \gg \Omega_c, \Omega_l$). Therefore, we study the STIRAP scheme for the system investigated in [35], where only the coupling $\propto (S^-a^\dagger + \text{h.c.})$ is present.

In [35], we study a singly charged QD where the electronic states are Zeeman split by an external magnetic field in the growth/z-direction (Faraday geometry). The electronic state $|\uparrow\rangle$ is coupled to the trion state $|\Uparrow\rangle$ (with angular momentum +3/2) by σ^+ circularly polarized light and the electronic state $|\downarrow\rangle$ is coupled to the trion state $|\Downarrow\rangle$ (with angular momentum $-3/2$) with σ^--polarized light. These transitions can be stimulated by a σ^+-polarized cavity field and a σ^--polarized classical laser field, respectively. The trion states are mixed with a resonant microwave field, whereas the electronic eigenstates are unchanged as they are far detuned from the microwave frequency and are now both coupled to the new trion eigenstates $|T_\Uparrow\rangle = 1/\sqrt{2}(|\Uparrow\rangle - |\Downarrow\rangle)$ and $|T_\Downarrow\rangle = 1/\sqrt{2}(|\Uparrow\rangle + |\Downarrow\rangle)$, and form a double Λ system (see [35] for a figure).

In a frame rotating with the laser frequency, the Hamiltonian reads

$$H = \frac{\Omega_c}{\sqrt{2}}\,(a^\dagger\,|\downarrow\rangle\langle T_\Uparrow| - a^\dagger\,|\downarrow\rangle\langle T_\Downarrow| + \text{h.c.}) + \frac{\Omega_l}{\sqrt{2}}(|\uparrow\rangle\langle T_\Uparrow| + |\uparrow\rangle\langle T_\Downarrow| + \text{h.c.})$$
$$+\delta' a^\dagger a + \Delta_+|T_\Uparrow\rangle\langle T_\Uparrow| + \Delta_-|T_\Downarrow\rangle\langle T_\Downarrow| + \tilde{\omega}_e S^z + H_{hf}, \tag{25}$$

where $\delta' = \omega_c - \omega_l - \omega_{mw}$ and $\Delta_\pm = \omega_\Downarrow - \omega_l \pm \Omega_{mw}$. Now, we derive the Hamiltonian where only the trion has been eliminated. If

$$\Delta_\pm \gg \Omega_l, \quad \Omega_c\sqrt{m} \tag{26}$$

holds, the trion can be adiabatically eliminated. This leads to the Hamiltonian

$$H_{el} = g_a\left(S^+a + \text{h.c.}\right) + g_n\left(S^+b + \text{h.c.}\right) + \frac{A}{2N}S^z b^\dagger b + \delta' a^\dagger a + \tilde{\omega}_e S^z$$
$$+\left(\frac{\Omega_c^2}{2\Delta_-} + \frac{\Omega_c^2}{2\Delta_+}\right)a^\dagger a|\downarrow\rangle\langle\downarrow| + \left(\frac{\Omega_l^2}{2\Delta_-} + \frac{\Omega_l^2}{2\Delta_+}\right)|\uparrow\rangle\langle\uparrow|, \tag{27}$$

where the coupling

$$g_a = \frac{\Omega_c\Omega_l}{2}\left(\frac{1}{\Delta_+} - \frac{1}{\Delta_-}\right). \tag{28}$$

We thus arrive, in addition to H_{hf}, at an effective JC-like coupling of the two electronic spin states to the cavity mode governed by

$$g_a(S^+a + \text{h.c.}), \tag{29}$$

i.e. the absorption of a cavity photon proceeds along with an upward flip of the electron spin (and the emission of a photon into the laser mode) and vice versa.

Next we present the STIRAP scheme: the couplings of the electronic states $|\uparrow\rangle$ and $|\downarrow\rangle$ are given by the optical fields (g_a) and the hyperfine coupling (g_n). The Hamiltonian describing the system is given by equation (27). It is block diagonal $H' = \bigoplus_m H_m$, where m denotes the initial photon number. The $(2m+1)$-dimensional Hamiltonian H_m, describing the evolution of the 'm-excitation subspace' can be written in the Fock basis $\{|m, \downarrow, 0\rangle, |m-1, \uparrow, 0\rangle, |m-1, \downarrow, 1\rangle, \ldots\}$, where the first number $m-k$ represents the Fock state of the cavity,

IOP Institute of Physics DEUTSCHE PHYSIKALISCHE GESELLSCHAFT

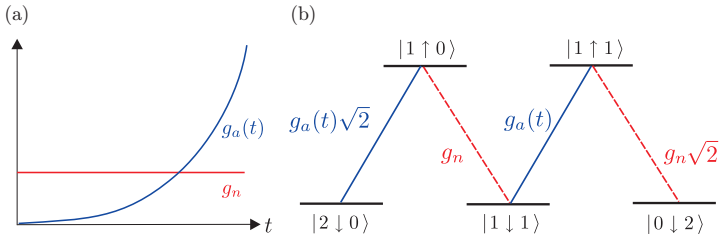

Figure 6. (a) Schematic view of the time dependence of the coupling g_a and the constant hyperfine coupling g_n. (b) Schematic view of the level scheme of the system with initially two photons. The hyperfine coupling g_n is 'always on', whereas $g_a(t)$ is an increasing function for which $g_a(T) \gg g_n$.

$\downarrow$ / $\uparrow$ denotes the electron spin down/up state and k is the excitation number of the nuclear spins. In this basis, H_m reads

$$H_m = \begin{pmatrix} \Delta_{G_0} & g_a\sqrt{m} & 0 & 0 & 0 & \dots \\ g_a\sqrt{m} & \Delta_{E_0} & g_n\sqrt{1} & 0 & 0 & \dots \\ 0 & g_n\sqrt{1} & \Delta_{G1} & g_a\sqrt{m-1} & 0 & \dots \\ 0 & 0 & g_a\sqrt{m-1} & \Delta_{E_1} & g_n\sqrt{2} & \dots \\ 0 & 0 & 0 & g_n\sqrt{2} & \Delta_{G_2} & \dots \\ \vdots & \vdots & \vdots & \vdots & \vdots & \ddots \end{pmatrix}, \tag{30}$$

with $\Delta_{G_k} = \left(\delta' + (\Omega_c^2/2\Delta_-) + (\Omega_c^2/2\Delta_+)\right)(m-k) - (A/2N)k - (\tilde{\omega}_e/2)$ and $\Delta_{E_l} = (\Omega_l^2/2\Delta_-) + (\Omega_l^2/2\Delta_+) + \delta'(m-l-1) + (A/2N)l + (\tilde{\omega}_e/2)$ for $k \in \{0, 1, 2 \dots m\}$ and $l \in \{0, 1, 2 \dots m-1\}$. In the following, we will denote the states with electron spin down as 'ground states', $|G_k\rangle = |m-k, \downarrow, k\rangle$ and the 'excited states' by $|E_l\rangle = |m-l-1, \uparrow, l\rangle$. The optical fields couple states G_k and E_l with $k = l$, whereas states with $k = l+1$ are coupled by the hyperfine coupling (see figure 6(b)).

We will show in the following that by slowly increasing the laser Rabi frequency and thus changing $g_a(t)$ such that $g_a(T) \gg g_n$, at the final time T (see figure 6(a)), an initial state $|\psi, \downarrow, 0\rangle$ with no nuclear spin excitations in the QD, and a state $|\psi\rangle$ in the cavity, evolves under the adiabatic change of H' to a state where the cavity is empty and its state has been mapped to the nuclear spins:

$$|\psi \downarrow 0\rangle_{t=0} \to |0 \downarrow \psi\rangle_{t\to T} \tag{31}$$

for $T \to \infty$. A prerequisite for the mapping is that the ground states of the Hamiltonian are all degenerate within each 'm-excitation'-subspace so that we can keep track of the phases of the individual eigenstates. This can be done by choosing the parameters such that Δ_{G_k} does not depend on k, which is fulfilled for $\delta' + (\Omega_c^2/2\Delta_-) + (\Omega_c^2/2\Delta_+) = -A/2N$ so that $\Delta_{G_k} = -(A/2N)m - (\tilde{\omega}_e/2)$.[4] Hence, the phases $\phi_m = \Delta_{G_m} t$ of the individual eigenstates that the system acquires during the time evolution (for perfect adiabaticity) are known and can be corrected, e.g., by applying a magnetic field $-|B|\hat{z}$ for a time $t = (A/(2N))/g_K\mu_K|B|$ after the

[4] It can be proven by induction that text H_m has an eigenvalue $E_{G_m} = \Delta_{G_m} \forall m$, i.e. that $\det(H_m - E_{G_m}\mathbb{1}) = 0$ for all $m \in \{0, 1 \dots \infty\}$ (where m is the initial photon number).

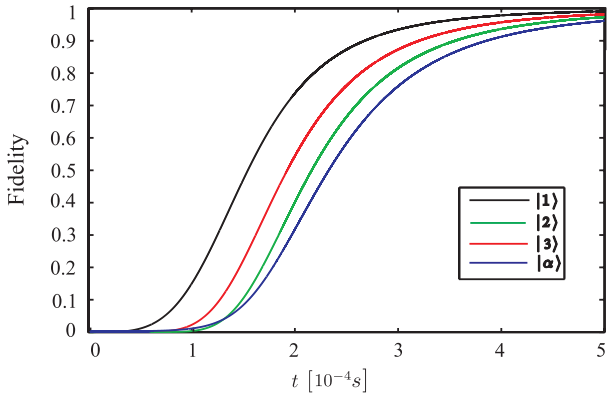

Figure 7. Plot of the fidelity of a variety of states versus time during the adiabatic evolution. $|1\rangle$, $|2\rangle$ and $|3\rangle$ denote the one-, five- and ten-photon Fock states, respectively. $|\alpha\rangle$ denotes the coherent state with average photon number 5. The total evolution time is chosen to be $T = 5 \times 10^{-4}$ s.

state transfer to the nuclei. Here g_K and μ_K denote the nuclear g-factor and the nuclear magnetic moment, respectively.

5.1. Numerical integration of the Schrödinger equation

To study the quality of the mapping of a state of the cavity to the nuclear spins, we numerically integrate the Schrödinger equation given by

$$\mathrm{i}\frac{\partial}{\partial t}|\psi(t)\rangle = H'(t)|\psi(t)\rangle, \tag{32}$$

where H' is the Hamiltonian given by equation (27). The simulation computes $|\psi(t+Dt)\rangle = \mathrm{e}^{-\mathrm{i}H'(t)Dt}|\psi(t)\rangle$ in T/Dt steps from $t=0$ to $t=T$. We assume that the change of $g_a(t)$ is quadratic in time, ensuring an initially slow and a finally fast increase of $g_a(t)$ and $g_a(T) \gg g_n(T)$, $g_a = 10\, g_n(t^2/T^2)$. Parameters are chosen as follows: we assume a hole g-factor $g_\mathrm{h} = 2.2$ and an electron g-factor $g_\mathrm{e} = 0.48$; the number of nuclei $N = 10^4$, the hyperfine coupling constant $A = 10\,\mu$eV, the laser and cavity Rabi frequency $\Omega_\mathrm{c} = \Omega_\mathrm{l} = 13\,\mu$eV, the detuning of the trion $\omega_\Downarrow - \omega_\mathrm{l} = 103\,\mu$eV, the effective Zeeman splitting $\tilde{\omega}_\mathrm{e} = 0\,\mu$eV and the microwave Rabi frequency $\Omega_\mathrm{mw} = 50\,\mu$eV. The fidelity of the mapping we are interested in is given by the overlap of the numerically evolved state $\rho(t) = |\psi_\mathrm{si}\rangle\langle\psi_\mathrm{si}|$ and the ideal output $|\psi_\mathrm{id}\rangle$

$$F = \langle\psi_\mathrm{id}|\rho(t)|\psi_\mathrm{id}\rangle. \tag{33}$$

To achieve a fidelity close to one, the total evolution time is chosen to be $T = 5 \times 10^{-4}$ s.[5] Figure 7 shows the fidelity plotted versus time for different kinds of states that will be discussed in the following, illustrating the different aspects of mapping.

[5] Note that this time is not directly comparable to the time for the Landau–Zener process in section 4 as here, a different setup is considered.

The one-photon Fock state $|1\rangle$ is mapped in $T = 5 \times 10^{-4}$ s with a fidelity of $F \approx 0.99$ to the nuclear spins. To see that not only population but also relative phases are properly mapped, we have simulated an approximately coherent state $|\alpha\rangle = \exp\left(-|\alpha|^2/2\right) \sum_{k=0}^{20} (\alpha^k/\sqrt{k!})|k\rangle$ with average photon number $|\alpha|^2 = 5$ and find a mapping fidelity of $F \approx 0.96$. Here the known phases ϕ_m have been compensated.

5.2. Error processes

The main error processes that lead to imperfections of the fidelity are the 'always-on' character of the hyperfine coupling, the non-adiabaticity due to finite times, non-perfect polarization of the nuclei and the decay of the cavity. These processes will be studied in the following.

The fact that the hyperfine coupling is 'always-on' leads to an 'error' that is intrinsic to our system. In contrast to conventional STIRAP that uses overlapping light pulses, we propose to adiabatically increase the coupling $g_a(t)$ so that $g_a(T) \gg g_n$ and therefore the mapping is imperfect as g_n is constant and cannot be 'switched off'. Treating the coupling g_n as a small perturbation in first-order perturbation theory at $t = T$, the fidelity is found to be

$$F = \frac{|\langle \xi^0 \mid \xi \rangle|^2}{\langle \xi \mid \xi \rangle} = \frac{1}{1 + m\, g_n^2/g_a(T)^2} \approx 1 - m \left(\frac{g_n}{g_a(T)}\right)^2, \tag{34}$$

where $|\xi^0\rangle$ is the ideal output state for which $g_n = 0$ (at $t = T$) and $|\xi\rangle = |\xi^0\rangle + |\xi^1\rangle + \cdots$ is the unnormalized eigenstate of H_m.

Another error arises from the non-adiabaticity due to finite times of realistic processes. For a quantitative estimate of the time T that is needed for an adiabatic passage to occur, we use the well-known adiabatic theorem [46] and numerically compute the minimum time T fulfilling

$$\frac{|\langle E_1^m(t)|(\mathrm{d}/\mathrm{d}t)(H' - \bigoplus_m E_{G_m} \mathbb{1})|\phi_0^m(t)\rangle|}{|E_1|^2} \leqslant \delta_{\mathrm{a}}, \quad \forall\, t \in [0,\ T\,]. \tag{35}$$

The left-hand side of (35) corresponds to the probability to find the system in an excited state $|E_l^m\rangle$ different from $|\phi_0^m\rangle$ (the (purely nuclear) eigenstates to the eigenvalue $E = 0$ of $H' - \bigoplus_m E_{G_m} \mathbb{1}$) and the fidelity decreases with δ_{a}. For $1/100 < \delta_{\mathrm{a}} < 1/10$, the minimum time fulfilling equation (35) for the mapping of one photon is in the range of $1\ \mu\mathrm{s} > T > 0.11\ \mu\mathrm{s}$.

To obtain an accurate description of the errors arising from non-adiabaticity, we use a perturbative approach to treat non-adiabatic corrections and compute the phases arising from non-adiabaticity [47]. As the Hamiltonian $H' = \bigoplus_m H_m$ is block-diagonal, states with different initial photon numbers m do not couple so that we can treat every 'm-photon' subspace separately. Moreover, we can use non-degenerate perturbation theory as the ground states $|G_k\rangle$ that are degenerate within each subspace are not coupled: $\langle G_{k'}|(\mathrm{d}/\mathrm{d}t)H|G_k\rangle$. Supposing to be at $t = 0$ in one of the ground states $|\phi_{G_k}(0)\rangle$ of $H'_m = H_m - E_{G_m}\mathbb{1}$ slowly varying in time, the first-order correction of the energy eigenvalue $E_0 = 0$ of H is given by

$$E_m^1 = \sum_{l \neq k} \frac{|\ \langle \phi_{E_l}|(\mathrm{d}/\mathrm{d}t)H'_m|\phi_{G_k}\rangle\ |^2}{E_l^3}. \tag{36}$$

The phases $\phi_m^1 = \int_0^T (E_m^1/\hbar)\,\mathrm{d}t$ that the system acquires can be found by numerical integration of E_m^1. For $T = 5 \times 10^{-4}$ s and initial photon number $m = 1$, $\phi_m^1 = -1.4 \times 10^{-5}$, and for $m = 2$, $\phi_m^1 = 0.004$, respectively. Thus, as expected, the errors arising from non-adiabaticity are small for sufficiently long times T.

As full polarization of the nuclear spins is hard to achieve, we are also interested in the effect of non-perfect polarization on the mapping fidelity. When the number of polarized spins is reduced from $N \to PN$, where $P = \langle A^z\rangle/\langle A^z\rangle_{\min}$ (as defined in section 2), $P \in [-1, 1]$ gives the polarization of the spin ensemble [21]. The nuclear spin part of H' now reads

$$H_{\text{pol}} = P\frac{A}{2}|\downarrow\rangle\langle\downarrow| + \frac{g_n}{2}\sqrt{P}(S^- b^\dagger + \text{h.c.}). \tag{37}$$

The structure of the Hamiltonian does not change, so the only change is a small variation of the parameters. Thus, the effect on the mapping fidelity is negligibly small. In practice, non-maximal polarization proceeds along with a nonzero variance of P (and the associated Overhauser field), which can have an influence on the mapping procedure. The main consequence is a small dephasing term, which arises from polarization-dependent corrections to H_{el} (equation (27)) in particular, from additional polarization-dependent Stark shifts. Hence, the mapping of Fock states is not affected, but for general superpositions the interface is degraded. The dephasing time can be estimated as $t \approx (1/g_a)(\Delta_{+/-}/\sigma_{\text{oh}})$, where σ_{oh} is the standard deviation of the Overhauser field. Since the mapping time T is $\sim 1/g_a$, increasing $\Delta_{+/-}$ and decreasing σ_{oh} can ensure that $T/t \ll 1$, making the dephasing over the whole mapping process small.

A further (smaller) effect of $P \not\approx 1$ is that the assumption that the collective nuclear spin operators A^+, A^- can be well approximated by the bosonic operators $b^\dagger, b$ for a small number of flipped spins is no longer that straightforward, as the exact expression for $A^+ \to \sqrt{N}\sqrt{1-(b^\dagger b/N)}b^\dagger$ has to be taken into account. Further corrections to the JC Hamiltonian in particular due to inhomogeneous coupling to the nuclear spins are discussed briefly in section 7 and in [34].

6. Quantum interface in the bad cavity limit

In previous sections, we have shown that a quantum interface can be achieved via direct mapping of the cavity field to the nuclear spins of the QD. But we have also seen that the cavity lifetimes required for high-fidelity storage are much larger than what is today's state of the art, i.e. as $g_{1,2} \ll 1/\tau_{\text{cavity}}$, we are, compared to the effective coupling, in the 'bad cavity limit'. A second problem with this approach is that the quantum information we want to map to the nuclei has to be coupled to a high-Q cavity. This is notoriously difficult although theoretical proposals exist [3] that should avoid reflection completely. Both problems can be circumvented employing ideas similar to [48, 49] by using the TMS Hamiltonian H_{sq} (see (11)) (note that we now return to the system proposed in section 2 for the rest of the paper). As discussed in [35] and elaborated in more detail below, it is possible to create entanglement between nuclei and the traveling-wave output field of the cavity. Then, quantum teleportation can be used to write the state of another traveling-wave light field onto the nuclei (figure 8)[6]. This approach gives an active role to cavity decay in the interface and can tolerate a bad effective cavity as long as strong coupling is achieved in equation (5). Moreover, it does not require coupling the quantum information to the cavity. Similarly, H_{bs} (equation (10)) enables read-out, by writing the state of the nuclei to the output field of the cavity. The entanglement between nuclear spins and output field can also be used to entangle nuclear spins in two distant cavities by interfering the output light of the cavities at a beamsplitter (figure 9).

[6] This maps the state up to a random (but known) displacement. It can be undone using H_{bs}, where the cavity is pumped with strong coherent light for a short time [50].

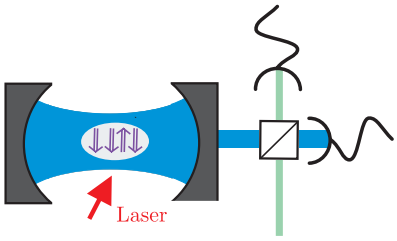

Figure 8. Quantum teleportation can be used to write the state of a traveling-wave light field onto the nuclei.

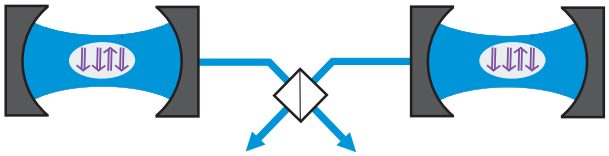

Figure 9. Nuclear spins of QDs in two distant cavities can be entangled by interfering the traveling wave output fields of the two cavities at a beamsplitter and measuring.

6.1. Entangling nuclei with the output field

The Hamiltonian of the nuclear spin–cavity system tuned to the squeezing interaction (11) and coupled to the environment is given by

$$H = g_2(a^\dagger b^\dagger + ab) + \mathrm{i}a\int\sqrt{\frac{\gamma}{2\pi}}c_\omega^\dagger\,\mathrm{d}\omega + \mathrm{h.c.} + \int\omega c_\omega^\dagger c_\omega\,\mathrm{d}\omega, \tag{38}$$

where c_ω are the annihilation operators of the bath and γ the cavity decay constant. We have specialized (11) to the case $\omega_1 = -\omega_2$ and transformed it to an interaction picture[7] with $H_0 = \omega_1(a^\dagger a - b^\dagger b) + \omega_1\int c_\omega^\dagger c_\omega\,\mathrm{d}\omega$ and performed the rotating-wave and Markov approximations in the description of the cavity decay [51]. The quantum Langevin equations of cavity and nuclear operators read

$$\dot{a}(t) = -\mathrm{i}g_2\,b^\dagger(t) - \frac{\gamma}{2}a(t) - \sqrt{\gamma}c_{\mathrm{in}}(t), \tag{39a}$$

$$\dot{b}(t) = -\mathrm{i}g_2\,a^\dagger(t). \tag{39b}$$

Here, c_{in} describes the vacuum noise coupled to the cavity and satisfies $[c_{\mathrm{in}}(t), c_{\mathrm{in}}^\dagger(t')] = \delta(t-t')$. The solutions of equations (39*a*) and (39*b*) are given (for $t \geqslant 0$) by

$$a(t) = p_-(t)a(0) + q(t)b^\dagger(0) + \sqrt{\gamma}\int_0^t p_-(t-\tau)c_{\mathrm{in}}(\tau)\mathrm{d}\tau, \tag{40a}$$

$$b(t) = q(t)a^\dagger(0) + p_+(t)b(0) + \sqrt{\gamma}\int_0^t q(t-\tau)c_{\mathrm{in}}^\dagger(\tau)\mathrm{d}\tau, \tag{40b}$$

[7] As was already the case in equation (11), all optical operators are also taken in a frame rotating with the laser frequency ω_{l}.

where

$$p_{\pm} = \mathrm{e}^{-(1/4)t\gamma}\left[\cosh(\nu t) \pm \frac{\gamma}{4\nu}\sinh(\nu t)\right], \tag{41}$$

$$q = -\mathrm{i}\frac{g_2}{\nu}\mathrm{e}^{-(1/4)\gamma t}\sinh \nu t, \tag{42}$$

with

$$\nu = \sqrt{\left(\frac{\gamma}{4}\right)^2 + g_2^2}. \tag{43}$$

While equations (40*a*) and (40*b*) describe a non-unitary time evolution of the open cavity–nuclei system, the overall dynamics of the system plus surrounding free field given by the Hamiltonian in equation (38) is unitary. Moreover, it is Gaussian (see appendix A), since all involved Hamiltonians are quadratic. Since all initial states are Gaussian (vacuum), the joint state of cavity, nuclei, and output fields is a pure Gaussian state at all times as well. This simplifies the analysis of the dynamics and in particular the entanglement properties significantly: the covariance matrix (defined by equation (A.4) in appendix A) of the system allows us to determine the entanglement of one part of the system with another one. In particular, we are interested in the entanglement properties of the nuclei with the output field.

The covariance matrix $\Gamma_{\mathrm{ns\text{–}c\text{–}o}}$ of the pure Gaussian state of nuclear spins, cavity and output field and thus the covariance matrix $\Gamma_{\mathrm{ns\text{–}o}}$ of the reduced nuclei–output field system can be found by analyzing the covariance matrix of the cavity–nuclei system $\Gamma_{\mathrm{ns\text{–}c}}$.

The elements $\langle X\rangle$ of the covariance matrix $\Gamma_{\mathrm{ns\text{–}c}}$ can be calculated by solving the Lindblad equation evaluated for the expectation values $\langle X\rangle$

$$\frac{\mathrm{d}}{\mathrm{d}t}\langle X\rangle = \mathrm{i}\langle[H_{\mathrm{sq}}, X]\rangle + \frac{\gamma}{2}\left(\langle 2a^{\dagger}Xa\rangle - \langle Xa^{\dagger}a\rangle - \langle a^{\dagger}aX\rangle\right). \tag{44}$$

We thus find the covariance matrix of the cavity–nuclei system to be

$$\Gamma_{\mathrm{ns\text{–}c}} = \begin{pmatrix} m & 0 & 0 & k \\ 0 & m & k & 0 \\ 0 & k & n & 0 \\ k & 0 & 0 & n \end{pmatrix}, \tag{45}$$

where

$$m = \mathrm{e}^{-\gamma t/2}\left[\frac{\gamma}{\nu}\sinh(2\nu t) + \left(\frac{g_2^2}{\nu^2} + \frac{\gamma^2}{8\nu^2}\right)\cosh(2\nu t) + \frac{g_2^2}{\nu^2}\right] - 1, \tag{46a}$$

$$n = 1 + 32\frac{g_2^2}{\nu^2}\mathrm{e}^{-\gamma t/2}\sinh(\nu t)^2, \tag{46b}$$

$$k = \mathrm{e}^{-\gamma t/2}\left[\frac{g_2\gamma}{2\nu^2}\sinh(\nu t)^2 + \frac{g_2}{\nu}\sinh(2\nu t)\right]. \tag{46c}$$

According to Williamson [52], there exists a symplectic transformation S (cf appendix A) such that $\Gamma_{\mathrm{D}} = S\Gamma_{\mathrm{ns\text{–}c}}S^{\mathrm{T}} = \mathrm{diag}(\lambda_1^s, \lambda_1^s, \lambda_2^s, \lambda_2^s)$, where $\{\lambda_1^s, \lambda_2^s\}$ are the symplectic eigenvalues of $\Gamma_{\mathrm{ns\text{–}c}}$. This allows us to calculate the covariance matrix of the pure nuclei–cavity–output field system

$$\Gamma_{\mathrm{ns\text{–}c\text{–}o}} = S'\Gamma_{\mathrm{D}'}(S'^{-1})^{\mathrm{T}}, \tag{47}$$

with $\Gamma_{D'}$ in 2×2 block-matrix form

$$\Gamma_{D'} = \begin{pmatrix} \cosh(2r_1)\mathbb{1}_2 & & \sinh(2r_1)\sigma_z & \\ & \cosh(2r_2)\mathbb{1}_2 & & \sinh(2r_2)\sigma_z \\ \sinh(2r_1)\sigma_z & & \cosh(2r_1)\mathbb{1}_2 & \\ & \sinh(2r_2)\sigma_z & & \cosh(2r_2)\mathbb{1}_2 \end{pmatrix}, \tag{48}$$

where $\cosh r_1 = \lambda_1^s$ and $\cosh r_2 = \lambda_2^s$ and

$$S' = \begin{pmatrix} S & \\ & \mathbb{1}_{4\times 4} \end{pmatrix}.$$

One of the symplectic eigenvalues $\{\lambda_1^s, \lambda_2^s\}$ is 1, indicating a pure—and therefore unentangled—mode in the system. This implies that there is a single 'output mode' in the out-field of the cavity to which the cavity–nuclear system is entangled and we can thus trace out the unentangled output mode.

The procedure for entangling the nuclei with the output field (write-in) is: let H_{sq} act for time t_1 to create a two-mode squeezed state $\psi(g_2, t_1)$: nuclei entangled with cavity and output field. To obtain a state in which the nuclei are only entangled to the output field, we switch the driving laser off ($g_2 = 0$) and let the cavity decay for a time $t_2 \gg \tau_{\mathrm{cav}}$, obtaining an almost pure two-mode squeezed state of nuclei and the output mode. We define the coupling as

$$g_t = \{g_2, t < t_1\ 0, t \geqslant t_1. \tag{49}$$

For the parameters used in section 3, $g_2 \sim 1.9 \times 10^{-3}\,\mu$eV. The entanglement of the different subsystems can be quantified: we compute the gEoF [43] of the reduced covariance matrix of the nuclei–output field system to quantify the entanglement of the nuclei with the output field (see figure 10). For a Gaussian state $\rho_{(\gamma,d)}$, the gEoF $E_{\mathrm{G}}(\rho_{(\gamma,d)})$ is defined as the minimal amount of average entanglement in a decomposition of $\rho_{(\gamma,d)}$ into Gaussian states, i.e. $E_{\mathrm{G}}(\rho_{(\gamma,d)}) = \min\{\int_{\gamma',d'} \mathrm{d}p(\gamma', d')E(\rho_{(\gamma',d')}) : \rho_{(\gamma,d)} = \int_{\gamma',d'} \mathrm{d}p(\gamma', d')\rho_{(\gamma',d')}\}$ [43]. Thus $E_{\mathrm{G}}(\rho_{(\gamma,d)})$ measures how costly it is (in terms of entanglement) to prepare $\rho_{(\gamma,d)}$ by mixing Gaussian states and gives an upper bound to the entanglement of formation (EoF). In the present case, it coincides with the logarithmic negativity [53]. The entanglement of the pure cavity–nuclei–output mode system can be quantified using the entanglement entropy S_{E} [54]. We plot the S_{E} of the nuclei–cavity system with the output mode (see figure 11(a)) and of the nuclei with the cavity–output mode system (see figure 11(b)). The entanglement is plotted versus $g_2 t$ for different ratios of the cavity decay constants and the coupling γ/g_2.

6.2. Write-in: teleportation channel

The entangled state between nuclei and the cavity output field allows us to map a state of a traveling light field to the nuclei using teleportation (see figure 8) [25].

To realize the teleportation, a Bell measurement has to be performed on the output mode of the cavity and the signal state to be teleported. This is achieved by sending the two states through a 50 : 50 beamsplitter and measuring the output quadratures [25]. To be able to do this, we need to know B_0, the output mode of the cavity. In the following, we derive an exact expression for this mode.

We fix a time t and denote by $B(y, t)$, $y \in \mathbb{N}$ a complete set of bath modes outside the cavity. $B(y, t)$ can be expressed as a superposition of bath operators $c(x, t)$

$$B(y, t) = \int z(y, x, t)c(x, t)\,\mathrm{d}x, \tag{50}$$

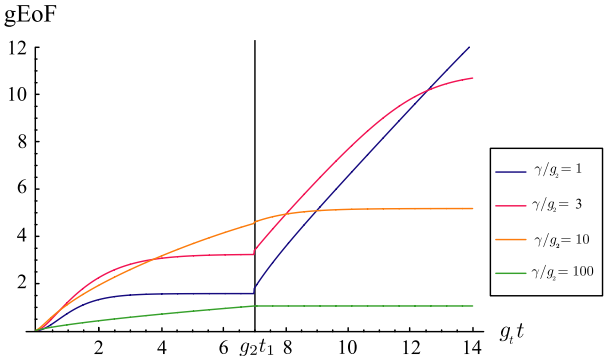

Figure 10. Plot of the gEoF of the nuclei with the output field versus t for different values of γ/g. At $g_2t_1 = 7$, the coupling is switched off. The curve saturates when all excitations have leaked out of the cavity.

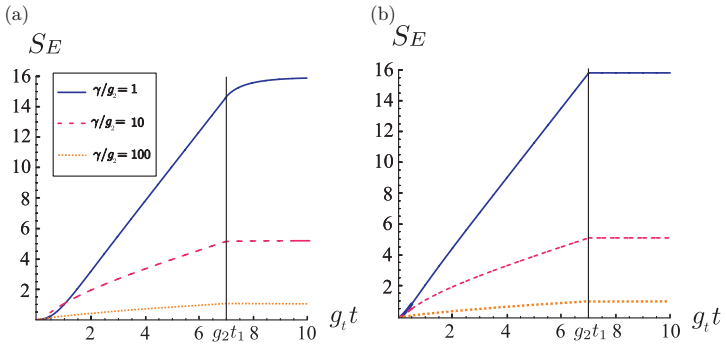

Figure 11. (a) Plot of the entanglement entropy S_E of the nuclei+cavity system with the output field versus t for different values of γ/g. At $g_2t_1 = 7$, the coupling is switched off. (b) Plot of the S_E of the nuclei with the cavity+output field versus g_2t for different values of γ/g_2.

where we introduce a complete set of orthonormal mode functions $z(y, x, t)$. The bath operators $c(x, t)$ are known from the input–output relations [51]

$$c(x,t) = \frac{\sqrt{\gamma}}{2} a(t-x)\chi_{[0,t]}(x), \tag{51}$$

where $a(t)$ is given by equation (40*a*) and

$$\chi_{[0,t]}(x) = \begin{cases} 1, & 0 \leqslant x \leqslant t, \\ 0, & x < 0, \ x > t. \end{cases} \tag{52}$$

To calculate $B(y, t)$, we thus need to determine $z(y, x, t)$. This can be done by calculating the variance $\langle c^\dagger(x,t), c(x',t)\rangle = \langle c^\dagger(x,t)c(x',t)\rangle - \langle c^\dagger(x,t)\rangle\langle c(x',t)\rangle$ following two different pathways: With equation (51), we find

$$\langle c^\dagger(x,t), c(x',t)\rangle = \frac{\gamma}{4} q(t-x')q(t-x)^*, \tag{53}$$

where $q(t)$ is given by equation (42). Another way to express $c(x,t)$ follows from (50):

$$c(x,t) = \sum_y z(y,x,t)^* B(y,t). \tag{54}$$

As shown in section 6.1 there exists only one output mode which we label $y = 0$. This mode contains all the output photons. Therefore $\langle B(y,t)^\dagger B(y',t)\rangle = K\,\delta_{y0}\delta_{y'0}$ and the variance using (54) reads

$$\langle c^\dagger(x,t), c(x',t)\rangle = K z(0,x,t) z(0,x',t)^*. \tag{55}$$

Comparing (53) to (55), we find

$$z(0,x,t) = \frac{q(t-x)^*}{\sqrt{\int |q(t-x)|^2\,\mathrm{d}x}} \tag{56}$$

and $K = (\gamma/4)\sqrt{\int |q(t-x)|^2\,\mathrm{d}x}$ and we have thus fully determined $B(0,t)$ (see figure 14). Note that the bath modes are given in a frame rotating with $\omega_1 + \omega_l$ to which we transformed in section 2 (ω_l) and section 6 (ω_1).

Therefore a state of a traveling light field can be teleported to the nuclear spins up to a random displacement that arises from the teleportation protocol [25, 55]. The random displacement can be undone, letting the beamsplitter interaction H_{bs} (given by equation (10)) act for a short time, while pumping the cavity with intense coherent light as suggested in [50].

Next, we want to consider the quality of the teleportation. Whereas before (see figures 10 and 11) the time evolution of the system for a fixed switch-off time $g_2 t_1 = 7$ was considered, we now consider the 'final' entangled state of nuclei and output field depending on $g_2 t_1$, where the cavity has decayed to the vacuum state, while the nuclei are (still) stationary.

The fidelity with which a quantum state can be teleported onto the nuclei is a monotonic function of the TMS parameter

$$r_1 = \tfrac{1}{2}\,\mathrm{arccosh}(m(t = t_1)) \tag{57}$$

with m defined in equation (46*a*). A typical benchmark [39] is the average fidelity with which an arbitrary coherent state can be mapped. This fidelity has a simple dependence on the TMS parameter r_1 of the state used for teleportation and is given by [56]

$$F_{\mathrm{tel}} = \frac{1}{1 + \mathrm{e}^{-2r_1}}. \tag{58}$$

We plot the teleportation fidelity dependent on the switch-off time t_1 (see figure 12).

Already for $r_1(t_1) \sim 1$, fidelities above 0.8 are obtained. After switching off the coupling we have to wait for the cavity to decay, which typically happens on a nanosecond timescale and does not noticeably prolong the protocol.

6.3. Read-out

The beamsplitter Hamiltonian H_{bs} (given by equation (10)) enables read-out of the state of the nuclei by writing it to the output field of the cavity. The quantum Langevin equations of cavity and nuclear operators lead to almost identical solutions as for H_{sq} (see equations (40*a*) and

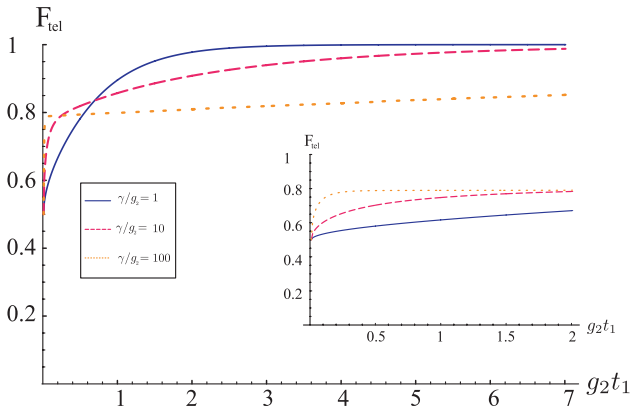

Figure 12. Plot of the teleportation fidelity versus $g_2 t_1$ for different values of γ/g_2.

(40*b*)): of course, now $a(t)$ is coupled to $b(t)$ instead of $b^\dagger(t)$ but the only other change to equations (40*a*) and (40*b*) is to replace ν by

$$\tilde{\nu} = \sqrt{(\gamma/4)^2 - g_1^2}. \tag{59}$$

This has the effect that all terms in equations (40*a*) and (40*b*) show exponential decay with t. The decay of the slowest terms $\sim e^{-2{g_1}^2/\gamma t}$ sets the timescale for read-out. To calculate the read-out fidelity, we need to know the state of the output field at time $t = T$. We assume that the state we want to read-out is a coherent state with displacement $\alpha_{\rm ns}$ at time $t = 0$ fully described by its covariance matrix $\gamma_b(0) = \mathbb{1}$ and its displacement $d_b(0) = \langle b \rangle = \alpha_{\rm ns}$ (while cavity and output field are in the vacuum state at $t = 0$). As the norm of the displacement $\|d(t)\|$ of the nuclei–cavity–output system

$$d(t) = \begin{pmatrix} d_a(t) \\ d_b(t) \\ d_{B_0}(t) \end{pmatrix} = \begin{pmatrix} \langle a(t) \rangle \\ \langle b(t) \rangle \\ \langle B_0(t) \rangle \end{pmatrix} \tag{60}$$

does not change under the beamsplitter transformation, the displacement of the output mode B_0 is given by

$$\begin{aligned} |d_{B_0}(t)| &= \sqrt{\|d(0)\|^2 - d_a(t)^2 - d_b(t)^2} \\ &= \sqrt{1 - (|q(t)|^2 + |p_+(t)|^2)}|\alpha_{\rm ns}|, \end{aligned} \tag{61}$$

where $q(t)$ and $p_+(t)$ are defined by equations (40*a*) and (40*b*) with ν replaced by $\tilde{\nu}$.

At finite times, the nuclear excitations and the cavity have not fully decayed, which leads to a loss of amplitude of the mapped state. The loss is very small for sufficiently large T. To assure high fidelity even for states with a large photon number, we can amplify the output field as in section 4.1. Then the state of the output field is $(\gamma_{B_0}, d_{B_0}) = (\kappa\mathbb{1}, \alpha_{\rm ns})$ with κ as defined in section 4.1. This leads to a read-out fidelity (see figure 13) given by

$$F_{\rm read} = |\langle \mathbb{1}, \alpha_{\rm ns} | \kappa\mathbb{1}, \alpha_{\rm ns} \rangle|^2 = 1 - (|q|^2 + |p_+|^2),$$

where we have used relations for the transition amplitudes (as in section 4.1) given by [42].

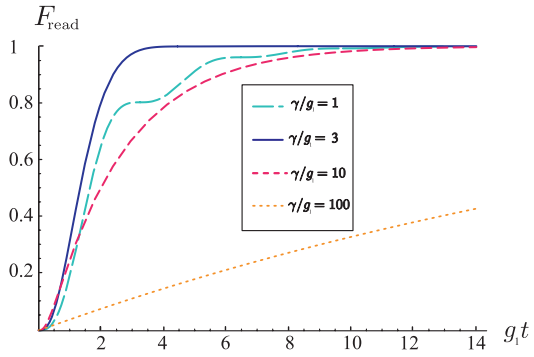

Figure 13. Plot of the read-out fidelity versus $g_1 t$ for different values of γ/g_1

6.4. Output mode

In figure 14, we plot the output mode of the cavity given by equation (50) for write-in and read-out, respectively, and for several choices of the parameters $g_{1,2}$ and γ. We are considering here only the idealized case of a one-sided and one-dimensional cavity. In general, the actual geometry of the cavity at hand has to be taken into account to determine B_0. In the following, we briefly discuss the shape of the mode function. It provides some insight into the dynamics of the mapping process, since due to (51) the weight of $c(x, T)$ in $B(0, t)$ reflects the state of the cavity mode at time $t - x$ in the past.

Write-in: Let us consider the two extreme cases of very strong and very weak cavity decay. In the former case ($\gamma \gg g_2$), the cavity mode can be eliminated, i.e. the nuclear spins couple directly and with constant strength $\sim g_2^2/\gamma$ to the output field: z_0 is a step function, which is 0 for $g_2 = 0$ and constant otherwise. This is reflected in figure 14, where for $\gamma = 100 g_2$ most of the excitations decay directly to the output mode such that z_0 takes a 'large' value at the time the squeezing is switched on and then increases only slowly in time. After switching the squeezing interaction off, the cavity quickly decays to the vacuum. For $\gamma \ll g_2$, instead, TMS builds up in the nuclei–cavity system as long as the squeezing interaction is on (3 μs in figure 14) and, after g_2 is switched off, the cavity decays to its standard exponential output mode. The intermediate cases in figure 14(a) show the shifting weight between 'initial step function' and subsequent exponential decay.

Read-out: In the case of the beamsplitter interaction, the same cases can be distinguished. For large γ/g_1, the cavity can be eliminated and the nuclear spins are mapped directly to the exponential output mode of a cavity decaying with an effective rate g_1^2/γ. For smaller γ, the output mode reflects the damped free evolution of the nuclei–cavity system, which in this case includes oscillations (excitations are mapped back and forth between nuclei and cavity at rate g_1) in absolute value and phase.

6.5. Linear optics with the nuclear spin mode

The interaction we have described can be used not only to map states to the nuclear spin ensemble but also for state generation and transformation. In fact, from a nuclear spin mode in the vacuum state, all single mode Gaussian states can be prepared. To see this, we have to show how any desired 2×2 correlation matrix Γ and displacement $d \in \mathbb{C}$ can be obtained.

IOP Institute of Physics DEUTSCHE PHYSIKALISCHE GESELLSCHAFT

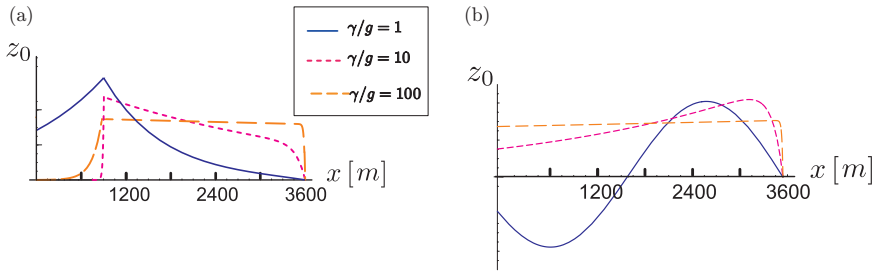

Figure 14. The output mode in one dimension: plot of z_0 versus position x, where $x = 0$ is the position of the cavity. (a) Write-in: the squeezing interaction is 'on' for 3 μs and then switched off. (b) Read-out: for $\gamma \gg g_2$ the excitations have not fully decayed to the output mode after $t = 12\,\mu$s. The read-out fidelity given by equation (62) corresponds to the probability that the excitations in the nuclear spins have decayed into the output mode of the cavity. For $\gamma/g_1 = 1$ and 10, the read-out fidelity is $F_{\text{read}} > 0.98$ after $t \approx 16$–$20\,\mu$s. For $\gamma/g_1 = 100$, however, it takes $\approx 200\,\mu$s to achieve $F_{\text{read}} > 0.98$. Note that for input and output modes to have similar shapes (e.g. for a network), it is best to consider the case where $\gamma/g_1 \gg 1$.

As we already remarked in a discussion of the write-in via teleportation, the beamsplitter Hamiltonian H_{bs} can be used to realize displacements of the nuclear mode. Driving the cavity mode with a strong laser to a coherent state with amplitude α (and the same phase as d) and switching on H_{bs} for a time $t = |\beta|/(g_1|\alpha|)$ provides, in the limit of large α, a good approximation to the displacement operation by β [50].

Concerning the CM, we assume that every CM of a pure Gaussian state is of the form $\Gamma = ODO^{\text{T}}$, where D is a positive diagonal matrix with determinant one and O is orthogonal and symplectic. O can be seen as the effect of time evolution under some quadratic Hamiltonian acting on the single-mode squeezed state with CM D. In the single mode case, any O represents a phase shift and is obtained by letting the nuclear system evolve 'freely' (without laser coupling, i.e. a polarized electron interacts off-resonantly with the nuclei) according to the Hamiltonian $\propto b^\dagger b$ for some time. Thus, the state with CM Γ can be generated in a two-step process: first generate the state with $\Gamma = D$ and then apply O.

Whereas in the preceding paragraphs we could show how to realize operations that can act on any input state, no such possibility seems to exist for squeezing in our context. Instead we show how to obtain the pure single-mode squeezed state with CM D from the vacuum state. Letting H_{sq} act on the vacuum results in a two-mode squeezed state with squeezing parameter r_2. Performing a homodyne measurement (of the X quadrature) on the optical part of this state projects the nuclear system into a squeezed state with squeezing $r_1 = \ln[\cosh(2r_2)]/2$ [57]; thus given enough TMS, any CM D can be produced.

One can go even further and simulate evolution according to any quadratic Hamiltonian on the nuclear–optical system: according to Krauss *et al* [58], the Hamiltonian given by equation (8) with the interaction part $g_1 ab^\dagger + g_2 a^\dagger b^\dagger + \text{h.c.}$ enables simulation of any Hamiltonian quadratic in $a, b, a^\dagger, b^\dagger$.

7. Remarks on internal nuclear dynamics and approximations

With regard to the realization of the proposed protocol and the applicability of the approximations leading to the Hamiltonians (10) and (11), there are three aspects to consider: spontaneous emission of the QD, the internal nuclear dynamics and errors in the bosonic description. We assume the strong coupling limit of cavity-QED and neglect spontaneous emission of the QD. The other two aspects will be studied in the following. Note that the results on the internal nuclear dynamics are corroborated by an independent work by Kurucz *et al* [59]. They introduce the bosonic description to analyze the performance of a nuclear spin quantum memory and show that the performance of the memory is enhanced due to a detuning between excitations in the mode b versus those in other modes $b_{k\neq 0}$ and that secular dipolar terms do not affect the memory.

7.1. Internal nuclear dynamics

Up to now, we have focused exclusively on the hyperfine interaction and neglected 'internal' nuclear dynamics, dominated by dipolar and quadrupolar interactions. Moreover, the hyperfine coupling leads to a dipolar interaction between nuclei mediated by the electron. We study the dipolar interaction between nuclear spins, which is significantly weaker than g_n, g_1 and g_2: the energy scale for dipolar interaction between two nuclei has been estimated to be $\sim 10^{-5}\,\mu$eV for GaAs [26]. However, since for 10^4–10^6 nuclei there are many of these terms, they might play a role at the 10–50 μs timescales considered.

7.1.1. Dipolar interaction. The Hamiltonian of the direct dipolar interaction between N nuclei is given by [60]

$$H_{\rm dd} = -\frac{\mu_0}{4\pi}\frac{1}{2}\sum_{i=1}^{N}\sum_{j\neq i=1}^{N}\frac{\mu_i\mu_j}{I_iI_j}\frac{1}{r_{ij}^3}\left(\frac{3(\mathbf{I}_i\mathbf{r}_{ij})(\mathbf{I}_j\mathbf{r}_{ij})}{r_{ij}^2}-\mathbf{I_i}\mathbf{I_j}\right), \tag{62}$$

where $\mathbf{r}_{ij}$ is the vector connecting spins i and j and $\boldsymbol{\mu}_i = (\mu_i/I_i)\mathbf{I}_i$ is the magnetic moment of the nuclear spin operator $\mathbf{I}_i$. $H_{\rm dd}$ can be written as

$$H_{dd} = \sum_{i=1}^{N}\sum_{j\neq i=1}^{N}\tilde{\gamma}_{ij}[A_{ij}I_i^zI_j^z + B_{ij}I_i^+I_j^- + (C_{ij}I_i^+I_j^+ + D_{ij}I_i^zI_j^- + \text{h.c.})], \tag{63}$$

where $A_{ij} = 1-3\cos^2\theta_{ij}$, $B_{ij} = -\frac{1}{2}(1-3\cos^2\theta_{ij})$, $C_{ij} = -\frac{3}{4}\sin^2\theta_{ij}\,\mathrm{e}^{-2\mathrm{i}\phi_{ij}}$, $D_{ij} = -\frac{3}{2}\sin\theta_{ij}\cos\theta_{ij}\,\mathrm{e}^{\mathrm{i}\phi_{ij}}$ and $\tilde{\gamma}_{ij} = \mu_0\mu_i\mu_j/4\pi r_{ij}^3$. In GaAs, the nearest-neighbor dipolar interaction strength is around $\tilde{\gamma} = 10^{-5}\,\mu$eV [26]. We want to calculate the strength of the dipolar interaction between the main bosonic mode (which is defined as the mode that is coupled to the electron spin) and other bath modes (here, we no longer assume homogeneous coupling of the nuclei to the electron). We therefore write the Hamiltonian in terms of collective nuclear spin operators, use, in a next step, the bosonic approximation and, finally, separate the relevant terms (the ones that couple the main bosonic mode to bath modes) and calculate the coupling strength of the main mode to the bath modes.

For highly polarized nuclear spins, the first term of $H_{\rm dd}$ can be written as

$$\sum_{i=1}^{N}\sum_{j\neq i=1}^{N}\tilde{\gamma}_{ij}A_{ij}I_i^zI_j^z \approx \frac{1}{2}\sum_{i=1}^{N}\sum_{j\neq i=1}^{N}\tilde{\gamma}_{ij}A_{ij}\left(\frac{1}{2}-I_i^+I_i^- - I_j^+I_j^-\right), \tag{64}$$

where we write $I_i^z = -\frac{1}{2} + I_i^+ I_i^-$ and neglect the second-order term $I_i^+ I_i^- I_j^+ I_j^-$, which requires two excitations to be nonzero; thus, in the highly polarized case, the contribution from these terms is by a factor of $p = (1-P)/2$ smaller than the terms we keep. The last term is (for spin-1/2 nuclei)

$$\sum_{i=1}^{N} \sum_{j\neq i=1}^{N} \tilde{\gamma}_{ij} D_{ij} I_i^z I_j^- \approx -\frac{1}{2} \sum_{i=1}^{N} \sum_{j\neq i=1}^{N} \tilde{\gamma}_{ij} D_{ij} I_j^-, \tag{65}$$

neglecting higher order terms. In extension to the definition of the collective operators $A^{\pm}$ in section 2, which we now label $A_0^{\pm}$, we introduce a complete set of collective operators $A_k^- = \sum_i \alpha_i^{(k)} I_i^-$ with $k = 0, \ldots, N-1$ with an orthogonal set of coefficients $\alpha_i^{(k)}$ for which $\sum_i \alpha_i^k = 1$ for every collective mode k. Defining a unitary matrix U with columns $\boldsymbol{\alpha}^{(k)} = (1/\sqrt{\sum_i \alpha_i^{(k)2}})(\alpha_1^{(k)}, \ldots, \alpha_N^{(k)})^{\mathrm{T}}$, we can write

$$(I_1^-, \ldots, I_N^-)^{\mathrm{T}} = U\mathbf{A}^-, \tag{66}$$

where

$$\mathbf{A}^- = \mathrm{diag}\left(\frac{1}{\sqrt{\sum_i \alpha_i^{(0)2}}}, \ldots, \frac{1}{\sqrt{\sum_i \alpha_i^{(N-1)2}}} \right) (A_0^-, \ldots, A_{N-1}^-)^{\mathrm{T}}.$$

Writing H_{dd} in terms of the collective operators $A_k^{-,+}$ and neglecting higher order terms,

$$H_{\mathrm{dd}} = \mathbf{A}^+ U^\dagger S U \mathbf{A}^- + (\mathbf{A}^- U^\dagger M U \mathbf{A}^- - \tfrac{1}{2} D U \mathbf{A}^- + \mathrm{h.c.}). \tag{67}$$

Here, $M_{ij} = \tilde{\gamma}_{ij} C_{ij}$ for $i \neq j$, $M_{ij} = 0$ for $i = j$, $S_{ij} = \tilde{\gamma}_{ij} B_{ij}$ for $i \neq j$ and $S_{ii} = \sum_{l=1}^{N} \tilde{\gamma}_{il} A_{il}$ for $i = j$. D is a vector with entries $D_j = \sum_{i\neq j=1}^{N} \tilde{\gamma}_{ij} D_{ij}$. Next, we write H_{dd} in terms of bosonic operators, using the bosonic approximation introduced in section 2, and map $\mathbf{A}^- \to \mathbf{b} = (b_0, \ldots, b_{N-1})^{\mathrm{T}}$. This allows us to separate relevant terms of H_{dd}, which couple the main bosonic mode b_0 to other (bath) modes b_k. Isolating the terms containing b_0, we find

$$b_0 \left[\sum_{k\neq 0} (U^\dagger 2MU)_{0k} b_k + (U^\dagger SU)_{0k} b_k^\dagger - \frac{1}{2} D_k U_{0k} \right] + \mathrm{h.c.} + (U^\dagger SU)_{00} b_0^\dagger b_0$$
$$+ (U^\dagger 2MU)_{00} b_0 b_0 + \mathrm{h.c.}, \tag{68}$$

where the notation $(U^\dagger SU)_{01}$ denotes the element $(0, l)$ of the matrix $U^\dagger SU$. The first term describes the passive coupling of the main mode b_0 to other modes b_k and acquires a factor of two, as the terms that describe the active coupling in equation (68) can be written $b_1 (U^\dagger MU)_{1k} b_k + b_k (U^\dagger MU)_{k1} b_1 = b_1 (U^\dagger 2MU)_{1k} b_k$ as $(U^\dagger MU)_{k1} = (U^\dagger MU)_{1k}$: the entries of U are real so that $(U^\dagger)^{\mathrm{T}} = U$ and $M = M^{\mathrm{T}}$, i.e. $M_{ij} = -\tilde{\gamma}_{ij} \frac{3}{4} \sin^2 \theta_{ij}\, \mathrm{e}^{-2\mathrm{i}\phi_{ij}} = M_{ji}$ as $\phi_{ji} = \pi + \phi_{ij}$. The second term in equation (68) describes the passive coupling of b_0 to the modes $b_k^\dagger$ and the third term displaces the main mode. The last two terms describe a constant energy shift ($\sim b_0^\dagger b_0$) and a squeezing term ($\sim b_0 b_0 + \mathrm{h.c.}$), respectively.

The terms that couple the main mode b_0 to bath modes can be written as

$$b_0 \left(\sum_{k\neq 0} (U^\dagger 2MU)_{0k} b_k + (U^\dagger SU)_{0k} b_k^\dagger - \frac{1}{2} D_k U_{0k} \right) + \mathrm{h.c.}$$
$$= b_0 \left(c_1 \tilde{b}_1 + c_2 \tilde{b}_2^\dagger - \frac{1}{2} \sum_{k\neq 0} D_k U_{0k} \right) + \mathrm{h.c.}, \tag{69}$$

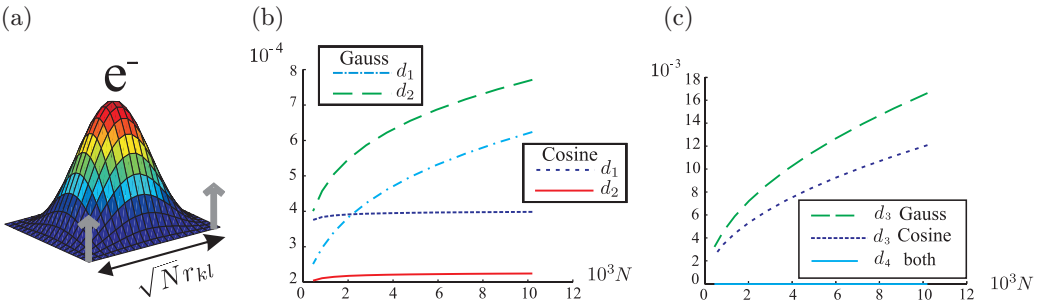

Figure 15. (a) Cosine-shaped wavefunction of the electron on a two-dimensional square grid with the nuclear spins located at the vertex points; (b) plot of the ratios $d_1 = \tilde{\gamma}(\Delta M_0)/g_2$ and $d_2 = \tilde{\gamma}(\Delta S_0)/g_2$ for a cosine- and a Gaussian-shaped wavefunction. For $N = 10^4$, both ratios d_1 and d_2 are of the order of 10^{-4}; together with (c), we see that the dipolar interaction is negligible. (c) Plot of the ratios $d_3 = \tilde{\gamma}(U^\dagger S U)_{00}/g_2$ and $d_4 = \tilde{\gamma}(U^\dagger 2MU)_{00}/g_2$ for a cosine- and a Gaussian-shaped wavefunction. For $N = 10^4$, d_3 is of the order of 10^{-2} and d_4 is zero due to the symmetry of the electron wavefunction.

where the linear combinations of bosonic modes b_k and $b_k^\dagger$ can be transformed to bosonic modes $\tilde{b}_1$ and $\tilde{b}_2^\dagger$. The coupling strength of b_0 to the first term in equation (69) is given by

$$[c_1\tilde{b}_1, (c_1\tilde{b}_1)^\dagger] = |c_1|^2 = \sum_{k\neq 0} |(U^\dagger 2MU)_{0k}|^2$$
$$= (U^\dagger 4MM^\dagger U)_{00} - |(U^\dagger 2MU)_{00}|^2 = (\Delta M_0)^2, \tag{70}$$

and $|c_2|^2 = (\Delta S_0)^2$ for the second term. ΔM_0 and ΔS_0 depend only on the electron wavefunction and the lattice geometry. To numerically calculate ΔM_0 and ΔS_0 and the effect of the last two terms in equation (68), we consider the case where the nuclei lie in a two-dimensional square plane with length $R = \sqrt{N} r_0$ of each side on a grid with equal spacings $r_0 (= 0.24$ nm in GaAs [26]) (see figure 15(a)). Consequently, $\theta_{ij} = \pi/2$, which simplifies many expressions in H_{dd}. These assumptions can be made as the height of the QD is small compared to its diameter, so that the variation of θ that is dependent on the height of the QD is small, $\theta_{ij} \approx \pi/2$.

To illustrate our results, we consider two simple choices for the electron wavefunction such that $\alpha_1^{(0)} = 1/\sum_1 f_{1/2}(\mathbf{r}_1) f_{1/2}(\mathbf{r}_1)$ with $\mathbf{r}_1 = (x_1, y_1)$,

$$f_1(\mathbf{r}_1) = \cos\left(\frac{\pi}{2}\frac{x_1}{R}\right)^2 \cdot \cos\left(\frac{\pi}{2}\frac{y_1}{R}\right)^2 \tag{71}$$

and

$$f_2(\mathbf{r}_1) = \exp(-\sqrt{2} r_1^2/R^2). \tag{72}$$

To show that the direct dipolar interaction is a weak effect compared to the optical–nuclear coupling g, we calculate the ratios

$$d_1 = \frac{\tilde{\gamma}(\Delta M_0)}{g_2} = \frac{\tilde{\gamma}(\Delta M_0)}{\frac{\Omega_c \Omega_1 g_n}{8\Delta'_{T_-}\tilde{\omega}_e}} = \frac{8\Delta'_{T_-}\tilde{\omega}_e}{\Omega_c\Omega_1}\frac{\tilde{\gamma}}{A}\frac{(\Delta M_0)}{\sqrt{\sum_{i=1}^N \alpha_i^{(0)2}}} \tag{73}$$

and $d_2 = \tilde{\gamma}\Delta S_0/g_2$. For the parameters used for the simulation in section 3, $(8\Delta'_{T_-}\tilde{\omega}_e/\Omega_c\Omega_l)(\tilde{\gamma}/A) \approx 4 \times 10^{-5}$ with $\tilde{\gamma}$ for GaAs [26]. A plot of d_1 and d_2 is shown in figure 15(b). d_1 and d_2 are both of the order of 10^{-4}–10^{-5} for $N > 1000$ nuclear spins and increase slowly with N. The last two terms in equation (68), $(U^\dagger SU)_{00}(b)^\dagger_0 b_0$ and $(U^\dagger 2MU)_{00}b_0b_0$ are small and zero, respectively, as can be seen in figure 15(c). The ratio of $d_3 = \tilde{\gamma}(U^\dagger SU)_{00}/g_2$ is of the order of 10^{-3}–10^{-2} for $N > 1000$ nuclear spins and the ratio $d_4 = \tilde{\gamma}(U^\dagger 2MU)_{00}/g_2$ is zero due to the symmetry of the electron wavefunction in this setting. Shifting the electron wavefunction such that it is no longer symmetric with respect to the coordinate origin, d_4 is of the order of 10^{-4}. We assume that the nuclei lie in a plane, so there is no displacement of b_0 as $D_{ij} = 0$ for $\theta_{ij} = \frac{\pi}{2}$. Therefore, we have shown that direct dipolar coupling is an effect that does not affect our protocol.

The hyperfine coupling between electron spin and nuclear spin leads to a mediated dipolar interaction between nuclear spins [61]. In the bosonic description, the electron couples solely to the b_0 mode; thus, the mediated coupling leads only to an energy shift

$$\frac{g_n^2}{4\tilde{\omega}_e} b_0^\dagger b_0 \tag{74}$$

that depends on the Zeeman splitting $\tilde{\omega}_e$ and the number of nuclear excitations. This was already present in equation (8) and is not affecting the protocol; in fact it can help as Kurucz *et al* [62] have shown.

For spin-1/2 systems, as considered here, the quadrupolar interaction is not present. For large spin I (e.g. 3/2 or 9/2) nuclei present in GaAs, there is a significant quadrupolar term. Depending on the strain, up to $g_q \lesssim 10^{-2}\,\mu$eV have been measured [63]. Therefore, for $I > 1/2$, dots with small strain have to be considered. The quadrupolar interaction [60] can be treated on a similar footing as the dipolar coupling in section 7.1.1.

7.2. Errors in the bosonic picture

We have relied on a simple bosonic description of the collective nuclear excitations and neglected all corrections to that simplified picture. For homogeneous coupling (α_j =const) this is the well-known Holstein–Primakoff approximation [32] and for systems cooled to a dark state [64] at moderate polarization ($\langle A^z\rangle$ of the order of $-1/2$) spin, replacing the collective spin operators by bosonic operators is accurate to $o(1/N)$. The generic inhomogeneous case is discussed in detail in [34]. In that case, the Hamiltonian (3) can be seen as a zeroth-order approximation in a small parameter $\sim q(1-P)$, where $q \geqslant 1/2$ and $q = 1/2$ for a homogeneous wavefunction. The first-order correction analyzed in [34] contains two contributions: (i) a polarization-dependent scaling of the coupling strength g_n, which has a negligible effect on the adiabatic transfer that we consider and (ii) an effective coupling of b to bath modes due to the inhomogeneity of the A^z term. This correction can be computed similarly to the one in the preceding subsections by rewriting A^z in terms of bosonic operators. The coupling strength of the leading term is found to be $\sim A/N = g_n/\sqrt{N}$ and is thus much weaker than $g_{1/2}$. Since $g_{1/2}$ also characterizes the energy splitting between different excitation-manifolds in the JC system, this term is further suppressed by energy considerations.

8. Summary and conclusions

We have shown how to realize a quantum interface between the polarized nuclear spin ensemble in a singly charged QD and a traveling optical field. The coupling is mediated by the electron

spin and the mode of a high-Q optical cavity to which the QD is strongly coupled. Our proposal exploits the strong hyperfine and cavity coupling of the electron to eliminate the electronic degree of freedom and obtain an effective coupling between cavity and nuclei. First, we have studied several possibilities to directly map the state of the cavity to the nuclei and discussed error processes and drawbacks of these schemes. Then, we have presented a more sophisticated interface that is robust to cavity decay. Read-out is achieved via cavity decay, while write-in is based on the generation of two-mode squeezed states of nuclei and output field and teleportation. For typical values of hyperfine interaction and cavity lifetimes, several ebits of entanglement can be generated before internal nuclear dynamics becomes non-negligible. All proposed schemes take advantage of the bosonic character of the nuclear system at high polarization, which implies that all the relevant dynamics of nuclei, cavity and output field are described by quadratic interactions. This allows the analytical solution of the dynamics and a detailed analysis of the entanglement generated. We show that apart from mapping a light state to the nuclei, the couplings described enable the preparation of arbitrary Gaussian states of the nuclear mode.

For highly polarized nuclear spin systems, the bosonic description provides a very convenient framework for the discussion of (dipolar and quadrupolar) 'internal' nuclear dynamics. It is seen that these processes do not appreciably affect the performance of the interface.

Our results give further evidence that nuclear spins in QDs can be a useful system for quantum information processing. In view of the recent impressive experimental progress in both dynamical nuclear polarization of QDs and QD cavity-QED, their use for QIP protocols may not be too far off.

Acknowledgments

This work was supported by the DFG through SFB 631 and the Excellence Cluster NIM.

Appendix A. Gaussian states and operations

Gaussian states and operations play a central role in quantum information with continuous variable systems [65]. To make this work self-contained, we briefly summarize here the main properties of Gaussian states and operations with particular regard to their entanglement.

Gaussian states are a family of states occurring very frequently in quantum optics, e.g. in the form of coherent, squeezed and thermal states. Despite being defined on an infinite-dimensional Hilbert space ($\mathcal{F}_+(\mathbb{R}^{2N})$, the symmetric Fock space over $\mathbb{R}^{2N}$), they are characterized by a finite number of real parameters, namely the first and second moments of N pairs of canonically conjugate observables $(Q_1, P_1, \ldots, Q_N, P_N) \equiv \vec{R}$.

One way to define them is that their characteristic function, i.e. the expectation values $\chi(\xi) = \mathrm{tr}(W_\xi \rho)$ of the displacement operators $W_\xi = \exp(\mathrm{i}\xi^{\mathrm{T}}\vec{R})$, $\xi \in \mathbb{R}^{2N}$, is a Gaussian function [66]:

$$\chi(\rho) = \exp(-\mathrm{i}\xi^{\mathrm{T}} d - 1/4\xi^{\mathrm{T}}\gamma\xi). \tag{A.1}$$

The displacement vector $d \in \mathbb{R}^{2N}$ and the $2N \times 2N$ real positive covariance matrix (CM) γ are given by the expectations and (co)variances of the R_k:

$$d_k = \mathrm{tr}[\rho R_k], \tag{A.2a}$$

$$\gamma_{kl} = \langle R_i R_j + R_j R_i \rangle - 2\langle R_i \rangle \langle R_j \rangle. \tag{A.2b}$$

All $d \in \mathbb{R}^{2N}$ are admissible displacement vectors and any real positive matrix γ is a valid CM if it satisfies $\gamma \geqslant \mathrm{i}\sigma_N$ when the symplectic matrix σ_N is

$$\sigma_N = \oplus_{l=1}^{N} \sigma_1 \quad \text{with} \quad \sigma_1 = \begin{pmatrix} 0 & -1 \\ 1 & 0 \end{pmatrix}. \tag{A.3}$$

The last condition summarizes all the uncertainty relations for the canonical operators R_j. These operators are related to the creation and annihilation operators $a_j^\dagger$ and a_j by the relations $Q_j = (a_j + a_j^\dagger)/\sqrt{2}$ and $P_j = -\mathrm{i}(a_j - a_j^\dagger)/\sqrt{2}$.

An example of a one-mode Gaussian state is a coherent state $|\alpha\rangle$, with covariance matrix $\gamma = \mathbb{1}$ and displacement $d = (\mathrm{Re}|\alpha|, \mathrm{Im}|\alpha|)/\sqrt{2}$.

Entanglement: All information about the entanglement properties of Gaussian states is encoded in the CM. Given a CM, there are efficient criteria to decide whether a Gaussian state is entangled or not.

To apply these criteria, it is useful to write the CM of bipartite $N \times M$ Gaussian states in the following form:

$$\gamma = \begin{pmatrix} A & C \\ C^{\mathrm{T}} & B \end{pmatrix}, \tag{A.4}$$

where the $2N \times 2N (2M \times 2M)$ matrix A (B) refers to the covariances of the quadrature operators associated with the first (second) system and C contains the covariances between the two systems. A (B) are the CM of the reduced state in the first (second) system only.

In the case of a two-mode system, the criteria [67, 68] are necessary and sufficient for separability: a state with CM γ is entangled if and only if $\det\gamma + 1 - \det A - \det B + 2\det C \ngeqslant 0$. In this case, entanglement is necessarily accompanied by a non-positive partial transpose (npt) [69]. For more modes, entangled states with positive partial transpose exist [70] and more general criteria for deciding entanglement have to be used [71, 72].

For pure states, the analysis of entanglement properties becomes particularly easy since all such states can be transformed to a simple standard form, namely a collection of two-mode squeezed states (TMSS) and vacuum states, by local unitaries [73]; hence the entanglement of such a state is fully characterized by the vector of TMS parameters. This also shows that for a $1 \times M$ system in a pure state, one can always identify a single mode such that only it (and not the $M - 1$ other modes) is entangled with the first system.

For many Gaussian states, it is also possible to make quantitative statements about the entanglement, i.e. to compute certain entanglement measures. For pure $N \times M$ states, the entropy of entanglement can be computed from the symplectic eigenvalues of the reduced CM A (or, equivalently, B). These are given by the modulus of the eigenvalues of $\sigma_N A$ [53]. All symplectic eigenvalues $\lambda \geqslant 1$ correspond to a TMSS with squeezing parameter $\mathrm{arccosh}(\lambda)/2$ in the standard form of the state at hand and contribute $\lambda^2 \log_2 \lambda^2 - (\lambda - 1)^2 \log_2(\lambda^2 - 1)$ to the entanglement entropy of the system. For mixed states, it is possible to compute the negativity [53] for any $N \times M$ system from the symplectic eigenvalues of the CM of the partially transposed state (which is related to the CM obtained by replacing all momenta P_j in the second system by $-P_j$). Every symplectic eigenvalue $\lambda < 1$ contributes $-\log_2 \lambda$ to the negativity.

For 1×1 Gaussian states with $\det A = \det B$ (so-called symmetric states), the EoF can be computed [74], and for more general states, a Gaussian version of EoF is available [43]. Even if the states are not certain to be Gaussian, several of the Gaussian quantities can serve as lower bounds for the actual amount of entanglement [75].

Gaussian operations: Operations that preserve the Gaussian character of the states they act on are called Gaussian operations [57]. Like the Gaussian states they are only a small family (in the set of all operations) but play a prominent role in quantum optics, since they comprise many of the most readily implemented state transformations and dynamics. With Gaussian operations and Gaussian states, many of the standard protocols of quantum information processing such as entanglement generation, quantum cryptography, quantum error correction and quantum teleportation can be realized [65].

Of particular interest for us are the Gaussian unitaries, i.e. unitary evolutions generated by Hamiltonians that are at most quadratic in the creation and annihilation operators. Unitary displacements W_ξ are generated by the linear Hamiltonian $\xi^{\mathrm{T}}\vec{R}$. All other Gaussian unitaries can be composed of three kinds [76], named according to their optical incarnations. The *phase shifter* ($H = a^\dagger a$) corresponds to the free evolution of a harmonic system. The *beamsplitter* ($H = ab^\dagger + a^\dagger b$) couples two modes. Both generators do not change the total photon number and are therefore examples of *passive* transformations. The remaining type of Gaussian unitary is *active*: the (single-mode) *squeezer* is generated by the squeezing Hamiltonian $H = a^2 + (a^\dagger)^2$, which, when acting on the vacuum state, decreases the variance in one quadrature (Q) by a factor $f < 1$ and increases the other one by $1/f$. Combining these building blocks in the proper way, all other unitaries generated by quadratic Hamiltonians, e.g. the TMS transformation ($H = ab + a^\dagger b^\dagger$), can be obtained.

Both active and passive transformations map field operators to a linear combination of field operators (disregarding displacements caused by linear parts in the Hamiltonians, which can always be undone by a further displacement), i.e. for all Gaussian unitaries we have in the Heisenberg picture

$$U\vec{R}U^\dagger = S\vec{R} \equiv \vec{R}'. \tag{A.5}$$

Here S is a symplectic map on $\mathbb{R}^{2N}$, i.e. S preserves the symplectic matrix σ_N, ensuring that R_i and $R_i{}'$ satisfy the same commutation relations. U_S denotes the unitary corresponding to the symplectic transformation S. Passive operations correspond to symplectic transformations that are also orthogonal.

In the Schrödinger picture, U_S transforms the Gaussian state with CM γ and displacement d such that $(\gamma, d) \mapsto (S\gamma S^{\mathrm{T}}, Sd)$. The TMS transformations

$$T(r) = \begin{pmatrix} \cosh(r)\mathbb{1} & \sinh(r)\sigma_x \\ \sinh(r)\sigma_x & \cosh(r)\mathbb{1} \end{pmatrix} \tag{A.6}$$

used in section 4.1 are an important example of active symplectic transformation.

Besides Gaussian unitaries, *Gaussian measurements* are another important and readily available tool. Gaussian measurements are generalized measurements represented by a positive-operator-valued measure $\{|\gamma, d\rangle\langle\gamma, d|\, \gamma, d, d \in \mathbb{R}^{2N}\}$ that is formed by all the projectors obtained from a pure Gaussian state $|\gamma, 0\rangle\langle\gamma, 0|\gamma, 0$ by displacements. The most important example is a limiting case of the above: the quadrature measurements (von Neumann measurements, which project on the (improper, infinitely squeezed) eigenstates of e.g. Q). In quantum optics, these are well approximated by *homodyne detection*. For example, the 'Bell- or EPR-measurement' that is part of the teleportation protocol is a measurement of the commuting quadrature operators $Q_1 + Q_2$ and $P_1 - P_2$.

Appendix B. Landau–Zener transitions

In a rotating frame with $U = \exp\left[-\frac{\mathrm{i}}{2}\int(\omega_1-\omega_2)\sigma_z + (\omega_1+\omega_2)\mathbb{1}\,\mathrm{d}t\right]$ the Heisenberg equations, given by equation (12), read

$$\dot{u}' = -\mathrm{i}g\exp\left(\mathrm{i}\int(\omega_1-\omega_2)\mathrm{d}t\right)v', \tag{B.1}$$

$$\dot{v}' = -\mathrm{i}g\exp\left(-\mathrm{i}\int(\omega_1-\omega_2)\mathrm{d}t\right)u'. \tag{B.2}$$

The initial boundary conditions of the coupled differential equations (B.1) and (B.2) are now chosen such that the photon operator a at time $t \to -\infty$ is mapped to the nuclear spin operator b at $t \to \infty$

$$u'_{-\infty} = 1, \quad |v'_{-\infty}| = 0. \tag{B.3}$$

Eliminating u' in equations (B.1) and (B.2) leads to the single equation

$$\ddot{v}' + \mathrm{i}\beta t\dot{v}' + g^2 v' = 0, \tag{B.4}$$

where $\dot{g} = 0$. Together with the substitution $v' = \mathrm{e}^{-(i/2)\int(\omega_1-\omega_2)\mathrm{d}t}U_1$, equation (B.4) reduces to the so-called Weber equation:

$$\ddot{U}_1 + \left(g^2 - \mathrm{i}\frac{\beta}{2} + \frac{\beta^2}{4}t^2\right)U_1 = 0. \tag{B.5}$$

Solving (B.5) as proposed by Landau and Zener and considering the asymptotic behavior of the solution at $t \to \infty$, it is found to be

$$\lim_{t\to\infty} U_1(t) = -K\frac{\sqrt{2\pi}}{\Gamma(\mathrm{i}\gamma_z+1)}\mathrm{e}^{-(1/4)\pi\gamma_z}\mathrm{e}^{\mathrm{i}\beta t^2}(\sqrt{\beta}t)^{\mathrm{i}\gamma_z}, \tag{B.6}$$

where $\gamma_z = g_1^2/\beta$ and the constant $K = \sqrt{\gamma_z}\exp(-\gamma_z\pi/4)$. The probability that the photonic operator a is mapped to the collective nuclear spin operator b is given by equation (15).

References

[1] DiVincenzo D P 2000 The physical implementation of quantum computation *Fortschr. Phys.* **48** 771

[2] Zoller P *et al* 2005 Quantum information processing and communication *Eur. Phys. J.* D **36** 203

[3] Cirac J I, Zoller P, Kimble H J and Mabuchi H 1997 Quantum state transfer and entanglement distribution among distant nodes in a quantum network. *Phys. Rev. Lett.* **78** 3221

[4] Kozekhin A E, Mølmer K and Polzik E S 2000 Quantum memory for light *Phys. Rev.* A **62** 033809

[5] Fleischhauer M and Lukin M D 2002 Quantum memory for photons: dark state polaritons *Phys. Rev.* A **65** 022314

[6] Maître X, Hagley E, Nogues G, Wunderlich C, Goy P, Brune M, Raimond J M and Haroche S 1997 Quantum memory with a single photon in a cavity *Phys. Rev. Lett.* **79** 769

[7] Julsgaard B, Sherson J, Cirac I, Fiurášek J and Polzik E S 2004 Experimental demonstration of quantum memory for light *Nature* **432** 482

[8] Wilk T, Webster S C, Kuhn A and Rempe G 2007 Single-atom single-photon quantum interface *Science* **317** 488–90

[9] Rosenfeld W, Berner S, Volz J, Weber M and Weinfurter H 2007 Remote preparation of an atomic quantum memory *Phys. Rev. Lett.* **98** 050504

[10] Choi K S, Deng H, Laurat J and Kimble H J 2008 Mapping photonic entanglement into and out of a quantum memory *Nature* **452** 67

[11] Blinov B B, Moehring D L, Duan L-M and Monroe C 2004 Observation of entanglement between a single trapped atom and a single photon *Nature* **428** 153

[12] Loss D and DiVincenzo D P 1998 Quantum computation with quantum dots *Phys. Rev.* A **57** 120

[13] Imamoğlu A, Awschalom D D, Burkard G, DiVincenzo D P, Loss D, Sherwin M and Small A 1999 Quantum information processing using quantum dot spins and cavity-QED *Phys. Rev. Lett.* **83** 4204

[14] Hanson R and Awschalom D D 2008 Coherent manipulation of single spins in semiconductors *Nature* **453** 1043

[15] Yao W, Liu R-B and Sham L J 2005 Theory of control of the spin–photon interface for quantum networks *Phys. Rev. Lett.* **95** 030504

[16] Reithmaier J P, Sek G, Loffler A, Hofmann C, Kuhn S, Reitzenstein S, Keldysh L V, Kulakovskii V D, Reinecke T L and Forchel A 2004 Strong coupling in a single quantum dot-semiconductor microcavity system *Nature* **432** 197

[17] Yoshie T, Scherer A, Hendrickson J, Khitrova G, Gibbs H M, Rupper G, Ell C, Shchekin O B and Deppe D G 2004 Vacuum rabi splitting with a single quantum dot in a photonic crystal nanocavity *Nature* **432** 200

[18] Hennessy K, Badolato A, Winger M, Gerace D, Atature M, Gulde S, Fält S, Hu E L and Imamoğlu A 2007 Quantum nature of a strongly coupled single quantum dot–cavity system *Nature* **445** 896

[19] Reithmaier J P 2008 Strong exciton–photon coupling in semiconductor quantum dot systems *Semicond. Sci. Technol.* **23** 123001

[20] Taylor J M, Imamoğlu A and Lukin M D 2003 Controlling a mesoscopic spin environment by quantum bit manipulation *Phys. Rev. Lett.* **91** 246802

[21] Taylor J M, Giedke G, Christ H, Paredes B, Cirac J I, Zoller P, Lukin M D and Imamoğlu A 2004 Quantum information processing using localized ensembles of nuclear spins arXiv:cond-mat/040764

[22] Landau L 1932 Zur theorie der energieübertragung bei stößen *Phys. Z. Sowjetunion* **1** 88

[23] Zener C 1932 Non-adiabatic crossing of energy levels *Proc. R. Soc.* A **137** 696

[24] Bergmann K, Theuer H and Shore B W 1998 Coherent population transfer among quantum states of atoms and molecules *Rev. Mod. Phys.* **70** 1003

[25] Braunstein S L and Kimble H J 1998 Teleportation of continuous quantum variables *Phys. Rev. Lett.* **80** 869

[26] Schliemann J, Khaetskii A and Loss D 2003 Electron spin dynamics in quantum dots and related nanostructures due to hyperfine interaction with nuclei *J. Phys.: Condens. Matter* **15** R1809

[27] Bracker A S *et al* 2005 Optical pumping of electronic and nuclear spin in single charge-tunable quantum dots *Phys. Rev. Lett.* **94** 047402

[28] Maletinsky P, Badolato A and Imamoğlu A 2007 Dynamics of quantum dot nuclear spin polarization controlled by a single electron *Phys. Rev. Lett.* **99** 056804

[29] Skiba-Szymanska J, Nikolaenko A V, Makhonin M N, Drouzas I, Skolnick M S, Krysa A B and Tartakovskii A I 2008 Strong Overhauser effect in individual InP/GaInP dots *Phys. Rev.* B **77** 165338

[30] Urbaszek B, Braun P-F, Marie X, Krebs O, Lemaitre A, Voisin P and Amand T 2007 Efficient dynamical nuclear polarization in quantum dots: temperature dependence *Phys. Rev.* B **76** 201301

[31] Maletinsky P 2008 *PhD Thesis* ETH Zürich http://e-collection.ethbib.ethz.ch/view/eth:30788

[32] Holstein T and Primakoff H 1940 Field dependence of the intrinsic domain magnetization of ferromagnet *Phys. Rev.* **58** 1098

[33] Christ H, Cirac J I and Giedke G 2009 Nuclear spin polarization in quantum dots—the homogeneous limit *Solid State Sci.* **11** 965

[34] Christ H 2008 Quantum computation with nuclear spins in quantum dots *PhD Thesis* TU München

[35] Schwager H, Cirac J I and Giedke G 2010 Quantum interface between light and nuclear spins in quantum dots *Phys. Rev.* B **81** 045309

[36] Brion E, Pedersen L H and Molmer K 2007 Adiabatic elimination in a lambda system *J. Phys. A: Math. Theor.* **40** 1033–43

[37] Xu X, Wu Y, Sun B, Huang Q, Cheng J, Steel D G, Bracker A S, Gammon D, Emary C and Sham L J 2007 Fast spin state initialization in a singly charged inas-gaas quantum dot by optical cooling *Phys. Rev. Lett.* **99** 097401
[38] Scully M O and Zubairy S M 1997 *Quantum Optics* (Cambridge: Cambridge University Press)
[39] Hammerer K, Wolf M M, Polzik E S and Cirac J I 2005 Quantum benchmark for storage and transmission of coherent states *Phys. Rev. Lett.* **94** 150503
[40] Furusawa A, Sørensen J L, Braunstein S L, Fuchs C A, Kimble H J and Polzik E S 1998 Unconditional quantum teleportation *Science* **282** 706
[41] Caves C M 1982 Quantum limits on noise in linear amplifiers *Phys. Rev.* D **26** 1817
[42] Scutaru H 1998 Transition probabilities for quasifree states *J. Math. Phys.* **39** 6403
[43] Wolf M M, Giedke G, Krüger O, Werner R F and Cirac J I 2003 Gaussian entanglement of formation *Phys. Rev.* A **69** 052320
[44] Parkins A S, Marte P, Zoller P, Carnal O and Kimble H J 1995 Quantum-state mapping between multilevel atoms and cavity light fields *Phys. Rev.* A **51** 1578
[45] Takahashi Y, Hagino H, Tanaka Y, Song B-S, Asano B-S and Noda S 2007 High-Q nanocavity with a 2-ns photon lifetime *Opt. Express* **15** 17206–13
[46] Messiah A 1985 *Quantenmechanik Band 2* (Berlin: de Gruyter and Co.)
[47] Shi Y and Wu Y-S 2004 Perturbative formulation and nonadiabatic corrections in adiabatic quantum-computing schemes *Phys. Rev.* A **69** 024301
[48] Clark S, Peng A, Gu M and Parkins S 2003 Unconditional preparation of entanglement between atoms in cascaded optical cavities *Phys. Rev. Lett.* **91** 177901
[49] Kraus B and Cirac J I 2004 Discrete entanglement distribution with squeezed light *Phys. Rev. Lett.* **92** 013602
[50] Matteo G A 1996 Paris Displacement operator by beam splitter *Phys. Lett.* A **217** 78
[51] Gardiner C W and Zoller P 2000 *Quantum Noise* 2nd edn (Berlin: Springer)
[52] Williamson J 1936 *Am. J. Math.* **58** 141
[53] Vidal G and Werner R F 2002 A computable measure of entanglement *Phys. Rev.* A **65** 032314
[54] Bennett C H, Bernstein H J, Popescu S and Schumacher B 1996 Concentrating partial entanglement by local operations *Phys. Rev.* A **53** 2046
[55] Vaidman L 1994 Teleportation of quantum states *Phys. Rev.* A **49** 1473
[56] Fiurášek J 2002 Improving the fidelity of continuous-variable teleportation via local operations *Phys. Rev.* A **66** 012304
[57] Giedke G and Cirac J I 2002 The characterization of Gaussian operations and distillation of Gaussian states *Phys. Rev.* A **66** 032316
[58] Kraus B, Hammerer K, Giedke G and Cirac J I 2002 Entanglement generation and Hamiltonian simulation in continuous-variable systems *Phys. Rev.* A **67** 042314
[59] Kurucz Z, Sørensen M W, Taylor J M, Lukin M D and Fleischhauer M 2009 Qubit protection in nuclear-spin quantum dot memories *Phys. Rev. Lett.* **103** 010502
[60] Slichter C P 1990 *Principles of Magnetic Resonance* (Berlin: Springer)
[61] Yao W, Liu R-B and Sham L J 2006 Theory of electron spin decoherence by interacting nuclear spins in a quantum dot *Phys. Rev.* B **74** 195301
[62] Kurucz Z and Fleischhauer M 2008 Continuous-variable versus electromagnetically-induced-transparency-based quantum memories *Phys. Rev.* A **78** 023805
[63] Maletinsky P, Kroner M and Imamoglu A 2009 Breakdown of the nuclear-spin-temperature approach in quantum-dot demagnetization experiments *Nat. Phys.* **5** 407–11
[64] Imamoğlu A, Knill E, Tian L and Zoller P 2003 Optical pumping of quantum-dot nuclear spins *Phys. Rev. Lett.* **91** 017402
[65] Braunstein S L and van Loock P 2005 Quantum information with continuous variables *Rev. Mod. Phys.* **77** 513

[66] Manuceau J and Verbeure A 1968 Quasi-free states of the CCR–Algebra and Bogoliubov transformations *Commun. Math. Phys.* **9** 293
[67] Duan L-M, Giedke G, Cirac J I and Zoller P 2000 Physical implementation for entanglement purification of Gaussian continuous-variable quantum states *Phys. Rev.* A **62** 032304
[68] Simon R 2000 Peres–Horodecki separability criterion for continuous variable systems *Phys. Rev. Lett.* **84** 2726
[69] Peres A 1996 Separability criterion for density matrices *Phys. Rev. Lett.* **77** 1413
[70] Werner R F and Wolf M M 2001 Bound entangled Gaussian states *Phys. Rev. Lett.* **86** 3658
[71] Giedke G, Kraus B, Lewenstein M and Cirac J I 2001 Separability properties of three-mode Gaussian states *Phys. Rev.* A **64** 052303
[72] Hyllus P and Eisert J 2006 Optimal entanglement witnesses for continuous-variable systems *New J. Phys.* **8** 51
[73] Giedke G, Eisert J, Cirac J I and Plenio M B 2003 Entanglement transformations of pure Gaussian states *Quant. Inf. Comp.* **3** 211
[74] Giedke G, Wolf M M, Krüger O, Werner R F and Cirac J I 2003 Entanglement of formation for Gaussian states *Phys. Rev. Lett.* **91** 107901
[75] Wolf M M, Giedke G and Cirac J I 2006 Extremality of Gaussian quantum states *Phys. Rev. Lett.* **96** 080502
[76] Braunstein S L 2005 Squeezing as an irreducible resource *Phys. Rev.* A **71** 055801

nature COMMUNICATIONS

ARTICLE

Received 25 Mar 2011 | Accepted 16 Mar 2012 | Published 24 Apr 2012

DOI: 10.1038/ncomms1788

Scalable architecture for a room temperature solid-state quantum information processor

N.Y. Yao[1], L. Jiang[2], A.V. Gorshkov[1,2], P.C. Maurer[1], G. Giedke[3], J.I. Cirac[3] & M.D. Lukin[1]

The realization of a scalable quantum information processor has emerged over the past decade as one of the central challenges at the interface of fundamental science and engineering. Here we propose and analyse an architecture for a scalable, solid-state quantum information processor capable of operating at room temperature. Our approach is based on recent experimental advances involving nitrogen-vacancy colour centres in diamond. In particular, we demonstrate that the multiple challenges associated with operation at ambient temperature, individual addressing at the nanoscale, strong qubit coupling, robustness against disorder and low decoherence rates can be simultaneously achieved under realistic, experimentally relevant conditions. The architecture uses a novel approach to quantum information transfer and includes a hierarchy of control at successive length scales. Moreover, it alleviates the stringent constraints currently limiting the realization of scalable quantum processors and will provide fundamental insights into the physics of non-equilibrium many-body quantum systems.

[1] Physics Department, Harvard University, Cambridge, Massachusetts 02138, USA. [2] Institute for Quantum Information, California Institute of Technology, Pasadena, California 91125, USA. [3] Max-Planck-Institut für Quantenoptik, Hans-Kopfermann-Strasse 1, Garching, D-85748, Germany. Correspondence and requests for materials should be addressed to N.Y.Y. (email: nyao@fas.harvard.edu).

© 2012 Macmillan Publishers Limited. All rights reserved.

The majority of realistic approaches to quantum information processing impose stringent requirements on the qubit environment, ranging from ultra-high vacuum to ultra-low temperature[1–3]. Such requirements, designed to isolate the qubit from external noise, often represent major experimental hurdles and may eventually limit the potential technological impact of a quantum information processor. For these reasons, developing a realistic framework for a feasible solid-state quantum processor capable of operating at room temperature is of both fundamental and practical importance. Nitrogen-vacancy (NV) colour centres in diamond stand out among other promising qubit implementations[4–7] in that their electronic spins can be individually polarized, manipulated and optically detected under room-temperature conditions. Each NV centre constitutes an individual two-qubit quantum register as it also contains a localized nuclear spin. The nuclear spin, which has an extremely long coherence time, can serve as a memory qubit, storing quantum information, while the electronic spin can be used to initialize, read-out, and mediate coupling between nuclear spins of adjacent registers. Magnetic dipole interactions allow for coherent coupling between NV centres spatially separated by tens of nanometers. Although, in principle, a perfect array of NV centres would enable scalable quantum information processing, in practice, the finite creation efficiency of such centres, along with the requirements for parallelism, necessitate the coupling of registers separated by significantly larger distances.

Recent advances involving the quantum manipulation of NV defects have allowed researchers to achieve sub-diffraction limited resolution, single-shot read-out, and dipole-coupling-mediated entanglement between neighbouring NV electronic spins[8–18]. Despite such substantial developments, it remains unclear whether these individual pieces, each of which invariably require a unique set of experimental conditions, can be seamlessly unified into a scalable room-temperature architecture[19]. Thus, the development of an architectural blueprint that combines the associated experimental facets, while demonstrating that such a combination can enable high-fidelity quantum operations, is of crucial importance.

In what follows, we describe and analyse a feasible architecture for a room-temperature, diamond-based quantum information processor. Our approach makes use of an array of single NV centres, created through ion implantation and subsequent annealing[11,20]. To overcome the challenge of coupling remote NV registers, we develop a novel method that enables coherent long-range interactions between NV centres, mediated by an optically un-addressable 'dark' spin chain data bus (DSCB)[21]. For concreteness, within our architecture, we will consider the specific implementation of such a DSCB by utilizing implanted nitrogen impurities (P1 centres) with spin 1/2, as shown in Fig. 1a[8,22]. We analyse realistic imperfections and decoherence mechanisms, concluding that the implementation of this architecture is feasible with current experimental technology. Moreover, we demonstrate the possibility of high-fidelity remote coupling gates, whose error rates fall below the threshold for quantum error correction in a two-dimensional (2D) surface code[23].

Results

The NV qubit register. Single NV registers contain a spin triplet electronic ground state ($S=1$) and can be optically pumped and initialized to the $|0\rangle_e$ spin state, which has no magnetic dipole coupling with other NV registers or impurities. After optical initialization, the electronic spin of each register remains in the $|0\rangle_e$ state, unless coherently transferred to the $|1\rangle_e$ state by a resonant microwave (MW) pulse, as shown in Fig. 1a[10–13]. The NV nuclear spin associated with nitrogen atoms ($I=1/2$ for ^{15}N) possesses an extremely long coherence time (^{13}C nuclear spins could also in principle be utilized) and will serve as the memory qubit in our system[24,25]; manipulation of the nuclear spin is accomplished with radio frequency (RF) pulses[26]. The Hamiltonian governing the

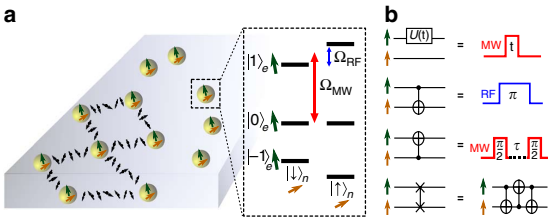

Figure 1 | Schematic representation of individual NV registers within bulk diamond. (**a**) Each NV register contains a nuclear spin $I=1/2$ (yellow), providing quantum memory, and an electronic spin $S=1$ (green). Dark spins (black) represent elements of an optically un-addressable spin chain, which coherently couples spatially separated NV registers. The NV level structure (in a high B field) is shown. A resonant MW (Ω_{MW}) pulse coherently transfers the electronic spin of the register from $|0\rangle_e$ to $|1\rangle_e$; subsequent manipulation of the nuclear spin is accomplished through an RF pulse (Ω_{RF}). The far detuned $|-1\rangle_e$ state can be neglected to create an effective two-qubit register. However, the full three-level NV structure will be utilized in horizontal DSCB-mediated coherent coupling of NV registers. (**b**) A universal set of two-qubit gates can easily be achieved with only MW and RF controls[26]. Electronic spin manipulation can be accomplished with a MW field, where t represents the duration of the MW pulse. By exploiting the hyperfine coupling between the electronic and nuclear spin, one can achieve controlled-NOT operations conditioned on either spin. In particular, a C_eNOT_n gate can be accomplished by utilizing a RF π-pulse, which flips the nuclear spin conditioned on the electronic spin being in $|1\rangle_e$. Similarly, a C_nNOT_e gate can be accomplished by utilizing the hyperfine interaction to generate a controlled-phase (CP) gate, where τ represents the duration of the wait time required to achieve such a hyperfine-driven CP gate. Performed between two single-qubit Hadamard gates ($\pi/2$-pulses) on the electronic spin, such a CP gate generates the desired C_nNOT_e gate. Finally, combining the C_eNOT_n and C_nNOT_e gates allows for the execution of a swap gate.

electronic and nuclear spins of the NV register is

$$H_{e,n} = \Delta_0 S_z^2 + \mu_e B S_z + \mu_n B I_z + A S_z I_z, \qquad (1)$$

with zero-field splitting $\Delta_0 = 2.87$GHz, electronic spin gyromagnetic ratio $\mu_e = -2.8$ MHz/Gauss, nuclear spin gyromagnetic ratio $\mu_n = -0.43$ kHz/Gauss, and hyperfine coupling $A = 3.0$ MHz[10]. The application of a magnetic field along the NV-axis ($\hat{z}$) ensures full addressability of the two-qubit system, resulting in the energy levels shown in Fig. 1a. A universal set of two-qubit quantum operations can easily be achieved with only MW and RF controls, as shown in Fig. 1b and detailed in Methods[26].

Furthermore, it is possible to selectively read-out the state of the NV register; for example, to read-out the nuclear qubit of a register, we apply a C_nNOT_e gate to couple the electronic and nuclear spins, thereby allowing for read-out of the electronic spin based on fluorescence detection. Our approach to scalability will ultimately involve a hierarchical design principle that ensures a spatial separation between NV registers, which is of order the optical wavelength; while this will, in principle, enable individualized read-out, additional use of a red Laguerre-Gaussian donut beam can further enhance read-out fidelities[14]. Indeed, the read-out of individual registers may be complicated by the strong fluorescence background from neighbouring NV centres. To suppress this background fluorescence, a red donut beam can be used, with its minimum located at the particular NV centre being read-out[14]. Whereas the fluorescence signal from the NV register located at the minimum persists, the remaining illuminated registers will be dominated by the stimulated

© 2012 Macmillan Publishers Limited. All rights reserved.

NATURE COMMUNICATIONS | DOI: 10.1038/ncomms1788

emission induced by the red donut beam. In addition to suppressing the background noise, the red donut beam can also suppress the nuclear decoherence of the remaining NV registers, by reducing the amount of time these registers spend in the electronic-excited state (Supplementary Note 1)[27]. Moreover, this approach may be particularly applicable in the case where NV registers are separated by sub-optical-wavelength distances. After each round of fluorescence detection, the electronic spin is polarized to the $|0\rangle_e$ state, while the I_z component of the nuclear spin, a quantum non-demolition observable, remains unchanged[28]. Therefore, it is possible to repeat this read-out procedure multiple times to improve the read-out fidelity[15,16]. A strong magnetic field $B_{z,0} \sim 1$ Tesla along the NV axis should be used to decouple the electronic and nuclear spins to achieve high-fidelity single-shot read-out of NV registers[16]. In addition to sub-wavelength read-out, optical donut beams also introduce the possibility of selectively manipulating individual NV registers with sub-wavelength resolution. In this case, we envision the use of a green Laguerre-Gaussian donut beam; whereas un-illuminated NV centres may respond to a resonant MW pulse, illuminated registers undergo a strong optical cycling transition that suppresses their response to MW pulses due to the quantum Zeno effect[29,30].

Approach to scalable architecture. One of the key requirements for fault-tolerant quantum computation is the ability to perform parallel gate operations. In our approach, this is achieved by considering a hierarchy of controllability. The lowest level of the hierarchy consists of an individual optically addressable plaquette with horizontal and vertical spatial dimensions ~100–500 nm, containing a single computational NV register, as shown in Fig. 2a. The plaquette dimensions are chosen such that register control and read-out can be achieved using conventional far-field or sub-wavelength optical techniques[10,14,24,30,31]. The second level, termed a *super-plaquette* (~10 μm ×10 μm), consists of a lattice of plaquettes whose computational registers are coupled through DSCBs. At the highest level of the hierarchy, we consider an array of super-plaquettes, where individual super-plaquettes are controlled by confined MW fields[32]. In particular, micro-solenoids can confine fields to within super-plaquettes, allowing for parallel operations at the super-plaquette level. For example, as shown in Fig. 2, independent MW pulses can allow for simultaneous operations on the electronic spins of all computational NV registers within all super-plaquettes. To control registers at the super-plaquette boundaries, we define a dual super-plaquette lattice (Fig. 2a). Localized MW fields, within such a dual lattice, can provide a smooth transition between the boundaries of neighbouring super-plaquettes.

Taking advantage of the separation of length scales inherent to optical control and MW confinement provides a mechanism to achieve parallelism; indeed, the hierarchical control of plaquettes, super-plaquettes and super-plaquette arrays allows for simultaneous single- and two-qubit gate operations, which are fundamental to fault-tolerant computation. One of the key differences between the currently proposed architecture and previous proposals[6,33], is that the design here does not rely on optically resolved transitions, which are only accessible at cryogenic temperatures.

The required 2D array of NV centres can be created via a two-step implantation process. We envision first implanting single nitrogen atoms along particular rows within each plaquette, as shown in Fig. 2b; subsequent annealing occurs until the creation of an NV centre, after which, a second nitrogen implantation step generates the spin chain data bus. The selective manipulation of individual registers within our 2D array is enabled by the application of a spatially dependent external magnetic field $B_z(y) = (\alpha y + B_{z,0})\hat{z}$; this 1D magnetic field gradient is sufficiently strong ($\alpha \sim 10^5$ T m^{-1}) to allow for spectroscopic MW addressing of individual NV registers, each of which occupies a unique row in the super-plaquette, as shown in Fig. 2b[32,34,35].

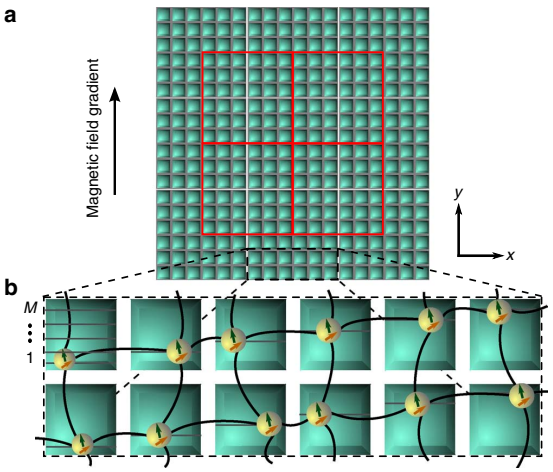

Figure 2 | The architecture for a room-temperature solid-state quantum computer. (**a**) A 2D hierarchical lattice allowing for length-scale-based control, which enables fully parallel operations. At the lowest level, individual plaquettes are outlined in grey and each contains a single computational NV register. At the second level of hierarchy, a super-plaquette, outlined in white, encompasses a lattice of plaquettes; each super-plaquette is separately manipulated by micro-solenoid confined MW fields. To allow for quantum information transfer across boundaries of super-plaquettes, there exists a dual super-plaquette lattice outlined in red. (**b**) The schematic NV register implantation within a super-plaquette. Two rows of individual plaquettes within a super-plaquette are shown. NV registers, consisting of an electronic (green) and nuclear (yellow) spin are shown within a staggered up-sloping array that is row-repetitive. Individual rows within a single plaquette are specified by an integer n with $n = 1$ being the bottom row and $n = M$ being the top row. To achieve a staggered structure, we specify a unique implantation row within each plaquette wherein single impurities are implanted and subsequently annealed. For a given row of plaquettes, the implantation row corresponding to the left-most plaquette is $n = 1$, whereas the plaquette to the immediate right has implantation row $n = 2$; this pattern continues until the final plaquette in a given row, which by construction, has the highest implantation row number. The implantation process is repeated for each row of plaquettes within the super-plaquette and creates an array of NV registers, which each occupy a unique row in the super-plaquette. Because each NV register occupies a unique row within the super-plaquette, the magnetic field gradient in the $\hat{y}$ direction allows for individual spectroscopic addressing of single registers. Coherent coupling of spatially separated NV registers in adjacent plaquettes is mediated by a DSCB and is schematically represented by the curved lines connecting individual registers. The second implantation step corresponds to the creation of these horizontal and vertical dark spin chains.

Dark spin chain data bus. To coherently couple two spatially separated NV centres, we consider two distinct approaches. First, we consider an approach, which is appropriate for spin-state transfer along the direction of the magnetic field gradient, in which individual addressing of spins is possible. This allows for an adiabatic sequential swap between neighbouring qubits and, consequently, between the ends of the chain. Alternatively, in the situation where individual addressing of spins is not possible (that is, in the direction transverse to the field gradient), we show that global control pulses achieve effective Hamiltonian evolution, which enables quantum state transfer through the spin chain. In both cases, we show that perfect state transfer and remote coupling gates are possible even

© 2012 Macmillan Publishers Limited. All rights reserved.

when the intermediate spin chain is completely unpolarized (infinite spin temperature).

We begin by analysing the adiabatic sequential swap in a spin-1/2 chain. This approach is suitable to couple registers in plaquettes that are vertically adjacent, relying on the individual addressability of qubits and utilizing the magnetic dipole coupling between spin-chain elements. As shown in the Supplementary Methods, under the secular approximation, the magnetic dipole coupling between a pair of neighbouring spins can be reduced to Ising form

$$H_{\rm int} = 4\kappa S_1^z S_2^z + \sum_{i=1,2} (\omega_0 + \delta_i) S_i^z, \qquad (2)$$

where κ is the relevant component of the dipole tensor, ω_0 captures the electronic Zeeman energy, and δ_i characterizes both the hyperfine term (nuclear spin dependent) and the magnetic field gradient. From the Ising Hamiltonian, an XX interaction between qubits can be distilled by driving with $H_{drive} = \sum_{i=1,2} \Omega_i S_x^i \cos[(\omega_0 + \delta_i)t]$, leading to (under the rotating wave approximation, in the rotating frame, with $|\Omega_1 + \Omega_2| \gg \kappa$, and in a rotated basis with $(x,y,z) \rightarrow (z, -y, x)$)

$$H_{\rm int} = \kappa(S_1^+ S_2^- + S_1^- S_2^+) + \Omega_1 S_1^z + \Omega_2 S_2^z. \qquad (3)$$

The spin-flip process in $H_{\rm int}$ is highly suppressed in the limit of $|\Omega_1 - \Omega_2| \gg \kappa$, whereas the same process is dominant in the case of $|\Omega_1 - \Omega_2| \ll \kappa$. Hence, by slowly ramping the Rabi frequencies Ω_1 and Ω_2 through one another, adiabatic swap of the quantum states of the two impurities can be achieved through rapid adiabatic passage, as shown in Fig. 3a. Generalizing to arbitrary length spin chains yields $H_{\rm int} = \sum_i \kappa(S_i^+ S_{i+1}^- + S_i^- S_{i+1}^+) + \sum_i \Omega_i S_i^z$, whereby the sequential adiabatic swap of quantum states along the spin chain can be achieved by successively tuning individual Rabi frequencies across one another. During the adiabatic swap of a single pair of spins, higher order interactions, such as those resulting from next-to-nearest neighbours, will be suppressed because of the differences in Rabi frequencies. By including the magnetic dipole coupling between the electronic spin of the NV register and the spin chain quantum channel, we arrive at an effective mixed spin chain with the DSCB connecting the two electronic spins of the vertically separated NV registers.

Crucially, such an adiabatic sequential swap is robust against variations in the coupling strength κ, which can be induced by the imprecise implantation of impurities that form the spin-1/2 chain; in particular, even for the case of varying $\kappa_{i,i+1}$, perfect adiabatic swap occurs so long as the rate at which Ω_i and Ω_{i+1} are ramped through one another is sufficiently small. Within the proposed architecture, the impurities forming the horizontal spin chain will not induce operational errors during the vertical adiabatic sequential swap as the design principle allows for selective spin echoing (Fig. 5).

Next, we consider a second method, termed free-fermion state transfer (FFST) developed in ref. 36, to coherently couple NV registers in the horizontal direction. In contrast to the adiabatic sequential swap, the method utilizes only global control over dark impurities and effective Hamiltonian evolution. The relaxation of the requirement of individual control over elements of the dark spin chain renders this second method, applicable for coherent coupling between NV registers in horizontally adjacent plaquettes, transverse to the direction of the field gradient. In particular, the protocol achieves coherent coupling through an unpolarized, infinite-temperature spin chain, employing purely Hamiltonian evolution under

$$H_{\rm FFST} = g(S_{\rm NV_1}^+ S_1^- + S_{\rm NV_2}^+ S_N^- + {\rm h.c.}) + \sum_{i=1}^{N-1} \kappa(S_i^+ S_{i+1}^- + S_i^- S_{i+1}^+) \qquad (4)$$

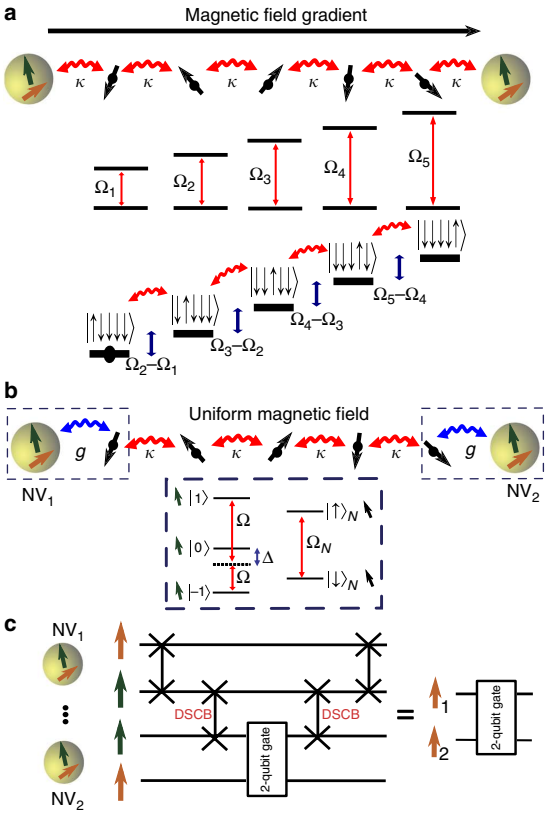

Figure 3 | DSCB-mediated coherent coupling of spatially separated NV registers. (**a**) Adiabatic sequential swap along the vertical direction, parallel to the magnetic field gradient. Individual addressing of impurities, enabled by the field gradient, allows for a slow ramping of the Rabi frequencies Ω_i and Ω_j through one another; this achieves adiabatic swap of the quantum states of the two impurities through rapid adiabatic passage. Thus, sequential adiabatic swap of quantum states along the spin chain can be achieved by successively tuning individual Rabi frequencies across one another. (**b**) FFST in the horizontal direction, transverse to the magnetic field gradient. The coupling strength between the end qubits and the spin chain is g, whereas the interchain coupling strength is κ. Schematic representation of the level structure of the NV electronic spin and a dark impurity spin. Controlling the NV-impurity coupling g is an essential component of FFST and occurs by driving the NV in two-photon resonance, with Rabi frequency Ω and detuning Δ. (**c**) Schematic circuit diagram outlining the protocol to achieve coherent coupling between the nuclear memory qubits of spatially separated NV registers. First, the nuclear and electronic qubits of a single register are swapped. Next, the electronic qubits of the two NV centres to be coupled are swapped through the DSCB. Finally, a two-qubit gate between the electronic and nuclear spin of the second register is performed, before the memory qubit is returned to the nuclear spin of the original NV centre.

as shown in Fig. 3b. This Hamiltonian, obtained in a similar fashion equation (3), results in coherent interactions between NV centres, which is best understood through an analogy with eigenmode tunneling in a many-body system. Specifically, the spin chain described by $H_{\rm FFST}$ can be viewed as a system of non-interacting fermions. As described in ref. 36, by tuning the NV centres into resonance with a single fermionic eigenmode, an effective three-state system can be

© 2012 Macmillan Publishers Limited. All rights reserved.

realized. Mediated by this fermionic eigenmode, the electronic states of two remote NV centres can be coherently swapped. Coupled with arbitrary two-qubit gates between the nuclear and electronic spin (Fig. 1b; Methods), an electronic swap gate enables universal computation between spatially remote nuclear spin memories, as shown in Fig. 3c. Crucially, such a swap gate is insensitive to the polarization of the intermediate dark spins and high-fidelity quantum state transfer can be achieved, provided that the fermionic mode is delocalized and that the coupling, g, of the NV qubit to the spin chain is controllable. As detailed in the Methods, by utilizing the three-level NV ground-state structure (Fig. 3b), it is possible to fully control the NV-chain coupling. This tunability also ensures that FFST is fundamentally robust to experimentally relevant coupling-strength disorder, which could be induced by implantation imprecision. Indeed, by separately tuning the NV-chain coupling on either side of the DSCB, it is possible to compensate for both disorder-induced asymmetry in the fermionic eigenmode as well as altered eigenenergies (Supplementary Methods)[36–38].

Implementation, operational errors and gate fidelities. The specific implementation of the DSCB can be achieved with implanted nitrogen impurity ions. Dipole coupling between neighbouring nitrogen electronic spins forms the DSCB, whereas dipole coupling between the NV and nitrogen electronic spins forms the qubit–DSCB interaction; non-secular terms of this magnetic dipole coupling are highly suppressed owing to the spatially dependent external magnetic field $B_z(y)$, resulting in the effective interaction found in equation (2). In addition, the nitrogen impurities possess a strong hyperfine coupling, the principal axis of which can take on four possible orientations due to tetrahedral symmetry[39–41]. Dynamic Jahn–Teller (JT) reorientation of the nitrogen impurity's hyperfine principal axis results in two particular considerations, namely the addressing of additional JT frequencies yielding a denser super-plaquette frequency spectrum and the JT-governed spin-lattice relaxation time T_1^N (Supplementary Methods). As T_1^N is characterized by an Arrhenius rate equation[40] at ambient temperatures, a combination of a static electric field and slight cooling by ~50 K allows for a substantial extension of the relaxation time to ~1 s; hence, in the following consideration of operational errors, we will assume that we are limited by T_1^{NV}, the spin-lattice relaxation time of the NV centre.

We now consider various imperfections, which may introduce operational errors. In particular, we consider the errors associated with the sequential swap-mediated coupling between vertically adjacent registers and the FFST between horizontally adjacent registers. We begin by discussing the analytic error estimate associated with each method, after which, we summarize the results of full numerical simulations (Supplementary Methods).

First, we consider the accumulated infidelity associated with the adiabatic sequential swap,

$$p_{err}^{SS} \approx N(p_{off}^{SS} + p_{adia} + p_{dip} + p_{T1}^{SS} + p_{T2}^{SS}). \qquad (5)$$

The first term, $p_{off}^{SS} \sim (\Omega_i/\Delta_g)^2$, represents off-resonant cross-talk induced by MW manipulations with Rabi frequency Ω_i. Here Δ_g characterizes the gradient-induced splitting achieved within the super-plaquette frequency spectrum (Supplementary Methods). The second term, p_{adia}, corresponds to the non-adiabatic correction resulting from an optimized adiabatic ramp profile[42–44]. The third term, $p_{dip} \sim (\kappa/\Omega_i)^2$, is directly obtained from equation (3) and corresponds to additional off-resonant errors. The fourth error term, p_{T1}^{SS} corresponds to the depolarization error induced by the finite NV T_1 time, while the final error term, p_{T2}^{SS} corresponds to the infidelity induced by dephasing. As each error term is considered within the context of a single adiabatic swap, the total error contains an additional factor of N, representing the chain length, which is plaquette size dependent.

We can similarly consider the accumulated infidelity associated with FFST,

$$p_{err}^{FFST} \approx p_{off}^{FFST} + p_f + p_g + p_{T1}^{FFST} + p_{T2}^{FFST}. \qquad (6)$$

In direct analogy to p_{err}^{SS}, the first term in p_{err}^{FFST} corresponds to the excitation of an NV register by off-resonant MW fields. The second term, p_f, corresponds to the undesired coupling with off-resonant fermionic modes. Since the coupling strength is characterized by $g/\sqrt{N}$[36], while the splitting of the eigenenergy spectrum $\sim\kappa/N$, such an off-resonant error induces an infidelity $\sim\left((g/\sqrt{N})/(\kappa/N)\right)^2$. The third error term, p_g, results from the protocol designed to control, g, the NV-chain coupling (see Methods for details). Directly analogous to p_{err}^{SS}, the fourth and fifth terms correspond to errors induced by the operational time, t_{FFST}, which causes both depolarization and dephasing.

Finally, we perform numerical simulations, taking into account the nitrogen JT frequencies, to characterize the infidelity of both the adiabatic sequential swap and FFST within the NV architecture, as shown in Fig. 4. The results of these calculations are in excellent agreement with the above theoretical predictions. In particular, these simulations reveal that, for sufficiently long $T_1^{NV} \sim 100$ms, operational infidelities in both DSCB methods can be kept below 10^{-2}.

These simulations clearly show that the T_1 time of the NV electronic spin is of critical importance in obtaining high-fidelity quantum operations. While at room temperature, T_1 appears to vary depending on the particular sample and on the specific properties of the local NV environment, such as strain, values on the order of 10 ms are generally obtained[24,39]. However, the spin-lattice relaxation mechanism governing T_1 is most likely related to an Orbach process[45,46], which is strongly temperature dependent. In such a case, modest cooling of the sample by ~50 K, is likely to extend T1

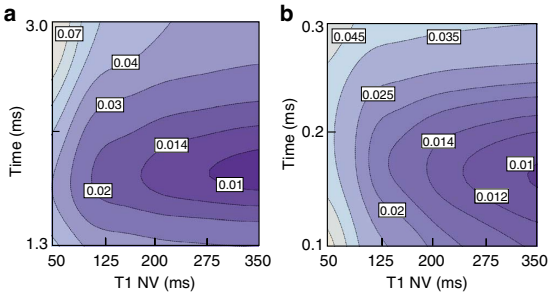

Figure 4 | Numerical simulation of the DSCB fidelity. (**a**) The operational infidelity associated with the adiabatic sequential swap for $N = 18$. The simulations account for the JT orientation of nitrogen impurities and utilize the optimized adiabatic ramp profile[42]. Simulations utilize an optimized coupling strength of 8.71 kHz (18.1 nm spacing). Full numerical integration of the time-dependent Schrödinger equation produces infidelity contour plots as a function of total swap time and T_1^{NV}. (**b**) Numerical simulations of the operational infidelity associated with FFST for $N = 7$. Non-nearest neighbour interactions are assumed to be refocused through dynamic decoupling as described in the Methods. Simulations, which utilize an optimized coupling strength of 12.6kHz (16 nm spacing), are based on a full diagonalization and also account for the JT orientation of nitrogen impurities. Infidelity contour plots are again shown as a function of total swap time and T_1^{NV}.

© 2012 Macmillan Publishers Limited. All rights reserved.

by more than an order of magnitude, thereby making high-fidelity gates possible.

Given that such numerical estimations suggest the possibility of achieving high-fidelity two-qubit operations between remote NV registers, the proposed architecture seems well suited to the implementation of topological quantum error correction. In particular, we imagine implementing a 2D surface code, which requires only nearest-neighbour two-qubit gates and single-qubit preparation and measurement[23,47,48]. Recent progress in optimizing this surface code has yielded an error threshold of ε~1.4% (ref. 49), which is above the estimated infidelity corresponding to both the adiabatic sequential swap and FFST; thus, in principle, implementation of such a 2D surface code can allow for successful topological quantum error correction, and hence, fault tolerant quantum computation[50].

Discussion

The above considerations indicate the feasibility of experimentally realizing a solid-state quantum computer capable of operating under ambient conditions at or near room temperature. We emphasize that a majority of the elements required for the realization of individual qubits in our architecture have already been demonstrated. In our approach, these techniques are supplemented by both a new mechanism for remote register coupling between NV centres as well as a hierarchical design principle, which facilitates scalability. The remote coupling mechanisms discussed can naturally be implemented via nitrogen ion implantation in ultra-pure diamond crystals and are robust to realistic imperfections and disorder[36]. Moreover, single errors during quantum state transfer are localized to individual transport channels and do not have a propagating effect on the remaining computation.

While we hope that the proposed architecture evinces the feasibility of room temperature quantum information processing, the implementation and integration of the various proposed elements still require significant advances in areas ranging from engineering to materials science. Crucially, recent results have demonstrated substantial progress towards overcoming challenges such as the optimization of planar microcoil arrays[51,52] and efficient beam steering in micromirror systems[53]. Furthermore, by eliminating requirements for cryogenic temperatures, our blueprint aims to make the realization of a scalable quantum computer significantly more practical.

The present work opens a number of new directions that can subsequently be explored. In particular, although we have considered the direct errors associated with DSCB-mediated coupling, it is instructive to note that the fidelity of such quantum gates can often be significantly improved, using techniques from optimal control theory[54,55]. For example, such methods of optimal control, while negating the detrimental effects of decoherence, can also simultaneously allow for the implementation of high-fidelity gates, despite both frequency and coupling disorder as induced by ion implantation errors. Indeed, the ability to precisely guide the quantum evolution via optimal control, even when the system complexity is exacerbated by environmental coupling, provides an alternative solution to improve single- and two-qubit gate fidelities[56]. In addition, it is well known that the local strain field surrounding each NV centre can significantly alter the register's properties; hence, through a detailed understanding of electric field induced strain, it may be possible to improve the coherence properties of the qubit. Moreover, the long coherence times of individual P1 centres, each of which harbours an associated nuclear spin, suggest the possibility of utilizing these dark spins as computational resources in and of themselves[57]. Beyond these specific applications, a number of scientific avenues can be explored, including, for example, understanding and controlling the non-equilibrium dynamics of disordered spin systems.

Methods

Controlling qubit-chain coupling in the NV architecture. To achieve an effective Hamiltonian of the form given by equation (4), it is essential to control the coupling strength between the NV register and the neighbouring impurity. Here we utilize the three levels of the NV electronic spin[58] to effectively control g, as shown in Fig. 3b, whereby the Hamiltonian (under MW driving) can be written as

$$\begin{aligned} H = &-\Delta(|1\rangle\langle 1| + |-1\rangle\langle -1|) \\ &-\Omega(|0\rangle\langle 1| + |0\rangle\langle -1| + \text{h.c.}) \\ &-\Omega_N S_N^x + 4\kappa S_{NV}^z S_N^z, \end{aligned} \tag{7}$$

where Ω represents the Rabi frequency on the NV register, Δ represents the associated detuning, and Ω_N represents the Rabi frequency on the nitrogen impurity. In this case, as the NV two-photon detuning is zero, it is convenient to define bright and dark states, $|B\rangle = \frac{|1\rangle + |-1\rangle}{\sqrt{2}}$ and $|D\rangle = \frac{|1\rangle - |-1\rangle}{\sqrt{2}}$; further, in the resulting two-level picture, the associated dressed states are $|+\rangle \approx |B\rangle + (\sqrt{2}\Omega/\Delta)|0\rangle$ and $|-\rangle \approx |0\rangle - (\sqrt{2}\Omega/\Delta)|B\rangle$, in the limit $\Omega \ll \Delta$. Hence, rewriting the Hamiltonian in this limit yields

$$\begin{aligned} H = &-\Delta|D\rangle\langle D| - (\Delta + (2\Omega^2/\Delta))|+\rangle\langle +| \\ &+(2\Omega^2/\Delta)|-\rangle\langle -| - (1/2)\Omega_N(|+\rangle_N\langle +|-|-\rangle_N\langle -|) \\ &+2\kappa(|B\rangle\langle D| + |D\rangle\langle B|)(|+\rangle_N\langle -| + |-\rangle_N\langle +|), \end{aligned} \tag{8}$$

where $|\pm\rangle_N = \frac{|\uparrow\rangle_N \pm |\downarrow\rangle_N}{\sqrt{2}}$ correspond to the two S_N^x-eigenstates of the nitrogen impurity. The coupling term can be further re-expressed as

$$\begin{aligned} &2\kappa\{(|+\rangle\langle D| + |D\rangle\langle +|) - (\sqrt{2}\Omega/\Delta)(|-\rangle\langle D| + |D\rangle\langle -|)\} \\ &*(|+_N\rangle\langle -_N| + |-_N\rangle\langle +_N|). \end{aligned} \tag{9}$$

Thus, by working within the NV subspace $\{|D\rangle, |-\rangle\}$, it is possible to completely control the coupling between the NV register and Nitrogen impurity, $g \sim \kappa(\Omega/\Delta)$, by tuning the Rabi frequency and detuning. It is possible to work in the required two-state subspace by ensuring that $\kappa \ll \Delta$ and hence, that the $|+\rangle$ state remains unpopulated, with corresponding off-resonant error κ^2/Δ^2.

Furthermore, we evince a possible scheme to coherently map the quantum information that is stored in the nuclear memory into the desired electronic subspace. For example, consider mapping $|0\rangle\otimes(\alpha|\uparrow\rangle + \beta|\downarrow\rangle)$ to $(\alpha|-\rangle + \beta|D\rangle)\otimes|\uparrow\rangle$, where the first (tensor) factor corresponds to the electronic state and the second corresponds to the nuclear state of a single NV. The proposed mapping can be achieved in a two-step process. First, by simultaneously performing a $\pi-$pulse on the transitions $|0\rangle\otimes|\downarrow\rangle \rightarrow |-1\rangle\otimes|\downarrow\rangle$ and $|0\rangle\otimes|\downarrow\rangle \rightarrow |1\rangle\otimes|\downarrow\rangle$ with oppositely signed Rabi frequencies, one can map $|0\rangle\otimes|\downarrow\rangle$ to $|D\rangle\otimes|\downarrow\rangle$. Next, one utilizes an RF pulse to flip the nuclear spin, which yields $|D\rangle\otimes|\downarrow\rangle \rightarrow |D\rangle\otimes|\uparrow\rangle$. Finally, turning Ω on in an adiabatic fashion ensures that the state preparation populates only $|D\rangle$ and $|-\rangle$, thereby mapping the quantum information into the desired electronic subspace.

Arbitrary two-qubit gates within the NV register. Whereas the DSCB enables long-range quantum logic between spatially separated NV electronic spins, universal two-qubit gates between the nuclear spin quantum memories require additional local logic between nuclear and electronic spins, as outlined in Fig. 1b. Here we specify, in detail, the implementation of such local logic gates. A strong MW pulse (with $\Omega_{MW} \gg A$) can perform an arbitrary electronic spin rotation independent of the nuclear spin state. This can be mapped to a nuclear spin rotation by implementing a swap gate between the nuclear and electronic spins. Such a swap gate can be decomposed into three controlled-NOT gates: $C_e\text{NOT}_n\, C_n\text{NOT}_e C_e\text{NOT}_n$. A $C_e\text{NOT}_n$ gate can be accomplished by utilizing an RF π-pulse (with $\Omega_{RF} \ll A$), which flips the nuclear spin conditioned on the electronic spin being in $|1\rangle_e$. Finally, a hyperfine-driven controlled-phase gate enables the remaining $C_n\text{NOT}_e$ gate (up to single Hadamards on the electronic spin). This demonstrates that a universal set of local two-qubit gates between NV electronic and nuclear spins can easily be achieved with only MW and RF controls[26]. Such arbitrary local logic is crucial to enable the preparation of nuclear spin quantum information and forms an important portion of DSCB-mediated remote coupling (Fig. 3c).

Specific implementation of architecture. In this section, we offer a specific implementation of the architectural design principle and discuss the various ingredients required to achieve DSCB-mediated coherent coupling between spatially separated NV registers. In particular, we consider the refocusing of non-nearest neighbour interactions along the horizontal spin chain.

© 2012 Macmillan Publishers Limited. All rights reserved.

NATURE COMMUNICATIONS | DOI: 10.1038/ncomms1788

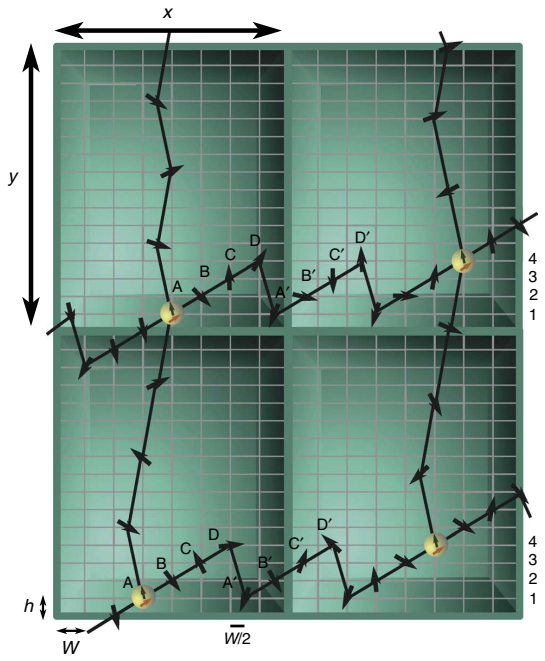

Figure 5 | Schematic Architectural Design. Specific impurity implantation within the architecture, which is designed to achieve parallel gate operations. Plaquettes, outlined in green, are chosen with $y \sim 600$ nm and $x \sim 550$ nm; the individual plaquette-lattice spacing is chosen with $h \sim 6$ nm and $w \sim 20$ nm. The magnetic field is oriented along the NV axis, which is normal to the shown computational plane (Supplementary Fig. S1) and the gradient is represented by the change in this field strength along the $\hat{y}$ direction. The distance between all nearest-neighbour pairs in the horizontal direction is ~21 nm ($\sqrt{h^2+w^2} = \sqrt{(3h)^2+(w/2)^2}$) and the $\hat{x}$ spacing between spin D and spin A' is given by $w/2$. We note that the figure is not drawn to scale and that all impurity spins sit on the horizontal lattice, whereas some impurity spins sit at midpoints of the vertical lattice. The particular lattice spacing is chosen to ensure that the spatial separation between individual nitrogen impurities forming the spin chain, as well as between NV registers and nitrogens does not exceed ~20 nm. The chosen plaquette-lattice spacing implies that neighbouring plaquettes are coupled by ~25 nitrogen impurities (black spins) in the $\hat{y}$ direction and by ~30 nitrogen impurities in the $\hat{x}$ direction. The zig–zag pattern of impurity implantation in the $\hat{y}$ direction ($w/2$ horizontal distance) ensures that all spin chain links are of identical length, thereby allowing for parallel sequential swap operations along $\hat{y}$. Additionally, such a pattern overcomes the limitation of imperfect NV conversion efficiency (Supplementary Note 2) by allowing each vertical spin chain to span a sufficiently large horizontal spacing. As the impurities forming the horizontal spin chain occupy unique rows relative to the vertical spin chain, during the adiabatic sequential swap, selective spin echoing of the horizontal chain impurities ensures that dipole coupling from such impurities will not induce operational errors. While the architecture is designed to showcase the ability to utilize the adiabatic sequential swap and FFST in differing directions, it is important to note that within the specific blueprint above, either implementation of the DSCB can be used in both directions.

The effective Hamiltonian evinced in equation (4) has nearest neighbour form; although next-nearest-neighbour interactions will represent a correction, we show that such interactions can be refocused within the current architectural design, and further, that, in principle, interactions beyond next-nearest-neighbour can also be refocused. In particular, the horizontal spin chain (N total spins) is arranged in a staggered saw-tooth fashion, as shown in Fig. 5. Within such an architecture, nearest neighbour coupling terms correspond to all pairs of adjacent spins, each separated by ~20 nm, with corresponding interaction Hamiltonian

$$H_N = \sum \kappa_N (S_A^+ S_B^- + S_B^+ S_C^- + S_C^+ S_D^- + S_D^+ S_{A'}^-) + \text{h.c.} \quad (10)$$

where the sum runs over all nearest neighbour pairs in a given dark spin chain. Thus, next-to-nearest neighbour terms for each spin correspond to the subsequent strongest interaction

$$H_{NN} = \sum \kappa_{NN} (S_A^+ S_C^- + S_B^+ S_D^-) + \kappa_{NN'} (S_C^+ S_{A'}^- + S_D^+ S_{B'}^-) + \text{h.c.} \quad (11)$$

where the prime denotes the next link in the saw-tooth chain as shown in Fig. 5. In addition to the impurity spins, FFST incorporates the electronic spin of the NV register into a mixed spin chain. It is important to note that the spin-flip Hamiltonians H_N and H_{NN} are derived from the secular approximated Ising coupling by the application of driving fields as per equation (3). As each row (1,2,3,4) is separately addressable by virtue of the magnetic field gradient (applying four frequencies per row to ensure that all JT and nuclear spin states are addressed), it is possible to apply a spin-echo procedure to refocus the next-nearest-neighbour terms. In particular, by flipping the spins in rows 1 and 2 (Fig. 5) after time $T_d/2$, where T_d is a small fraction of the desired evolution duration, the next-nearest-neighbour interactions are refocused since each term contains spins from only row 1 or 2. However, half of the nearest neighbour interactions are also refocused, leaving effective evolution under the Hamiltonian $H_{eff1} = \sum \kappa_N (S_A^+ S_B^- + S_C^+ S_D^-) + \text{h.c.}$ Analogously, by flipping the spins in rows 2 and 3, effective evolution under the Hamiltonian $H_{eff2} = \sum \kappa_N (S_B^+ S_C^- + S_D^+ S_{A'}^-) + \text{h.c.}$ is achieved, again with H_{NN} refocused. Combining the evolution according to H_{eff1} and H_{eff2} yields the desired nearest-neighbour Hamiltonian with next-to-nearest neighbour interactions refocused. However, as H_{eff1} and H_{eff2} do not commute, it will be necessary to employ piecewise evolution according to the Trotter–Suzuki formalism[59]. Further refocusing of higher order non-nearest neighbour interactions can also be achieved by extending the number of rows corresponding to the saw-tooth design; such an extension allows for the isolation of each specific pair of nearest neighbour interactions, thereby achieving the desired nearest-neighbour evolution through a Trotter sequence.

References

1. Stoneham, M. Is a room-temperature, solid-state quantum computer mere fantasy? *Physics* **2,** 34 (2009).
2. Stoneham, A. M., Fisher, A. J. & Greenland, P. T. Optically-driven silicon-based quantum gates with potential for high temperature operation. *J. Phys. Cond. Mat.* **15,** L447–451 (2003).
3. Hogan, J. Computing: quantum bits and silicon chips. *Nature* **424,** 484–486 (2003).
4. Loss, D. & DiVincenzo, D. P. Quantum computation with quantum dots. *Phys. Rev. A* **57,** 120–126 (1998).
5. Duan, L.- M., Blinov, B. B., Moehring, D. L. & Monroe, C. Scalable trapped ion quantum computation with a probabilistic ion-photon mapping. *Quantum Inf. Comp.* **4,** 165–173 (2004).
6. Benjamin, S. C., Browne, D. E., Fitzsimons, J. & Morton, J. J. L. Brokered graph-state quantum computation. *New J Phys* **8,** 141-1–141-9 (2006).
7. Makhlin, Y., Schön, G. & Shnirman, A. Quantum-state engineering with Josephson-junction devices. *Rev. Mod. Phys.* **73,** 357–400 (2001).
8. Epstein, R. J., Mendoza, F. M., Kato, Y. K. & Awschalom, D. D. Anisotropic interactions of a single spin and dark-spin spectroscopy in diamond. *Nature Phys.* **1,** 94–98 (2005).
9. Neumann, P. *et al.* Quantum register based on coupled electron spins in a room-temperature solid. *Nature Phys.* **6,** 249–253 (2010).
10. Childress, L. *et al.* Coherent dynamics of coupled electron and nuclear spin qubits in diamond. *Science* **314,** 281–285 (2006).
11. Balasubramanian, G. *et al.* Ultralong spin coherence time in isotopically engineered diamond. *Nature Mater.* **8,** 383–387 (2009).
12. Weber, J. R. *et al.* Quantum computing with defects. *Proc. Natl Acad. Sci. USA* **107,** 8513–8518 (2010).
13. Fuchs, G. D. *et al.* Excited-state spin coherence of a single nitrogen-vacancy centre in diamond. *Nature Phys.* **6,** 668–672 (2010).
14. Rittweger, E., Han, K. Y., Irvine, S. E., Eggeling, C. & Hell, S. W. STED microscopy reveals crystal colour centres with nanometric resolution. *Nature Photon.* **3,** 144–147 (2009).
15. Jiang, L. *et al.* Repetitive readout of a single electronic spin via quantum logic with nuclear spin ancillae. *Science* **326,** 267–272 (2009).
16. Neumann, P. *et al.* Single-shot readout of a single nuclear spin. *Science* **329,** 542–544 (2010).
17. Togan, E. *et al.* Quantum entanglement between an optical photon and a solid-state spin qubit. *Nature* **466,** 730–734 (2010).

© 2012 Macmillan Publishers Limited. All rights reserved.

18. Benjamin, S. C. & Smith, J. M. Driving a hard bargain with diamond qubits. *Nature Phys.* **4,** 78 (2011).
19. Stoneham, A. M., Harker, A. H. & Morley, G. W. Could one make a diamond-based quantum computer? *J. Phys.: Cond. Mat.* **21,** 1–11 (2009).
20. Tallairea, A. *et al.* Characterisation of high-quality thick single-crystal diamond grown by CVD with a low nitrogen addition. *Diamond Relat. Mater.* **15,** 1700–1707 (2006).
21. Bose, S. Quantum communication through an unmodulated spin chain. *Phys. Rev. Lett.* **91,** 207901 (2003).
22. Reynhardt, E. C., High, G. L. & van Wyk, J. A. Temperature dependence of spin-spin and spin-lattice relaxation times of paramagnetic nitrogen defects in diamond. *J. Chem. Phys.* **109,** 8471–8477 (1998).
23. Raussendorf, R. & Harrington, J. Fault-tolerant quantum computation with high threshold in two dimensions. *Phys. Rev. Lett.* **98,** 190504 (2007).
24. Dutt, M. V. G. *et al.* Quantum register based on individual electronic and nuclear spin qubits in diamond. *Science* **316,** 1312–1316 (2007).
25. Neumann, P. *et al.* Multipartite entanglement among single spins in diamond. *Science* **320,** 1326–1329 (2008).
26. Cappellaro, P., Jiang, L., Hodges, J. S. & Lukin, M. D. Coherence and control of quantum registers based on electronic spin in a nuclear spin bath. *Phys. Rev. Lett.* **102,** 210502 (2009).
27. Wildanger, D., Maze, J. R. & Hell, S. W. Diffraction unlimited all-optical recording of electron spin resonances. *Phys. Rev. Lett.* **107,** 017601 (2011).
28. Haroche, S. & Raimond, J. M. *Exploring the Quantum: Atoms, Cavities, and Photons* (Oxford Univ. Press, 2006).
29. Itano, W. M., Heinzen, D. J., Bollinger, J. J. & Wineland, D. J. Quantum Zeno effect. *Phys. Rev. A* **41,** 2295–2300 (1990).
30. Maurer, P. C. *et al.* Far-field optical detection and manipulation of individual spins with nanoscale resolution. *Nature Phys.* **6,** 912–918 (2010).
31. Gorshkov, A. V., Jiang, L., Greiner, M., Zoller, P. & Lukin, M. D. Coherent quantum optical control with sub-wavelength resolution. *Phys. Rev. Lett.* **100,** 093005 (2008).
32. Lee, H., Liu, Y., Ham, D. & Westervelt, R. M. Integrated cell manipulation system—CMOS/microfluidic hybrid. *Lab Chip* **7,** 331–337 (2007).
33. Jiang, L., Taylor, J. M., Sorensen, A. S. & Lukin, M. D. Distributed quantum computation based on small quantum registers. *Phys. Rev. A* **76,** 062323 (2007).
34. Ramadan, Q., Poenar, D. P. & Chen, Y. Customized trapping of magnetic particles. *Microfluid. Nanofluid.* **6,** 53–62 (2009).
35. Yu, X., Feng, X., Hu, J., Zhang, Z.- L. & Pang, D.- W. Controlling the magnetic field distribution on the micrometer scale and generation of magnetic bead patterns for microfluidic applications. *Langmuir* **27,** 5147–5156 (2011).
36. Yao, N. Y. *et al.* Robust quantum state transfer in random unpolarized spin chains. *Phys. Rev. Lett.* **106,** 040505 (2011).
37. Evers, F. & Mirlin, A. D. Anderson transitions. *Rev. Mod. Phys.* **80,** 1355–1417 (2008).
38. Balents, L. & Fisher, M. P. A. Delocalization transition via supersymmetry in one dimension. *Phys. Rev. B* **56,** 12970–12991 (1997).
39. Takahashi, S., Hanson, R., Tol, J., Sherwin, M. S. & Awschalom, D. D. Quenching spin decoherence in diamond through spin bath polarization. *Phys. Rev. Lett* **101,** 047601 (2008).
40. Loubser, J. H. N. & van Ryneveld, W. P. Dynamic Jahn-Teller and other effects in high-temperature electron spin resonance spectrum of Nitrogen in diamond. *Br. J. Appl. Phys.* **18,** 1029–1031 (1967).
41. Kedkaew, C., Limsuwan, P., Thongcham, K. & Meejoo, S. The spin Hamiltonian parameters calculation of N-14 and N-15 in natural type I diamond. *Int. J. Mod. Phys. B* **22,** 4740–4748 (2008).
42. Roland, J. & Cerf, N. J. Quantum search by local adiabatic evolution. *Phys. Rev. A* **65,** 041208 (2002).
43. Caneva, T. *et al.* Optimal control at the quantum speed limit. *Phys. Rev. Lett.* **103,** 240501 (2009).
44. Messiah, A. *Quantum Mechanics* (Dover Publications, 1962).
45. Jarmola, A., Acosta, V. M., Jensen, K., Chemerisov, D. & Budker, D. Temperature and magnetic field dependent longitudinal spin relaxation in nitrogen-vacancy ensembles in diamond. Preprint at arXiv:1112.5936v1 (2011).
46. Redman, D. A., Brown, S., Sands, R. H. & Rand, S. C. Spin dynamics and electronic states of N-V centers in diamond by EPR and four-wave-mixing spectroscopy. *Phys. Rev. Lett.* **67,** 3420–3423 (1991).
47. Bravyi, S. B. & Kitaev, A. Y. Quantum codes on a lattice with boundary. *Quantum Comput. and Comput.* **2,** 43–48 (2001).
48. Fowler, A. G., Stephens, A. M. & Groszkowski, P. High-threshold universal quantum computation on the surface code. *Phys. Rev. A* **80,** 052312 (2009).
49. Wang, D. S., Fowler, A. G. & Hollenberg, L. C. L. Surface code quantum computing with error rates over 1%. *Phys. Rev. A* **83,** 020302(R) (2011).
50. Jones, N. C. *et al.* A layered architecture for quantum computing using quantum dots. Preprint at arXiv:1010.5022 (2010).
51. Beyzavi, A. & Nguyen, N.- T. Modeling and optimization of planar microcoils. *J. Micromech. Microeng.* **18,** 095018 (2008).
52. Lee, H., Sun, E., Ham, D. & Weissleder, R. Chip-NMR biosensor for detection and molecular analysis of cells. *Nat. Med.* **14,** 869–874 (2008).
53. Knoernschild, C. *et al.* Independent individual addressing of multiple neutral atom qubits with a micromirror-based beam steering system. *Appl. Phys. Lett.* **97,** 134101 (2010).
54. Khaneja, N., Brockett, R. W. & Glaser, S. J. Time optimal control of spin systems. *Phys. Rev. A* **63,** 032308 (2001).
55. Yuan, H., Zeier, R. & Khaneja, N. Elliptic functions and efficient control of spin systems with unequal couplings. *Phys. Rev. A* **77,** 032340 (2008).
56. Grace, M. *et al.* Optimal control of quantum gates and suppression of decoherence in a system of interacting two-level particles. *J. Phys. B* **40,** S103–S125 (2007).
57. Morton, J. J. L. & Lovett, B. W. Hybrid solid-state qubits: the powerful role of electron spins. *Annu. Rev. Condens. Matter Phys.* **2,** 189–212 (2011).
58. Rabl, P. *et al.* Strong magnetic coupling between an electronic spin qubit and a mechanical resonator. *Phys. Rev. B* **79,** 041302R (2009).
59. Suzuki, M. Generalized Trotter's formula and systematic approximants of exponential operators and inner derivations with applications to many-body problems. *Commun. Math. Phys.* **51,** 183 (1976).

Acknowledgements

We gratefully acknowledge conversations with G. Goldstein, J. Maze, E. Togan, Y. Chu, J. Otterbach, Z.-X. Gong, L.-M. Duan, C. Laumann, C. Mathy, A. Zhai, J. Preskill, N. Schuch and Y.T.Siu. This work was supported by the NSF, DOE (FG02-97ER25308), CUA, DARPA QUEST, AFOSR MURI, NIST, the DFG within SFB631 and the Nano Initiative Munich (NIM), the Lee A. DuBridge Fellowship and the Sherman Fairchild Foundation.

Author contributions

N.Y. Y., L.J. and A.V.G. contributed equally to this work. All authors contributed extensively to all aspects of this work.

Additional information

Supplementary Information accompanies this paper at http://www.nature.com/naturecommunications

Competing financial interests: The authors declare no competing financial interests.

Reprints and permission information is available online at http://npg.nature.com/reprintsandpermissions/

How to cite this article: Yao, N. Y. *et al.* Scalable architecture for a room temperature solid-state quantum information processor. *Nat. Commun.* 3:800 doi: 10.1038/ncomms1788 (2012).

© 2012 Macmillan Publishers Limited. All rights reserved.

PHYSICAL REVIEW B **78**, 125314 (2008)

Entanglement generation via a completely mixed nuclear spin bath

H. Christ, J. I. Cirac, and G. Giedke
Max-Planck-Institut für Quantenoptik, Hans-Kopfermann-Strasse 1, D-85748 Garching, Germany
(Received 2 July 2008; revised manuscript received 16 August 2008; published 12 September 2008)

We show that qubits coupled sequentially to a mesoscopic static completely mixed spin bath via the Heisenberg interaction can become highly entangled. Straightforward protocols for the generation of multipartite entangled Greenberger-Horne-Zeilinger (GHZ) states are presented. We show the feasibility of an experimental realization in a quantum dot by the hyperfine interaction of an electron with the nuclear spins.

DOI: 10.1103/PhysRevB.78.125314 PACS number(s): 03.67.Mn, 73.21.La

I. INTRODUCTION

The quest to realize quantum information processing (QIP) has motivated an impressive race to implement high-precision preparation and manipulation of isolated two-level quantum systems (qubits) in a wide variety of physical settings.[1] A hallmark achievement for each such approach is the generation of quantum entanglement through controlled interaction between two or more qubits. Since switchable direct interactions between qubits often entail additional decoherence mechanisms, many QIP proposals rely on interactions *mediated* by an additional quantum system. As a rule this mediator (just as the qubits themselves) needs to be prepared in a pure state to achieve high-fidelity quantum operations, and it may look futile to use a high-entropy mesoscopic spin bath for this task. In contrast to these expectations, we show here that high-fidelity entanglement generation can be realized even if the qubits can interact only with an arbitrarily mixed spin bath, provided that this interaction can be switched on and off, single-qubit unitaries are available, and the bath has slow internal dynamics. This is motivated by and will be illustrated through the example of electron spin qubits in quantum dots (QDs),[2] where the ensemble of lattice nuclear spins represents a strongly coupled but slowly evolving spin bath.

Nuclear spins in quantum dots have received much theoretical[3–8] and experimental[9,10] attention in the QIP context as the main source of electron spin decoherence through the strong hyperfine coupling. It has also been noted that their slow internal dynamics and long (expected) decoherence time[11] make the ensemble of nuclear spins useful as a quantum memory[12] or for quantum computation.[13] These applications, however, require careful yet unachieved preparation of the nuclear system. What we show here is that the unprepared highly or even maximally mixed (nuclear) system is able to mediate coherent interaction between electrons and thereby allows the generation of highly entangled states of many (electron spin) qubits without any electron-electron interaction.

We consider a QD in the single-electron regime[14] and assume the availability of single-electron state preparation and measurement as well as the controlled shuttling of prepared electrons into and out of the QD, all of which have been demonstrated experimentally.[15] Additionally required is control of the detuning (e.g., by a magnetic or electric field), which switches the hyperfine (HF) interaction between resonant and off-resonant regimes. We first show how sequential interaction of three electrons with the nuclear bath can generate a maximally entangled pair of electron spins. More generally, the class of states that can be generated via the spin bath is characterized in terms of matrix product states. Finally we show that imperfect electron spin operations, inhomogeneous couplings between electron and nuclei, and modifications to the ideal static spin bath still allow for the scheme to be realized. In situations where the spin-orbit coupling is large, our scheme can be an interesting alternative to the standard exchange based setups, because it does not involve occupation of any higher orbital levels.[16,17]

II. ENTANGLEMENT GENERATION

We consider each electron coupled via the uniform Heisenberg interaction to the bath of N nuclear spins and to an external magnetic field B_z ($\hbar=1$),

$$H=\frac{A}{2N}(I^+S^-+S^+I^-)+\frac{A}{N}I^zS^z+g^*\mu_B B_zS^z. \tag{1}$$

$\mathbf{S}$ is the spin operator for the electron and $I^\mu=\Sigma_i I_i^\mu$ are the three components of the collective nuclear spin operators ($\mu=\pm,z$ and $[I^+,I^z]=-I^+$ and $[I^+,I^-]=2I^z$). g^* is the electron g factor and μ_B is the Bohr magneton. We consider spin-1/2 nuclei and neglect bath dynamics, the bath spins' Zeeman energies, and inhomogeneities in the Heisenberg couplings for now. We discuss the validity of these approximations toward the end of this paper.

We use the Dicke basis $\{|I,m,\beta\rangle\}$, where $I(I+1)$ is the eigenvalue of the collective angular momentum operator $\mathbf{I}^2$, the eigenvalue of I^z is given by m, and β is the permutation quantum number.[18] The initial state of the spin bath in the following is the identity

$$\rho_{\text{bath}}=\frac{1}{2^N}\sum_{I,m,\beta}|I,m,\beta\rangle\langle I,m,\beta|=\mathbb{1}_{2^N}/2^N. \tag{2}$$

In the following we omit β, which does not enter in the dynamics. This situation of a completely unknown bath state is, e.g., a suitable description for GaAs QDs even at temperatures as low as 100 mK.[9,10] In the following, time will be given in units of N/A. Even though the idea we present is applicable to any (quasi)static bath, we perform all estimations for GaAs, i.e., in particular $A^{-1}\approx 40$ ps.

The first electron spin (which we also refer to as ancilla

 ©2008 The American Physical Society

electron) is prepared in the state $|\uparrow\rangle$ and interacts *resonantly* for a time t_1 with the nuclear spin bath,

$$U|I,m,\uparrow\rangle = c_{Im}(t_1)|I,m,\uparrow\rangle + s_{Im}(t_1)|I,m+1,\downarrow\rangle, \quad (3)$$

with $U=e^{-iHt_1}$ and

$$c_{Im}(t_1) = \cos\left[\frac{(1+2I)t_1}{4}\right] - i\frac{1+2m}{1+2I}\sin\left[\frac{(1+2I)t_1}{4}\right],$$

$$s_{Im}(t_1) = \frac{-2i\sqrt{(I-m)(1+I+m)}}{1+2I}\sin\left[\frac{(1+2I)t_1}{4}\right].$$

Then the next electron spin, with initial state $|+\rangle = 1/\sqrt{2}(|\uparrow\rangle+|\downarrow\rangle)$, interacts for a time t_2 *off-resonantly* (e.g., in the presence of a large B_z) with the spin bath. For $g^*\mu_B B_z \gg A/\sqrt{N}$, the flip-flop part of the Hamiltonian can be approximately neglected,[19] yielding

$$V(t_2)|m,+\rangle = \frac{1}{\sqrt{2}}|m\rangle(e^{-i(\tilde{B}+m)t_2/2}|\uparrow\rangle + e^{+i(\tilde{B}+m)t_2/2}|\downarrow\rangle),$$

where $\tilde{B}=g^*\mu_B B_z N/A$ and the index I has been omitted for brevity. Remarkably, by choosing the interaction time $t_2=\pi$, the state of the electron is transformed to $(-i)^m|(-)^m\rangle$, i.e., for even $m=2k$ to $(-1)^k|+\rangle$ and for odd $m=2k+1$ to $-i(-1)^k|-\rangle$. For convenience we assume that $\tilde{B}t_2/2=2\pi\ell$, $\ell\in\mathbb{N}$, which is adjusted by the "free" parameter of the large field. With the third electron, also in $|+\rangle$ initially and with the same interaction, the state becomes

$$\pm c_{Im}(t_1)|I,m,\uparrow\rangle|\pm\pm\rangle \mp s_{Im}(t_1)|I,m+1,\downarrow\rangle|\mp\mp\rangle, \quad (4)$$

with upper (lower) signs referring to even (odd) m.

In the final step, the ancilla electron interacts resonantly with the nuclei again [cf. Eq. (3)], giving

$$\pm c_{Im}(t_1)|\pm\pm\rangle[c_{Im}(t_1)|m,\uparrow\rangle + s_{Im}(t_1)|m+1,\downarrow\rangle],$$

$$\mp s_{Im}(t_1)|\mp\mp\rangle[c^*_{Im}(t_1)|m+1,\downarrow\rangle + s_{Im}(t_1)|m,\uparrow\rangle] \quad (5)$$

for even/odd m, and is eventually measured projectively in the z basis. If the measurement outcome is $\downarrow$, it is clear from Eq. (5) that in each subspace the second and third electrons are in the maximally entangled state

$$|m+1\rangle(|++\rangle - e^{\pm i\phi_m}|--\rangle)/\sqrt{2}, \quad (6)$$

where the phase $\phi_m=2\arg(c_{Im})$ depends on the quantum numbers I and m, leading to a washing out of the entanglement when the average over the different subspaces is taken. However, for short times $[(2I+1)t_1 \ll 1$ for typical values of $I\sim\sqrt{N}]$, this phase tends to zero and near ideal entanglement is created, albeit at the price of a lower success probability, see Fig. 1.

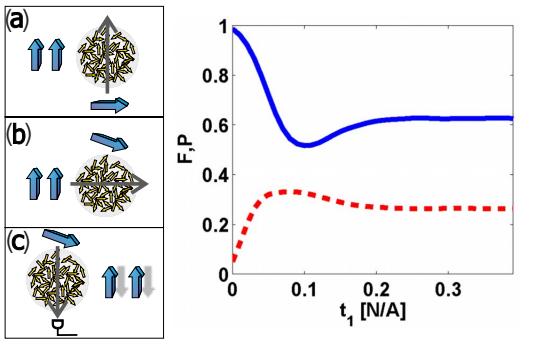

FIG. 1. (Color online) Left: Sketch of the protocol. (a) The z-polarized "control electron" interacts resonantly with the nuclear spin bath. (b) A sequence of x-polarized electrons interacts off-resonantly with the bath. (c) The control electron interacts resonantly again and is then measured in the z basis. Right: Time dependence of overlap F with Bell state $|\phi_-\rangle=(|++\rangle-|--\rangle)/\sqrt{2}$ (solid blue line) for $N=10^3$. The dashed red line shows the probability P for a $\downarrow$ measurement.

III. MULTIPARTITE ENTANGLEMENT

The presented scheme generalizes in a straightforward manner to multipartite entanglement creation. Following the same protocol using n electrons with arbitrary initial states $|\psi_1\rangle,\ldots,|\psi_n\rangle$, the final state becomes

$$|\Psi_n\rangle = \frac{1}{\sqrt{2}}\{\mathbb{1}+[(-1)^{m+1}i\sigma_z]^{\otimes n}\}|\psi_1,\ldots,\psi_n\rangle, \quad (7)$$

where the matrices are given in the standard z basis and we assumed the short-time limit $t_1\to 0$ for clarity. If $|\psi_k\rangle=|+\rangle$ for all k, this is an n-partite Greenberger-Horne-Zeilinger (GHZ) state. The m-dependent relative phase in the above equation restricts to generation of GHZ states with even particle number.

When multiple resonant interactions with the ancilla and varying interaction times are allowed, a larger class of states becomes accessible. To see which states can in principle be prepared, we exploit the similarity of our setup to the sequential entanglement generation scheme analyzed in Ref. 20. There it was shown that all the matrix product states (MPSs) of bond dimension d can be prepared if a string of qubits interacts sequentially with a d-dimensional ancilla system and *arbitrary unitaries* can be performed on ancilla and qubit in every step.

To apply this result to the present case, the ancilla electron and nuclear spin system together represent the control qubit: an effective $d=2$ system with Hilbert space spanned for given (I,m) by $\{|I,m,\uparrow\rangle,|I,m+1,\downarrow\rangle\}$. To see that arbitrary unitaries are possible, note that x rotations of the control qubit are caused by resonant interaction, while a static B_z field causes z rotations. From these, all single-qubit gates on the control qubit can be constructed. The off-resonant interaction considered before performs essentially a CNOT gate between the passing and the control qubit. In the CNOT gate the "control qubit" is the control and the passing electron is the target, in the $|\uparrow,\downarrow\rangle$ and $|\pm\rangle$ basis, respectively. Combined with single-qubit gates (on the passing electron), this seems to be enough to allow for arbitrary transformations on the coupled control-target system. However, the situation is more complicated since the effective gate performed by the off-resonant interaction *differs* for even and odd parities of the control qubit, namely, $V(\pi)=e^{(-1)^m i(\pi/4)\sigma_z}\sigma^m_{x,1}CNOT_{1\to 2}\sigma^m_{x,1}$. I.e., not only there is, as seen

before, a parity-dependent phase but also whether logical-0 or logical-1 controls the bit flip in the passing qubit depends on the parity of m. One way to remove this m-dependence and enable the generation of arbitrary states is to perform an "I^z parity measurement" by sending an electron $|+\rangle$ into the dot, and then measure it in the $|\pm\rangle$ basis after off-resonant interaction for a time π. Depending on the outcome, either the odd or the even states are projected out. Remarkably, gaining this single bit of information about the 2^N-dimensional bath then allows us to remove all m-dependences and perform clean CNOT gates. Hence the interactions outlined above are sufficient to prepare all $d=2$ MPSs with high fidelity. If the passing electrons can be brought into interaction with the ancilla again at any time, *arbitrary* two-qubit gates can be performed, which implies that all matrix product states with two-dimensional bonds can be sequentially created.[20]

Direct resonant interactions lead to very low-fidelity x rotations due to averaging over the different subspaces, indicating that prior measurement[21–23] or cooling[24] of the spin bath might be necessary. More sophisticated control schemes, however, allow for near-unit-fidelity single-qubit rotations with no prior preparation: In Ref. 25 it was proven that high-fidelity arbitrary single-qubit gates can be effected by a Hamiltonian $H=\delta\sigma_z+\Omega(\sigma_x\cos\phi+\sigma_y\sin\phi)$, when only the parameter ϕ can be controlled precisely. For δ and Ω it is sufficient to know that they are nonzero for some value of a controllable external parameter and zero for another. In our situation we have the three Hamiltonians $H_1=\Delta\sigma_z=B\mu_I\sigma_z/2$ (nuclear Zeeman), $H_2=\frac{A}{2N}[(m+1/2)\sigma_z+\xi_{I,m}\sigma_x]$ (resonant HF), and $H_3=\frac{A}{2N}[\pm(\tilde{B}+m+1/2)+\tilde{B}\mu_I/(\mu_B g^*)]\sigma_z$ (off-resonant HF) at hand. The Pauli matrices act on the control qubit, μ_I is the nuclear magnetic moment, and $\xi_{I,m}=\sqrt{I(I+1)-m(m+1)}$. The plus and minus signs for H_3 can be effected through spin flips of the passing electron (recall that $\sigma_x e^{iHt}\sigma_x=e^{i\sigma_x H\sigma_x t}$ and $\sigma_x\sigma_z\sigma_x=-\sigma_z$). These Hamiltonians can be switched on and off (adiabatically[26]) at will. Appropriate iterations of evolutions can lead to effective Hamiltonians of weighted sums and commutators of $H_{1,2,3}$. In particular, the subspace independence of the parameter $\Delta\propto B$ allows for generation of any weighted sum of σ_x and σ_y with the weights being (I,m) independent, thus making the results of Ref. 25 applicable. We have thus shown that while naive use of resonant interactions will lead to poor gate fidelities for the control qubit, enhanced control schemes still allow for full access to high-fidelity rotations. Hence, in principle, universal quantum computation on an electron spin quantum register can be performed, with all interactions mediated by the highly mixed spin bath.

IV. EXPERIMENTAL FEASIBILITY

We discuss now various couplings that have been neglected in the idealized Hamiltonian (1) but are present in the QD setup. We are concerned here only with their effects on the basic entanglement generation scheme. It is clear that the scheme can only work as long as it is fast compared to the electron T_2 time, since the coherence of the ancilla electron must be preserved. We see below that neither nuclear dynamics nor inhomogeneity place more stringent conditions on our scheme.

A. Inhomogeneity

The HF Hamiltonian in QDs has a slightly different form from the one in Eq. (1), because the collective bath operators have a spatial dependence $A/NI^\mu\to A^\mu\equiv\Sigma_i\alpha_i I_i^\mu$, with $\mu=\pm,z$. The coupling constants α_i are $\propto\mu_{I,i}|\psi_e(r_i)|^2$, with $|\psi_e(r_i)|^2$ being the probability of finding the electron at location r_i, and $A=\Sigma_j\alpha_j$ denotes now the effective (average) hyperfine coupling strength. We focus our analysis on short resonant interaction times $\Delta t_1\ll\sqrt{N}/A$. The electronic state after the above protocol conditioned on a $\downarrow$ measurement is proportional to

$$\sum_{\psi,\psi'}\langle\psi'|A^+e^{i(\sigma_1^z+\sigma_2^z)A^z t_2}+e^{i(\sigma_1^z+\sigma_2^z)A^z t_2}A^+|\psi\rangle|+\,+\rangle\times\text{H.c.},$$

where the Pauli matrices act on the off-resonant electrons and $|\psi\rangle=|i_1\cdots i_N\rangle$ and $|\psi'\rangle=|i_1'\cdots i_N'\rangle$ label the orthonormal basis of I_j^z eigenstates. Evaluating the matrix elements and introducing the normalization, we get

$$\rho(t_2)=\frac{1}{\mathcal{N}(t_2)}\sum_j\alpha_j^2\sum_{\substack{i_1,\ldots,i_N=\pm1/2\\ i_j=-1/2}}(|+_0+_0\rangle+|-_j-_j\rangle)\times\text{H.c.},\quad(8)$$

with the states $|+_0(t_2)\rangle=e^{i\omega_0 t_2/2}|\uparrow\rangle+e^{-i\omega_0 t_2/2}|\downarrow\rangle$ and $|-_j(t_2)\rangle=e^{i\omega_j t_2/2}|\uparrow\rangle+e^{-i\omega_j t_2/2}|\downarrow\rangle$, both of which depend on the nuclear spin configuration $\{i\}$ via the frequencies $\omega_0=\omega_0(\{i\})=\Sigma_\ell\alpha_\ell i_\ell$ and $\omega_j=\omega_0+\alpha_j$ and the normalization $\mathcal{N}(t_2)=\Sigma_j\alpha_j^2[3+\cos(\alpha_j t_2)]$. The time dependence of the states has been omitted for brevity in the above formula. Straightforwardly, one now determines the fidelity $F(t_2)=\langle\phi_-|\rho(t_2)|\phi_-\rangle$ with the desired maximally entangled state $|\phi_-\rangle\sim|+_0+_0\rangle+|-_0-_0\rangle$ as

$$F(t_2)=2\sum\alpha_j^2\Big/\sum_j\alpha_j^2[3+\cos(\alpha_j t_2)].\quad(9)$$

This expression readily gives the fidelity for arbitrary particle numbers and arbitrary distributions of coupling constants. For $N\gg1$, the obtained value is independent of particle number, and for the relevant situation of Gaussian coupling $F=0.90$, 0.83, and 0.78 for one dimension, two dimensions, and three dimensions, respectively. Including the difference in magnetic moments for Ga and As [^{75}As: $\mu_{I,\mathrm{As}}=1.44$; ^{69}Ga: $\mu_{I,\mathrm{Ga},1}=2.02$ (60%); and ^{71}Ga: $\mu_{I,\mathrm{Ga},2}=2.56$ (40%) (Ref. 7)], these values become $F=0.83$, 0.78, and 0.74, indicating that our scheme is not compromised by realistic inhomogeneities.

For small inhomogeneity we find the optimal time $t_2^{(\mathrm{opt})}$ by setting the time derivative of F zero and expanding the equation in terms of the deviations $\epsilon_j=\alpha_j-\alpha^*$, where $\alpha^*=\pi/t_2^{(\mathrm{opt})}$. Going to second order in the small parameters ϵ_j/α^*, the ensuing quadratic equation yields $\alpha^*=\eta_1[5-\sqrt{1+24(1-\eta_2/\eta_1^2)}]/4$, with $\eta_x=\frac{1}{N}\Sigma_j\alpha_j^x$. Plugging $t_2^{(\mathrm{opt})}$ back into Eq. (9) and keeping terms up to second order, we find $F(\pi/\alpha^*)=1-\frac{\pi}{2N}\Sigma_j(\epsilon_j/\alpha^*)^2$.

B. Nuclear Zeeman energies

For the times considered, nuclear Zeeman energies lead to an important relative phase $B_z\mu_{I,j}t_2$ for each of the two terms in the sum of the conditional state given in Eq. (8). Considering one homogeneously coupled species of nuclear spins, the state of Eq. (6) will have an additional m-dependent phase. In each invariant subspace this produces an overall phase $\propto B_z\mu_I t_2 m$ and a relative phase $\propto B_z\mu_I t_2$ between the two parts of the superposition. This might not seem harmful, but due to the parity effect, the *sign* of the phase depends on the parity of m. Since this phase is of order π, it could spoil the protocol. However, by simply waiting for an appropriate time t_p after each of the n electrons has passed, the total relevant phase is $(-1)^m nB_z\mu_I(t_2+t_p)$; with t_p+t_2 an integer multiple of $\pi/(\mu_I B_z)$, it is again m independent. By the same procedure, the nuclear Zeeman related phase can be removed for single-species inhomogeneous systems.

For systems with strongly varying nuclear magnetic moments $\mu_{I,j}$, the relative phase depends on "which nuclear spin has flipped" and the waiting time needs to be chosen such that all the relative phases are close to $2k\pi$. Otherwise the final fidelity may be strongly degraded. For the three species in GaAs this is the case, e.g., for $B_z(t_2+t_p)\approx 7\pi$, and assuming that a flat wave function still allows for a fidelity $\gtrsim 0.9$ with moderate overhead in time. In principle, one can completely cancel the undesired phase by removing the electrons from the QD and reversing the magnetic field for $t_p=t_2$.

C. Bath dynamics

The major internal dynamics of nuclear spins in QDs stems from the indirect hyperfine mediated interaction and the direct dipolar interaction.[6,8] Both mechanisms lead to bilocal errors that contain spin-flip terms $\propto(\Gamma_d^{kl}+\Gamma_i^{kl})I_k^+ I_l^-$ and phase changing zz terms $\propto\Gamma_d^{kl}I_k^z I_l^z$. The transition rates for direct and indirect interactions are Γ_{dd}/r_{kl}^3 and $\alpha_i\alpha_j/\Omega_e$, respectively, where Ω_e is the electron Zeeman energy and $r_{kl}=|\mathbf{r}_k-\mathbf{r}_l|$.

The dephasing interactions $\propto I_i^z I_j^z$ lead to a relative phase between the terms in Eq. (8), similar to the nuclear Zeeman energies. The energy difference, i.e., (in a mean-field treatment) the Zeeman splitting of a single nuclear spin in the field of its neighbors, is a few times Γ_{dd}.[24] Thus we need $N\Gamma_{dd}/(r_0^3 A)\ll 1$; given $\Gamma_{dd}/r_0^3\approx 0.1$ ms (Ref. 7) for nearest neighbors and $A\approx 40$ ps, this condition is readily fulfilled even for large dots.

We have seen above that for each term in the mixed state, the qubits rotate on the equatorial plane of the Bloch sphere with frequencies α_j when the jth nuclear spin has been flipped. If this particular spin is involved in a spin flip due to bath dynamics, the resulting rotation with "wrong" frequency spoils the entanglement. The errors in the rotation angle for the term containing the flip of the jth spin are $\epsilon_{d,i}^j=\sqrt{\Sigma_k(\Gamma_{d,i}^{kj}t)^2(\alpha_j-\alpha_k)^2(t_2^{\mathrm{opt}})^2}$, and the final overall errors are $\Sigma_j\alpha_j^2\epsilon_{d,i}^j/\Sigma_j\alpha_j^2$. We evaluate the above sums in the continuum limit for Gaussian couplings and get for the indirect flips a total error of $\delta_i\pi^2 A\gamma_3^2/(\gamma_4^2\Omega)$, where δ_i is determined by the integrals over the coupling constants. Taking $A/\Omega<1$ for the large (>1 T) fields that we require, we find errors of 2.4%, 2.0%, and 1.5% for one dimension, two dimensions, and three dimensions, respectively, for $N=10^4$ (we define N here as the number of nuclei within the $1/(2e)$ width of the Gaussian). For the direct nuclear dipole-dipole transitions, the error is of size $\delta_d\pi^2\gamma_3^2\Gamma_{dd}/(Ar_0^3\gamma_4^2)$, where numerical evaluation of the "dipolar integrals" δ_d yields 0.01%, 0.8%, and 5% for the same situation as above. This overall error is thus on the order of a few percent for realistic situations.

D. Storage

We implicitly assumed the possibility of storing the electrons protected from any bath. In QD structures this could be achieved by shuttling the electrons to a nuclear spin-free region or employing dynamical decoupling schemes; see, for example, Ref. 6. The required storage times of a few tens of microseconds should be readily achieved.

E. Imperfect electronic operations

A finite probability that an up electron is wrongly detected as a down electron (or vice versa) degrades the final entanglement. However, as only one electron needs to be measured, the effect is no worse for the n-partite GHZ state than for the Bell state $|\Phi^+\rangle$. The same goes for variations in the resonant interaction time t_1. In contrast, errors in the electron preparation and variations in the off-resonant interaction time t_2, since they affect each of the n electrons, lead to a fidelity reduction that scales exponentially with n. Variations in t_2 must be such that $\tilde{B}\delta t_2\ll 1$, with $\tilde{B}\gg A/\sqrt{N}$, which makes this the most stringent but still realistic[27,28] requirement for electron timing.

V. SUMMARY AND CONCLUSIONS

We have considered the Heisenberg interaction of electron spin qubits with a long-lived spin bath in a situation where *nothing* is known about the state of the bath. We have shown that nevertheless high-fidelity multipartite entanglement can be created via this bath.

The qubits interact neither directly with each other nor simultaneously with the bath at any time. Our protocol thus demonstrates that even the interaction with infinite temperature systems can mediate highly coherent operations and thus represent a valuable resource for quantum information processing that merits further investigation. In fact, when only one bit of information is extracted from the spin bath, arbitrary gates between the bath and the qubits are possible, and all matrix product states with two-dimensional bonds can be created by sequential interaction. The explicit protocols we presented can be realized in quantum dot setups and would (in typical GaAs dots) allow for the creation of entanglement between two electrons on a time scale of a few microseconds.

ACKNOWLEDGMENTS

This work was supported by the DFG within SFB 631 and within the excellence cluster NIM.

[1] P. Zoller *et al.*, Eur. Phys. J. D **36**, 203 (2005).
[2] D. Loss and D. P. DiVincenzo, Phys. Rev. A **57**, 120 (1998).
[3] A. V. Khaetskii, D. Loss, and L. Glazman, Phys. Rev. Lett. **88**, 186802 (2002).
[4] S. I. Erlingsson and Y. V. Nazarov, Phys. Rev. B **70**, 205327 (2004).
[5] C. Deng and X. Hu, Phys. Rev. B **73**, 241303(R) (2006).
[6] W. M. Witzel and S. Das Sarma, Phys. Rev. B **74**, 035322 (2006).
[7] J. Schliemann, A. Khaetskii, and D. Loss, J. Phys.: Condens. Matter **15**, R1809 (2003).
[8] W. Yao, R.-B. Liu, and L. J. Sham, Phys. Rev. Lett. **95**, 030504 (2005).
[9] J. R. Petta, A. C. Johnson, J. M. Taylor, E. A. Laird, A. Yacoby, M. D. Lukin, C. M. Marcus, M. P. Hanson, and A. C. Gossard, Science **309**, 2180 (2005).
[10] F. H. L. Koppens, J. A. Folk, J. M. Elzerman, R. Hanson, L. H. Willems van Beveren, I. T. Vink, H.-P. Tranitz, W. Wegscheider, L. P. Kouwenhoven, and L. M. K. Vandersypen, Science **309**, 1346 (2005).
[11] D. Paget, G. Lampel, B. Sapoval, and V. I. Safarov, Phys. Rev. B **15**, 5780 (1977).
[12] J. M. Taylor, A. Imamoğlu, and M. D. Lukin, Phys. Rev. Lett. **91**, 246802 (2003).
[13] J. M. Taylor, G. Giedke, H. Christ, B. Paredes, J. I. Cirac, P. Zoller, M. D. Lukin, and A. Imamoğlu, arXiv:cond-mat/0407640 (unpublished); H. Christ, Ph.D. thesis, TU München, 2008.
[14] R. Hanson, L. P. Kouwenhoven, J. R. Petta, S. Tarucha, and L. M. K. Vandersypen, Rev. Mod. Phys. **79**, 1217 (2007).
[15] R. Hanson and D. D. Awschalom, Nature (London) **453**, 1043 (2008).
[16] X. Hu and S. Das Sarma, Phys. Rev. Lett. **96**, 100501 (2006).
[17] W. A. Coish and D. Loss, Phys. Rev. B **75**, 161302(R) (2007).
[18] F. T. Arecchi, E. Courtens, R. Gilmore, and H. Thomas, Phys. Rev. A **6**, 2211 (1972).
[19] W. A. Coish and D. Loss, Phys. Rev. B **70**, 195340 (2004).
[20] C. Schön, E. Solano, F. Verstraete, J. I. Cirac, and M. M. Wolf, Phys. Rev. Lett. **95**, 110503 (2005).
[21] D. Klauser, W. A. Coish, and D. Loss, Phys. Rev. B **73**, 205302 (2006).
[22] D. Stepanenko, G. Burkard, G. Giedke, and A. Imamoğlu, Phys. Rev. Lett. **96**, 136401 (2006).
[23] G. Giedke, J. M. Taylor, D. D'Alessandro, M. D. Lukin, and A. Imamoğlu, Phys. Rev. A **74**, 032316 (2006).
[24] H. Christ, J. I. Cirac, and G. Giedke, Phys. Rev. B **75**, 155324 (2007).
[25] J. J. García-Ripoll and J. I. Cirac, Phys. Rev. Lett. **90**, 127902 (2003).
[26] We assume here perfect storage of the ancilla electron in a "protected" region free of HF interactions. HF Hamiltonians can then be switched adiabatically by shifting the electron wave function slowly from the protected region to the spin bath.
[27] M. Førre, J. P. Hansen, V. Popsueva, and A. Dubois, Phys. Rev. B **74**, 165304 (2006).
[28] J. M. Taylor, H.-A. Engel, W. Dür, A. Yacoby, C. M. Marcus, P. Zoller, and M. D. Lukin, Nat. Phys. **1**, 177 (2005).

PRL 104, 143601 (2010) PHYSICAL REVIEW LETTERS week ending 9 APRIL 2010

Optical Superradiance from Nuclear Spin Environment of Single-Photon Emitters

E. M. Kessler,[1] S. Yelin,[2,3] M. D. Lukin,[3,4] J. I. Cirac,[1] and G. Giedke[1]

[1]Max-Planck-Institut für Quantenoptik, Hans-Kopfermann-Strasse 1, D-85748 Garching, Germany
[2]Department of Physics, University of Connecticut, Storrs, Connecticut 06269, USA
[3]ITAMP, Harvard-Smithsonian Center for Astrophysics, Cambridge, Massachusetts 02138, USA
[4]Department of Physics, Harvard University, Cambridge, Massachusetts 02138, USA

(Received 8 February 2010; published 9 April 2010)

We show that superradiant optical emission can be observed from the polarized nuclear spin ensemble surrounding a single-photon emitter such as a single quantum dot or nitrogen-vacancy center. The superradiant light is emitted under optical pumping conditions and would be observable with realistic experimental parameters.

DOI: 10.1103/PhysRevLett.104.143601 PACS numbers: 42.50.Nn, 78.67.−n

Superradiance (SR) is a cooperative radiation effect resulting from spontaneous buildup and reinforcement of correlations between initially independent dipoles. Its most prominent feature is an emission intensity burst in which the system radiates much faster than an otherwise identical system of independent emitters. This phenomenon is of fundamental importance in quantum optics and since its first prediction by Dicke in 1954 [1] it has been studied extensively (for a review see [2]). The rich steady state properties of the associated dynamics can account for strong correlation effects including phase transitions and bistability [3,4]. Yet in its original form optical SR is difficult to observe due to dephasing dipole-dipole van der Waals interactions, which suppress a coherence buildup in atomic ensembles.

In this Letter, we show that cooperative emission can occur from the ensemble of nuclear spins surrounding a quantum emitter such as a self-assembled quantum dot (QD) or an nitrogen- vacancy (NV) center. The interaction of the nuclear spin ensemble and optical field is mediated by the electron spin of the emitter. Because of the indirect character of the interaction, the dephasing van der Waals interactions vanish in this setting.

We first explain the proposal using the example of an NV center in a diamond. Then, we adapt the model to QDs, which promise strong effects due to the large number of involved nuclei. Despite the inhomogeneity of the nuclear spin coupling and related dephasing processes, we predict a SR-like correlation buildup in the nuclear spin ensemble and a significant intensity burst of several orders of magnitude in the optical emission profile. Finally, we point out the possibility of observing phase transitions and bistability in the nuclear system.

The superradiant effect is based on the collective hyperfine (HF) interaction of the electronic spin of the defect (QD or NV) with N initially polarized proximal nuclear spins. It is dominated by the isotropic contact term [5,6] and reads in an external magnetic field ($\hbar = 1$):

$$H = \frac{g}{2}(A^+S^- + A^-S^+) + gA^zS^z + \omega_S S^z. \qquad (1)$$

Here S^μ and $A^\mu = \sum_{i=1}^N g_i \sigma_i^\mu$ ($\mu = +, -, z$) denote electron and collective nuclear spin operators, respectively. The coupling coefficients are normalized such that $\sum_i g_i^2 = 1$ and individual nuclear spin operators σ_i^μ are assumed to be spin $1/2$ for simplicity; g gives the overall HF coupling strength and ω_S denotes the electron Zeeman splitting. We neglect the typically very small nuclear Zeeman and nuclear dipole-dipole terms.

Let us first consider NV centers, in which the effect can be studied in a clean and relatively small spin environment. Because of their extraordinary quantum properties, such as ultralong decoherence times even at room temperature, NV centers have attracted wide interest [7] resulting, e.g., in the demonstration of entanglement and quantum gates between the electron and proximal nuclear spins [8]. Both the NV center's electronic ground (^3A) and optically excited states (^3E) are spin triplet ($S = 1$) [7]. In the absence of a magnetic field, the ground state sublevels $|m_S = \pm 1\rangle$ are split from $|m_S = 0\rangle$. In the following, we assume that a B field is applied along the NV axis to bring $|m_S = 0\rangle$ and $|m_S = 1\rangle$ close to degeneracy [9]. In this case, $|m_S = -1\rangle$ is off resonance and can be disregarded. We focus on low-strain NV centers with well-defined selection rules and assume that it is optically excited by selectively driving the weakly allowed transition from $|m_S = 1\rangle$ to a state $|E_x\rangle$ in the ^3E manifold which decays primarily into $|m_S = 0\rangle$ [10]; see Fig. 1(a). The nuclear spin environment of the NV center consists of proximal ^{13}C ($I = 1/2$) nuclei in the otherwise spinless ^{12}C matrix, which are HF coupled to the electronic spin of the defect center. The interaction is dominated by the Fermi-contact term such that the coupling is isotropic (to first order) and described by Eq. (1) (ω_S here contains both zero-field splitting and Zeeman energy). Nevertheless in the simulations conducted below, we included the small anisotropic dipole-dipole terms.

We describe now the coupling of the nuclear spin to the optical field as depicted in Fig. 1(b). It is best understood as a two-step process: first, strongly driving a dipole-forbidden optical transition of the $|m_S = 1\rangle$ spin state

 © 2010 The American Physical Society

PRL **104,** 143601 (2010) PHYSICAL REVIEW LETTERS week ending 9 APRIL 2010

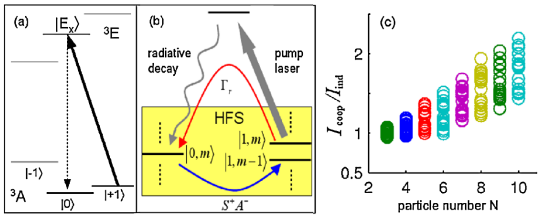

FIG. 1 (color online). (a) Simplified level scheme of NV center with relevant Λ system (cf. the text and [10]). (b) Sketch of relevant processes: electronic ground states are coupled by optical pumping and HF flipflops; the states are labeled by the z components of the electron and nuclear spin. (c) $I_{\mathrm{coop}}/I_{\mathrm{ind}}$ for randomly chosen nuclear environments of an NV center. The first nuclear shell is taken to be spinless, as due to their very strong coupling they would evolve largely independent from the ensemble.

(the allowed transition is far off resonant) pumps the electron into $|m_S = 0\rangle$. Such Raman spin-flip transitions have been demonstrated recently [10]. Since the short-lived excited state is populated negligibly throughout the process, we can eliminate it from the dynamics using standard techniques and obtain a master equation for the electron spin decaying with effective rate Γ_r:

$$\dot{\rho} = \Gamma_r(S^-\rho S^+ - \tfrac{1}{2}S^+S^-\rho - \tfrac{1}{2}\rho S^+S^-) - i[H,\rho], \quad (2)$$

each decay being accompanied by a Raman photon. Second, the return to state $|m_S = 1\rangle$, necessary for the next emission, occurs through H via a HF mediated electron spin flip (and nuclear spin flop). Thus, each Raman photon indicates a nuclear spin flop and the emission intensity $I(t)$ is proportional to the change in nuclear polarization. Starting from a fully polarized state, SR is due to the increase in the operative HF matrix element $\langle A^+A^-\rangle$. The scale of the coupling is set by $A := g\sum_i g_i$. For a small relative coupling strength $\epsilon = A/(2\Delta)$, where $\Delta := |\Gamma_r/2 + i\omega_S|$, the electron is predominantly in its $|m_S = 0\rangle$ spin state and we can project Eq. (2) to the respective subspace. The reduced master equation for the nuclear density operator reads

$$\dot{\rho} = c_r(A^-\rho A^+ - \tfrac{1}{2}A^+A^-\rho - \tfrac{1}{2}\rho A^+A^-) - ic_i[A^+A^-,\rho] - igm_S[A^z,\rho], \quad (3)$$

where $c_r = g^2/(2\Delta)^2\Gamma_r$ and $c_i = g^2/(2\Delta)^2\omega_S$.

As the electron is optically pumped into $|m_S = 0\rangle$, the last term—representing the electron's Knight field—in Eq. (3) vanishes. Assuming resonance ($\omega_S = 0$) the equation closely resembles the SR master equation which has been discussed extensively in the context of atomic physics [2] and thus SR effects might be expected. However, there is a crucial difference: the inhomogeneous nature ($g_i \neq$ const) of the operators A^μ. They do not preserve the collective spin, affecting the relative phase between nuclei. This could prevent the phased emission necessary for SR [2,11,12]. However, as we shall see, SR is still clearly present in realistic inhomogeneous systems. We take the ratio of the maximum intensity to the initial intensity (the maximum for independent spins) $I_{\mathrm{coop}}/I_{\mathrm{ind}}$ as our figure of merit in the following: if this relative intensity peak height is >1 it indicates cooperative effects.

To see that this effect can be observed at NV centers, we simulate Eq. (2) numerically [13]. The number N of effectively coupled nuclei can range from a few to a few hundred, since the concentration of ^{13}C can be widely tuned [14]. The HF constants g_i between the defect and the nearest ~40 nuclei were derived in [6] in an *ab initio* calculation. Nuclei outside this shell (~7 Å) have a coupling strength gg_i weaker than $2\pi \times 0.5$ MHz and are not considered here. The excited state lifetime of the NV center has been measured as $\tau \approx 13$ ns [15,16]. Thus, we adopt an effective rate $\Gamma_r = 2\pi \times 10$ MHz for the decay from $|m_S = 1\rangle$ to $|m_S = 0\rangle$ enabled by driving the Raman transition. The intensity enhancements predicted by exact simulations for small, randomly chosen, and initially polarized spin environments are shown in Fig. 1(c). In samples of higher ^{13}C concentration N can be larger and stronger effects are expected.

One characteristic feature of SR is the linear N dependence of the associated effects (already visible in Fig. 1). Since the number of nuclei to which the electron couples is much larger in a QD than in a NV center, QDs are particularly attractive candidates for the investigation of SR. In the following we study the dynamics of the QD system in different regimes and we show that strong signatures of SR can be expected in realistic settings.

Let us consider a self-assembled QD in which a single conduction band electron is coupled by isotropic Fermi-contact interaction to a large number of nuclear spins. Optical pumping of the electron is realized by a Raman process, driving a forbidden transition to a trion state [17], and including the HF coupling we again obtain dynamics as sketched in Fig. 1(b). For the optical pumping rate values $\Gamma_r = 2\pi \times (0.1\text{–}1)$ GHz are applicable [18,19]. A comparison with the HF coupling constants reported for different materials [20] shows that for InGaAs and CdSe QDs at resonance Eq. (3) are not valid since the relative coupling strength $\epsilon \geq 1$. We therefore consider the dynamics of the system under conditions of a finite electron inversion [using Eq. (2)]. In this regime, the electron can be seen as a driven and damped two-level system: the nuclei "pump" excitations into the electron, which are damped by the Raman-mediated decay; cooperative behavior manifests in enhanced HF interaction. This enhancement directly translates into increased electron inversion $\langle S^+S^-\rangle$ to which the emitted photon rate is proportional and thus SR from a single QD can be expected. Let us rephrase this, since SR from a *single* emitter is somewhat counter intuitive. Of course, on an optical time scale, antibunched single photons will be emitted at a rate below the optical decay rate. It is, in fact, typically much slower since the emitter is pumped into the optically inactive state $|m_S = 0\rangle$. SR on time scales $\sim 1/\Gamma_r$ consists

thus of lifting this "spin blockade" by HF coupling which becomes increasingly more efficient as nuclear cooperative effects kick in. As in the homogeneous case [2], this enhancement is associated with the transition through nuclear Dicke states $|J, m\rangle$, $|m| \ll J$. Although J is not preserved by inhomogeneous $A^{\pm}$, we can use the Dicke states to illustrate the dynamics. For instance, due to the large homogeneous component in A^{-}, its matrix elements show a strong increase $\propto J$ for states $|J, m\rangle$, $|m| \ll J$.

For large relative coupling strengths $\epsilon \gg 1$ the electron saturates and superradiant emission is capped by the decay rate $\Gamma_r/2$, prohibiting the observation of an intensity burst. In order to avoid this bottleneck regime, we choose a detuning $\omega_S = A/2$ such that $0 < \epsilon = A/\sqrt{\Gamma_r^2 + A^2} \leq 1$. In this parameter range, the early stage of the evolution—in which the correlation buildup necessary for SR takes place [2]—is well described by Eq. (3). The nuclear phasing is counteracted by the dephasing (inhomogeneous) part of the Knight term ($\propto g\sqrt{\mathrm{Var}(g_i)}/2$ [21]), which can cause transitions $J \rightarrow J - 1$. However, the system evolves in a many-body protected manifold (MPM) [22]: The term $\sim[A^{+}A^{-}, \rho]$ energetically separates different total nuclear spin-J manifolds. A rough estimate of the ratio between detuning and dephasing shows a dependence $\propto \epsilon^2$, with proportionality factor >1 (diverging in the homogeneous limit). Thus for values $\epsilon \approx 1$ the correlation buildup should be largely MPM protected. We now confirm these considerations and show by numerical simulation of Eq. (2) that a SR peaking of several orders of magnitude can be observed in the Raman radiation from an optically pumped QD; cf. Fig. 2. An exact numerical simulation of the dynamics is not feasible due to the large number of coupled nuclei and since the dynamics for inhomogeneous coupling cannot be restricted to a low-dimensional subspace. To obtain $I(t) \propto \frac{d}{dt}\sum_i \langle \sigma_i^{+}\sigma_i^{-}\rangle$, we therefore use an approximative scheme. By Eq. (2), these expectation values are related to fourth-order correlation terms involving both the electron and nuclear spins. We use a factorization assumption to reduce the higher-order expressions in terms of the covariance matrix $\gamma_{ij}^{+} = \langle \sigma_i^{+}\sigma_j^{-}\rangle$. Following [23], we apply the bosonic Wick's theorem, incorporating the fermionic character of same-site nuclear spin operators ($[\sigma_i^{+}, \sigma_i^{-}]_{+} = 1$) and replace, e.g., $\langle \sigma_i^{+}\sigma_j^{z}S^{-}\rangle \rightarrow (\gamma_{jj}^{+} - \frac{1}{2}) \times \langle \sigma_i^{+}S^{-}\rangle - \gamma_{ij}^{+}\langle \sigma_j^{+}S^{-}\rangle$. But the electron spin plays a special role and factorizing it completely leads to poor results. Therefore we also solve Eq. (2) for the main higher-order term involving the electron, the "mediated covariance matrix" $\gamma_{ij}^{-} = \langle \sigma_i^{+}S^{z}\sigma_j^{-}\rangle$. All other higher-order expectation values therein are factorized under consideration of special symmetries for operators acting on the same site.

In the regimes accessible to an exact treatment, i.e., the homogeneous case and for few inhomogeneously coupled particles, the factorization results agree well with the exact evolution (see the inset in Fig. 2). This shows that it quantitatively captures the effect of nuclear spin coherences while allowing a numerical treatment of hundreds of spins. Finally, in addition to the constant detuning $\omega_S = A/2$ for the displayed simulations we compensated the Overhauser field dynamically [24]. Furthermore, we assume a Gaussian spatial electron wave function. The results obtained with these methods are displayed in Figs. 2 and 3. For $\epsilon \approx 1$, the strong MPM protection suppresses dephasing, leading to pronounced SR signatures: A strong intensity burst, whose relative height scales $\propto N$ (for large N). For large $\epsilon \approx 1$, the relative height is reduced only by half compared to the ideal Dicke case. For smaller ϵ, it decreases further due to increased dephasing. For $\epsilon \leq 0.3$, where MPM protection is weak and the decay process is significantly slowed down ($c_r \propto \epsilon^2$), even the linear scaling is lost.

From Fig. 3, one extrapolates that for a fully polarized initial state a huge intensity overhead of several orders of magnitude ($\sim 10^3$–10^4) is predicted. If the initial state is not fully polarized, SR effects are reduced. However, even when, e.g., starting from a mixture of symmetric Dicke states $|J, J\rangle$ with polarization $P = 60\%$ [18,25] our simulations predict a strong intensity peak and (for $N \gg 1$) a

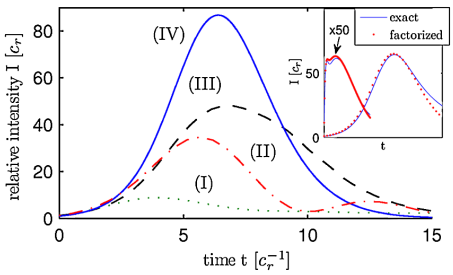

FIG. 2 (color online). Relative intensity under dynamical Overhauser field compensation: $N = 21^2$, $\omega_S = A/2$, and $\epsilon = 0.3$(I), 0.7(II), 0.99(III). (IV) shows the ideal Dicke SR profile [1] as a reference. Inset: comparison of exact evolution and factorization for $N = 9$ inhomogeneously coupled spins (left peak, scaled by factor 50) and $N = 21^2$ homogeneous spins ($\epsilon = 0.7$). Fully independent emitters lead to an exponential curve slowly decaying from 1 to zero and are therefore not depicted.

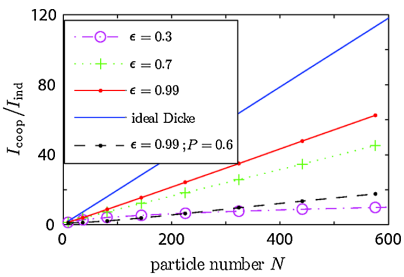

FIG. 3 (color online). $I_{\mathrm{coop}}/I_{\mathrm{ind}}$ for different values of ϵ—the Overhauser field is dynamically compensated and $\omega_S = A/2$ in all cases—compared to the ideal Dicke case. The dashed line corresponds to a partially polarized dot (cf. the text).

linear N dependence: $I_{\mathrm{coop}}/I_{\mathrm{ind}} \approx 0.03N$ ($\epsilon = 0.99$), i.e., only a factor 4 weaker than for full polarization.

Note that for the sake of simplicity, we consider $I = 1/2$ nuclei in our simulations. In terms of particle numbers N, this is a pessimistic assumption as typical QD host materials carry a higher spin. We can incorporate this effect by treating higher spins as $2I$ homogeneously coupled spins $I = 1/2$, thus increasing the effective particle number by the factor $2I$. Most QDs consist of a few different species of nuclei with strongly varying magnetic moments, increasing the inhomogeneity of the system. However, in the worst case the different species evolve independently, diminishing the effect by a small factor corresponding to the number of species. In our simulations, the effect was shown to be much smaller.

We have neglected the dipolar and quadrupolar interaction among the nuclear spins. The former is always negligible on the time scale considered here [5]. The latter is absent for nuclear spin $I = 1/2$ (NV centers, CdSe QDs) or strain-free QDs [18]. In strongly strained QDs it can be important [26], and a term $\sum_i \nu_i (I_i^{z_i})^2$ must be added to Eq. (1), where z_i is defined as the main axis of the local electric-field-gradient tensor.

Having seen that SR can be observed in experimentally accessible nuclear spin ensembles, let us briefly explore two further applications of this setting: nuclear spin polarization and phase transitions. We first note that the master equation Eq. (3) describes optical pumping of the nuclear spins. Its steady states are the eigenstates of A^z, which lie in the kernel of A^-, so-called dark states, and include the fully polarized state. Hence the setting described by Eqs. (2) and (3) can be used to polarize the nuclei [27], i.e., to prepare an initial state required for SR.

Finally, nuclear spin systems may be used to study further cooperative effects such as phase transitions. It is known [3] that in the thermodynamic limit an optically driven atomic system with collective decay—as described by Eq. (3) for homogeneous operators and $m_S = \omega_S = 0$—can undergo a second-order nonequilibrium phase transition in the steady state. In our setting an effective driving can be established by a dc magnetic field B_x perpendicular to the polarization direction. A semiclassical treatment of the equations of motion deduced from Eq. (2) predicts a similar phase transition in the combined system of electron and nuclear spins in certain regimes. Preliminary simulations confirm the validity of the semiclassical results and also indicate the appearance of related phenomena like bistability and hysteresis, which have recently been observed in polarization experiments, e.g., [28]. A detailed analysis of these topics and an analytical description of the SR dynamics presented here will be the subject of a forthcoming publication [29].

In conclusion, we have shown that the nuclear spin environment of individual QDs and NV centers shows superradiant optical emission under suitable optical pumping conditions. While in NV centers a collective intensity enhancement of up to 100% is predicted, the much larger nuclear spin ensembles in QDs could lead to relative peak heights of several orders of magnitude. This would be clear evidence of coherent HF dynamics of nuclear spin ensembles in QDs. The rich physics of SR systems, including bistability and phase transitions, could thus be studied in a long-lived mesoscopic solid-state system.

We acknowledge support by GIF, the DFG within SFB 631 and the Cluster of Excellence NIM, the NSF, DARPA, and the Packard Foundation.

[1] R. H. Dicke, Phys. Rev. **93**, 99 (1954).
[2] M. Gross and S. Haroche, Phys. Rep. **93**, 301 (1982).
[3] H. J. Carmichael, J. Phys. B **13**, 3551 (1980).
[4] S. Morrison and A. S. Parkins, Phys. Rev. A **77**, 043810 (2008).
[5] J. Schliemann *et al.*, J. Phys. Condens. Matter **15**, R1809 (2003).
[6] A. Gali *et al.*, Phys. Rev. B **77**, 155206 (2008).
[7] F. Jelezko and J. Wrachtrup, Phys. Status Solidi A **203**, 3207 (2006).
[8] M. V. G. Dutt *et al.*, Science **316**, 1312 (2007); P. Neumann *et al.*, Science **320**, 1326 (2008).
[9] A field of ~100 mT is sufficient to compensate the zero-field splitting between $|m_S = 1\rangle$ and $|m_S = 0\rangle$.
[10] P. Tamarat *et al.*, New J. Phys. **10**, 045004 (2008).
[11] C. Leonardi and A. Vaglica, Nuovo Cimento Soc. Ital. Fis. B **67**, 256 (1982).
[12] G. S. Agarwal, Phys. Rev. A **4**, 1791 (1971).
[13] Equation (2) allows for the full incorporation of anisotropies.
[14] A. T. Collins *et al.*, J. Phys. C **21**, 1363 (1988).
[15] A. Lenef *et al.*, Phys. Rev. B **53**, 13427 (1996).
[16] A. T. Collins *et al.*, J. Phys. C **16**, 2177 (1983).
[17] *Semiconductor Quantum Bits* edited by F. Henneberger and O. Benson (Pan Stanford Publishing, Singapore, 2009).
[18] A. Bracker *et al.*, Phys. Rev. Lett. **94**, 047402 (2005).
[19] G. Finkelstein *et al.*, Phys. Rev. B **58**, 12637 (1998); P. A. Dalgarno *et al.*, Appl. Phys. Lett. **89**, 043107 (2006).
[20] The HF coupling constants and typical numbers of nuclei (A/μeV, N) for important QD materials are [5,17] GaAs:(100, 10^4–10^6), CdSe:(10, 10^3), SiP:(0.1, 10^2).
[21] V. V. Temnov and U. Woggon, Phys. Rev. Lett. **95**, 243602 (2005).
[22] A. M. Rey *et al.*, Phys. Rev. A **77**, 052305 (2008).
[23] A. V. Andreev *et al.*, *Cooperative Effects in Optics* (IOP Publishing, Bristol, 1993).
[24] By applying a time dependent magnetic or spin-dependent AC Stark field such that $\omega_S(t) = g\langle A^z\rangle_t$, we ensure that the measured change in radiation intensity is due to a cooperative emission effect only.
[25] P. Maletinsky, Ph.D. thesis, ETH Zürich, 2008, http://e-collection.ethbib.ethz.ch/view/eth:30788.
[26] P. Maletinsky *et al.*, Nature Phys. **5**, 407 (2009).
[27] H. Christ *et al.*, Phys. Rev. B **75**, 155324 (2007).
[28] A. I. Tartakovskii *et al.*, Phys. Rev. Lett. **98**, 026806 (2007); P.-F. Braun *et al.*, Phys. Rev. B **74**, 245306 (2006); C. Latta *et al.*, Nature Phys. **5**, 758 (2009).
[29] E. M. Kessler *et al.* (unpublished).

PHYSICAL REVIEW B **86**, 085322 (2012)

Superradiance-like electron transport through a quantum dot

M. J. A. Schuetz,[1] E. M. Kessler,[1] J. I. Cirac,[1] and G. Giedke[1,2]
[1]*Max-Planck-Institut für Quantenoptik, Hans-Kopfermann-Strasse 1, 85748 Garching, Germany*
[2]*M5, Fakultät für Mathematik, TU München, L.-Boltzmannstrasse 1, 85748 Garching, Germany*
(Received 14 June 2012; published 27 August 2012)

We theoretically show that intriguing features of coherent many-body physics can be observed in electron transport through a quantum dot (QD). We first derive a master-equation-based framework for electron transport in the Coulomb-blockade regime which includes hyperfine (HF) interaction with the nuclear spin ensemble in the QD. This general tool is then used to study the leakage current through a single QD in a transport setting. We find that, for an initially polarized nuclear system, the proposed setup leads to a strong current peak, in close analogy with superradiant emission of photons from atomic ensembles. This effect could be observed with realistic experimental parameters and would provide clear evidence of coherent HF dynamics of nuclear spin ensembles in QDs.

DOI: 10.1103/PhysRevB.86.085322 PACS number(s): 85.35.Be, 76.70.Fz, 73.63.Kv, 42.50.Nn

I. INTRODUCTION

Quantum coherence is at the very heart of many intriguing phenomena in today's nanostructures.[1,2] For example, it is the essential ingredient to the understanding of the famous Aharonov-Bohm-like interference oscillations of the conductance of metallic rings[3] or the well-known conductance steps in quasi-one-dimensional wires.[4,5] In particular, nonequilibrium electronic transport has emerged as a versatile tool to gain deep insights into the coherent quantum properties of mesoscopic solid-state devices.[6,7] Here, with the prospect of spintronics and applications in quantum computing, a great deal of research has been directed towards the interplay and feedback mechanisms between electron and nuclear spins in gate-based semiconductor quantum dots.[8–14] Current fluctuations have been assigned to the random dynamics of the ambient nuclear spins[15] and/or hysteresis effects due to dynamic nuclear polarization.[15–18] Spin-flip-mediated transport, realized in few-electron quantum dots in the so-called spin-blockade regime,[19] has been shown to exhibit long time scale oscillations and bistability as a result of a buildup and relaxation of nuclear polarization.[15,16] The nuclear spins are known to act collectively on the electron spin via hyperfine interaction. In principle, this opens up an exciting test bed for the observation of collective effects which play a remarkable role in a wide range of many-body physics.[20–22]

In quantum optics, the concept of superradiance (SR), describing the cooperative emission of photons, is a paradigm example for a cooperative quantum effect.[1,23,24] Here, initially excited atoms emit photons collectively as a result of the buildup and reinforcement of strong interatomic correlations. Its most prominent feature is an emission intensity burst in which the system radiates much faster than an otherwise identical system of independent emitters. This phenomenon is of fundamental importance in quantum optics and has been studied extensively since its first prediction by Dicke in 1954.[23] Yet, in its original form the observation of optical SR has turned out to be difficult due to dephasing dipole-dipole van der Waals interactions, which suppress a coherence buildup in atomic ensembles.

This paper is built on analogies between mesoscopic solid-state physics and quantum optics: The nuclear spins surrounding a quantum dot (QD) are identified with an atomic ensemble, individual nuclear spins corresponding to the internal levels of a single atom and the electrons are associated with photons. Despite some fundamental differences—for example, electrons are fermions, whereas photons are bosonic particles—this analogy stimulates conjectures about the potential occurrence of related phenomena in these two fields of physics. Led by this line of thought, we address the question of whether superradiant behavior might also be observed in a solid-state environment where the role of photons is played by electrons. To this end, we analyze a gate-based semiconductor QD in the Coulomb blockade regime, obtaining two main results, of both experimental and theoretical relevance. First, in analogy to superradiant emission of photons, we show how to observe superradiant emission of electrons in a transport setting through a QD. We demonstrate that the proposed setup, when tuned into the spin-blockade regime, carries clear fingerprints of cooperative emission, with no van der Waals dephasing mechanism on relevant time scales. The spin blockade is lifted by the hyperfine (HF) coupling which becomes increasingly more efficient as correlations among the nuclear spins build up. This markedly enhances the spin-flip rate and hence the leakage current running through the QD. Second, we develop a general theoretical master-equation framework that describes the nuclear spin mediated transport through a single QD. Apart from the collective effects due to the HF interaction, the electronic tunneling current is shown to depend on the internal state of the ambient nuclear spins through the effective magnetic field (Overhauser field) produced by the hyperfine interaction.

The paper is structured as follows. In Sec. II, we highlight our key findings and provide an intuitive picture of our basic ideas, allowing the reader to grasp our main results on a qualitative level. By defining the underlying Hamiltonian, Sec. III then describes the system in a more rigorous fashion. Next, we present the first main result of this paper in Sec. IV: a general master equation for electron transport through a single QD which is coherently enhanced by the HF interaction with the ambient nuclear spins in the QD. It features both collective effects and feedback mechanisms between the electronic and the nuclear subsystem of the QD. Based on this theoretical

 ©2012 American Physical Society

framework, Sec. V puts forward the second main result, namely the observation of superradiant behavior in the leakage current through a QD. The qualitative explanations provided in Sec. II should make it possible to read this part independently of the derivation given in Sec. IV. Section VI backs up our analytical predictions with numerical simulations. When starting from an initially polarized nuclear spin ensemble, the leakage current through the QD is shown to exhibit a strong peak whose relative height scales linearly with the number of nuclear spins, which we identify as the characteristic feature of superradiant behavior. In Sec. VII we draw conclusions and give an outlook on future directions of research.

II. MAIN RESULTS

In this section we provide an intuitive exposition of our key ideas and summarize our main findings.

HF-assisted electron transport. We study a single electrically defined QD in the Coulomb-blockade regime which is attached to two leads, as schematically depicted in Fig. 1. Formally, the Hamiltonian for the total system is given by

$$H = H_Z + H_B + H_T + H_{\mathrm{HF}}. \tag{1}$$

Here, H_Z describes the electronic level structure inside the QD in the presence of an external magnetic field. Next, H_B refers to two independent reservoirs of noninteracting electrons, the left and right leads, respectively. The coupling between these and the QD is described in terms of a tunneling Hamiltonian H_T and H_{HF} models the *collective* hyperfine interaction between an electron confined inside the QD and an ensemble of N proximal nuclear spins surrounding the QD. Note that the specific form of H is given later in Sec. III.

Our analysis is built on a quantum master-equation approach, a technique originally rooted in the field of quantum optics. By tracing out the unobserved degrees of freedom of the leads we derive an effective equation of motion for the density matrix of the QD system ρ_S—describing the electron spin inside the QD as well as the nuclear spin ensemble—irreversibly coupled to source and drain electron reservoirs. In addition to the standard assumptions of a weak system-reservoir coupling (Born approximation), a flat reservoir spectral density, and a short reservoir correlation time (Markov approximation), we demand the hyperfine flip-flops to be strongly detuned with respect to the effective magnetic field seen by the electron throughout the dynamics. Under these conditions, the central master equation can be written as

$$\begin{aligned}\dot{\rho}_S(t) = &-i[H_Z + H_{\mathrm{HF}}, \rho_S(t)] \\ &+ \sum_{\sigma=\uparrow,\downarrow} \alpha_\sigma(t)\left[d_\sigma \rho_S(t) d_\sigma^\dagger - \frac{1}{2}\{d_\sigma^\dagger d_\sigma, \rho_S(t)\}\right] \\ &+ \sum_{\sigma=\uparrow,\downarrow} \beta_\sigma(t)\left[d_\sigma^\dagger \rho_S(t) d_\sigma - \frac{1}{2}\{d_\sigma d_\sigma^\dagger, \rho_S(t)\}\right],\end{aligned} \tag{2}$$

where the tunneling rates $\alpha_\sigma(t)$ and $\beta_\sigma(t)$ describe dissipative processes by which an electron of spin σ tunnels from one of the leads into or out of the QD, respectively. Here, the fermionic operator $d_\sigma^\dagger$ creates an electron of spin σ inside the QD. While a detailed derivation of Eq. (2) along with the precise form of the tunneling rates is presented in Sec. IV, here we focus on a qualitative discussion of its theoretical and experimental implications. Essentially, our central master equation exhibits two core features.

Nuclear-state-dependent electronic dissipation. First, dissipation only acts on the electronic subsystem with rates $\alpha_\sigma(t)$ and $\beta_\sigma(t)$ that depend dynamically on the state of the nuclear subsystem. This nonlinear behavior potentially results in hysteretic behavior and feedback mechanisms between the two subsystems as already suggested theoretically[11,14,20,21] and observed in experiments in the context of double QDs in the Pauli-blockade regime (see, e.g., Refs. 12, 13, and 18). On a qualitative level, this finding can be understood as follows: The nuclear spins provide an effective magnetic field for the electron spin, the Overhauser field, whose strength is proportional to the polarization of the nuclear spin ensemble. Thus, a changing nuclear polarization can either dynamically tune or detune the position of the electron levels inside the QD. This, in turn, can have a marked effect on the transport properties of the QD as they crucially depend on the position of these resonances with respect to the chemical potentials of the leads. In our model, this effect is directly captured by the tunneling rates dynamically depending on the state of the nuclei.

SR in electron transport. Second, the collective nature of the HF interaction H_{HF} allows for the observation of coherent many-body effects. To show this, we refer to the following example: Consider a setting in which the bias voltage and an external magnetic field are tuned such that only one of the two electronic spin components, say the level $|\uparrow\rangle$, lies inside the transport window. In this spin-blockade regime the electrons tunneling into the right lead are spin-polarized; that is, the QD acts as a spin filter.[25,26] If the HF coupling is sufficiently small compared to the external Zeeman splitting, the electron

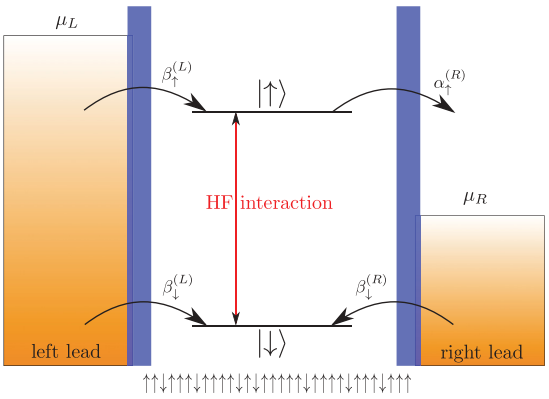

FIG. 1. (Color online) Schematic illustration of the transport system: An electrically defined QD is tunnel-coupled to two electron reservoirs, the left and right lead, respectively. A bias voltage $V = (\mu_L - \mu_R)/e$ is applied between the two leads in order to induce a current through the QD. An external magnetic field is used to tune the system into the sequential-tunneling regime and the QD effectively acts as a spin filter. The resulting spin blockade can be lifted by the HF interaction between the QD electron and the nuclear spins in the surrounding host environment.

is predominantly in its $|\downarrow\rangle$ spin state, making it possible to adiabatically eliminate the electronic QD coordinates. In this way we obtain an effective equation of motion for the nuclear density operator μ only. It reads

$$\dot{\mu} = c_r\left[A^-\mu A^+ - \frac{1}{2}\{A^+A^-,\mu\}\right] + ic_i[A^+A^-,\mu] + i\frac{g}{2}[A^z,\mu], \quad (3)$$

where $A^\mu = \sum_{i=1}^N g_i\sigma_i^\mu$ with $\mu = +,-,z$ are *collective* nuclear spin operators, composed of *all* N individual nuclear spin operators σ_i^μ, with g_i being proportional to the probability of the electron being at the location of the nucleus of site i. Again, we highlight the core implications of Eq. (3) and for a full derivation thereof, including the definition of the effective rates c_r and c_i, we refer to Sec. V. Most notably, Eq. (3) closely resembles the SR master equation which has been discussed extensively in the context of atomic physics[24] and therefore similar effects might be expected.

Superradiance is known as a macroscopic collective phenomenon which generalizes spontaneous emission from a single emitter to a many-body system of N atoms.[1] Starting from a fully polarized initial state the system evolves within a totally symmetric subspace under permutation and experiences a strong correlation buildup. As a consequence, the emission intensity is not of the usual exponentially decaying form, but conversely features a sudden peak occurring on a very rapid time scale $\sim 1/N$ with a maximum $\sim N^2$.

In this paper, we show that the same type of cooperative emission can occur from an ensemble of nuclear spins surrounding an electrically defined QD: The spin blockade can be lifted by the HF interaction as the nuclei pump excitations into the electron. Starting from a highly polarized, weakly correlated nuclear state (which could be prepared by, e.g., dynamic polarization techniques[12,13,22]), this process becomes increasingly more efficient, as correlations among the nuclei build up due to the collective nature of the HF interaction. This results in an increased leakage current. Therefore, the current is collectively enhanced by the electron's HF interaction with the ambient nuclear spin ensemble, giving rise to a superradiant-like effect in which the leakage current through the QD takes the role of the radiation field: To stress this relation, we also refer to this effect as *superradiant transport of electrons*.

Comparison to conventional SR. Compared to its conventional atomic counterpart, our system incorporates two major differences: First, our setup describes superradiant behavior from a *single* emitter, since in the strong Coulomb-blockade regime the electrons are emitted antibunched. As described above, the superradiant character is due to the nuclear spins acting collectively on the electron spin leading to an increased leakage current on time scales longer than single electron tunneling events. The second crucial difference is the *inhomogeneous* nature ($g_i \neq$ const) of the collective operators A^μ. Accordingly, the collective spin is not conserved, leading to dephasing between the nuclei which in principle could prevent the observation of superradiant behavior. However, as exemplified in Fig. 2, we show that under realistic conditions—taking into account a finite initial polarization of nuclear spins p and dephasing processes due to the inhomogeneous nature of the HF coupling—the leakage current through the QD still exhibits the characteristic peak whose relative height scales linearly with the number of nuclear spins. Even though the effect is reduced compared to the ideal case, for an experimentally realistic number of nuclei $N \approx 10^5$–10^6 a strong increase is still predicted. The experimental key signature of this effect, the relative peak height of the leakage current, can be varied by either tuning the external Zeeman splitting or the initial polarization of the nuclear spins.

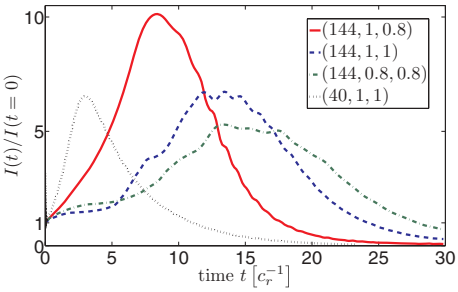

FIG. 2. (Color online) Normalized leakage current through a QD in the spin-blockade regime for N nuclear spins, initial nuclear polarization p, and external Zeeman splitting ω_0 in units of the total HF coupling constant $A_{\mathrm{HF}} \approx 100\ \mu$eV, summarized as $(N, p, \omega_0/A_{\mathrm{HF}})$. For homogeneous HF coupling the dynamics can be solved exactly (black dotted line). Compared to this idealized benchmark, the effects are reduced for realistic inhomogeneous HF coupling, but still present: The relative peak height becomes more pronounced for smaller detuning ω_0 or higher polarization p (solid red line compared to the blue dashed and green dash-dotted line, respectively). Even under realistic conditions, the relative peak height is found to scale linearly with N, corresponding to a strong enhancement for typically $N \approx 10^5$–10^6.

In the remainder of the paper, Eqs. (2) and (3) are derived from first principles; in particular, the underlying assumptions and approximations are listed. Based on this general theoretical framework, more results along with detailed discussions are presented. For both the idealized case of homogeneous HF coupling—in which an exact solution is feasible even for relatively large N—and the more realistic inhomogeneous case, further numerical simulations prove the existence of a strong superradiant peaking in the leakage current of single QD in the spin-blockade regime.

III. THE SYSTEM

This section gives an in-depth description of the Hamiltonian under study, formally introduced in Eq. (1). The system we consider consists of a single electrically defined QD in a transport setting as schematically depicted in Fig. 1. Due to strong confinement only a single orbital level is relevant. Moreover, the QD is assumed to be in the strong Coulomb-blockade regime so that at maximum one electron resides inside the QD. Therefore, the effective Hilbert space of the QD electron is span $\{|\uparrow\rangle, |\downarrow\rangle, |0\rangle\}$ where the lowest energy states for an additional electron in the QD with spin $\sigma = \uparrow, \downarrow$

are split by an external magnetic field. The Hamiltonian for the total system is given in Eq. (1).

Here, the first term,

$$H_Z = \sum_\sigma \epsilon_\sigma d_\sigma^\dagger d_\sigma, \tag{4}$$

describes the electronic levels of the QD. The Zeeman splitting between the two spin components is $\omega_0 = \epsilon_\uparrow - \epsilon_\downarrow$ (we set $\hbar = 1$) and the QD electron operators are $d_\sigma^\dagger = |\sigma\rangle\langle 0|$, describing transitions from the state $|0\rangle$ with no electron inside the QD to a state $|\sigma\rangle$ with one electron of spin σ inside the QD.

Electron transport through the QD is induced by attaching the QD to two electron leads (labeled as L and R), which are in thermal equilibrium at chemical potentials μ_L and μ_R, respectively. The leads themselves constitute reservoirs of noninteracting electrons,

$$H_B = \sum_{\alpha,k,\sigma} \epsilon_{\alpha k} c_{\alpha k\sigma}^\dagger c_{\alpha k\sigma}, \tag{5}$$

where $c_{\alpha k\sigma}^\dagger (c_{\alpha k\sigma})$ creates (annihilates) an electron in lead $\alpha = L, R$ with wave vector k and spin σ. The operators $c_{\alpha k\sigma}^\dagger (c_{\alpha k\sigma})$ fulfill the usual Fermi commutation relations: $\{c_{\alpha k\sigma}^\dagger, c_{\alpha' k'\sigma'}^\dagger\} = \{c_{\alpha k\sigma}, c_{\alpha' k'\sigma'}\} = 0$ and $\{c_{\alpha k\sigma}^\dagger, c_{\alpha' k'\sigma'}\} = \delta_{\alpha,\alpha'}\delta_{k,k'}\delta_{\sigma,\sigma'}$. The effect of the Coulomb interaction in the leads can be taken into account by renormalized effective quasiparticle masses. A positive source-drain voltage $V = (\mu_L - \mu_R)/e$ leads to a dominant tunneling of electrons from left to right. Microscopically, the coupling of the QD system to the electron reservoirs is described in terms of the tunneling Hamiltonian

$$H_T = \sum_{\alpha,k,\sigma} T_{k,\sigma}^{(\alpha)} d_\sigma^\dagger c_{\alpha k\sigma} + \text{H.c.}, \tag{6}$$

with the tunnel matrix element $T_{k,\sigma}^{(\alpha)}$ specifying the transfer coupling between the lead $\alpha = L, R$ and the system. There is no direct coupling between the leads and electron transfer is only possible by charging and discharging the QD.

The cooperative effects are based on the collective hyperfine interaction of the electronic spin of the QD with N initially polarized nuclear spins in the host environment of the QD.[27] It is dominated by the isotropic contact term[28] given by

$$H_{\text{HF}} = \frac{g}{2}(A^+ S^- + A^- S^+) + g A^z S^z. \tag{7}$$

Here S^μ and $A^\mu = \sum_{i=1}^N g_i \sigma_i^\mu$ with $\mu = +, -, z$ denote electron and collective nuclear spin operators, respectively. The coupling coefficients are normalized such that $\sum_i g_i^2 = 1$ and individual nuclear spin operators σ_i^μ are assumed to be spin-$\frac{1}{2}$ for simplicity; g is related to the total HF coupling strength A_{HF} via $g = A_{\text{HF}}/\sum_i g_i$. We neglect the typically very small nuclear Zeeman and nuclear dipole-dipole terms.[28] For simplicity, we also restrict our analysis to one nuclear species only. These simplifications are addressed in more detail in Sec. VI.

The effect of the HF interaction with the nuclear spin ensemble is twofold: The first part of the above Hamiltonian $H_{\text{ff}} = \frac{g}{2}(A^+ S^- + A^- S^+)$ is a Jaynes-Cummings-type interaction which exchanges excitations between the QD electron and the nuclei. The second term $H_{\text{OH}} = g A^z S^z$ constitutes a quantum magnetic field, the Overhauser field, for the electron spin generated by the nuclei. If the Overhauser field is not negligible compared to the external Zeeman splitting, it can have a marked effect on the current by (de)tuning the hyperfine flip-flops.

IV. GENERALIZED QUANTUM MASTER EQUATION

Electron transport through a QD can be viewed as a tool to reveal the QD's nonequilibrium properties in terms of the current-voltage I/V characteristics. From a theoretical perspective, a great variety of methods such as the scattering matrix formalism[29] and nonequilibrium Green's functions[7,30] have been used to explore the I/V characteristics of quantum systems that are attached to two metal leads. Our analysis is built upon the master equation formalism, a tool widely used in quantum optics for studying the irreversible dynamics of quantum systems coupled to a macroscopic environment.

In what follows, we employ a projection operator based technique to derive an effective master equation for the QD system—comprising the QD electron spin as well as the nuclear spins—which experiences dissipation via the electron's coupling to the leads. This dissipation is shown to dynamically depend on the state of the nuclear system potentially resulting in feedback mechanisms between the two subsystems. We derive conditions which allow for a Markovian treatment of the problem and list the assumptions our master equation based framework is based on.

A. Superoperator formalism: Nakajima-Zwanzig equation

The state of the global system that comprises the QD as well as the environment is represented by the full density matrix $\rho(t)$. However, the actual states of interest are the states of the QD which are described by the reduced density matrix $\rho_S = \text{Tr}_B[\rho]$, where $\text{Tr}_B \ldots$ averages over the unobserved degrees of freedom of the Fermi leads. We derive a master equation that governs the dynamics of the reduced density matrix ρ_S using the superoperator formalism. We start out from the von Neumann equation for the full density matrix

$$\dot\rho = -i[H(t), \rho], \tag{8}$$

where $H(t)$ can be decomposed into the following form which turns out to be convenient later on:

$$H(t) = H_0(t) + H_1(t) + H_T. \tag{9}$$

Here, $H_0(t) = H_Z + H_B + g\langle A^z\rangle_t S^z$ comprises the Zeeman splitting caused by the external magnetic field via H_Z and the Hamiltonian of the noninteracting electrons in the leads H_B; moreover, the time-dependent expectation value of the Overhauser field has been absorbed into the definition of $H_0(t)$. The HF interaction between the QD electron and the ensemble of nuclear spins has been split up into the flip-flop term H_{ff} and the Overhauser field H_{OH}, that is $H_{\text{HF}} = H_{\text{OH}} + H_{\text{ff}}$. The term $H_1(t) = H_{\Delta\text{OH}}(t) + H_{\text{ff}}$ comprises the Jaynes-Cummings-type dynamics H_{ff} and fluctuations due to deviations of the Overhauser field from its expectation value, that is, $H_{\Delta\text{OH}}(t) = g\delta A^z S^z$, where $\delta A^z = A^z - \langle A^z\rangle_t$.

The introduction of superoperators—operators acting on the space of linear operators on the Hilbert space—allows for a compact notation. The von Neumann equation is written

as $\dot{\rho} = -i\mathcal{L}(t)\rho$, where $\mathcal{L}(t) = \mathcal{L}_0(t) + \mathcal{L}_1(t) + \mathcal{L}_T$ is the Liouville superoperator defined via $\mathcal{L}_\alpha \cdot = [H_\alpha, \cdot]$. Next, we define the superoperator $\mathcal{P}$ as a projector onto the relevant subspace

$$\mathcal{P}\rho(t) = \mathsf{Tr}_B[\rho(t)] \otimes \rho_B^0 = \rho_S(t) \otimes \rho_B^0, \tag{10}$$

where ρ_B^0 describes separate thermal equilibria of the two leads whose chemical potentials are different due to the bias voltage $V = (\mu_L - \mu_R)/e$. Essentially, $\mathcal{P}$ maps a density operator onto one of product form with the environment in equilibrium but still retains the relevant information on the system state. The complement of $\mathcal{P}$ is $\mathcal{Q} = 1 - \mathcal{P}$.

By inserting $\mathcal{P}$ and $\mathcal{Q}$ in front of both sides of the von Neumann equation one can derive a closed equation for the projection $\mathcal{P}\rho(t)$, which for factorized initial condition, where $\mathcal{Q}\rho(0) = 0$, can be rewritten in the form of the generalized Nakajima-Zwanzig master equation,

$$\frac{d}{dt}\mathcal{P}\rho = -i\mathcal{P}\mathcal{L}\mathcal{P}\rho - \int_0^t dt'\, \mathcal{P}\mathcal{L}\mathcal{Q}\,\hat{T} e^{-i\int_{t'}^t d\tau \mathcal{Q}\mathcal{L}(\tau)} \mathcal{Q}\mathcal{L}\mathcal{P}\rho(t'), \tag{11}$$

which is nonlocal in time and contains all orders of the system-leads coupling.[31] Here, $\hat{T}$ denotes the chronological time-ordering operator. Since $\mathcal{P}$ and $\mathcal{Q}$ are projectors onto orthogonal subspaces that are only connected by $\mathcal{L}_T$, this simplifies to

$$\frac{d}{dt}\mathcal{P}\rho = -i\mathcal{P}\mathcal{L}\mathcal{P}\rho - \int_0^t dt' \mathcal{P}\mathcal{L}_T \hat{T} e^{-i\int_{t'}^t d\tau \mathcal{Q}\mathcal{L}(\tau)} \mathcal{L}_T \mathcal{P}\rho(t'). \tag{12}$$

Starting out from this exact integro-differential equation, we introduce some approximations: In the weak coupling limit we neglect all powers of $\mathcal{L}_T$ higher than two (Born approximation). Consequently, we replace $\mathcal{L}(\tau)$ with $\mathcal{L}(\tau) - \mathcal{L}_T$ in the exponential of Eq. (12). Moreover, we make use of the fact that the nuclear spins evolve on a time scale that is very slow compared to all electronic processes: In other words, the Overhauser field is quasistatic on the time scale of single electronic tunneling events.[22,32] That is, we replace $\langle A^z\rangle_\tau$ with $\langle A^z\rangle_t$ in the exponential of Eq. (12), which removes the explicit time dependence in the kernel. By taking the trace over the reservoir and using $\mathsf{Tr}_B[\mathcal{P}\dot{\rho}(t)] = \dot{\rho}_S(t)$, we get

$$\dot{\rho}_S(t) = -i(\mathcal{L}_Z + \mathcal{L}_{\mathrm{HF}})\rho_S(t) - \int_0^t d\tau\, \mathsf{Tr}_B(\mathcal{L}_T e^{-i[\mathcal{L}_0(t)+\mathcal{L}_1(t)]\tau} \times \mathcal{L}_T \mathcal{P}\rho(t-\tau)). \tag{13}$$

Here, we also used the relations $\mathcal{P}\mathcal{L}_T\mathcal{P} = 0$ and $\mathcal{L}_B\mathcal{P} = 0$ and switched the integration variable to $\tau = t - t'$. Note that, for notational convenience, we suppress the explicit time dependence of $\mathcal{L}_{0(1)}(t)$ in the following. In the next step, we iterate the Schwinger-Dyson identity:

$$e^{-i(\mathcal{L}_0+\mathcal{L}_1)\tau} = e^{-i\mathcal{L}_0\tau} - i\int_0^\tau d\tau'\, e^{-i\mathcal{L}_0(\tau-\tau')}\mathcal{L}_1 e^{-i(\mathcal{L}_0+\mathcal{L}_1)\tau'}. \tag{14}$$

In what follows, we keep only the first term of this infinite series (note that the next two leading terms are explicitly calculated in Appendix A). In quantum optics, this simplification is well known as an approximation of independent rates of variation.[33] In our setting it is valid, if $\mathcal{L}_1(t)$ is small compared to $\mathcal{L}_0(t)$ and if the bath correlation time τ_c is short compared to the HF dynamics, $A_{\mathrm{HF}} \ll 1/\tau_c$. Pictorially, this means that during the correlation time τ_c of a tunneling event, there is not sufficient time for the Rabi oscillation with frequency $g \lesssim A_{\mathrm{HF}}$ to occur. For typical materials,[34] the relaxation time τ_c is in the range of $\sim 10^{-15}$ s corresponding to a relaxation rate $\Gamma_c = \tau_c^{-1} \approx 10^5\,\mu$eV. Indeed, this is much faster than all other relevant processes. In this limit, the equation of motion for the reduced density matrix of the system simplifies to

$$\dot{\rho}_S(t) = -i(\mathcal{L}_Z + \mathcal{L}_{\mathrm{HF}})\rho_S(t) - \int_0^t d\tau\, \mathsf{Tr}_B\big(\mathcal{L}_T e^{-i\mathcal{L}_0(t)\tau}\mathcal{L}_T \rho_S(t-\tau)\otimes\rho_B^0\big). \tag{15}$$

Note, however, that this master equation is not Markovian as the rate of change of $\rho_S(t)$ still depends on its past. Conditions which allow for a Markovian treatment of the problem are addressed in the following.

B. Markov approximation

Using the general relation $e^{-i\mathcal{L}_0\tau}\mathcal{O} = e^{-iH_0\tau}\mathcal{O}e^{iH_0\tau}$ for any operator $\mathcal{O}$, we rewrite Eq. (15) as

$$\dot{\rho}_S(t) = -i[H_Z + H_{\mathrm{HF}}, \rho_S(t)] - \int_0^t d\tau\, \mathsf{Tr}_B\big([H_T, [\tilde{H}_T(\tau), e^{-iH_0\tau}\rho_S(t-\tau)e^{iH_0\tau}\otimes\rho_B^0]]\big). \tag{16}$$

In accordance with the previous approximations, we replace $e^{-iH_0\tau}\rho_S(t-\tau)e^{iH_0\tau}$ by $\rho_S(t)$ which is approximately the same since any correction to H_0 would be of higher order in perturbation theory.[35,36] In other words, the evolution of $\rho_S(t-\tau)$ is approximated by its unperturbed evolution, which is legitimate provided that the relevant time scale for this evolution τ_c is very short (Markov approximation). This step is motivated by the typically rapid decay of the lead correlations functions;[35] the precise validity of this approximation is elaborated below. In particular, this simplification disregards dissipative effects induced by H_T, which is valid self-consistently provided that the tunneling rates are small compared to the dynamics generated by H_0.

Moreover, in Eq. (16) we introduced the tunneling Hamiltonian in the interaction picture as $\tilde{H}_T(\tau) = e^{-iH_0\tau}H_T e^{iH_0\tau}$. For simplicity, we only consider one lead for now and add the terms referring to the second lead later on. Therefore, we can disregard an additional index specifying the left or right reservoir and write explicitly

$$\tilde{H}_T(\tau) = \sum_{k,\sigma} T_{k,\sigma} e^{-i[\epsilon_\sigma(t)-\epsilon_k]\tau} d_\sigma^\dagger c_{k\sigma} + \mathrm{H.c.} \tag{17}$$

Here, the resonances $\epsilon_\sigma(t)$ are explicitly time dependent as they dynamically depend on the polarization of the nuclear spins

$$\epsilon_{\uparrow(\downarrow)}(t) = \epsilon_{\uparrow(\downarrow)} \pm \frac{g}{2}\langle A^z\rangle_t. \tag{18}$$

The quantity

$$\omega = \epsilon_\uparrow(t) - \epsilon_\downarrow(t) = \omega_0 + g\langle A^z\rangle_t \tag{19}$$

can be interpreted as an effective Zeeman splitting which incorporates the external magnetic field as well as the mean magnetic field generated by the nuclei.

Since the leads are assumed to be at equilibrium, their correlation functions are given by

$$\mathrm{Tr}_B\left[c^\dagger_{k\sigma}(\tau)c_{k'\sigma'}\rho_B^0\right] = \delta_{\sigma,\sigma'}\delta_{k,k'}e^{-i\epsilon_k\tau}f_k, \tag{20}$$

$$\mathrm{Tr}_B\left[c_{k\sigma}(\tau)c^\dagger_{k'\sigma'}\rho_B^0\right] = \delta_{\sigma,\sigma'}\delta_{k,k'}e^{i\epsilon_k\tau}(1-f_k), \tag{21}$$

where the Fermi function $f_k = (1+\exp[\beta(\epsilon_k-\mu)])^{-1}$ with inverse temperature $\beta = 1/(k_BT)$ gives the thermal occupation number of the respective lead in equilibrium. Note that all terms comprising two lead creation $c^\dagger_{k\sigma}$ or annihilation operators $c_{k\sigma}$ vanish since ρ_B^0 contains states with definite electron number only.[35] The correlation functions are diagonal in spin space and the tunneling Hamiltonian preserves the spin projection; therefore, only corotating terms prevail. If we evaluate all dissipative terms appearing in Eq. (16), due to the conservation of momentum and spin in Eqs. (20) and (21), only a single sum over k,σ survives. Here, we single out one term explicitly, but all other terms follow analogously. We obtain

$$\dot\rho_S(t) = \cdots + \sum_\sigma \int_0^t d\tau\, \mathcal{C}_\sigma(\tau) d^\dagger_\sigma e^{-iH_0\tau}\rho_S(t-\tau)e^{iH_0\tau}d_\sigma, \tag{22}$$

where the correlation time of the bath τ_c is determined by the decay of the noise correlations,

$$\mathcal{C}_\sigma(\tau) = \sum_k |T_{k,\sigma}|^2 f_k e^{i[\epsilon_\sigma(t)-\epsilon_k]\tau} = \int_0^\infty d\epsilon\, J_\sigma(\epsilon)e^{i[\epsilon_\sigma(t)-\epsilon]\tau}. \tag{23}$$

Here, we made use of the fact that the leads are macroscopic and therefore exhibit a continuous density of states per spin $n(\epsilon)$. On top of that, we have introduced the spectral density of the bath as

$$J_\sigma(\epsilon) = D_\sigma(\epsilon)f(\epsilon), \tag{24}$$

where $D_\sigma(\epsilon) = n(\epsilon)|T_\sigma(\epsilon)|^2$ is the effective density of states. The Markovian treatment manifests itself in a self-consistency argument: We assume that the spectral density of the bath $J_\sigma(\epsilon)$ is flat around the (time-dependent) resonance $\epsilon_\sigma(t)$ over a range set by the characteristic width Γ_d. Typically, both the tunneling matrix elements $T_\sigma(\epsilon)$ as well as the density of states $n(\epsilon)$ are slowly varying functions of energy. In the so-called wide-band limit the effective density of states $D_\sigma(\epsilon)$ is assumed to be constant so that the self-consistency argument will exclusively concern the behavior of the Fermi function $f(\epsilon)$, which is intimately related to the temperature of the bath T. Under the condition, that $J_\sigma(\epsilon)$ behaves flat on the scale Γ_d, it can be replaced with its value at $\epsilon_\sigma(t)$, and the noise correlation simplifies to

$$\mathcal{C}_\sigma(\tau) = J_\sigma(\epsilon_\sigma(t))e^{i\epsilon_\sigma(t)\tau}\int_0^\infty d\epsilon\, e^{-i\epsilon\tau}. \tag{25}$$

Using the relation

$$\int_0^\infty d\epsilon\, e^{-i\epsilon\tau} = \pi\delta(\tau) - i\mathbb{P}\frac{1}{\tau}, \tag{26}$$

with $\mathbb{P}$ denoting Cauchy's principal value, we find that the Markov approximation $\mathrm{Re}[\mathcal{C}_\sigma(\tau)] \propto \delta(\tau)$ is fulfilled provided that the self-consistency argument holds. This corresponds to the white-noise limit where the correlation-time of the bath is $\tau_c = 0$. Pictorially, the reservoir has no memory and instantaneously relaxes to equilibrium. We can then indeed replace $e^{-iH_0\tau}\rho_S(t-\tau)e^{iH_0\tau}$ with $\rho_S(t)$ and extend the integration in Eq. (16) to infinity, with negligible contributions due to the rapid decay of the memory kernel. In the following, we derive an explicit condition for the self-consistency argument to be satisfied.

Let us first consider the limit $T = 0$: As schematically depicted in Fig. 3, in this case $f(\epsilon)$ behaves perfectly flat except for $\epsilon = \mu$, where the self-consistency argument is violated. Therefore, the Markovian approximation is valid at $T = 0$ given that the condition $|\epsilon_\sigma(t) - \mu| \gg \Gamma_\mathrm{d}$ is fulfilled. In this limit, all tunneling rates are constant over time and effectively decoupled from the nuclear dynamics. Note that for the observation of superradiant transport it is sufficient to restrict oneself to this case.

For a more general analysis, we now turn to the case of finite temperature $T > 0$. We require the absolute value of the relative change of the Fermi function around the resonance $\epsilon_\sigma(t)$ over a range of the characteristic width Γ_d to be much less than unity, that is,

$$\left|\frac{\partial f(\epsilon)}{\partial\epsilon}\Big|_{\epsilon_\sigma(t)}\right|\Gamma_\mathrm{d} \ll 1. \tag{27}$$

An upper bound for the first factor can easily be obtained as this quantity is maximized at the chemical potential μ, for all temperatures. Evaluating the derivative at $\epsilon_\sigma(t) = \mu$ results in the compact condition,

$$\Gamma_\mathrm{d} \ll 4k_BT. \tag{28}$$

Thus, finite temperature $T > 0$ washes out the rapid character of $f(\epsilon)$ at the chemical potential μ and, provided that Eq. (28) is fulfilled, allows for a Markovian treatment.

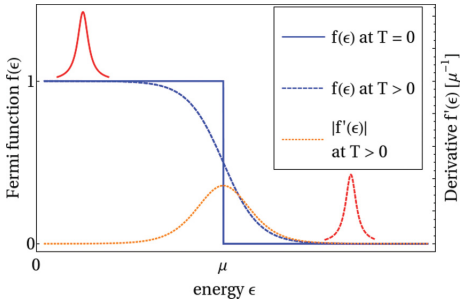

FIG. 3. (Color online) Fermi function for finite temperature (dashed blue line) and in the limit $T = 0$ (solid blue line). The absolute value of the derivative of the Fermi function $f'(\epsilon)$ (dotted orange line for finite temperature) is maximized at the chemical potential μ and tends to a δ function in the limit $T \to 0$. The Markovian description is valid provided that the Fermi function is approximately constant around the resonances $\epsilon_\sigma(t)$ on a scale of the width of these resonances, schematically shown in red [solid line for $\epsilon_\sigma(t) < \mu$ and dashed line for $\epsilon_\sigma(t) > \mu$].

Two distinct mechanisms contribute to the width Γ_d: dissipation due to coupling to the leads and the effect of $H_1(t)$. Both of them have been neglected self-consistently in the memory kernel when going from Eq. (12) to Eq. (15). Typically, the tunneling rates are of the order of ∼5–20 μeV, depending on the transparency of the tunnel barrier. Regarding the contribution due to $H_1(t)$, we first consider two limits of particular importance: For a completely mixed state the fluctuation of the nuclear field around its zero expectation value is of the order of $\sim A_{\rm HF}/\sqrt{N} \approx 0.1\,\mu$eV. In contrast, for a fully polarized state these fluctuations can be neglected, whereas the effective strength of the flip-flop dynamics is $\sim A_{\rm HF}/\sqrt{N}$ as well. Therefore, in both limits considered here, the dominant contribution to Γ_d is due to the coupling to the leads and the self-consistency condition could still be met with cryostatic temperatures $k_B T \gtrsim 10\,\mu$eV, well below the orbital level spacing. However, we note that in the course of a superradiant evolution, where strong correlations among the nuclei build up, the dominant contribution to Γ_d may come from the flip-flop dynamics, which are $A_{\rm HF}/4 \approx 25\,\mu$eV at maximum for homogeneous coupling. For realistic conditions, though, this effect is significantly reduced, as demonstrated in our simulations in Sec. VI.

C. General master equation for nuclear spin-assisted transport

Assuming that the self-consistency argument for a Markovian treatment is satisfied, we now apply the following modifications to Eq. (16): First, we neglect level shifts due to the coupling to the continuum states which can be incorporated by replacing the bare frequencies $\epsilon_\sigma(t)$ with renormalized frequencies. Second, one adds the second electron reservoir that has been omitted in the derivation above. Last, one performs a suitable transformation into a frame rotating at the frequency $\bar{\epsilon} = (\epsilon_\uparrow + \epsilon_\downarrow)/2$ leaving all terms invariant but changing H_Z from $H_Z = \epsilon_\uparrow d_\uparrow^\dagger d_\uparrow + \epsilon_\downarrow d_\downarrow^\dagger d_\downarrow$ to $H_Z = \omega_0 S^z$. After these manipulations one arrives at the central master equation as stated in Eq. (2) where the tunneling rates with $\alpha_\sigma(t) = \sum_{x=L,R} \alpha_\sigma^{(x)}(t)$, $\beta_\sigma(t) = \sum_{x=L,R} \beta_\sigma^{(x)}(t)$, and

$$\begin{aligned} \frac{\alpha_\sigma^{(x)}(t)}{2\pi} &= n_x(\epsilon_\sigma(t))\left|T_\sigma^{(x)}(\epsilon_\sigma(t))\right|^2[1 - f_x(\epsilon_\sigma(t))], \\ \frac{\beta_\sigma^{(x)}(t)}{2\pi} &= n_x(\epsilon_\sigma(t))\left|T_\sigma^{(x)}(\epsilon_\sigma(t))\right|^2 f_x(\epsilon_\sigma(t)) \end{aligned} \tag{29}$$

govern the dissipative processes in which the QD system exchanges single electrons with the leads. The tunneling rates, as presented here, are widely used in nanostructure quantum transport problems.[35,37,38] However, in our setting they are evaluated at the resonances $\epsilon_\sigma(t)$ which dynamically depend on the polarization of the nuclear spins [see Eq. (18)]. Note that Eq. (2) incorporates finite temperature effects via the Fermi functions of the leads. This potentially gives rise to feedback mechanisms between the electronic and the nuclear dynamics, since the purely electronic diffusion markedly depends on the nuclear dynamics.

Since Eq. (2) marks our first main result, at this point we quickly reiterate the assumptions our master equation treatment is based on.

(i) The system-lead coupling is assumed to be weak and therefore treated perturbatively up to second order (Born approximation).

(ii) In particular, the tunneling rates are small compared to the effective Zeeman splitting ω.

(iii) Level shifts arising from the coupling to the continuum states in the leads are merely incorporated into a redefinition of the QD energy levels $\epsilon_\sigma(t)$.

(iv) There is a separation of time scales between electron-spin dynamics and nuclear-spin dynamics. In particular, the Overhauser field $g\langle A^z\rangle_t$ evolves on a time scale that is slow compared to single electron tunneling events.

(v) The HF dynamics generated by $H_1(t) = H_{\rm ff} + H_{\Delta\rm OH}(t)$ is (i) sufficiently weak compared to H_0 and (ii) slow compared to the correlation time of the bath τ_c, which is $A_{\rm HF}\tau_c \ll 1$ (approximation of independent rates of variation). Note that the flip-flop dynamics can become very fast as correlations among the nuclei build up culminating in a maximum coupling strength of $A_{\rm HF}/4$ for homogeneous coupling. This potentially drives the system into the strong coupling regime where condition (i), that is $\omega \gg ||H_1(t)||$, might be violated. However, under realistic conditions of inhomogeneous coupling this effect is significantly reduced.

(vi) The effective density of states $D_\sigma(\epsilon) = n(\epsilon)|T_\sigma(\epsilon)|^2$ is weakly energy dependent (wide-band limit). In particular, it is flat on a scale of the characteristic widths of the resonances.

(vii) The Markovian description is valid provided that either the resonances are far away from the chemical potentials of the leads on a scale set by the characteristic widths of the resonances or the temperature is sufficiently high to smooth out the rapid character of the Fermi functions of the leads. This condition is quantified in Eq. (28).

In summary, we have derived a quantum master equation describing electronic transport through a single QD which is collectively enhanced due to the interaction with a large ancilla system, namely the nuclear spin ensemble in the host environment. Equation (2) incorporates two major intriguing features both of theoretical and experimental relevance: Due to a separation of time scales, only the electronic subsystem experiences dissipation with rates that depend dynamically on the state of the ancilla system. This nonlinearity gives rise to feedback mechanisms between the two subsystems as well as hysteretic behavior. Moreover, the collective nature of the HF interaction offers the possibility to observe intriguing coherent many-body effects. Here, one particular outcome is the occurrence of superradiant electron transport, as shown in the remainder of this paper.

Note that in the absence of HF interaction between the QD electron and the proximal nuclear spins, that is, in the limit $g \to 0$, our results agree with previous theoretical studies.[36]

V. SUPERRADIANCE-LIKE ELECTRON TRANSPORT

Proceeding from our general theory derived above, this section is devoted to the prediction and analysis of superradiant behavior of nuclear spins, evidenced by the strongly enhanced leakage current through a single QD in the Coulomb-blockade regime; see Fig. 1 for the scheme of the setup. A pronounced peak in the leakage current will serve as the main evidence for SR behavior in this setting.

We note that, in principle, an enhancement seen in the leakage current could also simply arise from the Overhauser field dynamically tuning the hyperfine flip-flops. However, we can still ensure that the measured change in the leakage current through the QD is due to cooperative emission only by dynamically compensating the Overhauser field. This can be achieved by applying a time-dependent magnetic or spin-dependent ac Stark field such that $H_{\rm comp}(t) = -g\langle A^z\rangle_t S^z$, which is done in most of our simulations below to clearly prove the existence of superradiant behavior in this setting. Consequently, in our previous analysis $H_0(t)$ is replaced with $H_0 = H_0(t) - g\langle A^z\rangle_t S^z = H_Z + H_B$ so that the polarization dependence of the tunneling rates is removed and we can drop the explicit time dependence of the resonances $\epsilon_\sigma(t) \to \epsilon_\sigma$. Under this condition, the master equation for the reduced system density operator can be written as

$$\begin{aligned}\dot\rho_S(t) = &-i[\omega_0 S^z + H_{\rm HF} + H_{\rm comp}(t), \rho_S(t)] \\ &+ \sum_{\sigma=\uparrow,\downarrow} \alpha_\sigma \left[d_\sigma \rho_S(t) d_\sigma^\dagger - \frac{1}{2}\{d_\sigma^\dagger d_\sigma, \rho_S(t)\}\right] \\ &+ \sum_{\sigma=\uparrow,\downarrow} \beta_\sigma \left[d_\sigma^\dagger \rho_S(t) d_\sigma - \frac{1}{2}\{d_\sigma d_\sigma^\dagger, \rho_S(t)\}\right]. \end{aligned} \tag{30}$$

In accordance with our previous considerations, in this specific setting the Markovian treatment is valid provided that the spectral density of the reservoirs varies smoothly around the (time-independent) resonances ϵ_σ on a scale set by the natural widths of the level and the fluctuations of the dynamically compensated Overhauser field. More specifically, throughout the whole evolution the levels are assumed to be far away from the chemical potentials of the reservoirs;[39,40] for an illustration see Fig. 3. In this wide-band limit, the tunneling rates $\alpha_\sigma, \beta_\sigma$ are independent of the state of the nuclear spins. The master equation is of Lindblad form which guarantees the complete positivity of the generated dynamics. Equation (30) agrees with previous theoretical results,[36] except for the appearance of the collective HF interaction between the QD electron and the ancilla system in the Hamiltonian dynamics of Eq. (30).

To some extent, Eq. (30) bears some similarity with the quantum theory of the laser. While in the latter the atoms interact with bosonic reservoirs, in our transport setting the QD is pumped by the nuclear spin ensemble and emits fermionic particles.[30,38]

If the HF dynamics is the slowest time scale in the problem, Eq. (30) can be recast into a form which makes its superradiant character more apparent. In this case, the system is subject to the slaving principle:[30] The dynamics of the whole system follow that of the subsystem with the slowest time constant, making it possible to adiabatically eliminate the electronic QD coordinates and to obtain an effective equation of motion for the nuclear spins. In this limit, the Overhauser field is much smaller than the Zeeman splitting so that a dynamic compensation of the OH can be disregarded for the moment. For simplicity, we consider a transport setting in which only four tunneling rates are different from zero (see Fig. 1). The QD can be recharged from the left and the right lead, but only electrons with spin projection $\sigma = \uparrow$ can tunnel out of the QD into the right lead. We define the total recharging rate $\beta = \beta_\downarrow + \beta_\uparrow = \beta_\downarrow^{(L)} + \beta_\downarrow^{(R)} + \beta_\uparrow^{(L)}$ and for notational convenience unambiguously set $\alpha = \alpha_\uparrow^{(R)}$. First, we project Eq. (30) onto the populations of the electronic levels and the coherences in spin space according to $\rho_{mn} = \langle m|\rho_S|n\rangle$, where $m,n = 0, \uparrow, \downarrow$. This yields

$$\dot\rho_{00} = \alpha\rho_{\uparrow\uparrow} - \beta\rho_{00}, \tag{31}$$

$$\begin{aligned}\dot\rho_{\uparrow\uparrow} = &-i\frac{g}{2}[A^z, \rho_{\uparrow\uparrow}] - i\frac{g}{2}(A^-\rho_{\downarrow\uparrow} - \rho_{\uparrow\downarrow}A^+) \\ &- \alpha\rho_{\uparrow\uparrow} + \beta_\uparrow\rho_{00}, \end{aligned} \tag{32}$$

$$\dot\rho_{\downarrow\downarrow} = +i\frac{g}{2}[A^z, \rho_{\downarrow\downarrow}] - i\frac{g}{2}(A^+\rho_{\uparrow\downarrow} - \rho_{\downarrow\uparrow}A^-) + \beta_\downarrow\rho_{00}, \tag{33}$$

$$\begin{aligned}\dot\rho_{\uparrow\downarrow} = &-i\omega_0\rho_{\uparrow\downarrow} - i\frac{g}{2}(A^z\rho_{\uparrow\downarrow} + \rho_{\uparrow\downarrow}A^z) \\ &- i\frac{g}{2}(A^-\rho_{\downarrow\downarrow} - \rho_{\uparrow\uparrow}A^-) - \frac{\alpha}{2}\rho_{\uparrow\downarrow}. \end{aligned} \tag{34}$$

We can retrieve an effective master equation for the regime in which on relevant time scales the QD is always populated by an electron. This holds for a sufficiently strong recharging rate, that is in the limit $\beta \gg \alpha$, which can be implemented experimentally by making the left tunnel barrier more transparent than the right one. Then, the state $|0\rangle$ is populated negligibly throughout the dynamics and can be eliminated adiabatically according to $\rho_{00} \approx \frac{\alpha}{\beta}\rho_{\uparrow\uparrow}$. In analogy to the Anderson impurity model, in the following this limit is referred to as *local moment regime*. The resulting effective master equation reads

$$\begin{aligned}\dot\rho_S = &-i[\omega_0 S^z + H_{\rm HF}, \rho_S] + \gamma\left[S^-\rho_S S^+ - \frac{1}{2}\{S^+S^-, \rho_S\}\right] \\ &+ \Gamma\left[S^z\rho_S S^z - \frac{1}{4}\rho_S\right], \end{aligned} \tag{35}$$

where

$$\gamma = \frac{\beta_\downarrow}{\beta}\alpha \tag{36}$$

is an effective decay rate and

$$\Gamma = \frac{\beta_\uparrow}{\beta}\alpha \tag{37}$$

represents an effective electronic dephasing rate. This situation is schematized in Fig. 4. The effective decay (dephasing) describes processes in which the QD is recharged with a spin down (up) electron after a spin up electron has tunneled out of the QD. As demonstrated in Ref. 41, additional electronic dephasing mechanisms only lead to small corrections to the dephasing rate Γ and are therefore neglected in Eq. (35).

In the next step we aim for an effective description that contains only the nuclear spins: Starting from a fully polarized state, SR is due to the increase in the operative HF matrix element $\langle A^+A^-\rangle$. The scale of the coupling is set by the total HF coupling constant $A_{\rm HF} = g\sum_i g_i$. For a sufficiently small *relative coupling strength*[27]

$$\epsilon = A_{\rm HF}/(2\Delta), \tag{38}$$

where

$$\Delta = |\alpha/2 + i\omega_0|, \tag{39}$$

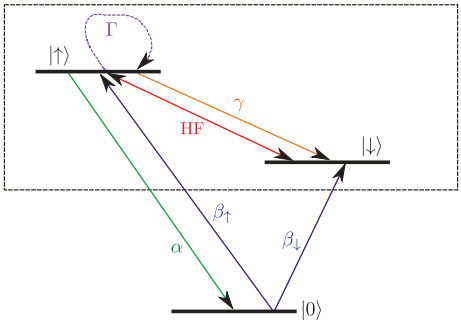

FIG. 4. (Color online) The electronic QD system in the local moment regime after the adiabatic elimination of the $|0\rangle$ level including the relevant dissipative processes. Within the effective system (box) we encounter an effective decay term and an effective pure dephasing term, with the rates γ and Γ, respectively. This simplification is possible for fast recharging of the QD, that is, $\beta \gg \alpha$.

the electron is predominantly in its $|\downarrow\rangle$ spin state and we can project Eq. (35) to the respective subspace. As shown in detail in Appendix B, in this limit the master equation for the reduced nuclear density operator $\mu = \mathrm{Tr}_{\mathrm{el}}[\rho_S]$ is given by Eq. (3), where the effective coefficients read

$$c_r = \frac{g^2\alpha}{4\Delta^2}, \tag{40}$$

$$c_i = \frac{g^2\omega_0}{4\Delta^2}. \tag{41}$$

This master equation is our second main result. In an optical setting, it has previously been predicted theoretically to exhibit strong SR signatures.[27] Conceptually, its superradiant character can be understood immediately in the ideal case of homogeneous coupling in which the collective state of all nuclear spins can be described in terms of Dicke states $|J,m\rangle$: The enhancement of the HF interaction is directly associated with the transition through nuclear Dicke states $|J,m\rangle, m \ll J$. In this idealized setting, the angular momentum operator $\mathbf{I} = \sqrt{N}\mathbf{A}$ of the nuclear spin ensemble obeys the SU(2) Lie algebra, from which one can deduce the ladder operator relation $I^-|J,m\rangle = \sqrt{J(J+1) - m(m-1)}|J,m-1\rangle$. This means that, starting from an initially fully polarized state $|J = N/2, m = N/2\rangle$, the nuclear system cascades down the Dicke ladder with an effective rate

$$\tilde{\Gamma}_{m\to m-1} = \frac{c_r}{N}(N/2+m)(N/2-m+1), \tag{42}$$

since, according to the first term in Eq. (3), the populations of the Dicke states evolve as

$$\dot{\mu}_{m,m} = -\frac{c_r}{N}(N/2+m)(N/2-m+1)\mu_{m,m} + \frac{c_r}{N}(N/2+m+1)(N/2-m)\mu_{m+1,m+1}. \tag{43}$$

While the effective rate is $\tilde{\Gamma}_{N/2\to N/2-1} = c_r$ at the very top of the the ladder it increases up to $\tilde{\Gamma}_{|m|\ll N/2} \approx \frac{c_r}{4}N$ at the center of the Dicke ladder. This implies the characteristic intensity peaking as compared to the limit of independent classical emitters the emission rate of which would be $\tilde{\Gamma}_{\mathrm{cl}} = \frac{c_r}{N}N_\uparrow = \frac{c_r}{N}(N/2+m)$.

However, there is also a major difference compared to the superradiant emission of photons from atomic ensembles: In contrast to its atomic cousin, the prefactor $c_r/N \propto 1/N^2$ is N-dependent, resulting in an overall time of the SR evolution $\langle t_D\rangle$ which increases with N. By linearizing Eq. (42) for the beginning of the superradiant evolution[24] as $\tilde{\Gamma}_{m\to m-1} \approx c_r(s+1)$, where $s = N/2 - m$ gives the number of nuclear flips, one finds that the first flip takes place in an average time c_r^{-1}, the second one in a time $(2c_r)^{-1}$, and so on. The summation of all these elementary time intervals gives an upper bound estimate for the process duration until the SR peaking as

$$\langle t_D\rangle \lesssim \frac{2}{c_r}\left[1 + \frac{1}{2} + \cdots + \frac{1}{N/2}\right] \approx \frac{2\ln(N/2)}{c_r}, \tag{44}$$

which, indeed, increases with the number of emitters as $\sim N\ln(N)$, whereas one obtains $\langle t_D\rangle \sim \ln(N)/N$ for ordinary SR.[24] Accordingly, in our solid-state system the characteristic SR peak appears at later times for higher N. The underlying reason for this difference is that in the atomic setting each new emitter adds to the overall coupling strength, whereas in the central spin setting a fixed overall coupling strength A_{HF} is distributed over an increasing number of particles. Note that in an actual experimental setting N is not a tunable parameter, of course. For our theoretical discussion, though, it is convenient to fix the total HF coupling strength A_{HF} and to extrapolate from our findings to an experimentally relevant number of nuclear spins N.

For large relative coupling strength $\epsilon \gg 1$ the QD electron saturates and superradiant emission is capped by the decay rate $\alpha/2$, prohibiting the observation of a strong intensity peak. In order to circumvent this bottleneck regime, one has to choose a detuning ω_0 such that $0 < \epsilon \leqslant 1$. However, to realize the spin-blockade regime, where the upper spin manifold is energetically well separated from the lower spin manifold, the Zeeman splitting has to be of the order of $\omega_0 \sim A_{\mathrm{HF}}$, which guarantees $\epsilon < 1$. In this parameter range, the early stage of the evolution—in which the correlation buildup necessary for SR takes place[24]—is well described by Eq. (3).

The inhomogeneous nature ($g_i \neq$ const) of the collective operators A^μ leads to dephasing between the nuclei, possibly preventing the phased emission necessary for the observation of SR.[24,27,42,43] The inhomogeneous part of the last term in Eq. (3)—the electron's Knight field—causes dephasing[44] $\propto g\sqrt{\mathrm{Var}(g_i)}/2$, possibly leading to symmetry reducing transitions $J \to J-1$. Still, it has been shown that SR is also present in realistic inhomogeneous systems,[27] since the system evolves in a many-body protected manifold (MPM): The second term in Eq. (3) energetically separates different total nuclear spin-J manifolds, protecting the correlation buildup for large enough ϵ.

The superradiant character of Eq. (3) suggests the observation of its prominent intensity peak in the leakage current through the QD in the spin-blockade regime. We have employed the method of full-counting-statistics (FCS)[45,46] in order to obtain an expression for the current and find (setting the electron's charge $e = 1$)

$$I(t) = \alpha\rho_{\uparrow\uparrow} - \beta_\downarrow^{(R)}\rho_{00}. \tag{45}$$

This result is in agreement with previous theoretical findings: The current through the device is completely determined by

the occupation of the levels adjacent to one of the leads.[29,37,39] The first term describes the accumulation of electrons with spin $\sigma = \uparrow$ in the right lead, whereas the second term describes electrons with $\sigma = \downarrow$ tunneling from the right lead into the QD. As done before,[27] we take the ratio of the maximum current to the initial current (the maximum for independent emitters) $I_{\rm coop}/I_{\rm ind}$ as our figure of merit: A relative intensity peak height $I_{\rm coop}/I_{\rm ind} > 1$ indicates cooperative effects. One of the characteristic features of SR is that this quantity scales linearly with the number of spins N.

In the local-moment regime, described by Eq. (35), the expression for the current simplifies to $I(t) = (1 - \beta_{\downarrow}^{(R)}/\beta)\alpha\langle S^+S^-\rangle_t \propto \langle S^+S^-\rangle_t$, showing that it is directly proportional to the electron inversion. This, in turn, increases as the nuclear system pumps excitations into the electronic system. A compact expression for the relation between the current and the dynamics of the nuclear system can be obtained immediately in the case of homogeneous coupling,

$$\frac{d}{dt}\langle S^+S^-\rangle_t = -\frac{d}{dt}\langle I^z\rangle_t - \gamma\langle S^+S^-\rangle_t. \tag{46}$$

Since the nuclear dynamics are, in general, much slower than the electron's dynamics, the approximate solution of this equation is $\langle S^+S^-\rangle_t \approx -\frac{d}{dt}\langle I^z\rangle_t/\gamma$. As a consequence, the current $I(t)$ is proportional to the time-derivative of the nuclear polarization,

$$I(t) \propto -\frac{d}{dt}\langle I^z\rangle_t. \tag{47}$$

Still, no matter how strong the cooperative effects are, on a time scale of single electron tunneling events, the electrons will always be emitted antibunched, since in the strong Coulomb-blockade regime the QD acts as a single-electron emitter.[47] Typically, the rate for single-electron emission events is even below the tunneling rate α due to the spin blockade. On electronic time scales $\sim 1/\alpha$, the SR mechanism manifests in lifting this blockade; as argued above, the efficiency of this process is significantly enhanced by collective effects.

Before we proceed with an in-depth analysis of the current $I(t)$, we note that an intriguing extension of the present work would be the study of fluctuations thereof (see, for example, Ref. 48 for studies of the shot noise spectrum in a related system). Insights into the statistics of the current could be obtained by analyzing two-time correlation functions such as $\langle n_\uparrow(t+\tau)n_\uparrow(t)\rangle$, where $n_\uparrow = d_\uparrow^\dagger d_\uparrow$. This can conveniently be done via the Quantum Regression Theorem,[49] which yields the formal result $\langle n_\uparrow(t+\tau)n_\uparrow(t)\rangle = \mathsf{Tr}_{\mathsf{S}}[n_\uparrow e^{\mathcal{W}\tau}(n_\uparrow\rho_S(t))]$. Here, $\mathcal{W}$ denotes the Liouvillian governing the system's dynamics according to $\dot\rho_S = \mathcal{W}\rho_S$ [see Eq. (35)] and $\mathsf{Tr}_{\mathsf{S}}[\cdots]$ refers to the trace over the system's degree of freedoms. This procedure can be generalized to higher-order correlation functions and full evaluation of the current statistics might reveal potential connections between current fluctuations and cooperative nuclear dynamics.

VI. ANALYSIS AND NUMERICAL RESULTS

A. Experimental realization

The proposed setup described here may be realized with state-of-the-art experimental techniques. First, the Markovian regime, valid for sufficiently large bias eV, is realized if the Fermi functions of the leads are smooth on a scale set by the natural widths of the levels and residual fluctuations due to the dynamically compensated Overhauser field. Since for typical materials[8] the hyperfine coupling constant is $A_{\rm HF} = 1$–$100\,\mu$eV and tunneling rates are typically[9] of the order of $\sim 10\,\mu$eV, this does not put a severe restriction on the bias voltage which is routinely[18,19] in the range of hundreds of μV or mV. Second, in order to tune the system into the spin-blockade regime, a sufficiently large external magnetic field has to be applied. More precisely, the corresponding Zeeman splitting ω_0 energetically separates the upper and lower manifolds in such a way that the Fermi function of the right lead drops from one at the lower manifold to zero at the upper manifold. Finite temperature T smears out the Fermi function around the chemical potential by approximately $\sim k_B T$. Accordingly, with cryostatic temperatures of $k_B T \sim 10\,\mu$eV being routinely realized in the laboratory,[10] this condition can be met by applying an external magnetic field of $\sim$5–10 T, which is equivalent to $\omega_0 \approx 100$–$200\,\mu$eV in GaAs.[8,50] The charging energy U, typically $\sim$1–4 meV,[9,19] sets the largest energy scale in the problem justifying the Coulomb-blockade regime with negligible double occupancy of the QD provided that the chemical potential of the left lead is well below the doubly occupied level. Last, we note that similar setups to the one proposed here have previously been realized experimentally by, for example, Hanson *et al.*[26,50]

Proceeding from these considerations, we now show by numerical simulation that an SR peaking of several orders of magnitude can be observed for experimentally relevant parameters in the leakage current through a quantum dot in the spin-blockade regime. We first consider the idealized case of homogeneous coupling for which an exact numerical treatment is feasible even for a larger number of coupled nuclei. Then, we continue with the more realistic case of inhomogeneous coupling for which an approximative scheme is applied. Here, we also study scenarios in which the nuclear spins are not fully polarized initially. Moreover, we discuss intrinsic nuclear dephasing effects and undesired cotunneling processes which have been omitted in our simulations. In particular, we show that the inhomogeneous nature of the HF coupling accounts for the strongest dephasing mechanism in our system. We note that this effect is covered in the second set of our simulations. Finally, we self-consistently justify the perturbative treatment of the Overhauser-field fluctuations as well as the HF flip-flop dynamics.

B. Superradiant electron transport

1. Idealized setting

The homogeneous case allows for an exact treatment even for a relatively large number of nuclei as the system evolves within the totally symmetric low-dimensional subspace $\{|J,m\rangle, m = -J,\ldots,J\}$. Starting from a fully polarized state, a strong intensity enhancement is observed; typical results obtained from numerical simulations of Eq. (30) are depicted in Fig. 5 for $N = 60$ and $N = 100$ nuclear spins. The corresponding relative peak heights display a linear dependence with N (cf. Fig. 6), which we identify as the characteristic feature of SR. Here, we have used the numerical

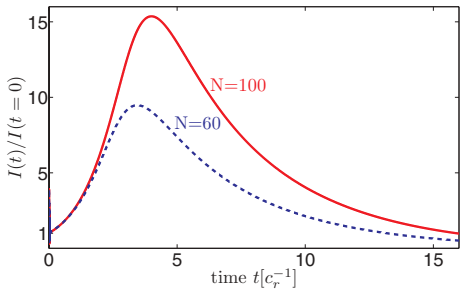

FIG. 5. (Color online) Typical time evolution of the normalized current for homogeneous coupling under dynamical compensation of the Overhauser field and a relative coupling strength of $\epsilon = 0.5$, shown here for $N = 60$ and $N = 100$ nuclear spins. The characteristic feature of SR, a pronounced peak in the leakage current proportional to N, is clearly observed.

parameters $A_{\rm HF} = 1$, $\omega_0 = 1$ and $\alpha = \beta_{\uparrow}^{(L)} = \beta_{\downarrow}^{(L)} = \beta_{\downarrow}^{(R)} = 0.1$ in units of $\sim$100 μeV, corresponding to a relative coupling strength $\epsilon = 0.5$.

Before we proceed, some further remarks on the dynamic compensation of the Overhauser field seem appropriate: We have merely introduced it in our analysis in order to provide a clear criterion for the presence of purely collective effects, given by $I_{\rm coop}/I_{\rm ind} > 1$. In other words, dynamic compensation of the Overhauser field is not a necessary requirement for the observation of collective effects, but it is rather an adequate tool to display them clearly. From an experimental point of view, the dynamic compensation of the Overhauser field might be challenging as it requires accurate knowledge about the evolution of the nuclear spins. Therefore, we also present results for the case in which the external magnetic field is constant and no compensation is applied. Here, we can distinguish two cases: Depending on the sign of the HF coupling constant $A_{\rm HF}$, the time dependence of the effective

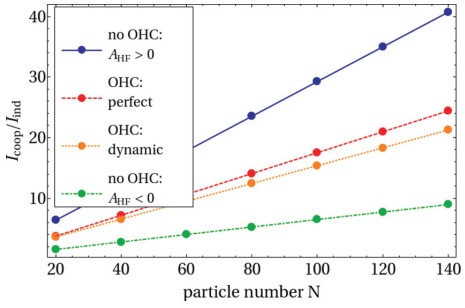

FIG. 6. (Color online) Ratio of the maximum current to the initial current $I_{\rm coop}/I_{\rm ind}$ as a function of the number of nuclear spins N for homogeneous coupling and a relative coupling strength of $\epsilon = 0.5$: Results for perfect compensation (dashed line) are compared to the case of dynamic compensation (dotted line) of the Overhauser field (OHC). Simulations without compensation of the Overhauser field set bounds for the enhancement of the leakage current, depending on the sign of the HF coupling constant $A_{\rm HF}$; solid and dash-dotted line for $A_{\rm HF} > 0$ and $A_{\rm HF} < 0$, respectively.

Zeeman-splitting ω can either give rise to an additional enhancement of the leakage current ($A_{\rm HF} > 0$) or it can counteract the collective effects ($A_{\rm HF} < 0$). As shown in Fig. 6, this sets lower and upper bounds for the observed enhancement of the leakage current.

In Fig. 6 we also compare the results obtained for dynamic compensation of the Overhauser field to the idealized case of perfect compensation in which the effect of the Overhauser term is set to zero, that is, $H_{\rm OH} = gA^zS^z = 0$. Both approaches display the same features justifying our approximation of neglecting residual (de)tuning effects of the dynamically compensated Overhauser field with respect to the external Zeeman splitting ω_0. This is also discussed in greater detail below.

2. *Beyond the idealized setting*

Inhomogeneous HF coupling. In principle, the inhomogeneous HF coupling could prevent the phasing necessary for SR. However, as shown below, SR is still present in realistically inhomogeneous systems. In contrast to the idealized case of homogeneous coupling, the dynamics cannot be restricted to a low-dimensional subspace so that an exact numerical treatment is not feasible due to the large number of nuclei. We therefore use an approximate approach which has previously been shown to capture the effect of nuclear spin coherences while allowing for a numerical treatment of hundreds of spins.[22,27] For simplicity, we restrict ourselves to the local moment regime in which the current can be obtained directly from the electron inversion $I(t) \propto \langle S^+S^-\rangle_t$. By Eq. (35), this expectation value is related to a hierarchy of correlation terms involving both the electron and the nuclear spins. Based on a Wick type factorization scheme, higher-order expressions are factorized in terms of the covariance matrix $\gamma_{ij}^{+} = \langle\sigma_i^+\sigma_j^-\rangle$ and the "mediated covariance matrix" $\gamma_{ij}^{-} = \langle\sigma_i^+S^z\sigma_j^-\rangle$. For further details, see Refs. 22 and 27.

The coupling constants g_j have been obtained from the assumption of a two-dimensional Gaussian spatial electron wave function of width $\sqrt{N}/2$. Specifically, we present results for two sets of numerical parameters, corresponding to a relative coupling strength of $\epsilon = 0.5$, where $A_{\rm HF} = 1, \omega_0 = 1$, $\gamma = 0.1$, and $\Gamma = 0.08$, and $\epsilon = 0.55$ with $A_{\rm HF} = 1, \omega_0 = 0.9$, $\gamma = 0.1$, and $\Gamma = 0.067$.

As shown in Figs. 7 and 8, the results obtained with these methods demonstrate clear SR signatures. In comparison to the ideal case of homogeneous coupling, the relative height is reduced, but for a *fully polarized* initial state we still find a linear enhancement $I_{\rm coop}/I_{\rm ind} \approx 0.043N$ ($\epsilon = 0.5$); therefore, as long as this linear dependence is valid, for typically $N \approx 10^5$–10^6 a strong intensity enhancement of several orders of magnitude is predicted ($\sim 10^3$–10^4).

Imperfect initial polarization. If the initial state is not fully polarized, SR effects are reduced: However, when starting from a mixture of symmetric Dicke states $|J, J\rangle$ with polarization $p = 80(60)\%$, we find that the linear N dependence is still present: $I_{\rm coop}/I_{\rm ind} \approx 0.0075(0.0025)N$ for $\epsilon = 0.5$; that is, the scaling is about a factor of $\sim$5(15) weaker than for full polarization.[51] Still, provided the linear scaling holds up to an experimentally realistic number of nuclei $N \approx 10^5$–10^6, this amounts to a relative enhancement of the

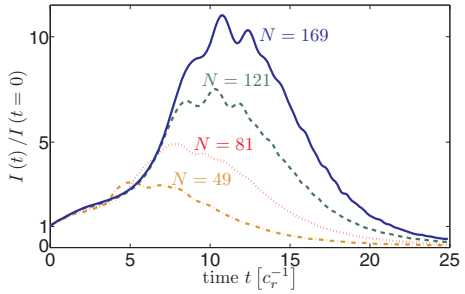

FIG. 7. (Color online) Typical time evolution of the normalized current for inhomogeneous coupling, shown here for up to $N = 13^2$ nuclear spins and a relative coupling strength $\epsilon = 0.55$. Compared to the idealized case of homogeneous coupling, the SR effects are reduced, but still clearly present. A Gaussian spatial electron wave function has been assumed and the Overhauser field is compensated dynamically.

order of $I_{\text{coop}}/I_{\text{ind}} \sim 10^2$–$10^3$. To clearly resolve this peak experimentally, any spurious current should not be larger than the initial HF-mediated leakage current. As we argue below, this condition can be fulfilled in our setup, since the main spurious mechanism, cotunneling, is strongly suppressed.

Nuclear Zeeman term and species inhomogeneity. In our simulations we have disregarded the nuclear Zeeman energies. For a single nuclear species, this term plays no role in the SR dynamics. However, in typical QDs several nuclear species with different g factors are present ("species inhomogeneity"). In principle, these are large enough to cause additional dephasing between the nuclear spins, similar to the inhomogeneous Knight field.[22] However, this dephasing mechanism only applies to nuclei which belong to different species.[22] This leads to few (in GaAs three) mutually decohered subsystems, each of which is described by our theory.

Nuclear interactions. Moreover, we have neglected the dipolar and quadrupolar interactions among the nuclear spins. First, the nuclear dipole-dipole interaction can cause diffusion and dephasing processes. Diffusion processes that can change A^z are strongly detuned by the Knight field and therefore are of minor importance, as corroborated by experimentally measured spin diffusion rates.[52,53] Resonant processes such as $\propto I_i^z I_j^z$ can lead to dephasing similar to the inhomogeneous Knight shift. This competes with the phasing necessary for the observation of SR as expressed by the first term in Eq. (3). The SR process is the weakest at the very beginning of the evolution where we estimate its strength as $c_r^{\min} \approx 10\,\mu\text{eV}/N$. An upper bound for the dipole-dipole interaction in GaAs has been given in Ref. 28 as $\sim 10^{-5}\,\mu$eV, in agreement with values given in Refs. 32 and 41. Therefore, the nuclear dipole-dipole interaction can safely be neglected for $N \lesssim 10^5$. In particular, its dephasing effect should be further reduced for highly polarized ensembles.

Second, the nuclear quadrupolar interactions can have two origins: strain (largely absent in electrically defined QDs) and electric field gradients originating from the electron. These have been estimated for typical electrically defined QDs in Ref. 41 to lead to an additional nuclear level splitting on the order of $\sim 10^{-5}\,\mu$eV. Moreover, they are absent for nuclear spin $I = 1/2$ (e.g., CdSe QDs). To summarize, the additional dephasing mechanisms induced by nuclear interactions are much smaller than the terms arising from the inhomogeneous Knight field.[32] As argued above and confirmed by our simulations, the latter does not prevent the observation of SR behavior due to the presence of the MPM-term in Eq. (3).

3. *Quantitative aspects*

Initially, the HF-mediated SR dynamics is rather slow, with its characteristic time scale set by c_r^{-1}; for experimentally realistic parameters—in what follows we use the parameter set ($\epsilon = 0.5, \alpha \approx 10\,\mu$eV, $N \approx 10^5$) for numerical estimates—this corresponds to $c_r^{-1} \approx 10\,\mu$s. Based on fits as shown in Fig. 9, we then estimate for the SR process duration $\langle t_D \rangle \approx 50 c_r^{-1} \approx 500\,\mu$s, which is still smaller than recently reported[54] nuclear decoherence times of $\sim$1 ms. Therefore, it should be possible to observe the characteristic enhancement of the leakage current before the nuclear spins decohere.

Leakage current. Accordingly, in the initial phasing stage, the HF-mediated lifting of the spin blockade is rather weak, resulting in a low leakage current, approximatively given by $I(t=0)/(e\hbar^{-1}) \approx \epsilon^2 \alpha / N$. Therefore, the initial current due to HF processes is inversely proportional to the number of nuclear

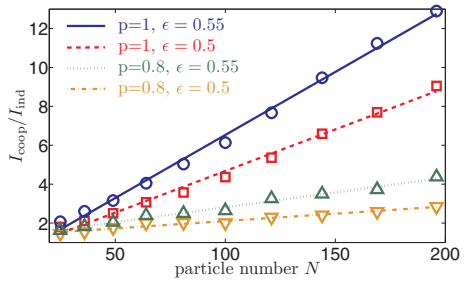

FIG. 8. (Color online) Ratio of the maximum current to the initial current $I_{\text{coop}}/I_{\text{ind}}$ as a function of the number of nuclear spins N for relative coupling strengths $\epsilon = 0.5$ and $\epsilon = 0.55$: Results for inhomogeneous coupling. The linear dependence is still present when starting from a nuclear state with finite polarization $p = 0.8$.

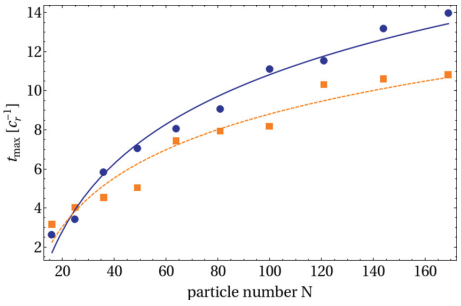

FIG. 9. (Color online) Total time until the observation of the characteristic SR peaking $t_{\max}$ for $\epsilon = 0.5$ (blue dots) and $\epsilon = 0.55$ (orange squares). Based on Eq. (44), logarithmic fits are obtained from which we estimate $t_{\max}$ for experimentally realistic number of nuclear spins $N \approx 10^5$.

spins N. However, as correlations among the nuclei build up, the HF-mediated lifting becomes more efficient, culminating in a maximum current of $I_{\max}/(e\hbar^{-1}) \approx \epsilon^2\alpha$, independent of N. For realistic experimental values—also taking into account the effects of inhomogeneous HF coupling and finite initial polarization $p \approx 0.6$—we estimate the initial (maximum) leakage current to be of the order of $I(t=0) \approx 6$ fA($I_{\max} \approx 10$ pA). Leakage currents in this range of magnitudes have already been detected in single QD spin-filter experiments,[26] as well as double QD Pauli-blockade experiments;[15,16,18,19] here, leakage currents below 10 and 150 fA, respectively, have been attributed explicitly to other spurious processes.[18,26] These are addressed in greater detail in the following.

Our transport setting is tuned into the sequential tunneling regime and therefore we have disregarded cotunneling processes which are fourth order in H_T. In principle, cotunneling processes could lift the spin blockade and add an extra contribution to the leakage current that is independent of the HF dynamics. However, note that cotunneling current scales as $I_{\rm ct} \propto \alpha^2$, whereas sequential tunneling current $I \propto \alpha$; accordingly, cotunneling current can always be suppressed by making the tunnel barriers less transparent.[26] Moreover, inelastic cotunneling processes exciting the QD spin can be ruled out for eV, $k_BT < \omega_0$ due to energy conservation.[25] The effectiveness of a single quantum dot to act as an electrically tunable spin filter has also been demonstrated experimentally:[26] The spin-filter efficiency was measured to be nearly 100%, with $I_{\rm ct}$ being smaller than the noise floor $\sim$10 fA. Its actual value has been calculated as $\sim 10^{-4}$ fA, from which we roughly estimate $I_{\rm ct} \sim 10^{-2}$ fA in our setting. This is smaller than the initial HF-mediated current $I(t=0)$ and considerably smaller than $I_{\max}$, even for an initially not fully polarized nuclear spin ensemble. Still, if one is to explore the regime where cotunneling cannot be neglected, phenomenological dissipative terms—effectively describing the corresponding spin-flip and pure dephasing mechanisms for inelastic and elastic processes, respectively—should be added to Eq. (30).

4. Self-consistency

In our simulations we have self-consistently verified that the fluctuations of the Overhauser field, defined via

$$\Delta_{\rm OH}(t) = g\sqrt{\langle A_z^2\rangle_t - \langle A_z\rangle_t^2}, \tag{48}$$

are indeed small compared to the external Zeeman splitting ω_0 throughout the entire evolution. This ensures the validity of our perturbative approach and the realization of the spin-blockade regime. From atomic SR it is known that in the limit of homogeneous coupling large fluctuations can build up, since in the middle of the emission process the density matrix becomes a broad distribution over the Dicke states.[24] Accordingly, in the idealized, exactly solvable case of homogeneous coupling we numerically find rather large fluctuations of the Overhauser field; as demonstrated in Fig. 10, this holds independently of N. In particular, for a relative coupling strength $\epsilon = 0.5$ the fluctuations culminate in $\max[\Delta_{\rm OH}]/\omega_0 \approx 0.35$. However, in the case of inhomogeneneous HF coupling the Overhauser field fluctuations are found to be smaller as the buildup of these fluctuations is hindered by the Knight term causing dephasing among the nuclear spins. As another limiting case, we also estimate the fluctuations for completely independent homogeneously coupled nuclear spins via the binominal distribution as $\max[\Delta_{\rm OH}] \sim 0.5A_{\rm HF}/\sqrt{N}$ (Ref. 55).

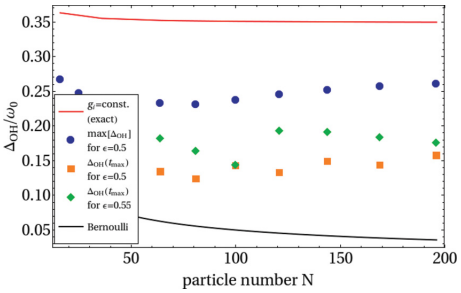

FIG. 10. (Color online) Fluctuations of the Overhauser field relative to the external Zeeman splitting ω_0. In the limit of homogeneous HF coupling, strong fluctuations build up towards the middle of the emission process (red line, $\epsilon = 0.5$). For inhomogeneous coupling this buildup of fluctuations is hindered by the dephasing between the nuclear spins, resulting in considerably smaller fluctuations: The value of the Overhauser fluctuations is shown at the time of the SR peak $t_{\max}$ for $\epsilon = 0.5$ (orange squares) and $\epsilon = 0.55$ (green diamonds). The Overhauser fluctuations reach a maximum value later than $t_{\max}$; see blue dots for $\epsilon = 0.5$. For independent homogeneously coupled nuclear spins, one can estimate the fluctuations via the binominal distribution (black line).

Moreover, we have also ensured self-consistently the validity of the perturbative treatment of the flip-flop dynamics; that is, throughout the entire evolution, even for maximum operative matrix elements $\langle A^+A^-\rangle_t$, the strength of the flip-flop dynamics $\|H_{\rm ff}\|$ was still at least five times smaller than ω_0.

VII. CONCLUSION AND OUTLOOK

In summary, we have developed a master equation based theoretical framework for nuclear-spin-assisted transport through a QD. Due to the collective nature of the HF interaction, it incorporates intriguing many-body effects as well as feedback mechanisms between the electron spin and nuclear spin dynamics. As a prominent application, we have shown that the current through a single electrically defined QD in the spin-blockade regime naturally exhibits superradiant behavior. This effect stems from the collective hyperfine interaction between the QD electron and the nuclear spin ensemble in the QD. Its most striking feature is a lifting of the spin blockade and a pronounced peak in the leakage current. The experimental observation of this effect would provide clear evidence of coherent HF dynamics of nuclear spin ensembles in QDs.

Finally, we highlight possible directions of research going beyond our present work: Apart from superradiant electron transport, the setup proposed here is inherently well suited for other experimental applications like dynamic polarization of nuclear spins (DNPs): In analogy to optical pumping, Eq. (3) describes *electronic* pumping of the nuclear spins. Its steady states are eigenstates of A^z, which lie in the

kernel of the collective jump operator A^-. In particular, for a completely inhomogeneous system the only steady state is the fully polarized one, the ideal initial state required for the observation of SR effects. When starting from a completely unpolarized nuclear state, the unidirectionality of Eq. (3)—electrons with one spin orientation exchange excitations with the nuclear spins, while electrons of opposite spin primarily do not—implies that the rather warm electronic reservoir can still extract entropy out of the nuclear system. More generally, the transport setting studied here possibly opens up the route towards the (feedback-based) electronic preparation of particular nuclear states in single QDs. This is in line with similar ideas previously developed in double QD settings (see, e.g., Refs. 12, 15, 18, 20, and 54).

In this work we have specialized on a single QD. However, our theory could be extended to a double QD (DQD) setting which is likely to offer even more possibilities. DQDs are routinely operated in the Pauli-blockade regime where despite the presence of an applied source-drain voltage the current through the device is blocked whenever the electron tunneling into the DQD has the same spin orientation as the one already present. The DQD parameters and the external magnetic field can be tuned such that the role of the states $|\sigma\rangle, \sigma = \downarrow, \uparrow$, in our model is played by a pair of singlet and triplet states, while all other states are off-resonant. Then, along the lines of our study, nonlinearities appear due to dependencies between the electronic and nuclear subsystems and collective effects enter via the HF-mediated lifting of the spin blockade.

While we have focused on the Markovian regime and the precise conditions for its validity, Eq. (15) offers a starting point for studies of non-Markovian effects in the proposed transport setting. All terms appearing in the memory kernel of Eq. (15) are quadratic in the fermionic creation and annihilation operators allowing for an efficient numerical simulation, without having to explicitly invoke the flatness of the spectral density of the leads. This should then shed light on possibly abrupt changes in the QD transport properties due to feedback mechanism between the nuclear spin ensemble and the electron spin.

Last, our work also opens the door towards studies of dissipative phase transitions in the transport setting: When combined with driving, the SR dynamics can lead to a variety of strong-correlation effects, nonequilibrium, and dissipative phase transitions,[1,56–58] which could now be studied in a mesoscopic solid-state system, complementing other approaches to dissipative phase transitions in QDs.[59–62]

ACKNOWLEDGMENTS

We thank O. Viyuela for fruitful discussions. We acknowledge support by the DFG within SFB 631 and the Cluster of Excellence NIM.

APPENDIX A: MICROSCOPIC DERIVATION OF THE MASTER EQUATION

In this appendix we provide some details regarding the derivation of the master equations as stated in Eqs. (2) and (30). It comprises the effect of the HF dynamics in the memory kernel of Eq. (13) and the subsequent approximation of independent rates of variation.

In the following, we show that it is self-consistent to neglect the effect of the HF dynamics $\mathcal{L}_1(t)$ in the memory kernel of Eq. (13) provided that the bath correlation time τ_c is short compared to the Rabi flips produced by the HF dynamics. This needs to be addressed as cooperative effects potentially drive the system from a weakly coupled into a strongly coupled regime. First, we reiterate the Schwinger-Dyson identity in Eq. (14) as an infinite sum over time-ordered nested commutators

$$e^{-i(\mathcal{L}_0+\mathcal{L}_1)\tau} = e^{-i\mathcal{L}_0\tau}\sum_{n=0}^{\infty}(-i)^n\int_0^\tau d\tau_1\int_0^{\tau_1}d\tau_2\ldots \times\int_0^{\tau_{n-1}}d\tau_n\,\tilde{\mathcal{L}}_1(\tau_1)\tilde{\mathcal{L}}_1(\tau_2)\ldots\tilde{\mathcal{L}}_1(\tau_n), \quad \text{(A1)}$$

where for any operator X

$$\tilde{\mathcal{L}}_1(\tau)X = e^{i\mathcal{L}_0\tau}\mathcal{L}_1 e^{-i\mathcal{L}_0\tau}X = [e^{iH_0\tau}H_1e^{-iH_0\tau},X] = [\tilde{H}_1(\tau),X]. \quad \text{(A2)}$$

More explicitly, up to second order Eq. (A1) is equivalent to

$$e^{-i(\mathcal{L}_0+\mathcal{L}_1)\tau}X = e^{-i\mathcal{L}_0\tau}X - ie^{-i\mathcal{L}_0\tau}\int_0^\tau d\tau_1[\tilde{H}_1(\tau_1),X] - e^{-i\mathcal{L}_0\tau}\int_0^\tau d\tau_1\int_0^{\tau_1}d\tau_2[\tilde{H}_1(\tau_1),[\tilde{H}_1(\tau_2),X]]+\cdots. \quad \text{(A3)}$$

Note that the time dependence of $\tilde{H}_1(\tau)$ is simply given by

$$\tilde{H}_1(\tau) = e^{i\omega\tau}H_+ + e^{-i\omega\tau}H_- + H_{\Delta\mathrm{OH}}, \quad H_\pm = \frac{g}{2}S^\pm A^\mp, \quad \text{(A4)}$$

where the effective Zeeman splitting $\omega = \omega_0 + g\langle A^z\rangle_t$ is time dependent. Accordingly, we define $\tilde{\mathcal{L}}_1(\tau) = \tilde{\mathcal{L}}_+(\tau) + \tilde{\mathcal{L}}_-(\tau) + \tilde{\mathcal{L}}_{\Delta\mathrm{OH}}(\tau) = e^{i\omega\tau}\mathcal{L}_+ + e^{-i\omega\tau}\mathcal{L}_- + \mathcal{L}_{\Delta\mathrm{OH}}$, where $\mathcal{L}_x\cdot = [H_x,\cdot]$ for $x = \pm,\Delta\mathrm{OH}$. In the next steps, we explicitly evaluate the first two contributions to the memory kernel that go beyond $n = 0$ and then generalize our findings to any order n of the Schwinger-Dyson series.

1. First-order correction

The first-order contribution $n = 1$ in Eq. (13) is given by

$$\Xi^{(1)} = i\int_0^t d\tau\int_0^\tau d\tau_1\,\mathrm{Tr}_B(\mathcal{L}_T e^{-i\mathcal{L}_0\tau}[\tilde{H}_1(\tau_1),X]). \quad \text{(A5)}$$

Performing the integration in τ_1 leads to

$$\Xi^{(1)} = \int_0^t d\tau\left\{\frac{g}{2\omega}(1-e^{-i\omega\tau})\mathrm{Tr}_B(\mathcal{L}_T[S^+A^-,\tilde{X}_\tau]) + \frac{g}{2\omega}(e^{i\omega\tau}-1)\mathrm{Tr}_B(\mathcal{L}_T[S^-A^+,\tilde{X}_\tau]) + ig\tau\,\mathrm{Tr}_B(\mathcal{L}_T[(A^z-\langle A^z\rangle_t)S^z,\tilde{X}_\tau])\right\}, \quad \text{(A6)}$$

where, for notational convenience, we introduced the operators $X = \mathcal{L}_T\rho_S(t-\tau)\rho_B^0$ and $\tilde{X}_\tau = e^{-iH_0\tau}[H_T,\rho_S(t-\tau)\rho_B^0]e^{iH_0\tau} \approx [\tilde{H}_T(\tau),\rho_S(t)\rho_B^0]$. In accordance with previous

approximations, we have replaced $e^{-iH_0\tau}\rho_S(t-\tau)e^{iH_0\tau}$ with $\rho_S(t)$ since any additional term besides H_0 would be of higher order in perturbation theory.[35,36] In particular, this disregards dissipative effects: In our case, this approximation is valid self-consistently provided that the tunneling rates are small compared to effective Zeeman splitting ω. The integrand decays on the leads-correlation time scale τ_c, which is typically much faster than the time scale set by the effective Zeeman splitting, $\omega\tau_c \ll 1$. This separation of time scales allows for an expansion in the small parameter $\omega\tau$, for example, $\frac{g}{\omega}(e^{i\omega\tau}-1) \approx ig\tau$. We see that the first-order correction can be neglected if the the bath correlation time τ_c is sufficiently short compared to the time scale of the HF dynamics, that is $g\tau_c \ll 1$. The latter is bounded by the total hyperfine coupling constant A_{HF} (since $||gA^x|| \leqslant A_{\mathrm{HF}}$) so that the requirement for disregarding the first-order term reads $A_{\mathrm{HF}}\tau_c \ll 1$.

2. Second-order correction

The contribution of the second term $n=2$ in the Schwinger-Dyson expansion can be decomposed into

$$\Xi^{(2)} = \Xi^{(2)}_{\mathrm{zz}} + \Xi^{(2)}_{\mathrm{ff}} + \Xi^{(2)}_{\mathrm{fz}}. \tag{A7}$$

The first term $\Xi^{(2)}_{\mathrm{zz}}$ contains contributions from $H_{\Delta\mathrm{OH}}$ only,

$$\begin{aligned}\Xi^{(2)}_{\mathrm{zz}} &= \int_0^t d\tau \int_0^\tau d\tau_1 \int_0^{\tau_1} d\tau_2 \mathsf{Tr}_{\mathsf{B}}(\mathcal{L}_T e^{-i\mathcal{L}_0\tau}[\tilde{H}_{\Delta\mathrm{OH}}(\tau_1), \\ &\quad [\tilde{H}_{\Delta\mathrm{OH}}(\tau_2), X]]) \qquad \text{(A8)} \\ &= -\int_0^t d\tau (g\tau)^2 \mathsf{Tr}_{\mathsf{B}}\Big[\mathcal{L}_T\Big(\delta A^z S^z \tilde{X}_\tau \delta A^z S^z \\ &\quad - \frac{1}{2}\{\delta A^z S^z \delta A^z S^z, \tilde{X}_\tau\}\Big)\Big]. \qquad \text{(A9)}\end{aligned}$$

Similarly, $\Xi^{(2)}_{\mathrm{ff}}$, which comprises contributions from H_{ff} only is found to be

$$\begin{aligned}\Xi^{(2)}_{\mathrm{ff}} = \frac{g^2}{4\omega^2}\int_0^t d\tau \{&(1+i\omega\tau - e^{i\omega\tau}) \\ &\times \mathsf{Tr}_{\mathsf{B}}[\mathcal{L}_T(S^+S^-A^-A^+\tilde{X}_\tau + \tilde{X}_\tau S^-S^+A^+A^-)] \\ &+(1-i\omega\tau - e^{-i\omega\tau})\mathsf{Tr}_{\mathsf{B}}[\mathcal{L}_T(S^-S^+A^+A^-\tilde{X}_\tau \\ &+\tilde{X}_\tau S^+S^-A^-A^+)]\}. \qquad \text{(A10)}\end{aligned}$$

Here, we have used the following simplification: The time-ordered products which include flip-flop terms only can be simplified to two possible sequences in which $\mathcal{L}_+$ is followed by $\mathcal{L}_-$ and vice versa. This holds since

$$\begin{aligned}\mathcal{L}_\pm\mathcal{L}_\pm X &= [H_\pm,[H_\pm,X]] \\ &= H_\pm H_\pm X + X H_\pm H_\pm - 2H_\pm X H_\pm = 0. \qquad \text{(A11)}\end{aligned}$$

Here, the first two terms drop out immediately since the electronic jump operators $S^\pm$ fulfill the relation $S^\pm S^\pm = 0$. In the problem at hand, also the last term gives zero because of particle number superselection rules: In Eq. (13) the time-ordered product of superoperators acts on $X = [H_T, \rho_S(t-\tau)\rho_B^0]$. Thus, for the term $H_\pm X H_\pm$ to be nonzero, coherences in Fock space would be required, which are consistently neglected (compare Ref. 36). This is equivalent to ignoring coherences between the system and the leads. Note that the same argument holds for any combination $H_\mu X H_\nu$ with $\mu,\nu = \pm$.

Similar results can be obtained for $\Xi^{(2)}_{\mathrm{fz}}$ which comprises $H_\pm$ as well as $H_{\Delta\mathrm{OH}}$ in all possible orderings. Again, using that the integrand decays on a time scale τ_c and expanding in the small parameter $\omega\tau$ shows that the second-order contribution scales as $\sim(g\tau_c)^2$. Our findings for the first- and second-order correction suggest that the nth-order correction scales as $\sim(g\tau_c)^n$. This is proven in the following by induction.

3. *n*th-order correction

The scaling of the nth term in the Dyson series is governed by the quantities of the form

$$\xi^{(n)}_{+-\ldots}(\tau) = g^n \int_0^\tau d\tau_1 \int_0^{\tau_1} d\tau_2 \cdots \int_0^{\tau_{n-1}} d\tau_n e^{i\omega\tau_1} e^{-i\omega\tau_2} \ldots, \tag{A12}$$

where the index suggests the order in which $H_\pm$ (giving an exponential factor) and $H_{\Delta\mathrm{OH}}$ (resulting in a factor of 1) appear. Led by our findings for $n=1,2$, we claim that the expansion of $\xi^{(n)}_{+-\ldots}(\tau)$ for small $\omega\tau$ scales as $\xi^{(n)}_{+-\ldots}(\tau) \sim (g\tau)^n$. Then, the $(n+1)$th terms scale as

$$\begin{aligned}\xi^{(n+1)}_{-(\Delta\mathrm{OH})+-\ldots}(\tau) &= g^{n+1}\int_0^\tau d\tau_1 \int_0^{\tau_1} d\tau_2 \cdots \int_0^{\tau_{n-1}} d\tau_n \\ &\quad \times \int_0^{\tau_n} d\tau_{n+1} \begin{pmatrix} e^{-i\omega\tau_1} \\ 1 \end{pmatrix} e^{+i\omega\tau_2} \cdots \qquad \text{(A13)} \\ &= g\int_0^\tau d\tau_1 \begin{pmatrix} e^{-i\omega\tau_1} \\ 1 \end{pmatrix} \xi^{(n)}_{+-\ldots}(\tau_1) \qquad \text{(A14)} \\ &\sim (g\tau)^{n+1}. \qquad \text{(A15)}\end{aligned}$$

Since we have already verified this result for $n=1,2$, the general result follows by induction. This completes the proof.

APPENDIX B: ADIABATIC ELIMINATION OF THE QD ELECTRON

For a sufficiently small relative coupling strength ϵ the nuclear dynamics are slow compared to the electronic QD dynamics. This allows for an adiabatic elimination of the electronic degrees of freedom yielding an effective master equation for the nuclear spins of the QD.

Our analysis starts out from Eq. (35), which we write as

$$\dot{\rho} = \mathcal{W}_0\rho + \mathcal{W}_1\rho, \tag{B1}$$

where

$$\begin{aligned}\mathcal{W}_0\rho &= -i[\omega_0 S^z,\rho] + \gamma\Big[S^-\rho S^+ - \frac{1}{2}\{S^+S^-,\rho\}\Big] \\ &\quad + \Gamma\Big[S^z\rho S^z - \frac{1}{4}\rho\Big], \qquad \text{(B2)} \\ \mathcal{W}_1\rho &= -i[H_{\mathrm{HF}},\rho]. \qquad \text{(B3)}\end{aligned}$$

Note that the superoperator $\mathcal{W}_0$ only acts on the electronic degrees of freedom. It describes an electron in an external magnetic field that experiences a decay as well as a pure dephasing mechanism. In zeroth order of the coupling parameter

ϵ the electronic and nuclear dynamics of the QD are decoupled and SR effects cannot be expected. These are contained in the interaction term $\mathcal{W}_1$.

Formally, the adiabatic elimination of the electronic degrees of freedom can be achieved as follows:[63] To zeroth order in ϵ the eigenvectors of $\mathcal{W}_0$ with zero eigenvector $\lambda_0 = 0$ are

$$\mathcal{W}_0 \mu \otimes \rho_{SS} = 0, \tag{B4}$$

where $\rho_{SS} = |\downarrow\rangle\langle\downarrow|$ is the stationary solution for the electronic dynamics and μ describes some arbitrary state of the nuclear system. The zeroth-order Liouville eigenstates corresponding to $\lambda_0 = 0$ are coupled to the subspaces of "excited" nonzero (complex) eigenvalues $\lambda_k \neq 0$ of $\mathcal{W}_0$ by the action of $\mathcal{W}_1$. Physically, this corresponds to a coupling between electronic and nuclear degrees of freedom. In the limit where the HF dynamics are slow compared to the electronic frequencies, that is, the Zeeman splitting ω_0, the decay rate γ, and the dephasing rate Γ, the coupling between these blocks of eigenvalues and Liouville subspaces of $\mathcal{W}_0$ is weak, justifying a perturbative treatment. This motivates the definition of a projection operator P onto the subspace with zero eigenvalue $\lambda_0 = 0$ of $\mathcal{W}_0$ according to

$$P\rho = \mathsf{Tr}_{\mathsf{el}}[\rho] \otimes \rho_{SS} = \mu \otimes |\downarrow\rangle\langle\downarrow|, \tag{B5}$$

where $\mu = \mathsf{Tr}_{\mathsf{el}}[\rho]$ is a density operator for the nuclear spins, $\mathsf{Tr}_{\mathsf{el}} \ldots$ denotes the trace over the electronic subspace, and, by definition, $\mathcal{W}_0 \rho_{SS} = 0$. The complement of P is $Q = 1 - P$. By projecting the master equation on the P subspace and tracing over the electronic degrees of freedom we obtain an effective master equation for the nuclear spins in second-order perturbation theory,

$$\dot{\mu} = \mathsf{Tr}_{\mathsf{el}}\big[P\mathcal{W}_1 P\rho - P\mathcal{W}_1 Q\mathcal{W}_0^{-1} Q\mathcal{W}_1 P\rho\big]. \tag{B6}$$

Using $\mathsf{Tr}_{\mathsf{el}}[S^z \rho_{SS}] = -1/2$, the first term is readily evaluated and yields the Knight shift seen by the nuclear spins,

$$\mathsf{Tr}_{\mathsf{el}}[P\mathcal{W}_1 P\rho] = +i\frac{g}{2}[A^z, \mu]. \tag{B7}$$

The derivation of the second term is more involved. It can be rewritten as

$$\begin{aligned} &-\mathsf{Tr}_{\mathsf{el}}\big[P\mathcal{W}_1 Q\mathcal{W}_0^{-1} Q\mathcal{W}_1 P\rho\big] \\ &\quad = -\mathsf{Tr}_{\mathsf{el}}\big[P\mathcal{W}_1(1-P)\mathcal{W}_0^{-1}(1-P)\mathcal{W}_1 P\rho\big] \qquad \text{(B8)} \\ &\quad = \int_0^\infty d\tau\, \mathsf{Tr}_{\mathsf{el}}[P\mathcal{W}_1 e^{\mathcal{W}_0\tau}\mathcal{W}_1 P\rho] \\ &\qquad - \int_0^\infty d\tau\, \mathsf{Tr}_{\mathsf{el}}[P\mathcal{W}_1 P\mathcal{W}_1 P\rho]. \qquad \text{(B9)} \end{aligned}$$

Here, we used the Laplace transform $-\mathcal{W}_0^{-1} = \int_0^\infty d\tau\, e^{\mathcal{W}_0\tau}$ and the property $e^{\mathcal{W}_0\tau} P = P e^{\mathcal{W}_0\tau} = P$.

Let us first focus on the first term in Eq. (B9). It contains terms of the form

$$\begin{aligned} &\mathsf{Tr}_{\mathsf{el}}[P[A^+S^-, e^{\mathcal{W}_0\tau}[A^-S^+, \mu\otimes\rho_{SS}]]] \\ &\quad = \mathsf{Tr}_{\mathsf{el}}[S^- e^{\mathcal{W}_0\tau}(S^+\rho_{SS})]A^+A^-\mu \qquad \text{(B10)} \\ &\qquad - \mathsf{Tr}_{\mathsf{el}}[S^- e^{\mathcal{W}_0\tau}(S^+\rho_{SS})]A^-\mu A^+ \qquad \text{(B11)} \\ &\qquad + \mathsf{Tr}_{\mathsf{el}}[S^- e^{\mathcal{W}_0\tau}(\rho_{SS}S^+)]\mu A^-A^+ \qquad \text{(B12)} \\ &\qquad - \mathsf{Tr}_{\mathsf{el}}[S^- e^{\mathcal{W}_0\tau}(\rho_{SS}S^+)]A^+\mu A^-. \qquad \text{(B13)} \end{aligned}$$

This can be simplified using the following relations: Since $\rho_{SS} = |\downarrow\rangle\langle\downarrow|$, we have $S^-\rho_{SS} = 0$ and $\rho_{SS}S^+ = 0$. Moreover, $|\uparrow\rangle\langle\downarrow|$ and $|\downarrow\rangle\langle\uparrow|$ are eigenvectors of $\mathcal{W}_0$ with eigenvalues $-(i\omega_0 + \alpha/2)$ and $+(i\omega_0 - \alpha/2)$, where $\alpha = \gamma + \Gamma$, yielding

$$e^{\mathcal{W}_0\tau}(S^+\rho_{SS}) = e^{-(i\omega_0+\alpha/2)\tau}|\uparrow\rangle\langle\downarrow|, \tag{B14}$$

$$e^{\mathcal{W}_0\tau}(\rho_{SS}S^-) = e^{+(i\omega_0-\alpha/2)\tau}|\downarrow\rangle\langle\uparrow|. \tag{B15}$$

This leads to

$$\begin{aligned} &\mathsf{Tr}_{\mathsf{el}}[P[A^+S^-, e^{\mathcal{W}_0\tau}[A^-S^+, \mu\otimes\rho_{SS}]]] \\ &\quad = e^{-(i\omega_0+\alpha/2)\tau}(A^+A^-\mu - A^-\mu A^+). \end{aligned} \tag{B16}$$

Similarly, one finds

$$\begin{aligned} &\mathsf{Tr}_{\mathsf{el}}[P[A^-S^+, e^{\mathcal{W}_0\tau}[A^+S^-, \mu\otimes\rho_{SS}]]] \\ &\quad = e^{+(i\omega_0-\alpha/2)\tau}(\mu A^+A^- - A^-\mu A^+). \end{aligned} \tag{B17}$$

Analogously, one can show that terms containing two flip or two flop terms give zero. The same holds for mixed terms that comprise one flip-flop and one Overhauser term with $\sim A^zS^z$. The term consisting of two Overhauser contributions gives

$$\begin{aligned} &\mathsf{Tr}_{\mathsf{el}}[P[A^zS^z, e^{\mathcal{W}_0\tau}[A^zS^z, \mu\otimes\rho_{SS}]]] \\ &\quad = -\tfrac{1}{4}[2A^z\mu A^z - [A^zA^z, \mu]]. \end{aligned} \tag{B18}$$

However, this term exactly cancels with the second term from Eq. (B9). Thus, we are left with the contributions coming from Eqs. (B16) and (B17). Restoring the prefactors of $-ig/2$, we obtain

$$\begin{aligned} &\mathsf{Tr}_{\mathsf{el}}\big[P\mathcal{W}_1 Q\big(-\mathcal{W}_0^{-1}\big)Q\mathcal{W}_1 P\rho\big] \\ &\quad = \frac{g^2}{4}\int_0^\infty d\tau [e^{-(i\omega_0+\alpha/2)\tau}(A^-\mu A^+ - A^+A^-\mu) \\ &\qquad + e^{+(i\omega_0-\alpha/2)\tau}(A^-\mu A^+ - \mu A^+A^-)]. \end{aligned} \tag{B19}$$

Performing the integration and separating real from imaginary terms yields

$$\begin{aligned} &\mathsf{Tr}_{\mathsf{el}}\big[P\mathcal{W}_1 Q\big(-\mathcal{W}_0^{-1}\big)Q\mathcal{W}_1 P\rho\big] \\ &\quad = c_r\left[A^-\mu A^+ - \frac{1}{2}\{A^+A^-, \mu\}\right] + ic_i[A^+A^-, \mu], \end{aligned} \tag{B20}$$

where $c_r = g^2/(4\omega_0^2 + \alpha^2)\alpha$ and $c_i = g^2/(4\omega_0^2 + \alpha^2)\omega_0$. Combining Eq. (B7) with Eq. (B20) directly gives the effective master equation for the nuclear spins given in Eq. (3) in the main text.

[1] T. Brandes, Phys. Rep. **408**, 315 (2004).
[2] D. D. Awschalom, N. Samarth, and D. Loss, *Semiconductor Spintronics and Quantum Computation* (Springer-Verlag, Berlin, 2002).
[3] D. Y. Sharvin and Y. V. Sharvin, JETP Lett. **34**, 272 (1981).
[4] B. J. van Wees, H. van Houten, C. W. J. Beenakker, J. G. Williamson, L. P. Kouwenhoven, D. van der Marel, and C. T. Foxon, Phys. Rev. Lett. **60**, 848 (1988).
[5] D. Wharam, T. J. Thornton, R. Newbury, M. Pepper, H. Ahmed, J. E. F. Frost, D. G. Husko, D. C. Peacock, D. A. Ritchie, and G. A. C. Jones, J. Phys. C **21**, 209 (1988).
[6] Y. V. Nazarov and Y. M. Blanter, *Quantum Transport* (Cambridge University Press, Cambridge, 2009).
[7] S. Datta, *Electronic Transport in Mesoscopic Systems* (Cambridge University Press, Cambridge, 1997).
[8] R. Hanson, L. P. Kouwenhoven, J. R. Petta, S. Tarucha, and L. M. Vandersypen, Rev. Mod. Phys. **79**, 1217 (2007).
[9] W. G. van der Wiel, S. De Franceschi, J. M. Elzerman, T. Fujisawa, S. Tarucha, and L. P. Kouwenhoven, Rev. Mod. Phys. **75**, 1 (2002).
[10] A. C. Johnson, J. R. Petta, J. M. Taylor, A. Yacoby, M. D. Lukin, C. M. Marcus, M. P. Hanson, and A. C. Gossard, Nature (London) **435**, 925 (2005).
[11] O. N. Jouravlev and Y. V. Nazarov, Phys. Rev. Lett. **96**, 176804 (2006).
[12] J. Baugh, Y. Kitamura, K. Ono, and S. Tarucha, Phys. Rev. Lett. **99**, 096804 (2007).
[13] J. R. Petta, J. M. Taylor, A. C. Johnson, A. Yacoby, M. D. Lukin, C. M. Marcus, M. P. Hanson, and A. C. Gossard, Phys. Rev. Lett. **100**, 067601 (2008).
[14] J. Iñarrea, G. Platero, and A. H. MacDonald, Phys. Rev. B **76**, 085329 (2007).
[15] F. H. L. Koppens, J. A. Folk, J. M. Elzerman, R. Hanson, L. H. Willems van Beveren, I. T. Vink, H. P. Tranitz, W. Wegschneider, L. P. Kouwenhoven, and L. M. K. Vandersypen, Science **309**, 1346 (2005).
[16] K. Ono and S. Tarucha, Phys. Rev. Lett. **92**, 256803 (2004).
[17] A. Pfund, I. Shorubalko, K. Ensslin, and R. Leturcq, Phys. Rev. Lett. **99**, 036801 (2007).
[18] T. Kobayashi, K. Hitachi, S. Sasaki, and K. Muraki, Phys. Rev. Lett. **107**, 216802 (2011).
[19] K. Ono, D. G. Austing, Y. Tokura, and S. Tarucha, Science **297**, 1313 (2002).
[20] M. S. Rudner and L. S. Levitov, Phys. Rev. Lett. **99**, 036602 (2007).
[21] M. Eto, T. Ashiwa, and M. Murata, J. Phys. Soc. Jpn. **73**, 307 (2004).
[22] H. Christ, J. I. Cirac, and G. Giedke, Phys. Rev. B **75**, 155324 (2007).
[23] R. H. Dicke, Phys. Rev. **93**, 99 (1954).
[24] M. Gross and S. Haroche, Phys. Rep. **93**, 301 (1982).
[25] P. Recher, E. V. Sukhorukov, and Daniel Loss, Phys. Rev. Lett. **85**, 1962 (2000).
[26] R. Hanson, L. M. K. Vandersypen, L. H. Willems van Beveren, J. M. Elzerman, I. T. Vink, and L. P. Kouwenhoven, Phys. Rev. B **70**, 241304(R) (2004).
[27] E. M. Kessler, S. Yelin, M. D. Lukin, J. I. Cirac, and G. Giedke, Phys. Rev. Lett. **104**, 143601 (2010).
[28] J. Schliemann, A. Khaetskii, and Daniel Loss, J. Phys.: Condens. Matter **15**, R1809 (2003).
[29] H. Bruus and K. Flensberg, *Many-Body Quantum Theory in Condensed Matter Physics* (Oxford University Press, New York, 2006).
[30] Y. Yamamoto and A. Imamoglu, *Mesoscopic Quantum Optics* (Wiley, New York, 1999).
[31] S. Welack, M. Esposito, U. Harbola, and S. Mukamel, Phys. Rev. B **77**, 195315 (2008).
[32] J. M. Taylor, J. R. Petta, A. C. Johnson, A. Yacoby, C. M. Marcus, and M. D. Lukin, Phys. Rev. B **76**, 035315 (2007).
[33] C. Cohen-Tannoudji, J. Dupont-Roc, and G. Grynberg, *Atom-Photon Interactions: Basic Processes and Applications* (Wiley, New York, 1992).
[34] C. Timm (private communication).
[35] C. Timm, Phys. Rev. B **77**, 195416 (2008).
[36] U. Harbola, M. Esposito, and S. Mukamel, Phys. Rev. B **74**, 235309 (2006).
[37] H.-A. Engel and D. Loss, Phys. Rev. B **65**, 195321 (2002).
[38] N. Zhao, J.-L. Zhu, R.-B. Liu, and C. P. Sun, New J. Phys. **13**, 013005 (2011).
[39] S. A. Gurvitz and Ya. S. Prager, Phys. Rev. B **53**, 15932 (1996).
[40] S. A. Gurvitz, Phys. Rev. B **57**, 6602 (1998).
[41] H. Bluhm, S. Foletti, I. Neder, M. Rudner, D. Mahalu, V. Umansky, and A. Yacoby, Nat. Phys. **7**, 109 (2010).
[42] G. S. Agrawal, Phys. Rev. A **4**, 1791 (1971).
[43] C. Leonardi and A. Vaglica, Nuovo Cimento Soc. Ital. Fis. B **67**, 256 (1982).
[44] V. V. Temnov and U. Woggon, Phys. Rev. Lett. **95**, 243602 (2005).
[45] D. A. Bagrets and Yu. V. Nazarov, Phys. Rev. B **67**, 085316 (2003).
[46] M. Esposito, U. Harbola, and S. Mukamel, Rev. Mod. Phys. **81**, 1665 (2009).
[47] C. Emary, C. Pöltl, A. Carmele, J. Kabuss, A. Knorr, and T. Brandes, Phys. Rev. B **85**, 165417 (2012).
[48] L. D. Contreras-Pulido and R. Aguado, Phys. Rev. B **81**, 161309(R) (2010).
[49] H. J. Carmichael, *Statistical Methods in Quantum Optics 1* (Springer, Berlin, 1999).
[50] R. Hanson, B. Witkamp, L. M. K. Vandersypen, L. H. Willems van Beveren, J. M. Elzerman, and L. P. Kouwenhoven, Phys. Rev. Lett. **91**, 196802 (2003).
[51] For finite polarization the initial covariance matrix has been determined heuristically from the dark-state condition $\langle A^- A^+ \rangle = 0$ in the homogeneous limit.
[52] D. Paget, Phys. Rev. B **25**, 4444 (1982).
[53] T. Ota, G. Yusa, N. Kumada, S. Miyashita, T. Fujisawa, and Y. Hirayama, Appl. Phys. Lett. **91**, 193101 (2007).
[54] R. Takahashi, K. Kono, S. Tarucha, and K. Ono, Phys. Rev. Lett. **107**, 026602 (2011).
[55] This limit is realized if strong nuclear dephasing processes prevent the coherence buildup of the SR evolution.
[56] H. J. Carmichael, J. Phys. B **13**, 3551 (1980).
[57] S. Morrison and A. S. Parkins, Phys. Rev. A **77**, 043810 (2008).
[58] E. M. Kessler, G. Giedke, A. Imamoglu, S. F. Yelin, M. D. Lukin, and J. I. Cirac, Phys. Rev. A **86**, 012116 (2012).
[59] C.-H. Chung, K. Le Hur, M. Vojta, and P. Wölfle, Phys. Rev. Lett. **102**, 216803 (2009).
[60] L. Borda, G. Zarand, and D. Goldhaber-Gordon, arXiv:cond-mat/0602019.
[61] A. J. Leggett, S. Chakravarty, A. T. Dorsey, M. P. A. Fisher, A. Garg, and W. Zwerger, Rev. Mod. Phys. **59**, 1 (1987).
[62] M. S. Rudner and L. S. Levitov, Phys. Rev. B **82**, 155418 (2010).
[63] J. I. Cirac, R. Blatt, P. Zoller, and W. D. Phillips, Phys. Rev. A **46**, 2668 (1992).

PHYSICAL REVIEW A **86**, 012116 (2012)

Dissipative phase transition in a central spin system

E. M. Kessler,[1] G. Giedke,[1,2] A. Imamoglu,[3] S. F. Yelin,[4,5] M. D. Lukin,[5] and J. I. Cirac[1]
[1]*Max-Planck-Institut für Quantenoptik, Hans-Kopfermann-Strasse 1 85748 Garching, Germany*
[2]*M5, Fakultät für Mathematik, TU München, L.-Boltzmannstrasse 1, 85748 Garching, Germany*
[3]*Institute of Quantum Electronics, ETH-Zürich, CH-8093 Zürich, Switzerland*
[4]*Department of Physics, University of Connecticut 2152 Hillside Road, U-3046 Storrs, Connecticut 06269-3046, USA*
[5]*Department of Physics, Harvard University, Cambridge, Massachusetts 02138, USA*
(Received 15 May 2012; published 23 July 2012)

We investigate dissipative phase transitions in an open central spin system. In our model the central spin interacts coherently with the surrounding many-particle spin environment and is subject to coherent driving and dissipation. We develop analytical tools based on a self-consistent Holstein-Primakoff approximation that enable us to determine the complete phase diagram associated with the steady states of this system. It includes first- and second-order phase transitions, as well as regions of bistability, spin squeezing, and altered spin-pumping dynamics. Prospects of observing these phenomena in systems such as electron spins in quantum dots or nitrogen-vacancy centers coupled to lattice nuclear spins are briefly discussed.

DOI: 10.1103/PhysRevA.86.012116 PACS number(s): 03.65.Yz, 05.30.Rt, 64.60.Ht

I. INTRODUCTION

Statistical mechanics classifies phases of a given system in thermal equilibrium according to its physical properties. It also explains how changes in the system parameters allow us to transform one phase into another, sometimes abruptly, which results in the phenomenon of phase transitions. A special kind of phase transitions occur at zero temperature: such transitions are driven by quantum fluctuations instead of thermal ones and are responsible for the appearance of exotic quantum phases in many areas of physics. These quantum phase transitions have been a subject of intense research in the last 30 years, and are expected not only to explain interesting behavior of systems at low temperature, but also to lead to new states of matter with desired properties (e.g., superconductors, -fluids, and -solids, topological insulators [1–6]).

Phase transitions can also occur in systems away from their thermal equilibrium. For example, this is the case when the system interacts with an environment and, at the same time, is driven by some external coherent source. Due to dissipation, the environment drives the system to a steady state, $\rho_0(g)$, which depends on the system and environment parameters, g. As g is changed, a sudden change in the system properties may occur, giving rise to a so-called *dissipative phase transition* (DPT) [7–14]. DPTs have been much less studied than traditional or quantum ones. With the advent of new techniques that allow them to be observed experimentally, they are starting to play an important role [15]. Moreover, they offer the intriguing possibility of observing critical effects nondestructively because of the constant intrinsic exchange between system and environment [16]. In equilibrium statistical mechanics a large variety of toy models exist that describe different kind of transitions. Their study led to a deep understanding of many of them. In contrast, in the case of DPT few models have been developed.

The textbook example of a DPT occurs in the Dicke model of resonance fluorescence [7,17]. There, a system of spins interacts with a thermal reservoir and is externally driven. Experimental [18] and theoretical studies [19–22] revealed interesting features such as optical multistability, first- and second-order phase transitions, and bipartite entanglement.

In this paper, we analyze another prototypical open system: The model is closely related to the central spin system which has been thoroughly studied in thermal equilibrium [23–25]. In its simplest form, it consists of a set of spin-$\frac{1}{2}$ particles (in the following referred to as the *nuclear spins*), uniformly coupled to a single spin-$\frac{1}{2}$ (referred to as the *electron spin*). In the model we consider, the central spin is externally driven and decays through interaction with a Markovian environment. Recently, the central spin model has found application in the study of solid-state systems such as electron and nuclear spins in a quantum dot [25] or a nitrogen-vacancy center.

In what follows, we first provide a general framework for analyzing DPT in open systems. In analogy with the analysis of low-energy excitations for closed systems, it is based on the study of the excitation gap of the system's Liouville operator $\mathcal{L}$. We illustrate these considerations using the central spin model. For a fixed dissipation strength γ, there are two external parameters one can vary: the Rabi frequency of the external driving field, Ω, and the Zeeman shift, ω. We present a complete phase diagram as a function of those parameters, characterize all the phases, and analyze the phase transitions occurring among them. To this end, we develop a series of analytical tools, based on a self-consistent Holstein-Primakoff approximation, which allows us to understand most of the phase diagram. In addition, we use numerical methods to investigate regions of the diagram where the theory yields incomplete results. Combining these techniques, we can identify two different types of phase transitions and regions of bistability, spin squeezing, and enhanced spin polarization dynamics. We also identify regions where anomalous behavior occurs in the approach to the steady state. Intriguingly, recent experiments with quantum dots, in which the central (electronic) spin is driven by a laser and undergoes spontaneous decay, realize a situation very close to the one we study here and show effects such as bistability, enhanced fluctuations, and abrupt changes in polarization in dependence of the system parameters [26,27].

 ©2012 American Physical Society

This paper is organized as follows. Section II sets the general theoretical framework underlying our study of DPT. Section III introduces the model and contains a structured summary of the main results. In Sec. IV we develop the theoretical techniques and use those techniques to analyze the various phases and classify the different transitions. Thereafter, in Sec. V numerical techniques are employed to explain the features of the phase diagram which are not captured by the previous theory. Possible experimental realizations and a generalization of the model to inhomogeneous coupling are discussed in Sec. VI. Finally, we summarize the results and discuss potential applications in Sec. VII.

II. GENERAL THEORETICAL FRAMEWORK

The theory of quantum phase transitions in closed systems is a well-established and extensively studied area in the field of statistical mechanics. The typical scenario is the following: a system is described by a Hamiltonian, $H(g)$, where g denotes a set of systems parameters (like magnetic fields, interactions strengths, etc.). At zero temperature and for a fixed set of parameters, g, the system is described by a quantum state, $\psi_0(g)$, fulfilling $[H(g) - E_{\psi_0}(g)]|\psi_0(g)\rangle = 0$, where $E_{\psi_0}(g)$ is the ground-state energy. As long as the Hamiltonian is gapped (i.e., the difference between $E_0(g)$ and the first excitation energy is finite), any small change in g will alter the physical properties related to the state $|\psi_0(g)\rangle$ smoothly and we remain in the same phase. However, if the first excitation gap $\Delta = E_{\psi_1}(g) - E_{\psi_0}(g)$ closes at a given value of the parameters, $g = g_0$, it may happen that the properties change abruptly, in which case a phase transition occurs.

In the following we adapt analogous notions to the case of DPT and introduce the concepts required for the subsequent study of a particular example of a generic DPT in a central spin model.

We consider a Markovian open system, whose evolution is governed by a time-independent master equation $\dot{\rho} = \mathcal{L}(g)\rho$. The dynamics describing the system are contractive, implying the existence of a steady state. This steady state $\rho_0(g)$ is a zero eigenvector to the Liouville superoperator $\mathcal{L}(g)\rho_0(g) = 0$. This way of thinking parallels that of quantum phase transitions, if one replaces $[H(g) - E_{\psi_0}(g)] \to \mathcal{L}(g)$. Despite the fact that these mathematical objects are very different (the first is a Hermitian operator, and the second a Hermiticity-preserving superoperator), one can draw certain similarities between them. For instance, for an abrupt change of $\rho_0(g)$ (and thus of certain system observables) it is necessary that the gap in the (in general complex) excitation spectrum of the system's Liouville operator $\mathcal{L}(g)$ closes. The relevant gap in this context is determined by the eigenvalue with largest real part different from zero (it can be shown that $\mathrm{Re}(\lambda) \leqslant 0$ for all eigenvalues of $\mathcal{L}$ [28]). The vanishing of the real part of this eigenvalue—from here on referred to as *asymptotic decay rate* (ADR) [29]—indicates the possibility of a nonanalytical change in the steady state and thus is a necessary condition for a phase transition to occur.

In our model system, the Liouvillian low-excitation spectrum, and the ADR in particular, can in large parts of the phase diagram be understood from the complex energies of a stable Gaussian mode of the nuclear field. We find first-order transitions where the eigenvalue of this stable mode crosses the eigenvalue of a metastable mode at zero in the projection onto the real axis. The real part of the Liouvillian spectrum closes *directly* as the stable mode turns metastable and vice versa. A finite difference in the imaginary parts of the eigenvalues across the transition prevents a mixing of the two modes and the emergence of critical phenomena, such as a change in the nature of the steady-state correlations at the critical point. In contrast, we also find a second-order phase transition where the ADR vanishes *asymptotically* as both mode energies become zero (in both real and imaginary part) in the thermodynamic limit. At this critical point a true degeneracy emerges in the Liouvillian spectrum and mixing of the two modes point gives rise to diverging correlations in the nuclear system. This observation parallels the classification of quantum phase transitions in closed systems. There, a direct crossing of the ground- and first-excited-state energy for finite systems (mostly arising from a symmetry in the system) typically gives rise to a first-order phase transition. An asymptotical closing of the first excitation gap of the Hamiltonian in the thermodynamic limit represents the generic case of a second-order transition [30].

Besides the analogies described so far [cf. Table I], there are obvious differences, like the fact that in DTP $\rho_0(g)$ may be pure or mixed, and that some of the characteristic behavior of a phase may also be reflected in how the steady state is

TABLE I. Nonexhaustive comparison of thermal phase transitions (TPTs), quantum phase transitions (QPTs), and DPTs. The concepts for DPTs parallel in many respects the considerations for QPTs and TPTs. $||\cdot||_{\mathrm{tr}}$ denotes the trace norm and S the entropy. Note that if the steady state is not unique, additional steady states may come with a nonzero imaginary part of the eigenvalue and then appear in pairs: $\mathcal{L}\rho = \pm iy\rho$ ($y \in \mathbb{R}$).

	TPT	QPT	DPT
System	Hamiltonian	Hamiltonian	Liouvillian
operator	$H = H^\dagger$	$H = H^\dagger$	$\mathcal{L}$–Lindblad
Relevant	Free energy	Energy eigenvalues	"Complex energy" eigenvalues
quantity	$F(\rho) = \langle H\rangle_\rho - T\langle S\rangle_\rho$	$E_\psi : H\|\psi\rangle = E_\psi\|\psi\rangle$	$\lambda_\rho : \mathcal{L}\rho = \lambda_\rho\rho$
	Gibbs state	Ground state	Steady state
State	$\rho_T = \underset{\rho\geqslant 0,\mathrm{Tr}(\rho)=1}{\mathrm{argmin}}\ [F(\rho)]$	$\|\psi_0\rangle = \underset{\|\psi\|=1}{\mathrm{argmin}}[\langle\psi\|H\|\psi\rangle]$	$\rho_0 = \underset{\|\rho\|_{\mathrm{tr}}=1}{\mathrm{argmin}}[\|\mathcal{L}\rho\|_{\mathrm{tr}}]$
	$\rho_T \propto \exp[-H/k_BT]$	$[H - E_{\psi_0}]\|\psi_0\rangle = 0$	$\mathcal{L}\rho_0 = 0$
Phase transition	Nonanalyticity in $F(\rho_T)$	$\Delta = E_{\psi_1} - E_{\psi_0}$ vanishes	ADR $= \max[\mathrm{Re}(\lambda_\rho)]$ vanishes

approached. Nonanalyticities in the higher excitation spectrum of the Liouvillian are associated to such dynamical phases.

III. MODEL AND PHASE DIAGRAM

A. The model

We investigate the steady-state properties of a homogeneous central spin model. The central spin—also referred to as electronic spin in the following—is driven resonantly via suitable optical or magnetic fields. Dissipation causes electronic spin transitions from the spin-up to the spin-down state. It can be introduced via standard optical pumping techniques [31,32]. Furthermore, the central spin is assumed to interact with an ensemble of ancilla spins—also referred to as nuclear spins in view of the mentioned implementations [25]—by an isotropic and homogeneous Heisenberg interaction. In general, this hyperfine interaction is assumed to be detuned. Weak nuclear magnetic dipole-dipole interactions are neglected.

After a suitable transformation which renders the Hamiltonian time-independent, the system under consideration is governed by the master equation

$$\begin{aligned}\dot{\rho} &= \mathcal{L}\rho \\ &= J\gamma\left(S^-\rho S^+ - \tfrac{1}{2}\{S^+S^-,\rho\}\right) - i[H_S + H_I + H_{SI},\rho],\end{aligned} \tag{1}$$

where $\{\cdot,\cdot\}$ denotes the anticommutator and

$$H_S = J\Omega(S^+ + S^-), \tag{2}$$

$$H_I = \delta\omega I_z, \tag{3}$$

$$H_{SI} = a/2(S^+I^- + S^-I^+) + aS^+S^-I_z. \tag{4}$$

S^α and I^α ($\alpha = +,-,z$) denote electron and collective nuclear spin operators, respectively. Collective nuclear operators are defined as the sum of N individual nuclear operators $I^\alpha = \sum_{i=1}^{N}\sigma_i^\alpha$. $J\Omega$ is the Rabi frequency of the resonant external driving of the electron (in rotating wave approximation), while $\delta\omega = \omega - a/2$ is the difference of hyperfine detuning ω and half the individual hyperfine coupling strength a. $\delta\omega$, for instance, can be tuned via static magnetic fields in the z direction. Note that $H_I + H_{SI} = a\vec{S}\vec{I} + \omega I_z$, describing the isotropic hyperfine interaction and its detuning. The rescaling of the electron driving and dissipation in terms of the total (nuclear) spin quantum number J[1] is introduced here for convenience and will be justified later. Potential detunings of the electron driving—corresponding to a term ΔS_z in the Hamiltonian part of the master equation—can be neglected if $\Delta \ll Ja$.

In the limit of strong dissipation $\gamma \gg a$ the electron degrees of freedom can be eliminated and Eq. (1) reduces to

$$\begin{aligned}\dot{\sigma} := \mathrm{Tr}_S(\dot{\rho}) = \gamma_{\mathrm{eff}}&\left(I^-\sigma I^+ - \frac{1}{2}\{I^+I^-,\sigma\}\right) \\ &- i[\Omega_{\mathrm{eff}}I_y + \delta\omega I_z],\end{aligned} \tag{5}$$

where $\gamma_{\mathrm{eff}} = \frac{a^2}{\gamma}$, $\Omega_{\mathrm{eff}} = \frac{\Omega a}{2\gamma}$, and σ is the reduced density matrix of the nuclear system. This is a generalization of the Dicke model of resonance fluorescence as discussed in [7,10,22].

Master Eq. (1) has been theoretically shown to display cooperative nuclear effects such as superradiance (even for inhomogeneous electron nuclear coupling) [33] and nuclear spin squeezing [34] in the transient evolution. In analogy to the field of cooperative resonance fluorescence, the system's rich steady-state behavior comprises various critical effects such as first- and second-order DPT and bistabilities. In the following we provide a qualitative summary of the phase diagram and of the techniques developed to study the various phases and transitions.

B. Phenomenological description of the phase diagram

For a fixed dissipation rate $\gamma = a$ the different phases and transitions of the system are displayed schematically in Fig. 1 in dependence on the external driving Ω and the hyperfine detuning ω. We stress the point that none of the features discussed in the following depends critically on this particular value of the dissipation. In Appendix A we discuss briefly the quantitative changes in the phase diagram for moderately lower (higher) values of γ. Further, we concentrate our studies on the quadrant $\Omega,\omega > 0$, in which all interesting features can be observed. In the following, we outline the key features of the phase diagram.

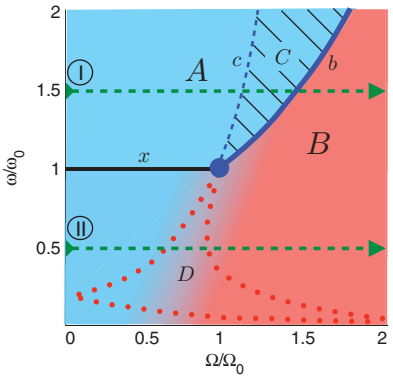

FIG. 1. (Color online) Schematic of the different phases and transitions of master Eq. (1). In the two main phases of the system A (blue) and B (red)—which together cover the whole phase diagram—the system is found in a RSTSS (cf. text). While phase A is characterized by normal spin-pumping behavior (large nuclear polarization in the direction of the dissipation) and a low effective temperature, phase B displays anomalous spin-pumping behavior (large nuclear polarization in opposing direction to the dissipation) and high temperature. They are separated by the first-order phase boundary b, which is associated with a region of bistability C (framed by the boundary c). Here a second non-Gaussian solution appears, besides the normal spin-pumping mode of A. The region of bistability C culminates in a second-order phase transition at (ω_0,Ω_0). Below this critical point the system is supercritical and no clear distinction between phases A and B exists. In this region a dynamical phase D emerges, characterized by anomalous behavior in the approach to the steady state. For a detailed description of the different phases and transitions, see Sec. III B.

[1]Note that the total spin quantum number J is conserved under the action of $\mathcal{L}$.

First we consider the system along the line segment x ($\omega = \omega_0, \Omega \leqslant \Omega_0$), where $\Omega_0 = \omega_0 = a/2$ (a is the individual hyperfine coupling constant) define a critical driving strength and critical hyperfine detuning, respectively. Here H_I vanishes and the steady state can be constructed analytically as a zero-entropy factorized state of the electron and nuclear system. The nuclear field builds up to compensate for the external driving—forcing the electron in its dark state $|\downarrow\rangle$—until the maximal polarization is reached at the critical value Ω_0. Above this point the nuclear system cannot compensate for the driving Ω anymore and a solution of a different nature, featuring finite electron inversion and entropy is found. The point Ω_0 shows diverging spin entanglement and is identified below as a second-order phase transition.

For the separable density matrix $\rho_0 = |\psi\rangle\langle\psi|$, $|\psi\rangle = |\downarrow\rangle \otimes |\alpha\rangle$ the only term in master Eq. (1) which is not trivially zero is the Hamiltonian term $S^+(\frac{a}{2} I^- + J\Omega)$. However, choosing $|\alpha\rangle$ as an approximate eigenstate of the lowering operator $I^-|\alpha\rangle \approx \alpha|\alpha\rangle$ (up to second order in $\epsilon = 1/\sqrt{J}$) with $\alpha = -2J\Omega/a \equiv -J\Omega/\Omega_0$, the corresponding term in Eq. (1) vanishes in the thermodynamic limit. In Appendix B 1 we demonstrate that approximate eigenstates $|\alpha\rangle$ can be constructed as squeezed and displaced vacua in a Holstein-Primakoff [35] picture up to a correction of order $1/J$. The squeezing of the nuclear state depends uniquely on the displacement such that these states represent a subclass of *squeezed coherent atomic states* [36]. Remarkably, this solution—where along the whole segment x the system settles in a separable pure state—exists for all values of the dissipation strength γ.

In the limit of vanishing driving $\Omega = 0$ the steady state trivially is given by the fully polarized state (being the zero eigenstate of the lowering operator), as the model realizes a standard optical spin-pumping setting for dynamical nuclear polarization [37]. With increasing Ω, the collective nuclear spin is rotated around the y axis on the surface of the Bloch sphere such that the effective Overhauser field in the x direction compensates exactly for the external driving field on the electron spin. As a consequence along the whole segment x the dissipation forces the electron in its dark state $|\downarrow\rangle$, and all electron observables, but also the entropy and some nuclear observables, are independent of Ω.

Furthermore, the steady state displays increased nuclear spin squeezing in the y direction (orthogonal to the mean polarization vector) when approaching the critical point. A common measure of squeezing is defined via the spin fluctuations orthogonal to the mean polarization of the spin system. A state of a spin-J system is called spin squeezed [36] if there exists a direction $\vec{n}$ orthogonal to the mean spin polarization $\langle\vec{I}\rangle$ such that

$$\xi_{\vec{n}}^2 \equiv 2\langle \Delta I_{\vec{n}}^2 \rangle / |\langle \vec{I} \rangle| < 1. \tag{6}$$

In [38] it was shown that every squeezed state also contains entanglement among the individual constituents. Moreover, if $\xi_{\vec{n}}^2 < \frac{1}{k}$ then the spin-squeezed state contains k-particle entanglement [39–41]. In Appendix B 1 we show that the squeezing parameter in the y direction for an approximate I^- eigenstate $|\alpha\rangle$ is given as $\xi_{\hat{e}_y}^2 = \sqrt{1-\alpha^2/J^2} + O(1/J) = \sqrt{1-(\Omega/\Omega_0)^2} + O(1/J)$. Note, however, that this equation is valid only for $\xi_{\hat{e}_y}^2 \geqslant 1/\sqrt{J}$. For higher squeezing the operator expectation values constituting the term of order $O(1/J)$ can attain macroscopic values of order $\sqrt{J}$. For $\Omega \lesssim \Omega_0$ we find that the nuclear spins are in a highly squeezed minimum uncertainty state, with k-particle entanglement.[2] Close to the critical point k becomes of the order of $\sqrt{J}$ [$\xi_{\hat{e}_y}^2 = O(1/\sqrt{J})$], indicating diverging entanglement in the system.

Since the lowering operator is bounded ($||I^-|| \leqslant J$), at $\Omega = \Omega_0$ where the nuclear field has reached its maximum value, the zero entropy solution constructed above ceases to exist. For large electron driving, where $\Omega \gg \Omega_0$ sets the dominant energy scale, the dissipation γ results in an undirected diffusion in the dressed state picture and in the limit $\Omega \to \infty$ the system's steady state is fully mixed. In order to describe the system for driving strength $\Omega > \Omega_0$, in Sec. IV A we develop a perturbative theory designed to efficiently describe a class of steady states where the electron and nuclear spins are largely decoupled and the nuclear system is found in a fully polarized and rotated state with potentially squeezed, thermal Gaussian fluctuations (also referred to as *rotated squeezed thermal spin states (RSTSS)* or the *Gaussian mode*). It is fully characterized by its mean polarization as well as the spin squeezing and effective temperature T_{eff} of the fluctuations (cf. Appendix C). Squeezed coherent atomic states, which constitute the solution along segment x, appear as a limiting case of this class for zero temperature $T_{\text{eff}} = 0$.

In order to describe these RSTSS solutions, we conduct a systematic expansion of the system's Liouville operator in orders of the system size $1/\sqrt{J}$, by approximating nuclear operators by their semiclassical values and incorporating bosonic fluctuations up to second order in an Holstein-Primakoff picture. The resulting separation of time scales between electron and nuclear dynamics is exploited in a formalized adiabatic elimination of the electron degrees of freedom. The semiclassical displacements (i.e., the electron and nuclear direction of polarization) are found self-consistently by imposing first-order stability of the nuclear fluctuations and correspond to the nuclear and electron steady-state expectation values derived from the semiclassical Bloch equations (i.e., after a brute force factorization $\langle S_i I_j\rangle \to \langle S_i\rangle\langle I_j\rangle$, for $i,j = x,y,z$) in the equations of motion (cf. Appendix D). For a given set of semiclassical solutions we derive a second-order reduced master equation for the nuclear fluctuations which, in the thermodynamic limit, contains all information on the nuclear state's stability, its steady-state quantum fluctuations and entanglement, as well as the low excitation dynamics in the vicinity of the steady state and thus allows for a detailed classification of the different phases and transitions.

Using this formalism, we find that the system enters a new phase at the critical point Ω_0, in which the nuclear field can no longer compensate for the external driving, leading to a finite electron inversion and a nuclear state of rising temperature

[2] As in Ref. [40] we call a pure state $|\psi\rangle$ of N-qubits k-particle entangled if $|\psi\rangle$ is a product of states $|\psi_l\rangle$ each acting on at most k qubits and at least one of these does not factorize. A mixed state is at least k-particle entangled if it cannot be written as a mixture of $l < k$-particle entangled states.

for increasing driving strength. At the transition between the two phases, the properties of the steady state change nonanalytically and in Sec. IV B2 we will find an asymptotic closing of the Liouvillian gap (cf. Sec. II) at the critical point, as the Liouvillian's spectrum becomes continuous in the thermodynamic limit. Below we characterize the critical point (ω_0, Ω_0) as a second-order phase transition.

Allowing for arbitrary hyperfine detunings ω, a phase boundary emerges from the second-order critical point (line b in Fig. 1), separating two distinct phases A (blue) and B (red) of the Gaussian mode. The subregion C of A indicates a region of bistability associated with the phase boundary b and is discussed below.

At $\Omega = 0$ the semiclassical equations of motion feature two steady-state solutions. Not only the trivial steady state of the spin-pumping dynamics—the fully polarized state in the $-z$ direction—but also an inverted state where the nuclear system is fully polarized in the$+z$ direction is a (unstable) solution of the semiclassical system. Quantum fluctuations account for the decay of the latter solution of anomalous spin-pumping behavior. The two semiclassical solutions (the corresponding quantum states are from here on referred to as the *normal* and *anomalous spin-pumping modes*, respectively) persist for finite Ω. As we show employing the formalism described above (Sec. IV B3), quantum fluctuations destabilize the mode of anomalous behavior in region A of the phase diagram. The stable Gaussian solution in phase A displays a behavior characterized by the competition of dissipation γ and the onsetting driving field Ω. The nuclear state is highly polarized in the direction set by the decay, and the electron spin starts aligning with the increasing external driving field. Furthermore, the normal spin-pumping mode of phase A is characterized by a low effective spin temperature.

The analysis of the low excitation spectrum of the Liouvillian (Sec. IV B4) shows a direct vanishing of the ADR at the phase boundary b between A and B, while the imaginary part of the spectrum is gapped at all times. At this boundary, the normal mode of phase A destabilizes while at the same the metastable anomalous mode turns stable defining the second phase B. The two mode energies are nondegenerate across the transition preventing a mixing of the two modes and the emergence of critical phenomena such as diverging entanglement in the system. Phase B—anomalous spin pumping—is characterized by a large nuclear population inversion, as the nuclear field builds up in opposite direction of the dissipation. At the same time the electron spin counter aligns with the external driving field Ω. In contrast to the normal mode of phase A, phase B features large fluctuations (i.e., high effective temperature) in the nuclear state, which increase for high Ω, until at some point the perturbative description in terms of RSTSS breaks down and the system approaches the fully mixed state. Note that region A also transforms continuously to B via the lower two quadrants of the phase diagram (Fig. 1). In this supercritical region [42] no clear distinction between the two phases exist.

To complete the phase diagram, we employ numerical techniques in order to study steady-state solutions that go beyond a RSTSS description in Sec. V. The subregion of A labeled C indicates a region of bistability where a second steady-state solution (besides the normal spin-pumping Gaussian solution described above) appears, featuring a non-Gaussian character with large fluctuations of order J. Since this mode cannot be described by the perturbative formalism developed in Sec. IV (which by construction is only suited for low fluctuations $\ll J$) we use numerical methods to study this mode in Sec. V for finite systems. We find that the non-Gaussian mode (in contrast to the Gaussian mode of region A) is polarized in the $+z$ direction and features large fluctuations of the order of J. Additionally this solution displays large electron-nuclear connected correlations $\langle S_i I_j \rangle - \langle S_i \rangle \langle I_j \rangle$. It emerges from the anomalous spin-pumping mode coming from region B and the system shows hysteretic behavior in region C closely related to the phenomenon of optical bistability [43].

A fourth region is found in the lower half of the phase diagram (D). In contrast to the previous regions, area D has no effects on steady-state properties. Instead, the region is characterized by an anomalous behavior in the low excitation dynamics of the system. The elementary excitations in region D are overdamped. Perturbing the system from its steady state leads to a nonoscillating exponential return. This behavior is discussed at the end of Sec. IV B3, where we study the low excitation spectrum of the Liouvillian in this region within the perturbative approach.

In summary, all the phases and transitions of the system are displayed in Fig. 1. Across the whole phase diagram one solution can be described as a RSTSS, a largely factorized electron-nuclear state with rotated nuclear polarization and Gaussian fluctuations. Phase A hereby represents a region of normal spin-pumping behavior. The system is found in a cold Gaussian state, where the nuclear spins are highly polarized in the direction set by the electron dissipation and the electron spin aligns with the external driving for increasing field strength. In contrast, phase B displays anomalous spin-pumping behavior. The nuclear system displays population inversion (i.e., a polarization opposing the electron pumping direction) while the electron aligns in opposite direction of the driving field. Furthermore, the state becomes increasingly noisy, quantified by a large effective temperature, which results in a fully mixed state in the limit of large driving strength $\Omega \to \infty$. Along segment x the state becomes pure and factorizes exactly with a nuclear field that cancels the external driving exactly. The nuclear state can be described using approximate eigenstates of the lowering operator I^- which display diverging squeezing approaching the second-order critical point Ω_0. From this critical point a first-order phase boundary emerges separating phases A and B. It is associated with a region of bistability (area C), where a second solution appears featuring a highly non-Gaussian character. The system shows hysteretic behavior in this region. Region D is a phase characterized by its dynamical properties. The system shows an overdamping behavior approaching the steady state, which can be inferred from the excitation spectrum of the Liouvillian.

Let us now describe the phases and transitions involving the Gaussian mode in detail.

IV. PERTURBATIVE TREATMENT OF THE GAUSSIAN MODE

As seen in the previous section along the segment x the system settles in a factorized electronic-nuclear state, where

the nuclear system can be described as a lowering operator eigenstate up to second order in $\epsilon = J^{-1/2}$. Motivated by this result, we develop in Sec. IV A a perturbative theory based on a self-consistent Holstein-Primakoff transformation that enables the description of a class of steady states, which generalizes the squeezed coherent atomic state solution along x to finite thermal fluctuations (RSTSS, Appendix C). A solution of this nature can be found across the entire phase diagram and we show that this treatment becomes exact in the thermodynamic limit.

In Sec. IV B we discuss this Gaussian mode across the whole phase diagram. Steady-state properties of the nuclear fluctuations derived from a reduced second-order master equation provide deep insights in the nature of the various phases and transitions. Observed effects include criticality in both the steady state and the low-excitation spectrum, spin squeezing and entanglement, as well as altered spin-pumping dynamics. Whenever feasible we compare the perturbative results with exact diagonalization techniques for finite systems and find excellent agreement even for systems of a few hundred spins only. First, in Sec. IV B2 we apply the developed theory exemplarily along the segment x to obtain further insights in the associated transition at Ω_0. In Sec. IV B3 we then give a detailed description of the different phases that emerge in the phase diagram due to the Gaussian mode. Thereafter, in Sec. IV B4 we conduct a classification of the different transitions found in the phase diagram.

A. The theory

In this section we develop the perturbative theory to derive an effective second-order master equation for the nuclear system in the vicinity of the Gaussian steady state.

For realistic parameters, the Liouville operator $\mathcal{L}$ of Eq. (1) does not feature an obvious hierarchy that would allow for a perturbative treatment. In order to treat the electron-nuclear interaction as a perturbation, we first have to separate the macroscopic semiclassical part of the nuclear fields. To this end we conduct a self-consistent Holstein-Primakoff approximation describing nuclear fluctuations around the semiclassical state up to second order.

The (exact) Holstein-Primakoff transformation expresses the truncation of the collective nuclear spin operators to a total spin J subspace in terms of a bosonic mode (b denotes the respective annihilation operator):

$$\begin{aligned} I^- &= \sqrt{2J - b^\dagger b}\, b, \\ I_z &= b^\dagger b - J. \end{aligned} \tag{7}$$

In the following we introduce a macroscopic displacement $\sqrt{J}\beta \in \mathbb{C}$ ($|\beta| \leqslant 2$) on this bosonic mode to account for a rotation of the mean polarization of the state, expand the operators of Eq. (7) and accordingly the Liouville operator of equation Eq. (1) in orders of $\epsilon = 1/\sqrt{J}$. The resulting hierarchy in the Liouvillian allows for an perturbative treatment of the leading orders and adiabatic elimination of the electron degrees of freedom whose evolution is governed by the fastest time scale in the system. The displacement β is self-consistently found by demanding first-order stability of the solution. The second order of the new effective Liouvillian then provides complete information on second-order stability, criticality, and steady-state properties in the thermodynamic limit.

The macroscopic displacement of the nuclear mode,

$$b \to b + \sqrt{J}\beta, \tag{8}$$

allows for an expansion of the nuclear operators [Eq. (7)] in orders of ϵ

$$\begin{aligned} I^-/J &= \sqrt{k}\sqrt{1 - \epsilon\frac{\beta b^\dagger + \beta^* b}{k} - \epsilon^2\frac{b^\dagger b}{k}}(\beta + \epsilon b) \\ &= \sum_i \epsilon^i \mathcal{J}_i^-, \end{aligned} \tag{9}$$

where

$$\mathcal{J}_0^- = \sqrt{k}\beta, \tag{10}$$

$$\mathcal{J}_1^- = \frac{1}{2\sqrt{k}}[(2k - |\beta|^2)b - \beta^2 b^\dagger], \tag{11}$$

$$\mathcal{J}_2^- = -\left[\frac{\beta^* b + \beta b^\dagger}{2\sqrt{k}}b + \frac{\sqrt{k}\beta}{8}\left(\left[\frac{\beta b^\dagger + \beta^* b}{k}\right]^2 + 4\frac{b^\dagger b}{k}\right)\right], \tag{12}$$

$$\vdots$$

and $k = 2 - |\beta|^2$. Analogously, one finds

$$I_z/J = \sum_{i=0}^{2} \epsilon^i \mathcal{J}_i^z, \tag{13}$$

$$\mathcal{J}_0^z = |\beta|^2 - 1, \tag{14}$$

$$\mathcal{J}_1^z = \beta b^\dagger + \beta^* b, \tag{15}$$

$$\mathcal{J}_2^z = b^\dagger b. \tag{16}$$

This expansion is meaningful only if the fluctuations in the bosonic mode b are smaller than $O(\sqrt{J})$. Under this condition, any nuclear state is thus fully determined by the state of the bosonic mode b and its displacement β.

According to the above expansions master Eq. (1) can be written as

$$\dot{\rho}/J = [\mathcal{L}_0 + \epsilon\mathcal{L}_1 + \epsilon^2\mathcal{L}_2 + O(\epsilon^3)]\rho, \tag{17}$$

where

$$\begin{aligned} \mathcal{L}_0\rho = \gamma\left(S^-\rho S^+ - \tfrac{1}{2}\{S^+S^-, \rho\}_+\right) - i[S^+(\Omega + a/2\mathcal{J}_0^-) \\ + S^-(\Omega + a/2\mathcal{J}_0^+) + aS^+S^-\mathcal{J}_0^z, \rho], \end{aligned} \tag{18}$$

$$\mathcal{L}_{1,2}\rho = -i[a/2(S^+\mathcal{J}_{1,2}^- + S^-\mathcal{J}_{1,2}^+) + (aS^+S^- + \delta\omega)\mathcal{J}_{1,2}^z, \rho]. \tag{19}$$

The zeroth-order superoperator $\mathcal{L}_0$ acts only on the electron degrees of freedom. This separation of time scales between electron and nuclear degrees of freedom implies that for a given semiclassical nuclear field (defined by the displacement β) the electron settles to a quasisteady state on a time scale shorter than the nuclear dynamics and can be eliminated adiabatically on a coarse-grained time scale. In the following we determine the effective nuclear evolution in the submanifold of the electronic quasisteady states of $\mathcal{L}_0$.

Let P be the projector on the subspace of zero eigenvalues of $\mathcal{L}_0$, that is, the zeroth-order steady states, and $Q = \mathbb{1} - P$. Since $\mathcal{L}_0$ features a unique steady state, we find $P\rho = \mathrm{Tr}_S(\rho) \otimes \rho_{ss}$, where Tr_S denotes the trace over the electronic subspace and $\mathcal{L}_0\rho_{ss} = 0$. By definition it is $P\mathcal{L}_0 = \mathcal{L}_0 P = 0$. After a generalized Schrieffer-Wolff transformation [44], we derive an effective Liouvillian within the zeroth-order steady-state subspace in orders of the perturbation,

$$\mathcal{L}_{\mathrm{eff}} = \epsilon P\mathcal{L}_1 P + \epsilon^2\left(P\mathcal{L}_2 P - P\mathcal{L}_1 Q\mathcal{L}_0^{-1} Q\mathcal{L}_1 P\right) + O(\epsilon^3). \tag{20}$$

After tracing out the electron degrees of freedom the dynamics of the nuclear fluctuations b are consequently governed by the reduced master equation

$$\dot{\sigma} := \mathrm{Tr}_S(P\dot{\rho}) = \mathrm{Tr}_S(\mathcal{L}_{\mathrm{eff}} P\rho). \tag{21}$$

The first-order term in ϵ of Eq. (20) can be readily calculated,

$$\mathrm{Tr}_s(P\mathcal{L}_1 P\rho) = -i[\langle A\rangle_{ss} b + \langle A^\dagger\rangle_{ss} b^\dagger, \sigma], \tag{22}$$

where A is an electronic operator,

$$A = \beta^*(aS^+S^- + \delta\omega) + \frac{a}{4\sqrt{k}}[(2k - |\beta|^2)S^+ - (\beta^*)^2 S^-]. \tag{23}$$

$\langle A\rangle_{ss}$ denotes the steady-state expectation value according to $\mathcal{L}_0$, which depends on the system parameters γ and Ω and on the semiclassical displacement β via optical Bloch equations derived from $\mathcal{L}_0$ as described below. Equation (22) represents a driving of the nuclear fluctuations to leading order in the effective dynamics. Thus, for the steady state to be stable to first order, we demand

$$\langle A\rangle_{ss} = 0. \tag{24}$$

This equation defines self-consistently the semiclassical nuclear displacement β in the steady state in dependence on the system parameters γ, Ω, and $\delta\omega$.

The calculation of the second-order term of Eq. (20) is more involved and presented in Appendix E. We find the effective nuclear master equation to second order,[3]

$$\begin{aligned}\dot{\sigma} = {} & 2R_a\left(b\sigma b^\dagger - \tfrac{1}{2}\{b^\dagger b,\sigma\}\right) + 2R_b\left(b^\dagger\sigma b - \tfrac{1}{2}\{bb^\dagger,\sigma\}\right) \\ & + c\left(b\sigma b - \tfrac{1}{2}\{bb,\sigma\}\right) + c^*\left(b^\dagger\sigma b^\dagger - \tfrac{1}{2}\{b^\dagger b^\dagger,\sigma\}\right) \\ & - i[(I_a + I_b + F)b^\dagger b + (\alpha + B^*)b^2 + (\alpha^* + B)(b^\dagger)^2, \sigma],\end{aligned} \tag{25}$$

with

$$B = -\frac{a\beta}{16\sqrt{k^3}}[(4k + |\beta|^2)\langle S^-\rangle_{ss} + \beta^2\langle S^+\rangle_{ss}], \tag{26}$$

$$\begin{aligned}F = {} & -\frac{a}{8\sqrt{k^3}}(4k + |\beta|^2)(\beta\langle S^+\rangle_{ss} + \beta^*\langle S^-\rangle_{ss}) \\ & + a(\langle S^+S^-\rangle_{ss} + \delta\omega/a),\end{aligned} \tag{27}$$

and

$$\begin{aligned}R_a &= \int_0^\infty dt\,\mathrm{Re}[\langle A^\dagger(t)A(0)\rangle_{ss}], \\ I_a &= \int_0^\infty dt\,\mathrm{Im}[\langle A^\dagger(t)A(0)\rangle_{ss}], \\ R_b &= \int_0^\infty dt\,\mathrm{Re}[\langle A(t)A^\dagger(0)\rangle_{ss}], \\ I_b &= \int_0^\infty dt\,\mathrm{Im}[\langle A(t)A^\dagger(0)\rangle_{ss}], \\ c &= \int_0^\infty dt\,\langle\{A(t),A(0)\}\rangle_{ss}, \\ \alpha &= \frac{1}{2i}\int_0^\infty dt\,\langle[A(t),A(0)]\rangle_{ss}.\end{aligned} \tag{28}$$

For a given set of system parameters the coefficients defining the nuclear dynamics [Eqs. (26), (27), and (28)] depend only on the nuclear displacement β. After choosing β self-consistently to fulfill Eq. (24) in order to guarantee first-order stability, Eq. (25) contains all information of the nuclear system within the Gaussian picture, such as second-order stability as well as purity and squeezing of the nuclear steady state. Also it approximates the Liouville operator's low excitation spectrum to leading order and thus contains information on criticality in the system. Equation (25) therefore forms the basis for the subsequent discussion of the RSTSS mode and the corresponding phases and transitions in Sec. IV.

In order to calculate the coefficients of Eq. (28), we have to determine integrated electronic autocorrelation functions of the type $\int_0^\infty dt\,\langle S^i(t)S^j(0)\rangle_{ss}$ and $\int_0^\infty dt\,\langle S^i(0)S^j(t)\rangle_{ss}$, where $i,j = +,-,z$. The dynamics of single electron operator expectation values are governed by the optical Bloch equations derived from $\mathcal{L}_0$,

$$\frac{d}{dt}\langle\Delta\vec{S}\rangle = \mathcal{M}\langle\Delta\vec{S}\rangle, \tag{29}$$

where $\Delta\vec{S} := \vec{S} - \langle\vec{S}\rangle_{ss}$ and $\vec{S} = (S^+, S^-, S_z)^T$ and

$$\mathcal{M} = \begin{pmatrix} -(\frac{\gamma}{2} - ia\mathcal{L}_0^z) & 0 & -2i\tilde{\Omega}^* \\ 0 & -(\frac{\gamma}{2} + ia\mathcal{L}_0^z) & 2i\tilde{\Omega} \\ -i\tilde{\Omega} & i\tilde{\Omega}^* & -\gamma \end{pmatrix}, \tag{30}$$

where we defined $\tilde{\Omega} = \Omega + \frac{a}{2}\sqrt{k}\beta$ and $\mathcal{L}_0^z$ is given in Eq. (14). The steady-state solutions can readily be evaluated:

$$\langle S^+\rangle_{ss} = 2i\frac{\tilde{\Omega}^*(\gamma + 2ia\mathcal{L}_0^z)}{\gamma^2 + 4a\mathcal{L}_0^{z2} + 8|\tilde{\Omega}|^2}, \tag{31}$$

$$\langle S_z\rangle_{ss} = -\frac{1}{2}\frac{\gamma^2 + 4a\mathcal{L}_0^{z2}}{\gamma^2 + 4a\mathcal{L}_0^{z2} + 8|\tilde{\Omega}|^2}. \tag{32}$$

Defining the correlation matrix $\mathbf{S} = \langle\Delta\vec{S}\Delta\vec{S}^\dagger\rangle_{ss}$ and $\mathbf{S}_t = \langle\Delta\vec{S}_t\Delta\vec{S}^\dagger\rangle_{ss}$, the quantum regression theorem [45] yields the simple result

$$\mathbf{S}_t = e^{\mathcal{M}t}\mathbf{S}, \tag{33}$$

$$\mathbf{S}_t^\dagger = \langle\Delta\vec{S}\Delta\vec{S}_t^\dagger\rangle_{ss} = \mathbf{S}e^{\mathcal{M}^\dagger t}. \tag{34}$$

[3] In [44] it has been shown that this type of master equation is of Lindblad form.

Finally, the time-integrated autocorrelation functions reduce to the simple expression

$$\mathcal{F}_1 = \int_0^\infty dt \mathbf{S}_t = \int_0^\infty dt e^{\mathcal{M}t}\mathbf{S} = -\mathcal{M}^{-1}\mathbf{S}, \quad (35)$$

$$\mathcal{F}_2 = \int_0^\infty dt \mathbf{S}_t^\dagger = \mathcal{F}_1^\dagger = -\mathbf{S}(\mathcal{M}^{-1})^\dagger. \quad (36)$$

These matrices straightforwardly define the coefficients of the effective master equation of the nuclear fluctuations [Eq. (25)]. In Appendix E 1 we provide explicit formulas to calculate the relevant coefficients.

B. Phase diagram of the Gaussian mode

In this section we use the theory developed above to study the RSTSS mode across the phase diagram. As outlined in the previous section we first determine self-consistently possible semiclassical displacements β, which guarantee first-order stability [Eq. (24)]. For each of these solutions we determine the effective master equation for the nuclear fluctuations [Eq. (25)], which in the thermodynamic limit contains all information on the steady state and the low excitation dynamics and we discuss properties like second-order stability, criticality, as well as purity and squeezing of the nuclear steady state. Using this information we provide a complete picture of the various phases and transitions involving the RSTSS solution.

1. Methods and general features

In order to determine the semiclassical displacements β which guarantee first-order stability, we show in Appendix D that Eq. (24) is equivalent to the steady-state conditions derived from the semiclassical Bloch equations of the system. Due to a symmetry in the equation, the steady-state displacements appear in pairs β_-, β_+. Any semiclassical displacement β can be straightforwardly converted to the mean spin polarizations up to leading order in ϵ according to Eqs. (10), (14), (31), and (32). In the thermodynamic limit the two sets of steady-state expectation values extracted from β_- and β_+ share the symmetry $(\pm\langle S_x\rangle, \langle S_y\rangle, \langle S_z\rangle, \langle I_x\rangle, \pm\langle I_y\rangle, \pm\langle I_z\rangle)$. In large parts of the phase diagram the solution β_- (β_+) displays high nuclear polarization in the same (opposite) direction as the the electron spin pumping. We define the corresponding quantum states as the normal (anomalous) spin-pumping mode.

The two solutions $\beta_\pm$ define two corresponding master equations of the nuclear fluctuations around the respective semiclassical expectation values according to Eq. (25). These master equations are subsequently used to determine second-order stability of the nuclear fluctuations and, if the dynamics turn out to be stable, the steady-state properties of the nuclear system. We emphasize that the effective master Eq. (25) not only can be used to determine steady-state properties, but also reproduces accurately the low excitation spectrum of the exact Liouvillian. It thus also describes the system dynamics in the vicinity of the steady state (increasingly accurate for large J).

From Eq. (25) one readily derives a dynamic equation for the first-order bosonic moments

$$\begin{pmatrix} \dot{\langle b\rangle} \\ \langle b^\dagger\rangle \end{pmatrix} = \Sigma \begin{pmatrix} \langle b\rangle \\ \langle b^\dagger\rangle \end{pmatrix}, \quad (37)$$

with

$$\Sigma = \begin{pmatrix} -(R_a - R_b) - i\chi & -2i\xi \\ 2i\xi^* & -(R_a - R_b) + i\chi \end{pmatrix}, \quad (38)$$

$$\chi = I_a + I_b + F, \quad (39)$$

$$\xi = \alpha^* + B, \quad (40)$$

where all parameters are functions of the semiclassical displacements $\beta_\pm$. This equation of motion—and thus the corresponding master equation itself– - features a fixed point if the eigenvalues of the matrix Σ have negative real part ($\mathrm{Re}[\lambda_{1,2}] < 0$). Due to the symmetry between β_+ and β_- one finds that the eigenvalues of the two Σ matrices corresponding to $\beta_\pm$ fulfill $\mathrm{Re}[\lambda_{1,2}(\beta_+)] = -\mathrm{Re}[\lambda_{1,2}(\beta_-)]$ such that across the whole phase diagram only one solution is stable at a time and defines the corresponding phase in the phase diagram. Note, however, that the unstable solution decays at a rate that is second order in ϵ. Preparing the system in this state consequently leads to slow dynamics, such that this solution exhibits metastability.

In the following we implicitly choose the stable β for which the real parts of the eigenvalues of Σ are negative and discard the unstable solution. Figure 2 displays a selection of steady-state expectation values in the thermodynamic limit across the phase diagram for the stable solution. Different expectation values illustrate the different nature of phases A and B and show distinct signatures of first- and second-order

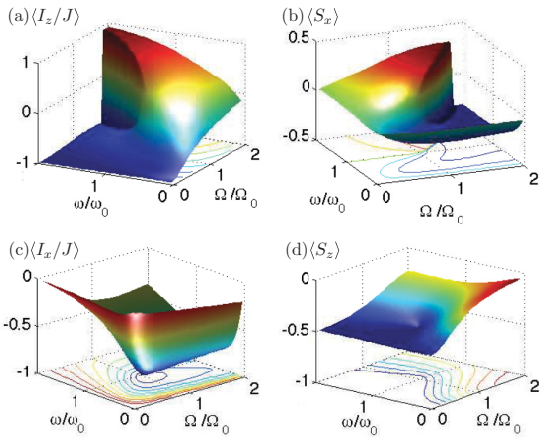

FIG. 2. (Color online) The system observables of the RSTSS solution in the thermodynamic limit show clear signatures of first- and second-order transitions ($\gamma = a$). (a) The nuclear polarization in the z direction $\langle I_z/J\rangle_{ss}$ switches abruptly from minus to plus at the phase boundary b. (b) The electron polarization in the x direction $\langle S_x\rangle_{ss}$ shows a similar discontinuous behavior along b. (c) The nuclear polarization in the x direction changes smoothly across the phase boundary b. Along the segment x ($\omega = \omega_0, \Omega < \Omega_0$) the nuclear field in the x direction builds up linearly to cancel the external driving. (d) The electron polarization in the z direction also does not show signatures of the first-order transition b. Along segment x the electron is fully polarized in the $-z$ direction up to the second-order critical point (ω_0, Ω_0), where it changes nonanalytically (see also Fig. 6).

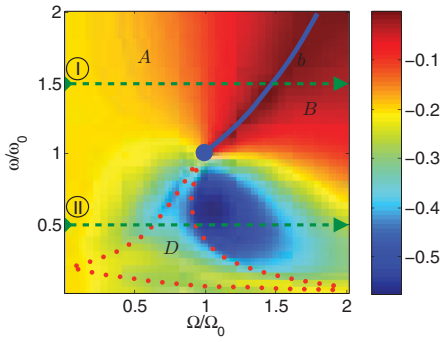

FIG. 3. (Color online) Asymptotic decay rate (ADR, cf. text) for $\gamma = a$ within the perturbative framework. Along b the ADR vanishes nonanalytically, indicating the stabilizing and destabilizing of the modes of regions A and B, respectively. b is a first-order phase boundary culminating in a second-order critical point at (ω_0, Ω_0). From here region D opens, which is characterized by a nonanalyticity in the ADR at a finite value. This indicates a change in the dynamic properties of the system which cannot be detected in steady-state observables. Within D the system shows an overdamped behavior in the vicinity of the steady state.

phase transitions which will be discussed in greater detail in Secs. IV B3 and IV B4. The approximate steady-state polarizations found in this way coincide with the exact values found via diagonalization techniques to an extraordinary degree ($\sim 10^{-3}$ relative deviation for $J = 150$). Corrections to the perturbative solutions are of the order $1/J$ since the first-order expectation values of the bosonic mode vanish by construction, since $\langle b \rangle = 0$ [compare Eqs. (9) and (13)]. In the thermodynamic limit the perturbative solution becomes exact.

The two eigenvalues of Σ are typically of the form $\lambda_{1,2} = a \pm ib$ (except in region D, which is discussed below) and define the complex energy of the mode. In this case the matrix Σ contains all information on the low excitation spectrum of the Liouvillian, which is approximated by multiples of the mode energies within the perturbative treatment.[4] The low excitation spectrum contains information about criticality of the system and the dynamics in the vicinity of the steady state and is used to discuss and classify the different transitions in the phase diagram. In particular, the eigenvalue of Σ with largest real part approximates the ADR in the thermodynamic limit in those regions of the phase diagram where the Gaussian mode is responsible for the lowest excitations in the Liouvillian spectrum (only in the region of bistability C this is not the case).

The ADR according to the perturbative descriptions based on Gaussian modes is displayed in Fig. 3. It is used to study the transitions involving the Gaussian mode in the thermodynamic limit. The ADR vanishes along a line b indicating a phase boundary separating the normal and anomalous spin-pumping phase, which is described in Sec. IV B4. Furthermore, a nonanalyticity of the ADR at a finite value defines region D, which characterizes a dynamical phase and is explained in Sec. IV B3.

The dynamical matrix of the first-order moments Σ provides information on the stability of the semiclassical solutions, the criticality of the Liouvillian, and the nonanalyticities of region D. In order to understand the character of the solutions in the different regions of the phase diagram we consider next the steady-state covariance matrix (CM) of the bosonic system. For a quadratic evolution like the one of Eq. (25) the steady-state CM contains all information on the state. We deduce the effective temperature and the squeezing of the nuclear spin system, which connects to criticality in the system.

For a one-mode system with vanishing displacements $\langle x \rangle$ and $\langle p \rangle$ [in the steady state of Eq. (25) this is always the case] the CM is defined as

$$\Gamma = \begin{pmatrix} 2\langle x^2 \rangle & 2\langle xp \rangle - i \\ 2\langle px \rangle + i & 2\langle p^2 \rangle \end{pmatrix}, \tag{41}$$

with the usual definitions $x = \frac{1}{\sqrt{2}}(b + b^\dagger)$ and $p = \frac{1}{\sqrt{2}i}(b - b^\dagger)$. Using Eq. (25) we straightforwardly calculate the steady-state CM $\Gamma_{\rm ss}$ across the phase diagram. As $\Gamma = \Gamma^T > 0$, Γ is symplectically diagonalizable, with

$$\Gamma = DO \begin{pmatrix} M^2 & 0 \\ 0 & M^{-2} \end{pmatrix} O^{-1}, \tag{42}$$

where O is orthogonal with $\det(O) = 1$. For a single mode, $D \geqslant 1$ and $M \geqslant 1$ are real numbers. While D is a measure of the purity of the state [$\mathrm{Tr}(\rho^2) = 1/\sqrt{|\Gamma|} = 1/D$], the smallest eigenvalue of Γ, $\lambda_{\rm min} \equiv DM^{-2}$ determines the amount of squeezing in the system [46]. $\lambda_{\rm min} < 1$ indicates squeezing in the bosonic mode. For $M = 1$, the CM Eq. (42) describes a thermal state of the bosonic mode and D can be straightforwardly associated to a dimensionless effective temperature

$$T_{\rm eff} = \ln\left[\frac{2}{\sqrt{D} - 1} + 1\right]^{-1}. \tag{43}$$

This definition is also meaningful for $M > 1$, since the squeezing operation is entropy-conserving. $T_{\rm eff}$ is also a measure for the entropy of the spin system, as to leading order it is connected to the bosonic mode via an unitary (i.e., entropy-conserving) transformation. The effective temperature of the different phases will be discussed below in Secs. IV B2 and IV B3 [cf. Fig. 7].

We stress the point that all properties of the CM derived within the second order of the perturbative approach are independent of the system size J. In particular, the amount of fluctuations (i.e., the purity) in the state does not depend on the particle number. In order to self-consistently justify the perturbative approach, D has to be small with regard to J. This implies that in the thermodynamic limit $J \to \infty$ the perturbative results to second (i.e., leading) order become exact.

The inverse purity D is displayed in Fig. 4(a). Except for for a small region around the Gaussian phase boundary b the fluctuations are much smaller than $J = 150$, which justifies the

[4]The inset of Fig. 9 clearly shows these bosonic characteristics of the exact spectrum for $J = 150$. Outside the region of bistability the real part of the spectrum is approximately equidistant.

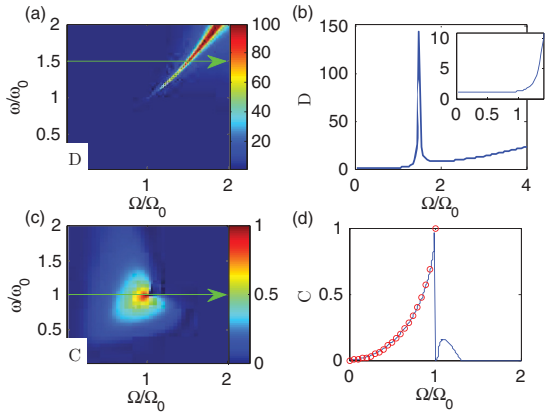

FIG. 4. (Color online) Properties of the steady state CM Γ_{ss} [Eq. (42)]. (a) The fluctuations D are low in most parts of the phase diagram except for a small wedge around the Gaussian phase boundary. (b) Fluctuations D along the line ① [green line of (a)]. The phase boundaries separate a mode with low fluctuations (enlarged in the inset), from a mode with large fluctuations. For large Ω fluctuations increase, and the system eventually approaches a fully mixed state. (c) The squeezing measure C (cf. text) in the thermodynamic limit. C approaches 1 at (ω_0,Ω_0), indicating diverging entanglement in the system. (d) C along the line $\omega=\omega_0$ (solid line). The red circles indicate the the squeezing parameter $1-\xi^2_{\tilde{e}_y}=1-\sqrt{1-(\Omega/\Omega_0)^2}$ (cf. text).

validity of the perturbative approach and explains the excellent agreement with the exact diagonalization for this system size.

The squeezing $\lambda_{\min}$ in the auxiliary bosonic mode does not necessarily correspond to spin squeezing in the nuclear system. In order to deduce the spin squeezing in the nuclear system from the squeezing of the bosonic mode a transformation according to Eq. (11) and Eq. (15) is necessary. In Appendix B 1 we show that for $|\beta|<1$ Eq. (11) can be reformulated to connect the spin fluctuations to a squeezed and rescaled bosonic mode

$$\mathcal{J}_1^- = \sqrt{2(1-|\beta|^2)}S^\dagger(r)bS(r), \tag{44}$$

where $S(r)=e^{(r^*b^2-rb^{\dagger 2})/2}$ is the squeezing operator and $\cosh(r)=\mu=(2k-|\beta|^2)/[2\sqrt{2k(1-|\beta|^2)}]$ and $\sinh(r)=-\nu=\beta^2/[2\sqrt{2k(1-|\beta|^2)}]$.

Thus, squeezing $\lambda_{\min}$ of the mode b does, in general, not imply reduced spin fluctuations in a direction orthogonal to the mean spin polarization since the transformation between spin fluctuations and b involves a squeezing operation itself and a scaling by a factor $0<\sqrt{2(1-|\beta|^2)}\leqslant\sqrt{2}$.

In general, we thus have to apply a more involved squeezing criterion. In [38] it was shown that for systems of N spin-$\frac{1}{2}$ particles and for all directions $\vec{n}$ the quantity

$$C_{\vec{n}} \equiv 1-\frac{2}{J}\langle\Delta I^2_{\vec{n}}\rangle-\frac{1}{J^2}\langle I_{\vec{n}}\rangle^2<1, \tag{45}$$

signals entanglement if $C_{\vec{n}}>0$ for some direction $\vec{n}$. Moreover, $\langle\Delta I^2_{\vec{n}}\rangle<J/2$ indicates a generalized spin squeezing of the state.[5]

In the following we use the quantity $C=\max\{0,C_{\vec{n}}|\vec{n}\in\mathbb{R}^3\}$ to investigate squeezing and bipartite entanglement in the nuclear system. In order to calculate $C_{\vec{n}}$ we reconstruct the approximate nuclear operators according to Eqs. (9) and (14) from the semiclassical displacement β and evaluate the expectation values according to the steady-state CM Eq. (41). Finally, we maximize $C_{\vec{n}}$ with regard to all possible directions $\vec{n}$ to obtain C. The results are discussed in Sec. IV B4. As discussed in more detail in the next section, the fact that $C\to1$ as $\Omega\to\Omega_0$ on the line segment x indicates a diverging entanglement length in the sense that $O(1/(1-C))=O(\sqrt{J})$-particle entanglement is present [40].

2. *A second-order phase transition: The segment x*

The segment x at $\omega=\omega_0$ (Fig. 1) represents a very peculiar region in the phase diagram, where the solution below the critical point can be constructed analytically as demonstrated in Sec. III B. The electron and nuclear system decouple, resulting in a zero entropy product steady state. A nuclear polarization builds up to cancel the external driving up to the point of maximal Overhauser field (Ω_0). At this point squeezing and entanglement in the system diverge, indicating a second-order phase transition. In the following we exemplarily employ the formalism developed above along this line to obtain further insight about the criticality at (ω_0,Ω_0). We calculate the analytical steady-state solution as well as the effective master equation governing the nuclear fluctuation dynamics in its vicinity. We find that here the spectrum of the Liouvillian becomes continuous (implying a closing gap) and real. At the same time the creation operators of the elementary excitations from the steady state turn Hermitian, giving rise to diverging spin entanglement.

The first-order stability condition Eq. (24) is fulfilled, if $\tilde{\Omega}=0$ [compare Eqs. (31) and (32)], which yields the possible semiclassical steady-state displacements

$$\begin{aligned}&\sqrt{k}\beta=-\Omega/\Omega_0,\\ \Leftrightarrow\ &\beta_\pm=-\sqrt{1\pm\sqrt{1-(\Omega/\Omega_0)^2}},\end{aligned} \tag{46}$$

corresponding to a normal ("−") and anomalous ("+") spin-pumping mode, respectively.

Next, we explicitly calculate the second-order corrective dynamics of the nuclear degrees of freedom for the normal mode. The vanishing of the effective driving $\tilde{\Omega}=0$ forces the electron in its dark state—implying $\langle S^+\rangle_{ss}=\langle S^-\rangle_{ss}=\langle S^+S^-\rangle_{ss}=0$—and directly yields $B=F=0$ [Eqs. (26) and (27)]. The remaining constants can be calculated as described above and introducing new bosonic operators (for the normal mode $\beta=\beta_-\leqslant1$)

$$d=\mu b+\nu b^\dagger, \tag{47}$$

[5] In distinction to the criterion Eq. (6) the squeezed component $J_{\vec{n}}$ is not necessarily orthogonal to the mean spin.

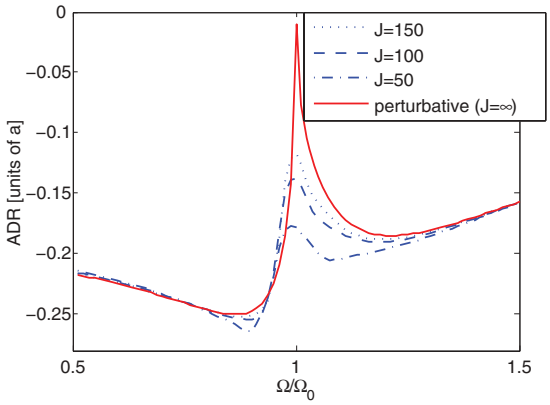

FIG. 5. (Color online) The ADR ($\gamma = a$) for $J = 50$, 100, 150 (broken lines) in comparison with the perturbatively calculated (solid line, cf. Sec. IV B2) along $\omega = \omega_0$. For finite systems one finds an avoided crossing at Ω_0. The size of the gap reduces with the system size until it closes in the thermodynamic limit (solid line). Below Ω_0 the ADR in the thermodynamic limit is given by Eq. (52).

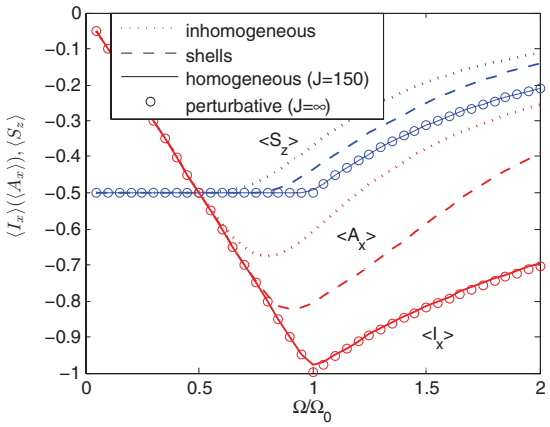

FIG. 6. (Color online) Electron inversion $\langle S_z \rangle$ and the nuclear field in the x direction $\langle I_x \rangle$ along $\omega = \omega_0$ in the thermodynamic limit according to the perturbative theory (circles) in comparison with the numeric values from exact diagonalization for a finite system of $J = 150$ (solid lines). The perturbative theory shows excellent agreement with the numerical solutions. Further, the numerically determined electron inversion and the expectation value of the inhomogeneous nuclear operator $\langle A_x \rangle$ are displayed for a model of two inhomogeneously coupled nuclear shells ($g_1 = 2g_2$) of size $J_{1,2} = 8$ (dashed lines) and for five inhomogeneously coupled nuclear spins (dotted lines) are displayed (discussion see Sec. VI).

with

$$\mu = \frac{2k - |\beta|^2}{2\sqrt{2k(1-|\beta|^2)}}, \tag{48a}$$

$$\nu = -\frac{\beta^2}{2\sqrt{2k(1-|\beta|^2)}}, \tag{48b}$$

one finds the effective evolution of the nuclear fluctuations given as

$$\dot{\sigma} = \Gamma_{\text{eff}}\left(d\sigma d^\dagger - \tfrac{1}{2}\{d^\dagger d, \sigma\}\right) - i[\Theta_{\text{eff}} d^\dagger d, \sigma], \tag{49}$$

with

$$\Gamma_{\text{eff}} = 2a^2 \text{Re}\left(\frac{1}{\gamma + i2a(|\beta|^2 - 1)}\right)(1 - |\beta|^2), \tag{50}$$

$$\Theta_{\text{eff}} = a^2 \text{Im}\left(\frac{1}{\gamma + i2a(|\beta|^2 - 1)}\right)(1 - |\beta|^2). \tag{51}$$

d and $d^\dagger$ fulfill boson commutation relations, since Eq. (47) defines a symplectic transformation ($|\mu|^2 - |\nu|^2 = 1$). The eigenvalues of the dynamical matrix Σ associated to Eq. (49) are straightforwardly given as $\lambda_{1,2} = -\Gamma_{\text{eff}}/2 \pm i\Theta_{\text{eff}}$. The real part—representing the ADR of the system in thermodynamic limit (compare Fig. 5)– -is always negative, indicating the stability of the normal spin-pumping mode (β_-). In an analogous calculation one shows that the semiclassical solution $\beta_+ > 1$ is not stable to second order since the eigenvalues of Σ have a positive real part, that is, the fluctuations diverge, violating the initial assumptions that the mode b has to be lowly occupied.

Selected steady-state expectation values derived from the stable displacement β_- to leading order in J (i.e., in the thermodynamic limit) are displayed in Fig. 6.

Already for $J = 150$ we find excellent agreement between the perturbative and exact mean polarizations. The nuclear field builds up to exactly cancel the external magnetic field Ω, forcing the electron in its dark state $|\downarrow\rangle$ along x and thus realizing the model of cooperative resonance fluorescence [7] even for weak dissipation $\gamma \leqslant a$ [compare Eq. (5)]. This solution is available only if $\Omega \leqslant \Omega_0$ (defining segment x), that is, up to the point where the nuclear field reaches its maximum. At this point the system enters a new phase of anomalous spin-pumping (described below) and the steady-state properties change abruptly.

Inserting solution β_- in the coefficients of master Eq. (49) yields

$$\Gamma_{\text{eff}} = 2a^2 \text{Re}\left(\frac{1}{\gamma - i2a\sqrt{1-(\Omega/\Omega_0)^2}}\right)\sqrt{1-(\Omega/\Omega_0)^2}, \tag{52}$$

$$\Theta_{\text{eff}} = a^2 \text{Im}\left(\frac{1}{\gamma - i2a\sqrt{1-(\Omega/\Omega_0)^2}}\right)\sqrt{1-(\Omega/\Omega_0)^2}. \tag{53}$$

In the close vicinity below the critical point Ω_0 the real part of the gap in the Liouvillian's spectrum closes as

$$\Gamma_{\text{eff}} \approx 2\frac{a^2}{\gamma}\sqrt{1-(\Omega/\Omega_0)^2}, \tag{54}$$

and the imaginary part as

$$|\Theta_{\text{eff}}| \approx 2\frac{a^3}{\gamma^2}[1-(\Omega/\Omega_0)^2], \tag{55}$$

indicating criticality. Figure 5 displays the ADR along $\omega = \omega_0$ in the thermodynamic limit [which is given on the segment x by Eq. (52)] and for finite systems. It displays an avoided crossing

at Ω_0 with a gap that vanishes in the thermodynamic limit. This closing of the gap coincides with diverging time scales in the system, which renders the model more susceptible to potential perturbing effects, a phenomenon well known in the context of criticality [43].

In contrast to the general form Eq. (25), Eq. (49) contains only one Lindblad term and the dynamics drive the system into the vacuum $|0_d\rangle$ of the squeezed mode d. As the system approaches the critical value $\Omega = \Omega_0$ (i.e., $\beta_- = -1$) the mode d adopts more and more a $\hat{p} = \frac{1}{\sqrt{2}i}(b - b^\dagger)$-like character and thus the squeezing of this mode's vacuum increases. The (in general complicated) transformation between the squeezing of the bosonic mode b and the spin operators (cf. Sec. IV B 1) can readily be established along x, since the operator d is trivially related to the spin operators [cf. Eq. (11)]

$$\begin{aligned}\mathcal{J}_1^- &= \frac{1}{2\sqrt{k}}[(2k - |\beta|^2)b - \beta^2 b^\dagger] \\ &= \sqrt{2(1-|\beta|^2)}(\mu b + \nu b^\dagger) \\ &= \sqrt{2(1-|\beta|^2)}d. \end{aligned} \tag{56}$$

The fluctuations in the y direction, for example, are consequently given as

$$\mathcal{J}_1^y = \sqrt{(1-|\beta|^2)}\hat{p}_d, \tag{57}$$

where $\hat{p}_d = \frac{1}{\sqrt{2}i}(d - d^\dagger)$. One readily shows that

$$\langle \Delta I_y^2 \rangle = J\langle \mathcal{J}_1^{y2} \rangle = J(1-|\beta|^2)\langle \hat{p}_d^2 \rangle, \tag{58}$$

up to order $O(1)$ and we used $\langle d \rangle = 0$ in the steady state. In the $\hat{p}$ vacuum $|0_p\rangle$ it is $\langle \hat{p}_d^2 \rangle = 1/2$, such that we evaluate

$$\begin{aligned}\xi^2_{\hat{e}_y} &= 2\langle \Delta I_y^2 \rangle / |\langle \vec{I} \rangle| \\ &= 2(1-|\beta|^2)\langle \hat{p}_d^2 \rangle = \sqrt{1 - \left(\frac{\Omega}{\Omega_0}\right)^2}, \end{aligned} \tag{59}$$

where we used $|\langle \vec{I} \rangle| = J$ and inserted the semiclassical displacement β_-.

This is the same result we derived in Sec. III B and Appendix B 1 by constructing approximate eigenstates of the lowering operator I^- and along x we find that $C \approx 1 - \xi^2_{\hat{e}_y}$, as shown in Fig. 4(d). Note that here $\hat{e}_y$ is orthogonal to the direction of the mean spin $\langle \vec{I} \rangle$. This allows us to deduce that $O(\sqrt{J})$ nuclear spins must be entangled close to the critical point, which establishes a "diverging entanglement length" in this system. To see this, we employ a variant of the criterion Eq. (6), as discussed in [39]. There, it was shown that $\xi^2_{\hat{e}_y} < 1/k$ sets a lower bound of $N\xi^{-2}_{\hat{e}_y}$ on the quantum Fisher information F_Q of the state. In [40] it was shown that for states containing at most k-particle entanglement, F_Q is upper bounded by Nk. Consequently, the values of $\xi^2_{\hat{e}_y}$ obtained close to the critical point [cf. Eq. (59) and Appendix B 1] imply that at least $O(\sqrt{J})$-particle entanglement must be present. Note that the bosonic description does not make it possible to describe the range $\xi^2_{\hat{e}_y} = O(1/J)$, that is, $k = O(J)$, where the fluctuations become larger than the expansion parameter.

The nuclear squeezing and entanglement in the system diverges approaching the critical point, as the Lindblad operator d (defining the steady state $|0_d\rangle$) becomes more and more $\hat{p}$-like. The fluctuations in the y direction tend to zero, while at the same time—due to the Heisenberg uncertainty relation—the steady state is in a superposition of an increasing number of I_z eigenstates. Since in a system with infinite range interactions (as the one we are considering) there is no obvious definition of a coherence length, the range of the involved I_z eigenstates can be considered as an analogous concept.

At the critical value $\Omega = \Omega_0$ the symplectic transformation Eq. (47) becomes ill defined (d becomes a $\hat{p}$-like operator) while both the dissipation rate and the mode energy tend to zero. While the coefficients in Eqs. (48) diverge, the total master equation is well defined [due to the factors $(1 - |\beta|^2)$ in Γ_{eff}] and straightforwardly can be written as

$$\dot{\sigma} = \frac{a^2}{2\gamma}\left(\hat{p}\sigma\hat{p} - \frac{1}{2}\{\hat{p}^2, \sigma\}\right). \tag{60}$$

The Liouville operator's spectrum is real and continuous with Hermitian creation operators of the elementary excitations.

We stress the point that along segment x in the phase diagram highly dissipative dynamics drive the system in a pure and separable steady state with zero effective temperature $T_{\text{eff}} = 0$ [cf. Fig. 7(b)]. At the critical point Ω_0 the steady state changes its nature abruptly as the system enters a high-temperature phase.

Furthermore, we remark that this steady state has no relation to the system's ground state. This is in contrast to the extensively studied Dicke phase transition [15,47,48] where the steady state is in close relation to the Hamiltonian's ground state (in fact, in the normal phase it is identical). In the present model dissipation drives the system to a highly excited state of the Hamiltonian and the observed critical phenomena are disconnected from the Hamiltonian's low excitation spectrum.

We have seen that at the critical point (ω_0, Ω_0) the gap of the Liouville operator's spectrum (in both real and imaginary part) closes in the thermodynamic limit [Eqs. (54) and (55)]. Approaching the critical point the steady-state fluctuations become more and more squeezed due to the increasing $\hat{p}$-like character of the mode d. The spin squeezing close to the critical point [Eq. (59)] can be interpreted as a diverging coherence length in a system with infinite range interactions

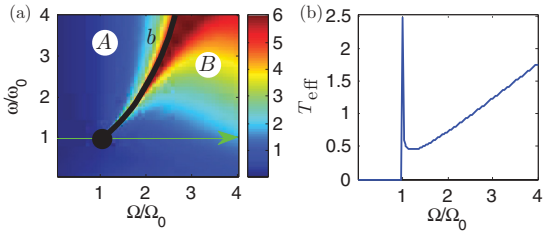

FIG. 7. (Color online) Effective temperature T_{eff} of the Gaussian mode. Temperatures $T_{\text{eff}} > 6$ are cut off, as the temperature diverges along the phase boundary b. (a) The first-order phase boundary b separates the low-temperature phase A from the high-temperature phase B. (b) T_{eff} along $\omega = \omega_0$: On segment x the system is in a zero entropy state ($T_{\text{eff}} = 0$). Above the second-order critical point $\Omega > \Omega_0$ the system enters a high-temperature phase. Here the temperature rises with increasing driving strength.

(the electron mediates interactions between remote spins). These are clear indications for a second-order phase transition, which is formalized in Sec. IV B4.

3. Phases

In the present section we study the different phases of the system, which involve the RSTSS solution (A, B, and D) using the analytic tools developed above. By construction, the RSTSS solution describes steady states where the electron and nuclear states factorize to leading order in the system size and the nuclear system is found in a fully polarized and rotated state with Gaussian fluctuations, which are fully characterized by their effective temperature and squeezing. Figure 2 displays different steady state observables of the Gaussian solution determined via the formalism described above in the thermodynamic limit.

In phase A the system is characterized by normal spin-pumping behavior. Only the semiclassical displacement β_- (normal mode) leads to a dynamical matrix Σ that has negative real parts of its eigenvalues, while for β_+ the eigenvalues have positive real parts, indicating the instability of that mode in second order. The nuclear system in the normal mode settles in a state highly polarized in the $-z$ direction following the direction of the electron spin pumping [Fig. 2(a)]. Meanwhile, increasing the external driving Ω and approaching the phase boundary b, a nuclear field in the x direction builds up, but only along x it can fully cancel the external driving [Fig. 2(c)]. Therefore, in general, the electron spin aligns more and more with the external field [Figs. 2(b) and 2(d)]. Furthermore, the effective temperature (and thus the entropy) of the phase is low, as displayed in Fig. 7(a).

In region B, in contrast, β_+ is the only stable solution, defining the phase of anomalous spin-pumping behavior. The nuclear system now shows strong population inversion; that is, the nuclear polarization is found in the direction opposite to the external pumping (z). In the same way the electron now aligns in opposite direction to the external driving field (x). Also, in contrast to phase A, the RSTSS now is in a high-temperature state. For larger electron driving the temperature increases until eventually the Gaussian description breaks down (as $D \propto J$) and for $\Omega \to \infty$ the system is found in a completely mixed state [compare Fig. 4(b)].

In the upper half of the phase diagram ($\omega > \omega_0$) phase A changes abruptly into phase B at the boundary b and certain steady-state spin observables [$\langle I_z \rangle$, $\langle S_x \rangle$ [Figs. 2(a) and 2(b)] and $\langle I_y \rangle$ (not displayed)] show distinct features of a first-order phase transition, changing sign as the normal (anomalous) mode destabilizes (stabilizes). This transition is discussed in greater detail in the following Sec. IV B4. Following this boundary toward the critical point (ω_0, Ω_0) the two phases become progressively more similar. Below the critical point ($\omega < \omega_0$) there is no clear distinction between the normal and anomalous spin-pumping mode anymore, a phenomenon known from thermodynamics as *supercriticality*. Phase A transforms continuously to phase B in this region. Close to the critical point, supercritical media typically respond very sensitively to the external control parameters of the phase diagram (e.g., temperature or pressure) [42]. In our system we observe that small changes in the parameter ω leads to large changes in electron spin observables.

Next, we consider the third region associated with the RSTSS solution, region D. We will find that this region differs from the previous ones by the fact that it cannot be detected in the system's steady state but rather in dynamical observables.

The eigenvalues of the dynamic matrix Σ can be calculated as $\lambda_{1,2} = -(R_a - R_b) \pm 2\sqrt{4|\xi|^2 - \chi^2}$ and provide information on the approximate low excitation spectrum of the Liouvillian. We can distinguish two cases for the low excitation spectrum, which differ only in the Hamiltonian properties of Eq. (25) (fully determined by χ and ξ [Eqs. (39) and (40)]. In the first case the quadratic bosonic Hamiltonian can be symplectically transformed to be diagonal in a Fock basis (i.e., to be of the form $\propto \tilde{b}^\dagger \tilde{b}$). This is the case if $\chi^2 > 4|\xi|^2$. As a consequence the two eigenvalues of Σ have an identical real part and imaginary parts $\pm 2\sqrt{\chi^2 - 4|\xi|^2}$. In the second case the Hamiltonian transforms symplectically into a squeezing Hamiltonian $\propto (\tilde{b}^{\dagger 2} + \tilde{b}^2)$. Here one finds $\chi^2 < 4|\xi|^2$, such that the eigenvalues become real and symmetrically distributed around $-(R_a - R_b)$. In region D in Fig. 1 we find the effective Hamiltonian for the nuclear fluctuations to be symplectically equivalent to a squeezing Hamiltonian.

Figure 8 shows the ADR exemplarily along the line $\omega = 0.5\omega_0$(Ⅱ in Fig. 1) calculated according to the perturbative theory and via exact diagonalization, respectively. The perturbative theory approximates accurately the low excitation spectrum of the Liouvillian. We find that in region D the ADR splits up when the coherent part of Eq. (25) changes to a squeezing Hamiltonian. As mentioned above, this nonanalyticity occurs at a nonzero value of the ADR and thus does not leave signatures in the steady state behavior. The steady state transforms smoothly along Ⅱ. However, the nature of dynamical observables change within region D as the system displays anomalous behavior approaching

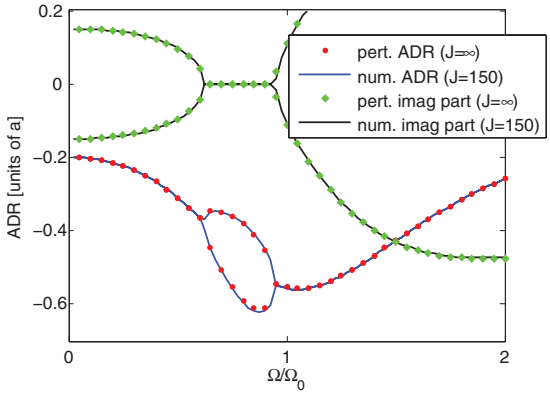

FIG. 8. (Color online) The ADR and the imaginary part of the respective eigenvalue ($\gamma = a$) for $J = 150$ (solid lines) in comparison with the perturbatively calculated value (dots) along Ⅱ. In the region where the coherent part of Eq. (25) is a squeezing Hamiltonian, the ADR (i.e., real part of the lowest Liouvillian eigenvalue pair) splits. At the same time the imaginary part of the lowest eigenvalue pair vanishes (black lines), indicating that the system is overdamped.

the steady state. The splitting of the ADR coincides with the vanishing of the imaginary part of the lowest nonzero Liouvillian eigenvalues. Thus, the system is overdamped in D. Perturbing the system from its steady state will not lead to a damped oscillatory behavior, but to an exponential, oscillation-free return to the steady state.

The blue area in the vicinity of region D in Fig. 3 does not represents a new phase but is another interesting feature of the system. Here, the ADR exceeds the value at $\Omega = 0$ by a factor of $\sim$3. For $\Omega = 0$ the model describes the standard spin-pumping setting. Large gaps in the low excitation spectrum indicate the possibility to improve the effective spin-pumping rate (remember that also in this region the steady state is fully polarized, however, not in the $-z$ direction, as is the case for the normal spin-pumping configuration $\Omega = 0$). Indeed, simulations show that starting from a fully mixed state, the system reaches the steady state faster than in the standard setting ($\Omega = 0$). This feature becomes more distinct in systems, where the electron pumping rate γ is limited. For $\gamma = 0.1a$ the time to reach the fully polarized steady state from a fully mixed state is shortened by a factor of $\sim$6.

4. Transitions

In this section we consider the transitions involving the RSTSS solution in greater detail providing a classification in analogy to quantum phase transitions in closed systems (compare Sec. II).

As seen in the previous section, certain steady-state observables show clear signatures of a first-order phase transition at b (Fig. 2). In order to understand this sharp transition we consider the ADR exemplarily along path ① in Fig. 9.

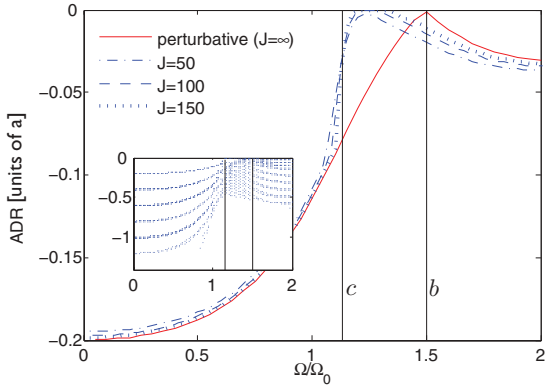

FIG. 9. (Color online) The ADR ($\gamma = a$) for $J = 50$, 100, 150 (broken lines) in comparison with the perturbatively calculated (solid line) along ①. The vertical black lines indicate the asymptotic boundaries of the region of bistability. In the whole region the ADR tends to zero in the thermodynamic limit due to the appearance of a non-Gaussian stable mode. (Inset) The next-higher excitations in the spectrum for $J = 150$ display equidistant splittings in regions far from the region of bistability. This is an indication for the bosonic character of the steady state, which is exploited in the perturbative approach.

The broken lines represent numeric results of exact diagonalization of the Liouvillian for $J = 50$, 100, and 150, while the solid line indicates the result of the perturbative approach. As described in Sec. IV B1, we implicitly choose the semiclassical displacement β_- (for $\Omega < 1.5\Omega_0$) or β_+ (for $\Omega > 1.5\Omega_0$) for which the ADR is negative, indicating a stable solution. For increasing system size the ADR is increasingly well approximated by the perturbative solution.

We stress the point that the red line represents the first Gaussian excitation energy only. However, within the region of bistability (indicated by two vertical bars and discussed below in Sec. V), a non-Gaussian mode is responsible for additional excitations in the exact spectrum. The Gaussian mode eigenvalue (red line) in this region is reproduced approximately by higher excitations of the exact spectrum (not displayed). The perturbative theory is still correct within the region of bistability but, as expected, it misses all non-Gaussian eigenstates of the exact Liouvillian.

At the boundary b ($\Omega \approx 1.5\Omega_0$) the gap in the real part of the spectrum of the Liouvillian closes nonanalytically, indicating critical behavior. This observation is supported by the effective temperature (and thus the fluctuations in the system), which is increased in the vicinity of the boundary b, and diverges at the boundary [Figs. 7(a) and 4(a)]. The vanishing of the ADR at b (i.e., the vanishing due to the RSTSS solution) can be observed at finite J (dashed lines in Fig. 9) and is not a feature appearing in the thermodynamic limit only. The position of this closing of the gap—which in the thermodynamic limit (solid line) is found at $\Omega \approx 1.5\Omega_0$—is shifted for finite system sizes to lower drivings Ω.

The origin of this closing of the Liouvillian gap becomes more transparent if we take the mode energy of the respective metastable solution into account.

In Fig. 10(a) the complex energy of both the stable and the unstable mode are displayed (i.e., the first eigenvalue of the matrix Σ [Eq. (37)]).

The normal spin-pumping mode (β_-; blue lines) is stable (Re[$\lambda(\beta_-)$] < 0) up to the critical point where it destabilizes

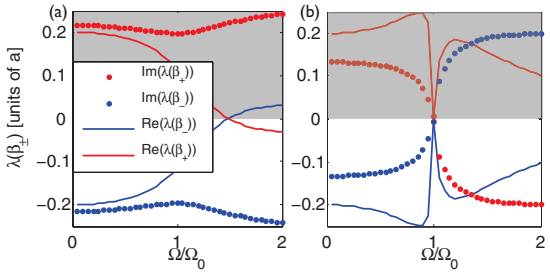

FIG. 10. (Color online) Complex energy of the two modes corresponding to the semiclassical solutions $\beta_\pm$ for $\gamma = a$. The solid line in the nonshaded area represents the ADR of Fig. 9 and Fig. 5, respectively. (a) Along ① ($\omega = 1.5\omega_0$). The eigenvalues miss each other in the complex plane. The real parts cross directly. (b) $\omega = \omega_0$. The eigenvalues degenerate asymptotically (in both real and imaginary parts) at the critical point. This closing of the gap originates from an avoided crossing in finite systems with the relevant gap vanishing in the thermodynamic limit (see also Fig. 5).

and the anomalous mode appears (β_+; red lines). At the critical point the two solutions are macroscopically different $\beta_- \neq \beta_+$ and their energy (i.e., $\mathrm{Im}[\lambda(\beta_\pm)]$) is distinct across the transition [dotted lines in Fig. 10(a)]. Although the projection of the eigenvalues on the real axis vanishes at the critical point for both modes (indicating the stabilizing/destabilizing of the modes) the eigenvalues pass each other in the complex plane at large distance. There is no degeneracy in the spectrum of the Liouvillian at the critical point and consequently there can be no mixing of the two modes; the real parts of the eigenvalues cross *directly* without influencing each other. Except for the change in stability the modes do not change their character approaching the phase boundary and no diverging correlations (indicated by the squeezing parameter C) can be observed. Together with the discontinuous change in system observables such as mean polarizations we classify this Gaussian transition as of first order.

Second, we consider the transition along $\omega = \omega_0$ (including the line segment x). In contrast to the situation before we find that the semiclassical displacements β_+ and β_- merge approaching the critical point such that the two modes become asymptotically identical at Ω_0 [Eq. (46)]. Approaching the critical point, the eigenvalues of the two modes tend to zero (both the real and the imaginary parts), causing the gap of the Liouvillian's spectrum to close [Fig. 10(b), Eqs. (54) and (55)]. As we have seen in Sec. IV B 2 at (ω_0, Ω_0) the spectrum becomes real and continuous, signaling criticality. The perturbative treatment intrinsically is a description in the thermodynamic limit. If we consider the exact spectrum we indeed find an avoided crossing due to the mode mixing at the critical point with a gap that is closing for $J \to \infty$ (cf. Fig. 5). As we discussed in Sec. IV B 2 the elementary excitations become $\hat{p}$-like, causing a diverging coherence length in the system [indicated by the diverging squeezing parameter C in Figs. 4(c) and 4(d)]. Together with the continuous but non-analytical change of the mean polarizations these properties classify the point (Ω_0, ω_0) as a second-order transition.

V. REGION OF BISTABILITY: NON-GAUSSIAN SOLUTION

As noted in Sec. III B along the Gaussian boundary b extends a region of bistability [C in (Fig. 1)]—culminating in the critical point (Ω_0, ω_0)—in which a second stable solution appears. Within the perturbative framework from Sec. IV this highly non-Gaussian solution could not be detected because it features large fluctuations of the order of the system size J. In the following we use numerical techniques to construct and study this mode for finite systems. In the thermodynamic limit the ADR tends to zero within C, such that there exists a two-dimensional subspace of steady states. Here we find two independent, physical solutions within the kernel of the Liouvillian, one of which will turn out to be the Gaussian normal spin-pumping mode described in Sec. IV. We analyze the nature and properties of the other, non-Gaussian solution, exemplarily along the line $\omega = 1.5\omega_0$ (① in Fig. 1).

Figure 9 displays the ADR for different particle numbers. Within the indicated region of bistability (the black vertical lines represent the boundaries c and b, respectively) the ADR tends to zero with increasing particle number. Already for $J = 150$ one finds a small region, where the ADR is small enough (of the order of $10^{-6}a$) that one can construct two linearly independent (quasi) steady-state solutions. Although we find the eigenmatrix ρ_1 associated with the ADR to be nonpositive and traceless (the latter being a consequence of $\mathcal{L}$ being the generator of a trace-preserving map) we can linearly combine it with the true steady state ρ_0 to obtain two linear independent, positive solutions with trace one, ρ_{lo} (corresponding to the normal spin-pumping mode) and ρ_{up}. These solutions span the two-dimensional space of steady states in that region.

Figure 11 illustrates the solutions ρ_{lo} and ρ_{up} around the bistable region in an equally weighted mixture. The density matrices are represented by their diagonal elements in the I_z basis. In the plane the blue dots (red diamonds) represent the polarization in the z direction $\langle I_z \rangle$ of the lower (upper) solution ρ_{lo} (ρ_{up}). Coming from below the critical region ($\Omega < 1.15\Omega_0$) the nuclear system is found in the Gaussian normal spin-pumping mode, fully polarized, slightly rotated away from the $-z$ direction and with fluctuations of the order of $\sqrt{J}$. This Gaussian solution persists within the critical region where it becomes noisier until eventually—approaching the right boundary b at $\Omega = 1.5\Omega_0$—it destabilizes. In the thermodynamic limit the lower solution is stable up to the right boundary, where a first-order transition occurs and the anomalous spin-pumping mode appears. Approaching boundary b from above ($\Omega > 1.5\Omega_0$) this mode transforms into a non-Gaussian solution, which—in contrast to the coexisting normal mode—features fluctuations of the order of J and is not fully polarized. It shows large electron-nuclear and nuclear-nuclear connected correlations $\langle S_i I_j \rangle - \langle S_i \rangle \langle I_j \rangle$, and can consequently not be approximated by the semiclassical solutions, which rely on negligibility of these correlations (cf. Appendix D). Approaching the left boundary c at $\Omega = 1.15\Omega_0$ this mode destabilizes eventually as the ADR becomes finite again and the normal mode is the only stable solution in the system.

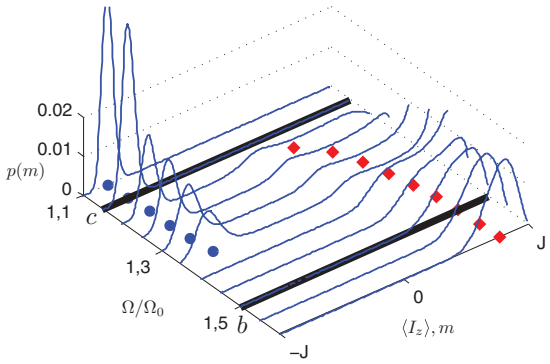

FIG. 11. (Color online) Diagonal elements $p(m) = \langle m | \rho | m \rangle$ of the nuclear density matrix in the z basis ($I_z | m \rangle = m | m \rangle$) across the region of bistability for $\omega = 1.5\omega_0$ ($J = 150$, $\gamma = a$). In the bistable region two stable modes– -the Gaussian normal spin-pumping mode (lower branch; ρ_{lo}) and a non-Gaussian (upper branch; ρ_{up})—coexist. At the boundary b the latter transforms into the anomalous spin-pumping mode, which is the sole stable solution above b. The blue dots (red diamonds) in the plane indicate the average polarization in the z direction $\langle I_z \rangle$ for the lower (upper) solution.

The bistable behavior of the system in region C bears close resemblance to the phenomenon of optical bistability for saturable absorbers [49], where connections to phase transitions have been established [43]. In this region the system displays strong hysteretic behavior. Recent experiments in quantum dots, realizing a setting close to our model system display distinct signatures of hysteresis upon application of an external driving field on the electronic spin [26,27]. Our results suggest the observed optical bistability in central spin systems as a possible pathway to understand these experimental results, which will be a subject of further studies.

VI. IMPLEMENTATIONS AND EXTENSIONS OF THE MODEL

In the present section we discuss potential physical realizations of the master Eq. (1) and address certain aspects of an extension of the model for inhomogeneous hyperfine couplings.

As mentioned above, the model we study is a generic central spin model with various potential physical implementations. The most prominent ones represent singly charged semiconductor quantum dots, where the electron spin couples to the nuclear spins of the host material [25,37], and diamond nitrogen vacancy (NV) centers coupled to either nuclear (^{13}C spins of the host material) or electron (e.g., nearby nitrogen impurities) spin ensembles [50,51]. Recently, diamond nanocrystals containing single NV centers coated with organic molecule spin labels, which are dipole coupled to the NV center spin have been manufactured [52].

NV centers represent a natural realization of the Master Eq. (1). Their ground state consists of three spin sublevels (of spin projection quantum number $m = 0, \pm 1$) featuring a zero field splitting due to anisotropic crystal fields of 2.88 GHz [50]. In a static magnetic field this zero field splitting can be compensated for and one of the transitions (e.g., $m = 0 \leftrightarrow 1$) is brought into near hyperfine resonance with the ancilla spin system, defining an effective two-level system. Since the $m = 0$ level does not carry a magnetic moment, the hyperfine interaction of the effective two-level system and the ancilla system takes the anisotropic form of Eq. (4). Potential counterrotating terms of the dipole-dipole interaction are neglected in the static magnetic field in a rotating wave approximation. Optical pumping of the electron spin in the $m = 0$ spin state and resonant driving (either by optical Raman transitions or radio frequency fields) realizes master Eq. (1) [32].

In general, the hyperfine interaction in such a setting will not be homogeneous and the truncation to a symmetric subspace of total spin J is not justified. In the following we consider an extension of the model taking into account the inhomogeneous nature of the hyperfine coupling in a shell model. Along x we show that up to the critical point steady states can be constructed analytically as electron-nuclear product states involving nuclear eigenstates of the (inhomogeneous) lowering operator. In analogy to the homogeneous case, such solutions cease to exist after the critical point at which we find diverging nuclear squeezing. These results are supported by numerical simulations that confirm the analytical considerations and provide further indications that other features of the phase diagram aside from the second order transition can be found in the inhomogeneous model.

In order to take into account inhomogeneities in the hyperfine coupling, we replace the homogeneous spin operators of Eq. (4) with inhomogeneous operators $I_\alpha \to A_\alpha$ ($\alpha = x,y,z$). We approximate the actual distribution of coupling strengths by n shells of spins with identical coupling

$$A_\alpha = \sum_{i=1}^{n} g_i A_\alpha^{(i)}, \tag{61}$$

where $A_\alpha^{(i)}$ represent homogeneous spin operators within the ith shell. Each homogeneous shell is assumed to be in a symmetric subspace J_i.

In analogy to the homogeneous case we can construct approximate eigenstates of the lowering operator $A^- |\alpha\rangle = \alpha |\alpha\rangle$. To this end we perform a Holstein-Primakoff transformation on the homogeneous spin operators within each shell and displace the respective bosonic mode b_i by β_i and expand the resulting operators in orders of $1/\sqrt{J_i}$. As we demonstrate in Appendix B 2 the choice of a particular displacement β_i uniquely defines the squeezing of the respective mode b_i if we demand that the corresponding state is an A^- eigenstate to second order in the expansion parameters, that is, of order $O(\sum_i 1/J_i)$. The corresponding eigenvalue is then given as $\alpha = \sum_{i=1}^{n} g_i \sqrt{k_i}\beta_i$ ($k_i = 2 - |\beta_i|^2$). As discussed in Sec. III B, $|\psi\rangle = |\downarrow\rangle \otimes |\alpha\rangle$ is a steady state of the evolution to second order, if $\alpha = \sum_i g_i \sqrt{k_i}\beta_i = -J\Omega/\Omega_0$. In contrast to the homogeneous case ($n = 1$) the latter condition does not determine the steady state uniquely. Several sets of displacements within the different shells can fulfill the steady-state condition. However, all these microscopic realizations lead to the same macroscopic behavior of the system such as the locking of the electron inversion $\langle S_z \rangle = 0$. Furthermore, at the critical point, the solution is unique again ($\beta_i = 1$ for all shells) and the considerations on entanglement of Appendix B 1 can be straightforwardly generalized to the inhomogeneous case with the result that also here at the critical point the entanglement in the system diverges, indicating a second-order phase transition. Obviously, above the critical point no such solution can be constructed and the system observables change nonanalytically.

Figure 6 shows numerical results which confirm the above considerations. We find numerically the exact steady-state solution for a model of two inhomogeneously coupled shells ($g_1 = 2g_2$) of size $J_{1,2} = 8$ (broken lines), as well as for a system of five nuclear spins with coupling strengths ($\{g_i\}_{i=1,\ldots,5} = \{0.67, 0.79, 0.94, 1.15, 1.4\}$, dotted lines). For low driving strengths Ω we find the Overhauser field building up linearly, as expected. The emergence of the thermodynamic phase transitions can be anticipated already for these low particle numbers.

These analytical and numerical arguments for the emergence of a second-order phase transition in the inhomogeneous case, suggest the possibility to find other features of the homogeneous phase diagram also in inhomogeneous systems, such as NV centers in diamond.

Another attractive realization of a central spin system is provided by singly charged semiconductor quantum dots: Up to several 10^4 nuclear spins are coupled to a central spin-$\frac{1}{2}$ electron; driving and spin pumping of the electronic state have been

demonstrated experimentally with high efficiency [31,53]. In this setting, however, the inhomogeneity of the hyperfine coupling and the absence of an $m = 0$ central spin state lead to a situation in which the effective nuclear Zeeman term H_I in Eq. (1) becomes inhomogeneous [it is composed of a Knight field, nuclear Zeeman energy, and the (homogeneous) detuning] and does not vanish for any choice of parameters. Therefore, the above argument for a persistence of the second-order phase transition does not apply. However, critical phenomena similar to the ones described above were observed in optically driven quantum dots [26]. The adaptation of our model to this and other more general settings is subject to future studies.

VII. CONCLUSIONS

In analogy to closed systems where critical phenomena arise from nonanalyticities of the Hamiltonian low-energy spectrum, in open systems critical phenomena are intimately related to the low excitation spectrum of the Liouville operator. We investigated a generic driven and damped central spin model and its rich steady-state behavior, including critical effects such as bistabilities, first- and second-order phase transitions, and altered spin-pumping dynamics. We developed a two-step perturbative theory involving the expansion of nuclear fluctuations up to second order in a self-consistent Holstein-Primakoff transformation and the subsequent adiabatic elimination of the electron degrees of freedom in the vicinity of the steady state, which enabled us to provide a complete picture of the system's phase diagram. Linking common ideas from closed-system phase transitions to the dissipative scenario, we were able to introduce a classification of the different transitions in the phase diagram.

The relevance of the considered model involves two aspects. On the one hand, Eq. (1) describes a simple yet rich model, which displays a large variety of critical phenomena. The limitation to symmetric states allows for an efficient (and in the thermodynamic limit exact) perturbative treatment that gives deep insights into the nature of dissipative critical phenomena from a fundamental point of view. On the other hand, the central spin model is general enough to have realizations in a large variety of physical systems (e.g., quantum dots, NV centers). Our understanding of the critical phenomena in this model could provide insight into recent observation of critical behavior in related systems [26,27]. Furthermore the main features of the phase diagram discussed above can also be found if the central (two-level) spin is replaced by a different physical system, for example, a larger spin or a bosonic mode. The theory developed in Sec. IV can straightforwardly be adapted to different scenarios and opens the possibility to study dissipative critical effects in a variety of different physical systems [15].

Finally, we showed that in a more realistic adaptation of the model incorporating an inhomogeneous hyperfine coupling, the second-order phase transition persists, indicating the possibility that the phase diagram remains qualitatively correct in this experimentally more realistic case. A more thorough analysis of the effects of inhomogeneities is subject to future work.

ACKNOWLEDGMENTS

We acknowledge support by the DFG within SFB 631 and the Cluster of Excellence NIM (E.M.K., G.G., and I.C.), the NSF (M.L. and S.F.Y.), CUA, and the Packard Foundation (M.L.), as well as the ECR (A.I.) and AFOSR under MURI Award No. FA9550-09-1-0588 (S.F.Y.).

APPENDIX A: PHASE DIAGRAM FOR ALTERNATIVE DISSIPATION STRENGTHS γ

In the main text of this article we discussed the steady-state phase diagram of the master Eq. (1) exemplarily in the case $\gamma = a$. However, we stress the point that the features we describe do not depend critically on this particular value, but rather prevail qualitatively for all dissipation strengths of this order of magnitude. Most importantly, we noted before the interesting phenomena that all considerations concerning the segment x, including the second-order phase transition at (ω_0,Ω_0) are entirely independent of the value of γ. In the following we briefly discuss the remaining regions of the phase diagram by means of two examples of a lower ($\gamma = 0.2a$) and higher ($\gamma = 5a$) dissipation strength.

The case of low dissipation ($\gamma = 0.2a$) bears strong resemblance to the case we discussed in the main text ($\gamma = a$), which is shown exemplarily in Fig. 12(a) for the nuclear steady-state polarization in the z direction $\langle I_z/J\rangle_{ss}$ [compare Fig. 2(a)]. The first-order boundary is only slightly shifted toward lower driving strength Ω, and all the other features prevail, qualitatively. One finds a region of bistability, as well as a high- and low-temperature phase (not displayed). However, one finds that with decreasing dissipation strength the steady state becomes increasingly noisy.

The situation for higher dissipation is slightly different. First, we note that as the dissipation is increased the first-order boundary is rotated clockwise until in the limit $\gamma \gg a$ [where the electron can be trivially adiabatically eliminated; compare Eq. (5)] it coincides with the line $(\omega_0,\Omega > \Omega_0)$. This behavior can already be seen for $\gamma = 5a$ in Fig. 12(b), which displays the nuclear steady state polarization in the z direction. Interestingly, with increasing dissipation, the system's steady state becomes more pure and the region of bistability shrinks in size. At the same time, the distinction in a high- and low-temperature phase becomes less clear. However, a second criterion characterizing the phases emerges in the form of the

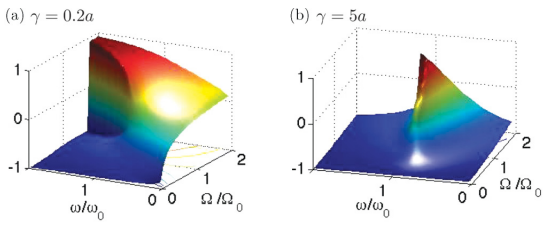

FIG. 12. (Color online) (a) The nuclear polarization in the z direction $\langle I_z/J\rangle_{ss}$ of the RSTSS solution in the thermodynamic limit for (a) $\gamma = 0.2a$ and (b) $\gamma = 5a$. In the first case [(a)] the phase diagram bears strong resemblance with the case $\gamma = a$ (compare Fig. 2). In the case of large dissipation [(b)] the first-order boundary is rotated clockwise toward the line $(\omega_0,\Omega > \Omega_0)$ and the distinction of the phases according to their nuclear polarization in the z direction becomes less prominent. Instead, other criteria like the polarization in the y direction (not displayed) emerge.

nuclear polarization in the y direction. In phase A (B) the system is highly polarized in the $-y$ direction (y direction). A more detailed analysis of this regime with the tools we have developed is an interesting subject for future studies.

APPENDIX B: APPROPRIATE EIGENSTATES OF THE LOWERING OPERATOR

1. Homogeneous case

In Sec. III B we have seen that we can construct the exact steady state along segment x if we assume the nuclear system to be in an eigenstate of the spin-lowering operator $I^-|\alpha\rangle = \alpha|\alpha\rangle$. Although it readily can be shown that this operator exactly features only the eigenvalue $\alpha = 0$, we can construct approximate eigenvalues in an expansion in $1/J$.

We stress the point that in the bosonic analog eigenstates of the annihilation operator are coherent minimum uncertainty states that display no squeezing. As we will see, the eigenvectors of the atomic lowering operator in contrast are squeezed coherent atomic states (on the southern hemisphere of the Bloch sphere), where the squeezing parameter depends uniquely on the rotation angle of the Bloch vector.

As noted in Sec. IV the Holstein-Primakoff transformation [Eq. (7)] provides an exact mapping between spin operators and a bosonic operator in the subspace of total spin quantum number J. In the following we show that approximate eigenstates of the lowering operator I^- can be expressed as a squeezed and displaced vacuum of the bosonic mode b

$$D(\beta)S(-r(\beta))|0\rangle =: |\beta\rangle, \tag{B1}$$

where $D(\beta) = e^{\sqrt{J}\beta b^\dagger - \sqrt{J}\beta^* b}$ and $S(r) = e^{(r^* b^2 - r b^{\dagger 2})/2}$ are the displacement and squeezing operators, respectively, and $|0\rangle \equiv |J\ -J\rangle$ the fully polarized nuclear state. We find the squeezing parameter uniquely defined by the displacement $r = r(\beta)$.

Without loss of generality we assume $\beta \in \mathbb{R}$ (and thus $r \in \mathbb{R}$); that is, the Bloch vector lies in the x-z plane. General states $\beta \in \mathbb{C}$ with arbitrary Bloch vectors on the southern hemisphere can straightforwardly be derived by a rotation around the z axis. Note that the corresponding states on the northern hemisphere can be constructed accordingly as eigenstates of the ascending operator I^+.

In order to show that Eq. (B1) defines an approximate eigenstate of I^- we first consider the transformation of the nuclear operator under the displacement and squeezing operator. Recall that according to Eq. (9) the displaced nuclear operators can be expanded in orders of $\epsilon = 1/\sqrt{J}$,

$$\begin{aligned} D^\dagger(\beta) I^- D(\beta) &= \sqrt{2J - (b^\dagger + \sqrt{J}\beta^*)(b + \sqrt{J}\beta)}\,(b + \sqrt{J}\beta) \\ &= J\mathcal{J}_0^- + \sqrt{J}\mathcal{J}_1^- + O(1), \end{aligned} \tag{B2}$$

where

$$\mathcal{J}_0^- = \sqrt{k}\beta, \tag{B3}$$

$$\begin{aligned} \mathcal{J}_1^- &= \sqrt{2(1-\beta^2)}(\mu b + \nu b^\dagger) \\ &= \sqrt{2(1-\beta^2)}S^\dagger(r) b S(r), \end{aligned} \tag{B4}$$

and $\cosh(r) = \mu = \frac{2k-\beta^2}{2\sqrt{2k(1-\beta^2)}}$ and $\sinh(r) = -\nu = \frac{\beta^2}{2\sqrt{2k(1-\beta^2)}}$, which defines $r = r(\beta)$ [the generalization to complex β is straightforward and leads to Eq. (44)]. Thus, it follows that

$$S^\dagger(-r)D^\dagger(\beta)\, I^- D(\beta)S(-r)|0\rangle = J\mathcal{J}_0^-|0\rangle + O(1), \tag{B5}$$

since $b|0\rangle = 0$.

Multiplying both sides by $D(\beta)S(-r)$ yields the desired approximate eigenvalue equation

$$I^-|\beta\rangle = J\sqrt{k}\beta|\beta\rangle + O(1). \tag{B6}$$

In the thermodynamic limit the term $O(1)$ is negligible and the eigenvalue equation is exact.[6]

Using the above representation we study the spin properties of the states $|\alpha\rangle$. In the following all expectation values are understood to be evaluated in the squeezed coherent state $|\beta\rangle$: $\langle O\rangle \equiv \langle\beta|\, O\, |\beta\rangle$.

Straightforwardly, one derives the nuclear mean polarizations

$$\langle I_x\rangle = \tfrac{1}{2}\langle\beta|(I^+ + I^-)|\beta\rangle = J\sqrt{k}\beta + O(1), \tag{B7}$$

$$\langle I_y\rangle = \tfrac{1}{2i}\langle\beta|(I^+ - I^-)|\beta\rangle = 0 + O(1), \tag{B8}$$

$$\langle I_z\rangle = J(\beta^2 - 1) + O(1), \tag{B9}$$

where in the last equation we used the expansion Eq. (14). Note that the Bloch vector is orthogonal [up to order $O(1)$] to the y direction for all (real) α and of length $|\langle\vec{I}\rangle| = \sqrt{\langle I_x\rangle^2 + \langle I_y\rangle^2 + \langle I_z\rangle^2} = J + O(1)$.

Using Eq. (B6) and the angular momentum commutation relations one readily calculates

$$\begin{aligned} \langle\Delta I_y^2\rangle &= -\frac{1}{2}\langle I_z\rangle + O(1), \\ &= \frac{1}{2}J(1-\beta^2) + O(1), \\ &= \frac{1}{2}J\sqrt{1-(\sqrt{k}\beta)^2} + O(1), \end{aligned} \tag{B10}$$

where, as usual, $\langle\Delta O^2\rangle := \langle O^2\rangle - \langle O\rangle^2$ and we used the identity $1-(\sqrt{k}\beta)^2 = (1-\beta^2)^2$.

Thus, we find for the squeezing parameter in the y direction,

$$\xi_y^2 = 2\langle\Delta I_y^2\rangle/|\langle\vec{I}\rangle| = \sqrt{1-(\sqrt{k}\beta)^2} + O(1/J). \tag{B11}$$

The squeezing diverges for the state that realizes the maximal eigenvalue of the lowering operator ($\sqrt{k}\beta = 1$). This corresponds to a state fully polarized in the x direction.

2. Inhomogeneous case

We approximate a system of inhomogeneous hyperfine coupling by grouping the nuclear spins into n shells. Within a shell i the nuclear spins have identical coupling g_i and the respective (homogeneous) spin operators $A_\alpha^{(i)}$ ($\alpha = x,y,z$) are truncated to a symmetric subspace J_i. The total spin operators

[6] This is true even for $\beta \to 0$ since all terms in the expansion Eq. (B2) that do not vanish upon application on $|0\rangle$ contain at least one factor β as well.

can then be written as

$$A_\alpha = \sum_{i=1}^{n} g_i A_\alpha^{(i)}. \tag{B12}$$

We define collective displacement and squeezing operators

$$\mathcal{D} = \Pi_{i=1}^{n} e^{\sqrt{J_i}\beta_i b_i^\dagger - \sqrt{J_i}\beta_i^* b_i}, \tag{B13}$$

$$\mathcal{S} = \Pi_{i=1}^{n} e^{(r_i^* b_i^2 - r_i b_i^{\dagger 2})/2}, \tag{B14}$$

where the b_i is the respective bosonic operator for shell i. Also here the squeezing parameter r_i depends uniquely [with the same functional dependence as before; cf. Eq. (B4)] on the displacement β_i within the shell, if we demand the first order in the eigenvalue equation to vanish,

$$A^- \mathcal{D}\mathcal{S}\,|0\rangle = \left(\sum_i J_i \sqrt{k_i}\beta_i\right) \mathcal{D}\mathcal{S}\,|0\rangle + O(1), \tag{B15}$$

where $k_i = \sqrt{2-\beta_i^2}$ and $|0\rangle \equiv |0\rangle^{\otimes n}$ is the vacuum of the shell modes.

We emphasize that, in general, the eigenvalues are highly degenerate. For a given eigenvalue α there are infinitely many microscopic realizations (i.e., sets of β_i) that fulfill $\alpha = \sum_i J_i\sqrt{k_i}\beta_i$. Only the maximal eigenvalue $\alpha = J$ features a unique steady state that displays diverging squeezing as one readily shows analogous to the homogeneous case.

APPENDIX C: ROTATED SQUEEZED THERMAL SPIN STATES

A key concept of the paper are RSTSSs, a generalization of squeezed coherent spin states to mixed states, parametrized via an effective temperature. They describe nuclear states which are fully polarized and rotated and feature fluctuations which can be described by a bosonic mode in a thermal (potentially squeezed) Gaussian state. In Sec. IV A we show that the truncation of every nuclear operator to a subspace of total spin J can be expressed in terms of a bosonic mode b and its displacement $\beta \in \mathbb{C}$, using a Holstein-Primakoff transformation [compare Eqs. (9) and (13)],

$$I^\alpha/J = \sum_n \epsilon^n \mathcal{J}_n^\alpha, \tag{C1}$$

where $\epsilon = 1/\sqrt{J}$, and the bosonic operators $\mathcal{J}_n^\alpha$ contain combinations of products of n bosonic operators $b, b^\dagger$. $\mathcal{J}_0^\alpha \in \mathbb{C}$ describes the semiclassical expectation value which is fully determined by the displacement β. β quantifies a rotation of the fully polarized nuclear state on the Bloch sphere. The higher order operators $\mathcal{J}_n^\alpha$ $(n > 0)$ describe quantum fluctuations around this semiclassical nuclear state. RSTSSs are those states where the mode b is in an undisplaced ($\langle b\rangle = 0$), squeezed thermal state, which is fully determined by its CM Γ [Eq. (41)]. These bosonic states constitute the natural steady states of the quadratic master Eq. (25), and we find in Sec. IV B that across the whole phase diagram one steady state of the system can always be described as a RSTSS.

Note that in the limit where the effective temperature of the Gaussian state is zero, we recover the class of squeezed coherent spin states [36], which constitute the solution along segment x.

APPENDIX D: SOLVING EQ. (24)

In order to find the solutions to Eq. (24) (which are numerically difficult to find) we first note that

$$\langle A\rangle_{ss} = 0 \Leftrightarrow \langle \dot{b}\rangle = \langle \dot{b^\dagger}\rangle = 0 \Leftrightarrow \langle \dot{\mathcal{J}_1^-}\rangle = \langle \dot{\mathcal{J}_1^+}\rangle = 0, \tag{D1}$$

where the time derivative is understood with respect to the first-order Liouvillian

$$\mathcal{L}_1\rho = -i\big[a\big(S_x\mathcal{J}_1^x + S_y\mathcal{J}_1^y\big) + (aS^+S^- + \delta\omega)\mathcal{J}_1^z, \rho\big], \tag{D2}$$

and in the usual way we define

$$\mathcal{J}_1^x = \tfrac{1}{2}(\mathcal{J}_1^+ + \mathcal{J}_1^-), \tag{D3}$$

$$\mathcal{J}_1^y = \tfrac{1}{2i}(\mathcal{J}_1^+ - \mathcal{J}_1^-). \tag{D4}$$

Using the relation $[J_1^i, J_1^j] = i\epsilon_{ijk}J_0^k$ one finds the equations

$$0 = \big\langle \dot{\mathcal{J}_1^x}\big\rangle = a\big(\langle S_y\rangle_{ss}\mathcal{J}_0^z - \langle S_z\rangle_{ss}\mathcal{J}_0^y\big) - \omega\mathcal{J}_0^y, \tag{D5}$$

$$0 = \big\langle \dot{\mathcal{J}_1^y}\big\rangle = -a\big(\langle S_x\rangle_{ss}\mathcal{J}_0^z - \langle S_z\rangle_{ss}\mathcal{J}_0^x\big) + \omega\mathcal{J}_0^x, \tag{D6}$$

$$0 = \big\langle \dot{\mathcal{J}_1^z}\big\rangle = a\big(\langle S_y\rangle_{ss}\mathcal{J}_0^x - \langle S_x\rangle_{ss}\mathcal{J}_0^y\big). \tag{D7}$$

Furthermore, from the definitions of the $\mathcal{J}_0^i$'s one finds

$$1 = \big(\mathcal{J}_0^x\big)^2 + \big(\mathcal{J}_0^y\big)^2 + \big(\mathcal{J}_0^z\big)^2. \tag{D8}$$

The steady-state expectation values $\langle S_i\rangle_{ss}$ are found directly via [cf. Eq. (18)],

$$\begin{aligned}\mathcal{L}_0\rho = {}& \gamma\big(S^-\rho S^+ - \tfrac{1}{2}\{S^+S^-,\rho\}_+\big)\\ & - i\big[S_x\big(2\Omega + a\mathcal{J}_0^x\big) + aS_y\mathcal{J}_0^y + aS^+S^-\mathcal{J}_0^z, \rho\big],\end{aligned} \tag{D9}$$

by solving the resulting optical Bloch equations,

$$0 = -\frac{\gamma}{2}\langle S_x\rangle + a\mathcal{J}_0^y\langle S_z\rangle - a\mathcal{J}_0^z\langle S_y\rangle, \tag{D10}$$

$$0 = -\frac{\gamma}{2}\langle S_y\rangle - \big(2\Omega + a\mathcal{J}_0^x\big)\langle S_z\rangle + a\mathcal{J}_0^z\langle S_x\rangle, \tag{D11}$$

$$0 = -\gamma(\langle S_z\rangle + 1/2) + \big(2\Omega + a\mathcal{J}_0^x\big)\langle S_y\rangle - a\mathcal{J}_0^y\langle S_x\rangle. \tag{D12}$$

This set of coupled equations for the six variables $\{\langle S_i\rangle, \mathcal{J}_0^j\}$ can be solved analytically and corresponds to the semiclassical Bloch equations (derived from a brute force factorization: $\langle S_iI_j\rangle \to \langle S_i\rangle\langle I_j\rangle$, for $i,j = x,y,z$ in the equations of motion). The solutions which feature second-order stability (see Section IV B1) are displayed in Fig. 2. Via Eqs. (10) and (14) β can be deduced unambiguously from a given set $\{\langle S_i\rangle, \mathcal{J}_0^j\}$.

APPENDIX E: DERIVING THE SECOND-ORDER TERM OF EQ. (20)

The first term of the second order of Eq. (20) is of the same form as the first order and can readily be calculated:

$$\begin{aligned}\mathrm{Tr}_S(P\mathcal{L}_2P\rho) &= -i\big[a/2(\langle S^+\rangle_{ss}\mathcal{J}_2^- + \langle S^-\rangle_{ss}\mathcal{J}_2^+)\\ &\quad + (a\langle S^+S^-\rangle_{ss} + \delta\omega)\mathcal{J}_2^z, \sigma\big],\\ &= -i[B^*b^2 + B(b^\dagger)^2 + Fb^\dagger b, \sigma],\end{aligned} \tag{E1}$$

with the β-dependent coefficients (remember that also the electron steady-state expectation values are functions of β)

$$B = -\frac{a\beta}{16\sqrt{k^3}}[(4k+|\beta|^2)\langle S^-\rangle_{ss} + \beta^2\langle S^+\rangle_{ss}], \quad \text{(E2)}$$

$$F = -\frac{a}{8\sqrt{k^3}}(4k+|\beta|^2)(\beta\langle S^+\rangle_{ss} + \beta^*\langle S^-\rangle_{ss}) + a(\langle S^+S^-\rangle_{ss} + \delta\omega/a). \quad \text{(E3)}$$

Next, we consider the second term of the second-order perturbative master equation

$$\begin{aligned} &-\mathrm{Tr}_s(P\mathcal{L}_1\mathcal{Q}\mathcal{L}_0^{-1}\mathcal{Q}\mathcal{L}_1 P\rho) \\ &= -\mathrm{Tr}_s[P\mathcal{L}_1(\mathbb{1}-P)\mathcal{L}_0^{-1}(\mathbb{1}-P)\mathcal{L}_1 P\rho] \\ &= \int_0^\infty d\tau \mathrm{Tr}_s(P\mathcal{L}_1 e^{\mathcal{L}_0\tau}\mathcal{L}_1 P\rho) \\ &\quad - \int_0^\infty d\tau \mathrm{Tr}_s(P\mathcal{L}_1 P\mathcal{L}_1 P\rho), \end{aligned} \quad \text{(E4)}$$

where we used the Laplace transform $-\mathcal{L}_0^{-1} = \int_0^\infty d\tau e^{\mathcal{L}_0\tau}$ and the property $e^{\mathcal{L}_0\tau}P = Pe^{\mathcal{L}_0\tau} = P$.

Noting that

$$\mathrm{Tr}_s(P\mathcal{L}_1 X) = -i\mathrm{Tr}_s([bA + b^\dagger A^\dagger, X]), \quad \text{(E5)}$$

and using Eq. (22) we find

$$-\int_0^\infty d\tau \mathrm{Tr}_s(P\mathcal{L}_1 P\mathcal{L}_1 P\rho) = \int_0^\infty d\tau \langle A^\alpha\rangle_{ss}\langle A^\beta\rangle_{ss}[b^\alpha,[b^\beta,\sigma]], \quad \text{(E6)}$$

where $\alpha,\beta = \dagger$, "void", and the Einstein sum convention is used.

In the same fashion we find

$$\begin{aligned} &\int_0^\infty d\tau \mathrm{Tr}_s(P\mathcal{L}_1 e^{\mathcal{L}_0\tau}\mathcal{L}_1 P\rho) \\ &= -\int_0^\infty d\tau \langle A^\alpha(\tau)A^\beta(0)\rangle_{ss}[b^\alpha,[b^\beta,\sigma]] \\ &\quad - \int_0^\infty d\tau \langle [A^\alpha(\tau),A^\beta(0)]\rangle_{ss}[b^\alpha,\sigma b^\beta]. \end{aligned} \quad \text{(E7)}$$

Here we defined the autocorrelation functions $\langle A^\alpha(\tau)A^\beta(0)\rangle_{ss} = \mathrm{Tr}_s(A^\alpha e^{\mathcal{L}_0\tau}A^\beta\rho_{ss})$ and $\langle [A^\alpha(\tau),A^\beta(0)]\rangle_{ss} = \mathrm{Tr}_s(A^\alpha e^{\mathcal{L}_0\tau}[A^\beta,\rho_{ss}])$ (cf., e.g., [54], pp. 22).

Putting together the results Eq. (E4) reduces to

$$\begin{aligned} &-\mathrm{Tr}_s(P\mathcal{L}_1\mathcal{Q}\mathcal{L}_0^{-1}\mathcal{Q}\mathcal{L}_1 P\rho) \\ &= -\int_0^\infty d\tau \langle \Delta A^\alpha(\tau)\Delta A^\beta(0)\rangle_{ss}[b^\alpha,[b^\beta,\sigma]] \\ &\quad - \int_0^\infty d\tau \langle [\Delta A^\alpha(\tau),\Delta A^\beta(0)]\rangle_{ss}[b^\alpha,\sigma b^\beta], \end{aligned} \quad \text{(E8)}$$

$\Delta O := O - \langle O\rangle_{ss}$. Since we choose the displacement β such that $\langle A^\alpha\rangle_{ss} = 0$ [Eq. (24)] it is $\Delta A^\alpha = A^\alpha$. Merging Eqs. (E1) and (E8), and regrouping the terms, one readily derives Eq. (25).

1. Calculation of the coefficients

In order to determine the coefficients Eq. (28) we have to calculate terms of the kind $\int_0^\infty d\tau\langle\Delta A^\alpha(\tau)\Delta A^\beta(0)\rangle_{ss}$ and $\int_0^\infty d\tau\langle\Delta A^\alpha(0)\Delta A^\beta(\tau)\rangle_{ss}$. Exemplarily, we calculate the two terms for $\alpha = \beta =$ "void".

First, defining $\vec{v} = [\frac{a}{4\sqrt{k}}(2k-|\beta|^2), -\frac{a}{4\sqrt{k}}\beta^2, \beta a]^T$ we can write $\Delta A = \vec{v}^*\cdot\Delta\vec{S}$ (and with $\vec{w} = [-\frac{a}{4\sqrt{k}}(\beta^*)^2, \frac{a}{4\sqrt{k}}(2k-|\beta|^2), \beta^* a]^T$ we find $\Delta A^\dagger = \vec{w}^*\cdot\Delta\vec{S}$). Likewise, it is $\Delta A^\dagger = \Delta\vec{S}^\dagger\cdot\vec{v}$ ($\Delta A = \Delta\vec{S}^\dagger\cdot\vec{w}$).

Consequently we compute

$$\begin{aligned} \int_0^\infty d\tau\langle\Delta A_\tau\Delta A\rangle_{ss} &= \vec{v}^*\left(\int_0^\infty d\tau\langle\Delta\vec{S}_\tau\Delta\vec{S}^\dagger\rangle_{ss}\right)\vec{w} \\ &= \vec{v}^*\left(\int_0^\infty d\tau e^{\mathcal{M}\tau}\langle\Delta\vec{S}\Delta\vec{S}^\dagger\rangle_{ss}\right)\vec{w} \\ &= \vec{v}^*(-\mathcal{M}^{-1}\langle\Delta\vec{S}\Delta\vec{S}^\dagger\rangle_{ss})\vec{w} = \vec{v}^*\mathcal{F}_1\vec{w}, \end{aligned} \quad \text{(E9)}$$

where we applied the quantum regression theorem in the second step and used the definitions of Sec. (IV A).

Noting that

$$\begin{aligned} \int_0^\infty d\tau\langle\Delta\vec{S}\Delta\vec{S}_\tau^\dagger\rangle_{ss} &= \left(\int_0^\infty d\tau\langle\Delta\vec{S}_\tau\Delta\vec{S}^\dagger\rangle_{ss}\right)^\dagger \\ &= (-\mathcal{M}^{-1}\langle\Delta\vec{S}\Delta\vec{S}^\dagger\rangle_{ss})^\dagger \\ &= -\langle\Delta\vec{S}\Delta\vec{S}^\dagger\rangle_{ss}\mathcal{M}^{-\dagger} = \mathcal{F}_2 = \mathcal{F}_1^\dagger, \end{aligned} \quad \text{(E10)}$$

we write

$$\int_0^\infty d\tau\langle\Delta A\Delta A_\tau\rangle_{ss} = \vec{v}^*\mathcal{F}_2\vec{w}. \quad \text{(E11)}$$

Analogously, we find the relations

$$\begin{aligned} \int_0^\infty d\tau\langle\Delta A_\tau^\dagger\Delta A\rangle_{ss} &= \vec{w}^*\mathcal{F}_1\vec{w}, \\ \int_0^\infty d\tau\langle\Delta A^\dagger\Delta A_\tau\rangle_{ss} &= \vec{w}^*\mathcal{F}_2\vec{w}, \\ \int_0^\infty d\tau\langle\Delta A_\tau\Delta A^\dagger\rangle_{ss} &= \vec{v}^*\mathcal{F}_1\vec{v}, \\ \int_0^\infty d\tau\langle\Delta A\Delta A_\tau^\dagger\rangle_{ss} &= \vec{v}^*\mathcal{F}_2\vec{v}, \\ &\vdots \end{aligned} \quad \text{(E12)}$$

such that all coefficients of the effective master Eq. (20) can be calculated by simple matrix multiplication.

[1] M. Vojta, Rep. Prog. Phys. **66**, 2069 (2003).
[2] S. Sachdev, Rev. Mod. Phys. **75**, 913 (2003).
[3] V. L. Ginzburg, Phys. Usp. **40**, 407 (2007).
[4] E. Kim and M. H. W. Chan, Nature (London) **427**, 225 (2004).

[5] D. Belitz and T. Kirkpatrick, Rev. Mod. Phys. **66**, 261 (1994).
[6] M. Hasan and C. Kane, Rev. Mod. Phys. **82**, 3045 (2010).
[7] H. J. Carmichael, J. Phys. B **13**, 3551 (1980).
[8] P. Werner, K. Volker, M. Troyer, and S. Chakravarty, Phys. Rev. Lett. **94**, 047201 (2005).
[9] L. Capriotti, A. Cuccoli, A. Fubini, V. Tognetti, and R. Vaia, Phys. Rev. Lett. **94**, 157001 (2005).
[10] S. Morrison and A. S. Parkins, J. Phys. B **41**, 195502 (2008).
[11] J. Eisert and T. Prosen, arXiv:1012.5013.
[12] M. J. Bhaseen, J. Mayoh, B. D. Simons, and J. Keeling, Phys. Rev. A **85**, 013817 (2012).
[13] S. Diehl, A. Tomadin, A. Micheli, R. Fazio, and P. Zoller, Phys. Rev. Lett. **105**, 015702 (2010).
[14] M. Žnidarič, Phys. Rev. E **83**, 011108 (2011).
[15] K. Baumann, C. Guerlin, F. Brennecke, and T. Esslinger, Nature (London) **464**, 1301 (2010).
[16] B. Öztop, M. Bordyuh, Ö. E. Müstecaplıoğlu, and H. E. Türeci, arXiv:1107.3108.
[17] K. Hepp and E. H. Lieb, Ann. Phys. **76**, 360 (1973).
[18] H. Gibbs, S. McCall, and T. Venkatesan, Phys. Rev. Lett. **36**, 1135 (1976).
[19] S. V. Lawande, R. R. Puri, and S. S. Hassan, J. Phys. B **14**, 4171 (1981).
[20] R. R. Puri, S. V. Lawande, and S. S. Hassan, Opt. Commun. **35**, 179 (1980).
[21] R. Bonifacio and L. A. Lugiato, Phys. Rev. A **18**, 1129 (1978).
[22] S. Schneider and G. J. Milburn, Phys. Rev. A **65**, 042107 (2002).
[23] M. Gaudin, J. Phys. France **37**, 1087 (1976).
[24] M. Bortz and J. Stolze, J. Stat. Mech. (2007) P06018.
[25] J. Schliemann, A. Khaetskii, and D. Loss, J. Phys.: Condens. Matter **15**, 1809R (2003).
[26] O. Krebs, P. Maletinsky, T. Amand, B. Urbaszek, A. Lemaitre, P. Voisin, X. Marie, and A. Imamoglu, Phys. Rev. Lett. **104**, 056603 (2010).
[27] A. Russell, V. I. Fal'ko, A. I. Tartakovskii, and M. S. Skolnick, Phys. Rev. B **76**, 195310 (2007).
[28] A. Rivas, S. F. Huelga, *Open Quantum Systems: An Introduction* (Springer, Berlin, 1999).
[29] Birger Horstmann, J. Ignacio Cirac, and Géza Giedke, arXiv:1207.1653v1 [quant-ph].
[30] S. Sachdev, *Quantum Phase Transitions* (Cambridge University Press, Cambridge, 1999).
[31] M. Atatüre, J. Dreiser, A. Badolato, A. Högele, K. Karrai, and A. Imamoglu, Science **312**, 551 (2006).
[32] P. Tamarat, N. B. Manson, J. P. Harrison, R. L. McMurtrie, A. Nizovtsev, C. Santori, R. G. Beausoleil, P. Neumann, T. Gaebel, F. Jelezko *et al*., New J. Phys. **10**, 045004 (2008).
[33] E. M. Kessler, S. Yelin, M. D. Lukin, J. I. Cirac, and G. Giedke, Phys. Rev. Lett. **104**, 143601 (2010).
[34] M. S. Rudner, L. M. K. Vandersypen, V. Vuletić, and L. S. Levitov, Phys. Rev. Lett. **107**, 206806 (2011).
[35] T. Holstein and H. Primakoff, Phys. Rev. **58**, 1098 (1940).
[36] M. Kitagawa and M. Ueda, Phys. Rev. A **47**, 5138 (1993).
[37] B. Urbaszek, X. Marie, T. Amand, O. Krebs, P. Voisin, P. Maletinsky, A. Hogele, and A. Imamoglu, arXiv:1202.4637.
[38] J. K. Korbicz, J. I. Cirac, and M. Lewenstein, Phys. Rev. Lett. **95**, 120502 (2005).
[39] L. Pezzé and A. Smerzi, Phys. Rev. Lett. **102**, 100401 (2009).
[40] P. Hyllus, W. Laskowski, R. Krischek, C. Schwemmer, W. Wieczorek, H. Weinfurter, L. Pezzé, and A. Smerzi, Phys. Rev. A **85**, 022321 (2012).
[41] G. Tóth, Phys. Rev. A **85**, 022322 (2012).
[42] A. Clifford and T. Clifford, *Fundamentals of Supercritical Fluids* (Oxford University Press, New York, 1999).
[43] C. M. Bowden and C. C. Sung, Phys. Rev. A **19**, 2392 (1979).
[44] E. M. Kessler, arXiv:1205.5440 [Phys. Rev. A (to be published)].
[45] M. Lax, Phys. Rev. **129**, 2342 (1963).
[46] M. S. Kim, J. Lee, and W. J. Munro, Phys. Rev. A **66**, 030301(R) (2002).
[47] D. Nagy, G. Konya, G. Szirmai, and P. Domokos, Phys. Rev. Lett. **104**, 130401 (2010).
[48] N. Lambert, C. Emary, and T. Brandes, Phys. Rev. Lett. **92**, 073602 (2004).
[49] P. D. Drummond and D. F. Walls, J. Phys. A **13**, 725 (1980).
[50] F. Jelezko and J. Wrachtrup, Phys. Status Solidi A **203**, 3207 (2006).
[51] E. Togan, Y. Chu, A. Imamoglu, and M. D. Lukin, Nature (London) **478**, 497 (2011).
[52] N. Chisholm, P. Maurer, G. Kucsko, P. Lo, N. Yao, B. Shields, H. Park, and M. Lukin, *American Physical Society, 42nd Annual Meeting of the APS Division of Atomic, Molecular and Optical Physics*, Abstract No. OPE.10 (2011), http://meetings.aps.org/link/BAPS.2011.DAMOP.E1.96.
[53] M. Kroner, K. M. Weiss, B. Biedermann, S. Seidl, S. Manus, A. W. Holleitner, A. Badolato, P. M. Petroff, B. D. Gerardot, R. J. Warburton, and K. Karrai, Phys. Rev. Lett. **100**, 156803 (2008).
[54] H. J. Carmichael, *Statistical Methods in Quantum Optics 1* (Springer, Berlin, 1999).

PHYSICAL REVIEW A **87**, 012108 (2013)

Noise-driven dynamics and phase transitions in fermionic systems

Birger Horstmann,[1,2] J. Ignacio Cirac,[1] and Géza Giedke[1,3]
[1]*Max-Planck-Institut für Quantenoptik, Hans-Kopfermann-Straße 1, 85748 Garching, Germany*
[2]*Deutsches Zentrum für Luft- und Raumfahrt, Institut für Technische Thermodynamik, Pfaffenwaldring 38-40, 70569 Stuttgart, Germany*
[3]*Zentrum Mathematik, Technische Universität München, L.-Boltzmannstrasse 3, 85748 Garching, Germany*
(Received 3 August 2012; published 10 January 2013)

We study abrupt changes in the dynamics and/or steady state of fermionic noise-driven systems produced by small changes in the system parameters. Specifically, we consider fermionic systems whose dynamics is described by master equations that are quadratic (and, under certain conditions, quartic) in creation and annihilation operators. We analyze phase transitions in the steady state as well as "dynamical transitions." The latter are characterized by abrupt changes in the rate at which the system asymptotically approaches the steady state. We illustrate our general findings with relevant examples of fermionic (and, equivalently, spin) systems and show that they can be realized in ion chains.

DOI: 10.1103/PhysRevA.87.012108 PACS number(s): 03.65.Yz, 05.30.Rt

I. INTRODUCTION

Motivated by the impressive experimental control over many-body quantum states and dynamics [1], open many-body quantum systems have received increasing experimental and theoretical attention in recent years. On one hand, the decoherence introduced by coupling to an environment or by quantum noise is a major challenge to quantum information processing [2], on the other hand, it can play a constructive role for quantum computing [3,4], state preparation [5–8], entanglement generation [9,10], quantum memories [11], or quantum simulation [12–16].

These exciting possibilities drive the interest in understanding the steady-state phase diagram of open systems in detail [17]. Of particular interest are points of transitions between different phases of the system. For closed systems at zero temperature, the phase diagram and quantum phase transition can be understood by studying the low-lying energy eigenstates of the system's Hamiltonian [18]. In particular, the nonanalyticity of certain expectation values as a function of an external parameter, that characterizes the quantum phase transition, can only occur if the gap of the Hamiltonian closes, i.e., the energy difference between ground state and first excited state vanishes. Quantum phase transitions are, thus, determined by the low-energy spectrum of the Hamiltonian governing the dynamics of wave functions,

$$\partial_t|\Phi\rangle = -\frac{i}{\hbar}\mathbf{H}|\Phi\rangle. \tag{1}$$

In this paper, we study abrupt changes in the physical properties of a many-body quantum system whose dynamics is described by a master equation,

$$\partial_t\rho = \boldsymbol{\mathcal{S}}\rho. \tag{2}$$

This equation describes the dynamics of an open system coupled to a Markovian reservoir where ρ is the system's density operator. The superoperator $\boldsymbol{\mathcal{S}}$ contains two parts: One is related to the system Hamiltonian (possibly renormalized due to the interaction with the environment), and the other is related to the quantum noise induced by the environment. Under the appropriate conditions, the system evolves to a steady state $\rho_{\rm ss}$, which corresponds to a (right) eigenstate of $\boldsymbol{\mathcal{S}}$ with eigenvalue 0. Note that this eigenvalue may be degenerate, or there may be other eigenvalues with zero real parts. In case this does not happen, the steady state is unique. Then, the other eigenvalues λ of $\boldsymbol{\mathcal{S}}$ have a negative real part, and the smallest absolute value of them Δ determines the *asymptotic decay rate* (ADR), that is, the rate at which the steady state is reached. A phase transition in the steady state, where its properties abruptly change when one slightly changes a parameter in the master equation, is accompanied by the vanishing of Δ. This situation has recently been studied by many authors (see, for example, Refs. [3,5,17,19,20]) and is typically referred to as a "dissipative quantum phase transition" or "noise-driven quantum phase transition." There is a natural analogy between noise-driven and (closed-system) quantum phase transitions: A unique ground state of the Hamiltonian is analogous to a unique steady state. The appearance of a phase transition is signaled by the vanishing of the gap or Δ, respectively.

Apart from its role in reflecting the appearance of a phase transition, the quantity Δ can play an additional role. It also represents a physical property of the system, namely, the rate at which the steady state is approached asymptotically or the system's response to perturbations in the steady state. This quantity may change abruptly itself. In that case, we can talk about a *dynamical transition* since a small change in the system parameters may lead to an abrupt change in the dynamics of the system. Actually, such a transition may, in principle, occur even if Δ remains finite, and thus, it is a different property than the transitions generally studied in this context.

In this paper, we investigate both kinds of transitions for simple fermionic systems. We concentrate on systems that are described by master equations and for which the Hamiltonian is, at most, quadratic in fermionic creation and annihilation operators. Specifically, we consider two kinds of noise terms: (i) general quadratic in the fermionic operators and (ii) quartic, but with some conditions (namely, that they correspond to Hermitian Lindblad operators). In the first case, the dynamics can be exactly solved [21–24], which has been exploited in several recent papers to study the interplay of noise and critical Hamiltonians in one-dimensional (1D) fermionic systems [19,23,25]. In the second case, even though the full dynamics cannot be obtained, we show that it is, nevertheless, possible to exactly determine the dynamics of certain expectation values

 ©2013 American Physical Society

from which dynamical and steady-state properties can be obtained. In this last case, we present analytical examples where dynamical transitions occur [26]. This situation has also been studied in Refs. [27–29] with particular regard to transport through a dephasing spin chain where exact solutions of the associated master equation could be obtained.

The formalism we develop is relatively general, and we illustrate it with explicit examples. In particular, we consider Hamiltonians which are intimately connected to physical situations that can be obtained in the laboratory, namely, anisotropic XY spin chains in transverse magnetic fields and that are mapped to a fermionic Hamiltonian by a Jordan-Wigner transformation. This family of Hamiltonians displays the prototype of a continuous phase transition [18]. The noise terms we consider can also be understood as particular physical processes occurring in the spin chain through its interaction with an environment [30]. Note that our framework also applies to the systems studied in Refs. [21,22,27,28] and, for the quadratic noise terms, is related to Refs. [19,23] where generic noise-driven phase transitions are analyzed.

This paper is structured as follows. In Sec. II, we introduce the Lindblad master equation, which allows describing decoherence due to the weak interaction with a Markovian bath and presents the covariance matrix (CM) formalism, which allows the exact treatment of quadratic fermionic systems. In Sec. III, we extend this formalism to decoherent systems with linear and Hermitian quadratic Lindblad operators. Then, we come to the calculation of the steady states and the ADRs for relevant interesting examples in this framework in Secs. IV–VI. Here, we explicitly demonstrate the presence of noise-driven phase transitions. In Sec. VII, we propose a possible implementation with cold ions before concluding in Sec. VIII.

II. NOTATION AND METHODS

In this section, we introduce our tools and notation, namely, the Lindblad master equation and the fermionic CM formalism, which is ideally suited for describing quasifree fermionic systems (see Sec. II C).

A. Lindblad master equation

We consider systems whose interaction with an environment leads to a time evolution governed by a Lindblad master equation [31],

$$\partial_t \rho = \mathcal{S}\rho = -\frac{i}{\hbar}[\mathbf{H},\rho] + \sum_\alpha \left(\mathbf{L}^\alpha \rho \mathbf{L}^{\alpha\dagger} - \frac{1}{2}\{\mathbf{L}^{\alpha\dagger}\mathbf{L}^\alpha,\rho\} \right), \tag{3}$$

where ρ is the density matrix of the system, $\mathbf{H}$ is its Hamiltonian, and the Lindblad operators $\mathbf{L}^\alpha$ determine the interaction between the system and the bath. This dynamical equation for an open system can be derived from two different points of view [32]: First, it can be derived from the full dynamics of system and bath. Here, three major approximations have to be used: The states of system and environment are initially uncorrelated, the coupling between system and bath is weak (Born approximation), and the environment equilibrates fast (Markov approximation). Second, any time evolution given by a quantum dynamical semigroup (i.e., a family of completely positive trace-preserving maps ϵ_t, which is strongly continuous and satisfies $\epsilon_t \epsilon_s = \epsilon_{t+s}$) is generated by an equation of the form Eq. (3).

We characterize the decoherence dynamics with the steady state and the asymptotic decay rate. A steady-state density matrix ρ_0 of the master equation (3) fulfills

$$\partial_t \rho_0 = \mathcal{S}\rho_0 = 0, \tag{4}$$

and is the (generically unique) eigenvector with eigenvalue 0 of the Liouvillian superoperator $\mathcal{S}$. The approach to the steady state is then governed by the nonzero eigenvalues (and eigenvectors) of $\mathcal{S}$, all of which have nonpositive real parts for Liouvillians of Lindblad form. Of particular interest is the eigenvalue with the largest real part since it governs the long-term dynamics. We refer to the absolute value of this largest real part as the ADR and denote it by Δ,

$$\Delta(\mathcal{S}) = \max\{|\mathrm{Re}\,\lambda| \neq 0 \colon \exists \rho_\lambda \colon \mathcal{S}(\rho_\lambda) = \lambda \rho_\lambda\}. \tag{5}$$

B. Quasifree fermions and spins

We consider systems with N fermionic modes described by creation and annihilation operators $a_j^\dagger$ and a_j. These operators obey the canonical anticommutation relations,

$$\{a_j, a_k\} = 0, \quad \{a_j^\dagger, a_k\} = \delta_{jk}. \tag{6}$$

Equivalently, we can use Hermitian fermionic Majorana operators,

$$c_{j,0} = a_j^\dagger + a_j, \quad c_{j,1} = (-i)(a_j^\dagger - a_j), \tag{7}$$

which, as generators of the Clifford algebra, satisfy the anticommutation relations,

$$\{c_{j,u}, c_{k,v}\} = 2\delta_{jk}\delta_{uv}. \tag{8}$$

We consider fermionic Hamiltonians that are quadratic in the Majorana operators. They describe quasifree fermions and are known to be exactly solvable. We parametrize them with the real antisymmetric matrix H,

$$\mathbf{H} = \frac{i}{4}\hbar \sum_{jkuv} H_{jk,uv} c_{j,u} c_{k,v}. \tag{9}$$

The 2×2 matrix $H_{jk} \equiv (H_{jk,uv})_{uv}$ describes the coupling between modes j and k.

All eigenstates and thermal states of such a quadratic fermionic Hamiltonian are Gaussian, i.e., they have a density operator, which is the exponential of a quadratic form in the Majorana operators. Gaussian states remain Gaussian under the evolution with quadratic Hamiltonians.

In the following, we will mostly be concerned with *translationally invariant* systems and nearest-neighbor interactions. In terms of the matrix H, the former means that H_{jk} depends only on the difference $j - k$, and for short, we write

$$H_{jk} \equiv H_{j-k}, \tag{10}$$

whereas, the latter implies that $H_s = 0$ for $s > 1$. We work with periodic boundary conditions, so $j - k$ is understood mod N.

An important reason to study one-dimensional fermionic systems with quadratic Hamiltonians is their intimate relation

to certain types of spin chains: The Jordan-Wigner transformation [33] maps fermionic operators onto Pauli spin operators via

$$c_{j,0} \leftrightarrow \prod_{k=1}^{j-1} \sigma_z^k \sigma_x^j, \quad c_{j,1} \leftrightarrow \prod_{k=1}^{j-1} \sigma_z^k \sigma_y^j. \tag{11}$$

Under this transformation, some spin chains are mapped to spinless quasifree fermionic systems, which can be solved exactly. A prominent example is the anisotropic XY chain in a transverse magnetic field [18] with the Hamiltonian,

$$\mathbf{H} = -J \sum_{j=1}^{N} \left[(1+\gamma)\sigma_x^j \sigma_x^{j+1} + (1-\gamma)\sigma_y^j \sigma_y^{j+1}\right] + B \sum_{j=1}^{N} \sigma_z^j, \tag{12}$$

where B is the magnetic field, J is the ferromagnetic coupling, and γ is the anisotropy parameter. Closed systems governed by this Hamiltonian show a quantum phase transition at $B = 2J$ in the thermodynamic limit, and the behavior in the presence of noise is studied in Sec. VI B.

We are interested in noise-driven open fermionic systems with dynamics described by a Lindblad master equation, characterized by a set of Lindblad operators L^α. We consider two classes of Lindblad operators: first, those given by arbitrary linear combinations of the Majorana operators (*linear* Lindblad operators),

$$\mathbf{L}^\alpha = \sum_{ju} L^\alpha_{j,u} c_{j,u}, \quad L^\alpha_{j,u} \in \mathbb{C}, \tag{13}$$

and second, those represented by quadratic expressions in the Majorana operators, which are, in addition, Hermitian (*Hermitian quadratic* Lindblad operators),

$$\mathbf{L}^\alpha = \frac{i}{4} \sum_{jkuv} L^\alpha_{jk,uv} c_{j,u} c_{k,v}, \tag{14}$$

with the real and antisymmetric matrix L^α.

C. Covariance matrix formalism

Now, we present a framework in which the noise-driven dynamics of the Lindblad master equation (3) can be solved exactly.

For every state of a fermionic system, its real and antisymmetric CM is defined by

$$\Gamma_{jk,uv} = \mathrm{tr}\left(\rho \frac{i}{2}[c_{j,u}, c_{k,v}]\right). \tag{15}$$

The magnitudes of the imaginary eigenvalues of Γ are smaller than or equal to unity ($\Gamma^2 \leqslant -\mathbb{1}$).

For Gaussian states, the correlation functions of all orders are related to the CM through Wick's theorem [34]. In particular, pure Gaussian states $\rho = |\Psi\rangle\langle\Psi|$ satisfy $\Gamma^2 = -\mathbb{1}$. In our notation, Γ_{jk} denotes a 2×2 matrix that describes the covariances between sites j and k.

III. LINDBLAD MASTER EQUATION IN THE COVARIANCE MATRIX FORMALISM

The CM formalism is especially useful if the operative dynamics leads to closed equations for the CM, which is the case for the two kinds of Lindblad operators Eqs. (13) and (14) that we study in the following.

A. Linear Lindblad operators

We consider a system with a quadratic Hamiltonian given by the antisymmetric matrix H [cf. Eq. (9)] and linear Lindblad operators as defined in Eq. (13). Using the anticommutation relations (8), we determine the dynamical equation for the CM Γ from Eq. (3) and obtain

$$\partial_t \Gamma = [H, \Gamma] - \sum_\alpha \{|L^\alpha\rangle\langle L^\alpha| + |L^{\alpha *}\rangle\langle L^{\alpha *}|, \Gamma\} - 2i(|L^\alpha\rangle\langle L^\alpha| - |L^{\alpha *}\rangle\langle L^{\alpha *}|), \tag{16}$$

where $|L^\alpha\rangle$ denotes the vector formed by the coefficients $L^\alpha_{j,u}$ in Eq. (13) and $|L^{\alpha *}\rangle$ denotes its complex conjugate. In terms of $|\Gamma\rangle$, the vector of components of Γ, this equation becomes

$$\partial_t |\Gamma\rangle = \mathcal{S}|\Gamma\rangle - |\mathcal{V}\rangle = (\mathcal{H} - \mathcal{M})|\Gamma\rangle - |\mathcal{V}\rangle, \tag{17}$$

with the superoperators,

$$\mathcal{H} = (H \otimes \mathbb{1} - \mathbb{1} \otimes H^T), \tag{18}$$

$$\mathcal{M} = \sum_\alpha [|L^\alpha\rangle\langle L^\alpha| \otimes \mathbb{1} + \mathbb{1} \otimes (|L^\alpha\rangle\langle L^\alpha|)^T + \text{c.c.}], \tag{19}$$

$$|\mathcal{V}\rangle = 2i \sum_\alpha (|L^\alpha\rangle \otimes |L^\alpha\rangle - \text{c.c.}). \tag{20}$$

Note that $\mathcal{H}$ is anti-Hermitian and $\mathcal{M}$ is Hermitian and positive semidefinite. The steady-state CM [see Eq. (4)] satisfies

$$(\mathcal{H} - \mathcal{M})|\Gamma_0\rangle = |\mathcal{V}\rangle. \tag{21}$$

Deviations $|\delta\Gamma\rangle = |\Gamma\rangle - |\Gamma_0\rangle$ then obey

$$\partial_t |\delta\Gamma\rangle = (\mathcal{H} - \mathcal{M})|\delta\Gamma\rangle, \tag{22}$$

and the approach to the steady state is governed by the the right eigenvalues of the superoperator $\mathcal{S} = \mathcal{H} - \mathcal{M}$, satisfying

$$\mathcal{S}|\Gamma_i\rangle = \lambda_i |\Gamma_i\rangle. \tag{23}$$

The eigenvalues whose real parts are closest to zero, thus, determine the asymptotics of the decoherence process. In the following, we refer to

$$\Delta = \max\{|\mathrm{Re}\,\lambda_i| \neq 0 \colon \exists \Gamma_i \quad \text{such that} \quad (\mathcal{S} - \lambda_i)|\Gamma_i\rangle = 0\}, \tag{24}$$

i.e., the asymptotic decay rate on the level of CMs simply as ADR.

B. Quadratic and Hermitian Lindblad operators

The second class of master equations, leading to closed equations for the CM, is of the form Eq. (3) with Lindblad operators that are quadratic and Hermitian as in Eq. (14). Lindblad equations with Hermitian Lindblad operators describe the dynamics of systems in contact with a classical bath. Let us choose a fluctuating external field as the source of decoherence (see Sec. VII). If, additionally, the Lindblad operators are

quadratic, the fluctuating Hamiltonian is quadratic. Thus, in this case, Gaussian states evolve into mixtures of Gaussian states under such evolutions, and we can expect a closed equation for the CM.

Before discussing the master equation in the CM formalism, let us first determine, in general, the steady-state density matrices [see Eq. (4)] of a master equation with only Hermitian Lindblad operators. In that case, we can rewrite the master equation in terms of $|\rho\rangle$, the vector of components of ρ as

$$\partial_t|\rho\rangle = \mathcal{S}|\rho\rangle = \left(\mathcal{H} - \frac{1}{2}\sum_\alpha (\mathcal{L}^\alpha)^2\right)|\rho\rangle, \tag{25}$$

with the superoperators,

$$\mathcal{H} = -i(\mathbf{H}\otimes\mathbf{1} - \mathbf{1}\otimes\mathbf{H}^T), \tag{26}$$

$$\mathcal{L}^\alpha = \mathbf{L}^\alpha\otimes\mathbf{1} - \mathbf{1}\otimes\mathbf{L}^{\alpha T}. \tag{27}$$

We observe that the superoperator $\mathcal{H}$ is anti-Hermitian and that the superoperators $\mathcal{L}^\alpha$ are Hermitian so that the $(\mathcal{L}^\alpha)^2$ are Hermitian and non-negative.

We consider all complex-valued vectors $|\rho\rangle$ instead of just the ones corresponding to positive density matrices with trace 1. Therefore, we have to check, after the calculation, if our results correspond to physically meaningful states. The steady states satisfy

$$\langle\rho_0|\left(\mathcal{H} - \frac{1}{2}\sum_\alpha (\mathcal{L}^\alpha)^2\right)|\rho_0\rangle = 0. \tag{28}$$

As stated above, $\mathcal{H}$ is anti-Hermitian, and all $(\mathcal{L}^\alpha)^2$ are Hermitian. Applying these properties, we can conclude from Eq. (28) that

$$\langle\rho_0|\sum_\alpha (\mathcal{L}^\alpha)^2|\rho_0\rangle = \langle\rho_0|\mathcal{H}|\rho_0\rangle = 0 \tag{29}$$

holds. It follows from the non-negativity of $(\mathcal{L}^\alpha)^2$ that

$$(\mathcal{L}^\alpha)^2|\rho_0\rangle = 0 \quad \forall\,\alpha. \tag{30}$$

Because the $\mathcal{L}^\alpha$ can be diagonalized, this implies $\mathcal{L}^\alpha|\rho_0\rangle = 0$. It follows that $\mathcal{H}|\rho_0\rangle$ vanishes identically. In terms of matrices ρ_0, we can summarize these conditions for steady states,

$$[\mathbf{H},\rho_0] = [\mathbf{L}^\alpha,\rho_0] = 0 \quad \forall\,\alpha. \tag{31}$$

It can be verified, with Eq. (3), that this condition for steady states is not only necessary, but also is sufficient. To summarize, steady states for Hermitian Lindblad operators correspond to density matrices commuting with the Hamiltonian and all Lindblad operators. Therefore, they are the identity up to symmetries shared by the Hamiltonian and the Lindblad operators.

Let us now return to exactly solvable systems in the CM formalism. For quadratic and Hermitian Lindblad operators and quadratic Hamiltonians, the master equation (3) becomes

$$\partial_t\Gamma = [H,\Gamma] + \frac{1}{2}\sum_\alpha [L^\alpha,[L^\alpha,\Gamma]]. \tag{32}$$

We can again reformulate this equation for the vector of components $|\Gamma\rangle$,

$$\partial_t|\Gamma\rangle = S|\Gamma\rangle = \left(\mathcal{H} - \frac{1}{2}\sum_\alpha (\mathcal{L}^\alpha)^2\right)|\Gamma\rangle, \tag{33}$$

with $\mathcal{H}$ as in Eq. (18) and $\mathcal{L}^\alpha = L^\alpha\otimes\mathbb{1} - \mathbb{1}\otimes L^\alpha$.

Since we found that steady states are trivial for Hermitian Lindblad operators, we concentrate on the asymptotics of the decoherence process. It is studied through the eigenvalues λ_i of the superoperator $\mathcal{S}$ and, in particular, its ADR as defined in Eq. (24).

C. Translationally invariant Hamiltonians

Naturally, translationally invariant systems are best treated in a Fourier-transformed picture. Any real antisymmetric matrix can be transformed into a real and antisymmetric block-diagonal matrix by an orthogonal transformation O. For the Hamiltonian matrix H, this means

$$H'_{mn,uv} = (OHO^T)_{mn,uv}, \quad H'_{mn} = \delta_{mn}\begin{pmatrix} 0 & \epsilon_m \\ -\epsilon_m & 0\end{pmatrix}, \tag{34}$$

where the real number ϵ_m is the energies of the elementary excitations. We, however, transform the Hamiltonian matrix with the unitary Fourier transform,

$$\widetilde{H}_{mn,uv} = (UHU^\dagger)_{mn,uv}, \quad U_{mn,uv} = \frac{1}{\sqrt{N}}e^{(2\pi i/N)mn}\delta_{uv}. \tag{35}$$

The resulting matrix $\widetilde{H}$ is anti-Hermitian but not real. For translationally invariant systems, for which the 2×2 matrices H_{jk} in Eq. (9) depend only on $j-k$, the matrix $\widetilde{H}$ is block diagonal with

$$\widetilde{H}_{mn} = \delta_{mn}\sum_{s=0}^{N-1} H_s e^{-(2\pi i/N)sm}. \tag{36}$$

The block diagonal is parametrized according to

$$\widetilde{H}_{nn} = \begin{pmatrix} ik_n & h_n \\ -h_n^* & il_n\end{pmatrix}, \quad k_n,l_n\in\mathbb{R}, \quad h_n\in\mathbb{C}. \tag{37}$$

For later use, we observe the properties,

$$h_{-n} = h_n^*, \quad k_{-n} = -k_n, \quad l_{-n} = -l_n, \tag{38}$$

which follow directly from Eq. (36) for real H_s.

For a system that is also invariant under reflections (in real space), $H_s = -H_s^T$ holds (in addition to $H_{-s} = -H_s^T$ implied by antisymmetry). In that case, we have $\widetilde{H}_{nn} = -\widetilde{H}_{nn}$, and therefore,

$$k_n = l_n = 0. \tag{39}$$

The spectrum of the Hamiltonian matrix determines the elementary excitation energies,

$$\epsilon_n = \left|\frac{k_n+l_n}{2} \pm \sqrt{\left(\frac{k_n-l_n}{2}\right)^2 + |h_n|^2}\right|. \tag{40}$$

It will be necessary to transform the CM Γ accordingly, defining

$$\widetilde{\Gamma} = U\Gamma U^\dagger. \tag{41}$$

By minimizing the energy expectation value,

$$\langle E\rangle = \mathrm{Tr}(H^T\Gamma) = \mathrm{Tr}(\widetilde{H}^\dagger\widetilde{\Gamma}), \tag{42}$$

we find the CM for the ground state. In the case of $k_n l_n < |h_n|^2$, it is

$$\widetilde{\Gamma}^0_{mn} = \delta_{mn}\{[(k_n-l_n)/2^2]+|h_n|^2\}^{-1/2}\begin{pmatrix} i\frac{k_n-l_n}{2} & -h_n \\ h_n^* & -i\frac{k_n-l_n}{2}\end{pmatrix}, \tag{43}$$

and, otherwise,

$$\widetilde{\Gamma}^0_{mn} = -i\delta_{mn}\mathrm{sgn}\,(k_n+l_n)\,\mathbb{1}_2. \tag{44}$$

For translationally invariant and reflection symmetric systems, $k_n l_n = 0$ holds, thus, $k_n l_n < |h_n|^2$ is fulfilled in such systems. Since the XY chain Eq. (12) is reflection symmetric, we can concentrate on the case of Eq. (43). Specifically, we obtain, for the Hamiltonian Eq. (12), that

$$h_n = -2B + 2J[(1+\gamma)e^{(2\pi i/N)n} + (1-\gamma)e^{-(2\pi i/N)n}], \tag{45}$$

$$k_n = l_n = 0, \tag{46}$$

which contains a continuous quantum phase transition at $B = 2J$ where the gap closes and an elementary excitation energy $\epsilon_n = |h_n| = 0$ exists. This Hamiltonian will be discussed further in Sec. VI.

IV. LINEAR LINDBLAD OPERATORS

Now, we apply the formalism introduced in the previous sections to some simple cases of physical interest. Here, we choose the simplest examples, i.e., linear Lindblad operators (see Sec. III A). We study two settings. In Sec. IV A, we look at systems without any unitary evolution, observing dynamic transitions when tuning the strength of competing decoherence processes. Here, we enrich our presentation with an example for noise-driven state engineering. In Sec. IV B, we consider systems governed by a Hamiltonian, which describes a quantum phase transition itself and are subject to noise and show that the noise-driven system undergoes a transition for the same values of the system parameters.

A. Purely noise-driven systems

The simplest example of two competing decoherence processes generated by linear Lindblad operators is

$$\mathbf{L}^\alpha_- = g\mu a_\alpha, \quad \mathbf{L}^\alpha_+ = g\nu a^\dagger_\alpha, \tag{47}$$

acting on site $\alpha \in \{1,\ldots,N\}$. It describes the competition between particle-loss and particle-gain processes. We observe that the master equation (16), without the Hamiltonian ($H = 0$), is diagonal in real space,

$$\partial_t\Gamma = -g^2(\mu^2+\nu^2)\Gamma - g^2(\mu^2-\nu^2)\bigoplus_{\alpha=1}^{N}(i\sigma_y). \tag{48}$$

In this simple case, the master equation is already diagonal, and we read off the single decoherence rate $\Delta = g^2(\mu^2+\nu^2)$. Solving the master equation for $\partial_t\Gamma_0 = 0$ gives the unique steady-state CM,

$$\Gamma_0 = -\frac{\mu^2-\nu^2}{\mu^2+\nu^2}\bigoplus_{\alpha=1}^{N}\begin{pmatrix}0 & 1\\ -1 & 0\end{pmatrix}, \tag{49}$$

which is block diagonal. This state is characterized by the particle number $\langle a^\dagger_\alpha a_\alpha\rangle = \nu^2/(\mu^2+\nu^2)$ at all sites. For pure particle-loss processes ($\nu = 0$), all sites are unoccupied $\langle a^\dagger_\alpha a_\alpha\rangle = 0$ in the steady state, whereas, for pure particle-gain processes ($\mu = 0$), all sites are occupied $\langle a^\dagger_\alpha a_\alpha\rangle = 1$. At $\mu = \nu$, the steady state is the unpolarized completely mixed state. Not surprisingly, the system does not display any phase transition.

More interesting may be the case in which noise can also induce correlations. A simple example of this kind is provided by the Lindblad operators,

$$\mathbf{L}^\alpha = g(\mu a_\alpha + \nu a^\dagger_{\alpha+1}), \tag{50}$$

acting on nearest neighbors. This set of Lindblad operators generates a master equation, which is diagonal after the Fourier transform (35),

$$\partial_t\widetilde{\Gamma} = -g^2(\mu^2+\nu^2)\widetilde{\Gamma} - g^2\mu\nu\left\{\bigoplus_{n=1}^{N}\cos(2\pi n/N)\sigma_z, \widetilde{\Gamma}\right\} - g^2(\mu^2-\nu^2)\bigoplus_{n=1}^{N} i\sigma_y - 2g^2\mu\nu\bigoplus_{n=1}^{N} i\,\sin(2\pi n/N)\sigma_x. \tag{51}$$

In this case, a spectrum of decoherence rates $g^2\{\mu^2+\nu^2 \pm 2\mu\nu[\cos\frac{2\pi n}{N} + \cos\frac{2\pi m}{N}], \mu^2+\nu^2 \pm 2\mu\nu[\cos\frac{2\pi n}{N} - \cos\frac{2\pi m}{N}]\}$ exists with a gap $g^2(\mu-\nu)^2$. The unique steady state is

$$\widetilde{\Gamma}_0 = -\frac{\mu^2-\nu^2}{\mu^2+\nu^2}\bigoplus_{n=1}^{N} i\sigma_y - \frac{2\mu\nu}{\mu^2+\nu^2}\bigoplus_{n=1}^{N} i\,\sin(2\pi n/N)\sigma_x. \tag{52}$$

This state is a paired fermionic state according to the definition of Kraus *et al.* [35]. Paired states show two-particle quantum correlations that cannot be reproduced by separable states (mixtures of Slater determinants). In Ref. [35], it is proven that Gaussian states are paired iff $Q_{kl} = \langle\frac{i}{2}[a_k, a_l]\rangle \neq 0$. This condition expresses the fact that separable states are convex combinations of states with a fixed particle number. For the CM (52), we get

$$Q_{kl} = \begin{cases}\frac{1}{2}\frac{\mu\nu\,\mathrm{sgn}(k-l)}{\mu^2+\nu^2}, & \text{if} \quad |k-l| = 1,\\ 0, & \text{if} \quad |k-l| \neq 1.\end{cases} \tag{53}$$

We conclude that (50) generates paired states, except for the trivial cases $\mu = 0$ or $\nu = 0$. Note that, even though the gap closes at $\mu = \nu$ (where maximal pairing is created), there is no phase transition at this point.

B. Noise-driven systems with Hamiltonians

A different form of transitions can arise in the presence of a Hamiltonian when tuning the parameters of the Hamiltonian. To show this, we solve the evolution of the Lindblad master equation (16) with a general quadratic and translationally invariant Hamiltonian [see Eqs. (9) and (37)]. We choose

the local Lindblad operators (47), again, because they are the simplest example. The diagonal master equation in Fourier space becomes

$$\partial_t \widetilde{\Gamma} = \left[\bigoplus_{n=1}^{N} \begin{pmatrix} ik_n & h_n \\ -h_n^* & il_n \end{pmatrix}, \widetilde{\Gamma}\right] - g^2(\mu^2+\nu^2)\widetilde{\Gamma} - g^2(\mu^2-\nu^2)\bigoplus_{n=1}^{N} i\sigma_y. \tag{54}$$

The corresponding steady-state CM in the weak-coupling limit $g \to 0$ is [36]

$$\widetilde{\Gamma}_0 = -\frac{\mu^2-\nu^2}{\mu^2+\nu^2}\bigoplus_{n=1}^{N} \frac{\mathrm{Re}\,(h_n)}{(k_n-l_n)^2/4+|h_n|^2} \times \begin{pmatrix} i(k_n-l_n)/2 & h_n \\ -h_n^* & -i(k_n-l_n)/2 \end{pmatrix}. \tag{55}$$

Transforming back to Γ_0 [and using Eq. (38)], we can read off the particle number $\langle 2a_j^\dagger a_j - 1\rangle = (\Gamma_0)_{jj,01}$ as

$$(\Gamma_0)_{jj,01} = \frac{1}{2}\frac{\mu^2-\nu^2}{\mu^2+\nu^2}\frac{1}{N}\sum_{n=1}^{N}\frac{\mathrm{Re}\,(h_n)^2}{(k_n-l_n)^2/4+|h_n|^2}. \tag{56}$$

Based on this result, we can now discuss how nonanalytic behavior in the steady state correlates with critical points of the system. A vanishing denominator in Eq. (56) is not *a priori* a sufficient condition for nonanalytic behavior because the numerator might vanish at the same point. This is relevant for interesting examples with $k_n - l_n = 0$, e.g., the XY chain in Eq. (45). We give a rigorous discussion in the following. In the thermodynamic limit, the sums over expectation values in Eq. (56) can be replaced by a loop integral around the origin of the complex plane with radius 1 where the integration variable is $z = \exp(\frac{2\pi i}{N}n)$. This is possible because h_n, k_n, and l_n are Fourier series. For local interactions, the denominator of the integrand is a polynomial in z [see Eq. (35)] and, thus, has a finite number of distinct roots. Applying the residue theorem, a nonanalyticity in $\langle a_j^\dagger a_j\rangle$ is possible only if a residue of the integrand, i.e., a root of its denominator, moves through the integral contour in the complex plane as a function of some external parameters. This happens for a vanishing denominator $|h_n|^2 + (k_n - l_n)^2/4 = 0$ for some real $n \in [0,N)$. In the special case of a reflection symmetric system $k_n + l_n = 0$, this coincides with a vanishing energy gap $\epsilon_n = 0$ [see Eq. (40)], a signature for a quantum phase transition. To summarize, for a reflection symmetric system with $|h_n|^2 + (k_n - l_n)^2/4 = 0$ in the weak-coupling limit, a quantum phase transition occurs in the noise-driven system for the same parameter values as in the corresponding closed system and is signaled by a nonanalyticity in $\langle a_j^\dagger a_j\rangle$. This calculation is explicitly performed in Sec. VI A for the XY chain [37].

V. QUADRATIC AND HERMITIAN LINDBLAD OPERATORS

In this section, we turn to the dynamical properties of the Lindblad master equation with quadratic and Hermitian Lindblad operators as introduced in Sec. III B. In the study of closed systems, quantum phase transitions are signaled by nonanalyticities in ground-state expectation values. In the noise-driven case, the steady state is the analog of the ground state. However, in Sec. III B, we have shown that, in the case of Hermitian Lindblad operators, the steady states are trivial and, thus, cannot evidence a phase transition. Therefore, we turn to the ADR, which determines the long-time dynamics of the decoherence process. We identify nonanalytical behavior of this rate both in the absence of any Hamiltonian (see Sec. V A) for competing decoherence processes and for the nonzero Hamiltonian, in which case, phase transitions of the corresponding closed system are reflected in a dynamical transition of this rate (see Sec. V B).

A. Purely noise-driven systems

A particular simple set of local and quadratic Lindblad operators is

$$\mathbf{L}_z^\alpha = g\mu\frac{i}{2}[c_{\alpha,1}, c_{\alpha,0}], \tag{57}$$

$$\mathbf{L}_x^\alpha = g\nu\frac{i}{2}[c_{\alpha+1,0}, c_{\alpha,1}]. \tag{58}$$

In this case, the Lindblad equation (32) becomes

$$\partial_t \Gamma_{kl,uv} = -4g^2\mu^2\Gamma_{kl,uv}(1-\delta_{kl}) - 4g^2\nu^2\Gamma_{kl,uv}(1-\delta_{2k+u+1,2l+v}\delta_{k+1,l} - \delta_{2k+u-1,2l+v}\delta_{k-1,l}). \tag{59}$$

We can read off the decoherence rates $-4g^2(\mu^2+\nu^2)$, $-4g^2\mu^2$, and $-4g^2\nu^2$. Thus, the ADR

$$\Delta = \begin{cases} 4g^2\mu^2, & \text{if} \quad \mu \leqslant \nu, \\ 4g^2\nu^2, & \text{if} \quad \nu < \mu \end{cases} \tag{60}$$

undergoes a dynamical transition as a function of μ/ν at $\mu = \nu$.

B. Noise-driven systems with Hamiltonians

Now, we add a quadratic Hamiltonian and calculate the asymptotic decay rate Δ in the limit of small couplings to the environment $g \to 0$. First, we derive it for the quadratic Lindblad operators from Eqs. (57) and (58) for $\nu = 0$ and $\mu = 1$. Later, we will present the results for the case of arbitrary μ and ν. For translationally invariant systems, the Fourier transformed master equation (59) is

$$\partial_t \widetilde{\Gamma}_{kl} \equiv (\widetilde{\mathcal{S}}\widetilde{\Gamma})_{kl} = [\widetilde{H}, \widetilde{\Gamma}]_{kl} - 4g^2\left(\widetilde{\Gamma}_{kl} - \frac{1}{N}\sum_{r,s=1}^{N}\widetilde{\Gamma}_{rs}\delta_{r-s,k-l}\right), \tag{61}$$

with the unitarily transformed superoperator $\widetilde{\mathcal{S}}$ to

$$\widetilde{\mathcal{S}} = (U\otimes U)\mathcal{S}(U\otimes U)^\dagger, \tag{62}$$

with U from Eq. (35). For weak couplings between system and bath $g \to 0$, the eigenvalues of $\widetilde{\mathcal{S}}$ (and, thus, of $\mathcal{S}$) can be determined by first-order perturbation expansion. To this end, we first diagonalize the unperturbed Hamiltonian part of $\widetilde{\mathcal{S}}$,

$$[\widetilde{H}, \widetilde{\Gamma}]_{kl} = \widetilde{H}_{kk}\widetilde{\Gamma}_{kl} - \widetilde{\Gamma}_{kl}\widetilde{H}_{ll} \stackrel{!}{=} \lambda\widetilde{\Gamma}_{kl}, \tag{63}$$

where we use the notation introduced in Eq. (36) for the Hamiltonian $\widetilde{H}$. The $4N^2$ eigenvalues λ^{mna} ($m,n = 1,\ldots,N$, $a = 1,\ldots,4$) are

$$\lambda^{mn1} = i(\alpha_m - \alpha_n + \beta_m - \beta_n), \tag{64}$$

$$\lambda^{mn2} = i(\alpha_m - \alpha_n - \beta_m + \beta_n), \tag{65}$$

$$\lambda^{mn3} = i(\alpha_m - \alpha_n + \beta_m + \beta_n), \tag{66}$$

$$\lambda^{mn4} = i(\alpha_m - \alpha_n - \beta_m - \beta_n), \tag{67}$$

with

$$\alpha_m = |k_m + l_m|/2, \tag{68}$$

$$\beta_m = \sqrt{|h_m|^2 + (k_m - l_m)^2/4}. \tag{69}$$

The corresponding eigenmatrices are denoted as $\widetilde{\Lambda}^{mna}$ with nonzero elements $\widetilde{\Lambda}^{mna}_{kl}$ only for $m = k$ and $n = l$, i.e., $\widetilde{\Lambda}^{mna}_{kl} = \delta_{mk}\delta_{nl}\widetilde{\Lambda}^{mna}_{mn}$. Perturbation theory demands calculating the matrix elements of the perturbative part of $\widetilde{\mathcal{S}}$, $-4g^2(\delta_{mk}\delta_{nl}\delta_{ab} - P^{mna}_{klb}/N)$ [see Eq. (61)], with

$$\begin{aligned} P^{mna}_{klb} &= \frac{N}{4g^2}\langle\widetilde{\Lambda}^{mna}|\frac{1}{2}\sum_{\alpha}(\mathcal{L}^{\alpha})^2|\widetilde{\Lambda}^{klb}\rangle + N\delta_{mk}\delta_{nl}\delta_{ab} \\ &= \sum_{q,r,s,t=1}^{N}\delta_{q-r,s-t}\mathrm{Tr}\big[\big(\widetilde{\Lambda}^{mna}_{st}\big)^{\dagger}\widetilde{\Lambda}^{klb}_{qr}\big] \\ &= \delta_{m-n,k-l}\mathrm{Tr}\big[\big(\widetilde{\Lambda}^{mna}_{mn}\big)^{\dagger}\widetilde{\Lambda}^{klb}_{kl}\big]. \end{aligned} \tag{70}$$

Thus, the eigenvalues of $\widetilde{\mathcal{S}}$ are determined by those of the Hermitian matrix P, and the largest eigenvalue smaller than N of P (restricted to a space of degenerate eigenvalues λ^{mna} of $[\tilde{H},\cdot]$) determines the ADR. We denote it by Δ_P and, thus, have that the asymptotic rate is $\Delta = 4g^2(1 - \frac{\Delta_P}{N})$. To find Δ_P, note that the matrix elements of P fulfill $|P^{mna}_{klb}| \leqslant 1$. Thus, an N-fold degeneracy of λ^{mna} is required for $\Delta_P = \Omega(N)$. Generically, this is possible only for the eigenvalue $\lambda^{mna} = 0$, i.e., $m = n$ and $a = 1,2$. The corresponding eigenmatrices are

$$\widetilde{\Lambda}^{mm1}_{kl} = \delta_{mk}\delta_{ml}\frac{1}{\sqrt{2}\beta_n}\begin{pmatrix} i\frac{k_m - l_m}{2} & -h_m \\ h^*_m & -i\frac{k_m - l_m}{2}\end{pmatrix}, \tag{71}$$

$$\widetilde{\Lambda}^{mm2}_{kl} = \delta_{mk}\delta_{ml}\frac{1}{\sqrt{2}}\begin{pmatrix}1 & 0\\ 0 & 1\end{pmatrix}. \tag{72}$$

As the eigenmatrices $\widetilde{\Lambda}^{mm2}$ give eigenvalues equal to N and 0 only, have no overlap with physical CMs, and yield $P^{mn2}_{kl1} = 0$, we focus on the matrices $\widetilde{\Lambda}^{mm1}$. The corresponding part of the perturbation matrix is

$$P_{mn} = P^{mm1}_{nn1} = \frac{2h_m h^*_n + 2h^*_m h_n - (k_m - l_m)(k_n - l_n)}{4\beta_m\beta_n}. \tag{73}$$

We diagonalize this matrix by introducing the three vectors $|a\rangle,|b\rangle,|c\rangle \in \mathbb{C}^N$ with the components,

$$a_m = \frac{k_m - l_m}{2\beta_m}, \quad b_m = \frac{\mathrm{Im}(h_m)}{\beta_m}, \quad c_m = \frac{\mathrm{Re}(h_m)}{\beta_m}, \tag{74}$$

and writing P_{mn} in terms of these un-normalized vectors,

$$P = |c\rangle\langle c| + |b\rangle\langle b| - |a\rangle\langle a|. \tag{75}$$

We now exploit the symmetries of h_n, k_n, and l_n stated in Eq. (38). First, we observe that $|c\rangle$ is orthogonal to $|a\rangle$ and $|b\rangle$. We have chosen the CMs corresponding to the three vectors (74) to be anti-Hermitian since this matrix remains anti-Hermitian even in the complex vector space. After transforming back into real space, the ones corresponding to $|a\rangle$ and $|b\rangle$ are purely imaginary so that they have no overlap with any physically meaningful real and antisymmetric CM. Only the matrix corresponding to $|c\rangle$ is real and antisymmetric and is given by

$$\Gamma_{\Delta} = \left(\sum_{m=1}^{N}\frac{|h_m|^2}{2\beta_m^2}\right)^{-1}\sum_n\frac{\mathrm{Re}(h_n)}{\beta_n}U^{\dagger}\Lambda^{nn1}U. \tag{76}$$

Therefore, it determines the ADR. We get

$$\Delta_P = \sum_{m=1}^{N}\frac{\mathrm{Re}(h_m)^2}{\beta_m^2} = \sum_{m=1}^{N}\frac{\mathrm{Re}(h_m)^2}{|h_m|^2 + (k_m - l_m)^2/4}, \tag{77}$$

and thus,

$$\Delta = \frac{4g^2}{N}\sum_{m=1}^{N}\frac{4\,\mathrm{Im}(h_m)^2 + (k_m - l_m)^2}{4|h_m|^2 + (k_m - l_m)^2}, \tag{78}$$

as the general form of the ADR.

We can extend our analysis to systems with the general Lindblad operators Eqs. (57) and (58) and find, in an analogous way, the two lowest decay rates,

$$\frac{\Delta_{\pm}}{4g^2} = \mu^2 + \nu^2 - \frac{\epsilon_z + \epsilon_x}{2} \pm \sqrt{\left(\frac{\epsilon_z - \epsilon_x}{2}\right)^2 + \epsilon^2}, \tag{79}$$

with

$$\begin{aligned} \epsilon_z &= \frac{\mu^2}{N}\sum_{m=1}^{N}\frac{\mathrm{Re}(h_m)^2}{\beta_m^2}, \\ \epsilon_x &= \frac{\nu^2}{N}\sum_{m=1}^{N}\frac{\mathrm{Re}[h_m\exp(-2\pi i m/N)]^2}{\beta_m^2}, \\ \epsilon &= \frac{\mu\nu}{N}\sum_{m=1}^{N}\frac{\mathrm{Re}(h_m)\mathrm{Re}[h_m\exp(-2\pi i m/N)]}{\beta_m^2}. \end{aligned} \tag{80}$$

We can now argue that the ADR itself reflects the criticality of the system. The argument is completely analogous to the one given in Sec. IV B. If the denominator becomes zero, we can expect nonanalyticity expressions Eqs. (80). In particular, in the reflection symmetric case $k_n + l_n = 0$ where the denominator agrees with the elementary excitation energies [$\epsilon_n^2 = |h_n|^2 + (k_n - l_n)^2/4 = 0$, see Eq. (40)], the nonanalyticity in the ADR signals the presence of a quantum phase transition in the Hamiltonian itself.

VI. EXAMPLE HAMILTONIANS

In this section, we will revisit the results obtained for the steady state and the ADR for linear and quadratic Lindblad operators in Secs. IV B and V B for the specific Hamiltonian (12) of the quantum XY chain.

The energies of the elementary excitations of this Hamiltonian are $\epsilon_n = |h_n|$. Thus, for the XY chain in Eq. (45), the

gap closes at $B = 2J$ in the thermodynamic limit, and the quantum XY chains exhibit a phase transition at this point. In fact, these models constitute the archetypal example of a continuous quantum phase transition [18]. In this section, we want to find properties of the noise-driven dynamics signaling this phase transition.

A. Linear Lindblad operators

Let us now apply the findings from Sec. IV B and Eq. (56) to the example system defined in Eq. (45), which contains a quantum phase transition at $B = 2J$. Then, the particle numbers become, for $k_n = l_n = 0$,

$$\langle 2a_n^\dagger a_n - 1\rangle = \frac{1}{2}\frac{\mu^2-\nu^2}{\mu^2+\nu^2}\left(1+\frac{1}{N}\sum_{n=1}^{N}\frac{h_n^*}{h_n}\right). \quad (81)$$

For $\gamma = 0$, we easily obtain $\Delta = 0$ [since, by Eq. (45), h_n is real in that case and then, by Eq. (78), Δ is zero for $k_n = l_n = 0$]. For $\gamma \neq 0$, we evaluate the sum $1/N \times \sum_{m=1}^{N} h_m^*/h_m$ in the thermodynamic limit by introducing the complex variable $z = \exp(-2\pi i m/N)$,

$$\lim_{N\to\infty}\frac{1}{N}\sum_{m=1}^{N}\frac{h_m^*}{h_m} = \frac{1}{2\pi i}\oint_{|z|=1}\frac{dz}{z}\frac{2J(1-\gamma)z^2-2Bz+2J(1+\gamma)}{2J(1+\gamma)z^2-2Bz+2J(1-\gamma)}, \quad (82)$$

where the integration contour is a circle of radius $|z| = 1$ around $z = 0$ in the complex plane. The complex integrand is analytic except for three distinct poles at

$$z^0 = 0, \quad z^\pm = \frac{1}{2J(1+\gamma)}[B \pm \sqrt{B^2 - 4J^2(1-\gamma^2)}]. \quad (83)$$

The contour integral is determined by the sum over the residues at those poles, which are inside the contour ($|z| < 1$). z^0 is always inside this contour. In the case of $\gamma > 0$, z^+ is inside the contour for $0 \leqslant B < 2J$ and is outside for $B > 2J$, whereas, z^- is always inside the contour. In the case of $\gamma < 0$, z^- is inside the contour for $B > 2J$ and is outside for $0 \leqslant B < 2J$, whereas, z^+ is always outside the contour. So residues cross the contour at the quantum phase transition $B = 2J$ (because, then, $h_n = 0$ for some n), leading to a nonanalytical behavior in the particle density of the steady state (see Fig. 1).

After applying the residue theorem, we get the particle number of the steady state,

$$\langle 2a_n^\dagger a_n - 1\rangle = \frac{\mu^2-\nu^2}{\mu^2+\nu^2}\begin{cases}\frac{1}{1+|\gamma|}, & B \leqslant 2J,\\ \frac{1}{1-\gamma^2}\left(1-\frac{\gamma^2}{\sqrt{1-\left(\frac{2J}{B}\right)^2(1-\gamma^2)}}\right), & B \geqslant 2J\end{cases} \quad (84)$$

for all γ, which does not depend on the sign of γ. For $B < 2J$, the particle number in the steady state does not vary with the magnetic field, whereas, its magnitude approaches $(\mu^2-\nu^2)/(\mu^2+\nu^2)$ for large magnetic fields $\sim(J/B)^2$. To summarize, the steady state undergoes a noise-driven phase transition at $B = 2J$ signaling the phase transition in the system.

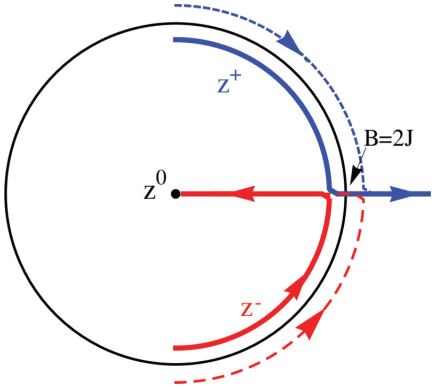

FIG. 1. (Color online) The poles $z^0, z^\pm$ [see Eq. (83)] are plotted for $J = 1$, $\gamma = \pm 0.1$. As B is changed from 0 to 20, the poles $z^+(z^-)$ for positive anisotropy $\gamma = +0.1$ move along the blue (red) solid curves, and z^+ crosses the contour at the critical value $B = 2J$. For negative $\gamma = -0.1$, z^- crosses at $B = 2J$. At the crossing, the integral Eq. (82) changes nonanalytically.

B. Quadratic and Hermitian Lindblad operators

As an example, we study the anisotropic XY chain in a transverse magnetic field with the Hamiltonian given in Eq. (12). This translationally invariant Hamiltonian is Jordan-Wigner transformed to a quadratic fermionic Hamiltonian with Hamiltonian matrix H given by

$$H_0 = \begin{pmatrix}0 & -2B\\ 2B & 0\end{pmatrix}, \quad (85)$$

$$H_1 = \begin{pmatrix}0 & 2J(1-\gamma)\\ -2J(1+\gamma) & 0\end{pmatrix}, \quad (86)$$

$$H_{-1} = \begin{pmatrix}0 & 2J(1+\gamma)\\ -2J(1-\gamma) & 0\end{pmatrix}. \quad (87)$$

After Fourier transforming [see Eq. (35)], this Hamiltonian matrix assumes the form given in Eq. (37) with parameters h_n, k_n, l_n given by Eq. (45).

We now apply the results from Sec. V B to the Hamiltonian Eq. (85) and the Lindblad operators,

$$\mathbf{L}^\alpha = g\mu\frac{i}{2}[c_{\alpha,1}, c_{\alpha,0}] \leftrightarrow g\sigma_z^\alpha. \quad (88)$$

After a brief discussion of the steady states and a derivation of the ADR in the thermodynamic ($N \to \infty$) and in weak coupling ($g \to 0$) limits, we present numerical results of the system dynamics for finite N and g and compare them with our analytic predictions.

First, we discuss the steady states of these systems (see Sec. III B). From Eq. (31), we have concluded that the steady-state density matrix is the identity up to symmetries shared by the Lindblad operators and the Hamiltonian. A rigorous derivation of the steady states for this example could start from the ansatz that the steady-state density matrix is diagonal in the Fock basis, following from $[\sigma_z^\alpha, \rho] = 0$. Then, the commutator $[\mathbf{H}, \rho] = 0$ must be exploited to get the steady state.

As the Lindblad operators correspond to local particle number operators, the important compatible symmetries for

the XY chains are the parity $\mathcal{P} = \sigma_z^1 \cdots \sigma_z^N$, discriminating between an odd and an even number of particles, and the total particle number $\mathcal{N} = (\mathbf{1} + \sum \sigma_z^j)/2$. For truly asymmetric XY chains $\gamma \neq 0.5$, the parity is the highest symmetry compatible with the Lindblad operators. In these cases, the steady-state density matrix is given by the identity in the two sectors of even and odd parities; the relative weight of these sectors is determined by the initial state. For the symmetric chain $\gamma = 0.5$, the steady-state density matrix is the identity only in the sectors with a constant total number of particles. Thus, for $\gamma \neq 0.5$, the steady-state magnetization is $\langle \sigma_z^j \rangle = 0$ regardless of the initial state, whereas, the magnetization of the initial state is conserved for $\gamma = 0.5$.

Second, we calculate the ADR (78) for the XY chains with Eq. (45) analogous to the integration in Sec. VI A.

After applying the residue theorem, we get the ADR,

$$\Delta = 4g^2 \begin{cases} \frac{|\gamma|}{1+|\gamma|}, & B \leqslant 2J, \\ \frac{\gamma^2}{1-\gamma^2}\left\{\left[1-\left(\frac{2J}{B}\right)^2(1-\gamma^2)\right]^{-1/2}-1\right\}, & B \geqslant 2J \end{cases} \tag{89}$$

for all γ in the case of $\mu = 1$. It does not depend on the sign of γ and is shown in Fig. 2 for several values of $\gamma \in [0,1]$. For $B < 2J$, the ADR does not vary with the magnetic field, whereas for large magnetic fields its magnitude decreases to zero and scales as $(J/B)^2$. The same behavior was found for the variance in the particle number in these models in a previous paper [38]. To summarize, the ADR undergoes a noise-driven phase transition at $B = 2J$ signaling the phase transition in the system.

The final result for the ADR (89) is valid in the limits $N \to \infty$ and $g \to 0$. In this section, we perform a numerical diagonalization of the Lindblad master equation superoperator $\mathcal{S}$ to compare the analytic result with the values for finite N and g. Furthermore, we extract the ADR from a simulation of the system dynamics and compare it with our prediction.

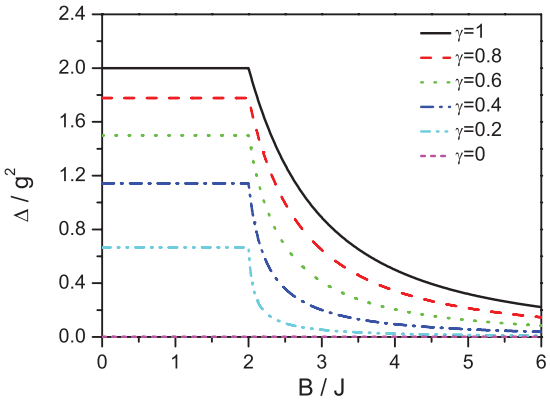

FIG. 2. (Color online) Asymptotic decay rate Δ [see Eq. (78)] of the XY chain (12) for different anisotropy parameters γ as a function of the magnetic field in the limits $N \to \infty$ and $g \to 0$. A phase transition in Δ is visible at $B = 2J$ for $\gamma \neq 0$.

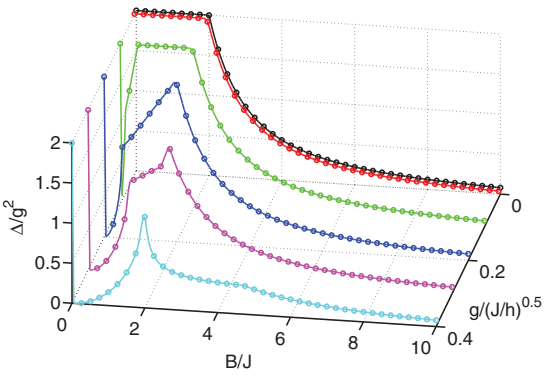

FIG. 3. (Color online) Asymptotic decay rate Δ [see Eq. (78)] of the XY chain (12) for different coupling strengths g, $\gamma = 1$, and $N = 100$ as a function of the magnetic field B. For $g \leqslant 0.1(J/\hbar)^{0.5}$, the results agree with the limit of weak coupling $g \to 0$ [see Eq. (89)].

In Fig. 3, we present the ADR for finite coupling strengths g. For $g^2 \leqslant 0.01J/\hbar$, the result of perturbation theory is in excellent agreement with the numerical diagonalization of the Lindblad master equation superoperator. Deviations are strongest at small magnetic fields for which the finite g is no longer a small perturbation. The nonanalytic behavior at the critical field value $B/J = 2$ is clearly visible. The additional structure in the ADR for finite g and small B/J arises from level crossings in the spectrum of the Liouvillian. At $B = 0$, the steady state becomes highly degenerate. The ADR (the largest *nonzero* real part) jumps to a finite value indicating a finite gap above the steady-state manifold.

We show the ADR Δ for different (finite) system sizes in Fig. 4. Even in small systems with $N = 10$ spins, the same qualitative behavior is found as in thermodynamic limit, i.e., the ADR signals the quantum phase transition in the system at

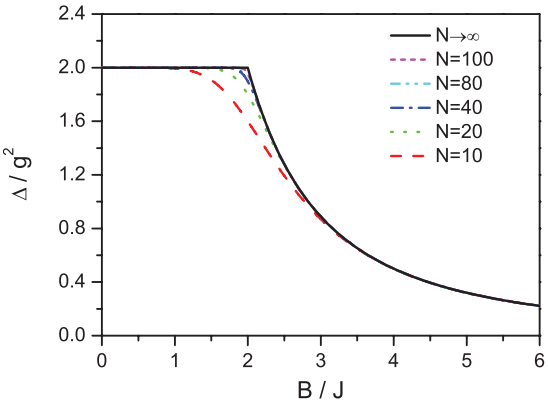

FIG. 4. (Color online) Asymptotic decay rate Δ [see Eq. (89)] of the XY chain (12) for different system sizes N and $\gamma = 1$, $g = 0.01(J/\hbar)^{0.5}$ as a function of the magnetic field B. For $N \geqslant 50$, the thermodynamic limit is reached, except for small variations at the phase transition $B = 2J$.

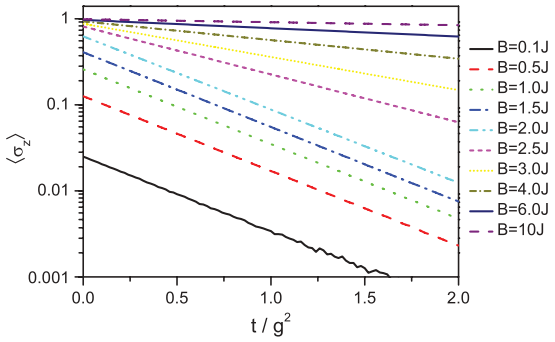

FIG. 5. (Color online) Evolution of the magnetization $\langle\sigma_z^j\rangle$ in time starting from the system ground state of the XY chain (12) for different magnetic fields B, $g = 0.01(J/\hbar)^{0.5}$, and $\gamma = 1$. The magnetization decreases exponentially in time.

$B = 2J$. However, finite values of g and N lead to a smearing out of the phase transition.

We have defined the ADR through a diagonalization of the master equation, trying to describe the long-time dynamics of the system. To demonstrate the deep relation between Δ and the noise-driven dynamics, we extract the decoherence rate from a dynamical calculation (see Fig. 5). Here, we start from the ground state of the system and study the decay of the magnetization in time after the system is brought into contact with a Markovian bath. In this example, the exponential decay expected after long evolution times is nicely visible. In Fig. 6, we compare the extracted decay rates for different magnetic fields with the result of the diagonalization. We find an exact agreement with the ADR numerically calculated with the same finite parameters.

We can calculate the ADR for the XY chain for general values of μ and ν in a similar way. In the spin picture, the

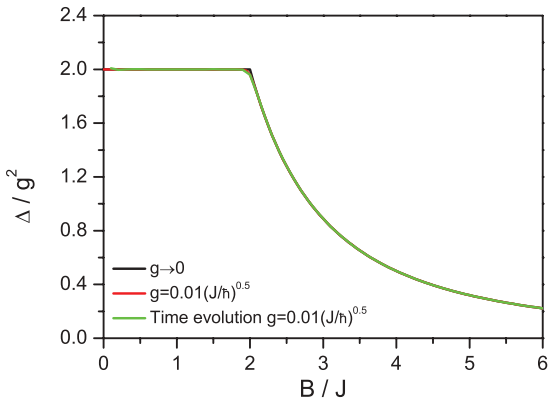

FIG. 6. (Color online) The ADRs Δ [see Eq. (89)] of the XY chain (12) for $\gamma = 1$, for $g = 0.01(J/\hbar)^{0.5}$, and for $g \to 0$ (result of perturbation theory) as a function of the magnetic field B are compared with the late-time decoherence rates extracted from Fig. 5. The agreement between the ADR and the late-time decoherence rate shows the validity of our calculations for finite times.

Lindblad operators are

$$\mathbf{L}_z^\alpha = g\mu\sigma_\alpha^z = g\mu\frac{i}{2}[c_{\alpha,1}, c_{\alpha,0}], \tag{90}$$

$$\mathbf{L}_x^\alpha = g\nu\sigma_\alpha^x\sigma_{\alpha+1}^x = g\nu\frac{i}{2}[c_{\alpha,0}, c_{\alpha+1,1}]. \tag{91}$$

We find for the constants in Eq. (79) in the case $\gamma = 1$,

$$\epsilon_z/\mu^2 = \begin{cases} \frac{1}{2}, & B \leqslant 2J, \\ 1 - \frac{1}{2}\left(\frac{2J}{B}\right)^2, & B \geqslant 2J, \end{cases} \tag{92}$$

$$\epsilon_x/\mu^2 = \begin{cases} 1 - \frac{1}{2}\left(\frac{B}{2J}\right)^2, & B \leqslant 2J, \\ \frac{1}{2}, & B \geqslant 2J, \end{cases} \tag{93}$$

$$\epsilon/(\mu\nu) = \begin{cases} -\frac{B}{2J}, & B \leqslant 2J, \\ -\frac{2J}{B}, & B \geqslant 2J. \end{cases} \tag{94}$$

In the symmetric case $\mu = \nu$, the ADR is constant ($\Delta = -4g^2\mu^2$). However, the next larger decoherence rate changes nonanalytically,

$$\Lambda_- = \begin{cases} -2g^2\mu^2\left[3 + \left(\frac{B}{2J}\right)^2\right], & \text{if } B < 2J, \\ -2g^2\mu^2\left[3 + \left(\frac{2J}{B}\right)^2\right], & \text{if } B > 2J. \end{cases} \tag{95}$$

VII. EXPERIMENTAL REALIZATION

We now discuss an experiment suited for the measurement of the asymptotic decoherence rate in spin systems. The quantum simulation of spin systems with trapped ions was proposed in Ref. [39] where the spin degree of freedom is represented by two hyperfine levels. The magnetic field can be simulated either by directly driving Rabi oscillations of the hyperfine transition or with position-independent Raman transitions induced by suitably aligned lasers. The spin-spin interaction is mediated via motional degrees of freedoms. State-dependent optical dipole forces (compare with state-dependent optical lattices) are generated by coupling the two hyperfine levels to electronically excited states with off-resonant laser beams. These dipole forces change the distance and, consequently, the Coulomb repulsion between two ions dependent on their internal states. This state-dependent Coulomb repulsion can be designed to give the required spin-spin interaction. The spin state can be measured by fluorescence imaging of the ions.

In this way, the quantum Ising chain [40,41] and frustrated Ising models [42] have been realized in recent experiments. In these experiments, the ions were first cooled to their zero-point motional ground state and optically pumped into a certain spin configuration representing the ground state of the system without spin-spin interactions. Then, the spin-spin interactions were adiabatically increased such that the system underwent a phase transition. Finally, it was checked that the final state represented the ground state of the simulated Hamiltonian. A large noncritical two-dimensional Ising system has been simulated with ions in a Penning trap [43]. In the digital approach to quantum simulation with trapped ions, the elements of a general toolbox, including Hamiltonian and noise-driven dynamics, have been demonstrated [44,45].

In the following, we describe how to extend analog quantum simulation to include an incoherent evolution. The Lindblad master equation (3) with Hermitian Lindblad operators $\mathbf{L}^\alpha = g\sigma_z^\alpha$ (see Sec. V B) can be realized by introducing fluctuations in the simulated magnetic field

$B^\alpha(t) = B^\alpha + \delta B^\alpha(t)$ [46] as shown in the following. The local magnetic fields $\delta B^\alpha(t)$ should be uncorrelated between different sites $\overline{\delta B^\alpha(t_1)\delta B^\beta(t_2)} = \delta_{\alpha\beta}\overline{\delta B^\alpha(t_1)\delta B^\alpha(t_2)}$. We restrict our derivation to a single Lindblad operator without loss of generality. Let, for example, $\delta B(t)$ constitute a Gaussian stochastic process of zero mean $\overline{\delta B(t)} = 0$ with the time correlations,

$$\overline{\delta B(t_1)\delta B(t_2)} = \frac{\overline{\delta B^2}}{\sqrt{2\pi}} \exp\left[-\frac{(t_1 - t_2)^2}{2T^2}\right]. \tag{96}$$

The correlation time T has to be much shorter than every process in the system (Markovian limit), i.e., $\|\mathcal{H}\|T < \omega T \ll 1$ with the spectral width ω of the Hamiltonian (difference between largest and smallest eigenvalues) and the superoperator $\mathcal{H}$ from Eq. (26). The averaged density matrix evolves like $|\rho(t)\rangle = \overline{\mathcal{U}(t)}|\rho(0)\rangle$ where the bar denotes the statistical average over the fluctuating magnetic field. The time-evolution operator $\overline{\mathcal{U}(t)}$ consists of contributions from $\mathcal{H}$ and

$$\mathcal{V}(t) = \frac{\delta B(t)}{\hbar}\mathcal{V} = -\frac{i\,\delta B(t)}{\hbar}(\mathbf{V}\otimes\mathbf{1} - 1\otimes\mathbf{V}^T), \tag{97}$$

with $\mathbf{V} = \sigma_z$. We can evaluate the statistical average of the time-evolution operator in the interaction picture for the superoperators,

$$\begin{aligned}
\overline{\mathcal{U}(t)} &= e^{\mathcal{H}t}\overline{\mathcal{T}\exp\left(\int_0^t d\tau\, e^{-\mathcal{H}\tau}\mathcal{V}(\tau)e^{\mathcal{H}\tau}\right)} = e^{\mathcal{H}t}\sum_{n=0}^{\infty}\overline{\int_{t\geqslant t_1\geqslant\cdots\geqslant t_n\geqslant 0} dt_1\cdots dt_n e^{-\mathcal{H}t_1}\mathcal{V}(t_1)e^{\mathcal{H}t_1}\cdots e^{-\mathcal{H}t_n}\mathcal{V}(t_n)e^{\mathcal{H}t_n}} \\
&= e^{\mathcal{H}t}\sum_{m=0}^{\infty}\left(\frac{1}{\hbar^2}\int_0^\infty \overline{\delta B(0)\delta B(\tau)}d\tau\right)^m \times \int_{t\geqslant t_1\geqslant\cdots\geqslant t_m\geqslant 0} dt_1\cdots dt_m e^{-\mathcal{H}t_1}\mathcal{V}^2 e^{\mathcal{H}t_1}\cdots e^{-\mathcal{H}t_m}\mathcal{V}^2 e^{\mathcal{H}t_m} \\
&= e^{\mathcal{H}t}\sum_{m=0}^{\infty}\left(\frac{\overline{\delta B^2}}{\hbar^2}\times\frac{T}{2}\right)^m \times \int_{t\geqslant t_1\geqslant\cdots\geqslant t_m\geqslant 0} dt_1\cdots dt_m e^{-\mathcal{H}t_1}\mathcal{V}^2 e^{\mathcal{H}t_1}\cdots e^{-\mathcal{H}t_m}\mathcal{V}^2 e^{\mathcal{H}t_m}, \\
\overline{\mathcal{U}(t)} &= \exp\left(\mathcal{H}t + \frac{1}{2}\frac{\overline{\delta B^2}T}{\hbar^2}\mathcal{V}^2 t\right),
\end{aligned} \tag{98}$$

with the time-ordering operator $\mathcal{T}$. Between the second and the third lines, we keep only even summation indices $m = 2n$ (zero-mean Gaussian process), evaluate the statistical average at adjacent times $t_{2n-1} - t_{2n} \leqslant T$ (correlation time T; that only adjacent times need to be considered is a consequence of time ordering, the Gaussian factorization of higher-order correlations, and the very short correlation times), and neglect the terms $\exp[\mathcal{H}(t_{2n-1} - t_{2n})] \ll 1$ (Markovian limit). To summarize, we have shown that the described fluctuations of the magnetic field generate Markovian dynamics [see Eq. (25)] with Lindblad operators $\mathbf{L}^\alpha = g\sigma_z^\alpha = g\mathbf{V}$ and decoherence strength,

$$g^2 = \frac{\overline{\delta B^2}T}{\hbar^2}. \tag{99}$$

In the case of the anisotropic XY chain [see Eq. (12)], the correlation time T is bounded by the width of the single-particle excitation spectrum $T^{-1} \gg \max(4B/\hbar, 8J/\hbar)$. In the recent experiment [40], $2J/\hbar \approx B/\hbar = 2\pi \times 4.4$ kHz was used, but experimentally available laser intensities allow $2J/\hbar \approx B/\hbar \approx 2\pi \times 40$ kHz. We propose creating fluctuations in the magnetic field with frequency $T^{-1} = 2\pi \times 1.6$ MHz and variance $\overline{\delta B^2}/\hbar^2 = (0.2B/\hbar)^2 \approx (2\pi \times 8\text{ kHz})^2$. This would result in the decoherence strength $g^2 \approx 2 \times 10^{-3}$ J/$\hbar$ and would require coherence times on the order of $2\pi/g^2 \approx 25$ ms. These coherence times can, in principle, be achieved in systems of trapped ions [47].

VIII. CONCLUSION

We have investigated the dynamics of noise-driven open quantum systems with regard to their steady states and asymptotic decay. We have shown that insight into different phases can be gained by spectral analysis of the Liouvillian in analogy to how the spectrum of the Hamiltonian reveals critical behavior in zero-temperature quantum phase transitions.

To illustrate this point, we have analyzed, in detail, the Liouvillian of fermionic systems under a translationally invariant quadratic Hamiltonian, coupled to a Markovian bath. We treat master equations with linear or quadratic and Hermitian Lindblad operators. In both cases, the master equation leads to a closed equation for the CM from which the steady-state CM and the rates at which it is approached can be obtained exactly (see also Ref. [19] for an elegant and comprehensive treatment of both fermionic and bosonic linear open systems and their critical properties and Ref. [28] for a detailed study of transport in spin chains under dissipation and dephasing). These results apply as well to a large class of 1D spin systems that can be mapped to quasifree fermions by a Jordan-Wigner transformation. We have proposed an experimental realization of this quantum simulation with trapped ions. Numerical calculations show that our results for the weak decoherence limit do apply to such finite systems.

We have focused on the limit of weak decoherence ($g \to 0$) and have shown how to deduce information about critical points from the spectrum of the Liouvillian. In particular, the ADR Δ, i.e., the smallest nonzero eigenvalue of the Liouvillian, can serve as an indicator of phase transitions even if the steady state of the system is trivial and steady-state expectation values, thus, cannot yield such information (as in the case of Hermitian Lindblad operators). Depending on the decoherence process considered, the critical point can be reflected in the spectrum of the system's Liouvillian in

TABLE I. Different noise-driven systems studied, characterized by their Lindblad operators and Hamiltonian H. Relevant properties of the ADR Δ and the steady state are listed. x_c denotes critical points of the Hamiltonian H.

Lindblad operator	ADR and gap	Steady state
	Hamiltonian $H = 0$	
$\mu a_\alpha, \nu a_\alpha^\dagger$	Gapped, no phase transition	Thermal
$\mu a_\alpha + \nu a_{\alpha+1}^\dagger$	Gap closes at $\mu = \nu$, no phase transition	Paired
$\frac{i\mu}{2}[c_{\alpha,0}, c_{\alpha,1}]$, $\frac{i\nu}{2}[c_{\alpha+1,0}, c_{\alpha,1}]$	Degenerate at $\mu = \nu$	$\propto \mathbb{1}$
	Hamiltonian $H \neq 0$: translationally invariant, critical at x_c	
$\mu a_\alpha, \nu a_\alpha^\dagger$	Degenerate at x_c	$\langle a^\dagger a \rangle$ nonanalytic at x_c
$\frac{i\mu}{2}[c_{\alpha,0}, c_{\alpha,1}]$, $\frac{i\nu}{2}[c_{\alpha+1,0}, c_{\alpha,1}]$	Nonanalytic at x_c	$\propto \mathbb{1}$

the form of a closing gap ($\Delta \to 0$), a degeneracy of Δ, or nonanalytic behavior of Δ. These results are summarized in Table I.

With this paper, we suggest the possibility to detect certain system properties through an observation of the decoherent dynamics: Phase transitions in closed systems can be reflected in nonanalytic changes in the ADR [25,26,28]. More generally, since the ADR and other decay rates represent physical properties of the system, such nonanalyticities can be seen as the signature of a transition to a different dynamical regime. This suggests studying the phase diagram of steady-state correlation functions $\langle A(t)B(t')\rangle$, which reflect these dynamical transitions.

ACKNOWLEDGMENTS

The authors thank M. M. Wolf and T. Roscilde, B.H. thanks M. Lubasch, L. Mazza, M. C. Bañuls, N. Schuch, and A. Pflanzer for fruitful discussions. The authors would like to acknowledge financial support from the DFG within the Excellence Cluster Nanosystems Initiative Munich (NIM) and the EU project MALICIA under FET-Open Grant No. 265522.

[1] K. Southwell, V. Vedral, R. Blatt, D. Wineland, I. Bloch, H. J. Kimble, J. Clarke, F. K. Wilhelm, R. Hanson, and D. D. Awschalom, Nature (London) **453**, 1003 (2008).
[2] P. W. Shor, Phys. Rev. A **52**, 2493 (1995).
[3] F. Verstraete, M. M. Wolf, and J. Ignacio Cirac, Nat. Phys. **5**, 633 (2009).
[4] B. Kraus, H. P. Büchler, S. Diehl, A. Kantian, A. Micheli, and P. Zoller, Phys. Rev. A **78**, 042307 (2008).
[5] S. Diehl, A. Micheli, A. Kantian, B. Kraus, H. P. Buchler, and P. Zoller, Nat. Phys. **4**, 878 (2008).
[6] S. Diehl, W. Yi, A. J. Daley, and P. Zoller, Phys. Rev. Lett. **105**, 227001 (2010).
[7] M. Roncaglia, M. Rizzi, and J. I. Cirac, Phys. Rev. Lett. **104**, 096803 (2010).
[8] W. Yi, S. Diehl, A. J. Daley, and P. Zoller, New J. Phys. **14**, 055002 (2012).
[9] C. A. Muschik, E. S. Polzik, and J. I. Cirac, Phys. Rev. A **83**, 052312 (2011).
[10] H. Krauter, C. A. Muschik, K. Jensen, W. Wasilewski, J. M. Petersen, J. I. Cirac, and E. S. Polzik, Phys. Rev. Lett. **107**, 080503 (2011).
[11] F. Pastawski, L. Clemente, and J. I. Cirac, Phys. Rev. A **83**, 012304 (2011).
[12] N. Syassen, D. M. Bauer, M. Lettner, T. Volz, D. Dietze, J. J. García-Ripoll, J. I. Cirac, G. Rempe, and S. Dürr, Science **320**, 1329 (2008).
[13] S. Dürr, J. J. García-Ripoll, N. Syassen, D. M. Bauer, M. Lettner, J. I. Cirac, and G. Rempe, Phys. Rev. A **79**, 023614 (2009).
[14] J.-J. García-Ripoll, S. Dürr, N. Syassen, D. M. Bauer, M. Lettner, G. Rempe, and J. I. Cirac, New J. Phys. **11**, 013053 (2009).
[15] A. J. Daley, J. M. Taylor, S. Diehl, M. Baranov, and P. Zoller, Phys. Rev. Lett. **102**, 040402 (2009).
[16] M. Kiffner and M. J. Hartmann, Phys. Rev. A **81**, 021806(R) (2010); New J. Phys. **13**, 053027 (2011).
[17] S. Diehl, A. Tomadin, A. Micheli, R. Fazio, and P. Zoller, Phys. Rev. Lett. **105**, 015702 (2010).
[18] S. Sachdev, *Quantum Phase Transitions* (Cambridge University Press, Cambridge, UK, 1999).
[19] J. Eisert and T. Prosen, arXiv:1012.5013.
[20] E. M. Kessler, G. Giedke, A. Imamoğlu, S. F. Yelin, M. D. Lukin, and J. I. Cirac, Phys. Rev. A **86**, 012116 (2012).
[21] T. Prosen, New J. Phys. **10**, 043026 (2008).
[22] T. Prosen, J. Stat. Mech. (2010) P07020.
[23] T. Prosen and B. Žunkovič, New J. Phys. **12**, 025016 (2010).
[24] S. R. Clark, J. Prior, M. J. Hartmann, D. Jaksch, and M. B. Plenio, New J. Phys. **12**, 025005 (2010).
[25] M. Höning, M. Moos, and M. Fleischhauer, Phys. Rev. A **86**, 013606 (2012).
[26] B. Horstmann, Ph.D. thesis, TU München, 2011.
[27] M. Žnidarič, J. Stat. Mech. (2010) L05002.
[28] M. Žnidarič, Phys. Rev. E **83**, 011108 (2011).
[29] V. Eisler, J. Stat. Mech. (2011) P06007.
[30] X. Zhao, W. Shi, L.-A. Wu, and T. Yu, Phys. Rev. A **86**, 032116 (2012).
[31] G. Lindblad, Commun. Math. Phys. **48**, 119 (1976).
[32] H.-P. Breuer and F. Petruccione, *The Theory of Open Quantum Systems* (Oxford University Press, Oxford, 2007).
[33] M. A. Nielsen, Michael Nielsen's blog (2005).
[34] G. Wick, Phys. Rev. **80**, 268 (1950).

[35] C. V. Kraus, M. M. Wolf, J. I. Cirac, and G. Giedke, Phys. Rev. A **79**, 012306 (2009).

[36] The exact steady-state CM for Eq. (54) differs from $\tilde{\Gamma}_0$ of Eq. (55) by $i2g^2 \bigoplus_n \frac{\mu^2-\nu^2}{(k_n-l_n)^2+4|h_n|^2}[-\mathrm{Im}(h_n)\sigma^z + \frac{k_n-l_n}{2}\sigma^x]$, which vanishes as $g \to 0$.

[37] The ADR itself, $g^2(\mu^2+\nu^2)$, does not change at the phase transition. However, note that there actually is a large manifold of eigenvalues of the Liouvillian whose real part is $-g^2(\mu^2+\nu^2)$ but with different imaginary parts, taken from the set $\{\lambda_\pm^{(n)} - \lambda_\pm^{(m)}\}$, where $\lambda_\pm^{(n)} = (k_n+l_n)/2 \pm \sqrt{(\frac{k_n-l_n}{2})^2+|h_n|^2}$ and all four combinations of the subscripts $\pm$ may occur. At the critical point, the discriminant vanishes, and each eigenvalue becomes (at least) fourfold degenerate.

[38] S. Braungardt, A. Sen(De), U. Sen, R. J. Glauber, and M. Lewenstein, Phys. Rev. A **78**, 063613 (2008).

[39] D. Porras and J. I. Cirac, Phys. Rev. Lett. **92**, 207901 (2004).

[40] A. Friedenauer, H. Schmitz, J. Glückert, D. Porras, and T. Schätz, Nat. Phys. **4**, 757 (2008).

[41] H. Schmitz, A. Friedenauer, C. Schneider, R. Matjeschk, M. Enderlein, T. Huber, J. Glückert, D. Porras, and T. Schätz, Appl. Phys. B **95**, 195 (2009).

[42] K. Kim, M.-S. Chang, S. Korenblit, R. Islam, E. E. Edwards, J. K. Freericks, G.-D. Lin, L.-M. Duan, and C. Monroe, Nature (London) **465**, 590 (2010).

[43] J. W. Britton, B. C. Sawyer, A. C. Keith, C.-C. J. Wang, J. K. Freericks, H. Uys, M. J. Biercuk, and J. J. Bollinger, Nature (London) **484**, 489 (2012).

[44] B. P. Lanyon, C. Hempel, D. Nigg, M. Müller, R. Gerritsma, F. Zähringer, P. Schindler, J. T. Barreiro, M. Rambach, G. Kirchmair, M. Hennrich, P. Zoller, R. Blatt, and C. F. Roos, Science **334**, 57 (2011).

[45] J. T. Barreiro, M. Muller, P. Schindler, D. Nigg, T. Monz, M. Chwalla, M. Hennrich, C. F. Roos, P. Zoller, and R. Blatt, Nature (London) **470**, 486 (2011).

[46] F. Marquardt and A. Püttmann, arXiv:0809.4403.

[47] D. J. Wineland, C. Monroe, W. M. Itano, D. Leibfried, B. E. King, and D. M. Meekhof, J. Res. Natl. Inst. Stand. Technol. **103**, 259 (1998).

PHYSICAL REVIEW A **87**, 022110 (2013)

Dissipative spin chains: Implementation with cold atoms and steady-state properties

Heike Schwager,[1] J. Ignacio Cirac,[1] and Géza Giedke[1,2]
[1]*Max-Planck-Institut für Quantenoptik, Hans-Kopfermann–Str. 1, D-85748 Garching, Germany*
[2]*M5, Zentrum Mathematik, TU München, L.-Boltzmannstr. 3, D–85748 Garching, Germany*
(Received 3 August 2012; published 13 February 2013)

We propose a quantum optical implementation of a class of dissipative spin systems, including the XXZ and Ising model, with ultracold atoms in optical lattices. By employing the motional degree of freedom of the atoms and detuned Raman transitions, we show how to obtain engineerable dissipation and a tunable transversal magnetic field, enabling the study of the dynamics and steady-states of dissipative spin models. As an example of effects made accessible this way, we consider small spin chains and weak dissipation and show by numerical simulation that steady-state expectation values display pronounced peaks at certain critical system parameters. We show that this effect is related to degeneracies in the Hamiltonian and derive a sufficient condition for its occurrence.

DOI: 10.1103/PhysRevA.87.022110 PACS number(s): 03.65.Yz, 03.67.Lx

I. INTRODUCTION

Quantum spin models play a fundamental role for the theoretical and experimental study of quantum many-body effects. They represent paradigmatic systems exhibiting, e.g., quantum phase transitions and peculiar forms of matter [1]. They also provide toy models for description of many solid state systems. Ultracold atoms in optical lattices [2] have emerged as a system that is especially suited to study the low-energy sector of quantum spin systems with the promise to eventually simulate theoretical models in large, controlled quantum systems.

To observe these effects, coupling to uncontrolled degrees of freedom has to be kept to a minimum, since it leads to dissipation and decoherence [3,4] which can mask or destroy the quantum effects. But in recent years, it has been shown how the coupling to an environment can be harnessed to generate useful quantum states [5–9] or perform quantum information tasks [9,10]. Moreover, the study of the phase diagram of open quantum systems has turned into a fruitful direction itself [11–16].

Our aim in the present work is twofold: In the first part of the paper, we propose a scheme to realize a quantum spin system using ultracold atoms in an optical lattice in which both coherent interaction and dissipation can be engineered and controlled, enabling the study the nonequilibrium and steady-state physics of open and driven spin systems. In the second part, we highlight a peculiar feature of the steady-state diagram for small spin chains: in the limit of weak dissipation, abrupt changes of steady-state expectation values for certain critical values of the system parameters are observed. We explain this feature and relate it to degeneracy properties of the system Hamiltonian and derive a sufficient condition for the occurrence of sharp peaks at critical system parameters.

II. PHYSICAL IMPLEMENTATION OF ONE-DIMENSIONAL SPIN CHAIN UNDER DISSIPATION

Ultracold bosonic atoms in optical lattices are ideal candidates to simulate spin Hamiltonians. Different theoretical and experimental approaches [17] have been employed to simulate quantum spin chains in optical lattices; for example, by optical driving of two hyperfine levels of cold bosons in the Hubbard regime [18]. Recently, a one-dimensional chain of interacting Ising spins has been implemented experimentally using a Mott-Insulator of spinless bosons in a tilted optical lattice [19].

In the following, we show theoretically how to add engineered dissipation to the toolbox of these systems [20,21]. Specifically, we show how to implement a system with the following properties: (i) dissipative dynamics of Lindblad form, (ii) a tunable magnetic field in x direction and (iii) an effective spin Hamiltonian such as, e.g., the XXZ, Heisenberg, or Ising model. In the next sections, we first introduce the setup and explain qualitatively how such a one-dimensional spin chain in a tunable magnetic field under engineerable dissipation can be realized with cold atoms in optical lattices. In the subsequent sections we give specific requirements and parameters and details of the derivation for (i)–(iii).

A. Setup and qualitative description

The system we consider is an optical lattice populated with a single atomic bosonic species. We assume to be in the Mott-insulator regime with filling factor 1, where the on-site interaction is much larger than the tunneling (hopping) between neighboring lattice sites. In this regime, the atoms are localized such that each lattice potential is occupied with one atom. We aim to use the motional ground and first-excited state of the atom (denoted by $|0\rangle$ and $|1\rangle$ [22], respectively) to realize an effective spin-$\frac{1}{2}$ system in each lattice site. To access the motional degree of freedom optically, we work in the Lamb-Dicke regime where the motion of the atom is restricted to a region small compared with the laser wavelength. We make use of the anharmonicity of the lattice potential and, as explained in the following, of decay of the atoms that leads to cooling of the system, to restrict the dynamics to the two-dimensional subspace of $\{|0\rangle,|1\rangle\}$ [23] (see Fig. 1). For the optical manipulation, we assume that the atoms have internal degrees of freedom that can be addressed with laser fields. We consider a Λ scheme with two ground states $|g\rangle$ and $|r\rangle$ (both trapped by the same optical lattice potential) and an excited state $|e\rangle$. The level scheme of the internal states of the atoms

 ©2013 American Physical Society

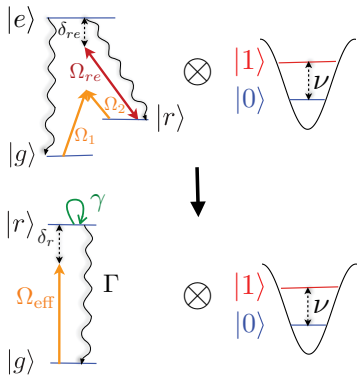

FIG. 1. (Color online) Relevant level structure and coupling and decay terms of single atom trapped at a lattice site. The upper-left part shows the internal levels of the atom: Λ system $|g\rangle$, $|r\rangle$, $|e\rangle$, off-resonantly driven by lasers. The right part shows motional states in the lattice potential. Lower part: After adiabatic elimination of $|e\rangle$, an effective two-level system with tunable decay rate Γ and dephasing rate γ is obtained.

is shown in Fig. 1. Off-resonant laser fields drive transitions between the two ground states $|g\rangle$ and $|r\rangle$ and the excited state $|e\rangle$. The system decays fast into the ground states and, as we show below, effectively decays into the state $|g\rangle$. Therefore, the atoms are optically pumped to the state $|g\rangle \otimes |0\rangle$ and the states $|r\rangle$ and $|e\rangle$ can be adiabatically eliminated. Eliminating the excited state $|e\rangle$ leads to the effective two-level system in the lower part of Fig. 1 with designable decay rates. Further elimination of the state $|r\rangle$ leads to an effective description in the internal ground state $|g\rangle$ (see Fig. 2). The optical couplings by laser fields give rise to effective Hamiltonians and effective dissipation (cooling) in the ground state $|g\rangle$ at each lattice site. Details are given in Sec. II B. In summary, we obtain an effective two-level system at each lattice site with Hilbert space spanned by $|g\rangle \otimes |0\rangle$ and $|g\rangle \otimes |1\rangle$ as depicted in Fig. 3.

In the following sections, we show that engineering the optical couplings as above leads to an effective master equation

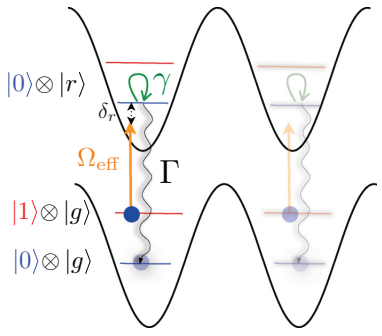

FIG. 2. (Color online) Effective two-level system $|g\rangle$-$|r\rangle$ in the optical lattice potential with motional states $|0\rangle$ and $|1\rangle$. Choosing resonance conditions as explained in Sec. II B, the atoms are selectively excited from $|g\rangle \otimes |1\rangle$ to the state $|r\rangle \otimes |0\rangle$ and spontaneously decay into $|g\rangle \otimes |0\rangle$.

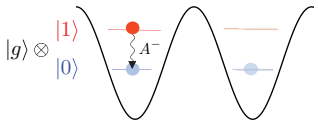

FIG. 3. (Color online) Decay of the effective two-level system $\{|0\rangle\},\{|1\rangle\}$ as described by the effective master equation derived in Sec. II B. The dissipation strength A^- is given in Eq. (7).

for the two-level system $|0\rangle$, $|1\rangle$ that describes (i) decay from $|1\rangle$ to $|0\rangle$ and (ii) an effective magnetic field in x direction. In the Mott insulator regime, tunnel couplings between neighboring lattice wells can be treated as a perturbation, which (iii) leads to an effective spin Hamiltonian. The resulting master equation [24] is given by

$$\dot{\rho}_t = \sum_k A^-(2\sigma_k^-\rho_t\sigma_k^+ - \{\sigma_k^+\sigma_k^-,\rho_t\}_+) - i[H,\rho_t]. \qquad (1)$$

Here, $\sigma_k^+ = |1\rangle\langle 0|_k$ is the operator that excites an atom at lattice site k from the motional state $|0\rangle$ to state $|1\rangle$ and $\sigma_k^- = (\sigma_k^+)^\dagger$. The sum runs over all N sites of the optical lattice potential. The first part in Eq. (1) describes decay from state $|1\rangle$ into state $|0\rangle$ as depicted in Fig. 3. It is derived in Sec. II B. The decay parameter A^- can be tuned by changing the Rabi frequencies of the lasers and the detunings and is given by Eq. (18) in Sec. II E. The Hamiltonian is given by $H = H_B + H_{\rm spin}$, where H_B describes the magnetic field in x direction given by

$$H_B = \sum_k B_x(\sigma_k^+ + \sigma_k^-), \qquad (2)$$

where B_x is proportional to an effective magnetic field in the x direction. It is derived in Sec. II C. The Hamiltonian $H_{\rm spin}$ describes the spin Hamiltonian

$$H_{\rm spin} = \sum_k \alpha_1\left(\sigma_k^x\sigma_{k+1}^x + \sigma_k^y\sigma_{k+1}^y\right) + \alpha_2\sigma_k^z\sigma_{k+1}^z, \qquad (3)$$

as derived in Sec. II D. The parameters α_1 and α_2 depend on the properties of the optical lattice potential and can be tuned. Therefore, the Hamiltonian $H_{\rm spin}$ describes the XXZ model, the Ising model, or the Heisenberg model. In the following three sections, we employ a perturbative approach to derive a master equation comprising dissipation of Lindblad form (i) as in Eq. (1), a magnetic field in x direction (ii) as in Eq. (2), and an effective spin Hamiltonian (iii) as in Eq. (3). For the sake of clarity, we derive (i)–(iii) in three separate steps employing the approximation of independent rates of variation as explained in Ref. [25].

B. Optical couplings of internal atomic states: dissipation of Lindblad form

In this section, we show that optically addressing the atoms with suitably tuned lasers allows to engineer decay as in Eq. (1).

We consider the internal levels $|g\rangle$, $|r\rangle$, $|e\rangle$ of an atom at site k. The ground states $|g\rangle$ and $|r\rangle$ can be coupled via the excited state $|e\rangle$ by a detuned Raman transition of two standing-wave laser fields with Rabi frequencies Ω_1 and Ω_2. Eliminating the excited state $|e\rangle$ leads to an effective coupling between $|g\rangle$

and $|r\rangle$ (see Fig. 1) with $\Omega_{\rm eff} = \Omega_1\Omega_2/\delta_{re}$ where δ_{re} is the detuning with respect to $|e\rangle$ (for details see Appendix A). To induce controlled dissipation, we couple $|r\rangle$ and $|e\rangle$ by an additional off-resonant laser field (indicated by a red arrow) in Fig. 1. Then adiabatic elimination of the excited state $|e\rangle$ leads to an effective two-level system (as shown in the lower part of Fig. 1) with states $|r\rangle$ and $|g\rangle$ which has designable decay rates Γ and γ as derived in [26] (see also Appendix A). Thereby, the excited state $|e\rangle$ that is broadened by spontaneous emission is eliminated, and the effective two-level system $|g\rangle$-$|r\rangle$ allows the motional states $|0\rangle$ and $|1\rangle$ of the lattice potential to be resolved (note that we are in the Lamb-Dicke regime), as can be seen in Fig. 2. Under appropriate resonance conditions that will be specified in the following, the atoms are excited from state $|1\rangle\otimes|g\rangle$ to state $|0\rangle\otimes|r\rangle$ and spontaneously decay into the state $|0\rangle\otimes|g\rangle$ as shown in Fig. 2. Adiabatically eliminating the state $|r\rangle$, this corresponds to an effective decay from state $|1\rangle\otimes|g\rangle$ into $|0\rangle\otimes|g\rangle$. Thus the atoms effectively remain in the internal ground state $|g\rangle$, such that the decay can be written as an effective decay from state $|1\rangle$ to $|0\rangle$ as depicted in Fig. 3.

In Appendix A, we derive in a perturbative approach (that corresponds to an adiabatic elimination of the state $|r\rangle$) a master equation that describes the dynamics of the two-level system $|0\rangle$, $|1\rangle$ of the atom. Assuming that the driving of level $|r\rangle$ is sufficiently weak such that

$$|\Omega_{\rm eff}| \ll \Gamma,\gamma,\nu,|\delta_r|, \tag{4}$$

and that the level broadening remains small

$$\Gamma+\gamma < \nu, \tag{5}$$

the master equation is given by

$$\dot\rho_t = \sum_k A^-(2\sigma_k^-\rho_t\sigma_k^+ - \{\sigma_k^+\sigma_k^-,\rho_t\}_+) + A^+(2\sigma_k^+\rho_t\sigma_k^- - \{\sigma_k^-\sigma_k^+,\rho_t\}_+) - i\big[H_{\rm eff}^{(1)},\rho_t\big]. \tag{6}$$

Here, A^+ determines the strength of the heating terms and A^- the strength of the decay terms. For simplicity, $A^\pm$ are chosen to be independent of the lattice site k. $A^\pm$ can be made dependent on the lattice site k by choosing different phases of the driving lasers as explained in Appendix A. Note that $A^+ \ll A^-$ is required for the validity of the approximation that restricts to the $|0\rangle$ and $|1\rangle$ subspace. A^- and A^+ are given by

$$A^\pm = \Omega_{\rm eff}^2\eta_1^2\frac{(\Gamma+\gamma)}{(\Gamma+\gamma)^2+(\delta_r\pm\nu)^2}. \tag{7}$$

Here, δ_r is the effective detuning given by Eq. (A5) in Appendix A, $\eta_1 = k_1/\sqrt{2M\nu}$ is the Lamb-Dicke parameter where k_1 is the wave number of the laser with Rabi frequency Ω_1, M is the atomic mass, and ν denotes the energy difference between the motional state $|0\rangle$ and $|1\rangle$ of the lattice potential. The Hamiltonian $H_{\rm eff}^{(1)}$ in the last term in Eq. (6) is given by

$$H_{\rm eff}^{(1)} = \sum_k \nu|1\rangle\langle1|_k + H_S, \tag{8}$$

where H_S describes ac Stark shifts on the motional levels that are $\ll\nu$ and are given in more detail in Appendix A. Now we have everything at hand to implement dissipation. If

$$\delta_r \approx \nu,$$

which can be achieved by choosing the laser frequency ω_l in $\delta_r = \omega_r - \omega_l$ accordingly, the strength of the dissipation is much larger than the strength of the heating:

$$A^+ \ll A^-. \tag{9}$$

Then, the master equation has only decaying terms and is of the form

$$\dot\rho_t = \sum_k A^-(2\sigma_k^-\rho_t\sigma_k^+ - \{\sigma_k^+\sigma_k^-,\rho_t\}_+) - i\big[H_{\rm eff}^{(1)},\rho_t\big]. \tag{10}$$

It describes decay of the atoms from state $|1\rangle$ into $|0\rangle$, while the atoms effectively remain in the internal state $|g\rangle$. By adiabatic elimination of the internal state $|r\rangle$, we have thus shown that a master equation can be derived that can be tuned such that it describes almost pure decay.

C. Optical couplings of internal atomic states: Effective magnetic field in *x* direction

To derive the effective magnetic field in x direction, we consider a detuned Raman transition. Two standing-wave laser fields with Rabi frequencies Ω_a and Ω_b couple the internal ground state $|g\rangle$ and the excited state $|e\rangle$ of the atoms, as depicted in Fig. 4. The coupling is described by the Hamiltonian

$$H_{ab} = \sum_k \Omega_a\cos(k_a x_k)|e\rangle\langle g|_k + \Omega_b\sin(k_b x_k)|e\rangle\langle g|_k + \text{H.c.}, \tag{11}$$

where k_a, k_b denote the wave numbers of the lasers and x_k is the displacement from the equilibrium position of the atom at lattice site k. As we are in the Lamb-Dicke regime, $\sin(k_b x_k) \approx \eta_b(\sigma_k^- + \sigma_k^+)$ [27] and $\cos(k_a x_k) \approx 1$. Under the condition

$$|\Omega_a|, |\Omega_b| \ll |\delta_e|, \tag{12}$$

where δ_e is the detuning of the driving lasers, as depicted in Fig. 4, the excited state $|e\rangle$ can be adiabatically eliminated and we get an effective Hamiltonian

$$H_{\rm eff}^{(2)} = H_B = \sum_k B_x\sigma_k^x, \tag{13}$$

which describes a tunable magnetic field in x direction, where B_x is proportional to the effective magnetic field strength in x direction, which is given by

$$B_x = \frac{2\Omega_a\Omega_b\eta_b}{\delta_e}.$$

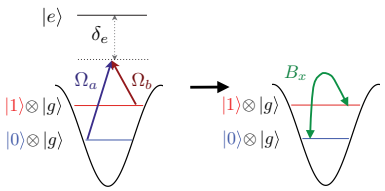

FIG. 4. (Color online) Level scheme and transitions used to implement the transverse magnetic field. Left: A detuned Raman transition couples the internal ground state $|g\rangle$ and the excited state $|e\rangle$ of the atom. Right: Adiabatic elimination of the excited state $|e\rangle$ leads to an effective magnetic field in x direction (see Sec. II C), which drives transitions between the motional states $|0\rangle$ and $|1\rangle$.

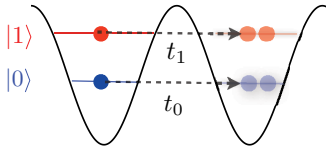

FIG. 5. (Color online) Tunneling between neighboring lattice wells with tunnel amplitudes t_0 and t_1. States with two atoms per lattice well are treated in perturbation theory in Sec. II D, as the on-site interaction is much larger than the tunneling amplitudes.

Thus, we have derived an effective magnetic field in x direction that drives transitions between the motional states $|0\rangle$ and $|1\rangle$ (as depicted on the right side of Fig. 4), while the atoms remain in the internal ground state $|g\rangle$.

D. Effective spin Hamiltonian

In the Mott-insulator regime, bosonic atoms trapped by a lattice potential with two motional states are described by the two-band Bose-Hubbard model [28] (see Appendix B). We denote the on-site interaction by U_{01}, U_{00}, and U_{11} [29] and by t_0 (t_1) the amplitudes for atoms in state $|0\rangle$ ($|1\rangle$) to tunnel to neighboring lattice sites. We assume that the on-site interaction $U_{01}, U_{00}, U_{11} \gg t_0, t_1$ such that tunneling between neighboring wells, which leads to states with two atoms in one lattice well, can be treated as a perturbation (see Fig. 5). Using second-order perturbation theory [25] (for a detailed derivation see Appendix B), we derive an effective spin Hamiltonian $H_{\rm spin}$ given by

$$H_{\rm eff}^{(3)} = H_{\rm spin} + B_z \sum_k |1\rangle\langle 1|_k, \tag{14}$$

with

$$H_{\rm spin} = \sum_k \alpha_1 \left(\sigma_k^x \sigma_{k+1}^x + \sigma_k^y \sigma_{k+1}^y\right) + \alpha_2 \sigma_k^z \sigma_{k+1}^z, \tag{15}$$

where $\alpha_1 = -4t_0t_1/U_{01}, \alpha_2 = 2[(t_0^2+t_1^2)/(2U_{01}) - t_0^2/U_{00} - t_1^2/U_{11}]$, and the magnetic field in z direction is

$$B_z = t_0^2/U_{00} - t_1^2/U_{11}, \tag{16}$$

using the Pauli spin matrices σ_k^x, σ_k^y with $\sigma_k^x = |0\rangle\langle 1|_k + |1\rangle\langle 0|_k)/2$. The Hamiltonian given by Eq. (14) is an effective spin Hamiltonian that is tunable by changing the lattice properties. If $\alpha_1, \alpha_2 > 0$, $H_{\rm eff}^{(3)}$ corresponds to the XXZ model with a magnetic field in z direction. If the lattice properties can be tuned such that one of the tunneling constants t_0 or $t_1 \to 0$, $H_{\rm spin}$ is an Ising Hamiltonian with a magnetic field in z direction. For $\alpha_1 = \alpha_2$, $H_{\rm spin}$ corresponds to the Heisenberg model.

E. Dissipative one-dimensional spin chain in magnetic field

In the previous sections, we showed—for the sake of clarity in separate steps—that optical couplings of the internal levels can be engineered such that we obtain a master equation of Lindblad form [Eq. (6)] fulfilling the demands (i)–(iii) of tunable dissipation, spin-interaction, and tunable transverse field. Combining these results, one has to carefully consider the order of magnitude of each term. Doing so, we find that the magnetic field B_z in z direction in Eq. (14) and the Stark shifts in Eq. (8) can be of the same order of magnitude as ν. Stark shifts and B_z lead to an effective energy difference between the motional states $|0\rangle$ and $|1\rangle$ given by

$$\tilde{\nu} = \nu + B_z + s_- - s_+,$$

where B_z is defined in Eq. (15) and s_-, s_+ are the ac Stark shifts in Eq. (8) (see Appendix A). Therefore, combining all results, the laser detuning δ_r that enters in $A^{\pm}$ has to be adjusted to $\tilde{\delta}_r$ such that $\tilde{\delta}_r - \nu = \delta_r - \tilde{\nu}$, which means that $\tilde{\delta}_r = \delta_r \pm (B_z + s_- - s_+)$.

Then, combining the results from Eqs. (6), (13), and (14), the master equation reads

$$\dot{\rho}_t = \sum_k A^+(2\sigma_k^+\rho_t\sigma_k^- - \{\sigma_k^-\sigma_k^+, \rho_t\}_+) + A^-(2\sigma_k^-\rho_t\sigma_k^+ - \{\sigma_k^+\sigma_k^-, \rho_t\}_+) - i[H, \rho_t], \tag{17}$$

where the rates $A^{\pm}$ are modified by the renormalized $\tilde{\delta}_r$:

$$A^{\pm} = \Omega_{\rm eff}^2 \eta_1^2 \frac{(\Gamma+\gamma)}{(\Gamma+\gamma)^2 + (\tilde{\delta}_r \pm \nu)^2}. \tag{18}$$

The Hamiltonian part of the master equation is given by

$$H = H_{\rm spin} + H_B + \tilde{\nu} \sum_k |1\rangle\langle 1|_k, \tag{19}$$

where $H_{\rm spin}$ is given by Eq. (15) and H_B by Eq. (13). The magnetic field in z direction and Stark shifts have been included in $\tilde{\nu}$. For $\tilde{\delta}_r \approx \nu$, as shown before, decay dominates over heating: $A^- \gg A^+$. Then, the master equation has only decaying terms and Eq. (17) describes a dissipative XXZ spin chain in a magnetic field with both x and z components. However, only B_x is fully tunable, while B_z is large (compared to B_x, $A^{\pm}$) and required to be so by the conditions for adiabatic elimination, cf. Eq. (4). However, an effective dissipative XXZ chain without any field in z direction would be advantageous for observing critical behavior in the steady-state dynamics that we study in the next sections. Therefore, we transform to a frame rotating with $\tilde{\nu}$. In the rotating frame, H_B becomes time dependent. To obtain a time-independent field in x direction, the detuned Raman lasers that lead to the effective magnetic field B_x have to be chosen time dependent, adapted to the rotating frame (i.e., suitably detuned from the two-photon resonance). This then yields a time-independent transversal magnetic field, and the master equation in the rotating frame is then given by

$$\dot{\rho}_t = \sum_k A^-(2\sigma_k^-\rho_t\sigma_k^+ - \{\sigma_k^+\sigma_k^-, \rho_t\}_+) - i[H_{\rm spin} + H_B, \rho_t]. \tag{20}$$

It corresponds to the master equation given by Eq. (1). In summary we have shown how to implement a one-dimensional spin chain with nearest-neighbor interaction described by the XXZ or the Ising model and a tunable effective magnetic field in x direction under dissipation. This system is an ideal test bed for studying steady-state dynamics of dissipative spin models, as discussed in the next section. Note that since we are in a rotating frame, observables other than the collective spin operator $\langle J_z\rangle$ become explicitly time dependent.

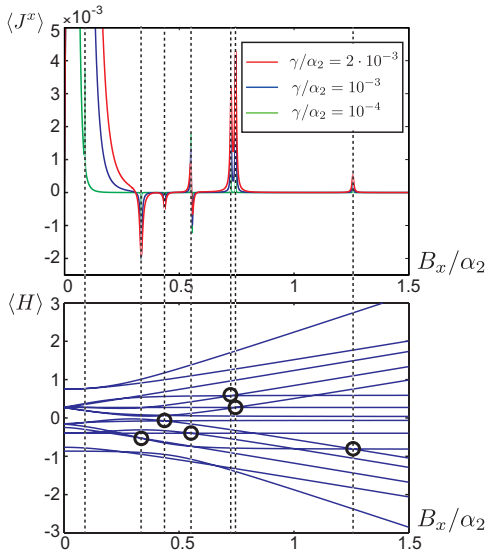

FIG. 6. (Color online) XXZ model with 4 spins, $\alpha_1 = \frac{1}{4}\alpha_2$ and open boundary conditions under local dissipation of form given by Eq. (20). Upper part: Steady-state expectation value $\langle J^x \rangle$ plotted versus the magnetic field B_x/α_2. Peaks are observed that narrow for decreasing the dissipation strength. Lower part: Spectrum of XXZ chain in the magnetic field B_x plotted versus B_x/α_2. Peaks in the steady-state expectation value (upper part) appear at crossing points of the Hamiltonian that are marked with black circles.

F. Steady-state behavior: Discontinuous steady-state behavior related to spectrum of Hamiltonian

A particular important characterization of dissipative dynamics is through their steady state: if it is unique (or distinguished by some conserved quantity) it allows for robust preparation of these states. Abrupt changes in the steady state as system parameters are varied may signal dissipative quantum phase transitions [12–16,30,31]. We study the steady-state behavior of short spin chains under dissipation in a magnetic field in the x direction by numerical simulations. We find that the one-dimensional XXZ model with four spins, as given by Eq. (15) where we chose as a typical example $\alpha_1 = \frac{1}{4}\alpha_2$, shows a surprising behavior: Changing the external magnetic field in the x direction makes peaks occur in the steady-state expectation values of the collective spin operators $J^{x/z} = \sum_k \sigma_k^{x/z}$ for weak dissipation; see Fig. 6. Here, we considered dissipation as in Eq. (20) with equal dissipation strength on each spin. We find that, upon decreasing the strength of the dissipation, the peaks become more narrow and each peak height approaches a finite value. For small γ we observe very narrow peaks. This indicates a discontinuity in the steady-state expectation values of the spin operators. We find that these narrow peaks appear exactly at points where the Hamiltonian becomes degenerate. In the following section we study this phenomenon in more generality.

III. DISCONTINUITIES IN STEADY-STATE DYNAMICS OF GENERAL CLASS OF ONE-DIMENSIONAL SPIN MODELS UNDER DISSIPATION

In the previous section we saw that, for the one-dimensional XXZ model, peaks in the steady-state expectation values of the collective spin operators appear, that are closely related to the spectrum of the Hamiltonian. In the following, we study in more generality and independent of a physical implementation local one-dimensional spin Hamiltonians under dissipation of different kinds. We present a condition that elucidates the discontinuous behavior of the steady state at degeneracy points of the Hamiltonian. Next, we study and explain this condition in more detail for Ising Hamiltonians.

A. Numerical studies of discontinuous behavior in steady state

We numerically simulate short spin chains. First, we study the one-dimensional Ising model with open boundary conditions, described by the Hamiltonian

$$H = H_{zz} + H_B, \tag{21}$$

with

$$H_{zz} = \alpha_3 \sum_k \sigma_k^z \sigma_{k+1}^z, \tag{22}$$

and H_B as in Eq. (2) subject to local or collective decay with Lindblad operators $\propto \sigma_k^-$ or $\sum_k \sigma_k^-$, respectively. The master equation describing the full system with local dissipation is given by

$$\dot{\rho}_t = \sum_k \gamma_k (2\sigma_k^- \rho_t \sigma_k^+ - \{\sigma_k^+ \sigma_k^-, \rho_t\}_+) - i[H, \rho_t]. \tag{23}$$

Changing the magnetic field B_x, we find that for weak dissipation the steady-state expectation values of the spin operators $\langle J^x \rangle$ and $\langle J^z \rangle$ change abruptly at particular values of B_x; see Fig. 7. Here, we considered dissipation as in Eq. (23) with equal dissipation strength on each spin, $\gamma_k = \gamma$. Upon decreasing the strength of the dissipation, i.e., decreasing γ, the peaks become more narrow and their height converges to some finite value, while the expectation value vanishes elsewhere. For $\gamma \to 0$, we observe very narrow peaks, which indicates discontinuities in the steady-state expectation values of the spin operators. We find that these narrow peaks appear only at degeneracy points of the spectrum of the Hamiltonian. That is, for every peak found at some value of $B_x = x_0$ for $\gamma \to 0$, at least one pair of degenerate eigenvalues λ_1, λ_2 of the local spin Hamiltonian H_{zz} can be found, i.e., $\lambda_1(x) = \lambda_2(x)$ at $x = x_0$. Note that the discontinuities in the steady state at critical system parameters are only observed for $\gamma \neq 0$. That is, the (weak) dissipation allows us to gain information about the Hamiltonian's properties that is not readily accessible in the case of $\gamma = 0$.

This effect can be observed for different kinds of spin Hamiltonians such as, for example, the XXZ model (see Fig. 6), both for periodic and open boundary conditions. Moreover, changing the type of dissipation, the observed behavior does not change qualitatively. For example, collective dissipation, which describes the dynamics of spins all coupled to the same bath and leads to the master equation

$$\dot{\rho}_t = \gamma (2J^- \rho_t J^+ - \{J^+ J^-, \rho_t\}_+) - i[H, \rho_t], \tag{24}$$

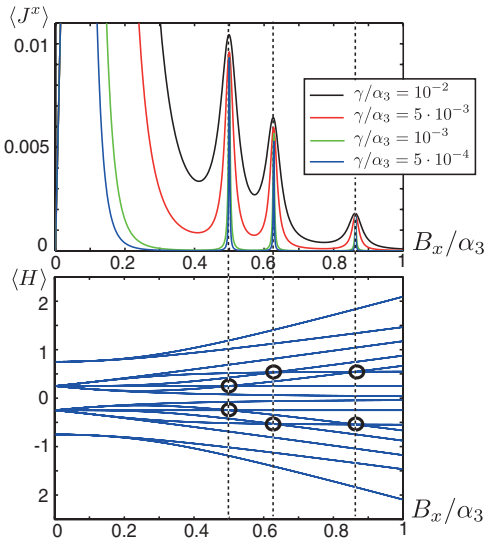

FIG. 7. (Color online) Ising model with 4 spins with open boundary conditions in a transverse magnetic field B_x and under local dissipation of form given by Eq. (23). Upper part: Steady-state expectation value $\langle J^x \rangle$ plotted versus B_x/α_3. Peaks are observed that become more narrow for decreasing dissipation strength. Lower part: Spectrum of the Hamiltonian plotted versus B_x/α_3. Peaks in the steady-state expectation value (upper part) appear at degeneracy points of the Hamiltonian that are marked with black circles.

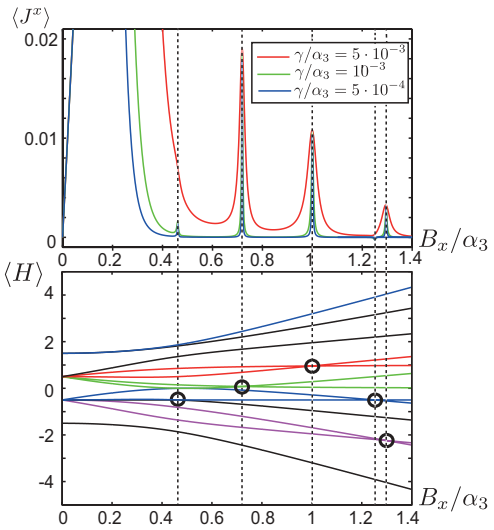

FIG. 8. (Color online) Ising model with 6 spins with periodic boundary conditions in a magnetic field B_x and under collective dissipation of the form given by Eq. (24) in the translation and reflection symmetric subspace $T = R = 1$. Upper part: Steady-state expectation value $\langle J^x \rangle$ plotted versus B_x/α_3. Lower part: Spectrum of the Hamiltonian plotted versus B_x/α_3.

where $J^{\pm} = \sum_k \sigma_k^{\pm}$ also leads to discontinuous behavior in the steady-state expectation values, as shown in Fig. 8 for the Ising model. Choosing an "inhomogeneous" dissipation which is of the form of the dissipative part in Eq. (23), where now the strengths of the dissipation γ_k are different for each spin, peaks can be observed for an even larger class of spin Hamiltonians: For $\gamma_k = \gamma$ and $H = H_H + H_B$, where H_H is the Heisenberg spin Hamiltonian, we do not observe any peaks. However, if we choose different dissipation strengths γ_k for each spin, we find peaks at the degeneracy points of the Hamiltonian, as can be seen in Fig. 9.

B. General condition for discontinuities in steady state

Since the Liouvillian depends smoothly on the system parameters, the observed discontinuities must be related to degeneracies in the spectrum of $\mathcal{L}$. As we shall see, in the weak-dissipation limit they are directly related to degeneracy points of the Hamiltonian.

We consider a system described by the master equation

$$\dot{\rho}(t) = \mathcal{L}\rho \equiv [\mathcal{L}_0(x) + \gamma \mathcal{L}_1]\rho(t), \tag{25}$$

where

$$\mathcal{L}_0(x)(\rho) = -i[H(x), \rho],$$

with a Hamiltonian $H(x)$ depending (analytically) on a parameter x. For simplicity, we consider the case in which $H_0(x)$ is nondegenerate for $x \neq x_0$. The term $\mathcal{L}_1$ contains dissipative terms and is independent of x. We are interested in the limit of weak dissipation ($\gamma \to 0$) and in the change of the steady state at the degeneracy point $x = x_0$.

The steady state $\rho_{ss}(x)$ is determined by $\mathcal{L}(x)\rho_{ss}(x) = 0$ and can be determined perturbatively. The kernel of $\mathcal{L}_0(x)$ is highly

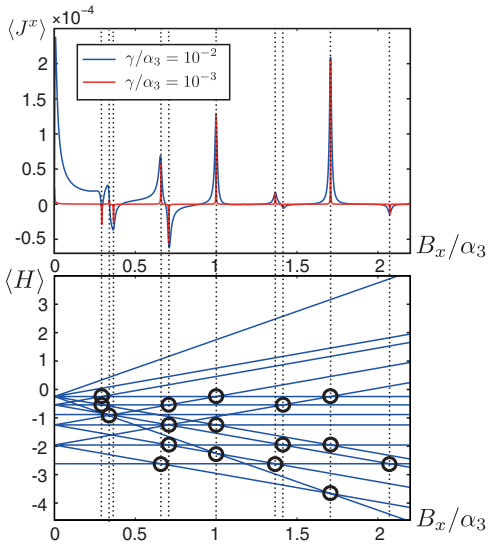

FIG. 9. (Color online) Heisenberg model with 4 spins with open boundary conditions in a magnetic field B_x and under local dissipation as given by Eq. (23) with different dissipation strengths γ_k. Upper panel: steady-state expectation value $\langle J^x \rangle$ plotted versus the B_x/α_3. Lower part: Spectrum of the Hamiltonian plotted versus B_x/α_3.

degenerate, being spanned by all eigenprojectors $|\lambda_i(x)\rangle\langle\lambda_i(x)|$ of the (nondegenerate) $H_0(x)$. This degeneracy is lifted by $\mathcal{L}_1$ and the steady state for $\gamma \to 0$ is for $x \neq x_0$ given by

$$\mathrm{P}^D(x)\mathcal{L}_1\mathrm{P}^D(x)\rho_{ss}(x) = 0, \tag{26}$$

where

$$\mathrm{P}^D(x)\rho = \sum_i |\lambda_i(x)\rangle\langle\lambda_i(x)|\rho|\lambda_i(x)\rangle\langle\lambda_i(x)|. \tag{27}$$

The possibility of discontinuous behavior of $\rho_{\rm ss}(x)$ at $x = x_0$ arises from the enlargement of the kernel of $\mathcal{L}_0(x)$ at this point: if λ_i and λ_j become degenerate at $x = x_0$ then coherences between the corresponding eigenvectors [i.e., $|\lambda_i(x)\rangle\langle\lambda_j(x)|, i \neq j$] become stationary at $x = x_0$. We denote by P^Δ the projector on these additional elements in the kernel of $\mathcal{L}_0(x_0)$ [32]. As we show in Appendix C, a discontinuity $\rho_{\rm ss}(x_0) \neq \lim_{x\to x_0}\rho_{\rm ss}(x)$ arises if

$$\mathrm{P}^\Delta\mathcal{L}_1 \lim_{x\to x_0}\rho_{ss}(x) \neq 0, \tag{28}$$

i.e., if $\mathcal{L}_1$ couples the steady state to the newly available subspace P^Δ in the kernel of $\mathcal{L}_0$. For simplicity, we made the assumption that the Hamiltonian is nondegenerate for $x \neq x_0$. If the Hamiltonian does have degeneracies outside x_0, but additional eigenvectors become degenerate at $x = x_0$ the argumentation follows identical lines, as also in this case, $\mathcal{L}_1$ can couple the steady state to a newly available subspace P^Δ.

Let us have another look at Figs. 6–9 in the light of the previous paragraph. Clearly, all the sharp isolated peaks occur for values of B_x (which plays the role of the parameter x), at which a degeneracy occurs, satisfying a necessary condition for Eq. (28). However, not all degeneracy points lead to discernible peaks, e.g., in Fig. 6. This can show that $\mathcal{L}_1$ does not couple the steady state to P^Δ or that the discontinuity is not witnessed by the expectation value of J^x. For most peaks studied here, however, the reason is simply that the corresponding peaks are too small and sharp to be resolved in the plot.

These points are illustrated in Fig. 10, which shows that the steady state changes abruptly at all degeneracy points of H for the four-spin XXZ model with local dissipation except for two such points (at $B_x \approx 0.16, 0.24$), where $\mathcal{L}_1$ does not couple to the coherences. To measure how quickly $\rho_{\rm ss}$ changes with B_x we use (in analogy to the ground-state fidelity introduced in Ref. [33] for the study of quantum phase transitions) the "steady-state infidelity" $I_{\delta B}(B_x) \equiv 1 - F(\rho(B_x), \rho(B_x + \delta B))$. Here $F(\rho,\sigma) = \mathrm{tr}[(\sigma^{1/2}\rho\sigma^{1/2})^{1/2}]^2 \in [0,1]$ denotes the Uhlmann fidelity [34] between two density matrices, which measures how similar ρ and σ are. Peaks in $I_{\delta B}(B_x)$ (for small δB) indicate that the steady state changes abruptly with B_x. For weak dissipation this happens close to all degeneracy points of the Hamiltonian when Eq. (28) holds.

Note also that, in Figs. 6–9, a large feature appears in the steady-state expectation value $\langle J^x\rangle$ around $B_x = 0$. It narrows for decreasing γ, but is not a sharp peak for any of the parameters used for γ. This broad peak represents the effect of one (or several, cf. Figs. 6 and 9) unresolved degeneracies around $B_x = 0$: Note that for all spin models considered, the degeneracy of their respective Hamiltonian is very high at $B_x = 0$ and is lifted slowly (certain eigenvalues touch and do not cross as $B_x \to 0$). Therefore, the finite values of γ used in the plots are not much smaller than all energy differences and we are not in the weak-dissipation limit. As γ is reduced, additional peaks are resolved (cf. Fig. 9).

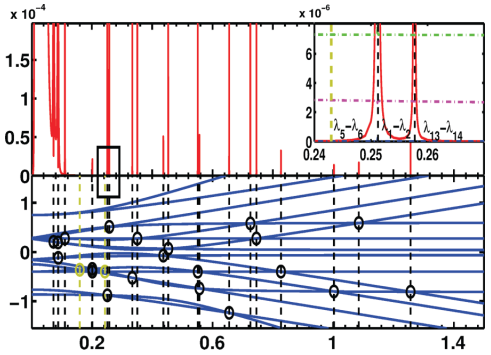

FIG. 10. (Color online) (Upper part) Steady-state infidelity $I_{\delta B}(B_x)$ (see text) for the four-spin XXZ model in transverse field B_x with local dissipation (cf. Fig. 6) for $\delta B = 3 \times 10^{-6}$ and weak dissipation $\gamma = 0.5 \times 10^{-4}$. (Lower part) Spectrum of $H_{\rm spin}$, dashed vertical lines indicate degeneracy points (encircled). Peaks in $I_{\delta B}$ line up with degeneracy points of $H(B_x)$, except for two (colored green) for which condition (28) does not hold. The inset shows the vicinity of $B_x \approx 0.25$, where three crossings of eigenvalues occur: (λ_5,λ_6), (λ_1,λ_2), and $(\lambda_{13},\lambda_{14})$. The dash-dotted horizontal lines show the 2-norm (scaled by 7×10^{-7}) of the left-hand side of Eq. (28) $C_{i,j} = \|\mathrm{P}^{\Delta_{i,j}}\mathcal{L}_1 \lim_{x'\to x}\rho_{ss}(x')\|_2$ for the three relevant projectors $\mathrm{P}^{\Delta_{i,j}}$, $(i,j) = (1,2)$ (green), $=(5,6)$ (blue), and $=(13,14)$ (magenta). $C_{5,6}$ vanishes at the crossing of (λ_5,λ_6), hence there is no peak in $I_{\delta B}$, while the other two lead to a peak in $I_{\delta B}$, since $C_{i,j}$ is finite.

C. Steady-state behavior for Ising Hamiltonians

To get a better insight into how the condition given by Eq. (28) explains the peaks seen in Fig. 8, we now specialize to the Ising model under collective dissipation given by Eq. (24). Then we see that the steady state apart from the degeneracy points and the condition for discontinuity becomes very simple. For a detailed derivation of what follows, see Appendix C.

The Hamiltonian in Eq. (21) with periodic boundary conditions is in general degenerate due to translational and reflection symmetry. To obtain a nondegenerate H, we restrict our consideration to a specific subspace with eigenvalue 1 for the translation operator T and the reflection operator R [35]. Note that the Hamiltonian is also symmetric under the spin-flip operation $F = \sigma_x^{\otimes N}$, i.e., $FHF^\dagger = H$. Using the properties of $\mathcal{L}_1$ and F invariance of H, we find that, if the system has a unique steady state of $\mathcal{L}(x)$, it is, in the limit of weak dissipation, given by the maximally mixed state $\propto\mathbb{1}$: plugging $\mathbb{1}$ into Eq. (26) we obtain $\mathrm{P}^D\mathcal{L}_1(\mathbb{1}) = \sum_i |\lambda_i(x)\rangle\langle\lambda_i(x)|J^z|\lambda_i(x)\rangle\langle\lambda_i(x)|$ and flip invariance of H implies $\langle\lambda_i(x)|J^z|\lambda_i(x)\rangle = 0$ for the eigenstates of a nondegenerate Hamiltonian H (see Appendix C).

Thus if the steady state is unique, it is always maximally mixed outside degeneracy points and we see a discontinuity at $x = x_0$ if for the degenerate eigenstates $|\lambda_1(x_0)\rangle, |\lambda_2(x_0)\rangle$ we have

$$\langle\lambda_1|J^z|\lambda_2\rangle \neq 0. \tag{29}$$

This can be checked to hold for the points at which peaks are observed in Fig. 8.

For the Ising model in a transverse magnetic field, for larger N the peaks decrease in height and disappear in the limit $N \longrightarrow \infty$. The spectrum for the Ising model in a transverse field is known analytically [36]. For large N, the spectrum is very dense and degeneracy points are so closely spaced that peaks are no longer resolvable (and vanish in the thermodynamic limit as bands develop). Nevertheless, for small spin systems, these features provide a method to dissipatively study degeneracies of the applicable Hamiltonian—anywhere in the spectrum, not just in the ground state. To the extent that $\mathcal{L}_1$ is tunable, it even provides access to the nature of the degenerate states via Eq. (28).

IV. CONCLUSIONS

We have shown that using cold atoms in an optical lattice in the Mott-insulator regime, dissipative spin chains with Hamiltonians such as the XXZ model, the Ising model, or the Heisenberg model can be realized. Optical driving of internal atomic states allows for the realization of a tunable transversal magnetic field and engineered dissipation.

This system is an ideal test bed for studying steady-state dynamics of dissipative spin models. We have discovered a peculiar feature of the steady-state diagram for small spin chains: in the limit of weak dissipation, the expectation values of the collective spin operators exhibit abrupt changes that hint at discontinuities in the steady state. These discontinuities occur at degeneracy points of the Hamiltonian. We have studied this phenomenon for different spin models with open and periodic boundary conditions subject to individual and collective dissipation. Finally, we have presented conditions that elucidate the discontinuous behavior of the steady state at degeneracy points of the Hamiltonian. Therefore, measurements of the steady-state dynamics of cold atoms in optical lattices would allow us to draw conclusions about the spectrum of the respective spin model.

ACKNOWLEDGMENTS

H. S. and G. G. thank L. Mazza for useful discussions on cold atoms. The authors gratefully acknowledge funding by the DFG within the SFB 631 and by the EU within project MALICIA under FET-Open grant number 265522.

APPENDIX A: DERIVATION OF EFFECTIVE DISSIPATIVE MASTER EQUATION

The internal levels of the atom that we consider are $|g\rangle$, $|r\rangle$, $|e\rangle$. Adiabatically eliminating the excited state $|e\rangle$ as discussed in Sec. II B, we get an effective two-level system $|g\rangle$ and $|r\rangle$ that is coupled with the effective Rabi frequency Ω_{eff}, as depicted in Fig. 1.

In the following, we derive in detail the master equation given by Eq. (6) in Sec. II B. The internal levels of the atom that we consider are $|g\rangle$, $|r\rangle$, $|e\rangle$, as depicted in the upper part of Fig. 1. The states $|g\rangle$-$|r\rangle$ are coupled by a detuned Raman transition via the excited state $|e\rangle$ by two standing-wave laser fields. The coupling is described by the Hamiltonians

$$H_{l1} = \sum_k \Omega_1 \cos(k_1 x_k)(|e\rangle\langle g|_k + \text{H.c.}), \tag{A1}$$

and

$$H_{l2} = \sum_k \Omega_2 \sin(k_2 x_k)(|r\rangle\langle g|_k + \text{H.c.}), \tag{A2}$$

where Ω_1 and Ω_2 are the Rabi frequencies of the two lasers and k_1 and k_2 are the wave numbers of the lasers and k denotes the lattice site. x_k is the displacement from the equilibrium position x_k^0 of the atom at lattice site k. The phase of the lasers is, for simplicity, chosen such that $\cos[k_1(x_k + x_k^0)] = \cos(k_1 x_k)$ and $\cos[k_2(x_k + x_k^0)] = \sin(k_2 x_k)$. Choosing different phases of the lasers makes $A^{\pm}$ in Eq. (7) dependent on the lattice site k. Adiabatic elimination of the excited state $|e\rangle$ leads to an effective coupling

$$H_1 = \sum_k \Omega_{\text{eff}} \eta_1 (\sigma_k^- + \sigma_k^+)(|r\rangle\langle g| + \text{H.c.}), \tag{A3}$$

with $\Omega_{\text{eff}} = \Omega_1\Omega_2/\delta_{re}$ where δ_{re} is the detuning with respect to $|e\rangle$ and η_1 is the Lamb-Dicke parameter. Here, we have expressed the deviation from the equilibrium position x_k in terms of harmonic oscillator operators truncated to the two lowest-lying levels $\sin(k_1 x_k) \approx \eta_1(\sigma_k^- + \sigma_k^+)$ where $\sigma_k^+ = |1\rangle\langle 0|_k$ and $\sigma_k^- = |0\rangle\langle 1|_k$ and $\cos(k_2 x_k) \approx 1$. The effective coupling with Rabi frequency Ω_{eff} between states $|r\rangle$ and $|g\rangle$ is shown in Fig. 1.

Coupling the state $|r\rangle$ to the excited state $|e\rangle$ with a third standing-wave laser field with Rabi frequency Ω_{er}, depicted with a red arrow in Fig. 1, we can derive an effective two-level system $|g\rangle$-$|r\rangle$ with designable decay rates as done in Ref. [26]. Here, we briefly review this result. Following Ref. [26], the upper level $|e\rangle$ can be adiabatically eliminated if the saturation parameter for the transition $|r\rangle$ and $|e\rangle$ is small:

$$s_{r,e} = \frac{(\Omega_{re}/2)^2}{\delta_{re}^2 + (\Gamma_{er} + \Gamma_{eg})^2/4} \ll 1. \tag{A4}$$

According to Ref. [26], the effective detuning and the effective decay rates are given by

$$\delta_r = \delta_{gr} - \delta_{re}\frac{(\Omega_{re}/2)^2}{[(\Gamma_{eg} + \Gamma_{er})/2]^2 + \delta_{re}^2}, \tag{A5}$$

$$\Gamma = \frac{(\Omega_{re}/2)^2}{[(\Gamma_{eg} + \Gamma_{er})/2]^2 + \delta_{re}^2}\Gamma_{eg}, \tag{A6}$$

$$\gamma = \frac{(\Omega_{re}/2)^2}{[(\Gamma_{eg} + \Gamma_{er})/2]^2 + \delta_{re}^2}\frac{\Gamma_{eg} + \Gamma_{er}}{2}; \tag{A7}$$

see also the lower part of Fig. 1. The effective two-level system $|g\rangle$-$|r\rangle$ with the effective decay rates Γ, γ and the effective detuning δ_r is the starting point of the following discussion. The full Hamiltonian describing the system is given by

$$H_{\text{full}} = H_1 + H_0, \tag{A8}$$

where H_1 describes the atom-light interaction given by Eq. (A3) and H_0 defines the energies of the system

$$H_0 = \sum_k \delta_r |r\rangle\langle r|_k + \nu |1\rangle\langle 1|_k. \tag{A9}$$

The effective dynamics of the system can be derived considering contributions to the Liouvillian up to second order in a perturbative approach. The full system is described by a Liouvillian given by

$$\dot{\rho}(t) = (\mathcal{L}_0 + \mathcal{L}_1)\rho(t), \tag{A10}$$

where $\mathcal{L}_0$ is given by

$$\begin{aligned}\mathcal{L}_0\rho(t) = \sum_k \Gamma\,(2|g\rangle\langle r|_k\rho(t)|r\rangle\langle g|_k - \{|r\rangle\langle r|_k, \rho(t)\}_+) \\ + \gamma(2|r\rangle\langle r|_k\rho(t)|r\rangle\langle r|_k - \{|r\rangle\langle r|_k, \rho(t)\}_+) \\ - i[H_0, \rho(t)].\end{aligned} \tag{A11}$$

The first part of the Liouvillian is the decay part with the effective decay rate Γ from state $|r\rangle$ to $|g\rangle$ and the dephasing rate γ. The projector

$$P_g = |g\rangle\langle g| \otimes (|0\rangle\langle 0| + |1\rangle\langle 1|) \tag{A12}$$

is stationary under $\mathcal{L}_0$. The perturbative part of the Liouvillian is given by

$$\mathcal{L}_1\rho(t) = -i[H_1, \rho(t)], \tag{A13}$$

where H_1 is given by Eq. (A3) and describes the interaction of the two-level system with the effective laser field. Treating $\mathcal{L}_1$ as a perturbation, we derive an effective Liouvillian in the stationary subspace of $\mathcal{L}_0$. The projection onto this subspace reads

$$\mathbb{P}\dot{\rho}(t) = \mathbb{P}\mathcal{L}\mathbb{P}\rho(t) + \mathbb{P}\mathcal{L}\mathbb{Q}\rho(t), \tag{A14}$$

where $\mathbb{P}\rho = |g\rangle\langle g| \otimes (|0\rangle\langle 0| + |1\rangle\langle 1|)\rho|g\rangle\langle g| \otimes (|0\rangle\langle 0| + |1\rangle\langle 1|)$ and $\mathbb{Q} = 1 - \mathbb{P}$. Projecting onto the subspace we want to eliminate, we get

$$\mathbb{Q}\dot{\rho}(t) = \mathbb{Q}\mathcal{L}\rho(t). \tag{A15}$$

In the following, we integrate Eq. (A15) to get the time evolution of the density matrix in the fast space, $\mathbb{Q}\rho(t)$. We insert the result in Eq. (A14) to get an equation of motion for the density matrix in the slow space. Therefore, we first go into the interaction picture, where the density matrix is given by $\tilde{\rho}(t) = e^{-\mathcal{L}_0 t}\rho(t)$. The equation of motion in the fast space reads

$$\mathbb{Q}\dot{\tilde{\rho}}(t) = \mathbb{Q}W_I(t)\tilde{\rho}(t), \tag{A16}$$

with $W_I(t) = e^{\mathcal{L}_0 t}\mathcal{L}_1 e^{\mathcal{L}_0 t}$. Solving this equation by iteration [37], we get

$$\begin{aligned}\mathbb{Q}\rho(t) = \mathbb{Q}e^{\mathcal{L}_0 t}\left[\int_0^t ds\, W_I(s)\mathbb{P}\tilde{\rho}(0)\right. \\ \left. + \int_0^t ds_1 \int_0^{s_1} ds_2 W_I(s_1)W_I(s_2)\mathbb{P}\tilde{\rho}(0)\right].\end{aligned} \tag{A17}$$

At time $t = 0$, $\tilde{\rho}(0) = \rho(0)$ and we assume that at $t = 0$, the population is in the ground state, i.e., $\tilde{\rho}(0) = \mathbb{P}\tilde{\rho}(0)$. Higher-order integrals are neglected with the assumption that

$$|\Omega_{\text{eff}}| \ll \Gamma, \gamma, |\delta_r|, \nu. \tag{A18}$$

We denote the first integral in Eq. (A17) by $R_1(t)$ and the second integral by $R_2(t)$ such that

$$\mathbb{Q}\rho(t) = R_1(t) + R_2(t). \tag{A19}$$

Inserting in Eq. (A14) leads to

$$\begin{aligned}\mathbb{P}\dot{\rho}(t) = \mathbb{P}\mathcal{L}\mathbb{P}\rho(t) + \mathbb{P}\mathcal{L}_0 R_1(t) + \mathbb{P}\mathcal{L}_1 R_1(t) \\ + \mathbb{P}\mathcal{L}_0 R_2(t) + \mathbb{P}\mathcal{L}_1 R_2(t).\end{aligned} \tag{A20}$$

The term $\mathbb{P}\mathcal{L}_0 R_1(t) = 0$, and $\mathbb{P}\mathcal{L}_1 R_2(t)$ is a third-order term and can be neglected. Neglecting terms rotating with $\exp(\pm i\nu t)$ we get the master equation given by Eq. (6) with ac Stark shifts given by

$$H_S = s_- \sigma_k^+ \sigma_k^- + s_+ \sigma_k^- \sigma_k^+, \tag{A21}$$

where

$$s_\pm = \Omega_{\text{eff}}^2 \eta_1^2 \frac{(\delta_r \pm \nu)}{(\Gamma + \gamma)^2 + (\delta_r \pm \nu)^2}.$$

APPENDIX B: DERIVATION OF SPIN HAMILTONIAN

In the Mott-insulator regime, bosonic atoms trapped by a lattice potential with two motional states are described by the two-band Bose-Hubbard model

$$H_{\text{BH}} = H_0 + H_t. \tag{B1}$$

Here, the sum runs over the N sites k of the optical lattice. The unperturbed Hamiltonian H_0 is given by

$$H_0 = \sum_k \left(\frac{U_{01}}{2}\hat{n}_{k0}\hat{n}_{k1} + \sum_{x=0,1} \frac{U_{xx}}{2}\hat{n}_{kx}(\hat{n}_{kx} - 1) + \nu\hat{n}_{k1} \right),$$

where $U_{xx'}$ is the on-site repulsion of two atoms on lattice site k, where one atom is in motional state $|x\rangle$ and the other one is in $|x'\rangle$ with $x, x' = 0, 1$, respectively. The operator $\hat{n}_{kx} = |x\rangle\langle x|_k$ counts the number of atoms at lattice site k in the motional states $x = 0, 1$ and ν is the energy difference between ground and first-excited motional states. We assume the system to be prepared in the ground state $|0\rangle$. Due to the anharmonicity of the potential, we do not leave the subspace of $n = 0$ and $n = 1$ excitations.

The perturbative part of the Hamiltonian describes the tunneling between neighboring lattice sites and is given by

$$H_t = \sum_k t_0 c_{k,0}^\dagger c_{k+1,0} + t_1 c_{k,1}^\dagger c_{k+1,1} + \text{H.c.} \tag{B2}$$

Here, the operators c_{kx} with $x = 0, 1$ are bosonic destruction operators for atoms in the two motional states $|0\rangle$ and $|1\rangle$ at lattice site k. t_0 (t_1) are the tunneling amplitudes from state $|0\rangle$ ($|1\rangle$) at lattice site k to state $|0\rangle$ ($|1\rangle$) at $k + 1$.

As the on-site interaction $U_{xx'} \gg t_0, t_1$, tunneling between neighboring wells that leads to states with two atoms in one lattice well can be treated as a perturbation. For that, we consider two neighboring lattice sites k and $k + 1$ and write the effective Hamiltonian in the basis of eigenvectors of H_0, $|x_k, y_{k+1}\rangle$, where for example $|0_k, 1_{k+1}\rangle$ is the notation for the state with one particle in well k in state $|0\rangle$, and one particle in well $k + 1$ in state $|1\rangle$. In perturbation theory [25], the

second-order effective Hamiltonian can be evaluated in the following way:

$$\langle x_k, y_{k+1}|H_{\rm eff}^{(3)}|x'_k, y'_{k+1}\rangle = \frac{1}{2}\sum_\chi \langle x_k, y_{k+1}|H_t|\chi\rangle \frac{1}{E'}\langle\chi|H_t|x'_k, y'_{k+1}\rangle, \quad \text{(B3)}$$

where

$$\frac{1}{E'} = \frac{1}{E_{xy}-E_\chi} + \frac{1}{E_{x'y'}-E_\chi},$$

and $|\chi\rangle$ are eigenstates of H_0 with two particles in one well (and no particle in the other one). $E_{xy} = \langle x_k, y_{k+1}|H_0|x_k, y_{k+1}\rangle$ and $E_\chi = \langle\chi|H_0|\chi\rangle$ are the unperturbed energies. Evaluating Eq. (B3) leads to the effective spin Hamiltonian $H_{\rm eff}^{(3)}$ given by

$$H_{\rm eff}^{(3)} = H_{\rm spin} + B_z\sum_k |1\rangle\langle 1|_k, \quad \text{(B4)}$$

with

$$H_{\rm spin} = \sum_k \alpha_1\left(\sigma_k^x\sigma_{k+1}^x + \sigma_k^y\sigma_{k+1}^y\right) + \alpha_2\sigma_k^z\sigma_{k+1}^z. \quad \text{(B5)}$$

Here,

$$\alpha_1 = -\frac{4t_0t_1}{U_{01}}, \quad \alpha_2 = 2\left(\frac{t_0^2+t_1^2}{U_{01}} - \frac{t_0^2}{U_{00}} - \frac{t_1^2}{U_{11}}\right),$$

and B_z, the magnetic field in z direction, is

$$B_z = \frac{t_0^2}{U_{00}} - \frac{t_1^2}{U_{11}}.$$

Thus, we have derived an effective XXZ-spin Hamiltonian with a magnetic field in the z direction.

APPENDIX C: CONDITION FOR DISCONTINUOUS BEHAVIOR

Here, we first derive a general condition for the discontinuous behavior in the steady state at a degeneracy point of a large class of spin Hamiltonians. Next, we focus on more specific Hamiltonians. We study the steady state of flip-invariant Hamiltonians outside the degeneracy point and, starting with the general condition for finding discontinuities in the steady state, we derive a more precise condition for flip-invariant Hamiltonians.

1. General condition for discontinuities in steady state

Here, we derive a general condition for discontinuous behavior in the steady state at the degeneracy point $x = x_0$ of a general Hamiltonian H, where $H = H(x)$ is an analytic function of x. We consider a system described by the master equation

$$\dot\rho(t) = (\mathcal{L}_0 + \mathcal{L}_1)\rho(t), \quad \text{(C1)}$$

where the Hamiltonian part of the Liouvillian is given by $\mathcal{L}_0(x) = \mathcal{L}_0 = -i[H(x),\cdot]$ and depends on a parameter x, and the local decay Liouvillian is

$$\mathcal{L}_1\rho(t) = \sum_k \gamma_k[2\sigma_k^-\rho(t)\sigma_k^+ - \{\sigma_k^+\sigma_k^-,\rho(t)\}_+]. \quad \text{(C2)}$$

First, we want to describe the system outside the degeneracy point, i.e., for $x \neq x_0$. We assume that in the vicinity of x_0, the Hamiltonian is nondegenerate (for $x \neq x_0$) and that the dissipation is weak. The steady state $\rho_{ss}(x)$ defined by $(\mathcal{L}_0(x) + \mathcal{L}_1)\rho_{ss}(x) = 0$ is, in the limit $\gamma \to 0$, given by

$$\mathrm{P}^D(x)\mathcal{L}_1\mathrm{P}^D(x)\rho_{ss} = 0, \quad \text{(C3)}$$

where $\mathrm{P}^D(x)$ is the projector onto the kernel($\mathcal{L}_0$). As the kernel of $\mathcal{L}_0$ is spanned by the eigenprojectors $|\lambda_i(x)\rangle\langle\lambda_i(x)|$ of H we have for arbitrary A

$$\mathrm{P}^D A = \sum_i |\lambda_i(x)\rangle\langle\lambda_i(x)|A|\lambda_i(x)\rangle\langle\lambda_i(x)|, \quad \text{(C4)}$$

where $|\lambda_i(x)\rangle$ are eigenstates of the Hamiltonian $H(x)$ which is assumed to be nondegenerate.

Now, let us consider the case that at $x = x_0$, the Hamiltonian has a degeneracy point at which two or more eigenvalues cross. At this degeneracy point, we expect a discontinuous behavior of the steady state that leads to the peaks we observe in our numerical simulation (see Figs. 6–9). At $x = x_0$ the projector onto the kernel of $\mathcal{L}_0$ has to be extended. It now also projects onto coherences between eigenstates of H: $|\lambda_1\rangle$,$|\lambda_2\rangle$ which are eigenvectors to the degenerate eigenvalues $\lambda_1 = \lambda_2$. Therefore the projector on the coherences reads

$$\mathrm{P}^\Delta A = |\lambda_1\rangle\langle\lambda_1|A|\lambda_2\rangle\langle\lambda_2| + \text{H.c.} \quad \text{(C5)}$$

It is convenient to define a continuous extension of the projector P^D at $x = x_0$, which reads

$$\mathrm{P}^D(x_0) = \lim_{x\to x_0}\mathrm{P}^D(x). \quad \text{(C6)}$$

Thus, at $x = x_0$, the full projector onto the kernel of $\mathcal{L}_0$ reads $\mathrm{P}^D(x_0) + P^\Delta$. Now the condition for the steady state $\rho_{ss}(x = x_0)$ at the degeneracy point is given by

$$[\mathrm{P}^D(x_0) + \mathrm{P}^\Delta]\mathcal{L}_1[\mathrm{P}^D(x_0) + \mathrm{P}^\Delta]\rho_{ss}(x_0) = 0. \quad \text{(C7)}$$

We want to find a sufficient condition for the steady state to change discontinuously. This means that

$$\rho_{ss}(x_0) - \lim_{x\to x_0}\rho_{ss}(x) \neq 0, \quad \text{(C8)}$$

where $\lim_{x\to x_0}\rho_{ss}(x)$ is the continuous extension of $\rho_{ss}(x)\ \forall\ x \neq x_0$ to $x = x_0$.

A discontinuity in the steady state as described by Eq. (C8) can occur only if

$$[\mathrm{P}^D(x_0) + \mathrm{P}^\Delta]\mathcal{L}_1[\mathrm{P}^D(x_0) + \mathrm{P}^\Delta]\lim_{x\to x_0}\rho_{ss}(x) \neq 0 \quad \text{(C9)}$$

holds, since otherwise the continuous extension $\lim_{x\to x_0}\rho_{ss}(x)$ would be a steady state as well. The last part of Eq. (C9) can be simplified using

$$[\mathrm{P}^D(x_0) + \mathrm{P}^\Delta]\lim_{x\to x_0}\rho_{ss}(x) = \lim_{x\to x_0}\rho_{ss}(x),$$

which holds since $\lim_{x\to x_0}\rho_{ss}(x)$ is per definition in the space onto which $\mathrm{P}^D(x_0)$ projects and P^Δ is orthogonal to that space. By Eq. (C3) we then see that Eq. (C9) reduces to the condition

$$\mathrm{P}^\Delta\mathcal{L}_1\lim_{x\to x_0}\rho_{ss}(x) \neq 0. \quad \text{(C10)}$$

If this condition is fulfilled, then $\rho_{ss}(x_0) - \lim_{x\to x_0}\rho_{ss}(x) \neq 0$ which means that the steady state shows discontinuous behavior at the degeneracy point $x = x_0$.

2. Condition for discontinuous behavior for Ising Hamiltonians

Here, we want to get a better insight into how the condition given by Eq. (C10) relates to the peaks observed in our numerical simulation. In the following, we will apply it to the Ising model in a transverse magnetic field. In the numerical simulation (see Fig. 8) for the Ising Hamiltonian with periodic boundary conditions under collective dissipation described by Eq. (24), we restrict our consideration to a specific subspace with eigenvalue 1 for the translation operator T and the reflection operator R: $T = R = 1$. First, we want to prove that if the steady state is unique, then it is the fully mixed state outside the degeneracy points as indicated by our numerical simulation. Then we show that, starting from the condition given by Eq. (C10), specialization to the Ising model allows us to derive a more precise condition for finding a discontinuity in the steady state at the degeneracy points.

First, we show that $\mathbb{1}$ satisfies $(\mathcal{L}_0 + \mathcal{L}_1)\mathbb{1} = 0$ outside the degeneracy point $x \neq x_0$. Therefore, for systems with a unique steady state, it is given by the fully mixed state for $x \neq x_0$ in the limit $\gamma \to 0$. The Hamiltonian given by Eq. (21) is assumed to be nondegenerate for $x \neq x_0$ and invariant under the spin-flip operator $F = \sigma_x^{\otimes N}$, i.e., $FHF^\dagger = H$. Thus, we want to show that, for $x \neq x_0$,

$$\mathrm{P}^D \mathcal{L}_1 \mathbb{1} = 0, \tag{C11}$$

where P^D is given by Eq. (C4). Then,

$$\mathrm{P}^D \mathcal{L}_1(\mathbb{1}) = 2\gamma(J^- J^+ - J^+ J^-) \propto \gamma J^z. \tag{C12}$$

Therefore, Eq. (C11) reads

$$\mathrm{P}^D \mathcal{L}_1(\mathbb{1}) = \mathrm{P}^D J^z = \sum_i |\lambda_i\rangle\langle\lambda_i|J^z|\lambda_i\rangle\langle\lambda_i| = 0. \tag{C13}$$

If we can show that Eq. (C13),

$$\langle\lambda_i|J^z|\lambda_i\rangle = 0 \;\forall\, i, \tag{C14}$$

then we have shown that the fully mixed state is a steady state of our system outside the degeneracy points of the Hamiltonian.

As the Hamiltonian is nondegenerate and invariant under the flip-operator F, the eigenvectors of H are eigenvectors of F: $F|\lambda_i\rangle = \alpha_i|\lambda_i\rangle$. Let $|\alpha\rangle$ denote an arbitrary eigenvector of H with F eigenvalue α. Since the spectrum of F is $\{\pm 1\}$, we have $|\alpha\rangle = \alpha^2|\alpha\rangle = \alpha F|\alpha\rangle$. Moreover, the flip F changes the sign of J^z, i.e, J^z and F anticommute: $\{F, J^z\}^+ = 0$. Therefore, we can write Eq. (C14) as

$$\begin{aligned}\langle\alpha|J^z|\alpha\rangle &= \alpha\langle\alpha|J^z F|\alpha\rangle \\ &= -\alpha\langle\alpha|FJ^z|\alpha\rangle = -\langle\alpha|J^z|\alpha\rangle,\end{aligned} \tag{C15}$$

where we have used $\alpha^2 = 1$. It follows that

$$\langle\alpha|J^z|\alpha\rangle = 0. \tag{C16}$$

Consequently, $\mathrm{P}^D\mathcal{L}_1(\mathbb{1}) = 0$ and we have shown that in the limit of weak dissipation, the steady state, if it is unique, is the fully mixed state. For the Ising model with up to eight atoms and collective dissipation, we know from our numerics that the steady state is unique.

To see that the steady state shows discontinuous behavior at the degeneracy point $x = x_0$, we need now only to show that the fully mixed state is not the steady state of the system. Thus, we need to show that

$$\mathrm{P}^\Delta \mathcal{L}_1(\mathbb{1}) = \mathrm{P}^\Delta J^z = \sum_{i,j,i\neq j}{}' |\lambda_i\rangle\langle\lambda_i|J^z|\lambda_j\rangle\langle\lambda_j| \neq 0, \tag{C17}$$

where P^Δ is given by Eq. (C5) and $\sum'$ sums over the labels of degenerate eigenvalues. Since the eigenvectors are orthogonal, Eq. (C17) holds if $\exists\, i \neq j$ such that

$$\langle\lambda_i|J^z|\lambda_j\rangle \neq 0. \tag{C18}$$

Therefore, Eq. (C18) gives a condition for finding discontinuous behavior of the steady state of the Ising model in a transverse field under collective dissipation. Note that this derivation can be easily extended to all nondegenerate Hamiltonians that are flip invariant.

[1] S. Sachdev, *Quantum Phase Transitions* (Cambridge University Press, Cambridge, MA, 1999).
[2] I. Bloch, Nat. Phys. **1**, 23 (2005).
[3] W. H. Zurek, Rev. Mod. Phys. **75**, 715 (2003).
[4] B. Baumgartner and H. Narnhofer, Rev. Math. Phys. **24**, 1250001 (2012).
[5] A. Beige, S. Bose, D. Braun, S. F. Huelga, P. L. Knight, M. B. Plenio, and V. Vedral, J. Mod. Opt. **47**, 2583 (2000).
[6] F. Benatti, R. Floreanini, and M. Piani, Phys. Rev. Lett. **91**, 070402 (2003).
[7] B. Kraus, H. P. Büchler, S. Diehl, A. Kantian, A. Micheli, and P. Zoller, Phys. Rev. A **78**, 042307 (2008).
[8] C. A. Muschik, E. S. Polzik, and J. I. Cirac, Phys. Rev. A **83**, 052312 (2011).
[9] F. Verstraete, M. M. Wolf, and J. I. Cirac, Nat. Phys. **5**, 633 (2009).
[10] K. G. H. Vollbrecht, C. A. Muschik, and J. I. Cirac, Phys. Rev. Lett. **107**, 120502 (2011).
[11] H. J. Carmichael, J. Phys. B **13**, 3551 (1980).
[12] F. Dimer, B. Estienne, A. S. Parkins, and H. J. Carmichael, Phys. Rev. A **75**, 013804 (2007).
[13] S. Morrison and A. S. Parkins, Phys. Rev. A **77**, 043810 (2008).
[14] S. Diehl, A. Micheli, A. Kantian, B. Kraus, H. P. Buchler, and P. Zoller, Nat. Phys. **4**, 878 (2008).
[15] J. Eisert and T. Prosen, arXiv:1012.5013.
[16] M. Müller, S. Diehl, G. Pupillo, and P. Zoller, Adv. At. Mol. Opt. Phys. **61**, 1 (2012).
[17] M. Lewenstein, A. Sanpera, and V. Ahufinger, *Ultracold Atoms in Optical Lattices* (Oxford University Press, Oxford, UK, 2012).
[18] J. J. García-Ripoll and J. I. Cirac, New J. Phys. **5**, 76 (2003).
[19] J. Simon, W. S. Bakr, R. Ma, M. E. Tai, P. M. Preiss, and M. Greiner, Nature (London) **472**, 307 (2011).
[20] D. Jaksch and P. Zoller, Ann. Phys. (NY) **315**, 52 (2005).
[21] C. Navarrete-Benlloch, I. de Vega, D. Porras, and J. I. Cirac, New J. Phys. **13**, 023024 (2011).
[22] $|0\rangle_j$ denotes the localized Wannier function at site j, where 0 is the band index.

[23] E. Charron, E. Tiesinga, F. Mies, and C. Williams, in *Quantum Communication, Computing, and Measurement 3*, edited by P. Tombesi and O. Hirota (Kluwer, New York, 2002), pp. 227–230.

[24] For details see Eq. (20).

[25] C. Cohen-Tannoudji, J. Dupont-Roc, and G. Grynberg, *Atom-Photon Interactions* (Wiley Intersciences, New York, 1992).

[26] I. Marzoli, J. I. Cirac, R. Blatt, and P. Zoller, Phys. Rev. A **49**, 2771 (1994).

[27] Note that $\sin(k_b x_k) \approx \eta_b(c_k + c_k^\dagger)$ where c_k are bosonic operators that describe the harmonic oscillator states of the trapping potential. As explained before, we work in the truncated subspace of $|0\rangle$ and $|1\rangle$ due to the anharmonicity of the trap and the cooling to the ground state such that the $\eta_b(c_k + c_k^\dagger) = \eta_b(\sigma_k^- + \sigma_k^+)$.

[28] D. Jaksch, C. Bruder, J. I. Cirac, C. W. Gardiner, and P. Zoller, Phys. Rev. Lett. **81**, 3108 (1998).

[29] $U_{xx'}$ is the on-site repulsion of two atoms on lattice site k, where one atom is in motional state $|x\rangle$ and the other one in $|x'\rangle$ with $x, x' = 0, 1$, respectively.

[30] P. Werner, K. Völker, M. Troyer, and S. Chakravarty, Phys. Rev. Lett. **94**, 047201 (2005).

[31] M. Žnidarič, Phys. Rev. E **83**, 011108 (2011).

[32] Here we use that if $H(x)$ is a holomorphic function of x (we are typically concerned with linear dependence on x only) the eigenvectors of $H(x)$ can be chosen as holomorphic (and thus continuous) functions of $x \in \mathbb{R}$ [38]. Then, $\lim_{x\to x_0} P^D(x_0)$ is well defined and we can define P^Δ as the difference of the projector on the kernel of $\mathcal{L}_0(x_0)$ and $\lim_{x\to x_0} P^D(x_0)$.

[33] P. Zanardi and N. Paunković, Phys. Rev. E **74**, 031123 (2006).

[34] A. Uhlmann, Rep. Math. Phys. **9**, 273 (1976).

[35] If initialized in this subspace (e.g., by optically pumping it to the fully polarized states $|0\rangle^{\otimes N}$), the system will remain there since both $\mathcal{L}_0$ and $\mathcal{L}_1$ respect these symmetries.

[36] P. Pfeuty, Ann. Phys. (NY) **57**, 79 (1970).

[37] A. Messiah, *Quantenmechanik Band 2* (de Gruyter, Berlin, 1985).

[38] T. Kato, *Perturbation Theory for Linear Operators* (Springer, Berlin, Heidelberg, 1995).

PRL 96, 080502 (2006) PHYSICAL REVIEW LETTERS week ending 3 MARCH 2006

Extremality of Gaussian Quantum States

Michael M. Wolf,[1] Geza Giedke,[1,2] and J. Ignacio Cirac[1]

[1]*Max-Planck-Institute for Quantum Optics, Hans-Kopfermann-Strasse 1, D-85748 Garching, Germany*
[2]*Institut für Quantenelektronik, ETH Zürich, Wolfgang-Pauli-Strasse 16, CH-8093 Zürich, Switzerland*

(Received 27 September 2005; published 2 March 2006)

We investigate Gaussian quantum states in view of their exceptional role within the space of all continuous variables states. A general method for deriving extremality results is provided and applied to entanglement measures, secret key distillation and the classical capacity of bosonic quantum channels. We prove that for every given covariance matrix the distillable secret key rate and the entanglement, if measured appropriately, are minimized by Gaussian states. This result leads to a clearer picture of the validity of frequently made Gaussian approximations. Moreover, it implies that Gaussian encodings are optimal for the transmission of classical information through bosonic channels, if the capacity is additive.

DOI: 10.1103/PhysRevLett.96.080502 PACS numbers: 03.67.Hk, 03.65.Ud

States with a Gaussian Wigner distribution, so-called *Gaussian states*, appear naturally in every quantum system which can be described or approximated by a quadratic bosonic Hamiltonian. They are ubiquitous in quantum optics as well as in the description of atomic ensembles, ion traps or nanomechanical oscillators. Moreover, Gaussian states became the core of quantum information theory with continuous variables.

Besides their practical relevance, Gaussian states play an exceptional role with respect to many of their theoretical properties. A particular property of Gaussian states is that they tend to be extremal within *all* continuous variable states if one imposes constraints on the covariance matrix (CM). The best known example of that kind is the extremality with respect to the entropy: within all states having a given CM, Gaussian states attain the maximum von Neumann entropy (cf. [1]). Similar extremality properties have recently been shown for the mutual information [2] and conditional entropies [3,4].

In this Letter we prove extremality results for Gaussian states with respect to entanglement measures, secret key rates, and the classical capacity of bosonic quantum channels. These findings are based on a general method, which exploits the central limit theorem as a active and local *Gaussification* operation. Our main focus lies on the entanglement, which will serve as a showcase for the general procedure. We prove that for any given CM, the entanglement, if measured in an appropriate way, is lower bounded by that of a Gaussian state. The same result is shown to hold true for many other quantities like the distillable randomness and the secret key rate. This result not only emphasizes the exceptional role of Gaussian states, it also leads to a clearer picture of the validity of frequently made Gaussian approximations. In practice, states deviate from exact Gaussians and their precise nature remains mostly unknown. Nevertheless, the CM can typically be determined, e.g., by homodyne detection, and one is tempted to calculate the amount of entanglement, or other quantities, from the CM under the assumption that the state is Gaussian. The derived extremality of Gaussian states now justifies this approach as it excludes an overestimation of the desired quantity, even in cases where the actual state is highly non-Gaussian. In this sense one stays on the safe side when *a priori* assuming the state to be Gaussian. We will see, however, that some care is in order, since the extremality property with respect to the entanglement turns out to depend on the chosen entanglement measure.

Before we derive the main results we will briefly recall the basic notions. Consider a bosonic system of N modes characterized by N pairs of canonical operators $(Q_1, P_1, \ldots, Q_N, P_N) =: R$ or equivalently by N bosonic annihilation operators $a_j = (Q_j + iP_j)/\sqrt{2}$. For any density operator ρ of the system we define a vector of means with components $d_j = \mathrm{tr}[\rho R_j]$, a CM $\Gamma_{kl} = \mathrm{tr}[\rho\{R_k - d_k, R_l - d_l\}_+]$ and introduce a *characteristic function* $\chi(\xi) = \mathrm{tr}[\rho \exp(i\xi \cdot R)]$, $\xi \in \mathbb{R}^{2N}$. The latter is the Fourier transform of the Wigner function and it thus completely characterizes the state [5]. For Gaussian states, the characteristic function has the form

$$\chi(\xi) = e^{i\xi\cdot d - 1/4\xi\cdot\Gamma\xi}, \tag{1}$$

such that they are entirely specified by d and Γ leading to a complete description within a finite dimensional phase space $\mathbb{R}^{2N}$. The underlying Hilbert space $\mathcal{H}$ is, however, infinite dimensional and we will denote the set of all bounded linear operators on $\mathcal{H}$ by $\mathcal{B}(\mathcal{H})$. Note that the following results also apply to finite dimensional systems by simply embedding $\mathbb{C}^d$ into $\mathcal{H}$.

Our results are based on a noncommutative central limit theorem, as discussed in [6,7], and operator-topology arguments from [7,8]. We will first state the main ingredient as a general Lemma and then discuss its applications to quantum information theory. Readers who are mainly interested in the applications may skip the proof of the Lemma.

Lemma 1.—Let f: $\mathcal{B}(\mathcal{H}^{\otimes N}) \to \mathbb{R}$ be a continuous functional, which is strongly superadditive and invariant under

 © 2006 The American Physical Society

local unitaries $f(U^{\otimes N}\rho U^{\dagger\otimes N}) = f(\rho)$. Then for every density operator ρ describing an N-partite system with finite first and second moments, we have that

$$f(\rho) \geq f(\rho_G), \tag{2}$$

where ρ_G is the Gaussian states with the same first and second moments as ρ.

Let us first remark on the requirements in Lemma 1. *Continuity* is understood in trace norm, i.e., $\|\rho^{(n)} - \rho\|_1 \to 0$ should imply $f(\rho^{(n)}) \to f(\rho)$. In fact, lower semicontinuity suffices, and we may restrict the domain of f to an appropriate compact subset of density operators like those satisfying an energy constraint. The latter typically restores continuity for functionals, which are known to be continuous in the finite dimensional case. *Strong superadditivity* means that given a state ρ acting on $(\mathcal{H}_{A_1} \otimes \mathcal{H}_{A_2}) \otimes (\mathcal{H}_{B_1} \otimes \mathcal{H}_{B_2})$ with restrictions ρ_i to $\mathcal{H}_{A_i} \otimes \mathcal{H}_{B_i}$, then $f(\rho) \geq f(\rho_1) + f(\rho_2)$, with equality if $\rho = \rho_1 \otimes \rho_2$. The latter is referred to as *additivity* and both properties are analogously defined for more than two parties.

Proof.—The main idea of the proof is covered by the following equation:

$$f(\rho) = \frac{1}{n} f(\rho^{\otimes n}) = \frac{1}{n} f(\tilde{\rho}) \tag{3}$$

$$\geq \frac{1}{n} \sum_{k=1}^{n} f(\tilde{\rho}_k) \to f(\rho_G). \tag{4}$$

In the first line we use additivity of f and set $\tilde{\rho} = U^{\otimes N}\rho^{\otimes n}U^{\dagger\otimes N}$, where U is a suitably chosen local unitary, which acts on n copies of the state. In the second line we first exploit strong superadditivity in order to bound $f(\tilde{\rho})$ from below by the sum over all reduced density operators $\tilde{\rho}_k$. Then we argue by the central limit theorem and a special choice of U, that each of these reduced states $\tilde{\rho}_k$ converges to the Gaussian ρ_G in the limit $n \to \infty$.

This idea is now made rigorous in two steps. First, we prove that each characteristic function $\tilde{\chi}_k$ converges pointwise to the corresponding Gaussian χ_G, and then we argue that this implies trace-norm convergence on the level of density operators. To simplify matters we will, without loss of generality, assume that ρ has vanishing first moments, i.e., $d_j = 0$. The general case is then obtained by applying local displacements, which by assumption will not change the value of f.

Let us begin with specifying the local unitary U as a passive symplectic operation acting on the canonical operators on site $\alpha \in \{1, \ldots, N\}$ as

$$\tilde{Q}_{\alpha,k} = \sum_{l=1}^{n} \frac{H_{kl}}{\sqrt{n}} Q_{\alpha,l}, \qquad \tilde{P}_{\alpha,k} = \sum_{l=1}^{n} \frac{H_{kl}}{\sqrt{n}} P_{\alpha,l}, \tag{5}$$

with

$$H = \begin{pmatrix} 1 & 1 \\ 1 & -1 \end{pmatrix}$$

being a Hadamard matrix and $n = 2^m$. Physically, U corresponds to an array of 50:50 beam splitters and half wave plates. Note that H has only entries ± 1, so that we can partition the sum

$$\tilde{Q}_{\alpha,k} = \frac{1}{\sqrt{n}} \Big(\sum_{l:H_{kl}=1}^{n_+} Q_{\alpha,l} - \sum_{j:H_{kj}=-1}^{n_-} Q_{\alpha,j} \Big), \tag{6}$$

and similarly for $\tilde{P}_{\alpha,k}$. Here $n_+ = n - n_-$ is the number of ones in the kth row of H. Note that either $n_+ = n$ in the first row, or $n_+ = n/2$ in all other rows.

The characteristic function $\tilde{\chi}_k$ of the reduced density operator $\tilde{\rho}_k$ is then given by

$$\tilde{\chi}_k(q, p) = \mathrm{tr}\Big[\rho^{\otimes n} \exp\Big(i \sum_{\alpha=1}^{N} q_\alpha \tilde{Q}_{\alpha,k} + p_\alpha \tilde{P}_{\alpha,k} \Big) \Big] \tag{7}$$

$$= \chi\Big(\frac{\xi}{\sqrt{n}}\Big)^{n_+} \chi\Big(\frac{-\xi}{\sqrt{n}}\Big)^{n_-}, \tag{8}$$

where χ is the characteristic function of ρ and $\xi = (q, p)$.

Following [7] we introduce a function $g\colon \mathbb{R} \to \mathbb{C}$ by $g(x) = \chi(x\xi)$, which is a *classical* characteristic function, i.e., the Fourier transform of a classical probability distribution with second moment $\xi^T\Gamma\xi/2$. To see this, note that χ is the Fourier transform of the Wigner function and recall that every one-dimensional marginal of a Wigner function (in particular the one corresponding to the direction ξ) is an admissible probability distribution. Characteristic functions are continuous at the origin, satisfy $g(0) = 1$, $|g(x)| \leq 1$, and in the case of finite second moments we can expand up to second order [9], such that

$$g(x) = 1 - \frac{\xi^T\Gamma\xi}{4} x^2 + o(x^2). \tag{9}$$

Pointwise convergence $\tilde{\chi}_k \to \chi_G$ follows then from Eq. (8) together with setting $x = 1$ in

$$\lim_{n\to\infty} g\Big(\frac{x}{\sqrt{n}}\Big)^{n_+} g\Big(\frac{-x}{\sqrt{n}}\Big)^{n_-} = \lim_{n\to\infty} \Big(1 - \frac{\xi^T\Gamma\xi}{4n} x^2\Big)^n \tag{10}$$

$$= \exp\Big[-\frac{1}{4} \xi^T\Gamma\xi x^2 \Big]. \tag{11}$$

For the remaining part we can combine the argumentations in Refs. [7,8]. In [7] it was proven that pointwise convergence of the characteristic functions implies convergence of the respective density operators within the weak operator topology. The latter was, however, shown to be equivalent to the trace-norm topology on density operators in Ref. [8]. □

A simple application of Lemma 1 is the rederivation of the maximum entropy principle by setting f equal to minus the von Neumann entropy $S(\rho) = -\mathrm{tr}[\rho \log \rho]$. Similarly, in the bipartite case with $N = N_A + N_B$ and $f(\rho) = S(\rho_A) - S(\rho)$, we recover the recently proven extremality result for the conditional entropy [4] for which strong

superadditivity is an immediate consequence of the strong subadditivity inequality for the entropy.

Entanglement measures.—Grouping the N tensor factors in Lemma 1 into $M \leq N$ parties and exploiting that every entanglement measure is by definition invariant under local unitaries, yields the following.

Proposition 1.—Let E be a continuous entanglement measure which is strongly superadditive. Then, for every density operator ρ describing an M-partite system with finite CM (and arbitrary, finite, number of modes per site), we have that any Gaussian state ρ_G with the same CM provides a lower bound $E(\rho_G) \leq E(\rho)$.

Most of the entanglement theory developed so far is devoted to bipartite systems. Whereas for pure states there is an essentially unique measure of entanglement, the von Neumann entropy of the reduced state, there are various different entanglement measures for mixed states [10]. Two of them have a clear operational meaning: the *distillable entanglement* E_D quantifies the amount of pure state entanglement that can asymptotically be extracted by means of local operations and classical communication (LOCC), and the *entanglement of formation* E_F (its regularized form, the *entanglement cost* E_c) measures the pure state entanglement required in order to prepare the state. Among all other measures, the *logarithmic negativity* E_N is the most popular one, as it is comparatively easy to calculate [11]. Let us now discuss the consequences of Proposition 1 for some entanglement measures:

(i) Distillable entanglement. E_D is additive (due to the asymptotic definition) and strongly superadditive (since restricted protocols lead to smaller rates). It was shown to be continuous in the interior of the set of distillable states [12]. As distillable Gaussian states are always in the interior [13], E_D fulfills all the requirements in the Lemma and analogous reasonings hold true in the multipartite case where ω is replaced by any M-partite target state. Moreover, in the bipartite case Prop. 1 leads immediately to a simple sufficient distillability criterion, since for Gaussian states it is known that $E_D > 0$ is equivalent to a simple inequality for the CM [13].

(ii) Entanglement of formation. Continuity of E_F was proven in [14] for finite and in [15] for infinite dimensional systems with energy constraint. Superadditivity of E_F is a notorious conjecture, which is proven to be equivalent to additivity of E_F and to many other additivity conjectures [16]. These are known for various special cases (cf. [4,16,17]) but remain to be proven in general.

(iii) Squashed entanglement. This is indeed strongly superadditive [18] and its continuity was proven (for finite dimensions) in Ref. [19].

(iv) Logarithmic negativity. E_N is additive, but fails to be strongly superadditive. In fact, E_N does not only fail the requirements for the proposition—Eq. (2) turns out to be false in this case. A simple counterexample is given by the state $|\varphi\rangle = \sqrt{1-\lambda^2}|00\rangle + \lambda|11\rangle$, with $\lambda = \frac{1}{4}$. In this case $E_N(\varphi) \simeq 0.57$, whereas $E_N(\varphi_G) \simeq 0.64$ [20]. Hence, despite the fact that E_N can easily be calculated, it is not a faithful entanglement measure in the sense that a Gaussian approximation of a non-Gaussian state could lead to an overestimated amount of entanglement.

Finally, it is interesting to note that Gaussian states not only give a lower bound, but they also provide an upper bound to the entanglement if only the CM is known. In fact, it is a simple consequence of the maximum entropy property that for a given energy (i.e., $\mathrm{tr}[\Gamma]$ fixed) the entanglement is maximized by a Gaussian state [21].

Secret key distillation.—We will now depart from the discussion of entanglement and see how Lemma 1 can be applied to the distillation of a classical secret key from quantum states under the assumption of collective attacks. Consider the case where two parties share m copies of a quantum state ρ_{AB} and aim at converting these into rm bits of a secret key under local operations and public communication. Allowing for the worst case scenario, in which an eavesdropper is given the entire purifying system of $\rho_{AB} = \mathrm{tr}_E[|\Psi_{ABE}\rangle\langle\Psi_{ABE}|]$, this can be understood as a mapping $\Psi_{ABE}^{\otimes m} \to \sigma^{\otimes rm} \otimes \rho_E$, where the secret bits $\sigma = \frac{1}{2}(|00\rangle\times\langle 00| + |11\rangle\langle 11|)$ are asymptotically uncorrelated with the state ρ_E of the eavesdropper. We call the asymptotic supremum over all achievable rates r the *distillable secret key* $K^{\mathrm{coll}}(\rho_{AB})$ of the state. By the same reasoning as for the distillable entanglement, K^{coll} (together with its multipartite generalizations with $\sigma = \frac{1}{2}(|0\ldots0\rangle\langle 0\ldots0| + |1\ldots1\rangle\langle 1\ldots1|)$) has the properties of being additive and strongly superadditive. Hence, under the assumption of continuity Lemma 1 implies the following.

Proposition 2.— Consider an M-partite system with an arbitrary, finite, number of modes per site. Then for every given finite first and second moments the Gaussian state ρ_G provides a lower bound to the distillable secret key $K^{\mathrm{coll}}(\rho) \geq K^{\mathrm{coll}}(\rho_G)$.

Channel capacities.—Let us finally apply Lemma 1 to the task of transmitting classical information through a bosonic Gaussian quantum channel T [2,4]. The latter may describe optical fibers, harmonic chains, or any other bosonic system for which we can describe the evolution in terms of a quadratic Hamiltonian H acting on system plus environment

$$T(\rho) = \mathrm{tr}_{\mathrm{env}}[V(\rho \otimes |\phi\rangle\langle\phi|_{\mathrm{env}})V^\dagger], \qquad V = e^{iHt}. \quad (12)$$

The classical capacity C of a quantum channel is the asymptotically achievable number of classical bits that can be reliably transmitted from a sender to a receiver per use of the channel. To make this a reasonable concept in the infinite dimensional setting, one imposes an energy constraint to the encoding. That is, any allowed set of input states ρ_i with respective probabilities p_i is such that the average state $\bar{\rho} = \sum_i p_i \rho_i$ satisfies an energy constraint $\bar{\rho} \in \mathcal{K} = \{\rho | \sum_j \mathrm{tr}[(Q_j^2 + P_j^2)\rho] \leq \kappa\}$. Under this constraint the capacity $C(T, \mathcal{K})$ of the channel is

$$C_1(T, \mathcal{K}) = \sup_{\{p_i, \rho_i\}} [S(T(\bar{\rho})) - \sum_i p_i S(T(\rho_i))], \quad (13)$$

$$C(T, \mathcal{K}) = \lim_{n\to\infty} \frac{1}{n} C_1(T^{\otimes n}, \mathcal{K}^{\otimes n}). \quad (14)$$

Consider now a fixed state $\bar{\rho}$ and define $\rho = V(\bar{\rho} \otimes |\phi\rangle \times \langle\phi|_{\text{env}})V^\dagger$. Then we can write

$$C_1(T, \bar{\rho}) = S(T(\bar{\rho})) - E_F(\rho). \quad (15)$$

If the notorious additivity conjecture is true [16], then not only E_F satisfies the requirements of Lemma 1 but also $C_1 = C$, i.e., the supremum over all $\bar{\rho} \in \mathcal{K}$ in Eq. (15) gives the capacity of T. By Proposition 1 together with the maximum entropy property of Gaussian states we have then, however, that $C(T, \bar{\rho}) \leq C(T, \bar{\rho}_G)$ as both terms in Eq. (15) become extremal for the Gaussian state $\bar{\rho}_G$, which has the same CM as $\bar{\rho}$. Since $\bar{\rho} \in \mathcal{K}$ iff $\bar{\rho}_G \in \mathcal{K}$ this shows:

Proposition 3.—Consider a bosonic Gaussian channel acting on a finite number of modes. Then there is an optimal encoding, which achieves the classical capacity with a Gaussian $\bar{\rho}$, if the capacity is additive.

For single mode channels for which the optimal ρ is a symmetric two-mode Gaussian state we then even know an optimal ensemble $\{p_i, \rho_i\}$ (which is continuous in this case). For such two-mode states it has been shown [22] that $E_F(\rho)$ equals the so-called *Gaussian entanglement of formation* [23], which in turn implies that the optimal ensemble consists of coherent states which are distributed in phase space according to an appropriate Gaussian distribution.

Summary and outlook.—We presented a general method which allows to prove extremality of Gaussian quantum states with regard to various applications. This re-emphasizes the exceptional role of these states and what is more, it justifies frequently made Gaussian (i.e., quadratic) approximations. As we saw, in particular, the asymptotic nature of many quantities in quantum information theory fits very well to the asymptotic nature of the central limit theorem. Hence, there are certainly many other similar applications. It is, for instance, straightforward to translate some results from the bosonic to the Fermionic world [24]. Moreover, via a state-channel duality one might apply similar techniques to channels and operations instead of states (cf. [6]). In fact, recently, Gaussian operations turned out to be optimal for certain tasks concerning classical teleportation and cloning of coherent states [25].

The authors are grateful to the Benasque Center for Science, where parts of this work were developed. M. M. W. thanks R. F. Werner and D. Perez-Garcia for interesting discussions.

[1] A. S. Holevo, M. Sohma, and O. Hirota, Phys. Rev. A **59**, 1820 (1999).
[2] A. S. Holevo and R. F. Werner, Phys. Rev. A **63**, 032312 (2001).
[3] F. Grosshans and N. J. Cerf, Phys. Rev. Lett. **92**, 047905 (2004).
[4] J. Eisert and M. M. Wolf, quant-ph/0505151.
[5] A. S. Holevo, *Probabilistic and Statistical Aspects of Quantum Theory* (North-Holland, Amsterdam, 1982).
[6] J. Quaegebeur, J. Funct. Anal. **57**, 1 (1984).
[7] C. D. Cushen and R. L. Hudson, J. Appl. Probab. **8**, 454 (1971).
[8] G. F. Dell'Antonio, Commun. Pure Appl. Math. **20**, 413 (1967); E. B. Davies, Commun. Math. Phys. **15**, 277 (1969); E. B. Davies, Commun. Math. Phys. **27**, 309 (1972).
[9] P. A. P. Moran, *An Introduction to Probability Theory* (Claredon, Oxford, 1968).
[10] M. Horodecki, Quantum Inf. Comput. **1** No. 1, 3 (2001).
[11] G. Vidal and R. F. Werner, Phys. Rev. A **65**, 032314 (2002); M. B. Plenio, Phys. Rev. Lett. **95**, 090503 (2005).
[12] G. Vidal, quant-ph/0203107.
[13] G. Giedke, L.-M. Duan, J. I. Cirac, and P. Zoller, Quantum Inf. Comput. **1** No. 3, 79 (2001); L.-M. Duan, G. Giedke, J. I. Cirac, and P. Zoller, Phys. Rev. Lett. **84**, 4002 (2000); R. F. Werner and M. M. Wolf, Phys. Rev. Lett. **86**, 3658 (2001).
[14] M. A. Nielsen, Phys. Rev. A **61**, 064301 (2000).
[15] M. E. Shirokov, quant-ph/0411091.
[16] P. W. Shor, Commun. Math. Phys. **246**, 453 (2004); K. Matsumoto, T. Shimono, and A. Winter, Commun. Math. Phys. **246**, 427 (2004); K. M. R. Audenaert and S. L. Braunstein, Commun. Math. Phys. **246**, 443 (2004).
[17] M. M. Wolf and J. Eisert, New J. Phys. **7**, 93 (2005).
[18] M. Christandl and A. Winter, J. Math. Phys. (N.Y.) **45**, 829 (2004).
[19] R. Alicki and M. Fannes, quant-ph/0312081.
[20] A similar example but with fixed *EPR uncertainty* [22] was found by J. Eisert (private communication).
[21] S. J. v. Enk and O. Hirota, Phys. Rev. A **71**, 062322 (2005).
[22] G. Giedke, M. M. Wolf, O. Krueger, R. F. Werner, and J. I. Cirac, Phys. Rev. Lett. **91**, 107901 (2003).
[23] M. M. Wolf, G. Giedke, O. Krueger, R. F. Werner, and J. I. Cirac, Phys. Rev. A **69**, 052320 (2004).
[24] R. L. Hudson, J. Appl. Probab. **10**, 502 (1973).
[25] N. J. Cerf, O. Krueger, P. Navez, R. F. Werner, and M. M. Wolf, Phys. Rev. Lett. **95**, 070501 (2005); K. Hammerer, M. M. Wolf, E. S. Polzik, and J. I. Cirac, Phys. Rev. Lett. **94**, 150503 (2005).

PRL 98, 130501 (2007) PHYSICAL REVIEW LETTERS week ending 30 MARCH 2007

Quantum Capacities of Bosonic Channels

Michael M. Wolf,[1] David Pérez-García,[2] and Geza Giedke[1]
[1]Max-Planck-Institute for Quantum Optics, Hans-Kopfermann-Strasse 1, D-85748 Garching, Germany
[2]Área de Matemática Aplicada, Universidad Rey Juan Carlos, Calle Tulipan, 28933 Móstoles (Madrid), Spain
(Received 15 June 2006; published 26 March 2007)

We investigate the capacity of bosonic quantum channels for the transmission of quantum information. We calculate the quantum capacity for a class of Gaussian channels, including channels describing optical fibers with photon losses, by proving that Gaussian encodings are optimal. For arbitrary channels we show that achievable rates can be determined from few measurable parameters by proving that every channel can asymptotically simulate a Gaussian channel which is characterized by second moments of the initial channel. Along the way we provide a complete characterization of degradable Gaussian channels and those arising from teleportation protocols.

DOI: 10.1103/PhysRevLett.98.130501 PACS numbers: 03.67.Hk, 42.81.Dp

One of the aims of quantum information theory [1] is to follow the ideas of Shannon and to establish a theory of information based on the rules of quantum mechanics. A key problem along this way is the calculation of the quantum capacity of noisy quantum channels. That is, the question how much quantum information (measured in number of qubits) can be transmitted coherently through a channel such as a lossy optical fiber, or stored reliably in a quantum memory—the future version of present-day hard drives? Despite substantial progress [2,3] a general computable formula for this capacity, comparable to Shannon's seminal coding theorem for classical information, is not in sight.

In this Letter, we focus on the special case of bosonic channels, in which a collection of bosonic modes is used to transmit (quantum) information. Arguably, this is the practically most important class of channels, since quantum information is almost invariably sent using photons: be it through the ubiquitous optical fibers, in free space, or in the microwave range via superconducting transmission lines (cf. [4]). In addition to the transmission in space, bosonic channels also play a major role for "transmission in time," i.e., in quantum memories. Several of the most advanced light-matter interfaces [5] make use of atomic ensembles to store photonic quantum information in collective atomic degrees of freedom which are in turn well described by bosonic modes. The quantum capacity of the corresponding channel is an adequate figure of merit for such devices.

The Letter has two parts in which we first deal with incomplete knowledge of the physical channel and then explicitly determine the capacity for some of the most relevant cases. In the first part we prove that the quantum capacity of any bosonic channel T is lower bounded by that of a corresponding Gaussian channel T_G, which can be derived from measurable moments of T. This implies that for determining and certifying achievable rates for the transmission of quantum information through T we need not know the channel exactly (which might be hardly possible in infinite dimensions), but merely its second moments, i.e., a few measurable parameters. In the second part we then explicitly calculate the quantum capacity of a class of Gaussian channels, which includes the important case of attenuation channels modeling optical fibers with photon losses and broadband channels where losses and photon number constraints might be frequency dependent. Along the way we provide two tools that might be of independent interest: a complete characterization of degradable Gaussian channels and of those arising from teleporting through Gaussian states.

Preliminaries.—Before we derive the main results we will briefly recall the basic notions [6,7]. Consider a bosonic system of N modes characterized by N pairs of canonical operators $(Q_1, P_1, \ldots, Q_N, P_N) =: R$ for which the commutation relations $[R_k, R_l] = i\sigma_{kl}$ are represented by the symplectic matrix $\sigma = \oplus_{k=1}^{N}(i\sigma_y)$. The exponentials $W_\xi := e^{i\xi R}$, $\xi \in \mathbb{R}^{2N}$ are called Weyl displacement operators. Their expectation value, the characteristic function, $\chi(\xi) := \mathrm{Tr}[\rho W_\xi]$ is the Fourier transform of the Wigner function and for Gaussian states

$$\chi(\xi) = e^{i\xi\cdot d - (1/4)\xi\cdot\gamma\xi}, \tag{1}$$

with first moments $d_k = \mathrm{Tr}[\rho R_k]$ and covariance matrix (CM) $\gamma_{kl} := \mathrm{Tr}[\rho\{R_k - d_k, R_l - d_l\}_+]$. Note that coherent, squeezed and thermal states in quantum optics are all Gaussian states.

Gaussian channels [7,8] transform Weyl operators as $W_\xi \mapsto W_{X\xi}e^{-(1/4)\xi Y\xi}$ and act on covariance matrices as

$$\gamma \mapsto X^T\gamma X + Y. \tag{2}$$

Particularly important instances of single-mode Gaussian channels are attenuation and amplification channels for which $X = \sqrt{\eta}\mathbb{1}$ and $Y = |\eta - 1|\mathbb{1}$. For $0 \le \eta \le 1$ this models a single mode of an optical fiber with transmissivity η where the environment is assumed to be in the vacuum state. The latter reflects the fact that thermal photons with optical frequencies are negligible at room temperature. For $\eta > 1$ the channel becomes an amplifi-

 © 2007 The American Physical Society

cation channel, where the noise term Y is now a consequence of the Heisenberg uncertainty.

Teleportation channels.—We will now derive the form of Gaussian channels which are obtained when teleporting through a centered bipartite Gaussian state. As this is useful for applying but not necessary for understanding the following it might be skipped by the reader. Let

$$\Gamma = \begin{pmatrix} \Gamma_A & \Gamma_C \\ \Gamma_C^T & \Gamma_B \end{pmatrix}$$

be the CM of a Gaussian state of $N_A + N_B$ modes with $N_A = N_B$. Assume Bob wants to teleport a quantum state of N_B modes with CM γ to Alice. Using the standard protocol [9] he sends pairs of modes from γ and Γ_B through 50:50 beam splitters, measures the Q and P quadratures, and then communicates the outcomes. Depending on the latter Alice applies displacements to the modes in Γ_A. The simplest way of deriving an expression for the output is to start with the Wigner representation and to assume that the state to be teleported is a centered Gaussian. The Wigner function before the measurement is up to normalization given by $\exp -\xi[M_{\mathrm{BS}}^T(\Gamma \oplus \gamma)^{-1} M_{\mathrm{BS}}]\xi$, where M_{BS} corresponds to the beam-splitter operation. With $\xi = (\xi_A, \xi_B, \xi_{B'})$ the final Wigner function is then proportional to

$$\int d\xi_B d\xi_{B'} e^{-\xi[M_X^T M_{\mathrm{BS}}^T (\Gamma \oplus \gamma)^{-1} M_{\mathrm{BS}} M_X]\xi}, \tag{3}$$

where M_X incorporates the displacements, i.e., it is the identity matrix plus an arbitrary $2N_B \times 2N_B$ off-diagonal block which maps the $2N_B$ measurement outcomes onto the respective displacements. To circumvent integrating Eq. (3) we can now go to the characteristic function, i.e., the Fourier transformed picture. The integration then boils down to picking out the upper left block of the inverted matrix $[M_X^T M_{\mathrm{BS}}^T (\Gamma \oplus \gamma)^{-1} M_{\mathrm{BS}} M_X]^{-1}$. The inversion is, however, trivial since $M_{\mathrm{BS}}^{-1} = M_{\mathrm{BS}}^T$ and M_X^{-1} is obtained from M_X by changing the sign of all off-diagonal entries. In this way we obtain that the input CM is transformed to

$$\gamma \mapsto X^T \gamma X + [\Gamma_A + \Gamma_C \Lambda X + (\Gamma_C \Lambda X)^T + X^T \Lambda^T \Gamma_B \Lambda X], \tag{4}$$

where $\Lambda = \mathrm{diag}(1, -1, 1, -1, \ldots)$ and X is such that $\sqrt{2}X$ is the matrix of displacement transformations, i.e., the gain which is typically chosen to be $\sqrt{2}\mathbb{1}$.

Clearly, Eq. (4) has the form (2) and following the above lines it is straight forward to show that the channel is Gaussian and maps any (not necessarily centered Gaussian) input characteristic function χ_{in} into

$$\chi_{\mathrm{out}}(\xi) = \chi_{\mathrm{in}}(X\xi)\chi_\Gamma(\xi \oplus \Lambda X \xi). \tag{5}$$

For standard protocols ($X = \mathbb{1}$) on single modes ($N_A = N_B = 1$) this was derived in [10].

Achievable rates for arbitrary channels.—The subject of interest is the quantum capacity $Q(T)$ of an arbitrary, *a priori* unknown, channel T. We will show how one can certify achievable rates for the transmission of quantum information through T by only looking at the CM Γ of a state $\rho_T = (T \otimes \mathrm{id})(\psi)$ which is obtained by sending half of an arbitrary entangled state ψ through the channel. Γ could be determined by homodyne measurements. The argument combines (i) the relation between entanglement distillation and quantum capacities observed in [11], (ii) the extremality of Gaussian states shown in [12], and (iii) the explicit form of Gaussian teleportation channels derived in the previous section. All together this leads to the chain of inequalities

$$Q(T) \geq D_{\leftarrow}(\rho_T) \geq D_{\leftarrow}(\mathcal{G}(\rho_T)) \geq Q(T_G). \tag{6}$$

Here $D_{\leftarrow}(\rho_T)$ is the distillable entanglement under protocols with one-way communication (from Bob to Alice). Since a classical side channel does not increase $Q(T)$ this is clearly a lower bound to the capacity as Alice and Bob could simply first distill ρ_T and then use the obtained maximally entangled states for teleportation [11]. The second inequality uses that replacing ρ_T by a Gaussian state $\mathcal{G}(\rho_T)$ with the same CM Γ can only decrease the distillable entanglement [12] (see Fig. 1 for an operational meaning). Finally, if we use the Gaussian state in turn as a resource for establishing a teleportation channel T_G we end up with the sought inequality $Q(T) \geq Q(T_G)$. T_G is then the Gaussian channel in Eqs. (4) and (5), which is for a fixed teleportation protocol (a fixed matrix X) completely determined by Γ.

Bounds on the quantum capacity of Gaussian channels were derived in [13,14] and we will show below that it can be calculated exactly for some important cases. Note that a simple bound for $Q(T)$ can be obtained from a lower bound to $D_{\leftarrow}[\mathcal{G}(\rho_T)]$, the conditional entropy of the Gaussian state with CM Γ, i.e., $Q(T) \geq S(\Gamma_A) - S(\Gamma)$.

Before we proceed, two comments on the quality of the above bound and its operational meaning are in order: The given argument holds for arbitrary T and ψ. However, since we bound by Gaussian quantities the inequality might

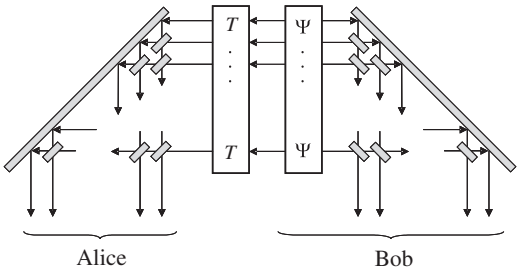

FIG. 1. In order to obtain a Gaussian channel from an arbitrary quantum channel T Bob (the sender) prepares n instances of an entangled state ψ half of which he sends through $T^{\otimes n}$. After applying two arrays of 50:50 beam splitters to the output $\rho_T^{\otimes n} = [(T \otimes \mathrm{id})(\psi)]^{\otimes n}$ the n reduced states will converge to a Gaussian state $\mathcal{G}(\rho_T)$ (with the same CM as ρ_T) which can in turn be used to establish a Gaussian teleportation channel T_G.

PRL 98, 130501 (2007) PHYSICAL REVIEW LETTERS week ending 30 MARCH 2007

become trivial [i.e., $Q(T_G) = 0$ though $Q(T) \gg 0$] if both T and ψ are too far from being Gaussian. On the other hand, if T is Gaussian and $|\psi\rangle = (\cosh r)^{-1} \sum_n (\tanh r)^n |nn\rangle$ is a two-mode squeezed state, then in the limit $r \to \infty$ the inequality becomes tight, i.e., $Q(T_G) \to Q(T)$ with exponentially vanishing gap. This also indicates how (bounds on) the rate achievable by a given channel can be probed experimentally: sending part of a two-mode squeezed state through T and measuring the second moments of the resulting state allows to compute $Q(T_G)$ using the formulas below.

Quantum capacity of Gaussian channels.—It was proven in [2] that the quantum capacity of a quantum channel T can be expressed as

$$Q(T) = \lim_{n\to\infty} \frac{1}{n} \sup_{\rho} J(\rho, T^{\otimes n}), \tag{7}$$

$$J(\rho, T) = S(T(\rho)) - S((T \otimes \mathrm{id})(\psi)), \tag{8}$$

where ψ is a purification of ρ and J is known as the coherent information. In general, the calculation of $Q(T)$ from the above formula is a daunting task since (i) the coherent information is known to be not additive, i.e., the regularization $n \to \infty$ is necessary, and (ii) due to lacking concavity properties there are local maxima which are not global ones. On top of this, for bosonic channels the optimization is over an infinite dimensional space.

Fortunately, for a class of Gaussian channels including the important case of the lossy channel, these obstacles can be circumvented by exploiting recent results on degradability of channels [3,15] and extremality of Gaussian states [12].

To this end consider a channel $T(\rho_S) = \mathrm{Tr}_E[U(\rho_S \otimes \varphi_E)U^\dagger]$ expressed in terms of a unitary coupling between the system S and the environment E which is initially in a pure state φ_E. The conjugate channel $T_c(\rho_S) = \mathrm{Tr}_S[U(\rho_S \otimes \varphi_E)U^\dagger]$ is defined as a mapping from the system to the environment. As shown in [3] the coherent information can be expressed in terms of a conditional entropy if there exists a channel T' such that $T' \circ T = T_c$; in this case T is called degradable. More precisely, if $\tilde{\rho}_{S'E'}$ is the extension of the state $\tilde{\rho}_{S'} = T' \circ T(\rho)$ to the environment E' of T', then

$$J(\rho, T) = S(\tilde{\rho}_{S'E'}) - S(\tilde{\rho}_{S'}) =: S(E'|S'). \tag{9}$$

The conditional entropy $S(E'|S')$ is known to be strongly subadditive [1], i.e., for a composite system $S(E'_{12}|S'_{12}) \le S(E'_1|S'_1) + S(E'_2|S'_2)$. This has important consequences: for a set $\{T_i\}$ of degradable channels $J(\rho, \otimes_i T_i) \le \sum_i J(\rho_i, T_i)$, where ρ_i are the corresponding reduced states, and if each T_i is a Gaussian channel, we have in addition

$$J(\rho, \otimes_i T_i) \le \sum_i J(\rho_i, T_i) \le \sum_i J(\mathcal{G}(\rho_i), T_i). \tag{10}$$

The last inequality follows from the extremality of Gaussian states with respect to the conditional entropy [7,12] together with the fact that for Gaussian channels T_c can be chosen to be Gaussian and the CM is transformed irrespective of whether the input was Gaussian or not. As a consequence, if T_i are degradable Gaussian channels, then

$$Q(\otimes_i T_i) = \sum_i \sup_{\rho_G} J(\rho_G, T_i), \tag{11}$$

where the supremum is now taken only over Gaussian input states ρ_G. Calculating the latter for Gaussian channels is now a feasible task which was solved for the single-mode case in [13] and in [14] for broadband channels under power constraints using Lagrange multipliers. In fact, if we impose a constraint on the input energy of the form $\sum_i \omega_i N_i = \mathcal{E}$, where N_i is the average input photon number of mode i with corresponding frequency ω_i, then the above argumentation still holds, since the constraint just depends on the CM. The importance of Eq. (11) stems from the fact that a large class of Gaussian channels is indeed degradable, as shown in [15] and extended below. In particular, we can apply Eq. (11) to attenuation (amplification) channels with transmissivity η (gain $\sqrt{\eta}$). Together with the optimization carried out in [13] [Eq. (5.9)] this yields (see Fig. 2)

$$Q(\eta) = \max\{0, \log_2|\eta| - \log_2|1 - \eta|\}. \tag{12}$$

Note that the quantum capacity of every degradable Gaussian channel can easily be calculated as J becomes a concave function of the CM such that local maxima are global ones.

Degradable Gaussian channels.—We will now investigate the condition under which Eq. (11) was derived and characterize the set of degradable Gaussian channels, extending the results of [15]. To this end we represent the channel in terms of a unitary coupling between the system with N_S modes and a (minimally represented) environment of $N_E \le 2N_S$ modes which are initially in the vacuum state with CM $\gamma_E = \mathbb{1}$. The interaction is described by a sym-

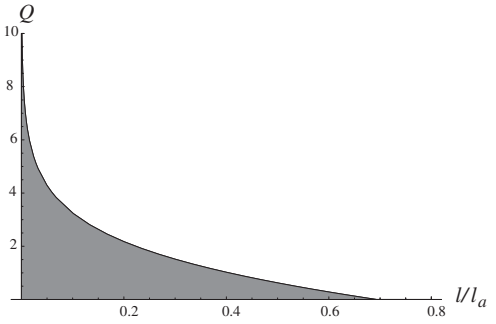

FIG. 2. Quantum capacity of a channel with photon losses as a function of the transmission length l in terms of the absorption length l_a, i.e., $\eta = e^{-l/l_a}$. For quantum memories l and l_a are storage and decay time. The capacity vanishes for $l/l_a = \ln 2 \approx 0.693$, where the channel can be considered to be part of a symmetric approximate cloning channel.

plectic matrix of size $2(N_E + N_S) \times 2(N_E + N_S)$ which we write in block form as

$$S = \begin{pmatrix} A & B \\ C & D \end{pmatrix}$$

[16]. The output CM of the channel T: $\gamma \mapsto X\gamma X^T + Y$ is then simply the lower right block of $S(\gamma_E \oplus \gamma)S^T$ (i.e., $D = X$ and $C\gamma_E C^T = Y$), whereas the conjugate channel T_c corresponds to the upper left block.

Let us first focus on the case $N_S = N_E$ and assume for simplicity that the blocks in S are nonsingular. A channel is degradable if $T_c \circ T^{-1}$ is completely positive which is for a Gaussian trace preserving map equivalent to the condition [8]

$$Y + i\sigma \geq iX\sigma X^T. \tag{13}$$

Inserting the above block structure and using [16] shows that complete positivity of $T_c \circ T^{-1}$ is equivalent to

$$0 \leq (\mathbb{1} + i\sigma) - K(\mathbb{1} + i\sigma)K^T, \qquad K = C^T D^{-T}\sigma D^{-1}C. \tag{14}$$

Expressing this in terms of X and Y finally gives [16]

$$(2X\sigma X^T\sigma^T - \mathbb{1})Y \geq 0. \tag{15}$$

Similarly we can derive a condition for degradability of T_c (antidegradability of T) which is again given by the expressions (14) and (15) which have then to be negative instead of positive semidefinite.

Since for $N_E = N_S = 1$ X is a 2×2 matrix and thus $X\sigma X^T\sigma^T = \mathbb{1}\det X$, condition (15) implies that either T or T_c is degradable, as shown in [15]. Hence, as antidegradable channels have zero quantum capacity (due to the no-cloning theorem), the quantum capacity of every Gaussian channel with $N_S = N_E = 1$ can easily be calculated. In fact, by using the freedom of acting unitarily before and after the channel (which does not change its capacity) one can generically bring the channel to a normal form [17,18] which only depends on the symplectic invariant $\det X$ such that $Q(T)$ of every such channel is given by Eq. (12) with $\eta = \det X$.

Let us finally briefly comment on the case $N_E \neq N_S$. If the environment is smaller than the system, then we can easily follow the above lines for instance by choosing a representation of the channel with larger N_E equal to N_S [19]. It is worth mentioning that if S corresponds to a passive (i.e., number preserving) operation, then for $N_E < N_S$ there are always unaffected modes such that $Q(T) = \infty$ without additional constraints. If $N_E > N_S$ then Eq. (15) is merely a necessary, whereas Eq. (14) is still a necessary and sufficient condition for degradability [19]. Applying the latter to a general single-mode channel with $N_S = 1$, $N_E = 2$ shows that generically one has neither degradability nor antidegradability. Hence, it remains open whether in this case the capacity is given by Eq. (11). However, we can easily derive an upper bound by exploiting the fact that every Gaussian channel T can be decomposed as $T = T_1 \circ T_2$, where T_2 is a minimal noise channel [8] for which $N_E = N_S$ with $X_2 = X$, $Y_2 \leq Y$ and T_1 is a classical noise channel for which $X_1 = \mathbb{1}$, $Y_1 = Y - Y_2$. Because of the bottleneck inequality for capacities (cf. [13]) we have $Q(T) \leq Q(T_2)$ where the latter is in the single-mode case again given by Eq. (12) with $\eta = \det X$. A lower bound is always given by the right-hand side of Eq. (11) as calculated in [13].

We appreciate discussions with J. I. Cirac and M. E. Shirokov and financial support by Spanish projects Ramon y Cajal and MTM2005-00082.

[1] M. A. Nielsen and I. L. Chuang, *Quantum Computation and Quantum Information* (Cambridge University Press, Cambridge, U.K., 2000).
[2] P. W. Shor, in The Quantum Channel Capacity and Coherent Information: Lecture Notes, MSRI Workshop on Quantum Computation, 2002 (unpublished); I. Devetak, IEEE Trans. Inf. Theory **51**, 44 (2005); S. Lloyd, Phys. Rev. A **55**, 1613 (1997).
[3] I. Devetak and P. W. Shor, quant-ph/0311131.
[4] A. Wallraff *et al.*, Nature (London) **431**, 162 (2004); A. Blais *et al.*, Phys. Rev. A **69**, 062320 (2004).
[5] D. F. Phillips *et al.*, Phys. Rev. Lett. **86**, 783 (2001); C. Liu *et al.*, Nature (London) **409**, 490 (2001); B. Julsgaard *et al.*, Nature (London) **432**, 482 (2004); T. Chanelière *et al.*, Nature (London) **438**, 833 (2005).
[6] A. S. Holevo, *Probabilistic and Statistical Aspects of Quantum Theory* (North-Holland Publishing, Amsterdam, 1982).
[7] J. Eisert and M. M. Wolf, quant-ph/0505151.
[8] G. Lindblad, J. Phys. A **33**, 5059 (2000); B. Demoen, P. Vanheuverzwijn, and A. Verbeure, Lett. Math. Phys. **2**, 161 (1977).
[9] L. Vaidman, Phys. Rev. A **49**, 1473 (1994); S. L. Braunstein and H. J. Kimble, Phys. Rev. Lett. **80**, 869 (1998).
[10] P. Marian, T. A. Marian, and H. Scutaru, Rom. J. Phys. **48**, 727 (2003).
[11] C. H. Bennett, D. P. DiVincenzo, J. A. Smolin, and W. K. Wootters, Phys. Rev. A **54**, 3824 (1996).
[12] M. M. Wolf, G. Giedke, and J. I. Cirac, Phys. Rev. Lett. **96**, 080502 (2006).
[13] A. S. Holevo and R. F. Werner, Phys. Rev. A **63**, 032312 (2001).
[14] V. Giovannetti, S. Lloyd, L. Maccone, and P. W. Shor, Phys. Rev. A **68**, 062323 (2003).
[15] F. Caruso and V. Giovannetti, Phys. Rev. A **74**, 062307 (2006).
[16] See footnote in Michael M. Wolf, David Perez-Garcia, Geza Giedke, quant-ph/0606132.
[17] A. S. Holevo, quant-ph/0607051.
[18] A. Serafini, J. Eisert, and M. M. Wolf, Phys. Rev. A **71**, 012320 (2005).
[19] The only assumption made in the derivation of condition (14) is nonsingularity of the diagonal blocks A and D.

Super-activation for Gaussian channels requires squeezing

Daniel Lercher[1,*], Géza Giedke[1,2,†], and Michael M. Wolf[1,‡]
[1]*Department of Mathematics, Technische Universität München, 85748 Garching, Germany*
[2]*Max-Planck-Institut für Quantenoptik, 85748 Garching, Germany*
(Dated: September 26, 2012)

The quantum capacity of bosonic Gaussian quantum channels can be non-additive in a particularly striking way: a pair of such optical-fiber type channels can individually have zero quantum capacity but super-activate each other such that the combined channel has strictly positive capacity. This has been shown in [Nature Photonics 5, 624 (2011)] where it was conjectured that squeezing is a necessary resource for this phenomenon. We provide a proof of this conjecture by showing that for gauge covariant channels a Choi matrix with positive partial transpose implies that the channel is entanglement-breaking. In addition, we construct an example which shows that this implication fails to hold for Gaussian channels which arise from passive interactions with a squeezed environment.

arXiv:1209.5574v1 [quant-ph] 25 Sep 2012

INTRODUCTION

A question at the heart of information theory—classical as well as quantum—is, how much information can be transmitted reliably through a given noisy channel. For classical memoryless channels Shannon posed and answered this questions in his groundbreaking work [1] in which he provided a tractable formula for the *capacity* of any such channel. In quantum information theory, despite considerable progress, no closed general expression is known for the classical or quantum capacity. What complicates matters in the quantum world is that quantum correlations between different channel uses can improve the performance or, mathematically speaking, lead to non-additivity effects. One of the most striking of these is *super-activation* of the quantum capacity: a pair of channels can individually have zero quantum capacity, but when combined give rise to a channel whose quantum capacity is strictly positive [2]. In [3] it was shown that this effect can occur for Gaussian channels. These describe evolutions of the continuous degrees of freedom of light in free space and in optical fibers as well as the time evolution of quantum memories which are based on collective excitations [4]. One of the channels used in the construction in [3] can indeed be regarded as a simple model of a single-mode optical fiber. The second channel, however, involves a high degree of squeezing within the interaction between a two-mode system and its environment—something considerably more difficult to realize. The authors of [3] write: "*Although an example using only linear optical elements would be desirable, we suspect, but cannot prove, that none exist.*" The present paper aims at settling this conjecture in the affirmative.

Currently, there is basically one approach towards super-activation. This is based on the fact that there are only two classes of channels known, which have provably zero quantum capacity: channels with a symmetric extension and so-called PPT channels. Since both classes are closed with respect to parallel composition, the only combination with a chance of successful super-activation is to take one channel from each class. In this work we show that if we restrict ourselves to passive Gaussian channels (i.e., those not involving squeezing), then the set of PPT channels becomes a strict subset of the set of channels with a symmetric extension, therefore rendering super-activation impossible.

PREREQUISITES

We begin with recalling basic notions and results needed for our purpose.

Gaussian states and channels: We consider a continuous variable system of n bosonic modes whose description involves n pairs of generalized position and momentum operators Q_k, P_k which may correspond to the quadratures of electromagnetic field modes. With the definition $R := (Q_1, P_1, \ldots, Q_n, P_n)$ the canonical commutation relations read

$$[R_k, R_l] = i\,(\sigma_n)_{kl}\,\mathbb{1}, \quad \text{with } \sigma_n := \bigoplus_{i=1}^{n} \begin{pmatrix} & 1 \\ -1 & \end{pmatrix} \tag{1}$$

being the symplectic form.
We associate with every density operator ρ its displacement vector d, with $d_k := \mathrm{tr}\,[\rho R_k]$ and its covariance matrix Γ with $\Gamma_{kl} := \mathrm{tr}\,[\rho\{R_k - d_k\mathbb{1}, R_l - d_l\mathbb{1}\}_+]$, $k,l = 1,\ldots,2n$. d and Γ contain the first and second moments of the corresponding phase space distribution.
A Gaussian state is defined as a quantum state with a Gaussian Wigner phase space distribution function, see [5]. In particular it is completely specified by d and Γ, the latter being any real symmetric matrix that satisfies

*Electronic address: daniel.lercher@ma.tum.de
†Electronic address: giedke@mpq.mpg.de
‡Electronic address: m.wolf@tum.de

the uncertainty relation

$$\Gamma \geq i\sigma_n. \tag{2}$$

In the following all states are assumed to be centered (i.e. $d = 0$) since displacements in phase space are local unitaries in Hilbert space which are irrelevant for our purpose.

A completely positive trace-preserving map which preserves the Gaussian nature of states is called *Gaussian channel*, see [6]. Again neglecting its effect on d it can be characterized by its action on covariance matrices, which is given by

$$\Gamma \mapsto X\Gamma X^T + Y, \qquad X, Y = Y^T \in \mathcal{M}_{2n}(\mathbb{R}). \tag{3}$$

For a pair of real matrices X and $Y = Y^T$ to describe a bona fide Gaussian channel it is necessary and sufficient that

$$Y + i\left(\sigma_n - X\sigma_n X^T\right) \geq 0. \tag{4}$$

Unitary Gaussian evolutions then correspond to $Y = 0$ and X being real symplectic, i.e. $X \in Sp(2n, \mathbb{R}) = \{S \in \mathcal{M}_{2n}(\mathbb{R}) |\, S\sigma_n S^T = \sigma_n\}$. Every Gaussian channel can be realized by a unitary dilation [7], invoking $n_E \leq 2n$ environmental modes. This means that there exist a unitary U representing S on Hilbert space and a Gaussian state ρ_E such that density matrices evolve as

$$\rho \mapsto \mathrm{tr}_E\left[U(\rho_E \otimes \rho)U^\dagger\right]. \tag{5}$$

On the level of covariance matrices Γ_E and Γ the overall evolution then looks like

$$(\Gamma_E \oplus \Gamma) \mapsto S\,(\Gamma_E \oplus \Gamma)\,S^T. \tag{6}$$

In the notation $S = \begin{pmatrix} S_1 & S_2 \\ S_3 & S_4 \end{pmatrix}$ that reflects the decomposition of the total system into the environment and the n-modes system, one finds $X = S_4$ and $Y = S_3\Gamma_E S_3^T$.

The Symplectic Orthogonal Group: A special case of a unitary Gaussian evolutions is the one generated by a passive Hamiltonian

$$H = \sum_{k,l=1}^{N} h_{kl} a_k^\dagger a_l + h.c.,\ h_{kl} \in \mathbb{C}, \tag{7}$$

with annihilation operator $a_k := (Q_k + iP_k)/\sqrt{2}$. Passive Hamiltonians comprise the set of quadratic Hamiltonians, which commute with the total particle number operator.

A unitary Gaussian evolution generated by a passive Hamiltonian as in (7) corresponds to a symplectic orthogonal matrix $S \in K(m) := Sp(2m, \mathbb{R}) \cap O(2m, \mathbb{R})$. Mathematically, $K(m)$ is the largest compact subgroup of the real symplectic group. Physically, it corresponds to the set of operations which can be implemented using beam splitters and phase shifters only [8].

$K(m)$ is isomorphic to $U(m)$ [9]. This can be verified easily: First one observes that elements $R \in \mathcal{M}_{2m}(\mathbb{R})$ in the commutant of σ_m have the form

$$[\sigma_m, R] = 0 \Leftrightarrow R = (r_{ij})_{i,j=1}^m, \qquad r_{ij} = \begin{pmatrix} a_{ij} & b_{ij} \\ -b_{ij} & a_{ij} \end{pmatrix},\ a_{ij}, b_{ij} \in \mathbb{R}. \tag{8}$$

With this result one verifies that the map

$$\Lambda : U(m) \to K(m), \qquad (c_{ij}) \mapsto (C_{ij}), \quad C_{ij} = \begin{pmatrix} \Re(c_{ij}) & \Im(c_{ij}) \\ -\Im(c_{ij}) & \Re(c_{ij}) \end{pmatrix} \tag{9}$$

is indeed a group isomorphism.

At this point we add two observations that will help us later to exploit the particular structure of real symplectic orthogonals (9). The set

$$\mathcal{C}_n := \left\{ \begin{pmatrix} A & B \\ -B & A \end{pmatrix} \middle|\ \begin{matrix} A, B \in \\ \mathcal{M}_n(\mathbb{R}) \end{matrix} \right\} \tag{10}$$

together with the operation of matrix multiplication forms a semigroup with neutral element. As such, it is isomorphic to $\mathcal{M}_n(\mathbb{C})$. An isomorphism is given by

$$\begin{pmatrix} A & B \\ -B & A \end{pmatrix} \mapsto A + iB\,. \tag{11}$$

And finally, for complex square matrices $A, B \in \mathcal{M}_n(\mathbb{C})$ one finds the following criterion for positive-semidefiniteness [10]

$$\begin{pmatrix} A & B \\ -B & A \end{pmatrix} \geq 0 \Leftrightarrow A \pm iB \geq 0\,. \tag{12}$$

Properties of Gaussian Channels: We call a quantum channel T PPT (for "positive partial transpose") if $\theta \circ T$ is completely positive, where θ denotes time reversal, which in Schrödinger representation corresponds to transposition. A Gaussian channel characterized by (X, Y) is PPT iff [11]

$$Y - i\left(\sigma_n + X\sigma_n X^T\right) \geq 0. \tag{13}$$

A Gaussian channel is entanglement-breaking if and only if Y admits a decomposition into real matrices M and N such that [12]

$$Y = M + N, \quad M \geq i\sigma_n, \quad N \geq iX\sigma_n X^T. \tag{14}$$

This reflects the fact that any entanglement-breaking quantum channel consists of a measurement, followed by a state preparation depending on the outcome of the measurement [13, 14]. As a consequence, every entanglement-breaking channel has a symmetric extension.

Definition 1. *In accordance with [15] we call a Gaussian channel characterized by (X, Y) "gauge covariant", if $[X, \sigma_n] = [Y, \sigma_n] = 0$.*

Definition 2. *We call a Gaussian channel "passive" if it can be generated by a passive Hamiltonian H (7) that couples the system to an environment in a Gibbs state ρ_E of a passive Hamiltonian H':*

$$\rho_E = \frac{\mathrm{e}^{-\beta H'}}{\mathrm{tr}\left[\mathrm{e}^{-\beta H'}\right]}, \quad H' = \sum_{k,l=1}^{n_E} h'_{kl} a_k^\dagger a_l + h.c. \quad (15)$$

One can show that, as a consequence of the normal mode decomposition of Gaussian states, (15) is equivalent to $[\Gamma_E, \sigma_{n_E}] = 0$, where Γ_E is the covariance matrix of the Gaussian state ρ_E and σ_{n_E} is the corresponding symplectic form. This implies for passive Gaussian channels

$$[Y, \sigma_n] = \left[S_3 \Gamma_E S_3^T, \sigma_n\right] = 0, \quad (16)$$

as one derives from the block structure of S_3 (9) and the analogous structure of the elements in the commutant of σ_n (8). Similarly we find $[X, \sigma_n] = [S_4, \sigma_n] = 0$. Hence, every passive Gaussian channel is gauge covariant.

MAIN RESULT

Proposition 3. *A gauge covariant Gaussian channel is entanglement-breaking iff it is PPT.*

Proof. Evidently, entanglement-breaking implies PPT, so we have to prove the reverse implication. To this end it is convenient to reorder the canonical coordinates as $(Q_1, \ldots, Q_N, P_1, \ldots, P_N)$. In this notation

$$\sigma_m = \begin{pmatrix} & \mathbb{1}_m \\ -\mathbb{1}_m & \end{pmatrix} \text{ and } Y = \begin{pmatrix} Y_1 & Y_2 \\ -Y_2 & Y_1 \end{pmatrix}.$$

The latter follows from (16) together with (8).
We prove first that we can restrict ourselves to the case $X = \hat{X} \oplus \hat{X}$, where by virtue of the symplectic singular value decomposition [16] the matrix $\hat{X}$ is diagonal and non-negative. Assume, this is not the case. Then we can replace the passive evolution U, which describes the interaction between system and environment, by $U' = (\mathbb{1}_E \otimes U_G) U (\mathbb{1}_E \otimes U_F)$. U_F and U_G are passive unitary evolutions that act only on the system. They correspond to symplectic transformations $F, G \in K(n)$ in phase space. We denote the resulting channel by T'. T is PPT iff T' is PPT. The same holds for the entanglement-breaking property. We find

$$\begin{aligned} X' &= GXF \quad (17) \\ &= \begin{pmatrix} G_1 & G_2 \\ -G_2 & G_1 \end{pmatrix} \begin{pmatrix} X_1 & X_2 \\ -X_2 & X_1 \end{pmatrix} \begin{pmatrix} F_1 & F_2 \\ -F_2 & F_1 \end{pmatrix}, \\ &\quad \text{with } F_1 + iF_2, G_1 + iG_2 \in U(n). \end{aligned}$$

Now we can exploit the isomorphism (11) and choose $F_{1,2}$ and $G_{1,2}$ such that $(G_1 + iG_2)(X_1 + iX_2)(F_1 + iF_2) =: \hat{X}$ is the singular value decomposition of $X_1 + iX_2$. Hence, $X' = \hat{X} \oplus \hat{X}$ with $\hat{X}$ diagonal and non-negative.

We will now exploit criterion (14) by showing that the decomposition of Y into $M := Y - X^2$ and $N := X^2$ obeys the required conditions, which read:

$$\begin{aligned} N - iX\sigma X^T &= X(\mathbb{1} - i\sigma)X^T \geq 0, \quad (18) \\ M - i\sigma &= \begin{pmatrix} Y_1 - \hat{X}^2 & Y_2 - i\mathbb{1} \\ -Y_2 + i\mathbb{1} & Y_1 - \hat{X}^2 \end{pmatrix} \geq 0 \end{aligned}$$

The first inequality in (18) follows simply from $(\mathbb{1} - i\sigma) \geq 0$. In order to arrive at the second inequality we use (12) and rewrite the inequality as

$$\begin{aligned} Y_1 - \hat{X}^2 \pm i(Y_2 - i\mathbb{1}) \geq 0 \;&\Leftrightarrow \\ Y_1 \pm iY_2 - (\hat{X}^2 \mp \mathbb{1}) \geq 0 \;&\Leftrightarrow \\ Y_1 \pm iY_2 - (\hat{X}^2 + \mathbb{1}) \geq 0 \;&\Leftrightarrow \\ \begin{cases} Y_1 + iY_2 + (\hat{X}^2 + \mathbb{1}) \geq 0 \\ Y_1 - iY_2 - (\hat{X}^2 + \mathbb{1}) \geq 0 \end{cases} \;&\Leftrightarrow \\ Y_1 \pm i\left(Y_2 - i(\mathbb{1} + \hat{X}^2)\right) \geq 0 \quad . \end{aligned} \quad (19)$$

Here we used two elementary facts: (i) a matrix is positive iff its complex conjugate is positive, and (ii) the sum of two positive matrices is again positive. In the last line, with (12), we recover the PPT criterion (13)

$$\begin{aligned} &Y - i(\sigma + X\sigma X^T) = Y - i\sigma(\mathbb{1} + X^2) = \\ &= \begin{pmatrix} Y_1 & Y_2 - i(\mathbb{1} + \hat{X}^2) \\ -Y_2 + i(\mathbb{1} + \hat{X}^2) & Y_1 \end{pmatrix} \geq 0\,, \end{aligned}$$

which concludes the proof. □

Proposition 4 (No super-activation without squeezing)**.** *Let T_1, T_2 be passive Gaussian quantum channels. If each channel either has a symmetric extension or satisfies the PPT property, then $Q(T_1 \otimes T_2) = 0$.*

Proof. Let $T_i\,(i = 1 \text{ or } 2)$ be PPT. T_i is gauge covariant, because it is passive, and according to Prop. 3 it is thus entanglement-breaking. In particular, it has a symmetric extension, which then also holds for $T_1 \otimes T_2$. Hence, the combined channel has zero quantum capacity. □

PASSIVE INTERACTIONS WITH A SQUEEZED ENVIRONMENT

We now consider an example of a Gaussian channel T for $n = n_E = 2$. T is generated by a passive interaction, as in (7), but the environment is assumed to be in a mixed squeezed state ρ_E (i.e. $\det \Gamma_E \neq 1$, $\Gamma_E \geq i\sigma_2$ and $\Gamma_E \ngeq \mathbb{1}_4$). T will be shown to be PPT but not

entanglement-breaking. We omit the index of $\mathbb{1}_2$ and choose

$$\Gamma_E = \tfrac{3+\sqrt{13}}{2}\begin{pmatrix} 5 & & 3 & \\ & 5 & & -3 \\ 3 & & 2 & \\ & -3 & & 2 \end{pmatrix}, \tag{20}$$

$$S = \sqrt{\tfrac{1}{3}}\left(\begin{array}{ccc|c} -\sqrt{2}\mathbb{1} & & & \mathbb{1} \\ & -\mathbb{1} & & \sqrt{2}\mathbb{1} \\ \hline \mathbb{1} & & & \sqrt{2}\mathbb{1} \\ & \sqrt{2}\mathbb{1} & & \mathbb{1} \end{array}\right). \tag{21}$$

S represents two beamsplitters: one of transmittivity $\frac{2}{3}$ that couples the first system mode to the first mode of the environment and a second of transmittivity $\frac{1}{3}$ that acts between the two remaining modes. The corresponding (X, Y), which characterize the Gaussian channel, then read

$$X = \sqrt{\tfrac{1}{3}}\begin{pmatrix} \sqrt{2}\mathbb{1} & \\ & \mathbb{1} \end{pmatrix}, \tag{22}$$

$$Y = \tfrac{3+\sqrt{13}}{6}\begin{pmatrix} 5 & & 3\sqrt{2} & \\ & 5 & & -3\sqrt{2} \\ 3\sqrt{2} & & 4 & \\ & -3\sqrt{2} & & 4 \end{pmatrix}. \tag{23}$$

Proposition 5. *The Gaussian channel determined by* (22) *exhibits the PPT property but it is not entanglement-breaking.*

Proof. Equations (4) and (13) are satisfied as one verifies explicitly.
It remains to show that T is not entanglement-breaking. With the inequalities (14) in mind we observe that this is equivalent to

$$\max_{(\lambda,M)\in\mathcal{D}} \lambda < 1, \quad \text{where} \tag{24}$$

$$\mathcal{D} = \left\{ (\lambda, M) \in \mathbb{R}\times\mathcal{M}_4(\mathbb{R}) \;\middle|\; \begin{array}{rl} M &= M^T, \\ M &\geq \lambda i\sigma, \\ Y - M &\geq \lambda i X\sigma X^T \end{array} \right\}.$$

This is a semi-definite program [17], so that the corresponding dual program can be used to construct a witness which certifies (24). Its specific form is given in the appendix. □

DISCUSSION

Squeezing is a useful resource in many contexts, such as entanglement generation, metrology, information coding or cryptography. When restricted to the practically relevant Gaussian regime, we know that it is sometimes even a necessary resource. This is the fact for entanglement generation [18] and, as we have proven in this work, as well for super-activation of the quantum capacity. In the latter case, however, the proof of necessity relies on the framework—the basic idea behind the construction of all currently known instances of super-activation. In order to make a stronger statement, we would need to know whether there are other types of channels with zero quantum capacity [19].

Another question, which suggests itself, is how much squeezing is necessary within the given framework. Unfortunately, we do at the moment not see an approach towards settling this quantitative question.

Acknowledgements: We acknowledge financial support from the European project COQUIT, the CHIST-ERA/BMBF project CQC and the QCCC programme of the Elite Network of Bavaria.

APPENDIX

In the following we show how to certify (24). Note that with the notation $\tilde{Y} = 0_4 \oplus Y$, $\tilde{X} = i\sigma \oplus iX\sigma X^T$, $\tilde{M} = M \oplus -M$, the two inequalities in the definition of $\mathcal{D}$ can be rewritten as

$$\lambda\tilde{X} + \tilde{Y} + \tilde{M} \geq 0. \tag{25}$$

In the following we confirm (24) by showing that for all $(\lambda, M) \in \mathcal{D}$, $\lambda \leq 0.94$. For this purpose, let us define the witness matrix Ω,

$$\Omega = (A + iB) \oplus (A + iC). \tag{26}$$

$$A = \begin{pmatrix} a_1 & & -a_3 & \\ & a_1 & & a_3 \\ -a_3 & & a_2 & \\ & a_3 & & a_2 \end{pmatrix}, \quad a = \begin{pmatrix} 0.512 \\ 0.722 \\ 0.592 \end{pmatrix},$$

$$B = \begin{pmatrix} & b_1 & & b_3 \\ -b_1 & & b_3 & \\ & -b_3 & & b_2 \\ -b_3 & & -b_2 & \end{pmatrix}, \quad b = \begin{pmatrix} -0.212 \\ 0.552 \\ -0.368 \end{pmatrix},$$

$$C = \begin{pmatrix} & c_1 & & c_3 \\ -c_1 & & c_3 & \\ & -c_3 & & c_2 \\ -c_3 & & -c_2 & \end{pmatrix}, \quad c = \begin{pmatrix} 0.39 \\ -0.3 \\ 0.368 \end{pmatrix}.$$

and state some of its properties:

(i) Ω is positive definite.

(ii) $\forall(\lambda, M) \in \mathcal{D}:\ \mathrm{tr}\left[\Omega\tilde{M}\right] = i\mathrm{tr}\left[(B-C)M\right] = 0$, since $(B-C)$ is anti-symmetric and M is symmetric.

(iii) $\mathrm{tr}\left[\Omega\tilde{X}\right] = 2(b_1 + b_2 + \frac{2}{3}c_1 + \frac{1}{3}c_2) = 1$

(iv) $\mathrm{tr}\left[\Omega\tilde{Y}\right] = \left(1 + \frac{\sqrt{13}}{3}\right)\left(5a_1 + 4a_2 - 6\sqrt{2}a_3\right) < 0.94$

Let now be $(\lambda, M) \in \mathcal{D}$. Applying (ii) and (iii) in the first line and (i) together with (25) in the third line leads to

$$\begin{aligned} \lambda - \mathrm{tr}\left[\Omega\tilde{Y}\right] &= -\lambda \mathrm{tr}\left[\Omega\tilde{X}\right] - \mathrm{tr}\left[\Omega\tilde{Y}\right] - \mathrm{tr}\left[\Omega\tilde{M}\right] \\ &= -\mathrm{tr}\left[\Omega\left(\lambda\tilde{X} + \tilde{Y} + \tilde{M}\right)\right] \qquad (27) \\ &\leq 0. \end{aligned}$$

With (iv) we obtain $\lambda < 0.94$.

[1] C. E. Shannon. A mathematical theory of communication. *Bell System Tech. J.*, 27:379–423,623–656, 1948.

[2] G. Smith, J. A. Smolin, and J. Yard. Quantum communication with zero-capacity channels. *Science*, 321:1812–1815, 2008. 1102.4580v1 [quant-ph].

[3] G. Smith, J. A. Smolin, and J. Yard. Quantum communication with gaussian channels of zero quantum capacity. *Nature Photonics*, 5:624–627, 2011. 0807.4935 [quant-ph].

[4] K. Hammerer, A.S. Sørensen, and E.S. Polzik. Quantum interface between light and atomic ensembles. *Rev. Mod. Phys.*, 82:10411093, 2010.

[5] A. S. Holevo. *Probabilistic and statistical aspects of quantum theory*, chapter on Gaussian states, pages 187–218. Edizioni della Normale, 2011.

[6] J. Eisert and M. M. Wolf. *Quantum information with continous variables of atoms and light*, chapter on Gaussian quantum channels, pages 23–42. Imperial College Press, 2007. quant-ph/0505151.

[7] F. Caruso, J. Eisert, V. Giovannetti, and A. S. Holevo. Multi-mode bosonic gaussian channels. *New Journal of Physics*, 10(083030), 2008. 0804.0511v3 [quant-ph].

[8] M. Reck and A. Zeilinger. Experimental realization of any discrete unitary operator. *Phys. Rev. Lett.*, 73:58–61, 1994.

[9] Arvind, B. Dutta, N. Mukunda, and R. Simon. The real symplectic groups in quantum mechanics and optics. *Pramana*, 45:471, 1995. quant-ph/9509002v3.

[10] This equivalence can be seen from the similarity transformation $\begin{pmatrix} A - iB & \\ & A + iB \end{pmatrix} = \frac{1}{\sqrt{2}}\begin{pmatrix} \mathbb{1} & i\mathbb{1} \\ i\mathbb{1} & \mathbb{1} \end{pmatrix}\begin{pmatrix} A & B \\ -B & A \end{pmatrix}\frac{1}{\sqrt{2}}\begin{pmatrix} \mathbb{1} & -i\mathbb{1} \\ -i\mathbb{1} & \mathbb{1} \end{pmatrix}$.

[11] In phase space, θ corresponds to the transformation $\Gamma \mapsto \tilde{\theta}\Gamma\tilde{\theta}^T$ with $\tilde{\theta} = \bigoplus_{i=1}^{n} \mathrm{diag}(1, -1)$.

[12] A. S. Holevo. Entanglement-breaking channels in infinite dimensions. *Problems of Information Transmission*, 44:171–184, 2008. 0802.0235v1 [quant-ph].

[13] M. Horodecki, P. W. Shor, and M. B. Ruskai. General entanglement breaking channels. *Rev. Math. Phys*, 15:629–641, 2003. quant-ph/0302031.

[14] A. S. Holevo, M. E. Shirokov, and R. F. Werner. Separability and entanglement-breaking in infinite dimensions. *Russian Math. Surveys*, 60(N2), 2005. quant-ph/0504204.

[15] A. S. Holevo. *Mathematical horizons for quantum physics*, chapter 5: Two mathematical problems in quantum information theory, pages 109–131. World Scientific, 2010.

[16] M. M. Wolf. Not-so-normal mode decomposition. *Phys. Rev. Lett.*, 100(070505), 2008. 0707.0604 [quant-ph].

[17] S. Boyd and L. Vandenberghe. *Convex optimization*, chapter 4.6 and 5.9, pages 167–169, 265–266. Cambridge University Press, 2011.

[18] M. M. Wolf, J. Eisert, and M. B. Plenio. The entangling power of passive optical elements. *Phys. Rev. Lett.*, 90(047904), 2003. quant-ph/0206171.

[19] G. Smith and J.A. Smolin. Detecting incapacity of a quantum channel. *Phys. Rev. Lett.*, 108(230507), 2012. quant-ph/0206171.

PHYSICAL REVIEW A **79**, 012306 (2009)

Pairing in fermionic systems: A quantum-information perspective

Christina V. Kraus,[1] Michael M. Wolf,[1,2] J. Ignacio Cirac,[1] and Géza Giedke[1]
[1]*Max Planck Institute for Quantum Optics, Hans-Kopfermann-Strasse 1, D-85748 Garching, Germany*
[2]*Niels Bohr Institute, Copenhagen University, Blegdamsvej 17, DK-2100 Copenhagen Ø, Denmark*
(Received 18 November 2008; published 8 January 2009)

The notion of "paired" fermions is central to important condensed-matter phenomena such as superconductivity and superfluidity. While the concept is widely used and its physical meaning is clear, there exists no systematic and mathematical theory of pairing that would allow us to unambiguously characterize and systematically detect paired states. We propose a definition of pairing and develop methods for its detection and quantification applicable to current experimental setups. Pairing is shown to be a quantum correlation different from entanglement, giving further understanding in the structure of highly correlated quantum systems. In addition, we will show the resource character of paired states for precision metrology, proving that the BCS states allow phase measurements at the Heisenberg limit.

DOI: 10.1103/PhysRevA.79.012306 PACS number(s): 03.67.Mn, 05.30.Fk, 71.10.−w

I. INTRODUCTION

The notion of pairing in fermionic systems is at least as old as the seminal work of Bardeen, Cooper, and Schrieffer explaining superconductivity [1]. The formation of fermionic pairs with opposite spin and momentum is not only the source for the vanishing resistance in solid-state systems, but it can also explain many other interesting phenomena, like superfluidity in helium-3 or inside a neutron star.

For instance, with recent progress in the field of ultracold quantum gases, fermionic pairing has gained again a lot of attention [2–9]. These experiments allow an excellent control over many parameters inherent to the system, offering a unique testing ground for existing theories and an exploration of new and exotic phases. However, the notion of pairing in these systems is less clear and sometimes even controversial. Recent experiments on the BEC-BCS crossover have caused a heated debate over whether the obtained data were in agreement with pairing [7,10–12]. In addition, pairing without superfluidity [13] has been observed in these experiments, raising fundamental questions on quantum correlations in fermionic many-body systems.

Motivated by these exciting experiments and the central role pairing plays in many physical phenomena, and by the perceived lack of accepted criteria to verify the presence of pairing in a quantum state, we propose a clear and unambiguous definition of pairing intended to capture its two-particle nature and to allow a systematic study of the set of paired states and its properties. We employ methods and tools from quantum-information theory to gain a better understanding of the set of fermionic states that display pairing. In particular, we develop tools for the systematic detection and for the quantification of pairing, which are applicable to current experiments. Our approach is inspired by concepts and methods from entanglement theory, thus building a bridge between quantum-information science and condensed-matter physics.

Since they contain nontrivial quantum correlations, paired states belong to the set of entangled many-body states. However, pairing will turn out to be not equivalent to any known concept of entanglement in systems of indistinguishable particles [14–29] but to represent a particular type of quantum correlation of its own. We will show that these correlations can be exploited for quantum-phase estimation. Hence pairing constitutes a resource in state estimation using fermions as much as entangled states with spins.

This paper is organized as follows. After the introduction of the language necessary for the description of fermionic systems in Sec. II, we will introduce the general framework of pairing theory in Sec. III. This part includes our definition of pairing and methods for its detection and quantification. In order to validate the theory, we will apply it to two different classes of fermionic states in Secs. IV and V. We start out with pairing in fermionic Gaussian states in Sec. IV. The interest in this family of states is twofold. First, the pairing problem can be solved completely in this case, so that Gaussian states are particularly interesting from a conceptual point of view. Second, there exists a relation between pure fermionic Gaussian states and the BCS states of superconductivity (see Sec. II D for the details), which are examples of paired states par excellence. This enables us to translate methods developed for the detection and quantification of pairing for Gaussian states to the BCS states. The reader interested in the application of our pairing theory to experimental application is referred to Sec. V. There we study pairing for number-conserving states, i.e., states commuting with the number operator. This class includes the states appearing in the BEC-BCS crossover, and we will develop tools for the detection of pairing tailored for these systems. In Sec. VI, we will show that certain classes of paired states constitute a resource for quantum-phase estimation, proving that pairing is a resource similar to entanglement.

II. FERMIONIC STATES

In this section, we review the basic concepts needed for the understanding of fermionic systems. We start out with some notation used for the description of fermionic systems in second quantization in Sec. II A. As pairing is a special sort of correlation, we continue with a review on quantum correlations and entanglement in systems of indistinguishable particles in Sec. II B. This general part is followed by

 ©2009 The American Physical Society

the introduction of fermionic Gaussian states and number-conserving states in Secs. II C and II D. The latter includes the introduction of BCS states and their relation to the Gaussian states. As this part is only necessary for the application of the pairing theory to these concrete examples in Secs. IV and V, it is possible to skip this part at the beginning, and then refer to it later on.

A. Basic notation

We consider fermions on an M-dimensional single-particle Hilbert space $\mathcal{H}=\mathbb{C}^M$. All observables are generated by the creation and annihilation operators $a_j^\dagger$ and a_j, $j=1,\ldots,M$, which satisfy the canonical anticommutation relations (CAR) $\{a_k,a_l\}=0$ and $\{a_k,a_l^\dagger\}=\delta_{kl}$. We say $a_j^\dagger$ creates a particle in mode (or single-particle state) e_j, where $\{e_j\}\subset\mathbb{C}^M$ denotes the canonical orthonormal basis of $\mathcal{H}$. In general, for any normalized $f\in\mathcal{H}$, we define $a_f\equiv\Sigma_k f_j a_j$, the annihilation operator for mode f.

Sometimes a description using the $2M$ Hermitian Majorana operators $c_{2j-1}=a_j^\dagger+a_j$, $c_{2j}=(-i)(a_j^\dagger-a_j)$, which satisfy $\{c_k,c_l\}=2\delta_{kl}$, is more convenient.

The Hilbert space of the many-body system, the antisymmetric Fock space over M modes, $\mathcal{A}_M$, is spanned by the orthonormal Fock basis defined by

$$|n_1,\ldots,n_M\rangle=(a_1^\dagger)^{n_1}\cdots(a_M^\dagger)^{n_M}|0\rangle, \tag{1}$$

where the vacuum state $|0\rangle$ fulfills $a_j|0\rangle=0\ \forall\ j$. The $n_j\in\{0,1\}$ are the eigenvalues of the mode occupation number operators $n_j=a_j^\dagger a_j$. The N-particle subspace spanned by vectors of the form (1) satisfying $\Sigma_i n_i=N$ is denoted by $\mathcal{A}_M^{(N)}$. The set of density operators on the Hilbert space $\mathcal{H}=\mathcal{A}_M,\mathcal{A}_M^{(N)}$ is denoted by $\mathcal{S}(\mathcal{H})$.

Linear transformations of the fermionic operators which preserve the CAR are called canonical transformations. They are of the form $c_k\mapsto c_k'=\Sigma_i O_{kl}c_l$, where $O\in O(2M)$ is an element of the real orthogonal group. These transformations can be implemented by unitary operations U_O on $\mathcal{A}_M$ which are (for $\det O=1$) generated by quadratic Hamiltonians in the c_j (see, e.g., [30]). The subclass of canonical operations that commute with the total particle number $N_{\mathrm{op}}=\Sigma_i n_i$ are called passive transformations. They take a particularly simple form in the complex representation $a_k\mapsto a_k'=\Sigma_l U_{kl}a_l$, where U is unitary on the single-particle Hilbert space $\mathcal{H}$, i.e., they describe (quasi)free time evolution of independent particles. Canonical transformations that do not commute with N_{op} are called active. They mix creation and annihilation operators.

B. Quantum correlations of fermionic states

The notion of "pairing" used in the description of superconducting solids, superfluid liquids, baryons in nuclei, etc. is always associated with a correlated fermionic system. The subject of quantum correlations in fermionic systems is vast (see [31], and for instance [32–34]). In recent years, there has been renewed interest from the perspective of quantum-information theory. There quantum correlations (also known as entanglement) of distinguishable systems (qubits) play a crucial role as a resource enabling certain state transformations or information-processing tasks. The detailed quantitative analysis of quantum correlations motivated by this has proven to be valuable also in the understanding of condensed-matter systems (see [35] for a review).

In contrast to the usual quantum-information setting, which studies the entanglement of distinguishable particles, the indistinguishable nature of the fermions is of utmost importance in the settings of our interest. The existing concepts for categorizing entanglement in systems of indistinguishable particles fall into two big classes: Entanglement of modes [14–22] and entanglement of particles. Entanglement of particles has been considered, e.g., in [23–29], leading to the concept of Slater rank [24,25], being the generalization of the Schmidt rank to indistinguishable particles. We show in Sec. III that our definition of pairing does not coincide with any of the existing ideas. We refrain from giving an exhaustive review on the existing concepts, referring the interested reader to the mentioned literature and references therein, and we restrict ourselves to the following definition:

Definition II.1. A pure fermionic state $\rho_p^{(N)}=|\Psi_p^{(N)}\rangle\langle\Psi_p^{(N)}|\in\mathcal{S}(\mathcal{A}_M^{(N)})$ is called a *product state*, if there exists a passive transformation $a_k\mapsto a_k'$ such that

$$|\Psi_p^{(N)}\rangle=\prod_{j=1}^{N}a_j'^\dagger|0\rangle. \tag{2}$$

A state ρ_s is called *separable*, if it can be written as the convex combination of product states, i.e.,

$$\rho_s=\sum_{p=1}^{K}\lambda_p\rho_p^{(N_p)}, \tag{3}$$

where $\Sigma_{p=1}^K\lambda_p=1$, $\lambda_p\geqslant 0$ and all $\rho_p^{(N_p)}\in\mathcal{S}(\mathcal{A}_M^{(N_p)})$ are product states. All other states are said to have "Slater number larger than 1" and are called *entangled* (in the sense of [24,25]).

We denote the set of all separable states by $\mathcal{S}_{\mathrm{sep}}$ and by $\mathcal{S}_{\mathrm{sep}}^{(N)}\equiv\mathcal{S}_{\mathrm{sep}}\cap\mathcal{S}(\mathcal{A}_M^{(N)})$ the set of all separable states of particle number N.

Note that the sets $\mathcal{S}_{\mathrm{sep}}$, $\mathcal{S}_{\mathrm{sep}}^{(N)}$ of separable states are convex and invariant under passive transformations. Both properties will be useful later on.

Separable states have only correlations resulting from their antisymmetric nature and classical correlations due to mixing. In the terminology of Refs. [24,25], they have Slater number one and describe unentangled particles. These states will certainly not contain correlations associated with pairing. (Note that they can be mode-entangled for an appropriate partition of modes.)

Besides basis change, there are other operations that do not create quantum correlations, and it is useful to see that the set of separable states is invariant under them.

Lemma II.2. Let $\rho\in\mathcal{S}_{\mathrm{sep}}$ be a separable state. Then the state after measuring the particle number $n_h=a_h^\dagger a_h$ in some mode h is separable for both possible outcomes $n_h=0,1$. Furthermore, $\rho_h\equiv\mathrm{tr}_{a_h}[\rho]$, the reduced state obtained by tracing out the mode a_h, is also separable.

Proof. As $\mathcal{S}_{\mathrm{sep}}$ is convex, it is sufficient to prove the claim for product states ρ. Let $|\Psi\rangle=\Pi_{j=1}^N a_{f_j}^\dagger|0\rangle$ be the vector in Hilbert space corresponding to ρ. Our aim is to show that $|\Psi\rangle$

$=|\Psi_0\rangle+|\Psi_1\rangle$, where $|\Psi_l\rangle$ are product states and $n_h=l$ eigenstates of the occupation number operator n_h. If h is in the span of $\{f_{1\leqslant k\leqslant N}\}$ or orthogonal to it, the state already is an n_h eigenstate and we are done. Otherwise, define f_{N+1} orthogonal to the $f_{k\leqslant N}$ such that $h\in\text{span}\{f_{1\leqslant k\leqslant N+1}\}$ and define another orthonormal basis $\{g_j\}$ for the span with $g_1=h$ and $g_2 \propto f_{N+1}-(hf_{N+1})h$ [here (hf_{N+1}) denotes the inner product on the single-particle Hilbert space]. Then we can write $|\Psi\rangle = a_{f_{N+1}}a^\dagger_{f_{N+1}}\Pi_{j=1}^N a^\dagger_{f_j}|0\rangle=(xa_{g_1}+ya_{g_2})\Pi_{j=1}^{N+1}a^\dagger_{g_j}|0\rangle$ for some $x,y\in\mathbb{C}$. Hence, $|\Psi\rangle=|\Psi_0\rangle+|\Psi_1\rangle$ with $|\Psi_0\rangle=x\Pi_{j=2}^{N+1}a^\dagger_{g_j}|0\rangle$ and $|\Psi_1\rangle=-ya^\dagger_h\Pi_{j=3}^{N+1}a^\dagger_{g_j}|0\rangle$, which both clearly are product states. The reduced state $\text{tr}_h[|\Psi\rangle\langle\Psi|]$ is the statistical mixture of $|\Psi_0\rangle$ and $|\Psi_1\rangle$ and therefore clearly separable. ■

C. Fermionic Gaussian states

Fermionic Gaussian states are represented by density operators that are exponentials of a quadratic form in the Majorana operators. A general multimode Gaussian state is of the form

$$\rho = K\exp\left[-\frac{i}{4}c^T G c\right], \tag{4}$$

where $c=(c_1,\ldots,c_{2M})$, K is a normalization constant, and G is a real antisymmetric $2M\times 2M$ matrix. Every antisymmetric matrix can be brought to a block-diagonal form

$$OGO^T=\bigoplus_{j=1}^{M}\begin{pmatrix}0 & -\beta_j\\ \beta_j & 0\end{pmatrix} \tag{5}$$

by a special orthogonal matrix $O\in\text{SO}(2M)$.

From Eq. (4), it is clear that Gaussian states have an interpretation as thermal (Gibbs) states corresponding to a Hamiltonian H that is a quadratic form in the c_k, i.e., $H=\frac{i}{4}c^TGc=\frac{i}{4}\Sigma_{k>l}G_{kl}[c_k,c_l]$, and the form Eq. (5) shows that every Gaussian state has a normal-mode decomposition in terms of M single-mode "thermal states" of the form $\sim\exp(-\beta a^\dagger a)$. From this one can see that the state is fully determined by the expectation values of quadratic operators a_ia_j and $a_i^\dagger a_j$. These are collected in a convenient form in the real and antisymmetric covariance matrix Γ, which is defined via

$$\Gamma_{kl}=\frac{i}{2}\text{tr}(\rho[c_k,c_l]). \tag{6}$$

It can be brought into block-diagonal form by a canonical transformation,

$$O\Gamma O^T=\bigoplus_{i=1}^{M}\begin{pmatrix}0 & \lambda_j\\ -\lambda_j & 0\end{pmatrix}. \tag{7}$$

For every valid density operator, $\lambda_j\in[-1,1]$, and the eigenvalues of Γ are given by $\pm i\lambda_j$. Hence, every Γ corresponding to a physical state has to fulfill $i\Gamma\leqslant\mathbb{1}$ or, equivalently, $\Gamma\Gamma^\dagger\leqslant\mathbb{1}$, and to each such Γ corresponds a valid Gaussian density operator where the relation between G and Γ is given by $\lambda_j=\tanh(\beta_j/2)$. The covariance matrix of the ground state of H is obtained in the limit $|\beta_j|\to\infty$, i.e., $\lambda_j\to\text{sgn}(\beta_j)$. In fact, this shows that every pure Gaussian state is the ground state to some quadratic Hamiltonian. The purity of the state can be easily determined from the covariance matrix as a Gaussian state is pure if and only if $\Gamma^2=-\mathbb{1}$ (see, e.g., [36]).

As mentioned, Gaussian states are fully characterized by their covariance matrix and all higher correlations can be obtained from Γ by Wick's theorem (see, e.g., [36]) via

$$i^p\text{tr}[\rho c_{j_1}\cdots c_{j_{2p}}]=\text{Pf}(\Gamma_{j_1,\ldots,j_{2p}}), \tag{8}$$

where $1\leqslant j_1<\cdots<j_{2p}\leqslant 2M$ and $\Gamma_{j_1,\ldots,j_{2p}}$ is the corresponding $2p\times 2p$ submatrix of Γ. $\text{Pf}(\Gamma_{j_1,\ldots,j_{2p}})^2=\det(\Gamma_{j_1,\ldots,j_{2p}})$ is called the Pfaffian.

In some cases it is more appropriate to use a different ordering of the Majorana operators, the so-called q-p ordering $c=(c_1,c_3,\ldots,c_{2M-1};c_2,c_4,\ldots,c_{2M})$, opposed to the mode-ordering introduced at the beginning. When using the q-p ordering, the relation between the real and complex representation is given by

$$c^T=\Omega a^T,\quad \Omega=\begin{pmatrix}\mathbb{1} & \mathbb{1}\\ i\mathbb{1} & -i\mathbb{1}\end{pmatrix}, \tag{9}$$

where $a=(a_1,\ldots,a_M,a_1^\dagger,\ldots,a_M^\dagger)$. The transformation matrix Ω fulfills $\Omega\Omega^\dagger=2\mathbb{1}$.

In the q-p ordering, the covariance matrix obtains the following block structure:

$$\tilde{\Gamma}=\begin{pmatrix}\Gamma_q & \Gamma_{qp}\\ -\Gamma_{qp}^T & \Gamma_p\end{pmatrix}. \tag{10}$$

Finally, for some purposes it is more convenient to use the complex representation, where the covariance matrix is of the form

$$\Gamma_c=\frac{1}{4}\Omega^\dagger\tilde{\Gamma}\bar{\Omega}=\begin{pmatrix}Q & R\\ \bar{R} & \bar{Q}\end{pmatrix}, \tag{11}$$

where $Q_{kl}=\langle i/2[a_k,a_l]\rangle$, $R_{kl}=\langle i/2[a_k,a_l^\dagger]\rangle$, and $\bar{Q}$ denotes the complex conjugate. Note that $R^\dagger=-R$ and $Q^T=-Q$ and hence $\Gamma_c^T=-\Gamma_c$. The condition $\tilde{\Gamma}\tilde{\Gamma}^\dagger\leqslant\mathbb{1}$ takes the form $4\Gamma_c\Gamma_c^\dagger\leqslant\mathbb{1}$.

The description of ρ by its covariance matrix is especially convenient to describe the effect of canonical transformations, i.e., time evolutions generated by quadratic Hamiltonians: if $c_k\mapsto\Sigma_l O_{kl}c_l$ in the Heisenberg picture, then $\Gamma\mapsto O\Gamma O^T$ in the Schrödinger picture. For a passive transformation $a_k\mapsto a_k'=\Sigma_l U_{kl}a_l$, the q-p-ordered Majorana operators transform as

$$c^T\mapsto c'^T=O_pc^T,\quad O_p=\begin{pmatrix}X & Y\\ -Y & X\end{pmatrix}, \tag{12}$$

where $X=\text{Re}(U)$ is the real part of the unitary U, and $Y=\text{Im}(U)$ is the imaginary part. Note that O_p is both orthogonal and symplectic. The behavior of Γ_c under a passive transformation is particularly simple: Q and R transform according to $Q\mapsto UQU^T$ and $R\mapsto URU^\dagger$.

Passive transformations can be used to transform *pure* fermionic states to a simple standard form, the so-called Bloch-Messiah reduction [37]. The q-p-ordered CM $\tilde{\Gamma}_{\text{BCS}}$ takes the form (10), where

$$\Gamma_q = -\Gamma_p = \bigoplus_k \begin{pmatrix} 0 & -2\,\mathrm{Im}(u_k v_k^*) \\ 2\,\mathrm{Im}(u_k v_k^*) & 0 \end{pmatrix}, \quad (13)$$

$$\Gamma_{qp} = \bigoplus_k \begin{pmatrix} |u_k|^2 - |v_k|^2 & 2\,\mathrm{Re}(u_k v_k^*) \\ -2\,\mathrm{Re}(u_k v_k^*) & |u_k|^2 - |v_k|^2 \end{pmatrix}. \quad (14)$$

In Hilbert space, the state in standard form is given by

$$|\Psi_{\mathrm{Gauss}}^{(\bar{N})}\rangle = \prod_k (u_k + v_k a_k^\dagger a_{-k}^\dagger)|0\rangle, \quad (15)$$

where $u_k, v_k \in \mathbb{C}$, $|u_k|^2 + |v_k|^2 = 1$, and $\bar{N} = \Sigma_k \langle a_k^\dagger a_k \rangle = 2\Sigma_k |v_k|^2$. This comprises the kind of "paired" states appearing in the BCS theory of superconductivity [1] with $k \equiv (\vec{k}, \uparrow)$, $-k \equiv (-\vec{k}, \downarrow)$. We will refer to these states as *Gaussian BCS states*. We would like to stress the fact that every pure Gaussian state is a Gaussian BCS state in some basis.

D. Number-conserving fermionic states

For the application to physical systems, we are interested in states for which the particle number is a conserved quantity. We call ρ a number-conserving state if $[\rho, N_{\mathrm{op}}] = 0$, where N_{op} denotes the total number operator. Thus, the density operator of a number-conserving state can be written as a mixture of N_{op} eigenstates. In particular, all separable states as defined in Def. II.1 are number-conserving.

The Gaussian BCS wave function (15) is not number-conserving (except for the case $\Sigma_k |u_k v_k| = 0$ that either u_k or v_k vanishes for every mode), but a relation to these states can be established via the identity

$$|\Psi_{\mathrm{Gauss}}^{(\bar{N})}\rangle = \sum_{N=0}^{2M} \lambda_N |\Psi_{\mathrm{BCS}}^{(N)}\rangle, \quad (16)$$

where the number-conserving $2N$-particle BCS state is given by

$$|\Psi_{\mathrm{BCS}}^{(N)}\rangle = C_N \left(\sum_{k=1}^{M} \alpha_k P_k^\dagger \right)^N |0\rangle, \quad (17)$$

where we have introduced the pair creation operator $P_k^\dagger = a_k^\dagger a_{-k}^\dagger$. The coefficients α_k are related to u_k and v_k via $\alpha_k = v_k / u_k$, and C_N is a normalization constant, which is seen to be

$$C_N = \left((N!)^2 \sum_{j_1 < \cdots < j_N} |\alpha_{j_1}|^2 \cdots |\alpha_{j_N}|^2 \right)^{-1/2}$$

by rewriting Eq. (17) as

$$C_N N! \sum_{j_1 < j_2 < \ldots < j_N} \alpha_{k_1} \cdots \alpha_{k_N} P_{k_1}^\dagger \cdots P_{k_N}^\dagger |0\rangle. \quad (18)$$

The coefficients $\lambda_N = (\Pi_k u_k)/(N! C_N)$ can be interpreted as the probability amplitude of being in state $|\Psi_{\mathrm{BCS}}^{(N)}\rangle$ since $\Sigma_N |\lambda_N|^2 = 1$. We will in general drop the term *number-conserving* and refer to states of the form (17) as *BCS states*.

Whenever the distribution of the λ_N is sharply peaked around some average particle number $\bar{N}$, expectation values of relevant observables for the number-conserving BCS states $|\Psi_{\mathrm{BCS}}^{(\bar{N})}\rangle$ are approximated well by the expectation values of the Gaussian BCS state. This relation will turn out to be very useful later on, as results on Gaussian states can be translated into results on number-conserving BCS states.

III. PAIRING THEORY

In this section, we introduce a precise definition of pairing as a property of quantum states.

A. Motivation and statement of the definition

The simplest system in which we can find pairing consists of two particles and four modes.[1] The prototypical paired state, for example the spin-singlet of two electrons with opposing momenta, is of the form

$$|\Phi\rangle = \frac{1}{\sqrt{2}} (a_1^\dagger a_2^\dagger + a_3^\dagger a_4^\dagger)|0\rangle. \quad (19)$$

The states describing many Cooper pairs in BCS theory are generalizations of $|\Phi\rangle$.

The state $|\Phi\rangle$ describes correlations between the two particles that cannot be reproduced by any uncorrelated state, and it can be completely characterized by one- and two-particle expectations (consisting of no more than two creation and annihilation operators each). This is a characteristic of the two-particle property "pairing" that we propose to make the central *defining* property of paired states in the general case of many modes, many particles, and mixed states. Since, moreover, we would call the state $|\Phi\rangle$ paired no matter what basis the mode operators a_i refer to and we want it to comprise all BCS states, we are led to the following list of requirements that a sensible definition of pairing should fulfill:

(i) States that have no internal quantum correlation must be unpaired. These are the separable states (3).

(ii) Pairing must reveal itself by properties related to one- and two-particle expectations only.

(iii) Pairing should be a basis-independent property.

(iv) The standard "paired" states appearing in the description of solid-state and condensed-matter systems, i.e., the BCS states with wave function (17), must be captured by our definition.

Further, it would be desirable that there exist examples of paired states that are a resource for some quantum-information application.

Let us define the following:

Definition III.1. The set of all operators $\{O_\alpha\}_\alpha$ on $\mathcal{A}_M$, which are the product of at most two creation and two annihilation operators, is called the set of *two-particle operators*. We denote it by A_2.

These operators capture all one- and two-particle properties of a state ρ and should therefore contain all information about pairing. We will call a state ρ paired if it can be distinguished from separable states by looking at observables in

[1] For three modes, all pure two-particle states are of product form.

A_2 alone. This is formalized in the following definition:

Definition III.2. A fermionic state ρ is called *paired* if there exists a set of operators $\{O_\alpha\}_\alpha \subseteq A_2$ such that the expectation values $\{\mathrm{tr}[\rho O_\alpha]\}$ cannot be reproduced by any separable state $\rho_s \in \mathcal{S}_{\mathrm{sep}}$. States that are not paired are called *unpaired*.

This definition automatically fulfills our first two requirements by definition. The third, basis independence, clearly holds, since the set of separable states is invariant under passive transformations. We will show that the last requirement is met, both for Gaussian and number-conserving BCS states, i.e., all of them are paired (see Lemma V.3 and Sec. IV B). Moreover, in Sec. VI we can show that there exist paired states that are a resource for quantum metrology.

For states with a fixed particle number, i.e., $\rho \in \mathcal{S}(\mathcal{A}_M^{(N)})$, it is sufficient to compare with expectation values on N-particle separable states $\rho_s^{(N)} \in \mathcal{S}_{\mathrm{sep}}^{(N)}$, as for all other states the expectation values of $\langle \Sigma_i n_i \rangle$ and $\langle (\Sigma_i n_i)^2 \rangle$ differ due to the particle number constraint. For number-conserving states, only number-conserving observables lead to nonvanishing expectation values and one can thus restrict to linear combinations of $a_i^\dagger a_j$, $a_i^\dagger a_j^\dagger a_k a_l$.

For Gaussian states, pairing must reveal itself by properties of the covariance matrix, as all higher correlations can be obtained from it via Eq. (8). This important fact enables us to give a complete solution of the pairing problem for fermionic Gaussian states, which we present in Sec. IV.

B. Relation of pairing and entanglement

Paired states are fermionic states exhibiting nontrivial quantum correlations. In particular, by definition paired states are inseparable, i.e., entangled in the sense of [24,25]. This raises immediately the following question: Is pairing equivalent to entanglement? Below, we provide examples of entangled but unpaired states that demonstrate that pairing is not equivalent to entanglement (of particles) but represents a special type of quantum correlation.[2]

Lemma III.3. There exist states that are entangled according to the Slater rank concept, but not paired.

Proof. Consider the state $|\Psi_4\rangle = \frac{1}{2}(a_1^\dagger a_2^\dagger a_3^\dagger a_4^\dagger + a_5^\dagger a_6^\dagger a_7^\dagger a_8^\dagger)|0\rangle$, which is entangled according to the Slater rank definition. However, one sees immediately that the one- and two-particle expectations for $|\Psi_4\rangle$ are the same as for $\rho_s^{(4)} = \frac{1}{2}|\Phi_1\rangle\langle\Phi_1| + \frac{1}{2}|\Phi_2\rangle\langle\Phi_2|$, where $|\Phi_1\rangle = a_1^\dagger a_2^\dagger a_3^\dagger a_4^\dagger|0\rangle$, $|\Phi_2\rangle = a_5^\dagger a_6^\dagger a_7^\dagger a_8^\dagger|0\rangle$. Since $\rho_s^{(4)}$ is a product state, $|\Psi_4\rangle$ is not paired. One can construct further examples in a similar manner using, e.g., other states with higher Slater rank. ■

Since pairing is defined via expectation values of one- and two-particle operators only, one might wonder whether pairing is related to entanglement of the two-particle reduced state. To study this relation, we recall the definition of the *two-particle density operator* and the closely related *two-particle density matrix* (see, e.g., [38]):

Definition III.4. Let ρ be the density operator of a fermionic state. Then $O_{(ij)(kl)}^{(\rho)} = \mathrm{tr}[\rho a_i^\dagger a_j^\dagger a_l a_k]$ is called the *two-particle reduced density matrix* (RDM). It is usually not normalized and fulfills $\mathrm{tr}[O^{(\rho)}] = \langle N_{\mathrm{op}}^2 \rangle - \langle N_{\mathrm{op}} \rangle$. The operator $\rho_2 = O^{(\rho)}/\mathrm{tr}[O^{(\rho)}]$ is called the *reduced two-particle density operator* (RDO).

Note the crucial difference between the two-particle RDM and the RDO. While the RDM contains all two-particle correlations of ρ, the RDO corresponds to the two-particle state of any two particles when the rest of the system is discarded. We would like to emphasize that pairing is *not* equivalent to entanglement of the RDO, and therefore it is a property of the one- and two-particle expectations:

Lemma III.5. Let $|\Psi_{\mathrm{BCS}}^{(N)}\rangle$ be a number-conserving BCS state as defined in Eq. (17) with $\alpha_k = 1 \,\forall\, k = 1, \ldots, M$. Then its two-particle RDO (see Def. III.4) $\rho_{\mathrm{BCS},2}^{(N)}$ is always paired. However, $\rho_{\mathrm{BCS},2}^{(N)}$ is entangled if and only if $M > 3N-2$.

The proof is given in Appendix E.

We would like to stress the point that Lemma III.5 shows the existence of paired states that are not entangled. Having assured that our definition of pairing does not coincide with entanglement, we now turn to methods of detecting and quantifying pairing.

C. Methods for detecting pairing

Taking Def. III.2, we aim at finding tools that can be used for the detection and quantification of pairing. These will be applied to systems of Gaussian states and number-conserving states in Secs. IV and V, respectively. In this section, we exploit the convexity of the set of unpaired states to introduce witness operators and obtain a geometrical picture of the set. The quantification of pairing via pairing measures will be discussed in Sec. III D.

Given a fermionic density operator, we are interested in an operational method to determine whether it is paired or not. As in the case of separability, this simple-sounding question will turn out to be rather difficult to answer in general.

Starting from Def. III.2, it is clear that the set of unpaired states is convex. This suggests the use of the Hahn-Banach separation theorem as a means to certify that a given density operator is not in the set of paired states. In analogy to the entanglement witnesses in quantum-information theory [39], we define the following:

Definition III.6. A *pairing witness* W is a Hermitian operator that fulfills $\mathrm{tr}[W\rho_u] \geqslant 0$ for all unpaired states ρ_u, and for which there exists a paired state ρ such that $\mathrm{tr}[W\rho] < 0$. We then say that W *detects* the paired state ρ.

The witness defines a hyperplane in the space of density operators such that the convex set of unpaired states lies wholly on that side of the plane characterized by $\mathrm{tr}[\rho W] > 0$. According to the Hahn-Banach theorem [40], for every unpaired state there exists a witness operator that detects it. In principle, a witness operator can be an operator involving an arbitrary number of creation and annihilation operators. However, since definition of pairing refers only to expectation values of operators in A_2, it is enough to restrict to

[2]Note that our basis-independent definition clearly has no relation to entanglement of modes, which is basis-dependent. The product states of Def. II.1 can be mode-entangled for some choice of partition of modes, e.g., $(1/\sqrt{2})(a_1^\dagger + a_2^\dagger)|0\rangle$ is entangled in modes $a_1^\dagger$ and $a_2^\dagger$.

operators from that set. This represents a significant simplification both mathematically (witness operators from a finite dimensional set) and experimentally, since operators involving more than two-body correlations are typically very difficult to measure.

The construction of entanglement witnesses detecting all entangled states is an unsolved problem in entanglement theory, and we will not be able to give a complete solution to the problem of finding all pairing witnesses either. However, in Sec. V we will construct witnesses for a large subclass of BCS states by using the correspondence between number-conserving and Gaussian BCS states.

Whether a state ρ is paired can be determined from a finite set of real numbers, namely the expectation values of a Hermitian basis $\{O_\alpha\}$ of A_2. This allows us to reformulate the pairing problem as a geometric question on convex sets in finite-dimensional Euclidean space, describe a complete set of pairing witnesses, and deduce a relation to the ground-state energies of quadratic Hamiltonians.

Consider a set $\{O_\alpha, \alpha=1,\ldots,K\}\subset A_2$ of Hermitian operators in A_2 that are not necessarily a basis. Denote by $\vec{O}$ the vector with components O_α. We define the set of all expectation values of $\vec{O}$ for separable states

$$C_{\vec{O}} = \{\vec{v} = \mathrm{tr}[\vec{O}\rho_s] : \rho_s \in S_{\mathrm{sep}}\} \subset \mathbb{R}^K. \tag{20}$$

For a state ρ, let $\vec{v}_\rho \equiv \mathrm{tr}[\vec{O}\rho]$. By definition, ρ is paired if $\vec{v}_\rho \notin C_{\vec{O}}$. As the set of separable states is convex, so is $C_{\vec{O}}$. Hence, we can use a result of convex analysis to check if $\vec{v}_\rho \notin C_{\vec{O}}$ (see, e.g., [41]):

Lemma III.7. Let $C\subset\mathbb{R}^N$ be a closed convex set, and let $\vec{v}\in\mathbb{R}^N$. Then

$$\vec{v}\in C \Leftrightarrow \forall\, \vec{r}\in\mathbb{R}^N : \vec{v}\cdot\vec{r} \geqslant E(\vec{r}) = \inf_{\vec{w}\in C} \vec{w}\cdot\vec{r}. \tag{21}$$

For our purposes, this translates into the following result:

Lemma III.8. For a vector of observables $\vec{O} = (O_1,\ldots,O_K)$ let $H(\vec{r}) = \vec{r}\cdot\vec{O}$ and $E(\vec{r}) = \inf_{\rho\in S_{\mathrm{sep}}}\{\mathrm{tr}[H(\vec{r})\rho]\}$. Then $W(\vec{r}) \equiv H(\vec{r}) - E(\vec{r})$ is a pairing witness, whenever $E(\vec{r}) \neq \inf_{\mathrm{all}\ \rho}\{\mathrm{tr}[\rho H(\vec{r})]\}$.

If $\{O_\alpha\}$ form a basis of A_2, then $W(\vec{r})$ is a complete set of witnesses in the sense that all paired states are detected by some $W(\vec{r})$, i.e., ρ is unpaired iff $\mathrm{tr}[W(\vec{r})\rho]\geqslant 0 \forall\ \vec{r}$.

Proof. The witness property of $W(\vec{r})$ is obvious from the definition of $E(\vec{r})$.

For the second part, "if" is clear and "only if" is seen as follows: By Lemma III.7, if $\mathrm{tr}[W(\vec{r})\rho]\geqslant 0\forall\ \vec{r}$, then $\vec{v}_\rho \in C$, i.e., the expectation values can be reproduced by a separable state. But since all expectation values of operators $\in A_2$ can be computed from $\vec{v}_\rho$, this implies all two-particle expectations of ρ can be thus reproduced, i.e., ρ is unpaired. □

For an M-mode system with annihilation operators a_i, a standard choice of O_α is, e.g., given by the real and imaginary parts of $\{(a_i^\dagger a_j^\dagger a_k a_l)_{i>j,k>l}, (a_i^\dagger a_j^\dagger)_{i>j}, (a_i^\dagger a_j)_{i\geqslant j}\}$, i.e., the dimension of A_2 (as a real vector space) is $K = M^2(M-1)^2/2 + 2M^2$.

Thus Lemma III.8 gives a necessary and sufficient criterion of pairing and provides a geometrical picture of the pairing problem. While the proof that a state is unpaired will in general be difficult as it requires knowledge of all $E(\vec{r})$ and experimentally the measurement of a complete set of observables, practical sufficient conditions for pairing can be obtained by restricting to a subset $O\subset A_2$. We will show in Sec. V A that for a certain choice of $\{O_\alpha\}\subset A_2$, the set $C_{\vec{O}}$ has a very simple form and allows a good visualization of the geometry of paired states and the detection of all BCS states up to passive transformations.

To provide a way to determite $E(\vec{r})$ used in Lemma III.8, we point out an interesting connection to the covariance matrices Γ_c [cf. Eq. (11)] of Gaussian states: even for number-conserving states, $E(\vec{r})$ is given by a quadratic minimization problem in terms of Γ_c.

Lemma III.9. Let $E(\vec{r})$ and $H(\vec{r})$ be as in Lemma III.8 and let $\vec{O} = \{a^\dagger_i a^\dagger_j a_k a_l, a^\dagger_i a_j\}$ and group the components of $\vec{r}$ in two subsets $(\vec{r})_{ijkl}$ and $(\vec{r})_{ij}$ corresponding to the one- and two-particle observables, respectively. Then $E(\vec{r})$ is given by a quadratic minimization problem over complex covariance matrices Eq. (11), in particular the off-diagonal block R of Γ_c. We have

$$E(\vec{r}) = \inf_{\substack{R=-R^\dagger \\ 4R^2=-1}} \{\vec{\gamma}^T M(\vec{r})\vec{\gamma} + w(\vec{r})^T\vec{\gamma}\}, \tag{22}$$

where $(\vec{\gamma})_{kl} = \langle a^\dagger_k a_l\rangle = -iR_{lk} + \frac{1}{2}\delta_{kl}$ and the $\vec{r}$-dependent quantities are $[M(\vec{r})]_{(ik)(jl)} = -\vec{r}_{ijkl} + \vec{r}_{ijlk}$ and $[w(\vec{r})]_{kl} = \vec{r}_{kl}$. The minimization can be extended over *all* (not necessarily pure separable) CMs without changing the result.

Proof. The minimum $\min_{\rho\in S_{\mathrm{sep}}}\{\langle H(\vec{r})\rangle_\rho\}$ is attained for *pure* separable states, i.e., product states. All pure fermionic product states are Gaussian; then by Wick's theorem, the expectation values of the $O_{ijkl} = a^\dagger_i a^\dagger_j a_k a_l$ factorize as $\langle a^\dagger_i a^\dagger_j a_k a_l\rangle_\rho = \langle a^\dagger_i a^\dagger_j\rangle\langle a_k a_l\rangle - \langle a^\dagger_i a_k\rangle\langle a^\dagger_j a_k\rangle + \langle a^\dagger_i a_l\rangle\langle a^\dagger_j a_k\rangle$. Since product states are also number-conserving, the first term vanishes. For the other two we use that $\langle a^\dagger_k a_l\rangle = -iR_{lk} + \frac{1}{2}\delta_{kl}$, i.e., they only depend on the off-diagonal block R. The pure state condition $\Gamma^2 = -1$ translates into $4R^2 = -1$ for product states $Q=0$.

We could extend over all CMs γ_c since only the block R appears in the expression to be minimized over, and since if $\Gamma_c(Q,R)$ is a valid CM, then so is $\Gamma_c(0,R)$. ■

This lemma provides a systematic way to construct pairing witnesses.

D. Pairing measures

It would be desirable if a theory of pairing not only answers the question of whether a state is paired, but also quantifies the amount of pairing inherent in a state. For this purpose, we introduce the notion of a pairing measure:

Definition III.10. Let ρ be an M-mode fermionic state. A pairing measure is a map

$$\mathcal{M}: \rho \mapsto \mathcal{M}(\rho) \in \mathbb{R}_+,$$

which is invariant under passive transformations and fulfills $\mathcal{M}(\rho)=0$ for every unpaired state ρ.

In addition, it is often useful to normalize $\mathcal{M}$ such that $\mathcal{M}(\rho_0)=1$ defines the "unit of pairing." The pair state $|\Phi\rangle$ of Eq. (19) would be an obvious choice for this unit, but as we see in Sec. IV D for Gaussian states a different unit is more natural, therefore we do not include normalization in the above definition.

In the geometric picture of the previous section, a candidate for a pairing measure that immediately comes to mind is the distance of $\vec{v}_\rho$ from the set C. This measure is positive, and it is invariant under passive transformations, as those correspond to a basis change in the space of expectation vectors.

The computation of this distance is, in general, very difficult and there is no evident operational meaning to this quantity. In the following sections, we will introduce a different measure that can be computed for relevant families of states and allow a physical interpretation in terms of quantifying a resource for precision measurements.

IV. PAIRING FOR GAUSSIAN STATES

In this section, we study pairing of fermionic Gaussian states. We start with the construction of pairing witnesses in Sec. IV A, which will later be a useful guideline for the construction of pairing witnesses for number-conserving states. Then we derive a simple necessary and sufficient criterion for pairing of Gaussian states. In Sec. IV C, we show how pure fermionic Gaussian states can be connected to an SU(2) angular momentum representation. This picture will guide us to the construction of a pairing measure.

A. Pairing witnesses for Gaussian states

Pairing witnesses for pure Gaussian states emerge naturally from the property that every such state is the ground state of a quadratic Hamiltonian (see Sec. II C). This leads to the following theorem:

Theorem IV.1. Let $0<\epsilon<1$ and let $0\leqslant|v_k|^2\leqslant 1-\epsilon$ and $\Sigma_k|v_k|^2>0$. Then the operator

$$H=\sum_{k=1}^{M} 2(1-\epsilon-|v_k|^2)(n_k+n_{-k})-2v_k u_k^* P_k^\dagger-2v_k^* u_k P_k \tag{23}$$

is a pairing witness, detecting

$$|\Psi_{\text{Gauss}}\rangle=\prod_k (u_k+v_k P_k^\dagger)|0\rangle.$$

Proof. Every Gaussian state is the ground state of a quadratic Hamiltonian. In particular, $|\Psi_{\text{Gauss}}\rangle$ is seen to be the ground state of

$$H_0=\sum_{k=1}^{M}(|u_k|^2-|v_k|^2)(n_k+n_{-k}-1)-2v_k u_k^* P_k^\dagger-2v_k^* u_k P_k$$

with the help of Eqs. (13) and (14), as the Hamiltonian matrix of H_0 and Γ can be brought simultaneously to the standard forms (5) and (7), respectively. Subtracting the minimal energy for separable states,

$$E_{\min}^{\text{sep}}=-(1-2\epsilon)\Sigma_k\langle n_k+n_{-k}\rangle-(|u_k|^2-|v_k|^2)$$

(note that $\langle P_k\rangle=0$ for separable states), we arrive at the Hamiltonian (23). For separable states ρ, the expectation values of $P_k^\dagger$ vanish, so that $\text{tr}[H\rho]\geqslant 0$. For the Gaussian BCS state, however, $\langle\Psi_{\text{Gauss}}|H|\Psi_{\text{Gauss}}\rangle=-4\epsilon\Sigma_k|v_k|^2<0$. ■

B. Complete solution of the pairing problem for fermionic Gaussian states

Every Gaussian state is completely characterized by its covariance matrix, so that the solution of the pairing problem must be related to it. The pairing problem is completely solved by the following theorem:

Theorem IV.2. Let ρ be the density operator of a fermionic Gaussian state with covariance matrix Γ_c defined in Eq. (11). Then ρ is paired iff $Q\neq 0$.

Proof. First, note that the condition $Q=0$ is independent of the choice of basis. If ρ is not paired, then there exists a separable state having the same covariance matrix as ρ. This implies $Q=0$, as separable states are convex combinations of states with fixed particle number, and thus $\langle i/2[a_k,a_l]\rangle=0$.

Now, let Γ_c be the covariance matrix of a paired Gaussian state, and assume that $Q=0$. As R is anti-Hermitian, there exists a passive transformation such that $R_{ij}=r_i\delta_{ij}$, and $Q=0$ is unchanged. But such a covariance matrix can be realized by a separable state fulfilling $\langle n_i\rangle=r_i$ in contradiction to the assumption.

Note that Thm. IV.2 implies that a Gaussian state is unpaired iff it is number-conserving.

C. Angular momentum algebra for Gaussian states

In this section, we will show that pairing of Gaussian states can be understood in terms of an SU(2) angular momentum algebra. The expectation values of the angular momentum operators can be visualized using a Bloch sphere, giving us further understanding of the structure of pairing in Gaussian states. It later leads to the construction of a pairing measure for these states. Define the operators [42,43]

$$j_k^{(x)}=\frac{1}{2}(P_k^\dagger+P_k),$$

$$j_k^{(y)}=\frac{i}{2}(P_k^\dagger-P_k),$$

$$j_k^{(z)}=\frac{1}{2}(1-n_k-n_{-k}).$$

They fulfill $[j_k^{(a)},j_k^{(b)}]=i\varepsilon_{abc}j_k^{(c)}$, $a,b,c\in\{x,y,z\}$, forming an SU(2) angular momentum algebra. For pure Gaussian states in the standard form (15), the expectation values of the angular momentum operators are given by $\langle j_k^{(x)}\rangle=\text{Re}(u_k v_k^*)$, $\langle j_k^{(y)}\rangle=\text{Im}(u_k v_k^*)$, and $\langle j_k^{(z)}\rangle=\frac{1}{2}(1-2|v_k|^2)$. As $j^2=\Sigma_{i=x,y,z}\langle j_k^{(i)}\rangle^2=\frac{1}{4}$ independent of u_k and v_k, the expectation values for every pure Gaussian state lie on the surface of a sphere with radius $\frac{1}{2}$. As we have shown in Thm. 4.2, every unpaired state ρ_u fulfills $\langle j_k^{(x)}\rangle_{\rho_u}=\langle j_k^{(y)}\rangle_{\rho_u}=0$, so that these states are

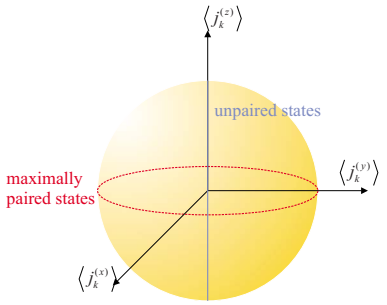

FIG. 1. (Color online) Bloch sphere representation of the expectation values of $j_k^{(x)}$, $j_k^{(y)}$, and $j_k^{(z)}$ for a variational BCS state. All pure states lie on the surface of the sphere. Unpaired states lie on the z axis, while the maximally paired states lie on the equator.

located on the z axis. The states on the equator have $\langle j_k^{(x)} \rangle^2 + \langle j_k^{(y)} \rangle^2 = \frac{1}{4}$, i.e. they correspond to $|u_k|^2 = |v_k|^2 = \frac{1}{2}$. The situation is depicted in Fig. 1. Referring to the states on the equator as maximally paired is suggested by the fact that they have maximal distance from the set of separable states. This intuitive picture is further borne out by two observations: first, the states on the equator display maximal entanglement between the involved modes [30]. Second, they have the property[3] that they achieve the minimal expectation value of any quadratic witness operator (up to basis change). To see this, recall from Sec. II C that any quadratic Hamiltonian of two modes $k, -k$ is (up to a common factor and basis change) of the form $\alpha \mathbb{1} + \sin\theta(n_k + n_{-k}) + \cos\theta(P_k^\dagger + P_k)$. It is a witness (i.e., has positive expectation for all product states) if $\alpha \geqslant |\max\{0, 2\sin\theta\}|$ and does detect some paired state as long as $\sin\theta > -1$. The minimum eigenvalue is $\sin\theta - 1 + \alpha$ and the minimum $\mathrm{tr}(W\rho) = -1$ is attained for $\rho = \frac{1}{2}(1 + P_k^\dagger)|0\rangle\langle 0|(1 + P_k)$.

The pairing measure, which is the topic of the next section, will confirm the characterization as maximally paired.

D. A pairing measure for Gaussian states

The angular momentum representation of paired states depicted in Fig. 1 suggests the introduction of a pairing measure via a quantity related to $|\langle j_k^{(x)} \rangle_{\rho_G}|^2 + |\langle j_k^{(y)} \rangle_{\rho_G}|^2 = |\langle a^\dagger{}_k a^\dagger{}_{-k} \rangle_{\rho_G}|^2$:

Definition IV.3. Let ρ be a fermionic state, and let $Q_{kl} = i/2\,\mathrm{tr}(\rho[a_k, a_l])$. Then we define

$$\mathcal{M}_G(\rho) = 2\|Q\|_2^2 = 2\sum_{kl} |Q_{kl}|^2. \tag{24}$$

Lemma IV.4. $\mathcal{M}_G$ as defined in Def. IV.3 is a pairing measure fulfilling $\mathcal{M}_G(\rho) \leqslant M$ for every M-mode Gaussian state.

Proof. Under a passive transformation $Q \mapsto UQU^T$, and hence $\|Q\|_2^2$ is invariant. Further, we know by Thm. 4.2 that $Q = 0$ for unpaired states.

[3]Maximally entangled states of two qubits share an analogous property about entanglement witnesses [44].

It remains to show that for an M-mode Gaussian state ρ we have $\mathcal{M}_G(\rho) \leqslant M$. Let Γ_c be the $2M \times 2M$ covariance matrix of ρ defined in Eq. (11). We show first that $\mathcal{M}(\rho)$ is maximized for pure Gaussian states. To do so, recall that an admissible covariance matrix for a Gaussian state in the real representation has to fulfill $i\Gamma \leqslant 1$ with equality iff Γ is the covariance matrix of a pure Gaussian state. This translates into $\Gamma_c \Gamma_c^\dagger \leqslant \mathbb{1}$ with equality iff Γ_c belongs to a pure Gaussian state. Using the form of Γ_c given in Eq. (11), this implies $2\,\mathrm{tr}[QQ^\dagger + RR^\dagger] \leqslant \mathrm{tr}[\mathbb{1}] = 2M$. Hence, $\|Q\|_2^2 \leqslant M - \|R\|_2^2$. It follows that for a fixed value of $\|R\|_2^2$, the value of $\|Q\|_2^2$ is maximal for a pure Gaussian state. Further, the standard form (15) implies that for every value of $\|R\|$ such a state exists, and that the maximal value is given by $\|Q\|_2^2 = 2\sum_{k=1}^M |u_k|^2 |v_k|^2 \leqslant M/2$, as $|u_k|^2 + |v_k|^2 = 1$. ■

Hence, for every pure Gaussian state with standard form (15) the value of the pairing measure is given by $\mathcal{M}_G(\rho) = 4\sum_{k=1}^M |u_k|^2 |v_k|^2$. Since $|v_k|^2 = 1 - |u_k|^2$, the measure attains its maximum value for $|u_k|^2 = |v_k|^2 = 1/2$, i.e., for the states already identified as maximally paired.

$\mathcal{M}_G(\rho)$ will appear again when we study the use of paired states for metrology applications, linking the pairing measure to the usefulness of a state for quantum phase estimation and giving support to the "resource" character of paired states.

V. PAIRING OF NUMBER-CONSERVING STATES

In the preceding section, we gave a complete solution to the pairing problem for fermionic Gaussian states. There, Wick's theorem lead to a reduction of the problem to properties of the covariance matrix. For number-conserving systems, the situation is more complicated, as now also operators of the form $a_i^\dagger a_j^\dagger a_k a_l$ have to be taken into account. However, we will derive pairing witnesses capable of detecting all number-conserving BCS states in Sec. V A using the concept of convex sets. For certain classes of BCS states, we will construct a family of improved witnesses using the analogy to the Gaussian states. Witnesses have the drawback that they depend on the choice of basis. That is, even if a witness detects ρ, it does not detect all states related to ρ by a passive transformation. We will show that the eigenvalues of the reduced two-particle density matrix can be used to obtain a sufficient criterion for pairing in Sec. V B that is basis-independent. We close the section with the construction of a pairing measure in Sec. V C.

A. Pairing of all BCS states and geometry of paired states

In a realistic physical setup, it may not be practical to perform all the measurements needed according to Lemma III.8 to check the necessary and sufficient condition for pairing. Having access only to a restricted set of measurements, necessary criteria for pairing can be derived. In this section, we consider the simplest case of a symmetric measurement involving four modes, i.e., we are looking at the following vector of operators:

$$\vec{O}_3 = \begin{pmatrix} n_k + n_{-k} + n_l + n_{-l} \\ n_k n_{-k} + n_l n_{-l} \\ a_k^\dagger a_{-k}^\dagger a_{-l} a_l + \mathrm{H.c.} \end{pmatrix}. \tag{25}$$

Remarkably, these expectation values will turn out to be sufficient to detect all BCS states as paired.

We are interested in $C_{\vec{O}_3}^{\text{unpaired}}=\{\text{tr}(\vec{O}_3\rho):\rho \text{ separable}\}$, the set of all expectation values of $\vec{O}_3$ that correspond to separable states. If for some ρ the vector $\vec{v}_\rho=\text{tr}(\vec{O}_3\rho)$ is found outside of $C_{\vec{O}_3}^{\text{unpaired}}$, then it follows from Lemma III.8 that ρ is paired. Membership in $C_{\vec{O}_3}^{\text{unpaired}}$ can be easily checked by the following Lemma:

Lemma V.1. A number-conserving state ρ has expectation values of $\vec{O}_3$ [see Eq. (25)] compatible with separability if and only if $\text{tr}(H_{k\pm}^{(p)}\rho)\geqslant 0$ for $k=1,2,3$, where

$$H_{1\pm}^{(p)}=\frac{1}{2}(n_k+n_{-k}+n_l+n_{-l})-(n_kn_{-k}+n_ln_{-l}) \pm (a_k^\dagger a_{-k}^\dagger a_{-l}a_l+\text{H.c.}), \tag{26}$$

$$H_{2\pm}^{(p)}=(n_kn_{-k}+n_ln_{-l})\pm(a_k^\dagger a_{-k}^\dagger a_{-l}a_l+\text{H.c.}), \tag{27}$$

$$H_{3\pm}^{(p)}=1-\frac{1}{2}(n_k+n_{-k}+n_l+n_{-l})+\frac{1}{2}(n_kn_{-k}+n_ln_{-l}) \pm\frac{1}{2}(a_k^\dagger a_{-k}^\dagger a_{-l}a_l+\text{H.c.}). \tag{28}$$

Hence, the extremal points of the set $C_{\vec{O}_3}^{\text{unpaired}}$ are given by $\text{tr}(H_{k\pm}^{(p)}\rho)=0$ for three of the witnesses (26)–(28). The faces of $C_{\vec{O}_3}^{\text{unpaired}}$ consist of points for which at least one of the expectation values $\text{tr}(H_{k\pm}^{(p)}\rho)$ vanishes. $H_{1\pm}^{(p)}$ and $H_{3\pm}^{(p)}$ are also pairing witnesses, while $H_{2\pm}^{(p)}$ is nonnegative on all number-conserving states.

Lemma V.2. Every number-conserving fermionic state fulfills $\text{tr}(H_{k\pm}\rho)\geqslant 0$, where

$$H_1=\frac{1}{2}(n_k+n_{-k}+n_l+n_{-l})-(n_kn_{-k}+n_ln_{-l}), \tag{29}$$

$$H_{2\pm}=(n_kn_{-k}+n_ln_{-l})\pm(a_k^\dagger a_{-k}^\dagger a_{-l}a_l+\text{H.c.}), \tag{30}$$

$$H_{3\pm}=2-\frac{1}{2}(n_k+n_{-k}+n_l+n_{-l})\pm(a_k^\dagger a_{-k}^\dagger a_{-l}a_l+\text{H.c.}). \tag{31}$$

The extremal points of the set $C_{\vec{O}_3}^{\text{all}}=\{\text{tr}(\vec{O}_3\rho):\rho\in\mathcal{S}(\mathcal{A}_M^{(N)}):M,N\in N\}$ are given by $\text{tr}(H_{k\pm}\rho)=0$ for three of the witnesses (29)–(31). The faces of $C_{\vec{O}_3}^{\text{all}}$ consist of points for which at least one of the expectation values $\text{tr}(H_{k\pm}\rho)$ vanishes.

The proofs of the two lemmas can be found in Appendix B. We denote by C^{unpaired} and C^{all} the polytopes containing all expectation vectors $\vec{v}_\rho$ corresponding to unpaired states or all number-conserving states, respectively. They are bounded by six and five planes, respectively, defined through the witnesses given in Lemmas V.1 and V.2. The situation is depicted in Fig. 2.

The witnesses $H_{1\pm}^{(p)}$ given in Eqs. (26) allow us to detect all number-conserving BCS states as paired:

Lemma V.3. The number-conserving BCS state $|\Psi_{\text{BCS}}^{(N)}\rangle$ given in Eq. (17) is (except for the trivially unpaired cases $\alpha_k=\delta_{kk_0}$ and $N=M$) detected by the witness $H_p^{(1)}$ by choosing any two modes (k,l).

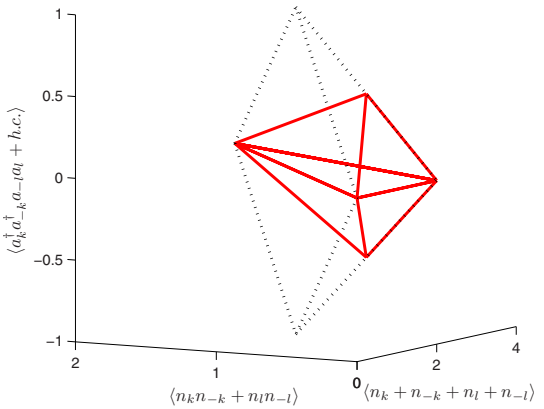

FIG. 2. (Color online) Expectation values of the vector Eq. (25). For all number-conserving states these lie within the convex set $C_{\vec{O}_3}^{\text{all}}$ indicated by the dashed back lines. The extreme points of the polytope are given by (0, 0, 0), (2, 0, 0), (4, 2, 0), and $(2,1,\pm 1)$. Unpaired states have expectation values in the smaller convex set $C_{\vec{O}_3}^{\text{unpaired}}$ (solid red), which has extreme points (0, 0, 0), (2, 0, 0), (4, 2, 0), and $(2,1/2,\pm 1/2)$.

Proof. The first two terms in $H_{1\pm}^{(p)}$ are designed such that their expectation value vanishes for states such as $|\Psi_{\text{BCS}}^{(N)}\rangle$: Since we either have a pair or no particles in the modes $(k,-k)$, we are in an eigenstate with eigenvalue 0 of the operators $n_k+n_{-k}-2n_kn_{-k}$.

The expectation value of the third term is found using the representation Eq. (18) as $|C_N|^2N!^2\text{Re}(\alpha_k\alpha_l^*)\Sigma_{j_1<\cdots<j_{N-1}\atop j_i\neq k,l}|\alpha_{j_1}|^2\cdots|\alpha_{j_{N-1}}|^2$, which is nonzero unless $N=M$ or all but one $\alpha_k\neq 0$. The sign can be adjusted by a passive transformation to give $\langle H_{1+}^{(p)}\rangle_{\text{BCS}}^{(N)}<0$. ■

This shows that indeed all BCS states are paired, as desired.

The witnesses $H_{p\pm}^{(1)}$, while detecting every BCS state as paired, are in general far from optimal. As the number-conserving BCS states appear in many physical setting, like in the BEC-BCS crossover [45], it is desirable to construction improved witnesses tailored for this class of states. For BCS states realized in nature, it is often appropriate to assume some symmetry of the wave function $|\Psi_{\text{BCS}}^{(N)}(\alpha_k)\rangle=(\Sigma_{k=1}^{2M}\alpha_kP_k^\dagger)^N|0\rangle$. For example, if $P_k^\dagger=a_{k\uparrow}^\dagger a_{-\vec{k}\downarrow}^\dagger$, $P_{k+M}^\dagger=a_{-\vec{k}\uparrow}^\dagger a_{\vec{k}\downarrow}^\dagger$ and if we are dealing with an isotropic setting, $\alpha_k=\alpha_{k+M}$ will hold. It is further often appropriate to assume that the number of modes is much bigger than the number of particles, i.e., $M\gg N$. For this kind of state we will construct pairing witnesses via the correspondence to the Gaussian picture. We sketch the idea of this construction leading to Thm. V.4, and give the details in the Appendix C.

We have shown in Sec. II D the connection of the Gaussian wave function and the number-conserving wave function

via $|\Psi_{\text{Gauss}}\rangle=\Sigma_{k=1}^{N}\lambda_N|\Psi_{\text{BCS}}^{(N)}(\alpha_k)\rangle$. Consider a number-conserving observable O and denote by $\langle O\rangle_{\text{Gauss}}$ and $\langle O\rangle_N$ its expectation value for the Gaussian and $2N$-particle BCS wave function, respectively. If the distribution of $|\lambda_N|^2$ is sharply peaked around some average particle number $\bar{N}$ with width Δ, then $\langle O\rangle_{\text{Gauss}}\approx\langle O\rangle_N$ for any integer $N\in[\bar{N}-\Delta,\bar{N}+\Delta]$. In Thm. IV.1, we have constructed witnesses H for all Gaussian BCS states. As these witnesses are optimal, they suggest to constitute an improved witness detecting the corresponding number-conserving BCS state. But H includes terms of the form $P_k^\dagger$ that do not conserve the particle number. Hence, this witness cannot be applied directly to the number-conserving case. Using Wick's theorem, $\langle P_k^\dagger P_{k+M}\rangle_{\text{Gauss}}=\bar{u}_k v_k\langle P_k^\dagger\rangle_{\text{Gauss}}$ holds under our symmetry assumption. This suggests that we replace the non-number-conserving operator $u_k v_k P_k^\dagger$ by the number-conserving operator $P_k^\dagger P_{k+M}$. We define operators

$$H_k=2(1-\epsilon-|v_k|^2)N_k-4(P_k^\dagger P_{k+M}+\text{H.c.}),\tag{32}$$

$$N_k=n_k+n_{-k}+n_{k+M}+n_{-(k+M)},\tag{33}$$

where $0\leqslant|v_k|^2\leqslant 1-\epsilon\,\forall\ k$ for $\epsilon>0$. Further, we introduce the notation $\alpha_k=v_k/\sqrt{1-|v_k|^2}$, $\tilde{N}=\Sigma_{k=1}^{M}|v_k|^2$ and we denote by N the biggest integer fulfilling $\bar{N}-\tilde{N}\geqslant 0$. Then the following holds:

Theorem V.4. Let M, $\tilde{N}\in\mathbb{N}$ and let $1\ll N<2M$. If $1>\epsilon\geqslant 18/\sqrt{\pi\bar{N}}$, the Hamiltonian $H(\{v_k\})=\Sigma_{k=1}^{M}H_k$ is a pairing witness detecting

$$|\Psi_{\text{BCS,sym}}^{(N)}\rangle=C_N\left(\sum_{k=1}^{M}\alpha_k(P_k^\dagger+P_{k+M}^\dagger)\right)^N|0\rangle.$$

The proof is given in Appendix C.

B. Eigenvalues of the two-particle reduced density matrix

In this section, we derive a basis-independent condition for detecting pairing. The two-particle reduced density matrix O contains all two-particle correlations. As a change of basis, $a_i^\dagger\mapsto\Sigma_k U_{ik}a_k^\dagger$ leaves the spectrum of O unchanged since

$$O_{(ij),(kl)}^{(\rho)}\to(U\otimes U)_{(ij),(mn)}O_{(mn),(pq)}^{(\rho)}(U\otimes U)_{(pq),(kl)}^\dagger,$$

and we are led to the following theorem:

Theorem V.5. Let ρ be an unpaired state, and let O be its two-particle RDM O. Then $\lambda_{\max}(O)\leqslant 2$, where $\lambda_{\max}$ denotes the maximal eigenvalue.

Proof. If ρ is unpaired, then there exists a separable state $\rho_s\in\mathcal{S}_{\text{sep}}$ having the same two-particle RDM. Any separable state is of the form $\rho_s=\Sigma_\alpha\mu_\alpha\rho^{(\alpha)}$, where $\rho^{(\alpha)}=|\psi^{(\alpha)}\rangle\langle\psi^{(\alpha)}|$, $|\psi^{(\alpha)}\rangle=\Pi_i a^\dagger{}_{\alpha_i}|0\rangle$, and $\Sigma_\alpha\mu_\alpha=1$. Here, $\{a_{\alpha_i}^\dagger\}_i$ denotes some basis of mode operators. The RDM is of the form $O^{(\rho)}=\Sigma_\alpha\mu_\alpha O^{(\alpha)}$, where $O^{(\alpha)}$ is the RDM for the state $\rho^{(\alpha)}$. The RDM is calculated in the basis $\{a_i^\dagger\}_i$, and the different bases are related by a unitary transformation $a_i^\dagger=\Sigma_j U_{ik}^{(\alpha)}a_{\alpha_k}^\dagger$, so that $O_{(ij)(kl)}^{(\alpha)}=\text{tr}[\rho^{(\alpha)}a_i^\dagger a_j^\dagger a_l a_k]=(U^{(\alpha)}\otimes U^{(\alpha)})_{(ij)(mn)}O_{(mn),(pq)}^{(\alpha,0)}(U^{(\alpha)}\otimes U^{(\alpha)})_{(pq)(kl)}^\dagger$, where $O_{(mn),(pq)}^{(\alpha,0)}=\langle a_{\alpha_m}^\dagger a_{\alpha_n}^\dagger a_{\alpha_q}a_{\alpha_p}\rangle_{\rho^{(\alpha)}}$. In the basis of the $\{a_{\alpha_i}^\dagger\}_i$, the expectation value $\langle a_{\alpha_m}^\dagger a_{\alpha_n}^\dagger a_{\alpha_q}a_{\alpha_p}\rangle_{\rho^{(\alpha)}}$ is of the simple form $\langle a_{\alpha_i}^\dagger a_{\alpha_j}^\dagger a_{\alpha_l}a_{\alpha_k}\rangle_{\rho^{(\alpha)}}=\delta_{ik}\delta_{jl}-\delta_{il}\delta_{jk}$. Hence, the spectrum of the $O^{(\alpha)}$ is given by $\text{spec}(O^{(\alpha)})=\{0,2\}\forall\ \alpha$. The two-particle RDM is Hermitian as $O_{(ij)(kl)}^\dagger=\bar{O}_{(kl)(ij)}=\langle a_k^\dagger a_l^\dagger a_j a_i\rangle=\langle a_i^\dagger a_j^\dagger a_l a_k\rangle=O_{(ij)(kl)}$. Then Weyl's theorem [46] implies $\lambda_{\max}(\Sigma_\alpha\mu_\alpha O^\alpha)\leqslant\Sigma_\alpha\mu_\alpha\lambda_{\max}(O^\alpha)\leqslant\Sigma_\alpha 2\mu_\alpha\leqslant 2$. ■

An example of a state detected as paired via criterion is the BCS state (17) with $N=2$, $M=3$, and all α_k equal. The largest eigenvalue of its two-particle RDM is given by $\lambda_{\max}=8/3$.

C. A pairing measure for number-conserving states

In Sec. IV D, we have derived a pairing measure for Gaussian states. The correspondence with number-conserving BCS states will be a guideline to derive a measure for number-conserving states. However, the measure of Def. IV.3 involves expectation values of the form $\langle a_k^\dagger a_{-k}^\dagger\rangle$ that vanish for states with fixed particle number. Yet, Wick's theorem suggests that a quantity involving expectation values of the form $\langle P_k^\dagger P_l\rangle$ will lead to a pairing measure. This is indeed the case, which is the content of the following theorem:

Theorem V.6. Let ρ be a number-conserving pure fermionic state. Then the following quantity defines a pairing measure:

$$\mathcal{M}(\rho)=\max\left\{\max_{\{a_i^\dagger\}_i}\sum_{kl=1}^{M}|\langle P_k^\dagger P_l\rangle_\rho|-\frac{1}{2}\sum_k\langle n_k\rangle_\rho,0\right\},\tag{34}$$

where $P_k^\dagger=a_k^\dagger a_{-k}^\dagger$ and the maximum is taken over all possible bases of modes $\{a_i^\dagger\}_i$. For mixed states ρ, a measure can be defined via

$$\mathcal{M}(\rho)=\min\sum_i p_i\mathcal{M}(\rho_i),\tag{35}$$

where the minimum is taken over all possible decompositions of $\rho=\Sigma_i p_i\rho_i$ into pure states ρ_i.

Proof. The positivity of $\mathcal{M}$ and its invariance under passive transformations follow directly from the definition. It remains to show that $\mathcal{M}$ is zero for separable states. We will prove in Lemma D.1, Appendix D, that any separable state of $2N$ particles fulfills $\Sigma_{kl}|\langle P_k^\dagger P_l\rangle|\leqslant N$, and that this bound can always be achieved, which concludes the proof. ■

We close the section by calculating the value of the pairing measure for two easy examples. Let

$$|\Psi_s\rangle=\bigotimes_{k=1}^{N}\frac{1}{\sqrt{2}}(P_k^\dagger+P_{-k}^\dagger)|0\rangle,\tag{36}$$

$$|\Psi_{\text{BCS}}^{(N,M)}\rangle=C_N\left(\sum_{k=1}^{M}P_k^\dagger\right)^N|0\rangle,\tag{37}$$

the tensor product of N spin-singlet states and the BCS state with equal weights, respectively. These states have a pairing measure $\mathcal{M}(|\Psi_s\rangle)=N$ and $\mathcal{M}(|\Psi_{\text{BCS}}^{(N,M)}\rangle=N(M-N)$, respectively. Thus, for the spin singlet the pairing measure has in addition the property that it is normalized to 1 and additive,

while it is subadditive for $|\Psi_{\mathrm{BCS}}^{(N,M)}\rangle$. Further, this example suggests that the pairing of $\mathcal{M}(|\Psi_{\mathrm{BCS}}^{(N,M)}\rangle = N(M-N)$ is stronger than for $|\Psi_s\rangle$. We will see indeed in Sec. VI B that states of the form $|\Psi_e\rangle$ allow interferometry at the Heisenberg limit.

VI. INTERFEROMETRY

The goal of quantum phase estimation is to determine an unknown parameter φ of a Hamiltonian $H_\varphi = \varphi H$ at the highest possible accuracy. The value of φ is inferred by measuring an observable O on a known input state that has evolved under H_φ. In a region where the expectation value $\langle O(\varphi)\rangle$ is bijective, φ can be inferred by inverting $\langle O(\varphi)\rangle$. In a realistic setup, however, $\langle O(\varphi)\rangle$ cannot be determined, as this would require an infinite number of measurements. Instead, one uses the mean value of the measurement results, o, as an estimate of $\langle O(\varphi)\rangle$. This will result in an error $\delta\varphi$ for the parameter to be estimated, as for a given value of φ we have $\langle O(\varphi)\rangle = o \pm \sqrt{\mathrm{Var}(o)}$. Linearizing around the real value of φ, it follows that the uncertainty of φ is given by [47,48]

$$\langle (\delta\varphi)^2\rangle = \frac{\mathrm{var}(O)}{|\partial\langle O\rangle/\partial\varphi|^2}, \tag{38}$$

where $\mathrm{var}(O) = \langle O^2\rangle - \langle O\rangle^2$, and we have used the fact that $\mathrm{var}(O) = \mathrm{var}(o)$. Further, it can be shown that the minimal uncertainty of φ is bounded by [49,50]

$$\langle (\delta\varphi)^2\rangle \mathrm{var}(H) \geqslant \frac{1}{4\nu}, \tag{39}$$

where ν is the number of times the estimation is repeated. Equation (39) derives from the Cramér-Rao bound and is asymptotically achievable in the limit of large ν.

For a given measurement scheme, i.e., for a given input state and a given observable O, the uncertainty in φ can be reduced by using N identical input states and average over the N measurement outcomes. As the preparation of a quantum state is costly, a precision gain that has a strong dependence on N is highly desirable. If these probe states are independent of each other, the precision scales like $1/\sqrt{N}$. This is the so-called standard quantum limit (SQL). Using distinguishable or bosonic systems, this limit can be beaten by a factor of $\sqrt{N}$ by using number-squeezed input states [51–54], N-particle path-entangled states ($\langle N,0| + \langle 0,N|$) (NOON states), or maximally entangled GHZ states $\frac{1}{\sqrt{2}}(|N,0\rangle + |0,N\rangle)$ [48,55–57]. Achieving this so-called Heisenberg limit is the big goal of quantum metrology.

Less is known for fermionic states where number squeezing and coherent N-particle states are prohibited by statistics. Nevertheless, there exist fermionic N-particle states that can achieve the Heisenberg limit for phase measurements in a Mach-Zehnder interferometer setup [58]. Taking the existence of such states as a starting point, we show that paired fermionic states can be used as a resource for phase estimation beyond the SQL. We will consider two different settings. The first setting will be the standard Ramsey-interferometer setup of metrology, where the coupling Hamiltonian is proportional to the number operator. Here, we will see that paired states lead to a precision gain of a factor of 2 compared to separable states. The second setup involves a more complex coupling. Here it will turn out that by using paired states, the Heisenberg limit, i.e., a phase sensitivity $(\delta\varphi)^2 \sim 1/N^2$, can be achieved.

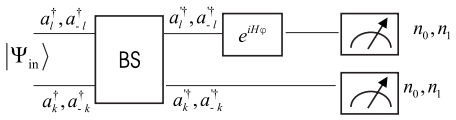

FIG. 3. Scheme of the Ramsey interferometer setup. The incoming wave function $|\Psi_{\mathrm{in}}\rangle$ enters a beam splitter (BS). Then particles in the modes $a_{\pm l}^\dagger$ evolve under the Hamiltonian φH. At the end, a particle number measurement is performed on all particles.

A. Ramsey interferometry with fermions

1. General setup

We consider the standard Ramsey interferometer setup (see Fig. 3) where a state in the modes $\{a_{k_j}^\dagger, a_{l_j}^\dagger\}_{j=-M}^{M}$ undergoes mode mixing at a beam splitter,

$$a_{\pm k_j}^\dagger \to a_{k_j}'^\dagger = \frac{1}{\sqrt{2}}(a_{\pm k_j}^\dagger + a_{\pm l_j}^\dagger), \tag{40}$$

$$a_{\pm l_j}^\dagger \to a_{\pm l_j}'^\dagger = \frac{1}{\sqrt{2}}(a_{\pm k_j}^\dagger - a_{\pm l_j}^\dagger), \tag{41}$$

before evolving under the action of the Hamiltonian

$$H_N = \sum_{j=1}^{M} (n_{l_j} + n_{-l_j}). \tag{42}$$

Finally, a particle number measurement is performed on the system, to compute the parity

$$\mathcal{P} = (-1)^{\Sigma_j n_0^{(j)} + n_1^{(j)}}, \tag{43}$$

where $n_0^{(j)} = a_{k_j}'^\dagger a_{k_j}'$ and $n_1^{(j)} = a_{-k_j}'^\dagger a_{-k_j}'$. According to Eq. (38), the phase sensitivity is given by

$$(\delta\varphi)^2 = \frac{1 - \langle\mathcal{P}\rangle^2}{\left|\frac{\partial}{\partial\varphi}\langle\mathcal{P}\rangle\right|^2}, \tag{44}$$

where we have exploited $\mathcal{P}^2 = 1$. Due to the fermionic statistics, the parity operator can be written in the form

$$\mathcal{P} = \prod_{j=1}^{M} [1 - 2(n_0^{(j)} + n_1^{(j)}) + 4 n_0^{(j)} n_1^{(j)}]. \tag{45}$$

In the next section, we will derive the best possible precision obtainable by using unpaired states, and compare this result to the precision achievable by using paired states. It will turn out that already at the two-particle level paired states have more power than the unpaired states for our setup.

2. Bound on unpaired states for the standard interferometer

In this section, we derive a lower bound on the phase sensitivity when using an unpaired state of $2N$ particles as input states.

Thorem VI.1. For the Ramsey interferometer described above, the phase sensitivity is bounded by

$$(\delta\varphi)^2 \geqslant \frac{1}{2\nu N}, \tag{46}$$

when an unpaired state of $2N$ particles is used as input state.

Proof. We will use Eq. (39) to derive the bound. Hence, we have to estimate an upper bound for the variance of the Hamiltonian H_N defined in Eq. (42). As H_N as well as H_N^2 contain operators from the set A_2 only, it is sufficient to prove the bound for product states, as for every unpaired state there exists a product state having the same expectations. In Lemma A.2 of Appendix A, we have shown that for pure separable states $\langle n_k n_l\rangle = |P_{kl}|^2 - P_{kk}P_{ll} + P_{kk}\delta_{kl}$, where $P \in \mathbb{C}^{4M\times 4M}$ is a projector of rank $2N$. We arrange the indices as $-l_M,\ldots,l_M,-k_M,\ldots,k_M$ and partition the projector P such that $P=\left(\begin{smallmatrix} A & B \\ B^\dagger & C\end{smallmatrix}\right)$, where $A,B,C \in \mathbb{C}^{2M\times 2M}$. Then

$$\mathrm{var}(H_N) = \sum_{i=1}^{2M} A_{ii} - \sum_{i,j=1}^{2M} |A_{ij}|^2 = \mathrm{tr}[BB^\dagger], \tag{47}$$

as H_N only involves the modes $-l_M,\ldots,l_M$. In the last step we have used $P^2=P$, implying $A-A^2=BB^\dagger$. As $\mathrm{rank}(P)=2N$, there exists some unitary U such that $P=U\mathrm{Id}_{2N}U^\dagger$, where $\mathrm{Id}_{2N}=\left(\begin{smallmatrix} 1_{2N} & 0 \\ 0 & 0\end{smallmatrix}\right) \in \mathbb{C}^{4M\times 4M}$. Partitioning the unitary $U=\left(\begin{smallmatrix} U_{11} & U_{12} \\ U_{21} & U_{22}\end{smallmatrix}\right)$, where $U_{ij} \in \mathbb{C}^{2M\times 2M}$, $i,j=1,2$, the projector P is of the form

$$P = \begin{pmatrix} U_{11}\mathrm{Id}_{2N}U_{11}^\dagger & U_{11}\mathrm{Id}_{2N}U_{21}^\dagger \\ U_{21}\mathrm{Id}_{2N}U_{11}^\dagger & U_{21}\mathrm{Id}_{2N}U_{21}^\dagger \end{pmatrix}.$$

Using the above representation of P and the cyclicity of the trace, we can write $\mathrm{var}(H_N)=\mathrm{tr}[\tilde{A}\tilde{B}]$ with Hermitian matrices $\tilde{A}=\mathrm{Id}_{2N}U_{11}^\dagger U_{11}\mathrm{Id}_{2N}$, $\tilde{B}=\mathrm{Id}_{2N}U_{21}^\dagger U_{21}\mathrm{Id}_{2N}$. The trace can be interpreted as a scalar product maximized for linearly dependent $\tilde{A}$ and $\tilde{B}$. Exploiting the unitarity of U, one sees immediately that the variance is maximized for $\tilde{A}=c/(1+c)\mathrm{Id}_{2N}$, $\tilde{B}=1/(1+c)\mathrm{Id}_{2N}$ for some constant c. Hence, $\mathrm{var}(H_N) \leqslant c/(1+c)^2\,\mathrm{tr}[1_{2N}] \leqslant N/2$. Inserting this into Eq. (39), we find that $(\delta\varphi)^2 \geqslant \frac{1}{2\nu N}$. ■

3. Interferometry with two particles

In this section, we will show that already a two-particle paired state can beat the bound for the phase sensitivity using unpaired states (46). Hence pairing manifests itself as useful quantum correlation already at the two-particle level. We show the following:

Theorem VI.2. Using the paired state

$$|\Psi_{\mathrm{in}}^{(2)}\rangle = \left(\sum_{j=1}^{M} \alpha_j a_{k_j}^\dagger a_{-k_j}^\dagger + \beta_j a_{l_j}^\dagger a_{-l_j}^\dagger\right)|0\rangle, \tag{48}$$

with normalization $\Sigma_j|\alpha_j|^2+|\beta_j|^2=1$ as input state for the Ramsey interferometer, the optimal phase sensitivity is given by

$$(\delta\varphi)^2_{\mathrm{min}} = \frac{1}{2[1+2\Sigma_{j=1}^{M}\,\mathrm{Re}(\alpha_j\beta_j^*)]} \geqslant \frac{1}{4}. \tag{49}$$

Proof. Take $|\Psi_{\mathrm{in}}^{(2)}\rangle$ as the input state. After an application of the beam splitter transformation (40) and an evolution under the Hamiltonian (42), the measurement outcome of the parity operator is calculated to be

$$\langle\mathcal{P}\rangle = 1 - \sin^2\varphi\left(1 + 2\sum_{j=1}^{M}\,\mathrm{Re}(\alpha_j\beta_j^*)\right). \tag{50}$$

Using Eq. (44), we obtain Eq. (49). The bound of $\frac{1}{4}$ can be obtained for a state where $\alpha_k=\beta_k\,\forall\ k$. ■

Theorem VI.2 shows that there exist two-particle paired states exceeding the bound on product states (46).

4. Interferometry with 2N-particle BCS states

Generalizing the result obtained in the last section, it follows immediately that states of the form $|\Psi_{\mathrm{in}}^{(2)}\rangle^{\otimes N}$ will lead to a phase sensitivity $(\delta\varphi)^2_{\mathrm{min}}=1/\{2N[1+2\Sigma_{j=1}^{M}\mathrm{Re}(\alpha_j\beta_j^*)]\}$. In this section, we will show that the same result can be achieved using BCS states.

Theorem VI.3. Let the paired state

$$|\Psi_{\mathrm{in}}^{(2N)}\rangle = c'\left(\sum_{j=1}^{M} \alpha_j a_{k_j}^\dagger a_{-k_j}^\dagger + \beta_j a_{l_j}^\dagger a_{-l_j}^\dagger\right)^N |0\rangle, \tag{51}$$

where we use the normalization condition $\Sigma_j|\alpha_j|^2+|\beta_j|^2=1$, be the input state for the Ramsey-type interferometer defined above. Then the optimal phase sensitivity is given by

$$(\delta\varphi)^2 = \frac{1}{2\bar{N}[1+2\Sigma_j\,\mathrm{Re}(\alpha_j\beta_j^*)]}. \tag{52}$$

Proof. As in previous sections, we will use the correspondence to the Gaussian state,

$$|\Psi_{\mathrm{in,Gauss}}^{(2\bar{N})}\rangle = c\,\exp\left[\sum_{j=1}^{M} \alpha_j a_{k_j}^\dagger a_{-k_j}^\dagger + \beta_j a_{l_j}^\dagger a_{-l_j}^\dagger\right]|0\rangle,$$

where $|N-\bar{N}| \ll \bar{N}$ for the calculation. After the state has passed through the interferometer, the expectation value of the parity operator is readily computed to be $\langle\mathcal{P}\rangle_{\mathrm{Gauss}}=\Pi_j(1-|c|^2|\alpha_j+\beta_j|^2\sin^2\varphi)$. As only number operators are involved, $\langle\mathcal{P}\rangle_{\mathrm{Gauss}} \approx \langle\mathcal{P}\rangle_N$, where $\langle\cdots\rangle_N$ denotes the expectation value of $\mathcal{P}$ for the state $|\Psi_{\mathrm{in}}^{(2N)}\rangle$. Expanding Eq. (44) for small values of φ and using $\bar{N}=|c|^2\Sigma_k|\alpha_k|^2+|\beta_k|^2=|c|^2$, one obtains Eq. (52), which has minimal value $(\delta\varphi)^2=1/(4N)$. This result is obtained when $\alpha_j=\beta_j\,\forall\ j$. ■

The above result shows that paired states result in a precision gain of up to a factor of 2 compared to the best precision obtainable for unpaired states (46).

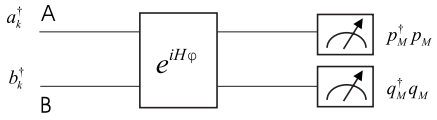

FIG. 4. Setup that allows interferometry with paired states at the Heisenberg limit. Particles in modes $a_k^\dagger$ and $b_k^\dagger$ evolve under the complex coupling Hamiltonian H (for the detailed form of H, refer to the text). In the end, particle numbers are measured.

The pairing measure derived in Secs. IV D and V C quantifies the precision gain obtainable by the use of paired states. To see this, denote by $|\Psi_{\text{in,Gauss}}^{(2\bar{N})\prime}\rangle$ the state after the beam splitter transformation. Then the pairing measure (Def. IV.3) for this state evaluates to

$$\mathcal{M}_G(|\Psi_{\text{in,Gauss}}^{(2\bar{N})\prime}\rangle) = \frac{N^2}{2}\left(1 + 2\sum_j \text{Re}(\alpha_j \beta_j^*)\right),$$

so that

$$(\delta\varphi)^2 = \frac{\bar{N}}{4\mathcal{M}_G(|\Psi_{\text{in,Gauss}}^{(2\bar{N})\prime}\rangle)}. \tag{53}$$

The above relation demonstrates that $\mathcal{M}$ is indeed quantifying a useful resource present in paired states. Whether this interpretation can be extended to mixed states will not be explored here.

B. Interferometry involving a pair-interaction Hamiltonian

So far we have seen that paired states lead to a gain of a factor of 2 in precision compared to unpaired states in a Ramsey-type interferometer. This section will show that paired states are even more powerful and can lead to a precision gain of a factor of N when measuring the phase of a pair-interaction Hamiltonian.

We consider a setup where two fermionic states enter the ports A and B of an interferometer. The particles entering port A can occupy the modes $\{a_k^\dagger\}_{k=-M}^M$, while the particles entering through port B can occupy the modes $\{b_k^\dagger\}_{k=-M}^M$. Then the two states evolve under the Hamiltonian H_c to be defined below and a particle number measurement is performed at the end. The situation is depicted in Fig. 4. We will compare the power of paired states over unpaired ones for two different settings. We start by introducing some basic notation.

1. Prerequisites

We define pair operators $P_k^\dagger = a_k^\dagger a_{-k}^\dagger$ and $Q_k^\dagger = b_k^\dagger b_{-k}^\dagger$ and their equally weighted superpositions

$$p_M^\dagger = \frac{1}{\sqrt{M}}\sum_{k=1}^M P_k^\dagger, \quad q_M^\dagger = \frac{1}{\sqrt{M}}\sum_{k=1}^M Q_k^\dagger. \tag{54}$$

The operators $p_M^\dagger$ and $q_M^\dagger$ fulfill the commutation relations

$$[p_M^\dagger, p_M] = -1 + \frac{1}{M}\hat{N}_a, \tag{55}$$

$$[q_M^\dagger, q_M] = -1 + \frac{1}{M}\hat{N}_b, \tag{56}$$

where $n_k = a_k^\dagger a_k$ so that $N_a = \Sigma_k(n_k + n_{-k})$, and $N_b = \Sigma_k(m_k + m_{-k})$ with $n_k = a_k^\dagger a_k$ and $m_k = b_k^\dagger b_k$ being the number operators for particles in modes $a_k^\dagger$ and $b_k^\dagger$, respectively.

We will compare the power of two paired states and two unpaired states entering through port A and B. The bound for unpaired states will be derived again via Eq. (39). As H_c and H_c^2 will be elements of A_2, it is sufficient, as in the last section, to compare the power of paired states to those of sparable states. The paired states will be of the form

$$|\Psi_N^{(M)}\rangle = |N\rangle_a^{(M)}|N\rangle_b^{(M)}, \tag{57}$$

$$|N\rangle_a^{(M)} = c_N^{(M)}(p_M^\dagger)^N|0\rangle, \quad |N\rangle_b^{(M)} = c_N^{(M)}(q_M^\dagger)^N|0\rangle, \tag{58}$$

with normalization constant $c_N^{(M)} = (NM!/M^N)^{-1/2}$, while the separable states are given by

$$|\Phi_N\rangle = |\phi^{(2N)}\rangle_a|\phi^{(2N)}\rangle_b, \tag{59}$$

where $|\phi^{(2N)}\rangle_{a,b}$ are separable states in the modes $a_k^\dagger$ and $b_k^\dagger$, respectively.

After the input state has evolved under the Hamiltonian H_φ into the state $|\Psi_N^{(M)}(\varphi)\rangle = e^{iH_c\varphi}|\Psi_N^{(M)}\rangle$, an observable O is used as an estimator to determine the parameter φ to a precision given by Eq. (38). Instead of working in the Schrödinger picture of state evolution, it turns out to be more convenient to tackle the problem in the Heisenberg picture, where O evolves according to $O \to O' = e^{-iH_c\varphi}Oe^{iH_c\varphi}$. We are interested in the phase sensitivity for small φ, so that we can expand Eq. (38) in powers of φ, arriving at

$$O(\varphi) = O - i\varphi[H_c, O] - \frac{1}{2}\varphi^2(H_c^2 O + OH_c^2 - 2H_c O H_c) + O(\varphi^3). \tag{60}$$

If the input state $|\Psi_N^{(M)}\rangle$ is an eigenvector of O with eigenvalue 0, we obtain the following simple expressions for $\langle O\rangle$ and $\text{var}(O)$:

$$\left|\frac{\partial}{\partial\varphi}\langle O\rangle\right|^2 = 4\varphi^2|\langle H_c O H_c\rangle|^2 + O(\varphi^3), \tag{61}$$

$$\text{var}(O) = \varphi^2\langle H_c O^2 H_c\rangle + O(\varphi^3), \tag{62}$$

so that the phase fluctuation $(\delta\varphi)^2$ simplifies to

$$(\delta\varphi)^2 = \frac{\langle HO^2H\rangle}{4|\langle HOH\rangle|^2} + O(\varphi). \tag{63}$$

An observable fulfilling this property is $O = (n_M^{(-)})^2$, where $n_M^{(-)} = \frac{1}{2}(p_M^\dagger p_M - q_M^\dagger q_M)$.

The commutation relations for $p_M^\dagger$ and $q_M^\dagger$ [Eq. (55)] imply that in the limit of infinitely many modes $M \to \infty$, the operators $p_M^\dagger$ and $q_M^\dagger$ become bosonic. We will thus start out with a scenario where the input states are in the bosonic limit and then turn our attention to a setting that is far from the bosonic limit.

2. Bosonic limit

In this section, we will consider the scenario $M\to\infty$, i.e., we are in the bosonic limit, where the limit is taken for the expectation values of the operators. We will consider a coupling of the form $H_c=\varphi H_\infty$, where

$$H_\infty=\frac{1}{2}(a_\infty^\dagger b_\infty+a_\infty b_\infty^\dagger), \tag{64}$$

and measure $(n_\infty^{(-)})^2$.

We start deriving the best precision for unpaired states using Eq. (39). We will use a finite M for input state, coupling Hamiltonian, and measurement and then take the limit $M\to\infty$. To be precise, the calculation will be done for $H_M=\frac{1}{2}(a_M^\dagger b_M+a_M b_M^\dagger)$ and $(n_M^{(-)})^2$. Then $\lim_{M\to\infty}\langle\phi_{a,b}|H_M|\phi_{a,b}\rangle=0$ due to the conservation of particle number. Hence,

$$\lim_{M\to\infty}\mathrm{var}(H_M)=\lim_{M\to\infty}\langle H_M^2\rangle=\lim_{M\to\infty}(\langle p_M^\dagger p_M\rangle+\langle q_M^\dagger q_M\rangle)^2=0,$$

as $\langle p_M^\dagger p_M\rangle=\frac{1}{M}\Sigma_{kl}|\langle P_k^\dagger P_l\rangle|^2\leq N/M$, where the last inequality results from the bound of the pairing measure on unpaired states Thm. V.6. The same holds for $\langle q_M^\dagger q_M\rangle$. Hence, in the limit $M\to\infty$ the variance of H_∞ vanishes. For the setting of paired states, however, we can obtain the following result:

Theorem VI.4. For paired input states, the interferometer depicted in Fig. 4 allows us to estimate the coupling parameter φ to a precision

$$(\delta\varphi)_{\mathrm{inf}}^2=\frac{1}{2N^2}. \tag{65}$$

Proof. Consider an interferometric setup depicted in Fig. 4, where the $2N$-particle input state and the coupling Hamiltonian are defined in Eqs. (57) and (64), respectively. We will again use a finite M for input state, coupling Hamiltonian, and measurement and then take the limit $M\to\infty$, i.e., we use $|\Psi_{\mathrm{in}}\rangle=|N\rangle_a^{(M)}|N\rangle_b^{(M)}$, $H_M=\frac{1}{2}(a_M^\dagger b_M+a_M b_M^\dagger)$, and $(n_M^{(-)})^2$. Making use of the relations

$$p_M|N\rangle_a^{(M)}=\alpha_N|N-1\rangle_a^{(M)}, \tag{66}$$

$$p_M^\dagger|N\rangle_a^{(M)}=\alpha_{N+1}|N+1\rangle_a^{(M)}, \tag{67}$$

where $\alpha_N=\sqrt{N(1-(N-1)/M)}$, a lengthy but straightforward calculation leads to $(\delta\varphi)_M^2=\frac{1}{2\alpha_{N+1}^2\alpha_N^2}+O(\varphi)$ using Eq. (63). Taking the limit $M\to\infty$ leads to the result of the theorem. ■

3. Interferometry far from the bosonic limit

In the preceding section, we have studied the power of paired states in the bosonic limit. As the power of bosonic particles for interferometry has been known for quite a while, the use of paired states where the fermionic nature of the particles survives might be a more interesting question. In this section, we will show that even far from the bosonic limit paired states can achieve a precision gain of order N for quantum metrology.

We will study a coupling Hamiltonian of the form $H_c=\varphi H_F$, where

$$H_F=\sum_{k=1}^{\infty}P_k^\dagger Q_k+P_k Q_k^\dagger. \tag{68}$$

First, we will give a bound for the phase sensitivity achievable by using product states at the input:

Theorem VI.5. Using product states of $2N$ particles as input states for the interferometric setting depicted in Fig. 4, the phase φ of the coupling Hamiltonian $H_c=\varphi H_F$, where H_F is defined in Eq. (68), can be measured to a precision $(\delta\varphi)^2\geq 1/(16N)$.

Proof. For every product state of the form (59), $\langle H_F\rangle=0$ due to particle number conservation. Hence, $\mathrm{var}(H_F)=\langle H_F^2\rangle$. We will bound this expectation value,

$$\begin{aligned}\langle H_F^2\rangle&=\sum_{k\neq l}\langle P_k^\dagger P_l\rangle\langle Q_l^\dagger Q_k\rangle+\mathrm{c.c.}+\sum_k\langle P_k^\dagger P_k\rangle\langle Q_k Q_k^\dagger\rangle\\&\leq 2\left(\sum_{k\neq l}|\langle P_k^\dagger P_l\rangle|^2\right)^{1/2}\left(\sum_{k\neq l}|\langle Q_k^\dagger Q_l\rangle|^2\right)^{1/2}\\&\quad+\sum_k\langle P_k^\dagger P_k\rangle\langle Q_k Q_k^\dagger\rangle+\mathrm{c.c.}\end{aligned}$$

From Lemma D.1 we know that $(\Sigma_{k\neq l}|\langle P_k^\dagger P_l\rangle|^2)^{1/2}\leq\sqrt{N}$. Further, $\langle P_k P_k^\dagger\rangle=\langle 1-(n_k-n_{-k})^2-n_k n_{-k}\rangle\leq 1$ and $\Sigma_k\langle P_k^\dagger P_k\rangle\leq N$. Thus $\mathrm{var}(H_{pq})\leq 2\sqrt{N}\sqrt{N}+2N=4N$, which leads immediately to our result via Eq. (39). ■

This bound can be beaten by a factor of $\sqrt{N}$ using paired states. A lengthy but straightforward calculation leads to the following result:

Theorem VI.6. Using paired states of the form (57) as input states for the interferometric setting depicted in Fig. 4, the phase φ of the coupling Hamiltonian $H_c=\varphi H_F$, where H_F is defined in Eq. (68), can be measured to a precision

$$(\delta\varphi)^2=\frac{M(M-1)}{8N(M-N)(M-1+MN-N^2)}. \tag{69}$$

This theorem implies $(\delta\varphi)^2\sim 1/N^2$ for all $M\geq 2N$. In conclusion, we have shown that paired states are a resource for quantum metrology. Theorem VI.6 is the main result of this section. We have remarked already at the beginning of this section that it has been proven before that the Heisenberg limit can be achieved using fermionic particles [58]. However, these states were constructed in an abstract way, while we prove that the BCS states that can be created easily in an experimental setup are a very powerful resource for quantum metrology.

VII. APPLICATION TO EXPERIMENTS AND CONCLUSION

In summary, we have developed a pairing theory for fermionic states. We have given a precise definition of pairing based on a minimal list of natural requirements. We have seen that pairing is not equivalent to entanglement of the whole state nor of its two-particle reduced density operator but represents a different kind of quantum correlation. Within the framework of fermionic Gaussian states, we could solve the pairing problem completely. For number-conserving states, we have given sufficient conditions for the

detection of pairing that can be verified by current experimental techniques, e.g., via spatial noise correlations [59–61], and we prescribed a systematic way to construct complete families of pairing witnesses.

To shed some light on the pairing debate [7,10–12], we would need access to the proportionality factor linking the quantity plotted in Fig. 4 of [7] to the local pair correlation correlation function $G_2(r,r)=\langle\Psi_\downarrow^\dagger(r)\Psi_\uparrow^\dagger(r)\Psi_\uparrow(r)\Psi_\downarrow(r)\rangle$.

Another important point of our work is the utility of fermionic states for quantum metrology. While it has been shown that, in principle, fermionic states can achieve the Heisenberg limit for precision measurements in a Ramsey-type interferometer [58], we could prove the usefulness of states that are available in the laboratory. Furthermore, the optimal precision for the Ramsey-type setup is proportional to the pairing measure introduced from an intuitive picture in Secs. II C and V. This endows the measure with an operational meaning. The results we have presented are just a first step in understanding pairing and its relation to other types of quantum correlations.

We hope that the pairing theory we have developed will help to get a better understanding of correlated many-body systems, and can provide a new perspective on quantum correlations and may serve as a starting point for further inquiries.

For example, one might attempt a finer characterization of pairing, e.g., $\Sigma_{k=1}^2 P_k^\dagger|0\rangle$ and $\Sigma_{k=1}^M P_k^\dagger|0\rangle$ represent paired states of rather different nature: it would be interesting to develop witnesses or measures that allow us to determine over how many modes the pairs in a given states extend and to relate these differences to applications in metrology or elsewhere. Moreover, the theory we developed has been concerned with finitely many modes only and it is an obvious question whether generalizing to an infinite-dimensional single-particle space gives rise to new phenomena.

Up to now we have concentrated on fermionic states. But the question of pairing in bosonic systems might be equally interesting and relevant for recent experiments [62].

What about higher-order correlations? The set of unpaired states contains both separable and highly correlated states. This is, for example, reflected in the fact that there are unpaired states that can be transformed to paired ones by single-mode particle number measurements [e.g., $(a_1^\dagger a_2^\dagger a_3^\dagger + a_4^\dagger a_5^\dagger a_6^\dagger)|0\rangle$ by measuring particle number in mode $b=a_3+a_6$]. A theory of higher-order correlated states could be developed along the lines discussed here, e.g., by changing the set of observables on which the states are compared to uncorrelated ones and defining as nth-order correlated those states whose expectation values on nth-order observables cannot be reproduced by $(m<n)$-correlated states.

Tools and methods from entanglement theory have been very useful in analyzing pairing. One very important such tool, however, is missing: positive maps, that is, transformations that do not correspond to a physical operations but nevertheless, when applied to a subsystem in a separable state with the rest, map density operators to (unnormalized) density operators and thus provides strong necessary conditions for separability. Finding an analogy might prove very useful for the analysis of many-body correlations. Another important object in the theory of entanglement is the set of LOCC operations (local operations and classical communication), i.e., the operations that cannot create entanglement. In the case of pairing, the analogous set would contain passive operations and discarding modes. Are there other physical transformations that cannot create pairing? Do paired states, then, possibly allow us to implement such transformations similar to entanglement enabling non-LOCC operations?

ACKNOWLEDGMENTS

We acknowledge support by the Elite Network of Bavaria QCCC, the DFG within SFB 631, the DFG Cluster of Excellence Munich-Centre for Advanced Photonics, QUANTOP, and the Danish Natural Science Research Council (FNU).

APPENDIX A: USEFUL PROPERTIES OF SEPARABLE STATES

We give two technical lemmas that involve useful properties of product states.

1. Bound of $a_i^\dagger a_j^\dagger a_k a_l$+H.c. on separable states

In this section, we prove a bound of a special two-body operator on product states:

Lemma A.1. Let $\rho\in S_{\text{sep}}$ be a separable state. Then

$$|\text{tr}[(a_i^\dagger a_j^\dagger a_k a_l + \text{H.c.})\rho_s]| \leqslant \tfrac{1}{2}. \tag{A1}$$

Proof. Let $\mathcal{H}_{ijkl}$ be the Hilbert space spanned by $a_i^\dagger$, $a_j^\dagger$, $a_k^\dagger$, $a_l^\dagger$ and define $A_{ijkl}=a_i^\dagger a_j^\dagger a_k a_l$+H.c. Then $\text{tr}[A_{ijkl}\rho]=\text{tr}[\rho^{(ijkl)}A_{ijkl}]$, where $\rho^{(ijkl)}=\Sigma_{n=0}^4\beta_{ijkl}^{(n)}|n\rangle\langle n|$ is a mixed separable state according to Lemma II.2, and $|n\rangle$ denotes the occupation number basis for the subspace $\mathcal{H}_{ijkl}$. It is easily checked that A_{ijkl} can have nonvanishing expectation value only for the two-particle state $|2\rangle=(\Sigma_{r=i,j,k,l}\mu_r a_r^\dagger)(\Sigma_{s=i,j,k,l}\nu_s a_s^\dagger)|0\rangle$. Using $|2\,\text{Re}(ab)|\leqslant|a|^2+|b|^2$ for any complex numbers a, b and the normalization conditions $\Sigma_r|\mu_r|^2=\Sigma_r|\nu_r|^2=1$, one arrives at

$$\begin{aligned}|\text{tr}[A_{ijkl}\rho]| &= 2|\text{Re}[(\mu_i\nu_j-\mu_j\nu_i)(\mu_k\nu_l-\mu_l\nu_k)^*]|\\ &= (|\mu_i|^2+|\mu_j|^2)(|\mu_k|^2+|\mu_l|^2)\\ &\quad+(|\nu_i|^2+|\nu_j|^2)(|\nu_k|^2+|\nu_l|^2)\\ &\leqslant 0.25+0.25=0.5.\end{aligned}$$

■

2. Expectation values of one- and two-body operators for separable states

In this section, we will prove that the one- and two-body operators for separable states can be expressed in terms of matrix elements of projectors.

Lemma A.2. Let $\rho\in\mathcal{S}_{\text{sep}}^{(N)}$ be a pure separable state. Then

$$\langle n_i\rangle = P_{ii}, \tag{A2}$$

$$\langle a_i^\dagger a_j^\dagger a_k a_l\rangle_\rho = (P\otimes P)_{(ij)(lk)} - (P\otimes P)_{(ij)(kl)}, \tag{A3}$$

where $P=P^2=P^\dagger$ is a projector of rank N.

Proof. Consider M modes. We go into the basis where the pure separable state is of the form $|\Phi\rangle=\Pi_{i=1}^N a_{\alpha_i}^\dagger|0\rangle$. In this basis $\langle a_{\alpha_i}^\dagger a_{\alpha_j}^\dagger a_{\alpha_k} a_{\alpha_l}\rangle_{|\Phi\rangle}=\delta_{il}\delta_{jk}-\delta_{ik}\delta_{jl}$, i.e., Eq. (A3) for $P=\mathrm{Id}_N$, where $\mathrm{Id}_N=\mathbb{1}_N\oplus 0_{M-N}\in\mathbb{C}^{M\times M}$. Now let $a_i^\dagger=\Sigma_k U_{ik}a_{\alpha_k}^\dagger$. Then

$$\begin{aligned}\langle a_i^\dagger a_j^\dagger a_k a_l\rangle_{\rho_s^{(N)}} &= (U\mathrm{Id}_N U^\dagger)\otimes(U\mathrm{Id}_N U^\dagger)_{(ij)(lk)} - (U\mathrm{Id}_N U^\dagger)\\ &\quad\otimes(U\mathrm{Id}_N U^\dagger)_{(ij)(kl)}\\ &= (P\otimes P)_{(ij)(lk)} - (P\otimes P)_{(ij)(kl)},\end{aligned}$$

and P is a projector of rank N.

For the one-particle operators, we obtain $\langle n_i\rangle=P_{ii}$ as

$$\begin{aligned}(N-1)\langle n_i\rangle &= \Sigma_{j\neq i}\langle n_i n_j\rangle\\ &= \Sigma_{j\neq i}P_{ii}P_{jj} - |P_{ij}|^2\\ &= \Sigma_j P_{ii}P_{jj} - P_{ij}P_{ji}\\ &= \mathrm{tr}[P]P_{ii} - (P^2)_{ii}\\ &= (N-1)P_{ii}.\end{aligned}$$

■

APPENDIX B: PROOF OF LEMMAS V.1 AND V.2

1. Proof of Lemma V.2

Proof. As $H_{1\pm}^{(p)}$, $H_{2\pm}^{(p)}$, $H_{3\pm}^{(p)}$ are built up of operators that are the product of at most two creation and annihilation operators, we can prove the lemma for separable states. In the first step, we will show that the three operators are positive on all separable states. Then we will show that all states within the set bounded by $H_{1\pm}^{(p)}$, $H_{2\pm}^{(p)}$, $H_{3\pm}^{(p)}$ correspond to a separable state. Finally we will show there exist states that are detected as paired by $H_{1\pm}^{(p)}$ and $H_{3\pm}^{(p)}$. Positivity of $H_{2\pm}^{(p)}$ on all number-conserving states will be shown in the proof of Lemma V.1 following below.

To show positivity of $H_{1\pm}^{(p)}$, $H_{2\pm}^{(p)}$, $H_{3\pm}^{(p)}$, it is sufficient to show the positivity for pure separable states, as the result for mixed states follows from convexity. From now on, let $\rho\in\mathcal{S}_{\mathrm{sep}}^{(N)}$.

a. $\mathrm{tr}[H_{1\pm}^{(p)}\rho]\geq 0$

In Lemma A.2 (see Appendix A), we have shown that the expectation values of number-conserving one- and two-body operators can be expressed in terms of matrix elements of projectors. Let P be the rank N projector such that $\langle a_i^\dagger a_j^\dagger a_k a_l\rangle_\rho=(P\otimes P)_{(ij)(lk)}-(P\otimes P)_{(ij)(kl)}$, $\langle n_i\rangle=P_{ii}$, and let $\tilde{P}=P|_{k-k,l,-l}$ the 4×4 principal submatrix of P where the indices run over k, $-k$, l, $-l$. Then we have the following inequalities:

$$\langle n_k n_{-k}\rangle = P_{kk}P_{-k-k} - |P_{k-k}|^2 \leq \frac{1}{2}(|P_{kk}|^2+|P_{-k-k}|^2) - |P_{k-k}|^2, \tag{B1}$$

$$\begin{aligned}|\langle a_k^\dagger a_{-k}^\dagger a_{-l}a_l + \mathrm{H.c.}\rangle| &= 2|\mathrm{Re}(P_{kl}P_{-k-l} - P_{k-l}P_{-kl})|\\ &\leq 2(|P_{kl}||P_{-k-l}| + |P_{k-l}||P_{-kl}|)\\ &\leq (|P_{kl}|^2 + |P_{-k-l}|^2 + |P_{k-l}|^2 + |P_{-kl}|^2).\end{aligned} \tag{B2, B3}$$

These results imply

$$\mathrm{tr}[\rho H_{1\pm}^{(p)}] \geq \frac{1}{2}\mathrm{tr}[\tilde{P}-\tilde{P}^2] + |P_{k-k}|^2 + |P_{l-l}|^2. \tag{B4}$$

We use the inclusion principle [46], stating that the eigenvalues of an $r\times r$ principal submatrix M_r of an $n\times n$ Hermitian matrix M fulfill $\lambda_k(M)\leq\lambda_k(M_r)\leq\lambda_{k+n-r}(M)$, where the eigenvalues are arranged in increasing order. As P is a projector, we have $0\leq\lambda_k(P)\leq\lambda_k(\tilde{P})\leq\lambda_{k+M-r}(P)\leq 1$. Hence,

$$\mathrm{tr}[H_{1\pm}^{(p)}\rho] \geq \frac{1}{2}\mathrm{tr}[\tilde{P}-\tilde{P}^2] \geq \frac{1}{2}\sum_k \lambda_k(\tilde{P})[1-\lambda_k(\tilde{P})] \geq 0. \tag{B5}$$

b. $\mathrm{tr}[H_{2\pm}^{(p)}\rho]\geq 0$

Define $O_1=n_k n_{-k}+n_l n_{-l}\geq 0$, $O_2^\pm = 1\pm a_k^\dagger a_{-k}^\dagger a_{-l}a_l + \mathrm{H.c.}\geq 0$. Then $H_{2\pm}^{(p)}=O_1 O_2^\pm$, and as $[O_1,O_2^\pm]=0$ we conclude that $H_{2\pm}^{(p)}=O_1O_2^\pm\geq 0$.

c. $\mathrm{tr}[H_{3\pm}^{(p)}\rho]\geq 0$

We will need the Lemma II.2: $\mathrm{tr}[H_{3\pm}^{(p)}\rho]=\mathrm{tr}[H_{3\pm}^{(p)}\rho_{kl}]$, where $\rho_{kl}=\Sigma_{n=0}^4\beta_n|n\rangle\langle n|$, $\beta_n\geq 0$, $\Sigma_{n=0}^4\beta_n=1$, and $|n\rangle$, $n=0,\ldots,4$ are separable n-particle states. Let $\langle H_{3\pm}^{(p)}\rangle_n=\langle n|H_{3\pm}^{(p)}|n\rangle$. Then a straightforward calculation leads to $\langle H_{3\pm}^{(p)}\rangle_0=1$, $\langle H_{3\pm}^{(p)}\rangle_1=\frac{1}{2}$, $\langle H_{3\pm}^{(p)}\rangle_2=\frac{1}{2}$, $\langle H_{3\pm}^{(p)}\rangle_3=0$, and $\langle H_{3\pm}^{(p)}\rangle_4=0$. Linearity of the trace implies $\mathrm{tr}[H_{3\pm}^{(p)}\rho]\geq 0$. Hence, all separable states lie within the set bounded by the planes defined by the witness operators $H_{1\pm}^{(p)}$, $H_{2\pm}^{(p)}$, $H_{3\pm}^{(p)}$.

Next, we show that each point within the polytope C^{unpaired} corresponds to a separable state. As S_{sep} is convex, it is sufficient to check that for every extreme point of C^{unpaired} there exists a separable state. This is indeed the case: The extreme points of C^{unpaired} are (0, 0, 0), (2, 0, 0), (4, 2, 0), $(2,1/2,\pm 1/2)$, which correspond, for example, to the separable states $|0\rangle$, $a_k^\dagger a_l^\dagger|0\rangle$, $a_k^\dagger a_{-k}^\dagger a_l^\dagger a_{-l}^\dagger|0\rangle$, and $(a_k^\dagger + a_l^\dagger)(a_{-k}^\dagger \pm a_{-l}^\dagger)/2|0\rangle$, respectively.

It remains to show that $H_{1\pm}^{(p)}$ and $H_{3\pm}^{(p)}$ are pairing witnesses. Define $|\Psi\rangle=\frac{1}{\sqrt{2}}(a_k^\dagger a_{-k}^\dagger + a_l^\dagger a_{-l}^\dagger)|0\rangle$. Then $\mathrm{tr}[H_{1\pm}^{(p)}|\Psi\rangle\langle\Psi|]=\mathrm{tr}[H_{3\pm}^{(p)}|\Psi\rangle\langle\Psi|]=-1$. ■

2. Proof of Lemma V.2

Proof. It is sufficient to prove the lemma for $\rho\in\mathcal{S}(\mathcal{A}_N)$, as the result for a general number-conserving state follows from convexity.

a. $\mathrm{tr}[H_1\rho]\geq 0$

$H_1=\frac{1}{2}(n_k-n_{-k})^2+\frac{1}{2}(n_l-n_{-l})\geq 0$.

b. $\mathbf{tr}[H_{2\pm}\rho]\geq 0$

Shown in the proof of Thm. V.2.

c. $\mathbf{tr}[H_{3\pm}\rho]\geq 0$

Let $\rho_{kl}=\Sigma_{n=1}^{4}\beta_n|0\rangle\langle n|$ be the reduced density operator in the modes $\pm k$, $\pm l$. We can rewrite $H_{3\pm}$ in the form $H_3=2-\frac{1}{2}(n_k+n_{-k}+n_l+n_{-l})[1\mp(a_k^\dagger a_{-k}^\dagger a_{-l}a_l+\text{H.c.})]$. Defining $O_{2\mp}=1\mp(a_k^\dagger a_{-k}^\dagger a_{-l}a_l+\text{H.c.})$, we obtain $\langle O_{2\mp}\rangle_0=\langle O_{2\mp}\rangle_1=\langle O_{2\mp}\rangle_3=\langle O_{2\mp}\rangle_4=1$, $\langle O_{2\mp}\rangle_2\leq 2$. This implies $\mathrm{tr}[\rho H_{3\pm}]\geq 4-(\beta_1+2\beta_2+3\beta_3+4\beta_4)\geq 4-\Sigma_{n=0}^{4}n\beta_n=4-\mathrm{tr}[(n_k+n_{-k}+n_l+n_{-l})\rho_{kl}]\geq 0$

As in the proof of Lemma V.1, it remains to show that the extreme points of C^{all} correspond to some fermionic state. It has been shown in the proof of Lemma V.1 that (0, 0, 0), (2, 0, 0), and (4, 2, 0) can be reached by some separable state. The remaining two extreme points, $(2,1,\pm 1)$, correspond, for example, to the state $\frac{1}{\sqrt{2}}(a_k^\dagger a_{-k}^\dagger+a_l^\dagger a_{-l}^\dagger)|0\rangle$. ■

APPENDIX C: PROOF OF THM. V.4

In this section, we will provide all the details leading to Thm. v.4, starting with the bound on separable states:

Lemma C.1. Let $\rho\in S_{\mathrm{sep}}$ with $\mathrm{tr}[N_{\mathrm{op}}\rho]=N$ and let $H(\{v_k\})$ be as in Thm. V.4. Then $\mathrm{tr}[H(\{v_k\})\rho_s]\geq 0$.

Proof. The operator H_k acts nontrivially only on the modes $a_k^\dagger$, $a_{-k}^\dagger$, $a_{k+M}^\dagger$, $a_{-(k+M)}^\dagger$. Denote by ρ_k the reduced density operator obtained when tracing out all but these four modes. According to Lemma II.2, $\rho_k=\Sigma_{n=0}^{4}\beta_k^{(n)}|n\rangle\langle n|$ is a convex combination of separable n-particle states $|n\rangle\langle n|$. We proved in Lemma A.1 that $|\mathrm{tr}[(P_k^\dagger P_{k+M}+\text{H.c.})\rho_s]|\leq 1/2$. Hence $\langle H(\{v_k\})\rangle\geq 2N(1-\epsilon)-2\Sigma_{k=1}^{M}(|v_k|^2\langle N_k\rangle+\beta_k^{(2)})$. Now $2\beta_k\leq\langle N_k\rangle\leq 4$ and $|v_k|^2\leq 1-\epsilon$ so that $|v_k|^2\langle N_k\rangle+\beta_k^{(2)})\leq 4$. Due to the particle number constraint $\Sigma_{k=1}^{M}\langle N_k\rangle=N$, this value can be taken for $k=1,\ldots,N/4$. Hence, $-2\Sigma_{k=1}^{M}(|v_k|^2\langle N_k\rangle+\beta_k^{(2)})\geq -2\times 4(1-\epsilon)N/4$ so that $\langle H(\{v_k\})\rangle\geq 0$. ■

To show the witness character of $H(\{v_k\})$, we also have to prove that there exists a BCS state that is detected by the Hamiltonian. We will need the following theorem about the distribution described by the $|\lambda_N|^2$ in Eq. (16):

Theorem C.2. Let $|\Psi_{\mathrm{Gauss}}\rangle=\Sigma_{N=0}^{M}\lambda_N^{(M)}|\Psi_{\mathrm{BCS}}^{(N)}\rangle$ like in Eq. (15) and (17). If $\Sigma_{k=1}^{M}|u_k|^2|v_k|^2=O(N^\gamma)$ for some $\gamma>0$, then in the limit $N\to\infty$ the $|\lambda_N|^2$ converge to a normal distribution,

$$|\lambda_N|^2=\frac{1}{\sqrt{2\pi}\sigma_{\bar{N}}}\exp\left[-\frac{(N-\bar{N})^2}{2\sigma_{\bar{N}}^2}\right], \tag{C1}$$

where $2\bar{N}=2\Sigma_{k=1}^{M}|v_k|^2$ is the mean particle number for the variational state, and the variance is given by $\sigma_{\bar{N}}^2=4\Sigma_{k=1}^{M}|v_k|^2|u_k|^2$.

Proof. For the proof we will need a theorem from probability theory known as Lyapunov's central limit theorem [63]:

Theorem C.3. (Lyapunov's central limit theorem). Let X_1, $X_2,\ldots$ be independent random variables with distribution functions F_1, $F_2,\ldots$, respectively, such that $EX_n=\mu_n$ and $\mathrm{var}\,X_n=\sigma_n^2<\infty$, with at least one $\sigma_n>0$. Let $S_n=X_1+\ldots+X_n$ and $s_n=\sqrt{\mathrm{var}(S_n)}=\sqrt{\sigma_1^2+\ldots+\sigma_n^2}$. If the Lyapunov condition

$$\frac{1}{s_n^{2+\delta}}\sum_{k=1}^{n}E|X_k-\mu_k|^{2+\delta}\underset{n\to\infty}{\to}0$$

is satisfied for some $\delta>0$, then the normalized partial sums $\frac{S_n-ES_n}{s_n}$ converge in distribution to a random variable with normal distribution $N(0,1)$.

Consider the observables $X_k=n_k+n_{-k}, k=1,\ldots,M$, where $n_{\pm k}=0,1$ is the number of particles with quantum numbers $\pm k$, respectively. The X_k can be considered as classical random variables since they commute mutually. In the variational BCS state, the random variable $S_M=\Sigma_{k=1}^{M}X_k$ is distributed according to the probability distribution

$$P(S_M=2N)=\sum_{k_1<\cdots<k_M=1}^{M}|v_{k_1}|^2\cdots|v_{k_N}|^2|u_{k_{N+1}}|^2\cdots|u_{k_M}|^2$$

$$=\left(\prod_k|u_k|^2\right)\sum_{k_1<\cdots<k_M=1}^{M}\frac{|v_{k_1}|^2\cdots|v_{k_N}|^2}{|u_{k_1}|^2\cdots|u_{k_N}|^2} \tag{C2}$$

$$=\frac{|C|^2}{(N!)^2|C_N|^2}=|\lambda_N^{(M)}|^2. \tag{C3}$$

With the help of Thm. C.3 applied to the random variable S_M, we can now complete the proof of Thm. C.2, i.e., show that $\lambda_N^{(M)}$ converges to a normal distribution for large M. We start calculating the expectation value μ_k of X_k. For a BCS state, $X_k=0,2$, as particles with quantum numbers $\pm k$ always appear in pairs. As $P(X_k=0)=|u_k|^2$, $P(X_k=2)=|v_k|^2$, we get $\mu_k=2|v_k|^2$ and $E(S_M)=2\Sigma_k|v_k|^2\equiv 2\bar{N}$. For calculating the variance, note that $X_k^2=n_k^2+n_{-k}^2+2n_kn_{-k}=0,4$, and $P(X_k^2=0)=|u_k|^2$, $P(X_k^2=4)=|v_k|^2$. Hence

$$\mathrm{var}(X_k)=4|u_k|^2|v_k|^2,\quad s_M^2=4\sum_k|u_k|^2|v_k|^2. \tag{C4}$$

To apply the central limit theorem, we consider $E(|X_k-\mu_k|^4)$. Using $P(|X_k-\mu_k|^4=\mu_k^4)=|u_k|^2$, $P[|X_k-\mu_k|^4=(2-\mu_k)^4]=|v_k|^2$, and $\mu_k=2|v_k|^2$, we arrive at

$$E(|X_k-\mu_k|^4)=16|u_k|^2|v_k|^2(|u_k|^6+|v_k|^6)$$
$$\leq 16|u_k|^2|v_k|^2(|u_k|^2+|v_k|^2)$$
$$=16|u_k|^2|v_k|^2. \tag{C5}$$

Setting $\delta=2$ in the Lyapunov condition, we obtain

$$\frac{1}{s_M^4}\sum_{k=1}^{M}E(|X_k-\mu_k|^4)\leq\frac{4}{s_M^2}=O(N^{-\gamma})\to 0, \tag{C6}$$

where we have applied the assumption of the theorem $\Sigma_{k=1}^{M}|v_k|^2|u_k|^2=O(N^\gamma)$ in the last step. The central limit theorem implies that S_M converges to a normal distribution with expectation values $2\bar{N}=2\Sigma_k|v_k|^2$ and variance $\sigma_{\bar{N}}^2=4\Sigma_k|v_k|^2|u_k|^2$. ■

With this result at hand, we can prove the following:

Lemma C.4. Let $H(\{v_k\})$ and $|\Psi_{\mathrm{BCS}}^{(N)}\rangle$ be defined as in Thm. 5.4. If $\epsilon>18/\sqrt{\pi N}$, then

$$\langle\Psi_{\mathrm{BCS,sym}}^{(N)}|H(\{v_k\})|\Psi_{\mathrm{BCS,sym}}^{(N)}\rangle<0.$$

Proof. We will use the correspondence of variational and number-conserving BCS states, deriving first a bound for $|\langle H(\{v_k\})\rangle_{\mathrm{var}}-\langle H(\{v_k\})\rangle_N|$, where $|\Psi_{\mathrm{Gauss}}\rangle=\Sigma_{k=1}^{2M}\lambda_n|\Psi_{\mathrm{BCS,sym}}^{(n)}\rangle$ with $|\Psi_{\mathrm{BCS,sym}}^{(n)}\rangle$ like in Thm. 5.4. To do so, we will need that the $|\lambda_n|^2$ are normally distributed. From $|u_k|^2=1-|v_k|^2\geqslant\epsilon$, where $\epsilon>18/(\sqrt{2\pi\bar{N}})$ and $\Sigma_{k=1}^{2M}|v_k|^2=\bar{N}$, it follows that $\sigma_{\bar{N}}=\Sigma_{k=1}^{2M}|v_k|^2|u_k|^2\geqslant\epsilon\bar{N}=O(\sqrt{\bar{N}})$. Hence, we know from Thm. C.2 that the $|\lambda_n|^2$ describe a normal distribution around $\bar{N}\approx N$ with standard deviation $\sigma_{\bar{N}}$.

Now, write $H(\{v_k\})=H_0-2W+2(1-\epsilon)\Sigma_{k=1}^{M}N_k$, where

$$H_0=-2\sum_{k=1}^{M}|v_k|^2N_k,$$

$$W=2\sum_k P_k^\dagger P_{k+M}+P_{k+M}^\dagger P_k.$$

We start with a bound for $|\langle H_0\rangle_{\mathrm{var}}-\langle H_0\rangle_N|\leqslant T_1+T_2$, where

$$T_1=\left|\sum_{\Delta\in[-\sigma_{\bar{N}}^2,\sigma_{\bar{N}}^2]}|\lambda_{N+\Delta}|^2(\langle H_0\rangle_{N+\Delta}-\langle H_0\rangle_N)\right|,$$

$$T_2=\left|\sum_{\Delta\notin[-\sigma_{\bar{N}}^2,\sigma_{\bar{N}}^2]}(|\lambda_{N+\Delta}|^2(\langle H_0\rangle_{N+\Delta}-\langle H_0\rangle_N)\right|. \quad \text{(C7)}$$

A bound for T_2 can be easily derived noting that

$$|\langle H_0\rangle_n-\langle H_0\rangle_{n'}|=8\left|\sum_k|v_k|^2(\langle n_k\rangle_n-\langle n_k\rangle_{n'})\right|, \quad \text{(C8)}$$

and for $n=N+\Delta>=N$ we have $\Sigma_k|v_k|^2(\langle n_k\rangle_n-\langle n_k\rangle_N)\leqslant\Sigma_k|v_k|^2\langle n_k\rangle_n\leqslant n$, as $|v_k|^2\leqslant 1$. Hence,

$$\begin{aligned}T_2&\leqslant 16\left|\sum_{\Delta\notin[0,\sigma_{\bar{N}}^2]}|\lambda_{N+\Delta}|^2|N+\Delta|\right|\\&\leqslant 8\frac{\sigma_{\bar{N}}}{\sqrt{2\pi}}e^{-\sigma_{\bar{N}}^2/2}+4N[1-\mathrm{erf}(\sigma_{\bar{N}}/\sqrt{2})]\\&\leqslant 8\frac{\sigma_{\bar{N}}}{\sqrt{2\pi}}+4N[1-\mathrm{erf}(\sigma_{\bar{N}}/\sqrt{2})],\end{aligned} \quad \text{(C9)}$$

where we have approximated the sum by an integral in the second step. For bounding T_1, we will show first that for $n=N+\Delta$, where $\Delta\in[-\sigma_{\bar{N}}^2,\sigma_{\bar{N}}^2]$, we have $\langle n_k\rangle_n-\langle n_k\rangle_{n-1}\geqslant 0$. Expanding the BCS wave function

$$|\Psi_{\mathrm{BCS,sym}}^{(n)}\rangle=C_n n!\sum_{j_1<\cdots<j_n=1}^{2M}\alpha_{j_1}\cdots\alpha_{j_n}P_{j_1}^\dagger\cdots P_{j_n}^\dagger|0\rangle, \quad \text{(C10)}$$

the expectation value of the number operator is easily calculated to be $\langle n_k\rangle_n=|C_n|^2(n!)^2|\alpha_k|^2S_k^{(n-1)}$, where

$$S_k^{(n)}=\sum_{\substack{j_1<\cdots<j_n=1\\ j_i\neq k}}^{2M}|\alpha_{j_1}|^2\cdots|\alpha_{j_n}|^2. \quad \text{(C11)}$$

If $0<|v_k|^2\leqslant 1-\epsilon$, there exists a lower bound on the coefficients $|\alpha_k|^2=|v_k|^2/\sqrt{1-|v_k|^2}\geqslant b\,\forall k$. Then $S_k^{(n-1)}$ and $S_k^{(n-2)}$ are related via

$$S_k^{(n-1)}\geqslant b\frac{2M-(n-1)}{n-1}S_k^{(n-2)}.$$

In the proof of Thm. C.2, we show that

$$\frac{|\lambda_n|^2}{|\lambda_{n-1}|^2}=\frac{|C_{n-1}|^2[(n-1)!]^2}{|C_n|^2(n!)^2}, \quad \text{(C12)}$$

resulting in

$$\begin{aligned}\langle n_k\rangle_n-\langle n_k\rangle_{n-1}\geqslant&\left(b\frac{2M-(n-1)}{n-1}-\frac{|\lambda_n|^2}{|\lambda_{n-1}|^2}\right)\\&\times|C_n|^2(n!)^2|\alpha_k|^2S_k^{(n-2)}.\end{aligned} \quad \text{(C13)}$$

For $n=N+\Delta$ and $\Delta\in[-\sigma_{\bar{N}}^2,\sigma_{\bar{N}}^2]$, the normal distribution of the $|\lambda_n|^2$ implies $|\lambda_n|^2/|\lambda_{n-1}|^2=\exp[(2\Delta-1)/(2\sigma_{\bar{N}}^2)]\leqslant e$. Hence, $b\frac{2M-(n-1)}{n-1}-\frac{|\lambda_n|^2}{|\lambda_{n-1}|^2}\geqslant 0\Leftrightarrow b\geqslant e\frac{n}{2M-(n-1)}>3\frac{n-1}{2M-(n-1)}$. For $M=q(n-1)$, this is equivalent to $|\alpha_k|^2\geqslant 3/(2q-1)$, which can be achieved for $q\gg 1$. The last condition is satisfied, as we are considering dilute systems, where $M\gg\bar{N}$. Thus, $\langle n_k\rangle_n-\langle n_k\rangle_{n-1}\geqslant 0$, implying $\Sigma_k|v_k|^2(\langle n_k\rangle_n-\langle n_k\rangle_{n-1})\leqslant 1$, as $|v_k|^2\leqslant 1$. Using Eq. (C8) and a telescope sum, we conclude that

$$\begin{aligned}T_1&\leqslant 8\left|\sum_{\Delta\in[-\sigma_{\bar{N}},\sigma_{\bar{N}}]}|\lambda_{N+\Delta}|^2|\Delta|\right|\\&\leqslant 8\left|\sum_\Delta|\lambda_{N+\Delta}|^2|\Delta|\right|\\&=16\frac{\sigma_{\bar{N}}}{\sqrt{2\pi}}.\end{aligned} \quad \text{(C14)}$$

Next, we derive the bound for the operator W. Its expectation value is given by

$$\langle W\rangle_n=|C_n|^2(n!)^2 2\sum_k|\alpha_k|^2\sum_{\substack{j_1<\cdots<j_{n-1}\\ j_i\neq k,k+M}}^{2M}|\alpha_{j_1}|^2\cdots|\alpha_{j_{n-1}}|^2. \quad \text{(C15)}$$

For $n\in[N-\Delta,N+\Delta]$, we use the same argumentation we have used for bounding $\langle n_k\rangle_n-\langle n_k\rangle_{n-1}$, to obtain

$$\langle W\rangle_n-\langle W\rangle_{n-1}\leqslant 2. \quad \text{(C16)}$$

Further, $\langle n_k\rangle_n=\langle P_k^\dagger P_{k-M}^\dagger+\mathrm{H.c.}\rangle_n/2+\langle n_k n_{k+M}\rangle_n$ due to the symmetry $\alpha_k=\alpha_{k+M}$. Hence, $\langle W\rangle_n\leqslant 2n$. Thus, up to a factor of 2 we obtain the same bound as for H_0. Putting all the pieces together, we find that

$$|\langle H(\{v_k\})\rangle_{\text{var}} - \langle H(\{v_k\})\rangle_N| \leq 2(1-\epsilon) + \frac{72}{\sqrt{2\pi}}\sigma_N + 12N[1-\text{erf}(\sigma_N/\sqrt{2})]. \tag{C17}$$

In the limit of large x, the error function $\text{erf}(x/\sqrt{2\pi})$ can be approximated by the following formula:

$$1-\text{erf}(x/\sqrt{2}) = 2\frac{\exp[-x^2/2]}{\sqrt{2\pi}}(x^{-1}-x^{-3}+\cdots). \tag{C18}$$

As $\sigma_N = O(\sqrt{N})$, we conclude

$$12N[1-\text{erf}(\sigma_N/\sqrt{2})] \leq 24\sigma_N \exp[-\sigma_N^2/2]/(\epsilon\sqrt{2\pi}) \to 0$$

for $N \gg 1$. A straightforward calculation results in $\langle H(\{v_k\})\rangle_{\text{var}} = -4N\epsilon$, leading immediately to the statement of the theorem. ■

APPENDIX D: LEMMA FOR THE PROOF OF THM. 5.6

Lemma D.1. Every pure separable state $\rho \in \mathcal{S}(\mathcal{A}_N)$ fulfills $\Sigma_{kl=1}^M |\langle P_k^\dagger P_l\rangle_\rho| \leq N/2$, and this bound is tight.

Proof. Using Lemma A.2, we obtain

$$\sum_{k,l=1}^M |\langle P_k^\dagger P_l\rangle| = \sum_{k,l=1}^M |P_{kl}P_{-k-l} - P_{k-l}P_{-kl}|, \tag{D1}$$

where $P = P^2 = P^\dagger$ and $\text{tr}[P] = N$. Using the triangle inequality, we get

$$\sum_{k,l=1}^M |\langle P_k^\dagger P_l\rangle| \leq \frac{1}{2}\sum_{k,l}(|P_{kl}|^2 + |P_{-k-l}|^2 + |P_{k-l}|^2 + |P_{-kl}|^2) = \frac{1}{2}\text{tr}[P^2] = N/2.$$

In the last step, we have used the property that the sum of the squares of a normal matrix is equal to the sum of squares of its eigenvalues. Taking the square root, we obtain the bound of our claim.

The bound is tight, as $P = \mathbb{1}_{2_N}$ implies $\Sigma_{kl}|\langle P_k^\dagger P_l\rangle| = N/2$, which is obtained for $|\Phi\rangle = \Pi_{i=1}^N a_i^\dagger|0\rangle$. ■

APPENDIX E: PROOF OF LEMMA 3.5

Proof. Let $|i,j\rangle = a_i^\dagger a_j^\dagger|0\rangle$ and consider the subspace spanned by the states $\{|k,-k\rangle, |l,-l\rangle, |k,l\rangle, |k,-l\rangle, |-k,l\rangle, |-k,-l\rangle\}$. In this basis, the two-particle RDO $\rho_2^{(N)}$ of $|\Psi_{\text{BCS}}^{(N)}\rangle$ is of the form

$$\rho_2^{(N)} = \frac{1}{4+2a_1}\begin{pmatrix} a_1 & a_2 & 0 \\ a_2 & a_1 & 0 \\ 0 & 0 & \mathbb{1}_4 \end{pmatrix}, \tag{E1}$$

where $a_1 = (M-1)/(N-1)$, $a_2 = (M-N)/(N-1)$. The witness operator $H_1^{(p)}$ of Thm. 5.1 has a negative expectation value on $\rho_2^{(N)}$, hence the state is paired in these modes.

For solving the entanglement question, we will use the following theorem [25] applicable to mixed fermionic states of two particles each living on a single-particle Hilbert space of dimension 4:

Theorem E.1. Let the mixed state acting on $\mathcal{A}_4$ have a spectral decomposition $\rho = \Sigma_{i=1}^r |\Psi_i\rangle\langle\Psi_i|$, where r is the rank of ρ, and the eigenvectors $|\Psi_i\rangle$ belonging to nonzero eigenvalues λ_i are normalized as $\langle\Psi_i|\Psi_j\rangle = \lambda_i\delta_{ij}$. Let $|\Psi_i\rangle = \Sigma_{a,b} w_{ab} a_a^\dagger a_b^\dagger|0\rangle$ in some basis, and define the complex symmetric $r\times r$ matrix C by

$$C_{ij} = \sum_{abcd} \epsilon^{abcd} w_{ab}^i w_{cd}^j, \tag{E2}$$

which can be represented using a unitary matrix as $C = UC_dU^T$, with $C_d = \text{diag}[c_1,\ldots,c_r]$ diagonal and $|c_1| \geq |c_2| \geq \cdots \geq |c_r|$. The state has Slater number 1 if and only if

$$|c_1| \leq \sum_{i=2}^r |c_i|. \tag{E3}$$

The spectral decomposition of $\rho_2^{(N)}$ is given by

$$\rho_2^{(N)} = |\Psi_+\rangle\langle\Psi_+| + |\Psi_-\rangle\langle\Psi_-| + |\Psi_{kl}\rangle\langle\Psi_{kl}| + |\Psi_{k-l}\rangle\langle\Psi_{k-l}| + |\Psi_{-kl}\rangle\langle\Psi_{-kl}| + |\Psi_{-k-l}\rangle\langle\Psi_{-k-l}|,$$

where $|\Psi_+\rangle = \sqrt{\frac{a_+}{5+a_+}}|\psi_+\rangle$, $|\Psi_-\rangle = \sqrt{\frac{1}{5+a_+}}|\psi_-\rangle$, and $|\Psi_{\pm k,\pm l}\rangle = \sqrt{\frac{1}{5+a_+}}|\pm k,\pm l\rangle$. Here $|\psi_\pm\rangle = \frac{1}{\sqrt{2}}(|k,-k\rangle \pm |l,-l\rangle)$ and $a_+ = (2M-N-1)/(N-1)$. Defining $\gamma^2 = 1/(5+a_+)$, one obtains

$$C = \gamma^2\begin{pmatrix} a_+ & 0 & 0 & 0 & 0 & 0 \\ 0 & -1 & 0 & 0 & 0 & 0 \\ 0 & 0 & 0 & -1 & 0 & 0 \\ 0 & 0 & -1 & 0 & 0 & 0 \\ 0 & 0 & 0 & 0 & 0 & 1 \\ 0 & 0 & 0 & 0 & 1 & 0 \end{pmatrix}, \tag{E4}$$

with spectrum $\text{spec}(C) = \gamma^2\{a_+,1,1,-1,-1,-1\}$. For $M \leq N$, the state $|\Psi_{\text{BCS}}^{(N)}\rangle$ is separable, so we can take $M > N$. Hence, $a_+\gamma^2$ is the eigenvalue with the biggest absolute value. According to Thm. E.1, the reduced state in the subspace of the four modes is entangled iff $|c_1| \leq \Sigma_{i=2}^r |c_i|$. For our example, this holds iff $M > 3N-2$. ■

[1] J. Bardeen, L. N. Cooper, and J. R. Schrieffer, Phys. Rev. **108**, 1175 (1957).
[2] M. Greiner, C. Regal, and D. Jin, Nature **426**, 537 (2003).
[3] S. Jochim, M. Bartenstein, A. Altmeyer, G. Hendl, S. Riedl, C. Chin, J. H. Denschlag, and R. Grimm, Science **302**, 2101 (2003).
[4] M. W. Zwierlein, C. A. Stan, C. H. Schunck, S. M. F. Raupach, S. Gupta, Z. Hadzibabic, and W. Ketterle, Phys. Rev. Lett. **91**, 250401 (2003).
[5] M. Zwierlein, J. Abo-Shaeer, A. Schirotzek, C. Schunck, and W. Ketterle, Nature **435**, 1047 (2005).
[6] M. W. Zwierlein, C. H. Schunck, A. Schirotzek, and W. Ketterle, Nature **442**, 54 (2006).
[7] G. B. Partridge, K. E. Strecker, R. I. Kamar, M. W. Jack, and R. G. Hulet, Phys. Rev. Lett. **95**, 020404 (2005).
[8] M. W. Zwierlein, C. A. Stan, C. H. Schunck, S. M. F. Raupach, A. J. Kerman, and W. Ketterle, Phys. Rev. Lett. **92**, 120403 (2004).
[9] C. A. Regal, M. Greiner, and D. S. Jin, Phys. Rev. Lett. **92**, 040403 (2004).
[10] G. B. Partridge, W. Li, R. I. Kamar, Y. Liao, and R. G. Hulet, Science **311**, 503 (2006).
[11] M. W. Zwierlein and W. Ketterle, Science **314**, 54a (2006).
[12] G. B. Partridge, W. Li, R. I. Kamar, Y. Liao, and R. G. Hulet, Science **314**, 54b (2006).
[13] C. Schunck, Y. Shin, A. Schirotzek, M. Zwierlein, and W. Ketterle, Science **316**, 867 (2007).
[14] P. Zanardi, Phys. Rev. A **65**, 042101 (2002).
[15] P. Zanardi and X. Wang, J. Phys. A **35**, 7947 (2002).
[16] D. Larsson and H. Johannesson, Phys. Rev. A **73**, 042320 (2006).
[17] M. M. Wolf, Phys. Rev. Lett. **96**, 010404 (2006).
[18] D. Gioev and I. Klich, Phys. Rev. Lett. **96**, 100503 (2006).
[19] M. Cramer, J. Eisert, and M. B. Plenio, Phys. Rev. Lett. **98**, 220603 (2007).
[20] Y. Shi, Phys. Rev. A **67**, 024301 (2003).
[21] R. Paskauskas and L. You, Phys. Rev. A **64**, 042310 (2001).
[22] M.-C. Banuls, J. I. Cirac, and M. M. Wolf, Phys. Rev. A **76**, 022311 (2007).
[23] H. M. Wiseman and J. A. Vaccaro, Phys. Rev. Lett. **91**, 097902 (2003).
[24] J. Schliemann, J. I. Cirac, M. Kus, M. Lewenstein, and D. Loss, Phys. Rev. A **64**, 022303 (2001).
[25] K. Eckert, J. Schliemann, D. Bruss, and M. Lewenstein, Ann. Phys. (N.Y.) **299**, 88 (2002).
[26] M. R. Dowling, A. C. Doherty, and H. M. Wiseman, Phys. Rev. A **73**, 052323 (2006).
[27] J. Schliemann, D. Loss, and A. H. MacDonald, Phys. Rev. B **63**, 085311 (2001).
[28] N. Schuch, F. Verstraete, and J. I. Cirac, Phys. Rev. A **70**, 042310 (2004).
[29] N. Schuch, F. Verstraete, and J. I. Cirac, Phys. Rev. Lett. **92**, 087904 (2004).
[30] S. Bravyi, Quantum Inf. Comput. **5**, 216 (2005).
[31] G. D. Mahan, *Many-Particle Physics*, 3rd ed. (Kluwer Academic, Dordrecht, 2000).
[32] P. Giorda and A. Anfossi, Phys. Rev. A **78**, 012106 (2008).
[33] C. Hainzl, E. Hamza, R. Seiringer, and J. P. Solovej, Commun. Math. Phys. **281**, 349 (2008).
[34] C. C. Tsuei and J. R. Kirtley, Rev. Mod. Phys. **72**, 969 (2000).
[35] L. Amico, R. Fazio, A. Osterloh, and V. Vedral, Rev. Mod. Phys. **80**, 517 (2008).
[36] V. Bach, E. Lieb, and J. Solovej, J. Stat. Phys. **76**, 3 (1994).
[37] C. Bloch and A. Messiah, Nucl. Phys. **39**, 95 (1962).
[38] A. Coleman and V. Yukalov, *Reduced Density Matrices* (Springer-Verlag, Berlin, 2000).
[39] M. Horodecki, P. Horodecki, and R. Horodecki, Phys. Lett. A **223**, 1 (1996).
[40] W. Rudin, *Functional Analysis*, 2nd ed. (McGraw-Hill, New York, 1991).
[41] R. Rockafellar, *Convex Analysis* (Princeton University Press, Princeton, NJ, 1970).
[42] P. W. Anderson, Phys. Rev. **112**, 1900 (1958).
[43] R. A. Barankov and L. S. Levitov, Phys. Rev. Lett. **93**, 130403 (2004).
[44] R. A. Bertlmann, K. Durstberger, B. C. Hiesmayr, and P. Krammer, Phys. Rev. A **72**, 052331 (2005).
[45] A. Leggett, *Modern Trends in the Theory of Condensed Matter*, edited by A. Pekalsky and R. Przystawa (Springer-Verlag, Berlin, 1980).
[46] R. Horn and C. Johnson, *Matrix Analysis* (Cambridge University Press, Cambridge, UK, 1985).
[47] D. J. Wineland, J. J. Bollinger, W. M. Itano, and D. J. Heinzen, Phys. Rev. A **50**, 67 (1994).
[48] J. J. Bollinger, W. M. Itano, D. J. Wineland, and D. J. Heinzen, Phys. Rev. A **54**, R4649 (1996).
[49] S. L. Braunstein and C. M. Caves, Phys. Rev. Lett. **72**, 3439 (1994).
[50] S. L. Braunstein, C. M. Caves, and G. Milburn, Ann. Phys. (N.Y.) **247**, 135 (1996).
[51] K. Eckert, P. Hyllus, D. Bruss, U. V. Poulsen, M. Lewenstein, C. Jentsch, T. Muller, E. M. Rasel, and W. Ertmer, Phys. Rev. A **73**, 013814 (2006).
[52] B. Yurke, S. L. McCall, and J. R. Klauder, Phys. Rev. A **33**, 4033 (1986).
[53] M. J. Holland and K. Burnett, Phys. Rev. Lett. **71**, 1355 (1993).
[54] P. Bouyer and M. A. Kasevich, Phys. Rev. A **56**, R1083 (1997).
[55] C. C. Gerry, Phys. Rev. A **61**, 043811 (2000).
[56] W. J. Munro, K. Nemoto, G. J. Milburn, and S. L. Braunstein, Phys. Rev. A **66**, 023819 (2002).
[57] S. F. Huelga, C. Macchiavello, T. Pellizzari, A. K. Ekert, M. B. Plenio, and J. I. Cirac, Phys. Rev. Lett. **79**, 3865 (1997).
[58] B. Yurke, Phys. Rev. Lett. **56**, 1515 (1986).
[59] E. Altman, E. Demler, and M. D. Lukin, Phys. Rev. A **70**, 013603 (2004).
[60] T. Rom, T. Best, D. van Oosten, U. Schneider, S. Foelling, B. Paredes, and I. Bloch, Nature **444**, 733 (2006).
[61] M. Greiner, C. A. Regal, J. T. Stewart, and D. S. Jin, Phys. Rev. Lett. **94**, 110401 (2005).
[62] S. Riedl, E. R. S. Guajardo, C. Kohstall, A. Altmeyer, M. J. Wright, J. H. Denschlag, R. Grimm, G. M. Bruun, and H. Smith, Phys. Rev. A **78**, 053609 (2008).
[63] P. Billingsley, *Probability and Measure*, 3rd ed. (Wiley-Interscience, New York, 1995).

8 Bibliography

[1] Aaronson, S., *Quantum Computing since Democritus*. Cambridge University Press (2013).

[2] Abragam, A., *Principles of Nuclear Magnetism*. Clarendon Press, Oxford (1961).

[3] Acín, A., Gisin, N., and Masanes, L., *From Bell's theorem to secure quantum key distribution*. Phys. Rev. Lett. **97**, 120405 (2006).

[4] Akimov, I. A., Feng, D. H., and Henneberger, F., *Electron spin dynamics in a self-assembled semiconductor quantum dot: The limit of low magnetic fields*. Phys. Rev. Lett. **97**, 056602 (2006).

[5] Andreas, B., Azuma, Y., Bartl, G., Becker, P., Bettin, H., Borys, M., et al., *Determination of the Avogadro constant by counting the atoms in a* ^{28}Si *crystal*. Phys. Rev. Lett. **106**, 030801 (2011), `arXiv:1010.2317`.

[6] Andreev, A. V., Emelyanov, V. I., and Ilinski, Y. A., *Cooperative effects in optics: Superradiance and phase transitions*. IOP Publishing, Bristol (1993).

[7] Arecchi, F. T., Courtens, E., Gilmore, R., and Thomas, H., *Atomic coherent states in quantum optics*. Phys. Rev. A **6**, 2211 (1972).

[8] Atatüre, M., Dreiser, J., Badolato, A., Högele, A., Karrai, K., and Imamoğlu, A., *Quantum-dot spin-state preparation with near-unity fidelity*. Science **312**, 551 (2006).

[9] Atatüre, M., Dreiser, J., Badolato, A., and Imamoğlu, A., *Observation of Faraday rotation from a single confined spin*. Nature Phys. **3**, 101 (2007), `quant-ph/0610110`.

[10] Awschalom, D. D., Bassett, L. C., Dzurak, A. S., Hu, E. L., and Petta, J. R., *Quantum spintronics: Engineering and manipulating atom-like spins in semiconductors*. Science **339**, 1174–1179 (2013).

[11] Balasubramanian, G., Neumann, P., Twitchen, D., Markham, M., Kolesov, R., Mizuochi, N., et al., *Ultralong spin coherence time in isotopically engineered diamond*. Nature Mater. **8**, 383–387 (2009).

[12] Barnes, E., Cywiński, L., and Das Sarma, S., *Nonperturbative master equation solution of central spin dephasing dynamics*. Phys. Rev. Lett. **109**, 140403 (2012), `arXiv:1203.6355`.

[13] Baumgartner, B. and Narnhofer, H., *The structures of state space concerning quantum dynamical semigroups*. Rev. Math. Phys. **24**, 1250001 (2012), `arxiv:1101.3914`.

[14] Bennett, C. H., Brassard, G., Crepeau, C., Jozsa, R., Peres, A., and Wootters, W. K., *Teleporting an unknown quantum state via dual classical and Einstein-Podolsky-Rosen channels*. Phys. Rev. Lett. **70**, 1895 (1993).

[15] Berezovsky, J., Mikkelsen, M. H., Stoltz, N. G., Coldren, L. A., and Awschalom, D. D., *Picosecond coherent optical manipulation of a single electron spin in a quantum dot*. Science **320**, 349 (2008).

[16] Bernien, H., Hensen, B., Pfaff, W., Koolstra, G., Blok, M. S., Robledo, L., et al., *Heralded entanglement between solid-state qubits separated by 3 meters*. Nature **497**, 86 (2013), arXiv:1212.6136.

[17] Bloch, I., Dalibard, J., and Zwerger, W., *Many-body physics with ultracold gases*. Rev. Mod. Phys. **80**, 885 (2008), 0704.3011.

[18] Bluhm, H., Foletti, S., Mahalu, D., Umansky, V., and Yacoby, A., *Enhancing the coherence of a spin qubit by operating it as a feedback loop that controls its nuclear spin bath*. Phys. Rev. Lett. **105**, 216803 (2010), arXiv:1003.4031.

[19] Bluhm, H., Foletti, S., Neder, I., Rudner, M., Mahalu, D., Umansky, V., et al., *Dephasing time of GaAs electron-spin qubits coupled to a nuclear bath exceeding 200μs*. Nature Phys. **7**, 109–113 (2011), arXiv:1005.2995.

[20] Bonifacio, R. and Lugiato, L., *Optical bistability and cooperative effects in resonance fluorescence*. Phys. Rev. A **18**, 1129–1144 (1978).

[21] Bortz, M., Eggert, S., Schneider, C., Stübner, R., and Stolze, J., *Dynamics and decoherence in the central spin model using exact methods*. Phys. Rev. B **82**, 161308(R) (2010), arXiv:1005.0001.

[22] Bortz, M. and Stolze, J., *Exact dynamics in the inhomogeneous central-spin model*. Phys. Rev. B **76**, 014304 (2007), arXiv:cond-mat/0612382.

[23] Bracker, A. S., Stinaff, E. A., Gammon, D., Ware, M. E., Tischler, J. G., Shabaev, A., et al., *Optical pumping of electronic and nuclear spin in single charge-tunable quantum dots*. Phys. Rev. Lett. **94**, 047402 (2005), cond-mat/0408466.

[24] Brandes, T., *Coherent and collective quantum optical effects in mesoscopic systems*. Phys. Rep. **408**, 315 (2005).

[25] Brataas, A. and Rashba, E. I., *Nuclear dynamics during Landau-Zener singlet-triplet transitions in double quantum dots*. Phys. Rev. B **84**, 045301 (2011), arXiv:1104.4591.

[26] Brataas, A. and Rashba, E. I., *Dynamical self-quenching of spin pumping into double quantum dots*. Phys. Rev. Lett. **109**, 236803 (2012), arXiv:1206.0100.

[27] Braun, P.-F., Urbaszek, B., Amand, T., Marie, X., Krebs, O., Eble, B., et al., *Bistability of the nuclear polarisation in InGaAs quantum dots*. Phys. Rev. B **74**, 245306 (2006), cond-mat/0607728.

[28] Braunstein, S. L. and Kimble, H. J., *Teleportation of continuous quantum variables*. Phys. Rev. Lett. **80**, 869 (1998).

[29] Braunstein, S. L. and van Loock, P., *Quantum information with continuous variables*. Rev. Mod. Phys. **77**, 513 (2005), arXiv:quant-ph/0410100v1.

[30] Bravyi, S. and Kitaev, A., *Universal quantum computation with ideal Clifford gates and noisy ancillas*. Phys. Rev. A **71**, 022316 (2005), arXiv:quant-ph/0403025.

[31] Breuer, H.-P., Burgarth, D., and Petruccione, F., *Non-markovian dynamics in a spin star system: Exact solution and approximation techniques*. Phys. Rev. B **70**, 045323 (2004).

[32] Breuer, H.-P. and Petruccione, F., *The Theory of Open Quantum Systems*. Oxford University Press (2007).

[33] Brown, S. W., Kennedy, T. A., Gammon, D., and Snow, E. S., *Spectrally resolved Overhauser shifts in single $GaAs/Al_xGa_{1-x}As$ quantum dots*. Phys. Rev. B **54**, R17339 (1996).

[34] Brunner, R., Shin, Y.-S., Obata, T., Pioro-Ladrière, M., Kubo, T., Yoshida, K., et al., *Two-qubit gate of combined single-spin rotation and interdot spin exchange in a double quantum dot*. Phys. Rev. Lett. **107**, 146801 (2011), arXiv:1109.3342.

[35] Bulaev, D. V., Trauzettel, B., and Loss, D., *Spin-orbit interaction and anomalous spin relaxation in carbon nanotube quantum dots*. Phys. Rev. B **77**, 235301 (2008).

[36] Burkard, G., Loss, D., and DiVincenzo, D. P., *Coupled quantum dots as quantum gates*. Phys. Rev. B **59**, 2070 (1999), cond-mat/9808026.

[37] Calsamiglia, J. and Lütkenhaus, N., *Maximum efficiency of a linear-optical Bell-state analyzer*. Appl. Phys. B **72**, 67 (2001), arXiv:quant-ph/0007058.

[38] Cappellaro, P., *Spin-bath narrowing with adaptive parameter estimation*. Phys. Rev. A **85**, 030301 (2012).

[39] Carmichael, H. J., *Analytical and numerical results for the steady state in cooperative resonance fluorescence*. J. Phys. B **13**, 3551 (1980).

[40] Chekhovich, E. A., Makhonin, M. N., Tartakovskii, A. I., Yacoby, A., Bluhm, H., Nowack, K. C., et al., *Nuclear spin effects in semiconductor quantum dots*. Nature Mater. **12**, 494 (2013).

[41] Chen, G., Bergman, D. L., and Balents, L., *Semiclassical dynamics and long time asymptotics of the central spin problem*. Phys. Rev. B **76**, 045312 (2007), arXiv:cond-mat/0703631.

[42] Chiribella, G., D'Ariano, G. M., and Perinotti, P., *Informational derivation of quantum theory*. Phys. Rev. A **84**, 012311 (2011), arXiv:1011.6451.

[43] Choi, M.-D., *Positive linear maps on C*-algebras*. Can. J. Math. **24**, 520 (1972).

[44] Christ, H., *Quantum Computation with Nuclear Spins in Quantum Dots*. Ph.D. thesis, TU München (2008).

[45] Churchill, H. O. H., Bestwick, A. J., Harlow, J. W., Kuemmeth, F., Marcos, D., Stwertka, C. H., et al., *Electron-nuclear interaction in 13c nanotube double quantum dots*. Nature Phys. **5**, 321 (2009), arXiv:0811.3236.

[46] Cirac, J. I., Dür, W., Kraus, B., and Lewenstein, M., *Entangling operations and their implementation using a small amount of entanglement*. Phys. Rev. Lett. **86**, 544 (2001), quant-ph/0007057.

[47] Cirac, J. I. and Zoller, P., *Quantum computations with cold trapped ions*. Phys. Rev. Lett. **74**, 4091 (1995).

[48] Cirac, J. I. and Zoller, P., *Goals and opportunities in quantum simulation*. Nature Phys. **8**, 264–266 (2012).

[49] Coish, W. A. and Baugh, J., *Nuclear spins in nanostructures*. phys. stat. sol. **246**, 2203 (2009), arXiv:0905.1743v2.

[50] Coish, W. A., Fischer, J., and Loss, D., *Exponential decay in a spin bath*. Phys. Rev. B **77**, 125329 (2008), arXiv:0710.3762.

[51] Coish, W. A. and Loss, D., *Hyperfine interaction in a quantum dot: Non-Markovian electron spin dynamics*. Phys. Rev. B **70**, 195340 (2004), cond-mat/0405676.

[52] Coish, W. A. and Loss, D., *Singlet-triplet decoherence due to nuclear spins in a double quantum dot*. Phys. Rev. B **72**, 125337 (2005), cond-mat/0506090.

[53] Cubitt, T. S., Eisert, J., and Wolf, M. M., *Extracting dynamical equations from experimental data is NP-hard*. Phys. Rev. Lett. **108**, 120503 (2012), arXiv:1005.0005.

[54] Cucchietti, F. M., Paz, J. P., and Zurek, W. H., *Decoherence from spin environments*. Phys. Rev. A **72**, 052113 (2005).

[55] Cushen, C. D. and Hudson, R. L., *A quantum-mechanical central limit theorem*. J. Appl. Prob. **8**, 454 (1971).

[56] Danieli, E. P., Álvarez, G. A., Levstein, P. R., and Pastawski, H. M., *Quantum dynamical phase transition in a system with many-body interactions*. Solid State Communications **141**, 422 – 426 (2007).

[57] Danon, J. and Nazarov, Y. V., *Nuclear tuning and detuning of the electron spin resonance in a quantum dot: Theoretical consideration*. Phys. Rev. Lett. **100**, 056603 (2008), arXiv:0710.0750.

[58] Danon, J., Vink, I. T., Koppens, F. H. L., Nowack, K. C., Vandersypen, L. M. K., and Nazarov, Y. V., *Multiple nuclear polarization states in a double quantum dot*. Phys. Rev. Lett. **103**, 046601 (2009), arXiv:0902.2653.

[59] De Greve, K., Yu, L., McMahon, P. L., Pelc, J. S., Natarajan, C. M., Kim, N. Y., et al., *Quantum-dot spin-photon entanglement via frequency downconversion to telecom wavelength*. Nature **491**, 421–425 (2012).

[60] de Lange, G., Wang, Z. H., Riste, D., Dobrovitski, V. V., and Hanson, R., *Universal dynamical decoupling of a single solid-state spin from a spin bath*. Science **330**, 60 (2010), arXiv:1008.2119.

[61] de Sousa, R. and Das Sarma, S., *Theory of nuclear-induced spectral diffusion: Spin decoherence of phosphorus donors in Si and GaAs quantum dots*. Phys. Rev. B **66**, 115322 (2003), cond-mat/0211567.

[62] Deng, C. and Hu, X., *Decoherence of nuclear spin quantum memory in quantum dots*. IEEE Trans. Nanotechnology **4** (2005), cond-mat/0406478.

[63] Deng, C. and Hu, X., *Selective dynamic nuclear spin polarization in spin-blocked double-dot*. Phys. Rev. B **71**, 033307 (2005), cond-mat/0402428.

[64] Devetak, I. and Shor, P. W., *The capacity of a quantum channel for simultaneous transmission of classical and quantum information*. Commun. Math. Phys. **256**, 287 (2005), quant-ph/0311131.

[65] Dicke, R. H., *Coherence in spontaneous radiation processes*. Phys. Rev. **93**, 99 (1954).

[66] Diehl, S., Rico, E., Baranov, M. A., and Zoller, P., *Topology by dissipation in atomic quantum wires*. Nature Phys. **7**, 971 (2011), arXiv:1105.5947.

[67] Diehl, S., Tomadin, A., Micheli, A., Fazio, R., and Zoller, P., *Dynamical phase transitions and instabilities in open atomic many-body systems*. Phys. Rev. Lett. **105**, 015702 (2010).

[68] Dieks, D., *Communication by EPR device*. Phys. Lett. A **92**, 271 (1982).

[69] DiVincenzo, D. P., *The physical implementation of quantum computation*. Fort. Phys. **48**, 771 (2000), arxiv:quant-ph/0002077.

[70] Dobrovitski, V. V., Taylor, J. M., and Lukin, M. D., *Long-lived memory for electronic spin in a quantum dot: Numerical analysis*. Phys. Rev. B **73**, 245318 (2006), cond-mat/0602499.

[71] Doherty, M. W., Manson, N. B., Delaney, P., Jelezko, F., Wrachtrup, J., and Hollenberg, L. C. L., *The nitrogen-vacancy colour centre in diamond*. Phys. Rep. **528**, 1 (2013), arXiv:1302.3288.

[72] Dolde, F., Jakobi, I., Naydenov, B., Zhao, N., Pezzagna, S., Trautmann, C., et al., *Room-temperature entanglement between single defect spins in diamond*. Nature Phys. **9**, 139–143 (2013).

[73] D'yakonov, M. I. and Perel, V. I., *Dynamic self-polarization of nuclei in solids*. JETP Lett. **16**, 398 (1972).

[74] Eckert, K., Schliemann, J., Bruss, D., and Lewenstein, M., *Quantum correlations in systems of indistinguishable particles*. Annals of Physics **299**, 88 (2002), mHQ-Ent, quant-ph/0203060.

[75] Eisert, J. and Prosen, T., *Noise-driven quantum criticality* (2011), arXiv:1012.5013.

[76] Eisert, J. and Wolf, M. M., *Quantum Information with Continuous Variables of Atoms and Light*, chap. Gaussian quantum channels, pp. 23–42. Imperial College Press (2007), quant-ph/0505151.

[77] Ekert, A., *Quantum cryptography based on Bell's theorem*. Phys. Rev. Lett. **67**, 661 (1991).

[78] Elzerman, J. M., Hanson, R., Willems van Beveren, L. H., Witkamp, B., Vandersypen, L. M. K., and Kouwenhoven, L. P., *Single-shot read-out of an individual electron spin in a quantum dot*. Nature **430**, 431 (2004).

[79] Erbe, B. and Schliemann, J., *Different types of integrability and their relation to decoherence in central spin models*. Phys. Rev. Lett. **105**, 177602 (2010), arXiv:1006.4983.

[80] Erbe, B. and Schliemann, J., *Hyperfine induced electron spin and entanglement dynamics in double quantum dots: The case of separate baths*. Phys. Rev. B **85**, 155127 (2012), arXiv:1201.5036.

[81] Erlingsson, S. I., Nazarov, Y. V., and Fal'ko, V. I., *Nucleus-mediated spin-flip transitions in GaAs quantum dots*. Phys. Rev. B **64**, 195306 (2001), cond-mat/0104148.

[82] Escher, B. M., de Matos Filho, R. L., and Davidovich, L., *General framework for estimating the ultimate precision limit in noisy quantum-enhanced metrology*. Nature Phys. **7**, 406–411 (2011).

[83] Farhi, E., Goldstone, J., Gutmann, S., and Sipser, M., *Quantum computation by adiabatic evolution* (2000), arXiv:quant-ph/0001106v1.

[84] Fischer, J., Trif, M., Coish, W. A., and Loss, D., *Spin interactions, relaxation and decoherence in quantum dots*. Solid State Comm. **149**, 1443 (2009), arXiv:0903.0527.

[85] Fleischhauer, M. and Lukin, M. D., *Dark-state polaritons in electromagnetically induced transparency*. Phys. Rev. Lett. **84**, 5094 (2000).

[86] Foletti, S., Bluhm, H., Mahalu, D., Umansky, V., and Yacoby, A., *Universal quantum control of two-electron spin quantum bits using dynamic nuclear polarization*. Nature Phys. **5**, 903 (2009).

[87] Furusawa, A., Sørensen, J. L., Braunstein, S. L., Fuchs, C. A., Kimble, H. J., and Polzik, E. S., *Unconditional quantum teleportation*. Science **282**, 706 (1998).

[88] Galland, C. and Imamoğlu, A., *All-optical manipulation of electron spins in carbon-nanotube quantum dots*. Phys. Rev. Lett. **101**, 157404 (2008).

[89] Gao, W. B., Fallahi, P., Togan, E., Miguel-Sanchez, J., and Imamoglu, A., *Observation of entanglement between a quantum dot spin and a single photon*. Nature **491**, 426–430 (2012).

[90] Gaudin, M., *Diagonalisation d'une classe d'hamiltoniens de spin*. J. Phys. France **37**, 1087–1098 (1976).

[91] Gaudreau, L., Granger, G., Kam, A., Aers, G. C., Studenikin, S. A., Zawadzki, P., et al., *Coherent control of three-spin states in a triple quantum dot*. Nature Phys. **8**, 54–58 (2012), arXiv:1301.7461.

[92] Gibbs, H., McCall, S., and Venkatesan, T., *Differential gain and bistability using a Sodium-filled Fabry-Perot interferometer*. Phys. Rev. Lett. **36**, 1135–1138 (1976).

[93] Giedke, G., Taylor, J. M., D'Alessandro, D., Lukin, M. D., and Imamoğlu, A., *Quantum measurement of a mesoscopic spin ensemble*. Phys. Rev. A **74**, 032316 (2006), quant-ph/0508144.

[94] Giedke, G., Wolf, M. M., Krüger, O., Werner, R. F., and Cirac, J. I., *Entanglement of formation for symmetric Gaussian states*. Phys. Rev. Lett. **91**, 107901 (2003), quant-ph/0304042.

[95] Gilchrist, A., Nemoto, K., Munro, W. J., Ralph, T. C., Glancy, S., Braunstein, S. L., et al., *Schrödinger cats and their power for quantum information processing*. J. Opt. B: Quantum Semiclass. Opt. **6**, S828 (2004).

[96] Giovannetti, V., Guha, S., Lloyd, S., Maccone, L., Shapiro, J. H., and Yuen, H. P., *Classical capacity of the lossy bosonic channel: The exact solution*. Phys. Rev. Lett. **92**, 027902 (2004), quant-ph/0308012.

[97] Giovannetti, V., Lloyd, S., and Maccone, L., *Advances in quantum metrology*. Nature Phot. **5**, 222–229 (2011).

[98] Gisin, N., Ribordy, G., Tittel, W., and Zbinden, H., *Quantum cryptography*. Rev. Mod. Phys. **74**, 145 (2002), arXiv:quant-ph/0101098.

[99] Gross, M. and Haroche, S., *Superradiance: An essay on the theory of collective spontaneous emission*. Physics Reports **93**, 301 (1982).

[100] Gullans, M., Krich, J. J., Taylor, J. M., Bluhm, H., Halperin, B. I., Marcus, C. M., et al., *Dynamic nuclear polarization in double quantum dots*. Phys. Rev. Lett. **104**, 226807 (2010), arXiv:1003.4508.

[101] Gullans, M., Krich, J. J., Taylor, J. M., Halperin, B. I., and Lukin, M. D., *Preparation of non-equilibrium nuclear spin states in double quantum dots*. Phys. Rev. B **88**, 035309 (2013), arXiv:1212.6953.

[102] Gywat, O., Krenner, H. J., and Berezovsky, J., *Spins in optically active quantum dots*. Wiley-VCH (2010).

[103] Hammerer, K., Sørensen, A., and Polzik, E. S., *Quantum interface between light and atomic ensembles*. Rev. Mod. Phys. **82**, 1041 (2010).

[104] Hanson, R. and Burkard, G., *Universal set of quantum gates for double-dot spin qubits with fixed interdot coupling*. Phys. Rev. Lett. **98**, 050502 (2007).

[105] Hanson, R., Dobrovitski, V. V., Feiguin, A. E., Gywat, O., and Awschalom, D. D., *Coherent dynamics of a single spin interacting with an adjustable spin bath*. Science **320**, 352 (2008).

[106] Hanson, R., Kouwenhoven, L. P., Petta, J. R., Tarucha, S., and Vandersypen, L. M. K., *Spins in few-electron quantum dots*. Rev. Mod. Phys. **79**, 1217 (2007), cond-mat/0610433.

[107] Hardy, L., *Quantum mechanics from five reasonable axioms* (2001), quant-ph/0101012v4.

[108] Hastings, M. B., *Superadditivity of communication capacity using entangled inputs*. Nature Phys. **5**, 255 (2009), arXiv:0809.3972.

[109] Hennessy, K., Badolato, A., Winger, M., Gerace, D., Atatüre, M., Gulde, S., et al., *Quantum nature of a strongly coupled single quantum dot-cavity system*. Nature **445**, 896 (2007), quant-ph/0610034.

[110] Hepp, K. and Lieb, E. H., *On the superradiant phase transition for molecules in a quantized radiation field: the Dicke maser model*. Annals of Physics **76**, 360 – 404 (1973).

[111] Hinrichsen, H., *Non-equilibrium phase transitions*. Physica A: Statistical Mechanics and its Applications **369**, 1 – 28 (2006).

[112] Hioe, F. T., *Phase transitions in some generalized Dicke models of superradiance*. Phys. Rev. A **8**, 1440–1445 (1973).

[113] Holevo, A. S., *Entanglement-breaking channels in infinite dimensions*. Probl. Inf. Transm. **44**, 3–18 (2008), arXiv:0802.0235.

[114] Holstein, T. and Primakoff, H., *Field dependence of the intrinsic domain magnetization of ferromagnet*. Phys. Rev. **58**, 1098 (1940).

[115] Horodecki, R., Horodecki, P., Horodecki, M., and Horodecki, K., *Quantum entanglement*. Rev. Mod. Phys. **81**, 865 (2009), arXiv:quant-ph/0702225.

[116] Huang, C.-W. and Hu, X., *Theoretical study of nuclear spin polarization and depolarization in self-assembled quantum dots*. Phys. Rev. B **81**, 205304 (2010), arXiv:1001.3707.

[117] Huelga, S. F., Macchiavello, C., Pellizzari, T., Ekert, A. K., Plenio, M. B., and Cirac, J. I., *Improvement of frequency standards with quantum entanglement*. Phys. Rev. Lett. **79**, 3865 (1997).

[118] Hüttel, A. K., Weber, J., Holleitner, A. W., Weinmann, D., Eberl, K., and Blick, R. H., *Nuclear spin relaxation probed by a single quantum dot*. Phys. Rev. B **69**, 073302 (2004).

[119] Imamoğlu, A., *Quantum computation using quantum dot spins and microcavities*. Fort. Phys. **48**, 987 (2000).

[120] Imamoğlu, A., Knill, E., Tian, L., and Zoller, P., *Optical pumping of quantum-dot nuclear spins*. Phys. Rev. Lett. **91**, 017402 (2003), `cond-mat/0303575`.

[121] Itano, W. M., Monroe, C., Meekhof, D., Leibfried, D., King, B., and Wineland, D., *Quantum harmonic oscillator state synthesis and analysis*. Prentiss, M. G. and Phillips, W. D. (editors), *Atom Optics*, vol. 2995, p. 43, SPIE (1997).

[122] Ivan, J. S. and Simon, R., *Entanglement of formation for Gaussian states* (2008), `arXiv:0808.1658`.

[123] Jaksch, D., Briegel, H.-J., Cirac, J. I., Gardiner, C. W., and Zoller, P., *Entanglement of atoms via cold controlled collisions*. Phys. Rev. Lett. **82**, 1975 (1999).

[124] Jamiołkowski, A., *Linear transformations which preserve trace and positive semidefiniteness of operators*. Rep. Math. Phys. **3**, 275 (1972).

[125] Jiang, L., Hodges, J. S., Maze, J. R., Maurer, P., Taylor, J. M., Cory, D. G., et al., *Repetitive readout of a single electronic spin via quantum logic with nuclear spin ancillae*. Science **326**, 267 (2009).

[126] Johnson, A. C., Petta, J. R., Taylor, J. M., Yacoby, A., Lukin, M. D., Marcus, C. M., et al., *Triplet-singlet spin relaxation via nuclei in a double quantum dot*. Nature **435**, 925 (2005), `cond-mat/0503687`.

[127] Jordan, S., *Quantum Algorithm Zoo*. http://math.nist.gov/quantum/zoo/ (2013).

[128] Kane, B. E., *A silicon-based nuclear spin quantum computer*. Nature **393**, 133 (1998).

[129] Kessler, E. M., Giedke, G., Imamoğlu, A., Yelin, S. F., Lukin, M. D., and Cirac, J. I., *Dissipative phase transition in central spin systems*. Phys. Rev. A **86**, 012116 (2012), `arXiv:1205.3341`.

[130] Khaetskii, A. V., Loss, D., and Glazman, L., *Electron spin decoherence in quantum dots due to interaction with nuclei*. Phys. Rev. Lett. **88**, 186802 (2002), `cond-mat/0201303`.

[131] Khaetskii, A. V., Loss, D., and Glazman, L., *Electron spin evolution induced by interaction with nuclei in a quantum dots*. Phys. Rev. B **67**, 195329 (2003), `cond-mat/0211678`.

[132] Kim, D., Carter, S. G., Greilich, A., Bracker, A. S., and Gammon, D., *Ultrafast optical control of entanglement between two quantum dot spins*. Nature Phys. **7**, 223–229 (2011), `arXiv:1007.3733`.

[133] Kitaev, A., *Quantum measurements and the Abelian Stabilizer Problem* (1995), `quant-ph/9511026`.

[134] Kitaev, A. Y., *Unpaired Majorana fermions in quantum wires*. Physics-Uspekhi **44**, 131 (2001), arXiv:cond-mat/0010440.

[135] Kitaev, A. Y., Shen, A. H., and Vyalyi, M. N., *Classical and Quantum Computation*. American Mathematical Society, Providence, RI (2002).

[136] Klauser, D., Coish, W. A., and Loss, D., *Nuclear spin state narrowing via gate–controlled Rabi oscillations in a double quantum dot*. Phys. Rev. B **73**, 205302 (2006), cond-mat/0510177.

[137] Kloeffel, C., Dalgarno, P. A., Urbaszek, B., Gerardot, B. D., Brunner, D., Petroff, P. M., et al., *Controlling the interaction of electron and nuclear spins in a tunnel-coupled quantum dot*. Phys. Rev. Lett. **106**, 046802 (2011), arXiv:1010.3330.

[138] Klotz, F., Jovanov, V., Kierig, J., Clark, E. C., Bichler, M., Abstreiter, G., et al., *Asymmetric optical nuclear spin pumping in a single uncharged quantum dot*. Phys. Rev. B **82**, 121307(R) (2010), arXiv:1007.2145.

[139] Knill, E., *Quantum computing with realistically noisy devices*. Nature **434**, 39 (2005), arXiv:quant-ph/0410199.

[140] Knill, E., Laflamme, R., and Milburn, G. J., *A scheme for efficient quantum computation with linear optics*. Nature **409**, 46 (2001).

[141] Koppens, F. H. L., Buizert, C., Tielrooij, K. J., Vink, I. T., Nowack, K. C., Meunier, T., et al., *Driven coherent oscillations of a single electron spin in a quantum dot*. Nature **442**, 766 (2006), cond-mat/0608459.

[142] Koppens, F. H. L., Folk, J. A., Elzerman, J. M., Hanson, R., Willems van Beveren, L. H., Vink, I. T., et al., *Control and detection of singlet-triplet mixing in a random nuclear field*. Science **309**, 1346 (2005), arXiv:cond-mat/0509053.

[143] Korbicz, J. K., Cirac, J. I., and Lewenstein, M., *Spin squeezing inequalities and entanglement of n qubit states*. Phys. Rev. Lett. **95**, 120502 (2005).

[144] Korenev, V., *The nuclear spin nanomagnet*. Phys. Rev. Lett. **99**, 256405 (2007), arXiv:0705.2167.

[145] Korenev, V., *Multitudes of stable states in a periodically driven electron-nuclear spin system in a quantum dot*. Phys. Rev. B **83**, 235429 (2011), arXiv:1006.5144.

[146] Korenev, V. L., *Dynamic self-polarization of nuclei in low-dimensional systems*. JETP Lett. **70**, 129 (1999).

[147] Kouwenhoven, L. P., Austing, D. G., and Tarucha, S., *Few-electron quantum dots*. Rep. Progr. Phys. **64**, 701 (2001).

[148] Kozekhin, A. E., Mølmer, K., and Polzik, E. S., *Quantum memory for light*. Phys. Rev. A **62**, 033809 (2000), quant-ph/9912014.

[149] Kraus, B., Büchler, H. P., Diehl, S., Kantian, A., Micheli, A., and Zoller, P., *Preparation of entangled states by quantum markov processes*. Phys. Rev. A **78**, 042307 (2008), arXiv:0803.1463.

[150] Krauter, H., Muschik, C. A., Jensen, K., Wasilewski, W., Petersen, J. M., Cirac, J. I., et al., *Entanglement generated by dissipation and steady state entanglement of two macroscopic objects*. Phys. Rev. Lett. **107**, 080503 (2011), arXiv:1006.4344.

[151] Krebs, O., Eble, B., Lemaître, A., Voisin, P., Urbaszek, B., Amand, T., et al., *Hyperfine interaction in InAs/GaAs self-assembled quantum dots: dynamical nuclear polarization versus spin relaxation*. Comptes Rendus Physique **9**, 874 – 884 (2008), arXiv:0904.1548.

[152] Krebs, O., Maletinsky, P., Amand, T., Urbaszek, B., Lemaître, A., Voisin, P., et al., *Anomalous Hanle effect due to optically created transverse Overhauser field in single InAs/GaAs quantum dots*. Phys. Rev. Lett. **104**, 056603 (2010), arXiv:0910.1744.

[153] Kurucz, Z., Sørensen, M. W., Taylor, J. M., Lukin, M. D., and Fleischhauer, M., *Qubit protection in nuclear-spin quantum dot memories*. Phys. Rev. Lett. **103**, 010502 (2009), arXiv:0902.4566.

[154] Laird, E. A., Barthel, C., Rashba, E. I., Marcus, C. M., Hanson, M. P., and Gossard, A. C., *Hyperfine-mediated gate-driven electron spin resonance*. Phys. Rev. Lett. **99**, 246601 (2007), arXiv:0707.0557.

[155] Lampel, G., *Nuclear dynamic polarization by optical electronic saturation and optical pumping in semiconductors*. Phys. Rev. Lett. **20**, 491 (1968).

[156] Latta, C., Högele, A., Zhao, Y., Vamivakas, A. N., Maletinsky, P., Kroner, M., et al., *Confluence of resonant laser excitation and bi-directional quantum dot nuclear spin polarization*. Nature Phys. **5**, 758 (2009), arXiv:0904.4767.

[157] Latta, C., Srivastava, A., and Imamoğlu, A., *Hyperfine interaction dominated dynamics of nuclear spins in self-assembled quantum dots*. Phys. Rev. Lett. **107**, 167401 (2011), arXiv:1104.1111.

[158] Laucht, A., Hofbauer, F., Hauke, N., Angele, J., Stobbe, S., Kaniber, M., et al., *Electrical control of spontaneous emission and strong coupling for a single quantum dot*. New J. Phys. **11**, 023034 (2009), arXiv:0810.3010.

[159] Law, C. K. and Eberly, J. H., *Arbitrary control of a quantum electromagnetic field*. Phys. Rev. Lett. **76**, 1055 (1996).

[160] Lawande, S. V., Puri, R. R., and Hassan, S. S., *Non-resonant effects in the fluorescent Dicke model I. exact steady state analysis*. J. Phys. B: Atom. Mol. Phys. **14**, 4171–4189 (1981).

[161] Le Hur, K., *Understanding Quantum Phase Transitions*, chap. Quantum Phase Transitions in Spin-Boson Systems: Dissipation and Light. Taylor and Francis (2010), arXiv:09094822.

[162] Lewenstein, M., Sanpera, A., and Ahufinger, V., *Ultracold Atoms in Optical Lattices*. Oxford University Press (2012).

[163] Liu, R.-B., Yao, W., and Sham, L. J., *Control of electron spin decoherence caused by electron-nuclear spin dynamics in a quantum dot*. New J. Phys. **9**, 226 (2007), cond-mat/0703690.

[164] Liu, Y.-K., Christandl, M., and Verstraete, F., *Quantum computational complexity of the N-representability problem: QMA complete*. Phys. Rev. Lett. **98**, 110503 (2007), arXiv:quant-ph/0609125.

[165] Lloyd, S., *Universal quantum simulators*. Science **273**, 1073 (1996).

[166] Loss, D. and DiVincenzo, D. P., *Quantum computation with quantum dots*. Phys. Rev. A **57**, 120 (1998), cond-mat/9701055.

[167] Makhonin, M. N., Kavokin, K. V., Senellart, P., Lemaître, A., Ramsay, A. J., Skolnick, M. S., et al., *Fast control of nuclear spin polarization in an optically pumped single quantum dot*. Nature Mater. **10**, 844 (2011), arXiv:1102.3636.

[168] Maletinsky, P., *Polarization and manipulation of a mesoscopic nuclear spin ensemble using a single confined electron spin*. Ph.D. thesis, ETH Zürich (2008).

[169] Maletinsky, P., Lai, C.-W., Badolato, A., and Imamoğlu, A., *Nonlinear dynamics of quantum dot nuclear spins*. Phys. Rev. B **75**, 035409 (2007), cond-mat/0609291.

[170] Masanes, L. and Mueller, M. P., *A derivation of quantum theory from physical requirements*. New J. Phys. **13**, 063001 (2011), arXiv:1004.1483.

[171] Mason, N., Biercuk, M. J., and Marcus, C. M., *Local gate control of a carbon nanotube double quantum dot*. Science **303**, 655–658 (2004).

[172] Maune, B. M., Borselli, M. G., Huang, B., Ladd, T. D., Deelman, P. W., Holabird, K. S., et al., *Coherent singlet-triplet oscillations in a silicon-based double quantum dot*. Nature **481**, 344–347 (2012).

[173] Maurer, P. C., Kucsko, G., Latta, C., Jiang, L., Yao, N. Y., Bennett, S. D., et al., *Room-temperature quantum bit memory exceeding one second*. Science **336**, 1283–1286 (2012).

[174] Meier, F. and Zhakharchenya, B. (editors), *Optical Orientation*, vol. 8 of *Modern Problems in Condensed Matter Sciences*. North-Holland, Amsterdam (1984).

[175] Merkulov, I. A., Efros, A. L., and Rosen, M., *Electron spin relaxation by nuclei in semiconductor quantum dots*. Phys. Rev. B **65**, 205309 (2002), cond-mat/0202271.

[176] Mikkelsen, M. H., Berezovsky, J., Stoltz, N. G., Coldren, L. A., and Awschalom, D. D., *Optically detected coherent spin dynamics of a single electron in a quantum dot*. Nature Phys. **3**, 770 (2007).

[177] Morrison, S. and Parkins, A., *Dynamical quantum phase transitions in the dissipative Lipkin-Meshkov-Glick model with proposed realization in optical cavity QED*. Phys. Rev. Lett. **100**, 040403 (2008).

[178] Müller, M., Diehl, S., Pupillo, G., and Zoller, P., *Engineered open systems and quantum simulations with atoms and ions*. Adv Atomic, Molecular and Optical Physics **61**, 1–80 (2012), arXiv:1203.6595.

[179] Neumann, P., Kolesov, R., Naydenov, B., Beck, J., Rempp, F., Steiner, M., et al., *Quantum register based on coupled electron spins in a room-temperature solid*. Nature Phys. **6**, 249 (2010).

[180] Neumann, P., Mizuochi, N., Rempp, F., Hemmer, P., Watanabe, H., Yamasaki, S., et al., *Multipartite entanglement among single spins in diamond*. Science **320**, 1326 (2008).

[181] Nielsen, M. A., *The fermionic canonical commutation relations and the Jordan-Wigner transform*. Michael Nielsen's Blog (2005).

[182] Nielsen, M. A. and Chuang, I. L., *Quantum Computation and Quantum Information*. Cambridge University Press, Cambridge (2000).

[183] Nikolaenko, A. E., Chekhovich, E. A., Makhonin, M. N., Drouzas, I. W., Van'kov, A. B., Skiba-Szymanska, J., et al., *Suppression of nuclear spin diffusion at a $GaAs/Al_xGa_{1-x}As$ interface measured with a single quantum-dot nanoprobe*. Phys. Rev. B **79**, 081303 (2009).

[184] Nowack, K. C., Shafiei, M., Laforest, M., Prawiroatmodjo, G. E. D. K., Schreiber, L. R., Reichl, C., et al., *Single-shot correlations and two-qubit gate of solid-state spins*. Science **333**, 1269 (2011).

[185] Obata, T., Pioro-Ladriere, M., Tokura, Y., Shin, Y. S., Kubo, T., Yoshida, K., et al., *Coherent manipulation of individual electron spin in a double quantum dot integrated with a micromagnet*. Phys. Rev. B **81**, 085317 (2010).

[186] Ono, K. and Tarucha, S., *Nuclear-spin-induced oscillatory current in spin-blockaded quantum dots*. Phys. Rev. Lett. **92**, 256803 (2004), `cond-mat/0309062`.

[187] Ota, T., Yusa, G., Kumada, N., Miyashita, S., Fujisawa, T., and Hirayama, Y., *Decoherence of nuclear spins due to direct dipole-dipole interactions probed by resistively detected nuclear magnetic resonance*. Appl. Phys. Lett. **91**, 193101 (2007), `arXiv:0710.3487`.

[188] Overhauser, A. W., *Polarization of nuclei in metals*. Phys. Rev. **92**, 411 (1953).

[189] Paget, D., Lampel, G., Sapoval, B., and Safarov, V. I., *Low field electron-nuclear spin coupling in Gallium Arsenide under optical pumping conditions*. Phys. Rev. B **15**, 5780 (1977).

[190] Partridge, G. B., Li, W., Kamar, R. I., Liao, Y., and Hulet, R. G., *Pairing and phase separation in a polarized fermi gas*. Science **27**, 120403 (2006).

[191] Partridge, G. B., Li, W., Kamar, R. I., Liao, Y., and Hulet, R. G., *Response to Comment on "Pairing and phase separation in a polarized fermi gas"*. Science **314**, 54b (2006).

[192] Petersen, G., Hoffmann, E. A., Schuh, D., Wegscheider, W., Giedke, G., and Ludwig, S., *Large nuclear spin polarization in gate-defined quantum dots using a single-domain nanomagnet*. Phys. Rev. Lett. **110**, 177602 (2013), `arxiv:1212.3140`.

[193] Petta, J. R., Johnson, A. C., Taylor, J. M., Laird, E. A., Yacoby, A., Lukin, M. D., et al., *Coherent manipulation of coupled electron spins in semiconductor quantum dots*. Science **309**, 2180 (2005).

[194] Petta, J. R., Lu, H., and Gossard, A. C., *A coherent beam splitter for electronic spin states*. Science **327**, 669 (2010), `arXiv:1010.0659`.

[195] Petz, D., *An Invitation to the Algebra of Canonical Commutation Relations*. Leuven University Press (1990).

[196] Pioro-Ladriere, M., Obata, T., Tokura, Y., Shin, Y. S., Kubo, T., Yoshida, K., et al., *Electrically driven single-electron spin resonance in a slanting Zeeman field*. Nature Phys. **4**, 776–779 (2008).

[197] Pla, J. J., Tan, K. Y., Dehollain, J. P., Lim, W. H., Morton, J. J. L., Jamieson, D. N., et al., *A single-atom electron spin qubit in silicon*. Nature **489**, 541–545 (2012).

[198] Poot, M. and van der Zant, H. S., *Mechanical systems in the quantum regime*. Phys. Rep. **511**, 273–335 (2012).

[199] Press, D., Ladd, T. D., Zhang, B., and Yamamoto, Y., *Complete quantum control of a single quantum dot spin using ultrafast optical pulses*. Nature **456**, 218 (2008).

[200] Puri, R. R., Lawande, S. V., and Hassan, S. S., *Dispersion in the driven Dicke model*. Opt. Comm. **35**, 179–184 (1980).

[201] Ramon, G. and Hu, X., *Dynamical nuclear spin polarization and the zamboni effect in gated double quantum dots*. Phys. Rev. B **75**, 161301(R) (2006), `cond-mat/0610585`.

[202] Raussendorf, R. and Briegel, H. J., *A one-way quantum computer*. Phys. Rev. Lett. **86**, 5188 (2001).

[203] Raussendorf, R. and Harrington, J., *Fault-tolerant quantum computation with high threshold in two dimensions*. Phys. Rev. Lett. **98**, 190504 (2007).

[204] Raz, R., *Exponential separation of quantum and classical communication complexity*. *STOC '99: Proceedings of the 31st annual ACM symposium on Theory of computing*, pp. 358–367, ACM Press, New York, NY, USA (1999).

[205] Recher, P. and Trauzettel, B., *Quantum dots and spin qubits in graphene*. Nanotechnology **21**, 302001 (2010).

[206] Reimann, S. M. and Manninen, M., *Electronic structure of quantum dots*. Rev. Mod. Phys. **74**, 1283 (2002).

[207] Reithmaier, J. P., Sek, G., Loffler, A., Hofmann, C., Kuhn, S., Reitzenstein, S., et al., *Strong coupling in a single quantum dot-semiconductor microcavity system*. Nature **432**, 197 (2004).

[208] Renner, R. and Cirac, J. I., *A de Finetti representation theorem for infinite dimensional quantum systems and applications to quantum cryptography*. Phys. Rev. Lett. **102**, 110504 (2009), `arXiv:0809.2243`.

[209] Ribeiro, H., Petta, J. R., and Burkard, G., *Harnessing the GaAs quantum dot nuclear spin bath for quantum control*. Phys. Rev. B **82**, 115445 (2010), `arXiv:1002.4630`.

[210] Roumpos, G., Master, C. P., and Yamamoto, Y., *Quantum simulation of spin ordering with nuclear spins in a solid state lattice*. Phys. Rev. B **75**, 094415 (2006), `quant-ph/0611218`.

[211] Rudner, M. S. and Levitov, L. S., *Electrically-driven reverse Overhauser pumping of nuclear spins in quantum dots*. Phys. Rev. Lett. **99**, 246602 (2007), `arXiv:0710.1076v1`.

[212] Rudner, M. S. and Levitov, L. S., *Self-polarization and cooling of spins in quantum dots*. Phys. Rev. Lett. **99**, 036602 (2007), `cond-mat/0609409`.

[213] Rudner, M. S. and Levitov, L. S., *Dynamical cooling of nuclear spins in double quantum dots*. Nanotechnology **21**, 274016 (2010), `arXiv:0705.2177`.

[214] Rudner, M. S., Vandersypen, L. M. K., Vuletić, V., and Levitov, L. S., *Generating entanglement and squeezed states of nuclear spins in quantum dots*. Phys. Rev. Lett. **107**, 206806 (2011), `arXiv:1101.3370`.

[215] Rugar, D., Budakian, R., Mamin, H. J., and Chui, B. W., *Single spin detection by magnetic resonance force microscopy*. Nature **430**, 329 (2004).

[216] Russell, A., Fal'ko, V. I., Tartakovskii, A. I., and Skolnick, M. S., *Bistability of optically-induced nuclear spin orientation in quantum dots*. Phys. Rev. B **76**, 195310 (2007), `quant-ph/0705.0110`.

[217] Sachdev, S., *Quantum Phase Transitions*. Cambridge University Press, Cambridge, MA (1999).

[218] Salis, G., Awschalom, D. D., Ohno, Y., and Ohno, H., *Origin of enhanced dynamic nuclear polarization and all-optical nuclear magnetic resonance in GaAs quantum wells*. Phys. Rev. B **64**, 195304 (2001), `cond-mat/0104564`.

[219] Schaibley, J. R., Burgers, A. P., McCracken, G. A., Duan, L.-M., Berman, P. R., Steel, D. G., et al., *Demonstration of quantum entanglement between a single electron spin confined to an InAs quantum dot and a photon* (2013), `arXiv:1210.5555`.

[220] Schliemann, J., Khaetskii, A., and Loss, D., *Electron spin dynamics in quantum dots and related nanostructures due to hyperfine interaction with nuclei*. J. Phys: Cond. Mat. **15**, R1809 (2003), `cond-mat/0311159`.

[221] Schmidt, M., Ludwig, M., and Marquardt, F., *Optomechanical circuits for nanomechanical continuous variable quantum state processing*. New J. Phys. **14**, 125005 (2012).

[222] Schneider, S. and Milburn, G., *Entanglement in the steady state of a collective-angular-momentum (Dicke) model*. Phys. Rev. A **65**, 042107 (2002).

[223] Schoelkopf, R. J. and Girvin, S. M., *Wiring up quantum systems*. Nature **451**, 664–669 (2008).

[224] Schuch, N., Cirac, I., and Verstraete, F., *Computational difficulty of finding matrix product ground states*. Phys. Rev. Lett. **100**, 250501 (2008).

[225] Schuch, N. and Verstraete, F., *Computational complexity of interacting electrons and fundamental limitations of density functional theory*. Nature Phys. **5**, 732–735 (2009), `arXiv:0712.0483`.

[226] Scully, M. O. and Zubairy, M. S., *Quantum Optics*. Cambridge University Press (1997).

[227] Shenvi, N., de Sousa, R., and Whaley, K. B., *Universal scaling of hyperfine-induced electron spin echo decay*. Phys. Rev. B **71**, 224411 (2005), `cond-mat/0502143`.

[228] Shnirman, A., Schön, G., and Hermon, Z., *Quantum manipulations of small Josephson junctions*. Phys. Rev. Lett. **79**, 2371 (1997).

[229] Shor, P. W., *Scheme for reducing decoherence in quantum computer memory*. Phys. Rev. A **52**, 2493 (1995).

[230] Shor, P. W., *Polynomial-time algorithms for prime factorization and discrete logarithms on a quantum computer*. SIAM J. Comp. **26**, 1484 (1997), `quant-ph/9508027`.

[231] Shore, B. W. and Knight, P. L., *The Jaynes-Cummings model*. J. Mod. Opt. **40**, 1195–1238 (1993).

[232] Shulman, M. D., Dial, O. E., Harvey, S. P., Bluhm, H., Umansky, V., and Yacoby, A., *Demonstration of entanglement of electrostatically coupled singlet-triplet qubits*. Science **336**, 202–205 (2012).

[233] Simmons, C. B., Prance, J. R., Van Bael, B. J., Koh, T. S., Shi, Z., Savage, D. E., et al., *Tunable spin loading and T_1 of a silicon spin qubit measured by single-shot readout*. Phys. Rev. Lett. **106**, 156804 (2011).

[234] Simon, P. and Loss, D., *Nuclear spin ferromagnetic phase transition in an interacting 2d electron gas*. Phys. Rev. Lett. **98**, 156401 (2007), `cond-mat/0611292`.

[235] Sklyanin, E., *Separation of variables in the gaudin model*. J Soviet Math **47**, 2473–2488 (1989).

[236] Skolnick, M. S. and Mowbray, D. J., *Self-assembled semiconductor quantum dots: Fundamental physics and device applications*. Annu. Rev. Mater. Res. **34**, 181 (2004).

[237] Slichter, C. P., *Principles of Magnetic Resonance*. Springer Verlag, Berlin, 3rd edn. (1996).

[238] Smith, G. and Smolin, J. A., *Detecting incapacity of a quantum channel*. Phys. Rev. Lett. **108**, 230507 (2012), `arXiv:1108.1807`.

[239] Smith, G., Smolin, J. A., and Yard, J., *Quantum communication with Gaussian channels of zero quantum capacity*. Nature Phot. **5**, 624 (2011), `arXiv:1102.4580`.

[240] Smith, G. and Yard, J., *Quantum Communication with Zero-Capacity Channels*. Science **321**, 1812 (2008).

[241] Song, Z., Zhang, P., Shi, T., and Sun, C.-P., *Effective boson-spin model for nuclei-ensemble-based universal quantum memory*. Phys. Rev. B **71**, 205314 (2005), `quant-ph/0409185`.

[242] Steger, M., Saeedi, K., Thewalt, M. L. W., Morton, J. J. L., Riemann, H., Abrosimov, N. V., et al., *Quantum information storage for over 180 s using donor spins in a ^{28}Si "semiconductor vacuum"*. Science **336**, 1280–1283 (2012).

[243] Stepanenko, D., Burkard, G., Giedke, G., and Imamoğlu, A., *Enhancement of electron spin coherence by optical preparation of nuclear spins*. Phys. Rev. Lett. **96**, 136401 (2006), `cond-mat/0512362`.

[244] Sun, B., Chow, C. M. E., Steel, D. G., Bracker, A. S., Gammon, D., and Sham, L. J., *Persistent narrowing of nuclear-spin fluctuations in inas quantum dots using laser excitation*. Phys. Rev. Lett. **108**, 187401 (2012).

[245] Taminiau, T. H., Wagenaar, J. J. T., van der Sar, T., Jelezko, F., Dobrovitski, V. V., and Hanson, R., *Detection and control of individual nuclear spins using a weakly coupled electron spin*. Phys. Rev. Lett. **109**, 137602 (2012).

[246] Tartakovskii, A. I., Wright, T., Russell, A., Fal'ko, V. I., Van'kov, A. B., Skiba-Szymanska, J., et al., *Nuclear spin switch in semiconductor quantum dots*. Phys. Rev. Lett. **98**, 026806 (2007), `cond-mat/0609371`.

[247] Taylor, J. M., Imamoğlu, A., and Lukin, M. D., *Controlling a mesoscopic spin environment by quantum bit manipulation*. Phys. Rev. Lett. **91**, 246802 (2003), `cond-mat/0308459`.

[248] Taylor, J. M., Petta, J. R., Johnson, A. C., Yacoby, A., Marcus, C. M., and Lukin, M. D., *Relaxation, dephasing, and quantum control of electron spins in double quantum dots*. Phys. Rev. B **76**, 035315 (2007), cond-mat/0602470.

[249] The Quantum Information Science and Technology Experts Panel, *A quantum information science and technology roadmap 2.0*. Tech. rep., ARDA (2004).

[250] Togan, E., Chu, Y., Imamoglu, A., and Lukin, M. D., *Laser cooling and real-time measurement of the nuclear spin environment of a solid-state qubit*. Nature **478**, 497–501 (2011).

[251] Tsyplyatyev, O. and Loss, D., *Spectrum of an electron spin coupled to an unpolarized bath of nuclear spins*. Phys. Rev. Lett. **106**, 106803 (2011), arXiv:1102.2426.

[252] Tyryshkin, A. M., Tojo, S., Morton, J. J. L., Riemann, H., Abrosimov, N. V., Becker, P., et al., *Electron spin coherence exceeding seconds in high-purity silicon*. Nature Mater. **11**, 143–147 (2012).

[253] Urbaszek, B., Marie, X., Amand, T., Krebs, O., Voisin, P., Maletinsky, P., et al., *Nuclear spin physics in quantum dots: an optical investigation*. Rev. Mod. Phys. **85**, 79 (2013), arXiv:1202.4637.

[254] Vaidman, L., *Teleportation of quantum states*. Phys. Rev. A **49**, 1473 (1994).

[255] Verstraete, F., Cirac, J. I., and Murg, V., *Matrix product states, projected entangled pair states, and variational renormalization group methods for quantum spin systems*. Adv. Phys. **57**, 143 (2008), arXiv:0907.2796.

[256] Verstraete, F., Wolf, M. M., and Ignacio Cirac, J., *Quantum computation and quantum-state engineering driven by dissipation*. Nature Phys. **5**, 633–636 (2009), arXiv:0803.1447.

[257] Vollbrecht, K. G. H., Muschik, C. A., and Cirac, J. I., *Entanglement distillation by dissipation and continuous quantum repeaters*. Phys. Rev. Lett. **107**, 120502 (2011), arXiv:1011.4115.

[258] Walls, D. F., Drummond, P. D., Hassan, S. S., and Carmichael, H. J., *Non-equilibrium phase transitions in cooperative atomic systems*. Prog. Theor. Phys. Suppl. **64**, 307 (1978).

[259] Wang, D. S., Fowler, A. G., and Hollenberg, L. C. L., *Quantum computing with nearest neighbor interactions and error rates over 1%*. Phys. Rev. A **83**, 020302(R) (2011), arXiv:1009.3686.

[260] Wang, X.-B., Hiroshima, T., Tomita, A., and Hayashi, M., *Quantum information with Gaussian states*. Phys. Rep. **448**, 1 – 111 (2007), arXiv:0801.4604.

[261] Weedbrook, C., Pirandola, S., Garcia-Patron, R., Cerf, N. J., Ralph, T. C., Shapiro, J. H., et al., *Gaussian quantum information*. Rev. Mod. Phys. **84**, 621 (2012), arXiv:1110.3234.

[262] Weiss, K. M., Elzerman, J. M., Delley, Y. L., Miguel-Sanchez, J., and Imamoğlu, A., *Coherent two-electron spin qubits in an optically active pair of coupled InGaAs quantum dots*. Phys. Rev. Lett. **109**, 107401 (2012).

[263] Werner, P., Völker, K., Troyer, M., and Chakravarty, S., *Phase diagram and critical exponents of a dissipative ising spin chain in a transverse magnetic field*. Phys. Rev. Lett. **94**, 047201 (2005), cond-mat/0402224.

[264] Wild, A., Kierig, J., Sailer, J., Ager, J. W., III, Haller, E. E., et al., *Few electron double quantum dot in an isotopically purified ^{28}Si quantum well*. Appl. Phys. Lett. **100**, 143110 (2012).

[265] Wildanger, D., Maze, J. R., and Hell, S. W., *Diffraction unlimited all-optical recording of electron spin resonances*. Phys. Rev. Lett. **107**, 017601 (2011).

[266] Witzel, W. M., Carroll, M. S., Cywiński, L., and Das Sarma, S., *Quantum decoherence of the central spin in a sparse system of dipolar coupled spins*. Phys. Rev. B **86**, 035452 (2012).

[267] Witzel, W. M., Carroll, M. S., Morello, A., Cywiński, L., and Das Sarma, S., *Electron spin decoherence in isotope-enriched silicon*. Phys. Rev. Lett. **105**, 187602 (2010).

[268] Witzel, W. M. and Das Sarma, S., *Nuclear spins as quantum memory in semiconductor nanostructures*. Phys. Rev. B **76**, 045218 (2007), `arXiv:0701480`.

[269] Witzel, W. M., de Sousa, R., and Das Sarma, S., *Quantum theory of spectral-diffusion-induced electron spin decoherence*. Phys. Rev. B **72**, 161306(R) (2005).

[270] Wolf, M. M., Giedke, G., Eisert, J., Plenio, M. B., Lewenstein, M., Werner, R. F., et al., *Gaussian states and operations* (2005).

[271] Wootters, W. K. and Zurek, W. H., *A single quantum cannot be cloned*. Nature **299**, 802 (1982).

[272] Wrachtrup, J. and Jelezko, F., *Processing quantum information in diamond*. J. Phys.: Condens. Matter **18**, S807 (2006), `quant-ph/0510152`.

[273] Wrachtrup, J., Kilin, S. Y., and Nizovtsev, A. P., *Quantum computation using ^{13}C nuclear spins near the single NV defect center in diamond*. Opt. Spectr. **91**, 459 (2000).

[274] Xu, X., Wu, Y., Sun, B., Huang, Q., Cheng, J., Steel, D. G., et al., *Fast spin state initialization in a singly charged inas-gaas quantum dot by optical cooling*. Phys. Rev. Lett. **99**, 097401 (2007), `cond-mat/0608225`.

[275] Xu, X., Yao, W., Sun, B., Steel, D. G., Bracker, A. S., Gammon, D., et al., *Optically controlled locking of the nuclear field via coherent dark-state spectroscopy*. Nature **459**, 1105 (2009).

[276] Yamamoto, M., Takada, S., Bauerle, C., Watanabe, K., Wieck, A. D., and Tarucha, S., *Electrical control of a solid-state flying qubit*. Nat Nano **7**, 247–251 (2012).

[277] Yao, N. Y., Jiang, L., Gorshkov, A. V., Gong, Z.-X., Zhai, A., Duan, L.-M., et al., *Robust quantum state transfer in random unpolarized spin chains*. Phys. Rev. Lett. **106**, 040505 (2011), `arXiv:1011.2762`.

[278] Yao, W., Liu, R.-B., and Sham, L. J., *Theory of electron spin decoherence by interacting nuclear spins in a quantum dot*. Phys. Rev. B **74**, 195301 (2006), `cond-mat/0508441`.

[279] Yeomans, J. M., *Statistical Mechanics of Phase Transitions*. Claredon Press, Oxford, UK (1992).

[280] Yoshie, T., Scherer, A., Hendrickson, J., Khitrova, G., Gibbs, H. M., Rupper, G., et al., *Vacuum Rabi splitting with a single quantum dot in a photonic crystal nanocavity*. Nature **432**, 200 (2004).

[281] Yuzbashyan, E. A., Altshuler, B. L., Kuznetsov, V. B., and Enolskii, V. Z., *Solution for the dynamics of the BCS and central spin problems*. J Phys A: Math Gen **38**, 7831 (2005).

[282] Zhang, W., Dobrovitski, V. V., Al-Hassanieh, K. A., Dagotto, E., and Harmon, B. N., *Hyperfine interaction induced decoherence of electron spins in quantum dots*. Phys. Rev. B **74**, 205313 (2006), `cond-mat/0609185`.

[283] Zhang, W., Hu, J.-L., Zhuang, J., You, J. Q., and Liu, R.-B., *Protection of center-spin coherence by a dynamically polarized nuclear spin core*. Phys. Rev. B **82**, 045314 (2010).

[284] Zhang, W., Konstantinidis, N. P., Dobrovitski, V. V., Harmon, B. N., Santos, L. F., and Viola, L., *Long-time electron spin storage via dynamical suppression of hyperfine-induced decoherence in a quantum dot*. Phys. Rev. B **77**, 125336 (2008), `arXiv:0801.0992`.

[285] Žnidarič, M., *Exact solution for a diffusive nonequilibrium steady state of an open quantum chain*. J. Stat. Mech. **2010**, L05002 (2010), `1005.1271`.

[286] Žnidarič, M., *Solvable quantum nonequilibrium model exhibiting a phase transition and a matrix product representation*. Phys. Rev. E **83**, 011108 (2011), `1011.0998`.

[287] Zoller, P., Beth, T., Binosi, D., Blatt, R., Briegel, H. J., Bruss, D., et al., *Quantum information processing and communication*. Eur. Phys. J. D **36**, 203 (2005), `quant-ph/0405025`.

[288] Zurek, W. H., *Decoherence and the transition from quantum to classical*. Physics Today **44**, 36 (1991).

[289] Zwierlein, M. W. and Ketterle, W., *Comment on "Pairing and phase separation in a polarized fermi gas"*. Science **314**, 54a (2006).